AD-A246 368

# LINEAR AND NON-LINEAR RESPONSE OF LIQUID AND SOLID

## PARTICLES TO ENERGETIC RADIATION

### FINAL REPORT

DENNIS R. ALEXANDER
PRINCIPAL INVESTIGATOR

JOHN P. BARTON
CO-PRINCIPAL INVESTIGATOR

**DTIC**
**S** ELECTE
FEB 2 1 1992
**D**
**D**

MARCH 11, 1991

U. S. ARMY RESEARCH OFFICE

CONTRACT/GRANT NUMBER

DAAL03-87-K-0138

UNIVERSITY OF NEBRASKA – LINCOLN

92-04276

92 2 14 124

# REPORT DOCUMENTATION PAGE

| 1. AGENCY USE ONLY (Leave blank) | 2. REPORT DATE | 3. REPORT TYPE AND DATES COVERED |
|---|---|---|
| | March 11, 1991 | Final 86-09-25 to 90-12-24 |

| 4. TITLE AND SUBTITLE | 5. FUNDING NUMBERS |
|---|---|
| Linear and Non-Linear Response of Liquid and Solid Particles to Energetic Radiation | DAAL03-87-K-0138 |

**6. AUTHOR(S)**

Dennis R. Alexander
John P. Barton

| 7. PERFORMING ORGANIZATION NAME(S) AND ADDRESS(ES) | 8. PERFORMING ORGANIZATION REPORT NUMBER |
|---|---|
| University of Nebraska-Lincoln<br>Room 248 WSEC<br>Center for Electro-Optics<br>Lincoln, NE 68588-0656 | |

| 9. SPONSORING/MONITORING AGENCY NAME(S) AND ADDRESS(ES) | 10. SPONSORING/MONITORING AGENCY REPORT NUMBER |
|---|---|
| U. S. Army Research Office<br>P. O. Box 12211<br>Research Triangle Park, NC 27709-2211 | |

**11. SUPPLEMENTARY NOTES**

The view, opinions and/or findings contained in this report are those of the author(s) and should not be construed as an official Department of the Army position, policy, or decision, unless so designated by other documentation.

| 12a. DISTRIBUTION/AVAILABILITY STATEMENT | 12b. DISTRIBUTION CODE |
|---|---|
| Approved for public release; distribution unlimited. | |

**13. ABSTRACT (Maximum 200 words)**

The principal purpose of the research is to investigate the linear and non-linear laser interaction with small aerosols and solid particles. Experimental work is devoted to excimer laser beam interaction at $\lambda = 248$ nm with small droplets of water, methanol, and fog oil at irradiances up to 200 GWatts/cm$^2$. Also of interest in this research is the interactions with solid particles including $Al_2O_3$, SiC, glass spheres, Al spheres, $CaF_2$ and W particles at both atmospheric and reduced pressures. Special attention is given to understanding the dynamics of the interaction processes by using a fast streak camera and excimer laser imaging at $\lambda = 193$ nm.

Jointly with the experimental work is the problem of understanding the electromagnetic interaction of focused laser beams with matter. Emphasis is given to developing computer codes to calculate internal and near electromagnetic fields for plane/focused laser beams incident upon spheres.

Another phase of this investigation is devoted to theoretical modeling the laser imaging system used to obtain nanosecond time scale shadow images of exploding droplets. In addition, theoretical models for both polarized and unpolarized particle thermometry are developed.

| 14. SUBJECT TERMS (25) Electromagnetic Laser Interaction with Droplets/Solids, Droplet Explosions, Nonlinear Laser Interaction with Aerosols, Scattering From Aerosols, Focused Beams, Internal and Near Fields, Morphology Dependent Resonances, Laser Ablation | | | 15. NUMBER OF PAGES |
|---|---|---|---|
| | | | 16. PRICE CODE |

| 17. SECURITY CLASSIFICATION OF REPORT | 18. SECURITY CLASSIFICATION OF THIS PAGE | 19. SECURITY CLASSIFICATION OF ABSTRACT | 20. LIMITATION OF ABSTRACT |
|---|---|---|---|
| UNCLASSIFIED | UNCLASSIFIED | UNCLASSIFIED | UL |

# TABLE OF CONTENTS

# 1. INTRODUCTION – STATEMENT OF THE PROBLEM

## ABSTRACT

The principal purpose of the research is to investigate the linear and non-linear laser interaction with small aerosols and solid particles. Experimental work is devoted to excimer laser beam interaction at $\lambda = 248$ nm with small droplets of water, methanol, and fog oil at irradiances up to 200 GWatts/cm$^2$. Also of interest in this research is the interactions with solid particles including $Al_2O_3$, SiC, glass spheres, Al spheres, $CaF_2$ and W particles at both atmospheric and reduced pressures. Special attention is given to understanding the dynamics of the interaction processes by using a fast streak camera and excimer laser imaging at $\lambda = 193$ nm.

Jointly with the experimental work is the problem of understanding the electromagnetic interaction of focused laser beams with matter. Emphasis is given to developing computer codes to calculate internal and near electromagnetic fields for plane/focused laser beams incident upon spheres.

Another phase of this investigation is devoted to theoretical modeling the laser imaging system used to obtain nanosecond time scale shadow images of exploding droplets. In addition, theoretical models for both polarized and unpolarized particle thermometry are developed.

## 2. SUMMARY OF RESULTS

During the period of this contract the principal investigator along with the co-principal investigator submitted twenty-eight manuscripts for publication in Scientific/Technical Journals, presented seventeen conference papers and submitted six semi-annual reports. In addition, research leading to three M.S. Theses and one Ph.D. Dissertation was supported by this contract. Three additional M.S. Theses and two Ph.D. Dissertations are in progress, which have been supported by this contract. (See Sections 4 and 6 for detailed lists.)

A summary of the results of this research are presented in the following abstracts of refereed papers, conference proceedings, dissertations, and theses.

## Internal and near-surface electromagnetic fields for a spherical particle irradiated by a focused laser beam

J. P. Barton, D. R. Alexander, and S. A. Schaub

*Laboratory for Electro-Optical Measurements, College of Engineering and Technology, University of Nebraska-Lincoln, Lincoln, Nebraska 68588-0525*

Theoretical expressions for the internal and external electromagnetic fields for an arbitrary electromagnetic beam incident upon a homogeneous spherical particle are derived, and numerical calculations based upon this theoretical development are presented. In particular, spatial distributions of the internal and near-surface electric field magnitude (source function) for a focused fundamental ($\text{TEM}_{00}$ mode) Gaussian beam of $1.06\,\mu\text{m}$ wavelength and $4\,\mu\text{m}$ beam waist diameter incident upon a $5$-$\mu\text{m}$-diam water droplet in air are presented as a function of the location of the beam focal point relative to the sphere center. The calculations indicate that the internal and near-surface electric field magnitude distribution can be strongly dependent upon relative focal point positioning and may differ significantly from the corresponding electric field magnitude distribution expected from plane-wave irradiation.

## Internal fields of a spherical particle illuminated by a tightly focused laser beam: Focal point positioning effects at resonance

J. P. Barton, D. R. Alexander, and S. A. Schaub

*Center for Electro-Optics, College of Engineering, University of Nebraska-Lincoln, Lincoln, Nebraska 68588-0525*

The spherical particle/arbitrary beam interaction theory developed in an earlier paper is used to investigate the dependence of structural resonance behavior on focal point positioning for a spherical particle illuminated by a tightly focused (beam diameter less than sphere diameter), linearly polarized, Gaussian-profiled laser beam. Calculations of absorption efficiency and distributions of normalized source function (electric field magnitude) are presented as a function of focal point positioning for a particle with a complex relative index of refraction of $\bar{n} = 1.33 + 5.0 \times 10^{-6} i$ and a size parameter of $a \approx 29.5$ at both nonresonance and resonance

conditions. The results of the calculations indicate that structural resonances are not excited during the on-center focal point positioning of such a tightly focused beam but structural resonances can be excited by proper on-edge focal point positioning. Electric wave resonances were found to be excited by moving the focal point from on-center towards the edge of the sphere *parallel* to the direction of the incident beam electric field polarization. Magnetic wave resonances were found to be excited by moving the focal point from on-center towards the edge of the sphere *perpendicular* to the direction of the incident beam electric field polarization.

# Focused laser beam interactions with methanol droplets: effects of relative beam diameter

Scott A. Schaub, Dennis R. Alexander, John P. Barton, and Mark A. Emanuel

The effect of the local diameter of a focused $CO_2$ laser beam on calculated internal source function distributions and experimentally observed explosive characteristics is examined for 165-$\mu$m spherical methanol droplets. Experimental results show that the location and the characteristics of the explosive process change as the droplet is moved out of the laser focal point along the axis of propagation. Theoretical calculations indicate that, when the beam diameter is of the same order of magnitude as the droplet diameter, a modification of Mie theory, accounting for the finite beam size of the laser, is necessary to provide results which are consistent with experimental observations.

# Theoretical model for the image formed by a spherical particle in a coherent imaging system: comparison to experiment

S. A. Schaub
D. R. Alexander, MEMBER SPIE
J. P. Barton
University of Nebraska-Lincoln
Center for Electro-Optics
Lincoln, Nebraska 68588-0525

Abstract. A simple theoretical model is presented that allows calculation of the image produced by a spherical absorbing particle illuminated by monochromatic, coherent laser light. Results presented in this paper are restricted to a single-lens imaging system, although generalization to more complex imaging system configurations would be straightforward. The method uses classic Lorenz-Mie scattering theory to obtain the electromagnetic field external to an absorbing spherical particle and a Fourier optics approach to calculate the intensities in the image plane. Experimental results evaluating focus characteristics are examined for 50 $\mu$m diameter water droplets using an $N_2$ laser imaging system in conjunction with a digital image processor, and the experimental images are comp⁻ ⸱⸱ to the results of the theoretical model. Comparative focus criteria r ults are particularly useful in aerosol science research involving dynamic particle size measurements in which criteria for focus and depth of field must be established.

Subject terms: spray analysis; image formation; focus effects.

Optical Engineering 28(5), 565-571 (May 1989).

# Scattering of incident KrF laser radiation resulting from the laser-induced breakdown of H₂O droplets

D. R. Alexander, S. A. Schaub, J. Zhang, D. E. Poulain, and J. P. Barton

*Center for Electro-Optics, University of Nebraska–Lincoln, Lincoln, Nebraska 68588-0525*

The time history of elastically scattered incident radiation (ESIR) is presented for 60-$\mu$m-diameter water droplets irradiated by KrF ($\lambda = 248$ nm) laser pulses with power densities in the range of 1–200 GW/cm². The ESIR shows a distinct two-peak structure that is dependent on the incident irradiance. The time delay between the arrival of the incident pulse and the first local minimum in the ESIR varied from 7 nsec at 200 GW/cm² to 21 nsec at 5 GW/cm². The time between incident pulse arrival and the first peak in the ESIR showed a similar irradiance dependence, with delays ranging from 4 to 12 nsec. Images of droplet breakup and the average velocities of ejected material are presented for times between 0 and 1000 nsec after the arrival of 3-GW/cm² laser pulses.

# Simplified scattering coefficient expressions for a spherical particle located on the propagation axis of a fifth-order Gaussian beam

Scott A. Schaub, John P. Barton, and Dennis R. Alexander
*Center for Electro-Optics, University of Nebrasaka–Lincoln, Lincoln, Nebraska 68588-0656*

Expanding on developments presented in an earlier paper, theoretical expressions for the scattering coefficients of a homogeneous, absorbing, spherical particle irradiated by a fifth-order Gaussian beam are presented for the special case of the particle center located on the propagation axis of the beam. For this case, evaluation of two-dimensional surface integrals, required in computing the scattering coefficients for the most general particle location, is reduced to a computationally more efficient one-dimensional integral. For a typical size parameter $\alpha = \pi d / \lambda = 17$, the CPU time required for calculation of scattering coefficients is reduced by a factor of $\sim 1500$ by using the simplified coefficient expressions. In addition, computation of electromagnetic field components is reduced from double summation to single summation expressions, further simplifying the field calculations.

# Fifth-order corrected electromagnetic field components for a fundamental Gaussian beam

J. P. Barton and D. R. Alexander
*Center for Electro-Optics, College of Engineering, University of Nebraska-Lincoln, Lincoln, Nebraska 68588-0525*

Fifth-order corrected expressions for the electromagnetic field components of a monochromatic fundamental Gaussian beam (i.e., a focused TEM₀₀ mode laser beam) propagating within a homogeneous dielectric media are derived and presented. Calculations of relative error indicate that the fifth-order Gaussian beam description provides a significantly improved solution to Maxwell's equations in comparison with commonly used paraxial (zeroth-order) and first-order Gaussian beam descriptions.

4

# Theoretical determination of net radiation force and torque for a spherical particle illuminated by a focused laser beam

J. P. Barton, D. R. Alexander, and S. A. Schaub

*Center for Electro-Optics, College of Engineering, University of Nebraska-Lincoln, Lincoln, Nebraska 68588-0525*

Series expressions for the net radiation force and torque for a spherical particle illuminated by an arbitrarily defined monochromatic beam are derived utilizing the spherical-particle/ arbitrary-beam interaction theory developed in an earlier paper. Calculations of net force and torque are presented for a 5-$\mu$m-diam water droplet in air optically levitated by a tightly focused (2 $\mu$m beam waist diameter) TEM$_{00}$-mode argon-ion ($\lambda = 0.5145 \mu$m) laser beam for on and off propagation axis, and on and off structural resonance conditions. Several features of these theoretical results are related to corresponding experimental observations.

# Measurement of hypersonic velocities resulting from the laser-induced breakdown of aerosols using an excimer laser imaging system

S. A. Schaub, D. R. Alexander, D. E. Poulain, and J. P. Barton

*Center for Electro-Optics, University of Nebraska-Lincoln, Lincoln, Nebraska 68588-0656*

In this article we describe a dual-pulse excimer-laser-based imaging system used in the determination of ejected material velocities resulting from the interaction of KrF laser radiation ($\lambda = 248$ nm, pulse width FWHM $= 17$ ns, $I \approx 10^{11}$ W/cm$^2$) with 20-$\mu$m aluminum particles under vacuum ($P = 10^{-5}$ Torr) conditions. Material velocities measured 200–400 ns after arrival of the incident pulse ranged from 450 to 1200 m/s.

# HIGH INTENSITY ULTRAVIOLET LASER INTERACTION
# WITH A METALLIC FILAMENT

G.M. Holtmeier, D.R. Alexander, and J. P. Barton

Center for Electro-Optics

University of Nebraska

Lincoln, NE 68588-0656

Abstract

Results of research conducted on the interaction of high intensity ultraviolet pulsed KrF laser radiation with a metallic filament are reported. Experimental results are presented on the time dependent material ejection dynamics associated with focused excimer laser beams interacting with a small diameter wire. Copper wire 75 $\mu$m in diameter was illuminated with a KrF ($\lambda = 248$ nm, pulse duration = 17 ns FWHM) excimer laser at an irradiance of 80 GW/cm$^2$. Interaction dynamics were recorded using both a real time and double stroked ultraviolet laser imaging technique. Temporal evolutions of both vaporized and molten material are reported. Material observed during 2-D shadow imaging on the shadow side of the wire was shown to originate from the front ablative surface without spallation of material on the shadow surface. Material emission velocities are reported utilizing two different imaging techniques. A maximum velocity of 1500 m/s was obtained for material ejected in a direction toward the ablating laser.

# Interactions of intense ultraviolet laser radiation with solid aerosols

D. E. Poulain, D. R. Alexander, J. P. Barton, S. A. Schaub, and J. Zhang
*Center for Electro-Optics, University of Nebraska-Lincoln, Lincoln, Nebraska 68588-0525*

Characterizations of the interaction of intense ultraviolet laser radiation ($\lambda = 248$ nm) with small solid aerosols are presented. Interaction dynamics, velocity measurements of expelled material, and thresholds for plasma formation are presented for aluminum, calcium fluoride, glass, silicon carbide, and tungsten particles. An excimer laser operating with a krypton fluoride gas mixture was used to irradiate small solid aerosol particles ($\approx 5$–$50\,\mu$m) under atmospheric and vacuum conditions down to $10^{-5}$ Torr. Focused laser radiation intensities varied from $10^7$ W/cm$^2$ to a maximum of $2 \times 10^{11}$ W/cm$^2$. Interactions of the laser radiation with the solid aerosols were recorded in real time by an ultraviolet laser imaging system. Velocities between 250 and 2000 m/s were measured for material ejected from particles undergoing laser interaction. Laser intensity thresholds for visible plasma emission ranged from a maximum of 650 MW/cm$^2$ for aluminum to a minimum of 59 MW/cm$^2$ for tungsten. Thresholds for plasma formation were determined to be relatively independent of ambient pressure.

6

# ELECTROMAGNETIC FIELDS

# FOR AN IRREGULARLY-SHAPED, NEAR-SPHERICAL PARTICLE

# ILLUMINATED BY A FOCUSED LASER BEAM

J. P. Barton, and D. R. Alexander

Center for Electro-Optics and Department of Mechanical Engineering

College of Engineering

University of Nebraska-Lincoln

Lincoln, Nebraska 68588-0656

## ABSTRACT

A theoretical procedure is derived for the determination of the internal and external electromagnetic fields for a monochromatic beam incident upon a homogeneous particle of arbitrarily-defined shape. The procedure is best-suited for the analysis of near-spherical particles (i.e. particles which deviate from a sphere by plus or minus a few tenths of a radii). Verification and demonstration calculations are presented. Also presented are calculations investigating the effect of a surface deformation on resonance excitation within an otherwise spherical particle.

# MODELING OF THE COHERENT IMAGING OF A SPHERICAL AEROSOL PARTICLE ILLUMINATED BY A PLANE WAVE AT OBLIQUE INCIDENCE

S.A. Schaub, D.R. Alexander, and J.P. Barton

Center for Electro-Optics

University of Nebraska-Lincoln

Lincoln, NE 68588-0656

(402) 472-3091

## Abstract

A theoretical model has been developed for the coherent imaging of a spherical aerosol particle illuminated by an off-axis incident plane wave. The modeling technique makes use of the arbitrary beam theory, presented by the authors in an earlier paper, to calculate the external electromagnetic field resulting from the laser/aerosol interaction. Scalar diffraction theory is used to propagate the dominant electric field component through the imaging lens and to the image plane. Demonstration calculations have been presented for both opaque and transparent particles ranging in size from 10 to 40 $\mu$m in diameter illuminated by off-axis $\lambda \approx 0.5$ $\mu$m incident radiation.

8

# Fundamental Gaussian beam solutions of Maxwell's equations

Ding Liu, J. P. Barton and D. R. Alexander

March 7, 1991

The Center for Electro-Optics, 248 WSEC, University of Nebraska-Lincoln, Lincoln, NE 68588

### Abstract

An exact fundamental Gaussian beam solution of Maxwell's equation is derived and its properties are discussed. Recursion relations are developed which enable the calculation of the solution to arbitray order in parameter s in a straightforward way. Results show that the solution does not exist in all space and the size of the region within which the solution exists is related to the parameter s.

# ELECTROMAGNETIC FIELD FOR A BEAM INCIDENT UPON TWO ADJACENT SPHERICAL PARTICLES

J.P. Barton, W. Ma, S.A. Schaub, and D.R. Alexander

Center for Electro-Optics

College of Engineering and Technology

University of Nebraska

Lincoln, NE 68588-0656

## ABSTRACT

Through an application of our previously derived single spherical particle/arbitrary beam interaction theory, an iterative procedure has been developed for the determination of the electromagnetic field for a beam incident upon two adjacent spherical particles. The two particles can differ in size and composition, and can have any positioning relative to each other and relative to

the focal point and propagation direction of the incident beam. Example calculations of internal and near field normalized source function ($\sim |\bar{E}|^2$) distributions are presented. Also presented are calculations demonstrating the effect of the relative positioning of the second adjacent particle on far field scattering patterns.

# THEORETICAL MODEL OF THE LASER IMAGING OF SMALL AEROSOLS: APPLICATIONS TO AEROSOL SIZING

S.A. Schaub, D.R. Alexander, and J.P. Barton
Center for Electro-Optics
University of Nebraska
Lincoln, NE 68588-0656
(402) 472-3091

## Abstract

A theoretical model is presented for the formation of small particle shadow images in a single lens laser imaging system. The model uses a modification of classical Lorenz-Mie theory, presented by the authors in an earlier paper, to calculate the external electromagnetic fields resulting from the interaction of a Gaussian laser beam with a finite absorbing spherical particle. Propagation of the electric field through the imaging system components is developed from a scalar viewpoint using the thin lens transformation and the Fresnel approximation to the Huygens-Fresnel propagation equation. The theoretical model is valid for either transparent or absorbing spheres and has no

restrictions on the allowable degree or direction of aerosol defocus. Direct comparisons between theoretical calculations and experimental observations are reported for 53 $\mu$m diameter transparent water droplets and 66 $\mu$m diameter absorbing nickel spheres for defocus ranging from −2 mm (toward lens) to +2 mm (away from lens). Theory and experiment showed good agreement in the boundary edge gradient and the location of the external peaks, while observable differences existed in the magnitude of the central spots. Theoretical results, comparing water and nickel aerosols, showed observable differences in the calculated average internal intensity (AII). In contrast, the boundary edge gradient (BEG) showed less dependence on changes in optical properties of the particle. These results indicate that criteria, such as the AII, used in focus determination must be reevaluated when applying in-focus sizing algorithms to aerosols with significantly different optical properties.

# Excimer Laser Produced Plasmas in Copper Wire Targets and Water Droplets

D. R. Alexander and Kyo-Dong Song

February 20, 1991

## Abstract

The elastically scattered incident radiation (ESIR) from a copper wire illuminated by a KrF laser pulse at $\lambda = 248$ nm shows a distinct two-peak structure which is dependent on the incident energy. Based on the results, the time required to reach the critical electron density ($n_c \approx 1.8 \times 10^{22}/cm^3$) can be estimated. Similar ESIR characteristics have been previously reported. Initiation of the broadband emission for the copper plasma starts at 6.5 ($\pm$ 1.45) ns after the arrival of the laser pulse as compared to 11 ($\pm$ 0.36) ns for water. Lifetimes of electrons in the subelectron states is estimated to be around $10^{-9}$ sec and may contribute in the time delay of the plasma initiation

for water droplets. In addition, the ionization potential of copper (430 - 530 nm) is around 6 eV, which is approximately two time smaller than the 13 eV ionization potential reported for water. These effects may also affect the plasma emission delay for water. The delay in the copper plasma after initiation is also contributed to energy losses by the interband transition ($4s^1$-$3d^{10}$).

# NONLINEAR INTERACTION OF KrF LASER
# RADIATION WITH SMALL WATER DROPLETS

D.R. Alexander, J.P. Barton, S.A. Schaub, and G.M. Holtmeier

Center for Electro-Optics
University of Nebraska-Lincoln
Lincoln, Nebraska 68588-0656

## Abstract

Results have been obtained for the interaction of KrF excimer laser radiation ($\lambda$ = 248 nm, $t_{pulse}$ = 17 ns) with 60 $\mu$m diameter distilled water droplets for irradiance values ranging from 3 to 230 GW/cm$^2$. Laser images of the droplet breakup during the time intervals from 0 to 100 ns indicate the dynamic breakup processes to be highly nonlinear. At low irradiance (3 GW/cm$^2$) material is ejected from both the illuminated and shadow hemispheres of the droplet, in qualitative agreement with the location of the electric field peaks predicted by plane wave Lorenz-Mie theory calculations. As the irradiance is increased, the interaction on the shadow hemisphere becomes stronger while the interaction on the illuminated hemisphere decreases. This nonlinear behavior is attributed to rapid electrical breakdown of the droplet near the shadow surface. The breakdown region destroys the ability of the droplet to redirect energy toward the front hemisphere of the

droplet. Without this mechanism, the localized electric field maxima near the illuminated surface of the droplet cannot arise. Measurements were also taken of the average material velocities during the time intervals from 0 to 50 ns after arrival of the high energy pulse. Velocities ranged from 1000 m/s at 3 GW/cm$^2$ to 6000 m/s at 230 GW/cm$^2$.

# Hybrid Inelastic Scattering Models for Particle Thermometry: Unpolarized Emissions

Jingyi Zhang        Dennis R. Alexander

March 8, 1991

### Abstract

A hybrid modeling technique is reported for studying inelastic (fluorescent and Raman) scattering from molecules embedded in particles of large optical size parameters. The modeling technique, which combines Lorenz-Mie theory (for determination of incident excitation field) with geometrical optics formulation (for determination of inelastic scattering efficiency function), provides an insight into the scattering processes and serves as a theoretical basis for guiding experiments and interpreting measurements in aerosol particle thermometry using inelastic light scattering techniques.

# Hybrid Inelastic Scattering Models for Particle Thermometry: Polarized Emissions

Jingyi Zhang        Dennis R. Alexander

March 8, 1991

### Abstract

The work of the previous paper is extended to the polarized inelastic (fluorescent and Raman) scattering from molecules embedded in solid particles of large size parameters. The hybrid modeling method, which combines Lorenz-Mie theory with geometrical optics formulation, has taken into account the contributions of transmitted and reflected/transmitted rays of secondary emissions. The coherent effects of light rays emitted from same point source have also been considered. The angular scattering patterns predicted with the method were consistent with expected physical behaviors and existing classical solutions. These results are important for current studies in laser diagnosis of aerosol particles using inelastically scattered light.

# EXPERIMENTAL AND THEORETICAL ANALYSIS OF LIQUID DROPLETS MOVING THROUGH A FOCUSED $CO_2$ LASER BEAM

J.P. Barton, D.R. Alexander, and S.A. Schaub
Center for Electro-Optics
College of Engineering
University of Nebraska-Lincoln
Lincoln, NE 68588-0525

## Abstract

A simplified theoretical model for predicting the threshold power for explosive fragmentation of liquid droplets falling through the focal point of a tightly-focused, continuous, Gaussian-profiled laser beam has been developed. Theoretically-predicted and corresponding experimentally-measured explosive fragmentation threshold power/droplet velocity ratios are compared for $CO_2$ laser irradiated water droplets within a size parameter range of 5 to 25. The theoretical and experimental data were in agreement within a factor of about two. Future refinements of the theoretical modeling and the experimental procedure are discussed.

## INTERACTION OF EXCIMER LASER RADIATION WITH SOLID PARTICLES

D.R. Alexander, D.E. Poulain, J.P. Barton, S.A. Schaub, and J. Zhang

Center for Electro-Optics
University of Nebraska-Lincoln
Lincoln, Nebraska 68588-0525

## Abstract

Results have been obtained for the interaction of KrF excimer laser radiation ($\lambda = 248$ nm, FWHM pulse width = 17 ns) with solid particles in air and under vacuum conditions down to approximately $10^{-5}$ Torr. Solid particles of glass spheres, Al spheres, $Al_2O_3$, W, SiC, ground fused silica (Suprasil), and polystyrene divinylbenzene have been imaged at various stages of the explosive process after interaction with the KrF laser operating at focused irradiance values of approximately $10^{11}$ W/cm$^2$. In addition to illustrating the dynamics of the explosive process, the excimer laser imaging system was also used to extract information regarding the velocities of the ejected material by the use of a dual imaging pulse. Although the velocity of the ejected material depends on several parameters, among these being the location of the particle within the focal region, typical velocities ranged from 200 to 2000 m/s. Streak camera images were also taken which revealed that the lifetime of plasma emission ranged from about 40 to 2700 ns depending on the particular material and surrounding pressure.

# ELECTROMAGNETIC FIELD CALCULATIONS FOR A TIGHTLY-FOCUSED LASER BEAM INCIDENT UPON A SPHERICAL PARTICLE

J.P. Barton, D.R. Alexander, and S.A. Schaub
Center for Electro-Optics
College of Engineering
University of Nebraska
Lincoln, Nebraska 68588

## ABSTRACT

New applications and extensions of our spherical particle/arbitrary beam electromagnetic interaction theory are presented. The topics include a further analysis of focal point positioning effects at resonance, the determination of the net radiation force and torque on the particle, the determination of the spatial distribution of radiation forces within and upon the surface of the particle, and the determination of the interactive internal and external electromagnetic fields for a beam incident upon two adjacent particles of differing size and material and of arbitrary spatial positioning. Future work will involve further refinement of these developments and an effort to obtain direct comparisons between theoretical calculations and corresponding experimental measurements.

## NONLINEAR EFFECTS OF EXCIMER LASER INTERACTION WITH WATER DROPLETS

D.R. Alexander, J.P. Barton, S.A. Schaub, and G. Holtmeier

Center for Electro-Optics
University of Nebraska-Lincoln
Lincoln, Nebraska 68588-0525

## Abstract

During this funding period results have been obtained for the interaction of KrF excimer laser radiation ($\lambda = 248$ nm, $t_{pulse} = 17$ ns) with 60 $\mu$m distilled water droplets for irradiance values ranging from 3 to 230 GW/cm$^2$. Laser images of the droplet breakup during the time interval from 0 to 100 ns indicate the dynamic breakup processes to be highly nonlinear. At low irradiance (3 GW/cm$^2$) the material is ejected from both the illuminated and shadow hemispheres of the droplet, closely resembling internal electric field strengths obtained from plane wave Lorenz-Mie theory calculations. As the irradiance is increased to 6 GW/cm$^2$ the interaction on the shadow hemisphere becomes stronger while the interaction on the illuminated hemisphere decreases. At high irradiance (230 GW/cm$^2$) the droplets fragment in essentially a symmetric manner. Average material velocity from 0 to 50 ns after arrival of the high energy pulse ranged from 1000 m/s at 3 GW/cm$^2$ to 6000 m/s at 230 GW/cm$^2$.

# LASER INTERACTION WITH A METALLIC FILAMENT: ABLATION DYNAMICS AND PLASMA FORMATION

D.R. Alexander, G. M. Holtmeier, Kyo-Dong Song, and J. P. Barton
Center for Electro-Optics
College of Engineering
University of Nebraska
Lincoln, NE 68588-0656

## RECENT PUBLICATIONS, SUBMITTALS FOR PUBLICATION, AND PRESENTATIONS:

### ABSTRACT

Experimental results are presented on the time dependent material ejection dynamics associated with focused excimer laser beams interacting with a small diameter wire. Copper wire 75 $\mu$m in diameter was illuminated with a KrF excimer laser at an irradiance of 80 GW/cm$^2$. Interaction dynamics were recorded using both real time and double strobed ultraviolet laser imaging techniques. Temporal evolutions of both vaporous and molten material are reported for the laser beam/wire interactions. Material observed during 2-D shadow imaging on the shadow side of the wire was shown to originate from the illuminated surface without spallation of material on the shadow surface. Material emission velocities are reported utilizing two different imaging techniques. A maximum velocity of 1500 m/s was obtained for material ejected in a direction toward the illuminating laser. The elastically scattered incident radiation (ESIR) for both solid copper wires and H$_2$O drops show a distinct two-peak structure which is dependent on the incident energy. Broad band plasma emission for copper starts at $6.5 \pm 1.4$ ns after the pulse arrival as compared to $11 \pm 0.36$ ns for water drops. Future work will include the use of a femtosecond laser to investigate laser interactions at higher irradiances (200 GW/cm$^2$) and associated nonlinear behavior.

# ELECTROMAGNETIC FIELDS FOR A BEAM INCIDENT
# UPON A NONSPHERICAL PARTICLE

J.P. Barton and D.R. Alexander
Center for Electro-Optics
College of Engineering
University of Nebraska
Lincoln, Nebraska 68588-0656

## ABSTRACT

A theoretical procedure has been developed for the determination of the internal and external electromagnetic fields for a monochromatic beam incident upon a homogeneous particle of arbitrarily-defined shape. The procedure is best suited for the analysis of near-spherical particles (i.e., particles which deviate from a sphere by plus-or-minus a few tenths of a radii). Verification and demonstration calculations are presented. Also presented are calculations investigating the effect of particle shape on internal heating distributions for $CO_2$ laser heated water droplets, and calculations investigating the effect of surface deformation on resonance excitation within an otherwise spherical particle. Future work will include consideration of modifications of the theoretical procedure that would allow solutions for elongated particles, and the comparison of theoretical calculations with corresponding experimental measurements.

# THEORETICAL DETERMINATION OF THE ELECTROMAGNETIC FIELDS
# FOR A LASER BEAM INCIDENT UPON
# TWO ADJACENT SPHERICAL PARTICLES OF ARBITRARY ARRANGEMENT

J.P. Barton, W. Ma, S.A. Schaub and D.R. Alexander

Center for Electro-Optics
College of Engineering
University of Nebraska-Lincoln
Lincoln, NE 68588-0656

## ABSTRACT

Applying our previously derived spherical particle/arbitrary beam interaction theory, a procedure has been developed for the determination of the electromagnetic fields for a beam incident upon two adjacent spherical particles. Example calculations of internal and near field normalized source function ($\sim |\bar{E}|^2$) distributions are presented. Also presented are calculations demonstrating the effect of the presence and the positioning of a second adjacent particle on far field scattering patterns for beam illumination.

17

# MODELING OF A COHERENT IMAGING SYSTEM

S.A. Schaub, D.R. Alexander, and J.P. Barton

University of Nebraska-Lincoln
Center for Electro-Optics
Lincoln, NE 68588-0656

## Abstract

A theoretical model is presented for the formation of spherical particle images in a laser-based imaging system. The model uses Lorenz-Mie theory in obtaining the electromagnetic fields at the imaging lens surface, the thin lens expression to propagate the field through the lens, and the Fresnel propagation equation to calculate the intensity distribution in the image plane. Comparisons between the theoretical calculations and experimental images are made for transparent water droplets at various degrees of particle defocus.

## 3. DESCRIPTION OF RESEARCH

Detailed descriptions of the experimental and theoretical investigation conducted during the research project are given in the reprints and preprints of the scientific manuscripts submitted with this Final Report. (See List of Publications, Section 6, and Appendices.)

# 4. PERSONNEL SUPPORTED BY THIS CONTRACT

In addition to the principal investigator, Dennis R. Alexander, and co-principal investigator, John P. Barton, the main contributors to this research project include the following graduate students:

- Ph.D. –

    Scott Schaub, "Modeling of the Coherent Imaging of Small Aerosol Particles," November 1990.

    Jingy Zhang, "Florescence Methods for Determination of Temperature in Aerosol Particles," Defense scheduled for April 1991.

    Kyo-Dong Song, "Excimer Laser Produced Plasmas in Copper Wire Targets and Water Droplets," (In Progress).

- M.S. –

    Mark A. Emanuel, Master of Science Thesis, "Laser Interaction with Spherical Aerosols and Cylinder Fluid Columns," 1987.

    Dana E. Poulain, Master of Science Thesis, "Interactions of Solid Aerosols with Intense Ultraviolet Laser Radiation," 1989.

    Wen Ma, Master of Science Thesis, "Laser Beam Interaction with Two Adjacent Spherical Particles of Arbitrary Arrangement," 1990.

    Gregg M. Holtmeier, Master of Science Thesis, "High Intensity Ultraviolet Laser Interaction with a Metallic Cylinder," 1990.

    Sik-Wah Chiang, Master of Science Thesis, "Laser Interaction with Aerosol Particles," (In Progress).

One copy of previously unsubmitted theses and/or dissertations are included as an addendum to this Final Report.

## 5. ACKNOWLEDGEMENTS

# 6. LIST OF PUBLICATIONS

### (a) Publications in Technical Journals

1. J. P. Barton, D. R. Alexander, and S. A. Schaub, "Internal and Near-Surface Electromagnetic Fields for a Spherical Particle Irradiated by a Focused Laser Beam," *J. of Appl. Phys.*, **64**, No. 4, 1632-1639, 1988.

2. J.P. Barton, D.R. Alexander, and S.A. Schaub, "Internal Fields of a Spherical Particle Illuminated by a Tightly-focused Laser Beam: Focal Point Positioning Effects at Resonance," *J. of Appl. Phys.*, **65**, No. 8, 2900-2906, 1989.

3. S. A. Schaub, D. R. Alexander, J. P. Barton, and M. A. Emanuel, "Focused Laser Beam Interactions With Methanol Droplets: Effects of Relative Beam Diameter," *Appl. Opt.*, **28**, 1666-1669, 1989.

4. S. A. Schaub, D. R. Alexander, and J. P. Barton, "Theoretical Model for the Image Formed by a Spherical Particle in a Coherent Imaging System: Comparison to Experiment," *Optical Engineering*, **28**, No. 5, 565-571, 1989.

5. D.R. Alexander, S.A. Schaub, J. Zhang, D. Poulain, and J.P. Barton, "Scattering of Incident KrF Laser Radiation Resulting from the Laser Induced Breakdown of $H_2O$ Droplets," *Opt. Lett.*, **14**, No. 8, 548-550, 1989.

6. S.A. Schaub, J.P. Barton and D.R. Alexander, "Simplified Scattering Coefficient Expressions for a Spherical Particle Located on the Propagation Axis of a Fifth-Order Gaussian Beam," *Appl. Phys. Lett.*, **55**, No. 26, 2709-2711, 1989.

7. J.P. Barton and D.R. Alexander, "Fifth-order Corrected Electromagnetic Field Components for a Fundamental Gaussian Beam," *J. of Appl. Phys.*, **66**, No. 7, 2800-2802, 1989.

8. J.P. Barton, D.R. Alexander and S.A. Schaub, "Theoretical Determination of Net Radiation Force and Torque for a Spherical Particle Illuminated by a Focused Beam," *J. of Appl. Phys.*, **66**, No. 10, 4594-4602, 1989.

9. S.A. Schaub, D.R. Alexander, D.E. Poulain, and J.P. Barton, "Measurement of Hypersonic Velocities Resulting from the Laser-induced Breakdown of Aerosols Using an Excimer Laser Imaging System," *Rev. Sci. Instrum.*, **60**, No. 12, 3688-3691, 1989.

10. G.M. Holtmeier, D.R. Alexander and J.P. Barton, "High Intensity Ultraviolet Laser Interaction with a Metallic Filament," accepted for publication in *J. of Appl. Phys.*, 1991.

11. D.E. Poulain, D.R. Alexander, J.P. Barton, S.A. Schaub, and J. Zhang, "Interactions of Intense Ultraviolet Laser Radiation with Solid Aerosols," *J. of Appl. Phys.*, **67**, No. 5, 2283-2288, 1990.

12. J.P. Barton and D.R. Alexander, "Electromagnetic Fields for an Irregularly-Shaped Near-Spherical Particle Illuminated by a Focused Laser Beam," accepted for publication *J. of Appl. Phys.*, 1990.

13. S.A. Schaub, D.R. Alexander, and J.P. Barton, "Modeling of the Coherent Imaging of a Spherical Aerosol Particle Illuminated by a Plane Wave at Oblique Incidence," submitted to *J. Opt. Soc. Am. A*, November 1990.

14. D. Liu, D.R. Alexander, and J.P. Barton, "Fundamental Gaussian Beam Solutions of Maxwell's Equations," in preparation to *J. of Appl. Phys.*, March 1991. (Not in Appendix.)

15. J.P. Barton, W. Ma, S.A. Schaub and D.R. Alexander, "Electromagnetic Field for a Beam Incident Upon Two Adjacent Spherical Particles," accepted for publication in *Appl. Opt.*, 1991.

16. S.A. Schaub, D.R. Alexander and J.P. Barton, "Theoretical Model of the Laser Imaging of Small Aerosols: Applications to Aerosol Sizing," accepted for publication in *Appl. Opt.*, 1991.

17. D.R. Alexander and Kyo-Dong Song, "Excimer Laser Produced Plasma in Copper Wire Targets and Water Droplets," in preparation, *J. of Appl. Phys.*, January 1991. (Not in Appendix)

18. D.R. Alexander, J.P. Barton, S.A. Schaub and G.M. Holtmeier, "Nonlinear Interaction of KrF Laser Radiation with Small Water Droplets," to be published in *Appl. Opt.*, 1991.

19. J. Zhang, D.R. Alexander and J.P. Barton, "Hybrid Inelastic Scattering Models for Particle Thermometry: Unpolarized Emissions," in preparation, March 1991. (Not in Appendix.)

20. J. Zhang, D.R. Alexander and J.P. Barton, "Hybrid Inelastic Scattering Models for Particle Thermometry: Polarized Emissions," in preparation, March 1991. (Not in Appendix.)

(b) **Conference Proceedings**

21. J.P. Barton, D.R. Alexander, and S.A. Schaub, "Experimental and Theoretical Analysis of Liquid Droplets Moving Through a Focused $CO_2$ Laser Beam" Proceedings of the 1988 U.S. Army CRDEC Conference on Obscuration and Aerosol Research, Aberdeen Proving Ground, Maryland, June 1988.

22. D. R. Alexander, D. E. Poulain, J. P. Barton, S. A. Schaub, and J. Zhang, "Interaction of Excimer Laser Radiation With Solid Particles," Proceedings of the 1988 U.S. Army CRDEC Conference on Obscuration and Aerosol Research, Aberdeen Proving Ground, Maryland, June 1988.

23. J.P. Barton, D.R. Alexander and S.A. Schaub, "Electromagnetic Field Calculations for a Tightly-Focused Laser Beam Incident upon a Spherical Particle," Proceedings of the 1989 U.S. Army CRDEC Conference on Obscuration and Aerosol Research, Aberdeen Proving Ground, Maryland, June 26-30, 1989.

24. D.R. Alexander, J.P. Barton, S.A. Schaub and G. Holtmeier, "Nonlinear Effects of Excimer Laser Interaction with Water Droplets," Proceedings of the 1989 CRDEC Scientific Conference on Obscuration and Aerosol Research, Aberdeen Proving Ground, Maryland, June 1989.

25. D.R. Alexander, G.M. Holtmeier, K.D. Song and J.P. Barton, "Laser Interaction with a Metallic Filament: Ablation Dynamics and Plasma Formation," Proceedings of the 1990 U.S. Army CRDEC Conference on Obscuration and Aerosol Research, Aberdeen Proving Ground, Maryland, June 25-27, 1990.

26. J.P. Barton and D.R. Alexander, "Electromagnetic Field for a Beam Incident Upon a Nonspherical Particle," Proceedings of the 1990 CRDEC Scientific Conference on Obscuration and Aerosol Research, Aberdeen Proving Ground, Maryland, June 25-27, 1990.

27. J.P. Barton, W. Ma, S.A. Schaub and D.R. Alexander, "Theoretical Determination of the Electromagnetic Fields for a Laser Beam Incident upon Two Adjacent Spherical Particles of Arbitrary Arrangement," Proceedings of the 2nd International Congress on Optical Particle Sizing, Tempe, Arizona, 1990.

28. D.R. Alexander, S.A. Schaub, and J.P. Barton, "Modeling of a Coherent Imaging System: Application to Focus Determination in Aerosol Sizing," Proceedings of the 2nd International Congress on Optical Particle Sizing, Tempe, Arizona, 1990.

(c) **Conference Presentations**

29. D. R. Alexander, J. P. Barton, S. A. Schaub, M. A. Fitzwater, "Beam Propagation Effects Resulting from the Electric Field Strengths for Spheres and Cylinders: Internal and Near Field," Presentation at the Workshop on the Physics of Directed Energy Propagation in the Atmosphere, U. S. Army Atmospheric Sciences Laboratory (ASL) at New Mexico State University, Las Cruces, New Mexico, January 27-28, 1987.

30. D. R. Alexander, S. A. Schaub, J. P. Barton, "Scattered Internal and External Near-Fields for Spherical and Cylinder-Like Particles," Invited Paper presentation at the Symposium on Scattering of Laser Radiation by Particulates, Optical Society of America, Rochester, New York, October 21, 1987.

31. J. P. Barton, D. R. Alexander, S. A. Schaub, "Internal and Near-Surface Electromagnetic Fields For a Spherical Particle in a Focused Laser Beam," poster presentation at the 1988 U. S. Army CRDEC Conference on Obscuration and Aerosol Research, Aberdeen Proving Ground, Maryland, June 1988.

32. D. R. Alexander, D. E. Poulain, J. P. Barton, S. A. Schaub, and J. Zhang, "Nonlinear Effects of Excimer Laser Radiation With Solid Particles in a Vacuum," Presentation at the 1988 U. S. Army CRDEC Conference on Obscuration and Aerosol Research, Aberdeen Proving Ground, Maryland, June 1988.

33. D. R. Alexander and J. P. Barton, "Gaussian Laser Beam Illumination of a Spherical Particle at Resonance Conditions," Presentation at the 19th European Conference on Laser Interaction with Matter, Madrid, Spain, October 3, 1988.

34. J.P. Barton, D.R. Alexander and S.A. Schaub, "Experimental and Theoretical Analysis of Liquid Droplets Moving Through a Focused $CO_2$ Laser Beam," Presentation at the 1988 U.S. Army CRDEC Scientific Conference on Obscuration and Aerosol Research, Aberdeen, Maryland, 1988.

35. D.R. Alexander, S.A. Schaub, J. Zhang, D.E. Poulain, and J.P. Barton, "Laser Induced Breakdown of $H_2O$ Droplets at 0.248 $\mu$m," Presentation at the Workshop on the Physics of Directed Energy Propagation in the Atmosphere, Las Cruces, New Mexico, February 28-March 1, 1989.

36. J.P. Barton, D.R. Alexander, and S.A. Schaub, "Electromagnetic Fields for a Focused Laser Beam Incident Upon a Spherical Particle," Presentation at the Workshop on the Physics of Directed Energy Propagation in the Atmosphere, Las Cruces, New Mexico, February 28-March 1, 1989.

37. J.P. Barton, D.R. Alexander and S.A. Schaub, "Electromagnetic Calculations for a Tightly-focused Laser Beam Incident Upon a Spherical Particle," Poster presentation at the 1989 CRDEC Scientific Conference on Obscuration and Aerosol Research, Aberdeen Proving Ground, Maryland, June, 1989.

38. D.R. Alexander, D.E. Poulain, S.A. Schaub, J. Zhang and J.P. Barton, "Interaction of Intense $\lambda = 248$ nm KrF Laser Radiation with Solid Particles and Thin Wires," Presentation at the 20th Annual Meeting of the Fine Particle Society, Boston, Massachusetts, August 23, 1989.

39. D.R. Alexander, J.P. Barton, S.A. Schaub and G. Holtmeier, "Nonlinear Effects of Excimer Laser Interaction with Water Droplets," Presented at the 1989 CRDEC Scientific Conference on Obscuration and Aerosol Research, Aberdeen Proving Ground, Maryland, June 1989.

40. J.P. Barton and D.R. Alexander, "Electromagnetic Fields for a Beam Incident upon a Nonspherical Particle," Presentation at the 1990 U.S. Army CRDEC Scientific Conference on Obscuration and Aerosol Research, Aberdeen, Maryland, 1990.

41. D.R. Alexander, S.A. Schaub and J.P. Barton, "Modeling of a Coherent Imaging System: Application to Focus Determination in Aerosol Sizing," Presentation at the 2nd International Congress on Optical Particle Sizing, Tempe, Arizona, March 5-8, 1990.

42. J.P. Barton, W. Ma, S.A. Schaub and D.R. Alexander, "Theoretical Determination of the Electromagnetic Fields for a Laser Beam Incident upon two Adjacent Spherical Particles of Arbitrary Arrangement," Presentation at the 2nd International Congress on Optical Particle Sizing, Tempe, Arizona, March 5-8, 1990.

43. D.R. Alexander, G.M. Holtmeier and K.D. Song, "KrF Laser Interaction with a Metallic Filament: Ablation Dynamics and Plasma Formation," Presented at the 1990 U.S. Army CRDEC Conference on Obscuration and Aerosol Research, Aberdeen Proving Ground, Maryland, June 25-27, 1990.

44. J.P. Barton and D.R. Alexander, "Electromagnetic Field Calculations for a Tightly Focused Laser Beam Incident Upon a Microdroplet," Invited Paper for presentation at SPIE's Optical Engineering SOUTHCENTRAL '91 Nonlinear Optics Conference, May 1991.

45. D.R. Alexander, S.A. Schaub, G.M. Holtmeier, and J.P. Barton, "Nonlinear Laser Interactions with Water Droplets," submitted for presentation at SPIE's Optical Engineering SOUTHCENTRAL '91 Nonlinear Optics Conference, May 1991.

## (d) Technical Reports

46. "Linear and Non-Linear Response of Liquid and Solid Particles to Energetic Radiation," U.S. Army Research Office, Research Triangle Park, N.C., Semi-Annual Report #1, July 1, 1987 – December 31, 1987.

47. "Linear and Non-Linear Response of Liquid and Solid Particles to Energetic Radiation," U.S. Army Research Office, Research Triangle Park, N.C., Semi-Annual Report #2, January 1, 1988 – June 30, 1988.

48. "Linear and Non-Linear Response of Liquid and Solid Particles to Energetic Radiation," U.S. Army Research Office, Research Triangle Park, N.C., Semi-Annual Report #3, July 1, 1988 – December 31, 1988.

49. "Linear and Non-Linear Response of Liquid and Solid Particles to Energetic Radiation," U.S. Army Research Office, Research Triangle Park, N.C., Semi-Annual Report #4, January 1, 1989 – June 30, 1989.

50. "Linear and Non-Linear Response of Liquid and Solid Particles to Energetic Radiation," U.S. Army Research Office, Research Triangle Park, N.C., Semi-Annual Report #5, July 1, 1989 – December 31, 1989.

51. "Linear and Non-Linear Response of Liquid and Solid Particles to Energetic Radiation," U.S. Army Research Office, Research Triangle Park, N.C., Semi-Annual Report #6, January 1, 1990 – June 30, 1990.

## 7. REPORT OF INVENTIONS

One patent on the "Forming of Fine Particles" has been filed with the U.S. Patent Office. Patent claims have been granted and a U.S. Patent will be granted in approximately six months.

# LINEAR AND NON-LINEAR RESPONSE OF LIQUID AND SOLID

## PARTICLES TO ENERGETIC RADIATION

## FINAL REPORT

## (APPENDICES)

DENNIS R. ALEXANDER
PRINCIPAL INVESTIGATOR

JOHN P. BARTON
CO-PRINCIPAL INVESTIGATOR

MARCH 11, 1991

# 8. APPENDICES

(a) Reprints and Preprints of Publications in Technical Journal, Item 6(a)

# Internal and near-surface electromagnetic fields for a spherical particle irradiated by a focused laser beam

J. P. Barton, D. R. Alexander, and S. A. Schaub

*Laboratory for Electro-Optical Measurements, College of Engineering and Technology, University of Nebraska-Lincoln, Lincoln, Nebraska 68588-0525*

Theoretical expressions for the internal and external electromagnetic fields for an arbitrary electromagnetic beam incident upon a homogeneous spherical particle are derived, and numerical calculations based upon this theoretical development are presented. In particular, spatial distributions of the internal and near-surface electric field magnitude (source function) for a focused fundamental (TEM$_{00}$ mode) Gaussian beam of 1.06 $\mu$m wavelength and 4 $\mu$m beam waist diameter incident upon a 5-$\mu$m-diam water droplet in air are presented as a function of the location of the beam focal point relative to the sphere center. The calculations indicate that the internal and near-surface electric field magnitude distribution can be strongly dependent upon relative focal point positioning and may differ significantly from the corresponding electric field magnitude distribution expected from plane-wave irradiation.

## I. INTRODUCTION

The interaction of a focused laser beam with a spherical particle is a topic of current research interest with applications occurring in a variety of areas of study including particle sizing, laser fusion, Raman scattering diagnostics, optical levitation, and laser beam/aerosol cloud penetration. The electromagnetic field that results from a focused laser beam incident upon a spherical particle is a function of the properties of the beam (wavelength, power, mode, beam waist diameter), the properties of the particle (diameter, complex index of refraction), and the relative focal point positioning. Presented here is a theoretical development that permits the determination of the internal and external electromagnetic fields for a focused laser beam incident upon a homogeneous spherical particle as a function of these parameters. For illustration, calculations of equatorial and transverse plane electric field magnitude (source function) distributions for a focused fundamental (TEM$_{00}$ mode) Gaussian beam ($\lambda = 1.06\,\mu$m, $w_0 = 2\,\mu$m) incident upon a spherical water droplet ($d = 5\,\mu$m) are presented for both on-center and off-center focal point positioning. Such calculations could be used, for example, to predict the location and required threshold power for spontaneous evaporative nucleation (within the droplet) or the location and required threshold power for electrical breakdown (either within or near the surface of the droplet).

Previously, Dusel, Kerker, and Cooke[1] and Green et al.[2] have presented internal electric field magnitude (source function) distributions for a plane electromagnetic wave incident upon a homogeneous spherical particle. But such a plane-wave assumption would be appropriate only if the sphere diameter is much less than the local beam diameter, and this is often not the situation when a focused laser beam is used for illumination. Morita et al.,[3] Tsai and Pogorzelski,[4] Tam and Corriveau,[5] Kim and Lee,[6] and Gouesbet, Grehan, and Maheu[7] have all considered the problem of a fundamental Gaussian beam incident upon a homogeneous spherical particle, but these works appear primarily concerned with far-field scattering and no internal or near-surface electromagnetic field distributions are presented. In addition, the first four of these papers utilize simple zero-order Gaussian beam descriptions. The most recent work of Gouesbet, Grehan, and Maheu[7] utilizes the more accurate first-order focused fundamental Gaussian beam description of Davis[8] (which is used here) but only on-center focusing is considered and, even for this simplified case, the expansion of the incident field into the coefficients used in the series expressions for the electromagnetic field components requires a difficult numerical integration over a semi-infinite plane.

An alternative to the approach of Gouesbet, Grehan, and Maheu[7] is derived and utilized in this paper and, for the first time, internal and near-surface electric field magnitude distributions are presented. The theoretical development is a simple extension of the classic plane wave Lorentz–Mie theory as presented in Born and Wolf[9] and the expansion of the incident field requires numerical integration of finite surface integrals only. The theoretical development is applicable for any incident beam for which an accurate mathematical description is known, and thus results for off-center focusing can be straightforwardly determined. In addition, as more accurate mathematical Gaussian beam descriptions are developed, these can be easily incorporated into the analysis.

## II. THEORY

The specific problem considered here is that of an arbitrary harmonic electromagnetic beam within an infinite, linear, isotropic, nonmagnetic, nonelectrically conducting, homogeneous media incident upon a linear, isotropic, nonmagnetic, finite electrically conducting sphere of radius $a$. A spherical coordinate system with the origin at the sphere center is chosen (Fig. 1). The initial part of the development is similar to the plane-wave Lorentz–Mie theory development as presented in Born and Wolf.[9] Appropriately,
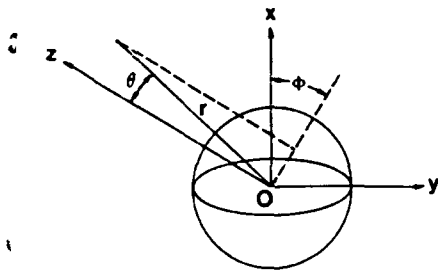
FIG. 1. Geometry for an arbitrary electromagnetic beam incident upon a spherical particle.

all electromagnetic quantities are assumed to vary in time as $\exp(-i\omega t)$. (The complex exponential is dropped from all subsequent expressions.)

The procedure is to first obtain a general electromagnetic field solution and then relate electromagnetic field expressions for the incident, scattered, and internal electromagnetic fields by applying boundary conditions at the surface of the sphere. The general electromagnetic field solution is obtained by expressing the field as a sum of two subfields: the electric wave field (designated by the superscript $e$) which is assumed to have a zero radial magnetic field component ($^{e}H_r = 0$) and the magnetic wave field (designated by the superscript $m$) which is assumed to have a zero radial electric field component ($^{m}E_r = 0$). The advantage of doing this is that each subfield can be expressed solely as a function of a single respective scalar potential, $\Pi$. In terms of the scalar potential associated with the electric wave field ($^{e}\Pi$) and the scalar potential associated with the magnetic wave field ($^{m}\Pi$) the electromagnetic field components are

$$E_r = \frac{\partial^2(r\Pi)}{\partial r^2} + k^2 r\Pi, \qquad (1)$$

$$E_\theta = \frac{1}{r}\frac{\partial^2(r^e\Pi)}{\partial\theta\,\partial r} + \frac{k''}{r\sin\theta}\frac{\partial(r^m\Pi)}{\partial\phi}, \qquad (2)$$

$$E_\phi = \frac{1}{r\sin\theta}\frac{\partial^2(r^e\Pi)}{\partial\phi\,\partial r} - \frac{k''}{r}\frac{\partial(r^m\Pi)}{\partial\theta}, \qquad (3)$$

$$H_r = \frac{\partial^2(r^m\Pi)}{\partial r^2} + k^2 r^m\Pi, \qquad (4)$$

$$H_\theta = -\frac{k'}{r\sin\theta}\frac{\partial(r^e\Pi)}{\partial\phi} + \frac{1}{r}\frac{\partial^2(r^m\Pi)}{\partial r\,\partial\theta}, \qquad (5)$$

and

$$H_\phi = \frac{k'}{r}\frac{\partial(r^e\Pi)}{\partial\theta} + \frac{1}{r\sin\theta}\frac{\partial^2(r^m\Pi)}{\partial r\,\partial\phi}. \qquad (6)$$

In Eqs. (1)–(6), $k' = ik_0\bar{\epsilon}$, $k'' = ik_0$, and $k = k_0\sqrt{\bar{\epsilon}}$, where $k_0 = \omega/c$, and the complex dielectric constant, $\bar{\epsilon} = \epsilon + i4\pi\sigma/\omega$, where $\sigma$ is the electrical conductivity. Both $^{e}\Pi$ and $^{m}\Pi$ satisfy the Helmholtz equation

$$\nabla^2\Pi + k^2\Pi = 0. \qquad (7)$$

That the electromagnetic field of Eqs. (1)–(6) with the condition of Eq. (7) satisfies Maxwell's equations can be verified by direct substitution.

It is at this point that the derivation for an arbitrary incident beam differs from the traditional derivation for an incident plane wave. Instead of choosing a series solution with a form corresponding to that for a transverse polarized plane wave propagating along the $z$ axis, the most general separation of variables solution of the Helmholtz equation [Eq. (7)] is chosen:

$$r\Pi = \sum_{l=0}^{\infty}\sum_{m=-l}^{l}[\tilde{A}_{lm}\psi_l(kr) + \tilde{B}_{lm}\chi_l(kr)]Y_{lm}(\theta,\phi), \qquad (8)$$

where $\tilde{A}_{lm}$ and $\tilde{B}_{lm}$ are arbitrary constants, $\psi_l$ and $\chi_l$ are the Ricatti–Bessel functions, and $Y_{lm}(\theta,\phi)$ is the spherical harmonic function.

The electric wave and magnetic wave scalar potentials for the incident field (designated by the superscript $i$), the scattered field (designated by the superscript $s$), and the internal field (designated by the superscript $w$) are expressed in a form consistent with Eq. (8). (In the following, the subscript int refers to properties within the sphere and the subscript ext refers to properties outside the sphere.) For the incident field,

$$r^e\Pi^{(i)} = \sum_{l=0}^{\infty}\sum_{m=-l}^{l}A_{lm}\psi_l(k_{ext}r)Y_{lm}(\theta,\phi) \qquad (9)$$

and

$$r^m\Pi^{(i)} = \sum_{l=0}^{\infty}\sum_{m=-l}^{l}B_{lm}\psi_l(k_{ext}r)Y_{lm}(\theta,\phi), \qquad (10)$$

where the $\chi_l$ functions have been excluded since this function is unbounded at the origin and the incident field should be describable everywhere, including the origin. For the scattered field

$$r^e\Pi^{(s)} = \sum_{l=0}^{\infty}\sum_{m=-l}^{l}a_{lm}\xi_l^{(1)}(k_{ext}r)Y_{lm}(\theta,\phi) \qquad (11)$$

and

$$r^m\Pi^{(s)} = \sum_{l=0}^{\infty}\sum_{m=-l}^{l}b_{lm}\xi_l^{(1)}(k_{ext}r)Y_{lm}(\theta,\phi), \qquad (12)$$

where $\xi_l^{(1)} = \psi_l - i\chi_l$ functions are chosen since these functions, in the limit of large $r$, correspond to outward traveling spherical waves, appropriate for the scattered field. For the internal field,

$$r^e\Pi^{(w)} = \sum_{l=0}^{\infty}\sum_{m=-l}^{l}c_{lm}\psi_l(k_{int}r)Y_{lm}(\theta,\phi) \qquad (13)$$

and

$$r^m\Pi^{(w)} = \sum_{l=0}^{\infty}\sum_{m=-l}^{l}d_{lm}\psi_l(k_{int}r)Y_{lm}(\theta,\phi), \qquad (14)$$

where once again the $\chi_l$ functions have been excluded since these functions are unbounded at the origin.

Substitution of Eqs. (9)–(14) into Eqs. (1)–(6) provides expressions for the incident, scattered, and internal electromagnetic fields. For brevity, only the expressions for the electric field components are given here. Expressions for the magnetic field components are given in Appendix A. The $l = 0$ terms in these series expressions have been removed since, as can be seen (note: $\partial Y_{00}/\partial\theta = 0$), these terms make no contribution. For the incident electric field,

$$E_r^{(i)} = \frac{1}{r^2} \sum_{l=1}^{\infty} \sum_{m=-l}^{l} [l(l+1)A_{lm}\psi_l(k_{ext}r)Y_{lm}(\theta,\phi)],$$

(15)

$$E_\theta^{(i)} = \frac{1}{r} \sum_{l=1}^{\infty} \sum_{m=-l}^{l} \left( k_{ext}A_{lm}\psi_l'(k_{ext}r)\frac{\partial Y_{lm}(\theta,\phi)}{\partial \theta} \right.$$
$$\left. + imk_{ext}^{II}B_{lm}\psi_l(k_{ext}r)\frac{Y_{lm}(\theta,\phi)}{\sin\theta} \right),$$

(16)

and

$$E_\phi^{(i)} = \frac{1}{r} \sum_{l=1}^{\infty} \sum_{m=-l}^{l} \left( imk_{ext}A_{lm}\psi_l'(k_{ext}r)\frac{Y_{lm}(\theta,\phi)}{\sin\theta} \right.$$
$$\left. - k_{ext}^{II}B_{lm}\psi_l(k_{ext}r)\frac{\partial Y_{lm}(\theta,\phi)}{\partial \theta} \right),$$

(17)

for the scattered electric field,

$$E_r^{(s)} = \frac{1}{r^2} \sum_{l=1}^{\infty} \sum_{m=-l}^{l} [l(l+1)a_{lm}\xi_l^{(1)}(k_{ext}r)Y_{lm}(\theta,\phi)],$$

(18)

$$E_\theta^{(s)} = \frac{1}{r} \sum_{l=1}^{\infty} \sum_{m=-l}^{l} \left( k_{ext}a_{lm}\xi_l^{(1)\prime}(k_{ext}r)\frac{\partial Y_{lm}(\theta,\phi)}{\partial \theta} \right.$$
$$\left. + imk_{ext}^{II}b_{lm}\xi_l^{(1)}(k_{ext}r)\frac{Y_{lm}(\theta,\phi)}{\sin\theta} \right),$$

(19)

and

$$E_\phi^{(s)} = \frac{1}{r} \sum_{l=1}^{\infty} \sum_{m=-l}^{l} \left( imk_{ext}a_{lm}\xi_l^{(1)\prime}(k_{ext}r)\frac{Y_{lm}(\theta,\phi)}{\sin\theta} \right.$$
$$\left. - k_{ext}^{II}b_{lm}\xi_l^{(1)}(k_{ext}r)\frac{\partial Y_{lm}(\theta,\phi)}{\partial \theta} \right),$$

(20)

and for the internal electric field

$$E_r^{(w)} = \frac{1}{r^2} \sum_{l=1}^{\infty} \sum_{m=-l}^{l} [l(l+1)c_{lm}\psi_l(k_{int}r)Y_{lm}(\theta,\phi)],$$

(21)

$$E_\theta^{(w)} = \frac{1}{r} \sum_{l=1}^{\infty} \sum_{m=-l}^{l} \left( k_{int}c_{lm}\psi_l'(k_{int}r)\frac{\partial Y_{lm}(\theta,\phi)}{\partial \theta} \right.$$
$$\left. + imk_{int}^{II}d_{lm}\psi_l(k_{int}r)\frac{Y_{lm}(\theta,\phi)}{\sin\theta} \right),$$

(22)

and

$$E_\phi^{(w)} = \frac{1}{r} \sum_{l=1}^{\infty} \sum_{m=-l}^{l} \left( imk_{int}c_{lm}\psi_l'(k_{int}r)\frac{Y_{lm}(\theta,\phi)}{\sin\theta} \right.$$
$$\left. - k_{int}^{II}d_{lm}\psi_l(k_{int}r)\frac{\partial Y_{lm}(\theta,\phi)}{\partial \theta} \right),$$

(23)

where the superscript prime refers to the derivative of the function with respect to its argument.

The coefficients that describe the scattered field, $a_{lm}$ and $b_{lm}$, and the coefficients that describe the internal field, $c_{lm}$ and $d_{lm}$, can be related to the coefficients that describe the incident field, $A_{lm}$ and $B_{lm}$, by application of the boundary condition that the tangential components of the electric and magnetic fields be continuous across the sphere surface. From Eqs. (2), (3), (5), and (6) it can be observed that the boundary conditions will be satisfied if

$$k^{I}r\Pi, \quad k^{II}r^m\Pi, \quad \frac{\partial(r\Pi)}{\partial r}, \quad \text{and} \quad \frac{\partial(r^m\Pi)}{\partial r}$$

are continuous across the surface of the sphere. Noting that $\Pi_{ext} = \Pi^{(i)} + \Pi^{(s)}$ and $\Pi_{int} = \Pi^{(w)}$, and using Eqs. (9)–(14) to substitute into the four boundary conditions, results, after equating like terms, in four simultaneous algebraic equations that are solved to directly relate $a_{lm}$, $b_{lm}$, $c_{lm}$, and $d_{lm}$ to $A_{lm}$ and $B_{lm}$:

$$a_{lm} = \frac{\psi_l'(k_{int}a)\psi_l(k_{ext}a) - \bar{n}\psi_l(k_{int}a)\psi_l'(k_{ext}a)}{\bar{n}\psi_l(k_{int}a)\xi_l^{(1)\prime}(k_{ext}a) - \psi_l'(k_{int}a)\xi_l^{(1)}(k_{ext}a)}A_{lm},$$

(24)

$$b_{lm} = \frac{\bar{n}\psi_l'(k_{int}a)\psi_l(k_{ext}a) - \psi_l(k_{int}a)\psi_l'(k_{ext}a)}{\psi_l'(k_{int}a)\xi_l^{(1)\prime}(k_{ext}a) - \bar{n}\psi_l(k_{int}a)\xi_l^{(1)}(k_{ext}a)}B_{lm},$$

(25)

$$c_{lm} = \frac{\xi_l^{(1)\prime}(k_{ext}a)\psi_l(k_{ext}a) - \xi_l^{(1)}(k_{ext}a)\psi_l'(k_{ext}a)}{\bar{n}^2\psi_l(k_{int}a)\xi_l^{(1)\prime}(k_{ext}a) - \bar{n}\psi_l'(k_{int}a)\xi_l^{(1)}(k_{ext}a)}A_{lm},$$

(26)

and

$$d_{lm} = \frac{\xi_l^{(1)\prime}(k_{ext}a)\psi_l(k_{ext}a) - \xi_l^{(1)}(k_{ext}a)\psi_l'(k_{ext}a)}{\psi_l(k_{int}a)\xi_l^{(1)\prime}(k_{ext}a) - \bar{n}\psi_l'(k_{int}a)\xi_l^{(1)}(k_{ext}a)}B_{lm},$$

(27)

where $\bar{n}$ is the complex relative index of refraction defined as

$$\bar{n} = (\bar{\epsilon}_{int}/\epsilon_{ext})^{1/2}.$$

(28)

The final step is to determine the coefficients $A_{lm}$ and $B_{lm}$ that describe the incident electromagnetic field. This can be done for any physical incident electromagnetic field for which the radial components of the electric and magnetic fields are known over a spherical surface of radius $a$ (or actually, a spherical surface of any radius). Assuming $E_r^{(i)}(a,\theta,\phi)$ is known, this function of $\theta$ and $\phi$ only can be expanded in a series of spherical harmonics

$$E_r^{(i)}(a,\theta,\phi) = \sum_{l=0}^{\infty} \sum_{m=-l}^{l} e_{lm}Y_{lm}(\theta,\phi)$$

(29)

where

$$e_{lm} = \int_0^{2\pi} \int_0^{\pi} \sin\theta E_r^{(i)}(a,\theta,\phi)Y_{lm}^*(\theta,\phi)d\theta\,d\phi.$$

(30)

But evaluating Eq. (15) at $r = a$ and equating with Eq. (29) shows that

$$\frac{l(l+1)}{a^2}A_{lm}\psi_l(k_{ext}a) = e_{lm},$$

(31)

1634    J. Appl. Phys., Vol. 64, No. 4, 15 August 1988

Barton, Alexander, and Schaub    1634

and thus

$$A_{lm} = \frac{a^2}{l(l+1)\psi_l(k_{ext}a)} \int_0^{2\pi} \int_0^\pi \sin\theta E_r^{(i)}(a,\theta,\phi)$$

$$\times Y_{lm}^*(\theta,\phi)d\theta\,d\phi. \tag{32}$$

Similarly for the magnetic field it follows that

$$B_{lm} = \frac{a^2}{l(l+1)\psi_l(k_{ext}a)} \int_0^{2\pi} \int_0^\pi \sin\theta H_r^{(i)}(a,\theta,\phi)$$

$$\times Y_{lm}^*(\theta,\phi)d\theta\,d\phi. \tag{33}$$

In summary, the internal and external electromagnetic fields for an arbitrary beam incident upon a homogeneous sphere can be determined as follows. The $A_{lm}$ and $B_{lm}$ coefficients that describe the incident field are generated by computing the surface integrals of Eqs. (32) and (33). Equations (24)–(27) are then used to determine the coefficients $a_{lm}$, $b_{lm}$ and $c_{lm}$, $d_{lm}$ that respectively describe the scattered and internal fields. Finally, Eqs. (15)–(23) are evaluated to determine the electric field distribution. The magnetic field distribution can be evaluated using the equations presented in Appendix A.

An expression for the time-averaged power absorbed by the sphere can be obtained by integrating the radial component of the external field Poynting vector over a spherical surface enclosing the sphere. In the limit of a large integration radius, it follows that

$$W_{abs} = -\frac{c}{8\pi} k_0^2 \epsilon_{ext} \sum_{l=1}^\infty \sum_{m=-l}^l l(l+1)\left[ |a_{lm}|^2 + |b_{lm}|^2 \right.$$

$$\left. + \mathrm{Re}(A_{lm}a_{lm}^* + B_{lm}b_{lm}^*) \right]. \tag{34}$$

## III. NUMERICAL VERIFICATION

A computer program was written incorporating the aforementioned arbitrary incident beam theory. The required Ricatti–Bessel functions are evaluated using the recursion technique presented by Ross[10] and the required spherical harmonic functions are evaluated using derived recursion formulas based on the associated Legendre function recursion relationships presented by Press et al.[11] The surface integrals of Eqs. (32) and (33) are determined using standard numerical integration procedures. The assumed known incident electromagnetic field components are provided by a subroutine independent from the main computer program. In this way, the same main computer program could be used for different prescribed incident electromagnetic fields.

As a test of the arbitrary incident beam theory and the computer program, a Lorentz–Mie theory type incident plane wave was assumed. Consistent with the Lorentz–Mie theory development as presented in Born and Wolf,[9] the incident linearly polarized plane electromagnetic wave is assumed to propagate in the $+z$ axis direction with an electric field polarization in the $x$ axis direction. Thus, after removing the $\exp(-i\omega t)$ time dependence,

$$\mathbf{E}^{(i)} = E_0 e^{ik_{ext}z}\hat{x} \tag{35}$$

and

$$\mathbf{H}^{(i)} = \sqrt{\epsilon_{ext}}\, E_0 e^{ik_{ext}z}\hat{y}, \tag{36}$$
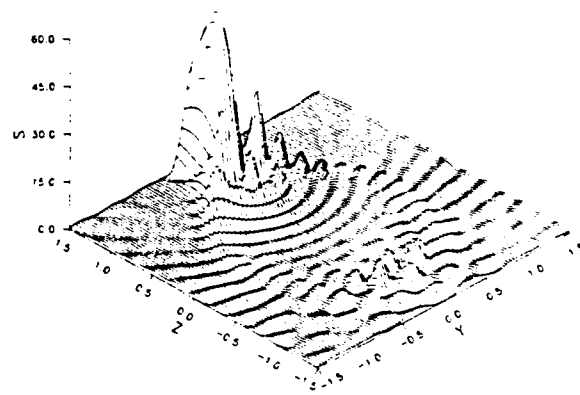
where $E_0$ is the incident electromagnetic wave electric field amplitude. Substituting the incident electromagnetic field described by Eqs. (35) and (36) into the computer program produced results, as expected, identical to those of plane wave Lorentz–Mie theory. For illustration, Fig. 2 shows a computer program generated plot of the normalized source function,

$$\tilde{S} = |\mathbf{E}|^2/|E_0|^2, \tag{37}$$

in the equatorial (y-z) plane for a 5-$\mu$m-diam (radius, $a = 2.5\,\mu$m) water droplet in air with 1.06 $\mu$m wavelength (Nd:YAG laser wavelength) plane-wave irradiation. (Size parameter $\alpha = 2\pi a/\lambda = 14.82$, complex relative index of refraction $\bar{n} = 1.33 + 5.0\times10^{-6}i$.[12]) Spatial coordinates are normalized relative to the sphere radius. These results agreed identically with corresponding plane wave results generated by a separate Lorentz–Mie theory based computer program.

An additional test of the validity of the arbitrary incident beam theory and the computer program was to again choose an incident linearly polarized plane electromagnetic wave but this time with arbitrary propagation direction and arbitrary electric field direction. As expected, the results were identical to that of plane-wave Lorentz–Mie theory after taking into consideration a proper rotation of axis.

Another verification was obtained by comparing the time-averaged power absorbed by the sphere as determined from the far-field Poynting vector surface integration of Eq. (34) to the time-averaged power absorbed as determined from internal sphere ohmic heating considerations. The time-average ohmic heating per unit volume within the sphere is given by

$$\tfrac{1}{2}\mathrm{Re}(\mathbf{J}\cdot\mathbf{E}^*) = \tfrac{1}{2}\sigma_{int}|\mathbf{E}|^2, \tag{38}$$

where the electrical conductivity $\sigma_{int}$ can be related to the complex index of refraction by $\sigma_{int} = 4\pi c\,\mathrm{Re}(\bar{n})\mathrm{Im}(\bar{n})k_0\epsilon_{ext}$. An integration of the time-averaged ohmic heating per volume over the volume of the sphere gives the total time-averaged ohmic heating:

$$W_{abs} = \int_0^a \int_0^\pi \int_0^{2\pi} \tfrac{1}{2}\, \sigma_{int} \,|E(r,\theta,\phi)|^2 r^2$$

$$\times \sin\theta \, d\phi \, d\theta \, dr. \tag{39}$$

In all cases, the results of Eqs. (34) and (39) were in agreement.

## IV. FOCUSED GAUSSIAN BEAM RESULTS

Calculations were performed for a focused fundamental Gaussian beam incident upon a water droplet in air for conditions analogous to those of Fig. 2 ($\lambda = 1.06\,\mu$m, $d = 5.0$ $\mu$m.) A first-order focused fundamental Gaussian beam model as developed by Davis[8] was used for the incident beam description. (Refer to Appendix B.) The beam is assumed to propagate in the $+z$ axis direction with predominate electric field polarization along the $x$ axis (TEM$_{00}$ mode). Even though this focused fundamental Gaussian beam description does not exactly satisfy Maxwell's equations, it was found to be a good approximation as long as the beam waist radius ($w_0$) is greater than a wavelength. For these calculations, a beam waist radius of $2\,\mu$m ($w_0/a = 0.8$) was chosen.

Figure 3 shows an equatorial ($y$-$z$) plane plot of the normalized source function for on-center focal point positioning. The source function is normalized relative to the beam focal point electric field amplitude. The intensity profile of the incident Gaussian beam, modified by some backscatter from the droplet, is apparent along the right-hand side of the plot. The incident Gaussian beam calculation of Fig. 3 can be compared with the corresponding incident plane wave calculation of Fig. 2. Both Figs. 2 and 3 indicate a peak in the electric field magnitude just off the shadow side surface of the droplet, but internal to the droplet the Gaussian beam calculations indicate a much stronger channeling of the beam energy through the center of the droplet, as might be expected.

The influence of off-center focal point positioning was investigated. The time-averaged power absorbed $W_{abs}$ was calculated, using Eq. (34), as a function of focal point positioning along the $x$, $y$, and $z$ axes. The maximum power absorbed was found to occur for on-center focal point positioning and a normalized power absorbed,

$$\widetilde{W}_{abs} = W_{abs}/W_{abs,FP}, \tag{40}$$

was defined relative to the on-center focal point positioning value,

$$W_{abs,FP} = 2.663 \times 10^{-4} (c/8\pi) a^2 E_0^2.$$

Figure 4 shows the normalized power absorbed versus focal point positioning along the $z$ axis. The power absorbed by the droplet decreases as the focal point is moved away from the droplet center because of the spreading of the beam. For the conditions here, the effect is nearly symmetrical with regard to illuminated side or shadow side focal point positioning. As might be expected, as the focal point is removed from the droplet along the $z$ axis, the normalized source function distribution internal and near-surface the droplet approaches that of a plane wave due to incident beam spreading. For example, Fig. 5 shows the equatorial plane normalized source function for focal point positioning 10



FIG. 4. Normalized power absorbed vs focal point positioning along the $z$ axis. Focused TEM$_{00}$ mode Gaussian beam incident upon a homogeneous sphere. $\alpha = 14.82$, $\bar{n} = 1.33 + 5.0 \times 10^{-6} i$, and $w_0/a = 0.8$ (5-$\mu$m-diam water droplet in air at $\lambda = 1.06\,\mu$m).
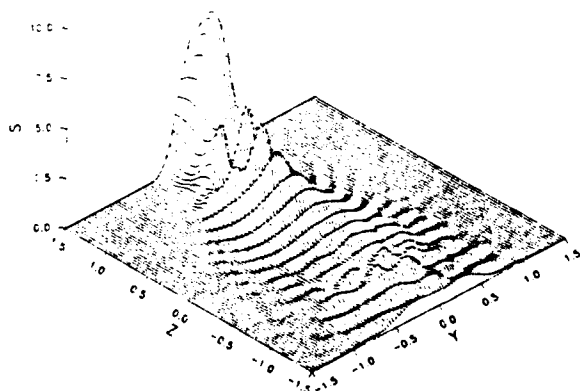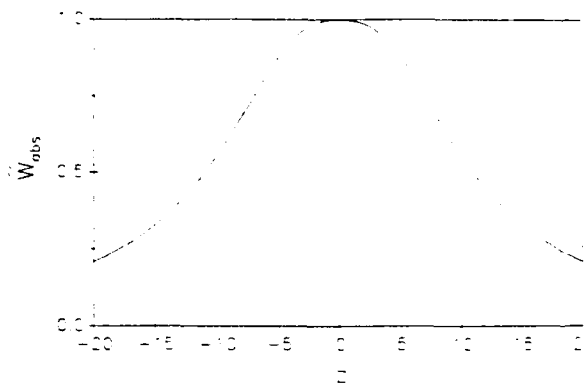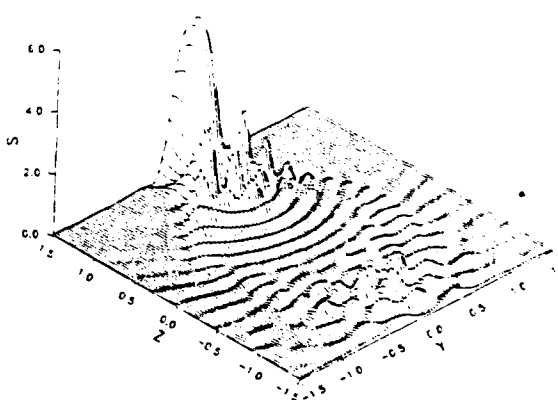


FIG. 3. Normalized source function in the equatorial ($y$-$z$) plane for a transverse polarized TEM$_{00}$ mode focused Gaussian beam propagating in the $+z$ direction incident upon a homogeneous sphere with on-center focal point positioning. $\alpha = 14.82$, $\bar{n} = 1.33 + 5.0 \times 10^{-6} i$, and $w_0/a = 0.8$ (5-$\mu$m-diam water droplet in air at $\lambda = 1.06\,\mu$m).



FIG. 5. Normalized source function in the equatorial ($y$-$z$) plane for a transverse polarized TEM$_{00}$ mode focused Gaussian beam propagating in the $+z$ axis direction incident upon a homogeneous sphere with $z/a = -10$ focal point positioning. $\alpha = 14.82$, $\bar{n} = 1.33 + 5.0 \times 10^{-6} i$, and $w_0/a = 0.8$ (5-$\mu$m-diam water droplet in air at $\lambda = 1.06\,\mu$m).

1636     J. Appl. Phys., Vol. 64, No. 4, 15 August 1988

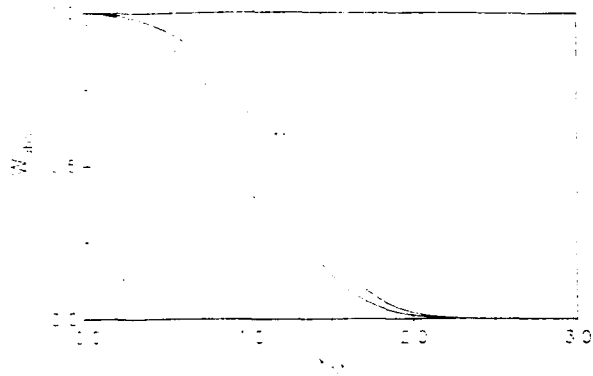Barton, Alexander, and Schaub     1636

FIG. 6. Normalized power absorbed vs focal point positioning along the x and y axes. Focused $TEM_{00}$ mode Gaussian beam incident upon a homogeneous sphere. $\alpha = 14.82$, $\bar{n} = 1.33 + 5.0 \times 10^{-6}i$, and $w_0/a = 0.8$ (5-$\mu$m-diam water droplet in air at $\lambda = 1.06 \mu$m).



FIG. 8. Normalized source function in the equatorial (y-z) plane for a transverse polarized $TEM_{01}$ mode focused Gaussian beam propagating in the $+z$ axis direction incident upon a homogeneous sphere with $y/a = 1.0$ focal point positioning. $\alpha = 14.82$, $\bar{n} = 1.33 + 5.0 \times 10^{-6}i$, and $w_0/a = 0.8$ (5-$\mu$m-diam water droplet in air at $\lambda = 1.06 \mu$m).

sphere radii in front of the droplet ($z/a = -10$) which compares closely in form with the corresponding incident plane wave calculation of Fig. 2.

The normalized power absorbed for focal point positioning along the x and y axes is given in Fig. 6. Again, as expected, the power absorbed is reduced as the focal point is moved away from the sphere center. For the conditions considered here, the decrease in power absorbed is slightly greater for focal point positioning parallel to the direction of primary electric field polarization (along the x axis) than for an equal distance perpendicular to the direction of primary electric field polarization (along the y axis). Figure 7 shows the equatorial plane source function for focal point positioning half a radius along the y axis ($y/a = 0.5$), and Fig. 8 shows a similar plot for focal point positioning a full radius along the y axis (at the side of the droplet, $y/a = 1.0$). The concentration of beam energy to the side of focal point posi-
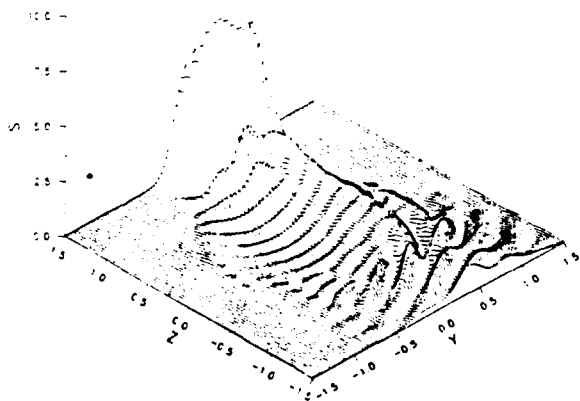
tioning is apparent and the distribution of the normalized source function is quite different from either that of on-center focal point positioning (Fig. 3) or that of the incident plane wave (Fig. 2).

The effect of focal point positioning along the x axis is demonstrated by the transverse (x-z) plane normalized source function plots of Figs. 9, 10, and 11. Figure 9 is for on-center focal point positioning, Fig. 10 is for focal point positioning one-half radius along the x axis ($x/a = 0.5$), and Fig. 11 is for focal point positioning one radius along the x axis (at the top of the droplet, $x/a = 1.0$). The discontinuity in the normalized source function at the surface of the droplet arises due to the presence of surface charges, a characteristic of such plots in the plane of polarization. Once again, the concentration of the beam energy towards the location of the focal point and the effect on the distribution of the normalized source function is apparent.
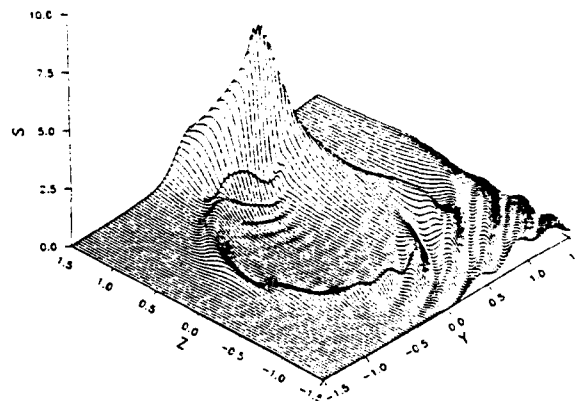


FIG. 7. Normalized source function in the equatorial (y-z) plane for a transverse polarized $TEM_{01}$ mode focused Gaussian beam propagating in the $+z$ axis direction incident upon a homogeneous sphere with $y/a = 0.5$ focal point positioning. $\alpha = 14.82$, $\bar{n} = 1.33 + 5.0 \times 10^{-6}i$, and $w_0/a = 0.8$ (5-$\mu$m-diam water droplet in air at $\lambda = 1.06 \mu$m).



FIG. 9. Normalized source function in the transverse (x-z) plane for a transverse polarized $TEM_{01}$ mode focused Gaussian beam propagating in the $+z$ axis direction incident upon a homogeneous sphere with on-center focal point positioning. $\alpha = 14.82$, $\bar{n} = 1.33 + 5.0 \times 10^{-6}i$, and $w_0/a = 0.8$ (5-$\mu$m-diam water droplet in air at $\lambda = 1.06 \mu$m).
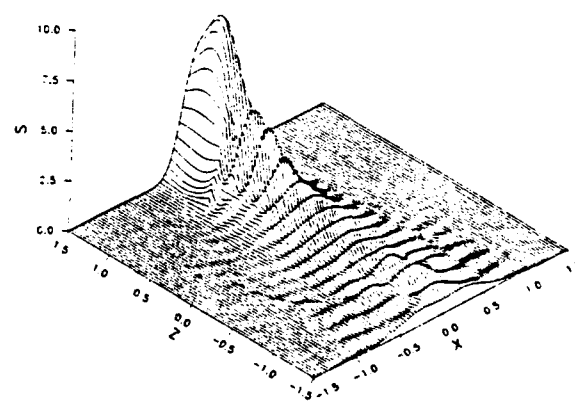
FIG. 10. Normalized source function in the transverse (x-z) plane for a transverse polarized TEM$_{00}$ mode focused Gaussian beam propagating in the $+z$ axis direction incident upon a homogeneous sphere with $x/a = 0.5$ focal point positioning. $\alpha = 14.82$, $\bar{n} = 1.33 + 5.0 \times 10^{-6}i$, and $w_0/a = 0.8$ (5-$\mu$m-diam water droplet in air at $\lambda = 1.06\,\mu$m).

## V. CONCLUSIONS

Theoretical expressions for the internal and external electromagnetic fields for an arbitrary electromagnetic beam incident upon a homogeneous spherical particle have been derived and, for the first time, numerical calculations of internal and near-surface electric field magnitude distributions for a focused fundamental Gaussian beam incident upon a spherical particle have been presented. In particular, calculations for a focused fundamental Gaussian beam of 1.06 $\mu$m wavelength and 4 $\mu$m beam waist diameter incident upon a 5-$\mu$m-diam water droplet in air indicate that the electric field magnitude (source function) distribution internal and near-surface the droplet can be strongly dependent upon focal point positioning and may differ significantly from the electric field magnitude distribution that results from plane-wave irradiation. A more thorough investigation of the dependence of power absorbed and electric field magnitude distribution on such parameters as beam waist diameter,
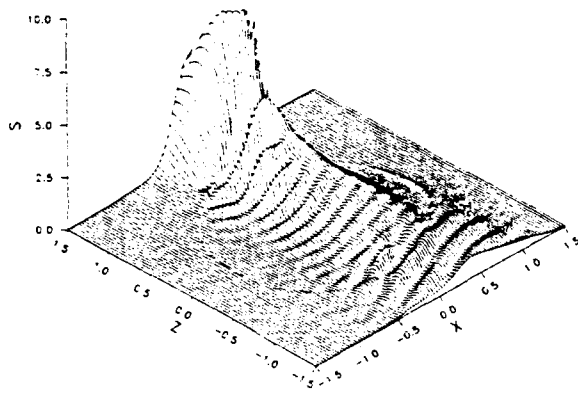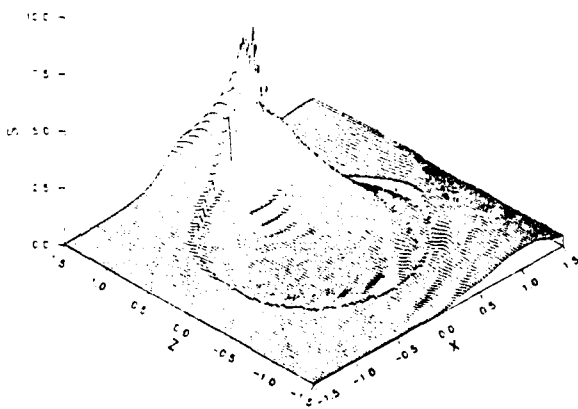


FIG. 11. Normalized source function in the transverse (x-z) plane for a transverse polarized TEM$_{00}$ mode focused Gaussian beam propagating in the $+z$ axis direction incident upon a homogeneous sphere with $x/a = 1.0$ focal point positioning. $\alpha = 14.82$, $\bar{n} = 1.33 + 5.0 \times 10^{-6}i$, and $w_0/a = 0.8$ (5-$\mu$m-diam water droplet in air at $\lambda = 1.06\,\mu$m).

beam focal point positioning, droplet size, and droplet complex index of refraction, including a comparison with experimental laser beam/liquid droplet explosive vaporization data[13] and experimental laser beam/liquid droplet elastic and stimulated Raman scattering data,[14] will be presented in a later paper.

## ACKNOWLEDGMENT

## APPENDIX A: MAGNETIC FIELD EQUATIONS

### Incident magnetic field

$$H_r^{(i)} = \frac{1}{r^2} \sum_{l=1}^{\infty} \sum_{m=-l}^{l} [l(l+1)B_{lm}\psi_l(k_{ext}r)Y_{lm}(\theta,\phi)],$$
(A1)

$$H_\theta^{(i)} = \frac{1}{r} \sum_{l=1}^{\infty} \sum_{m=-l}^{l} \left( -imk_{ext}^1 A_{lm}\psi_l(k_{ext}r)\frac{Y_{lm}(\theta,\phi)}{\sin\theta} \right.$$
$$\left. + k_{ext}B_{lm}\psi_l'(k_{ext}r)\frac{\partial Y_{lm}(\theta,\phi)}{\partial\theta} \right),$$
(A2)

and

$$H_\phi^{(i)} = \frac{1}{r} \sum_{l=1}^{\infty} \sum_{m=-l}^{l} \left( k_{ext}^1 A_{lm}\psi_l(k_{ext}r)\frac{\partial Y_{lm}(\theta,\phi)}{\partial\theta} \right.$$
$$\left. + imk_{ext}B_{lm}\psi_l'(k_{ext}r)\frac{Y_{lm}(\theta,\phi)}{\sin\theta} \right).$$
(A3)

### Scattered magnetic field

$$H_r^{(s)} = \frac{1}{r^2} \sum_{l=1}^{\infty} \sum_{m=-l}^{l} [l(l+1)b_{lm}\xi_l^{(1)}(k_{ext}r)Y_{lm}(\theta,\phi)],$$
(A4)

$$H_\theta^{(s)} = \frac{1}{r} \sum_{l=1}^{\infty} \sum_{m=-l}^{l} \left( -imk_{ext}^1 a_{lm}\xi_l^{(1)}(k_{ext}r)\frac{Y_{lm}(\theta,\phi)}{\sin\theta} \right.$$
$$\left. + k_{ext}b_{lm}\xi_l^{(1)\prime}(k_{ext}r)\frac{\partial Y_{lm}(\theta,\phi)}{\partial\theta} \right),$$
(A5)

and

$$H_\phi^{(s)} = \frac{1}{r} \sum_{l=1}^{\infty} \sum_{m=-l}^{l} \left( k_{ext}^1 a_{lm}\xi_l^{(1)}(k_{ext}r)\frac{\partial Y_{lm}(\theta,\phi)}{\partial\theta} \right.$$
$$\left. + imk_{ext}b_{lm}\xi_l^{(1)\prime}(k_{ext}r)\frac{Y_{lm}(\theta,\phi)}{\sin\theta} \right).$$
(A6)

### Internal magnetic field

$$H_r^{(w)} = \frac{1}{r^2} \sum_{l=1}^{\infty} \sum_{m=-l}^{l} [l(l+1)d_{lm}\psi_l(k_{int}r)Y_{lm}(\theta,\phi)],$$
(A7)

$$H_\theta^{(w)} = \frac{1}{r} \sum_{l=1}^{\infty} \sum_{m=-l}^{l} \left( -imk_{int}^1 c_{lm}\psi_l(k_{int}r)\frac{Y_{lm}(\theta,\phi)}{\sin\theta} \right.$$
$$\left. + k_{int}d_{lm}\psi_l'(k_{int}r)\frac{\partial Y_{lm}(\theta,\phi)}{\partial\theta} \right),$$
(A8)

and

$$H_\theta^{(w)} = \frac{1}{r} \sum_{l=1}^{\infty} \sum_{m=-l}^{l} \left( k_{\text{int}}^{-1} c_{lm} \psi_l^{\prime}(k_{\text{int}} r) \frac{\partial Y_{lm}(\theta,\phi)}{\partial \theta} \right.$$

$$\left. + i m k_{\text{int}} d_{lm} \psi_l^{\prime}(k_{\text{int}} r) \frac{Y_{lm}(\theta,\phi)}{\sin \theta} \right). \tag{A9}$$

## APPENDIX B: FOCUSED GAUSSIAN BEAM DESCRIPTION

$$E_x^{(i)} = E_0 \psi_0^* \exp(i k_{\text{ext}} z), \tag{B1}$$

$$E_y^{(i)} = 0, \tag{B2}$$

$$E_z^{(i)} = -(2Q^* x/l) E_x^{(i)}, \tag{B3}$$

$$H_x^{(i)} = 0, \tag{B4}$$

$$H_y^{(i)} = \sqrt{\epsilon_{\text{ext}}} E_x^{(i)}, \tag{B5}$$

and

$$H_z^{(i)} = -(2Q^* y/l) H_y^{(i)}, \tag{B6}$$

where

$$l = k_{\text{ext}} w_0^2, \tag{B7}$$

$$Q = 1/(i + 2\zeta), \tag{B8}$$

$$\zeta = z/l, \tag{B9}$$

$$\psi_0 = iQ \exp(-iQ\rho^2), \tag{B10}$$

and

$$\rho = \sqrt{x^2 + y^2}/w_0. \tag{B11}$$

[1] P. W. Dusel, M. Kerker, and D. D. Cooke, J. Opt. Soc. Am. **69**, 55 (1979).
[2] W. M. Greene, R. E. Spjut, E. Bar-Ziv, A. F. Sarofim, and J. P. Longwell, J. Opt. Soc. Am. B **2**, 998 (1985).
[3] N. Morita, T. Tanaka, T. Yamasaki, and Y. Nakanishi, IEEE Trans. Antennas Propag. **AP-16**, 724 (1968).
[4] W.-C. Tsai and R. J. Pogorzelski, J. Opt. Soc. Am. **65**, 1457 (1975).
[5] W. G. Tam and R. Corriveau, J. Opt. Soc. Am. **68**, 763 (1978).
[6] J. S. Kim and S. S. Lee, J. Opt. Soc. Am. **73**, 303 (1983).
[7] G. Gouesbet, G. Grehan, and B. Maheu, J. Opt. (Paris) **16**, 83 (1985).
[8] L. W. Davis, Phys. Rev. A **19**, 1177 (1979).
[9] M. Born and E. Wolf, *Principles of Optics* (Pergamon, Oxford, 1970).
[10] W. D. Ross, Appl. Opt. **11**, 1919 (1972).
[11] W. H. Press, B. P. Flannery, S. A. Teukolsky, and W. T. Vetterling, *Numerical Recipes: The Art of Scientific Computing* (Cambridge University, Cambridge, England, 1986).
[12] G. M. Hale and M. R. Querry, Appl. Opt. **12**, 555 (1973).
[13] D. R. Alexander and J. G. Armstrong, Appl. Opt. **26**, 533 (1987).
[14] J. Z. Zhang, D. H. Leach, and R. K. Chang, Opt. Lett. **13**, 270 (1988).

# Internal fields of a spherical particle illuminated by a tightly focused laser beam: Focal point positioning effects at resonance

J. P. Barton, D. R. Alexander, and S. A. Schaub

*Center for Electro-Optics, College of Engineering, University of Nebraska-Lincoln, Lincoln, Nebraska 68588-0525*

The spherical particle/arbitrary beam interaction theory developed in an earlier paper is used to investigate the dependence of structural resonance behavior on focal point positioning for a spherical particle illuminated by a tightly focused (beam diameter less than sphere diameter), linearly polarized, Gaussian-profiled laser beam. Calculations of absorption efficiency and distributions of normalized source function (electric field magnitude) are presented as a function of focal point positioning for a particle with a complex relative index of refraction of $\bar{n} = 1.33 + 5.0 \times 10^{-6}i$ and a size parameter of $\alpha \approx 29.5$ at both nonresonance and resonance conditions. The results of the calculations indicate that structural resonances are not excited during the on-center focal point positioning of such a tightly focused beam but structural resonances can be excited by proper on-edge focal point positioning. Electric wave resonances were found to be excited by moving the focal point from on-center towards the edge of the sphere *parallel* to the direction of the incident beam electric field polarization. Magnetic wave resonances were found to be excited by moving the focal point from on-center towards the edge of the sphere *perpendicular* to the direction of the incident beam electric field polarization.

## I. INTRODUCTION

In an earlier paper,[1] theoretical expressions for the internal and external electromagnetic fields of a homogeneous spherical particle illuminated by an arbitrarily defined beam were derived. In particular, calculations of absorption efficiency and distributions of normalized source function (electric field magnitude) were presented for a spherical particle illuminated by a tightly focused (beam diameter less than sphere diameter), linearly polarized, Gaussian-profiled, monochromatic beam. This situation corresponds to the important experimental arrangement of focusing a high-quality $TEM_{00}$ mode laser beam upon a small liquid droplet in air (or upon any suspended spherical particle). In this paper, additional calculations are presented in which the effect of beam focal point positioning on the absorption efficiency and internal normalized source function distribution is investigated for spherical particles at structural resonance conditions.

A spherical particle has a series of associated structural resonances which can be excited by incident radiation. For transparent (weakly absorbing) particles, resonance excitation is exhibited by an accompanying significant increase in the absorption and scattering of the incident radiation by the particle. Resonance effects have been experimentally observed through measurements of elastic scattering,[2,3] inelastic scattering,[4,5,6] and radiation pressure.[3,7]

Plane-wave Lorenz–Mie theory has been used to understand and predict resonance behavior, and excellent agreement with experimental measurements has been obtained.[2-7] However, plane-wave theory is not applicable for experiments utilizing tightly focused laser beams where the local beam diameter is less than the spherical particle diameter. Indeed, Ashkin and Dziedzic[3,7] have reported that resonances are not excited when such a tightly focused beam is aligned through the center of the spherical particle. But

Baer[8] and Zhang, Leach, and Chang[9] have observed *increased* resonance inelastic scattering when a tightly focused beam is aligned along the *edge* of a spherical particle.

In this paper, the spherical particle/arbitrary beam interaction theory developed in our earlier paper[1] is used to investigate the dependence of structural resonance behavior on focal point positioning when the beam diameter is tightly focused to less than the particle diameter. Corresponding plane-wave calculations are also presented for comparison. These calculations provide insight into understanding the experimental observations stated in the previous paragraph and also provide new observations which could be tested as part of future experiments.

## II. INCIDENT PLANE-WAVE CALCULATIONS

Previous investigators have used plane-wave Lorenz–Mie theory to analyze the structural resonance behavior of spherical particles and a brief review of this work, including calculations corresponding to the incident beam conditions of the next section, is useful here. In Lorenz–Mie theory a plane wave of transverse polarized electromagnetic radiation propagating within an infinite homogeneous dielectric medium is incident upon a homogeneous spherical particle of complex relative index of refraction $\bar{n}$. The spatial coordinates are referenced to the center of the spherical particle, as shown in Fig. 1. The incident plane wave is assumed to propagate in the $+z$-axis direction with electric field polarization in the $x$-axis direction.

Following the development approach of the Lorenz–Mie theory, the electromagnetic field components internal to and scattered by the spherical particle can each be mathematically expressed in the form of an infinite series of partial waves. The partial waves, in turn, are of two types: electric waves, which have no radial component of magnetic field, and magnetic waves, which have no radial component
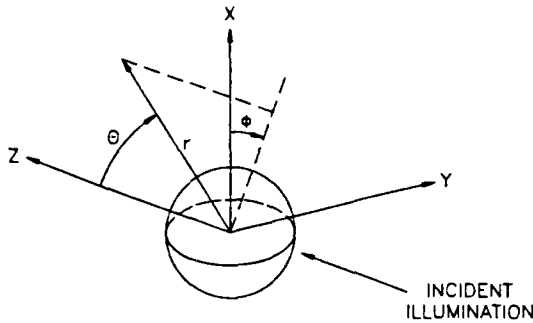
FIG. 1. Geometry for a plane-wave or focused Gaussian beam incident upon a spherical particle.

of electric field. Series expressions for the scattered electromagnetic fields, including a complete derivation, can be found in Born and Wolf,[10] and series expressions for the internal electromagnetic field components can be found in Kerker and Cooke.[11]

The coefficient for the $l$ th electric wave term within the scattered field series is given by

$$a_l = \frac{\psi_l'(\bar{n}\alpha)\psi_l(\alpha) - \bar{n}\psi_l'(\alpha)\psi_l(\bar{n}\alpha)}{\xi_l^{(1)}(\alpha)\psi_l'(\bar{n}\alpha) - \bar{n}\xi_l^{(1)'}(\alpha)\psi_l(\bar{n}\alpha)} , \qquad (1)$$

and the coefficient for the $l$ th magnetic wave term within the scattered field series is given by

$$b_l = \frac{\bar{n}\psi_l(\alpha)\psi_l'(\bar{n}\alpha) - \psi_l'(\alpha)\psi_l(\bar{n}\alpha)}{\bar{n}\xi_l^{(1)}(\alpha)\psi_l'(\bar{n}\alpha) - \xi_l^{(1)'}(\alpha)\psi_l(\bar{n}\alpha)} , \qquad (2)$$

where the prime refers to the derivative with respect to the argument, $\xi_l^{(1)} = \psi_l - i\chi_l$, $\psi_l$, and $\chi_l$ are the Riccati–Bessel functions, and $\alpha$ is the size parameter, $2\pi a/\lambda$, where $a$ is the sphere radius and $\lambda$ is the wavelength of the incident radiation.

Conditions for $l$ th mode electric wave structural resonance can be determined by setting the denominator of $a_l$ equal to zero and, likewise, conditions for $l$ th mode magnetic wave structural resonance can be determined by setting the denominator of $b_l$ equal to zero. (The $c_l$, $d_l$ coefficients for the internal field have the same respective denominators as the $a_l$, $b_l$ coefficients of the scattered field, thus the conditions for internal field structural resonance are identical to the conditions for the scattered field structural resonance.) For a specified value of $\bar{n}$, the solution of these equations requires a complex size parameter, the imaginary part of which describes the strength and width of the resonance (in electrical circuit analogy, the $Q$ of the resonance) and the real part of which corresponds (approximately) to the actual sphere radius/incident wavelength combination at which the resonance occurs. There is an infinite sequence of roots for each equation, with the root having the smallest real part designated as the first-order resonance, the root having the next to smallest real part designated as the second-order resonance, and so on.[12,13,14]

To illustrate resonance behavior, calculations were performed for a spherical particle in air with $\bar{n} = 1.33 + 5.0 \times 10^{-6}i$ and $\alpha$ values of the order of 29.5. These parameters correspond to an approximately 10-$\mu$m-diam water droplet with 1.06-$\mu$m (Nd:YAG laser) wavelength illumination. The absorption efficiency of the particle $Q_{abs}$, defined as the ratio of the total power absorbed by the particle to the power incident upon the projected area of the particle, can be expressed in terms of the incident plane-wave coefficients

$$Q_{abs} = \frac{2}{\alpha^2} \sum_{l=1}^{\infty} (2l+1)[\mathrm{Re}(a_l + b_l)$$
$$- (|a_l|^2 + |b_l|^2)] , \qquad (3)$$

and is given in Fig. 2 for a range of size parameters from 28 to 32. Each peak in absorption efficiency seen in Fig. 2 can be directly related to the first-order resonance indicated. Higher-order resonances of lower modes are also present within this range of size parameters, but are weak and not observable. As discussed by Chylek, Kiehl, and Ko,[12,13] for larger size parameters the first-order resonances become narrow while the higher-order (second, third, etc.) resonances heighten and become dominant.

Plots of the normalized source function within the spherical particle provides additional information with regard to the formation of structural resonances. The normalized source function is defined as

$$\tilde{S} = |\mathbf{E}|^2/E_0^2 , \qquad (4)$$

where $\mathbf{E}$ is the local electric field vector and $E_0$ is the electric field amplitude of the incident plane wave. The local volumetric heating rate is directly proportional to the normalized source function. In this paper, plots of the internal normalized source function distribution are presented either in the transverse ($x$-$z$) plane or the equatorial ($y$-$z$) plane. External sphere source function values are suppressed to zero in order to emphasize the internal sphere distribution and spatial coordinates are normalized by the sphere radius. (A tilde above a spatial quantity indicates that it has been normalized relative to the particle radius $a$.)

To compare internal sphere source function distributions at nonresonance, electric wave resonance, and magnetic wave resonance conditions, calculations were performed for the nonresonance case of $\alpha = 29.5$, the adjacent 34th mode, first-order electric wave resonance case of $\alpha = 29.753$, and the adjacent 34th mode, first-order magnetic wave resonance case of $\alpha = 29.365$ (refer to Fig. 2).
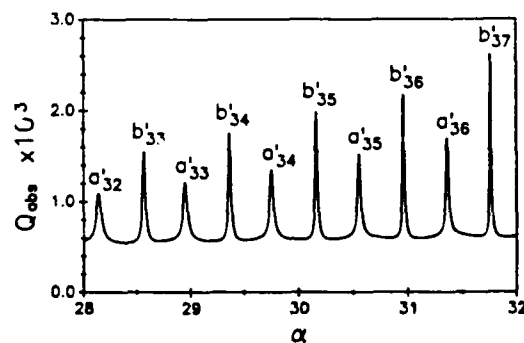


FIG. 2. Absorption efficiency vs size parameter for a plane wave incident upon a spherical particle. $\bar{n} = 1.33 + 5.0 \times 10^{-6}i$.

2901     J. Appl. Phys., Vol. 65, No. 8, 15 April 1989

Barton, Alexander, and Schaub     2901

Calculations for plane-wave illumination are shown in Figs. 3–6. Figure 3 is the normalized source function in the transverse $(x$-$z)$ plane for the nonresonance case of $\alpha = 29.5$. An equatorial $(y$-$z)$ plane plot for the same non-resonance case is given in Fig. 4. For the 34th mode, first-order electric wave resonance, it was found that, though there was insignificant difference in the equatorial plane normalized source function distribution in comparison with the nonresonance case (Fig. 4), there was a significant increase in the normalized source function in the transverse plane, as shown in Fig. 5. For the 34th mode, first-order magnetic wave resonance, little difference with the nonresonance case was observed in the transverse plane, but a significant increase in normalized source function was present in the equatorial plane, as shown in Fig. 6. In general, it was found that electric wave resonances were excited predominately in the transverse plane (parallel to the direction of incident electric field polarization) and magnetic wave resonances were excited predominately in the equatorial plane (perpendicular to the direction of incident electric field polarization) for plane-wave illumination.

The ring formation of the normalized source function just inside the surface of the sphere for the plane-wave illumination resonance cases, seen in Figs. 5 and 6, was reported by Chylek, Pendleton, and Pinnick,[15] who also observed that, in general, an $l$ th mode resonance will have $2l$ peaks arou .d the circumference, which is the case here. A physical exp anation for the occurrence of structural resonances, which is consistent with the ring formation of the normalized source function just beneath the surface of the particle, is the "surface wave" description first proposed by van de Hulst[16] and later discussed by other investigators.[17,18] van de Hulst proposed that structural resonances occur when surface waves constructively interfere about the circumference of the particle.

## III. INCIDENT BEAM CALCULATIONS

The theory of our earlier paper[1] was used to investigate structural resonance behavior for a spherical particle illuminated by a tightly focused laser beam as a function of focal point positioning. A focused, linearly polarized, Gaussian-profiled, monochromatic beam (a "focused Gaussian
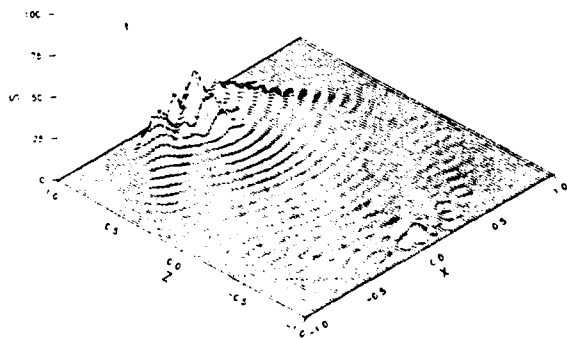
FIG. 4. Normalized source function in the equatorial $(y$-$z)$ plane for a transverse $(x$ direction) polarized plane wave propagating in the $+ z$-axis direction incident upon a sphere with $\bar{n} = 1.33 + 5.0 \times 10^{-6} i$ and $\alpha = 29.5$ (nonresonance).
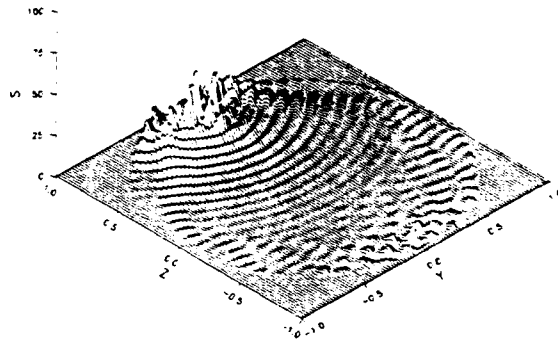
beam") propagating in the $+z$-axis direction and linearly polarized in the $x$-axis direction (refer to Fig. 1) is assumed. The beam was expressed mathematically using the first-order corrected paraxial beam description of Davis.[1,19] The coordinates $(x_0, y_0, z_0)$ are used to indicate the position of the center of the spherical particle relative to the focal point of the beam.

That an arbitrary beam can excite the same structural resonances as a plane wave is physically reasonable, and is also confirmed mathematically. As discussed in our earlier paper,[1] the derivation approach for the arbitrary beam incident upon a homogeneous spherical particle theory, similar to the Lorenz–Mie approach, is to express the internal and scattered electromagnetic fields of the spherical particle in the form of an infinite series of electric and magnetic waves. However, unlike the plane-wave Lorenz–Mie solution, the most general series form is chosen. The result is a nested series with each radial mode $l$ having $(2l + 1)$ associated angular modes. (For each radial mode $l$ the angular mode index $m$ may have integer values from $-l$ to $+l$.) The coefficients of the scattered field electric wave and magnetic wave $l$ th radial mode, $m$th angular mode terms, taken from our earlier paper,[1] are, respectively,

FIG. 3. Normalized source function in the transverse $(x$-$z)$ plane for a transverse $(x$ direction) polarized plane wave propagating in the $+ z$-axis direction incident upon a sphere with $\bar{n} = 1.33 + 5.0 \times 10^{-6} i$ and $\alpha = 29.5$ (nonresonance).

FIG. 5. Normalized source function in the transverse $(x$-$z)$ plane for a transverse $(x$ direction) polarized plane wave propagating in the $+ z$-axis direction incident upon a sphere with $\bar{n} = 1.33 + 5.0 \times 10^{-6} i$ and $\alpha = 29.753$ (34th mode, first-order electric wave resonance). (Note: Normalized source function truncated for values exceeding 100.)

2902     J. Appl. Phys., Vol 65. No. 8, 15 April 1989

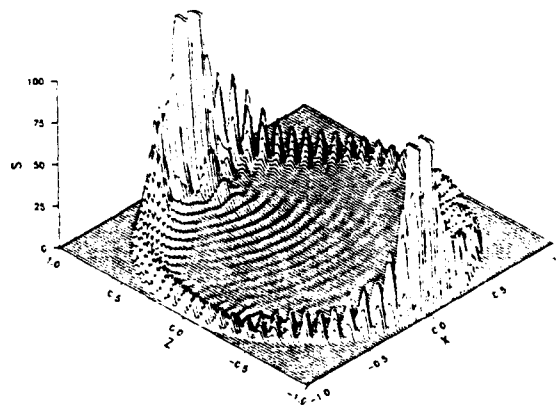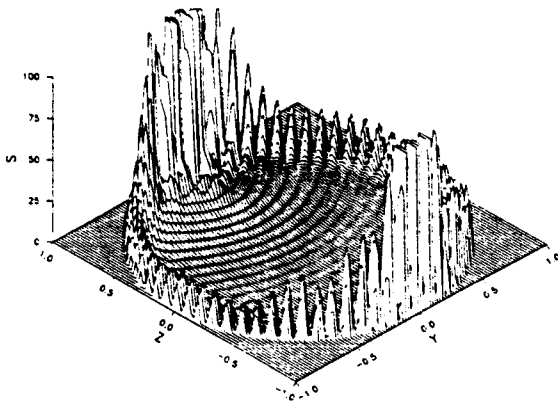Barton, Alexander, and Schaub     2902

FIG. 6. Normalized source function in the equatorial ($y$-$z$) plane for a transverse ($x$ direction) polarized plane wave propagating in the $+z$-axis direction incident upon a sphere with $\bar{n} = 1.33 + 5.0 \times 10^{-6} i$ and $\alpha = 29.365$ (34th mode, first-order magnetic wave resonance). (Note: Normalized source function truncated for values exceeding 100.)

$$a_{lm} = -a_l A_{lm} \qquad (5)$$

and

$$b_{lm} = -b_l B_{lm} , \qquad (6)$$

where $A_{lm}$ and $B_{lm}$ are incident field coefficients, the value of which are dependent upon the character of the incident beam, and $a_l$ and $b_l$ are the Lorenz–Mie plane-wave coefficients given in Eqs. (1) and (2). Since the scattered field electric wave and magnetic wave mode coefficients of the arbitrary beam theory are proportional to the respective plane-wave coefficients, structural resonance occurs at the same size parameters for arbitrary beam illumination as for plane-wave illumination. However, unlike the plane-wave resonance case, a particular beam radial resonance mode has associated with it $(2l + 1)$ angular modes. The relative excitation of each of these angular modes depends upon the character of the incident beam.

Beam calculations were performed for the same $\bar{n} = 1.33 + 5.0 \times 10^{-6} i$, $\alpha \approx 29.5$ conditions that were used for the plane-wave calculations of the previous section. A constant beam waist radius of $w_0 = 1.887\lambda$ was chosen. (For $\lambda = 1.06$-$\mu$m illumination, this would correspond to a 4-$\mu$m waist diameter beam incident upon an $\approx 10$-$\mu$m-diam particle.)

To explore the general effect of beam focal point positioning on structural resonance excitation, the spherical particle absorption efficiency was calculated for focal point positioning along the $x$, $y$, and $z$ axes of the spherical particle. A modified absorption efficiency $\tilde{Q}_{abs}$, defined as the ratio of the power absorbed by the spherical particle to the *total* power of the incident beam, was utilized. An expression for the power absorbed by the particle $W_{abs}$ was given in our earlier paper.[1] Dividing this expression by the total power of the incident beam

$$(c/16) E_0^2 w_0^2 ,$$

where, here, $E_0$ is the electric field amplitude at the beam focal point, provides a series expression for the modified absorption efficiency

$$\tilde{Q}_{abs} = -\frac{2\alpha^2}{\pi \bar{w}_0^2 a^4 E_0^2} \sum_{l=1}^{\infty} \sum_{m=-l}^{m=l} l(l+1) \left[ |a_{lm}|^2 + |b_{lm}|^2 \right.$$
$$\left. + \mathrm{Re}(A_{lm} a_{lm}^* + B_{lm} b_{lm}^*) \right] . \qquad (7)$$

Figure 7 shows the modified absorption efficiency for the $\alpha = 29.5$ (nonresonance), $\alpha = 29.753$ (34th mode, first-order electric wave resonance), and $\alpha = 29.365$ (34th mode, first-order magnetic wave resonance) cases for incident beam focal point positioning on the particle's $x$ axis ($0.0 \leqslant -\bar{x}_0 \leqslant 2.0$, $\bar{y}_0 = 0.0$, $\bar{z}_0 = 0.0$). As can be observed, the modified absorption efficiency is approximately equal for all three cases for focal point positioning near the center of the particle, but as the focal point of the beam is moved along the $x$ axis towards the surface of the particle, the modified absorption efficiency increases for the electric wave resonance case until it peaks at a focal point position just outside the particle surface before decreasing to zero as the beam is moved on away from the particle. In contrast, the modified absorption efficiency for the nonresonance and magnetic resonance cases decrease monotonically as the beam focal point position is moved away from the particle center.

Figure 8 presents the modified absorption efficiency for the same three cases presented in Fig. 7, but for beam focal point positioning along the $y$ axis ($\bar{x}_0 = 0.0$, $0.0 \leqslant -\bar{y}_0 \leqslant 2.0$, $\bar{z}_0 = 0.0$). In this arrangement, it is the magnetic wave resonance that is excited as the beam is moved from the center towards the particle surface, while the nonresonance and electric wave resonance cases decrease monotonically.

The lack of resonance excitation for on-center focal point positioning is consistent with the observation of Ashkin and Dziedzic[3,7] that resonances in radiation pressure did not appear for beams tightly focused through the center of a droplet. The excitation of resonance for beam focal point positioning near the surface of the spherical particle may explain the observations of Baer[8] and Zhang and co-workers[9] which indicated that increased resonance inelastic scattering can be obtained using such edge illumination. Apparently, to excite a structural resonance with a tightly focused beam it is necessary to position the focal point of the beam near the resonance ring formation that occurs for plane-wave illumination. According to van de Hulst's sur-



FIG. 7. Modified absorption efficiency vs focal point positioning along the $x$ axis. Transverse ($x$ direction) polarized focused Gaussian beam incident upon a sphere. $\bar{n} = 1.33 + 5.0 \times 10^{-6} i$, $\bar{w}_0 \alpha = 11.86$, and $\alpha = 29.365, 29.5,$ and $29.753$.

FIG. 8. Modified absorption efficiency vs focal point positioning along the $y$ axis. Transverse ($x$ direction) polarized focused Gaussian beam incident upon a sphere. $\bar{n} = 1.33 + 5.0 \times 10^{-6}i$, $\bar{w}_0\alpha = 11.86$, and $\alpha = 29.365, 29.5$, and 29.753.
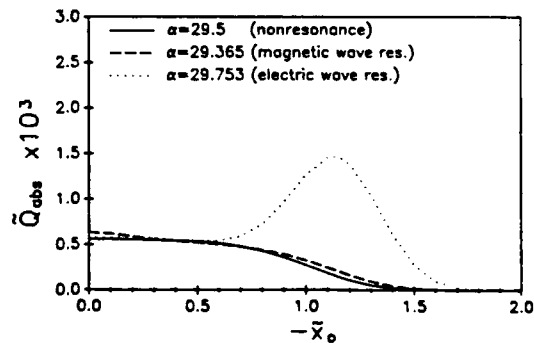


FIG. 9. Modified absorption efficiency vs focal point positioning along the $z$ axis. Transverse ($x$ direction) polarized focused Gaussian beam incident upon a sphere. $\bar{n} = 1.33 + 5.0 \times 10^{-6}i$, $\bar{w}_0\alpha = 11.86$, and $\alpha = 29.365, 29.5$, and 29.753.

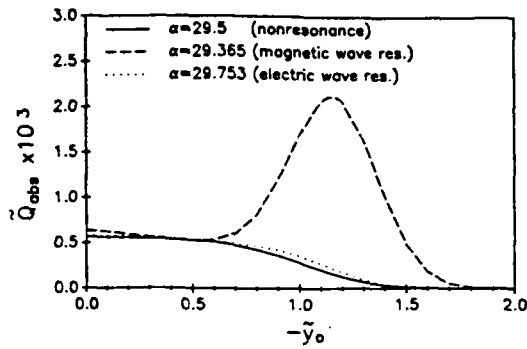face wave description, edge illumination is required to create the surface waves that constructively interfere to create the resonance.

In general, the calculations presented in Figs. 7 and 8 also suggest that only electric wave resonances are excited for edge illumination in the direction of incident electric field polarization and only magnetic wave resonances are excited for edge illumination perpendicular to the direction of incident electric field polarization. This observation, which was verified for the other resonance modes shown in Fig. 2, could be tested experimentally.

Another interesting observation is that the peak in structural resonance excitation occurs for beam focal point positioning outside the surface of the spherical particle. A possible physical explanation for this may lie within the "localization principle" discussed by van de Hulst[16] in which he indicates that, for radii much greater than a wavelength, the $l$th partial wave may be associated with a ray passing through a radial position

$$\bar{r} = (l + 1/2)/\alpha \qquad (8)$$

from the particle center. [Grehan and co-workers[20,21] have applied the localization principle to provide a mathematically simple, but approximate, determination of the interaction coefficients for their generalized Lorenz–Mie theory (GLMT) analysis.] Since for an $l$th mode structural resonance, it is the $l$th partial wave that is in resonance, a beam that is predominately characterized by that particular partial wave will excite the structural resonance. For the calculations considered here with $l = 34$, Eq. (7) gives $\bar{r} = 1.160$ for the $\alpha = 29.753$, electric wave resonance case, and $\bar{r} = 1.175$ for the $\alpha = 29.365$, magnetic wave resonance case. The peaks in the curves of Figs. 7 and 8 correspond approximately with these respective values. It appears then that van de Hulst's localization principle as expressed in Eq. (6) can be used to predict the approximate beam focal point positioning for maximum structural resonance excitation for an arbitrary $l$th mode resonance. This observation was also verified for several other complex relative index of refraction and resonance mode number combinations.

The modified absorption efficiency for focal point positioning along the $z$ axis (the incident beam propagation axis) for the nonresonance, electric wave resonance, and magnetic
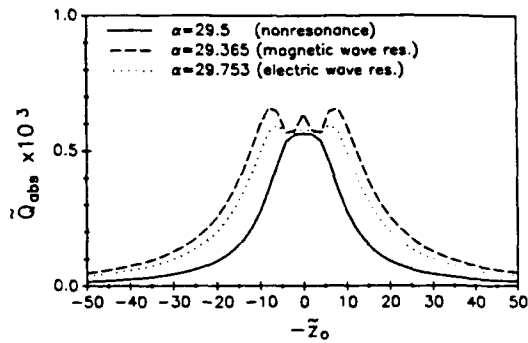
wave resonance cases is given in Fig. 9. For the nonresonance case, the modified absorption efficiency decreases monotonically as the beam focal point is moved away from the spherical particle due to the spreading of the beam incident upon the particle. However, for the resonance cases, moving the focal point of the tightly focused beam a relatively short distance away from the center of the sphere can actually increase the modified absorption efficiency when the beam spreads so as to provide illumination along the edge of the sphere that excites the structural resonances.

In general it was found, as was the case for plane-wave illumination, that electric wave resonances were predominately excited in the transverse plane (parallel to the direction of incident polarization) and magnetic wave resonances were predominately excited in the equatorial plane (perpendicular to the direction of incident polarization). The normalized source function distribution in the transverse ($x$-$z$) plane for the focused Gaussian beam positioned at the top edge of the particle ($\bar{x}_0 = -1.0$, $\bar{y}_0 = 0.0$, $\bar{z}_0 = 0.0$) is shown in Fig. 10 for the nonresonance case and in Fig. 11 for the electric wave resonance case. The normalized source function distribution in the equatorial ($y$-$z$) plane for the focused Gaussian beam positioned at the right edge of the particle ($\bar{x}_0 = 0.0$, $\bar{y}_0 = -1.0$, $\bar{z}_0 = 0.0$) is shown in Fig. 12 for the nonresonance case and in Fig. 13 for the magnetic



FIG. 10. Normalized source function in the transverse ($x$-$z$) plane for a transverse ($x$ direction) polarized focused Gaussian beam incident upon a sphere at nonresonance. $\bar{n} = 1.33 + 5.0 \times 10^{-6}i$, $\bar{w}_0 = 0.402$, $\bar{x}_0 = -1.0$, $\bar{y}_0 = 0.0$, $\bar{z}_0 = 0.0$, and $\alpha = 29.5$.
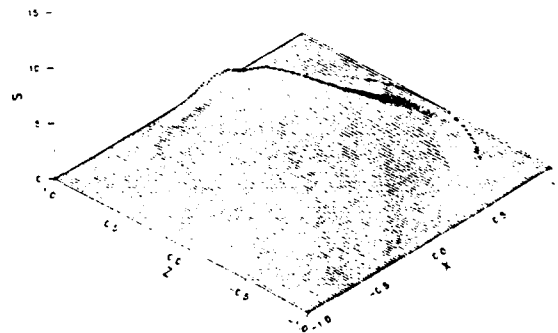
FIG. 11. Normalized source function in the transverse ($x$-$z$) plane for a transverse ($x$ direction) polarized focused Gaussian beam incident upon a sphere at electric wave resonance. $\bar{n} = 1.33 + 5.0 \times 10^{-6}i$, $\bar{w}_0 = 0.399$, $\bar{x}_0 = -1.0$, $\bar{y}_0 = 0.0$, $\bar{z}_0 = 0.0$, and $\alpha = 29.753$.



FIG. 13. Normalized source function in the equatorial ($y$-$z$) plane for a transverse ($x$ direction) polarized focused Gaussian beam incident upon a sphere at magnetic wave resonance. $\bar{n} = 1.33 + 5.0 \times 10^{-6}i$, $\bar{w}_0 = 0.404$, $\bar{x}_0 = 0.0$, $\bar{y}_0 = -1.0$, $\bar{z}_0 = 0.0$, and $\alpha = 29.365$.
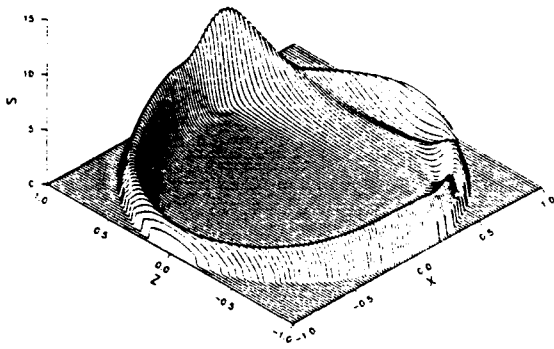
wave resonance case. For the resonance cases of Figs. 11 and 13 the beam excites a structural resonance producing a ring of increased normalized source function just inside the surface of the particle somewhat similar to the ring formation observed for plane-wave resonance illumination (Figs. 5 and 6). However, the ring formation for resonance beam illumination does not exhibit the $2l$ circumferential peaks that were observed for resonance plane-wave illumination but consists more of a solid ring. The difference in ring structure between the resonance plane wave and resonance beam cases is a consequence of the fact that for the plane-wave resonance only a single angular mode is "excited" while for beam resonance a series of angular modes ($-l \leqslant m \leqslant +l$) can be excited.

## IV. SUMMARY

The theory of our earlier paper[1] has been used to investigate the structural resonance behavior of a spherical particle illuminated by a tightly focused Gaussian beam. For the $\bar{n} = 1.33 + 5.0 \times 10^{-6}i$, $\alpha \approx 29.5$, and $w_0 = 1.887\lambda$ conditions considered here, it appears that:

(1) Electric wave resonances are excited predominately in the transverse plane (parallel to the direction of incident electric field polarization) and magnetic wave resonances
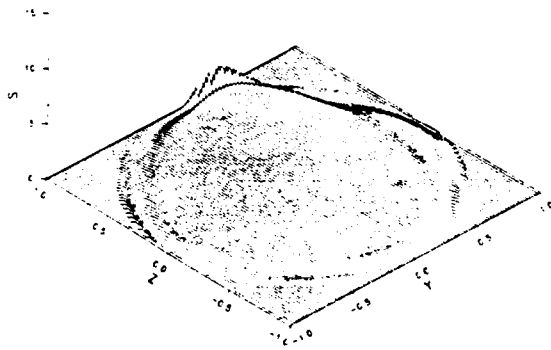
are excited predominately in the equatorial plane (perpendicular to the direction of incident electric field polarization).

(2) Structural resonances are not excited for on-center focal point positioning, but can be excited by on-edge focal point positioning.

(3) Electric wave resonances are excited for on-edge illumination in the direction of incident electric field polarization and magnetic wave resonances are excited by on-edge illumination perpendicular to the direction of incident electric field polarization.

(4) van de Hulst's "localization principle" can be used to predict the approximate radial location for focal point positioning that will provide maximum excitation of an arbitrary $l$ th mode structural resonance.

(5) The $2l$ circumferential peaks in the ring formation of normalized source function that occurs for plane-wave resonance are not exhibited for on-edge beam resonance excitation.

Observation (2) has already been verified by the experiments of Ashkin and Dziedzic.[3,7] Observations (1), (3), (4), and (5) could be tested as part of future experiments.

## ACKNOWLEDGMENT

FIG. 12. Normalized source function in the equatorial ($y$-$z$) plane for a transverse ($x$ direction) polarized focused Gaussian beam incident upon a sphere at nonresonance. $\bar{n} = 1.33 + 5.0 \times 10^{-6}i$, $\bar{w}_0 = 0.402$, $\bar{x}_0 = 0.0$, $\bar{y}_0 = -1.0$, $\bar{z}_0 = 0.0$, and $\alpha = 29.5$.
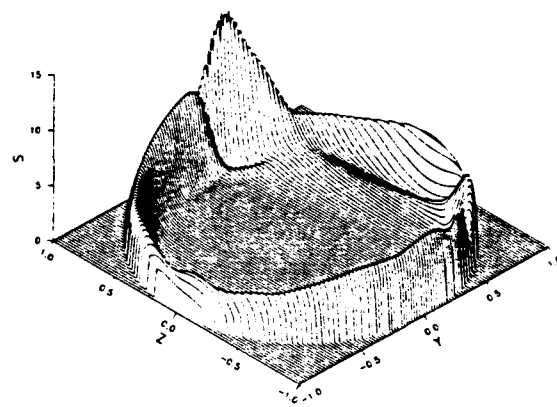
[1] J. P. Barton, D. R. Alexander, and S. A. Schaub, J. Appl. Phys. 64, 1632 (1988).
[2] P. Affolter and B. Eliasson, IEEE Trans. Microwave Theory Tech. MTT-21, 573 (1978).
[3] A. Ashkin and J. M. Dziedzic, Appl. Opt. 20, 1803 (1981).
[4] R. E. Benner, P. W. Barber, J. F. Owen, and R. K. Chang, Phys. Rev. Lett. 44, 475 (1980).
[5] R. Thurn and W. Kiefer, Appl. Opt. 24, 1515 (1985).
[6] J. B. Snow, S-X. Qian, and R. K. Chang, Opt. Lett. 10, 37 (1985).
[7] A. Ashkin and J. M. Dziedzic, Phys. Rev. Lett. 38, 1351 (1977).
[8] T. Baer, Opt. Lett. 12, 392 (1987).
[9] J-Z. Zhang, D. H. Leach, and R. K. Chang, Opt. Lett. 13, 270 (1988).
[10] M. Born and E. Wolf, Principles of Optics (Pergamon, Oxford, 1970).
[11] M. Kerker and D. D. Cooke, Appl. Opt. 12, 1378 (1973).

2905    J. Appl. Phys., Vol. 65, No. 8, 15 April 1989

Barton, Alexander, and Schaub    2905

[12]P. Chylek, J. T. Kiehl, and M. K. W. Ko, Appl. Opt. 17, 3019 (1978).

[13]P. Chylek, J. T. Kiehl, and M. K. W. Ko, Phys. Rev. A 18, 2229 (1978).

[14]P. R. Conwell, P. W. Barber, and C. K. Rushforth, J. Opt. Soc. Am. A 1, 62 (1984).

[15]P. Chylek, J. D. Pendleton, and R. G. Pinnick, Appl. Opt. 24, 3940 (1985).

[16]H. C. van de Hulst, *Light Scattering by Small Particles* (Dover, New York, 1981).

[17]A. B. Pluchino, Appl. Opt. 20, 2987 (1981).

[18]J. D. Murphy, P. J. Moser, A. Nagel, and H. Uberall, IEEE Trans. Antennas Propag. AP-28, 924 (1980).

[19]L. W. Davis, Phys. Rev. A 19, 1177 (1979).

[20]G. Grehan, B. Maheu, and G. Gouesbet, Appl. Opt. 25, 3539 (1986).

[21]B. Maheu, G. Grehan, and G. Gouesbet, Appl. Opt. 26, 23 (1987).

# Focused laser beam interactions with methanol droplets: effects of relative beam diameter

Scott A. Schaub, Dennis R. Alexander, John P. Barton, and Mark A. Emanuel

The effect of the local diameter of a focused $CO_2$ laser beam on calculated internal source function distributions and experimentally observed explosive characteristics is examined for 165-$\mu$m spherical methanol droplets. Experimental results show that the location and the characteristics of the explosive process change as the droplet is moved out of the laser focal point along the axis of propagation. Theoretical calculations indicate that, when the beam diameter is of the same order of magnitude as the droplet diameter, a modification of Mie theory, accounting for the finite beam size of the laser, is necessary to provide results which are consistent with experimental observations.

## I. Introduction

When investigating the interaction of high energy laser beams with aerosol droplets, the effect of the finite diameter of focused laser beams is of interest. In cases where the beam diameter is significantly larger than the droplet diameter, the plane wave approximation is apparently valid. However, in situations when the beam diameter is of the same order of magnitude as the droplet diameter, the validity of plane wave theory is uncertain. This situation is frequently encountered in experimentation[1-3] since the use of focused laser beams is often necessary to obtain sufficiently high laser intensities. In this paper the differences that plane wave and focused laser beams have on the laser–aerosol interaction for 165-$\mu$m spherical methanol droplets are examined from both a theoretical and experimental viewpoint.

## II. Theory

The theoretical development for a plane electromagnetic wave incident on a homogeneous absorbing sphere was first presented by Mie[4] in 1908 and by Debye[5] in 1909. This mathematical solution has been used extensively in attempts to better understand the interaction between laser light and spherical aerosol particles. The extension of Mie theory to arbitrary incident beams has been presented in detail by Barton

et al.[6] and allows the calculation of both the internal and external electric and magnetic fields for any arbitrary incident beam for which an accurate mathematical description is known. The fundamental (TEM$_{00}$ mode) Gaussian beam description used in this paper has been derived by Davis.[7] In the theoretical calculations to follow, only the first-order corrections, as presented by Davis, are used in the description of the incident Gaussian beam. This beam description has been applied to a similar Gaussian beam/spherical particle interaction analysis[8] and has provided accurate results as long as the wavelength is small compared to the laser beam diameter.

## III. Experimental

In the experimental arrangement shown in Fig. 1, a cw $CO_2$ laser (Advanced Kinetics model MIRL-100) operating at a wavelength of 10.6 $\mu$m in the fundamental TEM$_{00}$ mode is focused to a beam waist diameter, $2w_0$, of ~120 $\mu$m. (The beam diameter is expressed as $2w$ where $w$ represents the radial location at which the laser intensity falls to $1/e^2$, its value along the propagation axis. Quantities subscripted with 0 are evaluated at the focal point of the laser.) Monodisperse spherical droplets are generated using a vibrating orifice generator (TSI model 3450) and fall through the laser beam while being simultaneously imaged using a pulsed $N_2$ laser system ($\lambda$ = 337 nm, 10-ns FWHM). By changing the vibrating frequency and the orifice size of the generator, drops from ~20 to 500 $\mu$m can be generated. The characteristics of the explosion phenomena are observed by viewing real time images of the drop explosions utilizing the $N_2$ imaging system. These images, obtained using 10-ns illumination pulses, can be viewed at various time intervals during the explosion process. In addition to providing a
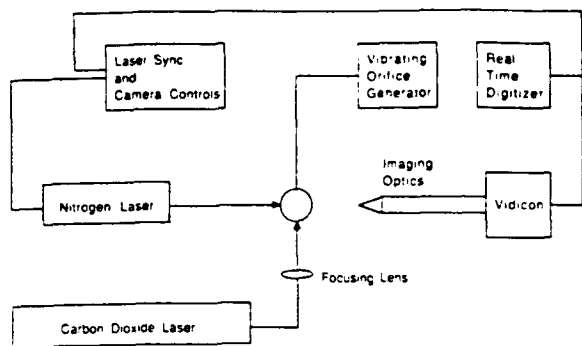
Fig. 1. Schematic of the experimental configuration.



Fig. 2. Interaction of a 165-$\mu$m methanol droplet ($\bar{n}$ = 1.395 + 0.0163$i$) with $\lambda$ = 10.6-$\mu$m radiation at an incident laser intensity of ~100 kW/cm$^2$. The droplet is located at the laser focal point ($2w$ = 120 $\mu$m); the laser is propagating from left to right.
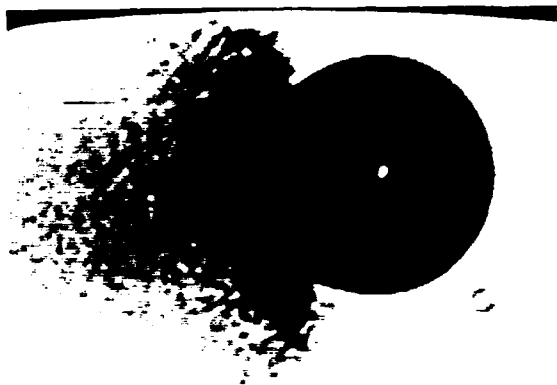


Fig. 3. Interaction of a 165-$\mu$m methanol droplet ($\bar{n}$ = 1.395 + 0.0163$i$) with $\lambda$ = 10.6-$\mu$m radiation at an incident laser intensity of ~15 kW/cm$^2$. The droplet is located ~7 mm behind the laser focal point ($2w$ = 800 $\mu$m); the laser is propagating from left to right.
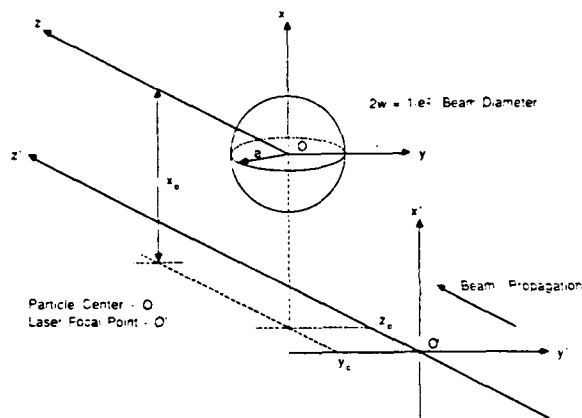


Fig. 4. Schematic of the geometry used for the theoretical calculations.

means for visualizing the explosion process, the $N_2$ imaging system also allows for accurate determination of particle size using a real time digitizer and particle sizing software.[9]

## IV. Results

The liquid used for the experiments considered here was methanol which has a complex refractive index of $\bar{n}$ = 1.395 + 0.0163$i$ (Ref. 10) at an incident wavelength of 10.6 $\mu$m. Figure 2 shows the explosive characteristics of a 165-$\mu$m methanol droplet located at the laser focal point. Figure 3 shows the same size methanol drop which has been positioned ~7 mm behind the laser focal point. In these photographs, the $CO_2$ laser is propagating from left to right. For both the focal point and 7-mm cases, the laser power was adjusted to a level slightly above that required to initiate explosive behavior. The laser intensities corresponded to ~100 kW/cm$^2$ for the focal point case and 15 kW/cm$^2$ for the 7-mm case. Examining Fig. 2, it is apparent that at this stage of the drop explosion, the illuminated hemisphere of the droplet has been fragmented extensively while the shadow hemisphere of the drop remains completely intact. Note that the beam diameter (120 $\mu$m)
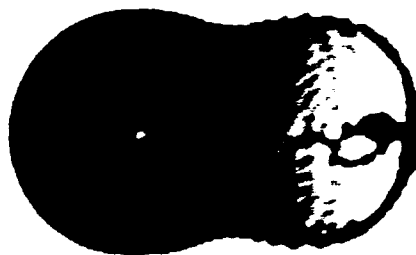
is smaller than the droplet diameter (165 $\mu$m) for the focused beam case shown in Fig. 2. In contrast, Fig. 3 shows the same size methanol droplet located 7 mm behind the laser focal point. This location would correspond to a beam diameter of ~800 $\mu$m which is significantly larger than the droplet diameter and more closely approximates plane wave illumination. At this position, the shadow hemisphere of the droplet is the first to show evidence of explosive vaporization. These observations suggest that the size of the laser beam relative to the droplet diameter has a direct effect on the explosive characteristics of large methanol droplets.

The geometry used for the theoretical calculations is shown in Fig. 4. A stationary particle of radius $a$, located at an arbitrary position ($x_0, y_0, z_0$) is illuminated by a fundamental Gaussian beam propagating in the $+z$ direction with linear polarization in the $x$ direction. Although the experimental observations shown in Figs. 2 and 3 were obtained using a stream of droplets falling through a focused laser beam, certain qualita-

Fig. 5. Computer generated plot of the normalized internal source function distribution within a 165-$\mu$m methanol droplet ($\bar{n}$ = 1.395 + 0.0163$i$) illuminated by a plane wave ($\lambda$ = 10.6 $\mu$m).



Fig. 7. Computer generated plot of the normalized internal source function distribution within a 165-$\mu$m methanol droplet ($\bar{n}$ = 1.395 + 0.0163$i$) illuminated by a Gaussian beam ($\lambda$ = 10.6 $\mu$m, $\bar{w}_0$ = 0.75, $\bar{x}_0$ = $\bar{y}_0$ = 0). The droplet is located 1.65 mm behind the laser focal point ($\bar{z}_0$ = 20).
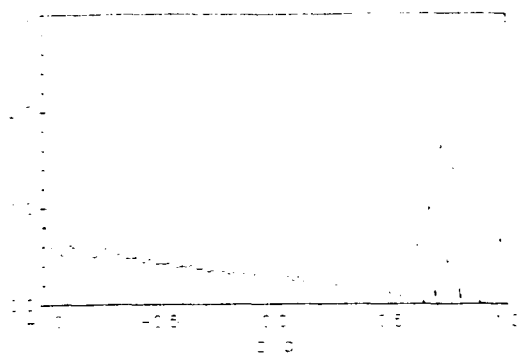


Fig. 6. Computer generated plot of the normalized internal source function distribution within a 165-$\mu$m methanol droplet ($\bar{n}$ = 1.395 + 0.0163$i$) illuminated by a Gaussian beam ($\lambda$ = 10.6 $\mu$m, $\bar{w}_0$ = 0.75, $\bar{x}_0$ = $\bar{y}_0$ = 0). The droplet is located 7 mm behind the laser focal point ($\bar{z}_0$ = 85).
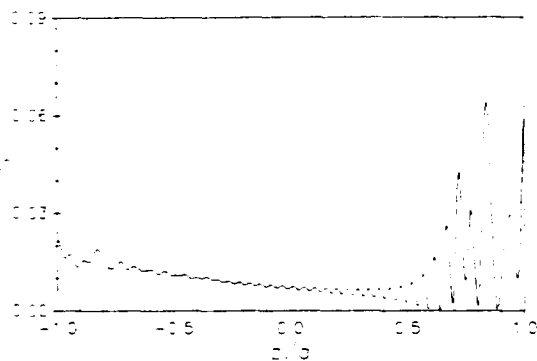


Fig. 8. Computer generated plot of the normalized internal source function distribution within a 165-$\mu$m methanol droplet ($\bar{n}$ = 1.395 + 0.0163$i$) illuminated by a Gaussian beam ($\lambda$ = 10.6 $\mu$m, $\bar{w}_0$ = 0.75, $\bar{x}_0$ = $\bar{y}_0$ = 0). The droplet is located at the laser focal point ($\bar{z}_0$ = 0).

tive comparisons can still be made. The series of plots which follow show the normalized internal source function distribution for $\bar{w}_0$ = 0.75 (experimental case) and $\bar{z}_0$ varying from the plane wave case ($\bar{z}_0 \to \infty$) to the focal point case ($\bar{z}_0$ = 0). Here, the normalized source function $\tilde{S}$ and the normalized beam waist $\bar{w}_0$ are defined as

$$\tilde{S} = \frac{|\mathbf{E}|^2}{|\mathbf{E}_0|^2}, \quad 2\bar{w}_0 = \frac{2w(z=0)}{a},$$

where $\mathbf{E}$ represents the electric field at an arbitrary location, $\mathbf{E}_0$ represents the peak value of the incident electric field at the focal point, $2w$ represents the local beam diameter, and $a$ represents the radius of the particle. $\bar{z}_0$ is the axial position of the particle with respect to the laser focal point normalized by the particle radius $a$. Physically, the source function is directly proportional to the time average power per unit volume deposited in the sphere due to resistance or joule heating. Since the maximum values of the normalized internal source function in the $y$-$z$ plane (see Fig. 4) occurred along the $y$ = 0 line for the cases considered, only center line plots are presented.
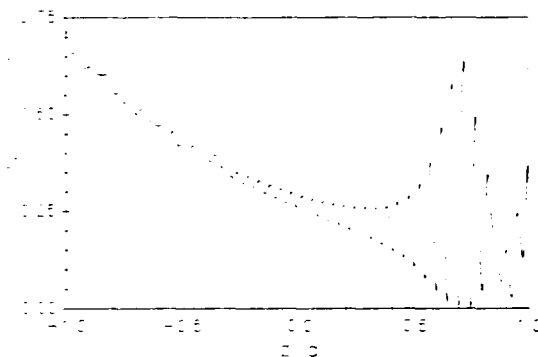
Figure 5 shows the normalized internal source function distribution for a 165-$\mu$m diam methanol droplet undergoing plane wave illumination. Note that the peak values of the source function occur exclusively within the shadow hemisphere of the droplet with smaller values appearing within the illuminated hemisphere. To illustrate the effect of decreasing beam diameter, examine Figs. 6–8 which show the normalized internal source function distributions for the same size methanol droplet located in a fundamental Gaussian beam with $\bar{w}_0$ = 0.75 and $\bar{z}_0$ equal to 85 (7-mm out of focal point), 20 (1.65-mm out of focal point), and 0 (focal point), respectively. As expected due to the large local beam diameter (800 $\mu$m at $\bar{z}_0$ = 85), Fig. 6 shows virtually the same normalized source function distribution as that calculated using plane wave Mie theory. The only notable difference is the magnitude of the normalized source function. For plane wave Mie theory, the source function is normalized based on an assumed uniform incident electric field. For the arbitrary incident beam theory, however, the source function is normalized by the electric field at the focal point of the incident Gaussian laser beam. Therefore,

as the particle is moved away from the laser focal point along the propagation axis, the corresponding incident beam intensity decreases. For smaller values of $z_0$, as shown in Figs. 6–8, the maximum value of the normalized source function within the illuminated hemisphere of the droplet increases relative to the peak values within the shadow hemisphere. Figure 8, which shows the theoretical calculations corresponding to the experimentally measured beam waist diameter (120 $\mu$m), indicates that the peak source function value occurs on the illuminated surface of the droplet. A qualitative explanation for the explosive process is to associate the transition between shadow and illuminated side explosive vaporization as the point at which relative source function values are approximately equal within the shadow and illuminated hemispheres of the droplet. This explanation is supported by the trends shown in the theoretical calculations as well as the experimental observations shown in Figs. 2 and 3. Examining peak source function values within each hemisphere may not always be a valid approach since the actual energy absorbed within the two hemispheres may be dramatically different even if peak source function values within each hemisphere are the same. This difference in absorption is due to the different source function distributions exhibited within the shadow and illuminated hemispheres of weakly absorbing particles. The source function distribution within the illuminated hemisphere tends to be more uniformly distributed while the distribution within the shadow hemisphere is much more localized.

Another interesting observation from Figs. 2 and 3 is the difference in the manner in which the droplets are exploding. In Fig. 2, the illuminated hemisphere of the droplet is fragmented into a large number of smaller droplets which are propagating back toward the laser beam. In contrast, Fig. 3 shows a considerably different interaction on the shadow hemisphere suggesting the growth of a vapor bubble near the shadow surface. One possible reason for the difference can be attributed to the different source function distributions within the two hemispheres which were discussed previously. For example Fig. 8, which corresponds to the experimental observations presented in Fig. 2, shows a relatively uniform source function distribution within the illuminated hemisphere of the droplet with smaller localized peaks occurring in the shadow hemisphere of the droplet. In contrast Fig. 3, which corresponds closely to plane wave calculations, shows localized regions in the shadow hemisphere where the source function values are maximum. In addition to the distribution of absorbed energy, the time scale of the process may also influence the way that the droplets explode. Since the laser intensity incident on the droplet shown in Fig. 3 (7-mm case) is approximately a factor of 7 less than the laser intensity illumination incident on the droplet shown in Fig. 2 (focal point case), the heating process resulting in explosive vaporization is much slower for the 7-mm case presented in Fig. 3.

## V. Conclusions

Although classical Mie theory is adequate in many cases for describing the internal source function distribution within spherical absorbing particles, there are situations when the Gaussian beam theory must be utilized to account for the experimentally observed explosive characteristics. In particular, for a 165-$\mu$m methanol droplet located at the focal point of a 120-$\mu$m diam laser beam, the Gaussian beam theory correctly predicts that the initial explosive vaporization will occur within the illuminated hemisphere of the droplet. Using classical Mie theory for the focal point case would show the largest energy absorption to occur within the shadow hemisphere contrary to experimental observation. As the methanol droplets are moved away from the laser focal point along the propagation axis to a point 7 mm behind the focal point, the location of initial explosive vaporization shifts from the illuminated hemisphere to the shadow hemisphere of the droplet. At this position, the beam diameter is much larger than the droplet diameter and thus both plane wave Mie theory and the Gaussian beam theory give results consistent with experimental observation. In general, for situations when the particle diameter is the same order of magnitude as the beam diameter, the Gaussian beam theory should be used to account for the finite size of the laser beam.

## References

1. J. H. Eickmans, W.-F. Hsieh, and R. K. Chang, "Laser-Induced Explosion of $H_2O$ Droplets: Spatially Resolved Spectra," Opt. Lett. 12, 22 (1987).
2. P. Chylek, M. A. Jarzembski, V. Srivastava. R. G. Pinnick, J. D. Pendleton, and J. P. Cruncleton, "Effect of Spherical Particles on Laser-Induced Breakdown of Gases," Appl. Opt. 26, 760 (1987).
3. V. Barinov and S. Sorokin, "Explosion of Water Drops Under the Action of Optical Radiation," Sov. J. Quantum Electron. 3, 89 (1973).
4. G. Mie, "Beiträge zur Optik trüber Medien, speziell kolloidaler Metallösungen," Ann. Phys. 25, 377 (1908).
5. P. Debye, "Der Lichtdruck auf Kugeln von beliebigem Material," Ann. Phys. 30, 57 (1909).
6. J. P. Barton, D. R. Alexander, and S. A. Schaub, "Internal and Near-Surface Electromagnetic Fields for a Spherical Particle Irradiated by a Focused Laser Beam," J. Appl. Phys., 64, 1632 (1988).
7. L. Davis, "Theory of Electromagnetic Beams," Phys. Rev. A 19, 1177 (1979).
8. G. Gouesbet, B. Maheu, and G. Grehan, "The Order of Approximation in a Theory of the Scattering of a Gaussian Beam by a Mie Scatter Center," J. Opt. Paris 16, 239 (1985).
9. K. D. Ahlers and D. R. Alexander, "Microcomputer Based Digital Image Processing System Developed to Count and Size Laser-Generated Small Particle Images," Opt. Eng. 24, 1060 (1985).
10. M. Querry, U. Missouri–Kansas City; private communication (July 1987).

# Theoretical model for the image formed by a spherical particle in a coherent imaging system: comparison to experiment

S. A. Schaub
D. R. Alexander, MEMBER SPIE
J. P. Barton
University of Nebraska-Lincoln
Center for Electro-Optics
Lincoln, Nebraska 68588-0525

**Abstract.** A simple theoretical model is presented that allows calculation of the image produced by a spherical absorbing particle illuminated by monochromatic, coherent laser light. Results presented in this paper are restricted to a single-lens imaging system, although generalization to more complex imaging system configurations would be straightforward. The method uses classic Lorenz-Mie scattering theory to obtain the electromagnetic field external to an absorbing spherical particle and a Fourier optics approach to calculate the intensities in the image plane. Experimental results evaluating focus characteristics are examined for 50 $\mu$m diameter water droplets using an $N_2$ laser imaging system in conjunction with a digital image processor, and the experimental images are compared to the results of the theoretical model. Comparative focus criteria results are particularly useful in aerosol science research involving dynamic particle size measurements in which criteria for focus and depth of field must be established.

Subject terms: spray analysis; image formation; focus effects.

## CONTENTS

## 1. INTRODUCTION

During recent years there has been a growing interest in the field of dynamic particle size measurements. Applications such as combustion optimization, industrial and agricultural spray application, and cloud simulation for aircraft icing studies all require detailed knowledge of both particle size and particle size distribution. One method commonly used to measure particle and spray characteristics utilizes laser interferometry and light scattering.[1,2] Although restricted to spherical droplets,[3] this method provides valuable size and velocity information for a variety of applications. Another method of obtaining data on particle characteristics, which is addressed in this paper, uses a laser-based imaging system coupled to a digital image processor.[4,5]

The specific imaging system under consideration has been described in detail in previous work[5,6] and can be summarized as shown in Fig. 1. In this system, an object located at plane $z_0$ is illuminated by an $N_2$ laser (Molectron model UV-12, $\lambda$ = 337 nm, 2.5 mJ/pulse, 10 ns FWHM). The image is formed by passing the scattered light through a plano-convex lens (f = 50 mm, D = 25 mm) onto a vidicon tube (plane $z_3$). The video signal is then sent to a Recognition Concepts, Inc., Trapix 5532 digital image processor for analysis. To obtain accurate particle size data, the imaging system must be calibrated using particles of known sizes, and the calibration data must be incorporated into an automated algorithm, allowing for rapid processing of video frames containing particle images. For particles in focus, the calibration and algorithm implementation is straightforward. However, for sizing dynamic sprays, special algorithms are required since most particles in a spray are slightly defocused due to the spatial distribution of particles throughout the spray. The computer-based sizing algorithms must have the capability of determining when a particle is in focus and its correct size. Such a computer algorithm has been developed,[6,7] to count and size particles in dynamic sprays based on criteria derived from experimental calibrations using a monodisperse droplet generator and a chrome-on-glass static calibration reticle.[8] The technique makes use of the intensity gradient at the particle edge and the measured average intensity (gray level) of the particle, both of which change as the particle is moved in and out of focus. By carefully positioning particles of known size at various locations with respect to the object plane (plane $z_0$), we obtained an empirical criteria to determine particle size as a function of the
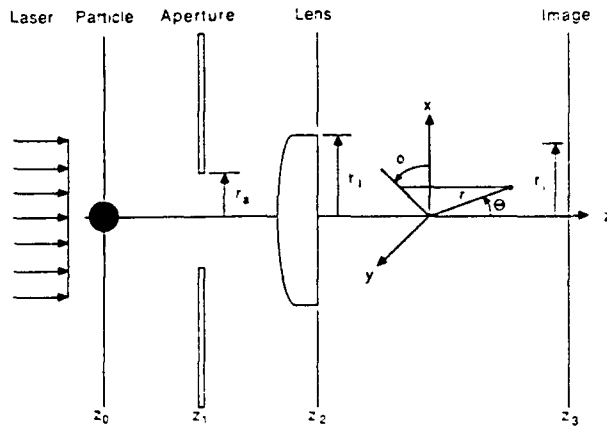
Laser  Particle  Aperture  Lens  Image



Fig. 1. Imaging system geometry.

measured average gray level of the particle. The particle edge gradient and average gray level have been shown[6,7] to provide excellent criteria on which to base in-focus and out-of-focus determination. Although empirical results can provide accurate algorithms for particle sizing for a particular optical system, a theoretical model would be useful in examining such things as the effect of changing aperture size on the observed particle images, the variation in average gray level with the degree of particle defocus, and the relationship between the actual particle edge and the observed edge intensity gradient of a defocused particle.

In a recent paper by Thompson and Malyak,[9] an approach using the Huygens-Fresnel principle was used to calculate the intensity distribution for opaque disks illuminated by a coherent laser source. Results showed that the depth of field for a coherent imaging system is much larger than for a similar incoherent system. In this paper, we consider the more general case of a spherical absorbing particle undergoing monochromatic coherent illumination and outline a simple method for calculating the image produced by the particle. Calculated results based on the theoretical model are compared to experimentally observed images for both in-focus and out-of-focus 50 μm diameter water droplets, and implications to particle sizing are discussed.

## 2. PROBLEM FORMULATION

In formulating the physical problem to be solved, we begin with the actual experimental arrangement shown in Fig. 1. The $N_2$ laser is propagating in the $+z$ direction and is assumed, for calculation purposes, to be linearly polarized in the x direction. Although the output beam of the $N_2$ laser is inherently randomly polarized, we assume as a first approximation that the coherence length of the $N_2$ laser is such that at any instant of time the particle is essentially illuminated by a linearly polarized plane wave. The spherical particle, of arbitrary radius a, located at plane $z_0$ is assumed to be isotropic, homogeneous, and non-magnetic and to possess a finite electrical conductivity. Accepting that the laser/aerosol interaction can be modeled as a linearly polarized plane wave incident on a spherical absorbing particle, the electromagnetic field distribution can be obtained everywhere internal and external to an absorbing spherical particle using the classic Lorenz-Mie theory.[10,11] A more recent outline of the theoretical details of the derivation can be found in Born and Wolf.[12] The equations used for the external electric

field calculations are shown in the appendix. These equations yield exact knowledge (within numerical accuracy) of the electromagnetic field at every point within the aperture located at plane $z_1$. Although we use the most general form of the Lorenz-Mie equations for calculations presented in this paper, it is possible that simplifications,[12] for specific cases of droplet size, optical properties, or imaging system geometry, can be incorporated into the analysis.

To remain consistent with the scalar diffraction theory outlined by Goodman,[13] we assume that the x-component (direction of polarization) of the electric field will be the only significant electric field component throughout the imaging system. The validity of this assumption can be readily verified by examining the magnitude of the three field components at the aperture (plane $z_1$).

In addition, the actual physical problem depicted in Fig. 1 can be simplified based on several experimental observations. For the aperture size of 5.5 mm used in the imaging system, it was observed that the particle image at plane $z_3$ was not significantly affected as the aperture was moved toward the lens. This observation is not entirely unexpected since, with λ being much less than $r_a$ and the distance $z_2$ to $z_1$ not being excessively large, we would expect that diffraction effects would be small in proceeding from plane $z_1$ to $z_2$. If we neglect diffraction effects due to the aperture, then the aperture serves only to decrease the effective lens diameter. As the aperture size becomes small, however, this assumption is no longer valid. For calculations presented in this paper, the aperture is assumed to be positioned directly in front of the lens. This simplification results in elimination of a very time-consuming numerical integration that would be required to proceed from plane $z_1$ to $z_2$.

One also observes that the particle image formed on the vidicon (plane $z_3$) appears essentially symmetric with respect to the z axis. Although it is apparent that the electric field components will be functions of angle as well as radial location (see the appendix), the angular dependence of the x-component of the electric field has been found to be very weak based upon direct computation. Therefore, we assume that the x-component of the electric field can be treated as axisymmetric. This simplification allows field calculations to be performed in the radial direction only. It is also apparent that since the x-component of the electric field is axisymmetric for a specific incident polarization direction, the calculations will also be valid for randomly polarized light in which the direction of polarization is changing in an arbitrary manner. The mathematical details incorporating the above discussion are presented in the following section.

## 3. THEORETICAL MODEL

The geometry for the simplified model is shown in Fig. 2. In the following discussion the x-component of the external electric field is denoted by $E_m$, where the subscript refers to the field evaluated at plane $z_m$. As discussed previously, the electric field at plane $z_1$ is known exactly from Lorenz-Mie theory (see the appendix). $E_2$ can be related to the $E_1$ by assuming that the paraxial thin lens expression[13] is valid,

$$E_2(x_2,y_2) = \exp(ikn\Delta_0) \exp\left[-\frac{ik}{2f}(x_1^2 + y_1^2)\right] E_1(x_1,y_1)$$

$$= \exp(ikn\Delta_0) \exp\left[-\frac{ik}{2f}(x_2^2 + y_2^2)\right] E_1(x_2,y_2) . \qquad (1)$$
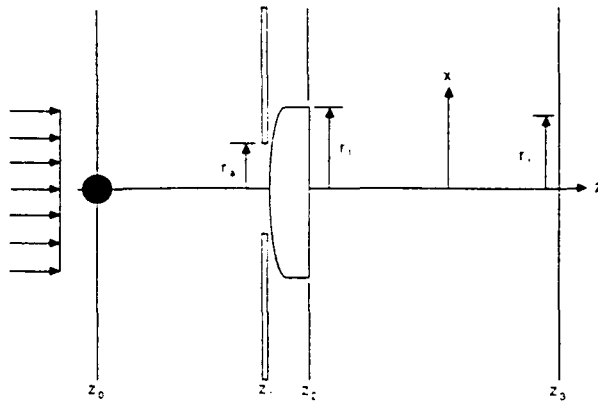
**Fig. 2. Simplified geometry used for calculations.**

where f is the focal length of the lens, $\Delta_0$ is the thickness of the lens, and $k = 2\pi/\lambda$. By thin lens, we mean that the thickness of the lens is such that a light ray enters and leaves the lens at essentially the same x-y coordinates, thus making $(x_1, y_1)$ and $(x_2, y_2)$ interchangeable. Note that the lens in the imaging system is assumed to be ideal and free from any aberrations. Using the Fresnel approximation[13] in proceeding from plane $z_2$ to $z_3$,

$$E_3(x_3, y_3) = \frac{\exp[ik(z_3 - z_2)]}{i\lambda(z_3 - z_2)} \iint_A E_2(x_2, y_2)$$

$$\times \exp\left\{\frac{ik}{2(z_3 - z_2)}[(x_3 - x_2)^2 + (y_3 - y_2)^2]\right\} dx_2 dy_2 \quad . \quad (2)$$

Substituting Eq. (1) into Eq. (2),

$$E_3(x_3, y_3) = \frac{\exp[ik(z_3 - z_2)]}{i\lambda(z_3 - z_2)} \iint_A \exp(ikn\Delta_0) \exp\left[-\frac{ik}{2f}(x_2^2 + y_2^2)\right]$$

$$\times E_1(x_2, y_2) \exp\left\{\frac{ik}{2(z_3 - z_2)}[(x_3 - x_2)^2\right.$$

$$\left. + (y_3 - y_2)^2]\right\} dx_2 dy_2 \quad . \quad (3)$$

For convenience, Eq. (3) can be written in terms of r-$\phi$ coordinates (i.e., $x_m = r_m\cos\phi_m$ and $y_m = r_m\sin\phi_m$ for plane $z_m$),

$$E_3(r_3, \phi_3) = \frac{\exp[ik(z_3 - z_2)]}{i\lambda(z_3 - z_2)} \int_0^{2\pi} \int_0^{r_a} \exp(ikn\Delta_0)$$

$$\times \exp\left\{-\frac{ik}{2f}[(r_2\cos\phi_2)^2 + (r_2\sin\phi_2)^2]\right\}$$

$$\times E_1(r_2, \phi_2) \exp\left\{\frac{ik}{2(z_3 - z_2)}[(r_3\cos\phi_3 - r_2\cos\phi_2)^2\right.$$

$$\left. + (r_3\sin\phi_3 - r_2\sin\phi_2)^2]\right\} r_2 dr_2 d\phi_2 \quad . \quad (4)$$

Based on the experimental observations discussed earlier, we utilize the axisymmetric field assumption and let $E_1(r_2, \phi_2) = E_1(r_2)$ only. Also, since we will ultimately be concerned only with intensity at plane $z_3$, constant phase factors can be omitted, giving

$$E_3(r_3, \phi_3) = \frac{1}{i\lambda(z_3 - z_2)} \int_0^{r_a} E_1(r_2) r_2 \exp\left(-\frac{ik}{2f} r_2^2\right) \int_0^{2\pi} \exp\left\{\frac{ik}{2(z_3 - z_2)}\right.$$

$$\times [r_3^2 + r_2^2 - 2r_2r_3\cos(\phi_2 - \phi_3)]\right\} d\phi_2 dr_2 \quad . \quad (5)$$

In addition to simplifying the electric field description, the axisymmetric assumption also allows exact evaluation of the angular integral in Eq. (5). Utilizing orthogonality along with the identity[13]

$$\exp(ia\sin x) = \sum_{k=-\infty}^{\infty} J_k(a)\exp(ikx) \quad , \quad (6)$$

Equation (5) can be simplified, giving

$$E_3(r_3) = \frac{2\pi}{i\lambda(z_3 - z_2)} \exp\left[\frac{ikr_3^2}{2(z_3 - z_2)}\right] \int_0^{r_a} E_1(r_2)J_0(\beta)$$

$$\times \exp\left\{-\frac{ikr_2^2}{2}\left[\frac{1}{f} - \frac{1}{(z_3 - z_2)}\right]\right\} r_2 dr_2 \quad , \quad (7)$$

where $J_0$ is the Bessel function of the first kind of order zero and

$$\beta = \frac{kr_2r_3}{(z_3 - z_2)} \quad . \quad (8)$$

In terms of intensity at the image plane, Eq. (7) can be written

$$I_3(r_3) = E_3(r_3)E_3^*(r_3)$$

$$= \left[\frac{2\pi}{\lambda(z_3 - z_2)}\right]^2 \left| \int_0^{r_a} E_1(r_2)J_0(\beta) \right.$$

$$\times \left. \exp\left\{-\frac{ikr_2^2}{2}\left[\frac{1}{f} - \frac{1}{(z_3 - z_2)}\right]\right\} r_2 dr_2 \right|^2 \quad , \quad (9)$$

where the asterisk denotes the complex conjugate. To remain consistent with the Lorenz-Mie theory development (see the appendix), Eq. (9) is written in terms of dimensionless variables,

$$\bar{I}_3(\bar{r}_3) = \left[\frac{\alpha}{(\bar{z}_3 - \bar{z}_2)}\right]^2 \left| \int_0^{\bar{r}_a} \hat{E}_1(\bar{r}_2)J_0(\hat{\beta}) \right.$$

$$\times \left. \exp\left\{\frac{-i\alpha\bar{r}_2^2}{2}\left[\frac{1}{\bar{f}} - \frac{1}{(\bar{z}_3 - \bar{z}_2)}\right]\right\} \bar{r}_2 d\bar{r}_2 \right|^2 \quad , \quad (10)$$

where

$$\hat{\beta} = \frac{\bar{r}_2\bar{r}_3\alpha}{(\bar{z}_3 - \bar{z}_2)} \quad , \qquad \alpha = \frac{2\pi a}{\lambda} \quad ,$$

$$\bar{r} = \frac{r}{a} \quad , \qquad \bar{z} = \frac{z}{a} \quad , \qquad \bar{f} = \frac{f}{a} \quad . \quad (11)$$

## 4. RESULTS AND DISCUSSION

To determine whether the theoretical model provided results consistent with experimental observations, the $N_2$ laser imaging system was configured in a manner identical to Fig. 2. The 50 μm diameter spherical water droplets were generated using
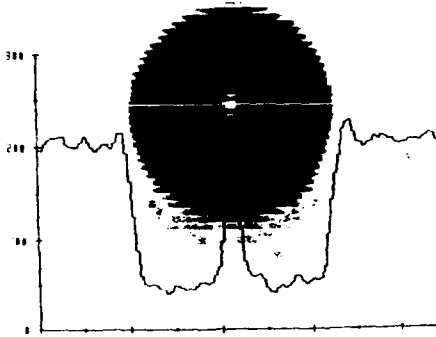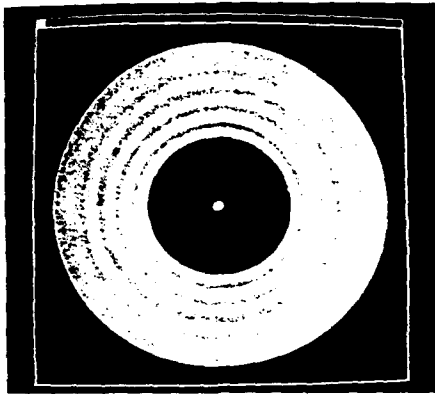
Fig. 3. 50 $\mu$m diameter water droplet located at the focal point $(\tilde{z}_1 - \tilde{z}_0 = 2100, \tilde{r}_a = 110)$. Theoretical calculations (top); observed image (bottom).



Fig. 4. 50 $\mu$m diameter water droplet moved out of focus 10 radii toward the lens $(\tilde{z}_1 - \tilde{z}_0 = 2090, \tilde{r}_a = 110)$. Theoretical calculations (top); observed image (bottom).

a vibrating orifice generator (TSI model 3450) and allowed to fall in the $-x$ direction through the $N_2$ laser imaging system at a velocity of approximately 8 m/s. The particle location and the aperture size could be changed using micrometer positioners and a variable size aperture. Unless otherwise noted, the following parameter values, corresponding to the actual experimental arrangement, were used for the computations: radius of water droplet a = 25 $\mu$m, incident wavelength $\lambda$ = 337 nm, complex refractive index[14] $\bar{n}$ = 1.345 + $8.7 \times 10^{-9}$i, size parameter $\alpha$ = 466, lens focal length $\bar{f}$ = 2000, distance from particle to aperture $(\tilde{z}_1 - \tilde{z}_0)$ = 2100 (in-focus case), distance from lens to image plane $(\tilde{z}_3 - \tilde{z}_2)$ = 42,000, radius of aperture $\tilde{r}_a$ = 110, radius of lens $\tilde{r}_\ell$ = 500, radius of image $\tilde{r}_i$ = 50.

For comparison, we examined four specific cases. Figures 3 through 6 show photographs of both the experimentally observed images obtained using the $N_2$ imaging system and the theoretically calculated intensities for a 50 $\mu$m diameter water droplet located at the focal point $(\tilde{z}_1 - \tilde{z}_0 = 2100, \tilde{r}_a = 110)$, 10 radii toward the lens $(\tilde{z}_1 - \tilde{z}_0 = 2090, \tilde{r}_a = 110)$, 10 radii away from the lens $(\tilde{z}_1 - \tilde{z}_0 = 2110, \tilde{r}_a = 110)$, and 12 radii away from the lens with a decreased aperture size $(\tilde{z}_1 - \tilde{z}_0 = 2112, \tilde{r}_a = 40)$, respectively. The theoretical images were generated and displayed on a DEC Microvax II/GPX workstation and represent relative intensity values in the image plane for $\bar{r} = r/a$ values from 0 to 2.5 (i.e., the dark outer circular edge corresponds to 2.5 particle radii). The experimental images are displayed on a video monitor and represent a digitized, enlarged picture of the particle image. Although the quality of the experimental image is limited by the resolution of the imaging
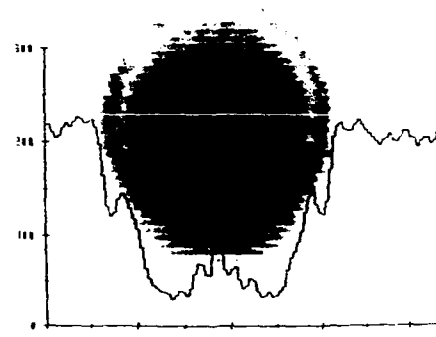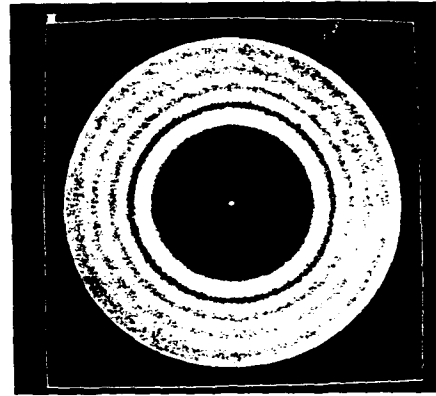
system (1 pixel = 1 $\mu$m and 256 gray levels), several interesting comparisons can be made.

As expected for an in-focus droplet, Fig. 3 shows a sharply defined boundary in both the theoretical and experimental images. Also evident is the bright center spot appearing in both photographs. The graph superimposed on the experimental image corresponds to the intensity distribution through the diameter of the particle, defined by the horizontal white line. Note that the actual droplet size is the same in both the theoretical and experimental images. The apparent difference results from the discrete amounts of enlargement obtainable using the image processor.

As the droplet is moved out of focus 10 radii toward the lens $(\tilde{z}_1 - \tilde{z}_0 = 2090)$, the experimental image, shown in Fig. 4, again exhibits a relatively bright center spot. In addition, two concentric rings of lesser intensity appear near the center spot as well as one ring slightly inside the boundary of the droplet. There also is a slight increase in light intensity just outside the edge of the particle. These general features are also observed in the theoretical calculations.

Figure 5 shows the same size water droplet but moved out of focus 10 radii away from the focusing lens $(\tilde{z}_1 - \tilde{z}_0 = 2110)$. Note that both the experimental and theoretical images show less intense ring structure internal to the particle edge than a corresponding particle moved an equal distance toward the lens. The difference in intensity distributions exhibited by particles that are an equal distance out of focus but on opposite sides of the object plane of the lens has been observed previously[6,7] and becomes more significant as the particle size decreases. The
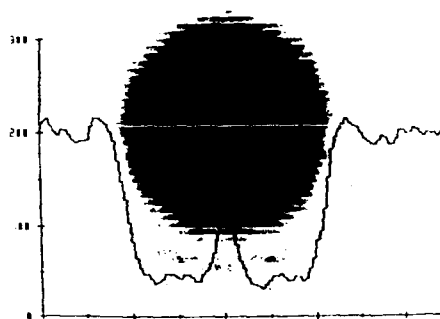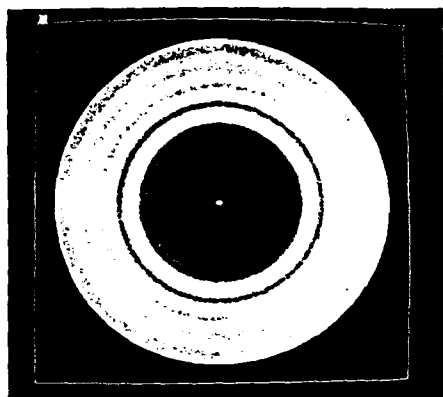
Fig. 5. 50 $\mu$m diameter water droplet moved out of focus 10 radii away from the lens ($\hat{z}_1 - \hat{z}_0 = 2110$, $\hat{r}_a = 110$). Theoretical calculations (top); observed image (bottom).
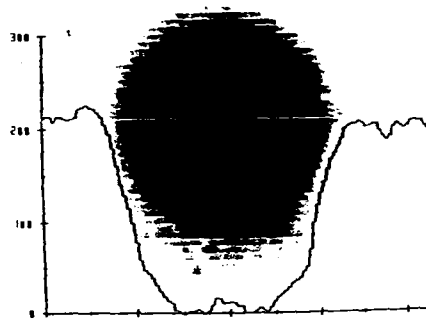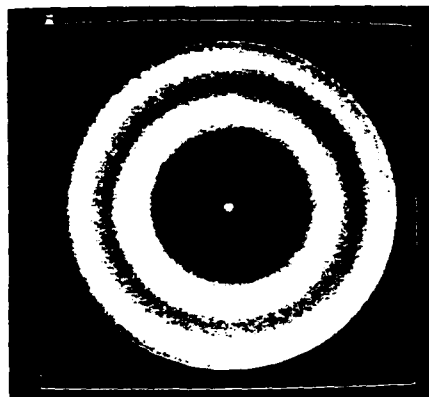


Fig. 6. 50 $\mu$m diameter water droplet moved out of focus 12 radii away from the lens and with decreased aperture size ($\hat{z}_1 - \hat{z}_0 = 2112$, $\hat{r}_a = 40$). Theoretical calculations (top); observed image (bottom).

intensity external to the edge of the particle, however, appears to be very similar for the two cases.

As a final case, Fig. 6 shows an out-of-focus particle moved 12 radii away from the lens ($\hat{z}_1 - \hat{z}_0 = 2112$) along with a decreased aperture size ($\hat{r}_a = 40$). In this case, both the theoretical and experimental images show evidence of a blurred particle edge as well as a significant decrease in the spatial frequency of the diffraction rings. The images differ, however, in the intensity of the center spot, which appears brighter for the theoretical calculations than for the experimental image.

In general, the theoretical calculations for all of the cases presented show center intensities higher than the intensities observed experimentally. Also apparent in the experimental images are the slightly different intensity distributions observed on the top and bottom of the droplet as compared to the left and right sides of the droplet. Several factors may contribute to the observed differences between experiment and theory. Among these are the simplified incident beam description used to model the laser pulse, the existence of lens aberrations, which were neglected in the present analysis, the assumption of symmetry about the z axis, the simplified lens transformation, and the relatively high velocity of the droplets (8 m/s) in the vertical direction.

To obtain a more quantitative representation of the effect of droplet location on the calculated intensities, plots of normalized intensity as a function of normalized radial location are shown in Figs. 7 and 8 for 50 $\mu$m diameter water droplets as they are moved out of focus toward the lens and away from the lens,

respectively. Note that the intensity values are normalized by the maximum intensity for the focal point (in-focus) case. In both figures, it is evident that the intensity gradient near the particle edge decreases significantly as the particle is moved out of focus. As pointed out previously[9,13] for coherent imaging systems, the actual particle edge corresponds to approximately 0.25 the incident intensity. Also evident are the high intensities that appear near the center of the droplet. This high intensity, commonly referred to as Poisson's spot, is approximately four times the intensity of the incident light for the in-focus case ($\hat{z}_1 - \hat{z}_0 = 2100$). As already noted, the intensity distribution is not the same for particles an equal distance on each side of the object plane. This fact adds additional uncertainty to the already difficult problem of sizing dynamic sprays.

We also see that below a certain threshold intensity value, the average intensity internal to the particle edge increases as the particle is moved out of focus. This observation is consistent with the concept of using measured average gray level as an indication of the degree of particle defocus. The optimum threshold value for the system described in Fig. 1 was determined[6] experimentally to be approximately one-half the incident intensity.

Figure 9 shows the effect of changing aperture size for a fixed particle location ($\hat{z}_1 - \hat{z}_0 = 2112$). Readily apparent is the decrease in spatial frequency of the relative intensity maximum as the aperture size is decreased. This effect should be expected since a decreasing effective lens size serves to restrict the lens to collection of low-frequency portions of the object only. We
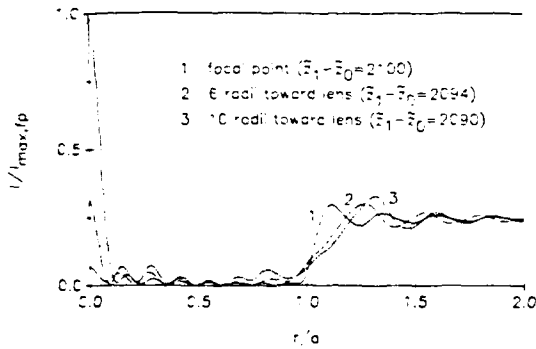
Fig. 7. Normalized intensity as a function of normalized radial position for a 50 μm diameter water droplet moved out of focus toward the focusing lens with $r_a = 110$.
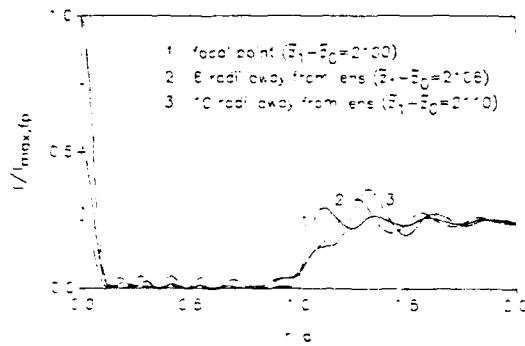


Fig. 8. Normalized intensity as a function of normalized radial position for a 50 μm diameter water droplet moved out of focus away from the focusing lens with $r_a = 110$.
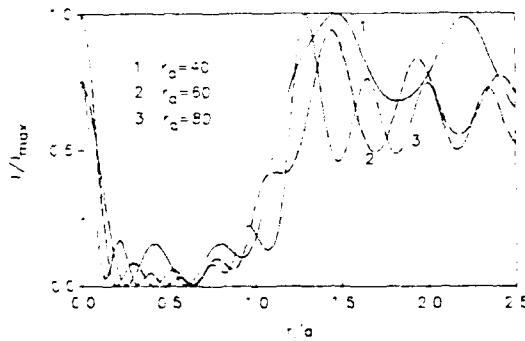


Fig. 9. Normalized intensity as a function of normalized radial position for a 50 μm diameter water droplet moved out of focus 12 radii away from the lens ($\hat{z}_1 - \hat{z}_0 = 2112$) using various aperture sizes.

also see that the smaller aperture sizes result in smaller intensity gradients near the particle edge.

## 5. CONCLUSIONS

Although the theoretical model presented has been simplified extensively over the actual physical problem, the results agree qualitatively with experimental observations. For the cases ex-

amined, the locations of the higher intensity diffraction rings agree well with experimental observations. The theoretical model provides results that confirm the validity of using the particle edge intensity gradient and the measured average gray level as focus criteria for the sizing of dynamic particle sprays. The theoretical approach can also be easily extended to more complex imaging system geometries involving multilens systems and to situations in which the axisymmetric field assumption is not appropriate, such as off-axis imaging.

## 6. APPENDIX

This section presents the near-field Lorenz-Mie theory equations for the scattered, incident, and external electric fields for a spherical particle illuminated by a plane wave, with the following assumptions:

(1) Stationary, homogeneous, isotropic, absorbing sphere of radius a in a homogeneous, isotropic, nonabsorbing medium.
(2) Both the particle and the medium are nonmagnetic ($\mu = 1$).
(3) Particle is illuminated by a plane, monochromatic electromagnetic wave of unit amplitude linearly polarized in the x direction, propagating in the +z direction.
(4) All time-dependent quantities are assumed to vary as $\exp(-i\omega t)$.

### 6.1. Scattered field

$$\tilde{E}_r^{(s)} = \frac{\cos\phi}{(\alpha\bar{r})^2} \sum_{\ell=1}^{\infty} \ell(\ell+1)a_\ell \xi_\ell^{(1)}(\alpha\bar{r}) P_\ell^{(1)}(\cos\theta) , \tag{A1}$$

$$\tilde{E}_\theta^{(s)} = -\frac{\cos\phi}{\alpha\bar{r}} \sum_{\ell=1}^{\infty} \left[ a_\ell \xi_\ell^{(1)\prime}(\alpha\bar{r}) P_\ell^{(1)\prime}(\cos\theta)\sin\theta \right.$$
$$\left. - b_\ell \xi_\ell^{(1)}(\alpha\bar{r}) P_\ell^{(1)}(\cos\theta) \frac{i}{\sin\theta} \right] . \tag{A2}$$

$$\tilde{E}_\phi^{(s)} = -\frac{\sin\phi}{\alpha\bar{r}} \sum_{\ell=1}^{\infty} \left[ a_\ell \xi_\ell^{(1)\prime}(\alpha\bar{r}) P_\ell^{(1)}(\cos\theta)\frac{1}{\sin\theta} \right.$$
$$\left. - ib_\ell \xi_\ell^{(1)}(\alpha\bar{r}) P_\ell^{(1)\prime}(\cos\theta)\sin\theta \right] . \tag{A3}$$

The external scattering coefficients $a_\ell$ and $b_\ell$ are given by

$$a_\ell = \frac{i^{(\ell-1)}(2\ell+1)}{\ell(\ell+1)} \frac{\psi_\ell'(\bar{n}\alpha)\psi_\ell(\alpha) - \bar{n}\psi_\ell(\bar{n}\alpha)\psi_\ell'(\alpha)}{\bar{n}\psi_\ell(\bar{n}\alpha)\xi_\ell^{(1)\prime}(\alpha) - \psi_\ell'(\bar{n}\alpha)\xi_\ell^{(1)}(\alpha)} , \tag{A4}$$

$$b_\ell = \frac{i^{(\ell-1)}(2\ell+1)}{\ell(\ell+1)} \frac{\bar{n}\psi_\ell'(\bar{n}\alpha)\psi_\ell(\alpha) - \psi_\ell(\bar{n}\alpha)\psi_\ell'(\alpha)}{\psi_\ell(\bar{n}\alpha)\xi_\ell^{(1)\prime}(\alpha) - \bar{n}\psi_\ell'(\bar{n}\alpha)\xi_\ell^{(1)}(\alpha)} , \tag{A5}$$

where $\psi_\ell$, $\chi_\ell$, and $\xi_\ell^{(1)} = \psi_\ell - i\chi_\ell$ are the Ricatti-Bessel functions, which are related to the Bessel functions of half-integer order; $P_\ell^{(1)}$ is the associated Legendre function of order 1; $\bar{n}$ is the complex refractive index of the sphere; $\alpha = 2\pi a/\lambda$ is the size parameter; and $\bar{r} = r/a$ is the normalized radial coordinate. Primed quantities denote differentiation with respect to the argument of the function. Note that all electric field quantities are normalized based on an assumed uniform incident electric field of unit magnitude.

The technique used to compute the Ricatti-Bessel functions is described in detail by Ross.[15] Computation of the associated

Legendre function is accomplished by using standard recursion formulas such as those presented by Abramowitz and Stegun.[16]

## 6.2. Incident field

$$\tilde{E}_r^{(i)} = \exp(i\alpha\bar{r}\cos\theta)\sin\theta\cos\phi ,$$ (A6)

$$\tilde{E}_\theta^{(i)} = \exp(i\alpha\bar{r}\cos\theta)\cos\theta\cos\phi ,$$ (A7)

$$\tilde{E}_\phi^{(i)} = -\exp(i\alpha\bar{r}\cos\theta)\sin\phi .$$ (A8)

## 6.3. External field

In terms of Cartesian coordinates,

$$\tilde{E}_x^{ext} = (\tilde{E}_r^{(i)} + \tilde{E}_r^{(s)})\sin\theta\cos\phi + (\tilde{E}_\theta^{(i)} + \tilde{E}_\theta^{(s)})\cos\theta\cos\phi$$

$$- (\tilde{E}_\phi^{(i)} + \tilde{E}_\phi^{(s)})\sin\phi ,$$ (A9)

$$\tilde{E}_y^{ext} = (\tilde{E}_r^{(i)} + \tilde{E}_r^{(s)})\sin\theta\sin\phi + (\tilde{E}_\theta^{(i)} + \tilde{E}_\theta^{(s)})\cos\theta\sin\phi$$

$$+ (\tilde{E}_\phi^{(i)} + \tilde{E}_\phi^{(s)})\cos\phi ,$$ (A10)

$$\tilde{E}_z^{ext} = (\tilde{E}_r^{(i)} + \tilde{E}_r^{(s)})\cos\theta - (\tilde{E}_\theta^{(i)} + \tilde{E}_\theta^{(s)})\sin\theta .$$ (A11)

## 7. REFERENCES

1. W. M. Farmer, "Measurements of particle size, number density, and velocity using a laser interferometer," Appl. Opt. 11(11). 2603–2612 (1972).
2. W. D. Bachalo and M. J. Houser, "Phase/Doppler spray analyzer for simultaneous measurements of drop size and velocity distributions," Opt. Eng. 23(5), 583–590 (1984).
3. D. R. Alexander, K. J. Wiles, S. A. Schaub, and M. P. Seeman, "Effects of non-spherical drops on a phase doppler spray analyzer," in Particle Sizing and Spray Analysis, N. Chigier and G. W. Stewart, eds., Proc. SPIE 573, 67–72 (1985).
4. B. A. Weiss, P. Derov, D. DeBiase, and H. C. Simmons, "Fluid particle sizing using a fully automated optical imaging system," Opt. Eng. 23(5), 561–566 (1984).
5. K. D. Ahlers and D. R. Alexander, "Microcomputer based digital image processing system developed to count and size laser-generated small particle images," Opt. Eng. 24(6), 1060–1065 (1985).
6. K. J. Wiles, "Development of a system for secondary liquid injection into a mach 2 supersonic flow to study drop size and distribution by video imaging techniques," master's thesis, Univ. of Nebraska, Lincoln (1985).
7. M. P. Seeman, "Aerosol spray characterization using a PDPA and laser imaging video processing system," master's thesis, Univ. of Nebraska, Lincoln (1987).
8. E. D. Hirleman, "Calibration standard reticles for particle sizing instruments," Laser ElectroOptics Ltd. product announcement RR-50.0-3.0-0.08-102-CF-No. 114 (1982).
9. B. J. Thompson and P. H. Malyak, "Accuracy of measurement in coherent imaging of particulates in a three-dimensional sample," in Particle Sizing and Spray Analysis, N. Chigier and G. W. Stewart, eds., Proc. SPIE 573, 12–20 (1985).
10. G. Mie, "Beiträge zur Optik trüber Medien, speziell kolloidaler Metallösungen," Ann. Phys. 25, 377–445 (1908).
11. P. Debye, "Der Lichtdruck auf Kugeln von beliebigem Material," Ann. Phys. 30, 57–136 (1909).
12. M. Born and E. Wolf, Principles of Optics, 6th Edition, Pergamon Press, Oxford, England 633–664 (1987).
13. J. W. Goodman, Introduction to Fourier Optics, McGraw-Hill, New York (1968).
14. G. M. Hale and M. R. Querry, "Optical constants of water in the 200-nm to 200-μm wavelength region," Appl. Opt. 12(3), 555–563 (1973).
15. W. D. Ross, "Computation of Bessel functions in light scattering studies," Appl. Opt. 11(9), 1919–1923 (1973).
16. M. Abramowitz and I. A. Stegun, eds., Handbook of Mathematical Functions, pp 332–334. Dover, New York (1972).

**Scott A. Schaub** received his BS degree in mechanical engineering in 1985 and his MS degree in 1986 from the University of Nebraska-Lincoln. He is currently working toward his Ph.D. degree in energetics and mechanics. His research interests include high energy laser interaction with solid and liquid aerosols and dynamic particle size measurements. He is a member of the OSA.

**Dennis R. Alexander** is a professor and director of the Center for Electro-Optics in the Mechanical Engineering Department at the University of Nebraska-Lincoln. Dr. Alexander received his degrees from Kansas State University in nuclear engineering. His research has been in the area of applied optical measurements. Of particular interest is the in situ sizing and characterization of aerosols using laser imaging techniques coupled with computer digital image processing algorithms. His research interests also include the theoretical modeling and the experimental interaction of high energy lasers with aerosols. Dr. Alexander has been a visiting scientist at Los Alamos Scientific Laboratory and Amoco Oil Company Research Facility. He is a member of the Fine Particle Society, the American Society of Mechanical Engineers, the American Nuclear Society, the American Society for Engineering Education, and SPIE.

**John P. Barton** received his BS degree in mechanical and aerospace engineering from the University of Missouri-Columbia in 1973 and his MS and Ph.D. degrees in mechanical engineering from Stanford University in 1974 and 1980, respectively. Currently, Dr. Barton is an assistant professor within the Mechanical Engineering Department at the University of Nebraska-Lincoln, where he is associated with the Center for Electro-Optics. Dr. Barton's research interests include the experimental and theoretical analysis of general laser beam/aerosol particle interactions.

# Scattering of incident KrF laser radiation resulting from the laser-induced breakdown of H₂O droplets

D. R. Alexander, S. A. Schaub, J. Zhang, D. E. Poulain, and J. P. Barton

*Center for Electro-Optics, University of Nebraska-Lincoln, Lincoln, Nebraska 68588-0525*

The time history of elastically scattered incident radiation (ESIR) is presented for 60-μm-diameter water droplets irradiated by KrF ($\lambda = 248$ nm) laser pulses with power densities in the range of 1–200 GW/cm². The ESIR shows a distinct two-peak structure that is dependent on the incident irradiance. The time delay between the arrival of the incident pulse and the first local minimum in the ESIR varied from 7 nsec at 200 GW/cm² to 21 nsec at 5 GW/cm². The time between incident pulse arrival and the first peak in the ESIR showed a similar irradiance dependence, with delays ranging from 4 to 12 nsec. Images of droplet breakup and the average velocities of ejected material are presented for times between 0 and 1000 nsec after the arrival of 3-GW/cm² laser pulses.

Knowledge of the physical mechanisms that govern the laser-induced breakdown (LIB) of aerosols is important in a variety of applications, and significant progress has been made in both the theoretical modeling[1-3] and the experimental analysis[4-6] of the problem. Much of the experimental research, however, has been confined to the visible and infrared wavelengths, and, as noted by Biswas et al.,[5] ambiguities still remain in regard to the plasma emission dependence on the incident laser wavelength and energy. In this Letter we present results showing the time history of elastically scattered incident radiation (ESIR) and typical examples showing the dynamics of the explosive breakup process for 60-μm-diameter distilled water droplets irradiated by a pulsed KrF laser under atmospheric conditions.

A schematic of the experimental setup is shown in Fig. 1. The high-energy laser beam is produced by a KrF excimer laser (Questek model 2860, $\lambda = 248$ nm, FWHM pulse duration ≈ 17–22 nsec) and is focused to a spot size of approximately $10^4 \ \mu\text{m}^2$. The beam from an identical excimer laser, oriented perpendicular to the high-energy laser beam, is synchronized with the high-energy pulses by using a digital delay unit (Questek 9200 laser sync/delay unit) and serves as the illumination source for imaging studies. The uncertainty in the delay time between the high-energy laser pulse and the imaging pulse is approximately ±5 nsec. The images are viewed with a UV-sensitive vidicon (Cohu 2006 camera system) in conjunction with a digital image-processing system[7] and are stored on an optical memory disk recorder (Panasonic model TQ-2023F). Monodispersed spherical water droplets are generated by a vibrating orifice generator (TSI model 3450) and fall vertically (perpendicular to both excimer laser beams) through the path of the high-energy laser beam. A Hamamatsu streak-camera system equipped with a slow-speed streak unit (model M2548) and a spectrograph (Instruments SA model HR-320) with a diffraction grating of 150 lines/mm is oriented at an angle of 120° with respect to the incident axis of the high-energy laser beam and is used to

obtain the time-resolved spectral information from the LIB phenomena. Two fiber-optic probes monitor the time history of the incident and the transmitted laser pulses.

Observations of the time history of the ESIR showed a distinct two-peak structure, with a weak intensity increase during the initial stage of the incident laser pulse followed by a period in which the intensity decreased to a local minimum. Later stages then show a sharp rise in the scattered intensity. These effects can be analyzed in a more quantitative manner by examining Fig. 2, which presents the time history of the ESIR, the broadband emission, and the incident pulse for a 60-μm-diameter water droplet irradiated by a 100-GW/cm² KrF laser pulse. We define several parameters in Fig. 2 that can be used to characterize the aerosol/laser interactions. The arrival of the incident pulse is defined as the time when the intensity reaches $1/e^2$, its maximum value. $P_{T1}$ and $P_{T2}$ are, respectively, the delay times from the incident pulse arrival to the first and second peak of the ESIR, $V_T$ is the delay time from the incident pulse arrival to
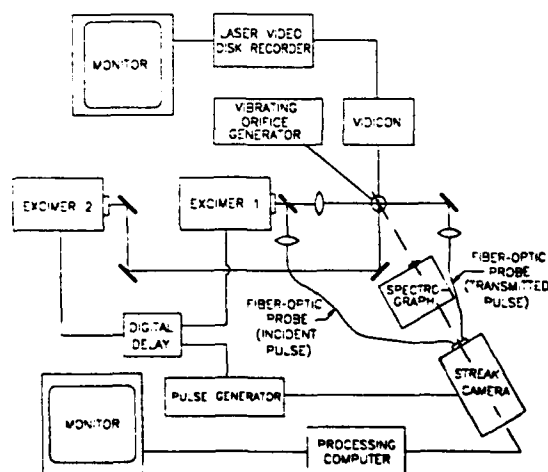


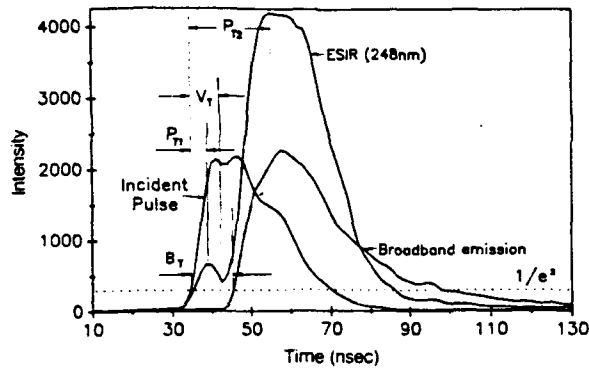Fig. 1. Schematic of the experimental setup.

Fig. 2. Intensities as a function of time for the incident pulse, the ESIR, and the broadband emission for a 60-$\mu$m-diameter water droplet illuminated by a 100-GW/cm$^2$ KrF laser pulse.

the first local minimum of the ESIR, and $B_T$ is the delay time between the incident pulse arrival and the start of broadband emission ($1/e^2$ peak value).

As shown in Fig. 3, $V_T$ showed a strong dependence on the incident irradiance, varying from approximately 7 nsec at 200 GW/cm$^2$ to 21 nsec at 5 GW/cm$^2$. $V_T$ is relatively long (21 nsec) at low irradiances since the major portion of the laser fluence is required for initiation of the plasma. However, at high irradiance values sufficient energy can be supplied during the initial rise of the incident pulse for plasma formation. As one would expect, $P_{T1}$ starts at the peak of the incident pulse and decreases as the incident irradiance increases. Values of $P_{T1}$ ranged from 4 nsec at 200 GW/cm$^2$ to approximately 12 nsec at 1 GW/cm$^2$, with the values remaining essentially constant for irradiance values greater than 25 GW/cm$^2$. These trends contrast with that of $P_{T2}$, which is only a weak function of the incident irradiance and remains essentially constant at 24 nsec. The constant value of $P_{T2}$ reflects the time that the laser pulse is supplying energy into the plasma. Figure 4 gives typical profiles of the time history of the incident pulse and the ESIR for irradiance levels ranging from 1 to 200 GW/cm$^2$ and clearly shows the irradiance dependence of the ESIR.

The time-history dependence of the ESIR on the incident irradiance is not surprising since the absorption and reflection of the incident radiation from an expanding plasma are dependent on plasma geometry as well as electron density, both of which are changing rapidly in time for the laser/aerosol interaction.[8,9] Although the details of the laser/aerosol interaction are not completely understood, we offer the following qualitative explanation of the results. At low irradiance values the droplet remains geometrically intact for the duration of the incident pulse with no accompanying plasma formation. At 1 GW/cm$^2$ [Fig. 4(a)] the ESIR results solely from scattering from the water droplet (the images of the water droplets show no breakup). This value compares favorably with the results of Pinnick et al.,[10] in which the breakdown threshold irradiance for water at 266 nm was 0.7 GW/cm$^2$, although it was concluded that thresholds are also dependent on the incident fluence. As the incident irradiance is increased [Figs. 4(b)–4(d)], plasma

formation is initiated before the end of the incident pulse. In this case the initial rise in the ESIR can be attributed to scattering from the water droplet before plasma formation. The subsequent decrease in ESIR may result from the destruction of the droplet geometry and/or an increase in absorption of the incident radiation by the expanding plasma whose electron density is increasing but is still less than the critical electron density ($n_c = 1.85 \times 10^{22}$ cm$^{-3}$ at $\lambda = 248$ nm). As the electron density increases and eventually exceeds the critical density the plasma becomes more reflective, accounting for the secondary peak, $P_{T2}$.
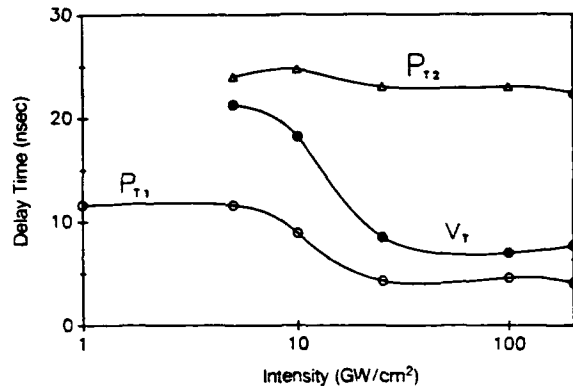


Fig. 3. Delay time between the arrival of the incident pulse and the first peak, the first valley, and the second peak observed in the ESIR as a function of irradiance for 60-$\mu$m-diameter water droplets illuminated by a KrF laser.
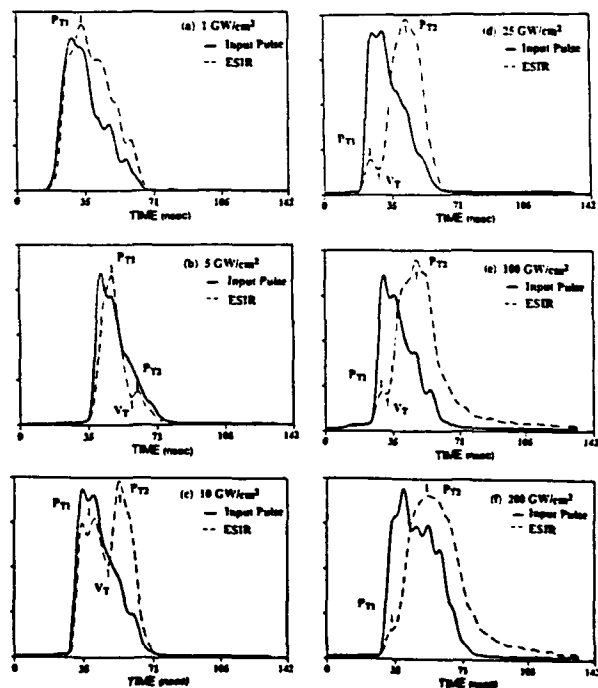


Fig. 4. Intensities of the incident pulse (solid curves) and the ESIR (dashed curves) as a function of time for 60-$\mu$m-diameter water droplets illuminated by KrF laser pulses of 1–200 GW/cm$^2$. The vertical scale is in arbitrary intensity units.
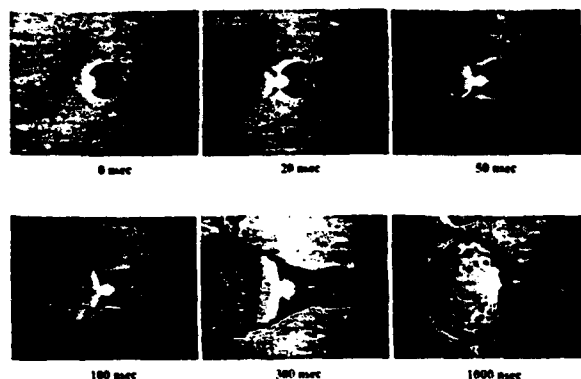
Fig. 5. Typical images of 3-GW/cm² KrF laser pulses incident upon 60-μm-diameter water droplets at 0, 20, 50, 100, 300, and 1000 nsec after the arrival of the high-energy pulse. The high-energy pulse is propagating from right to left. The bright spots appearing on the illuminated and shadow surfaces of the droplet are produced by the 17-nsec incident pulse saturating the vidicon. The lag in the vidicon makes these spots visible in later photographs.
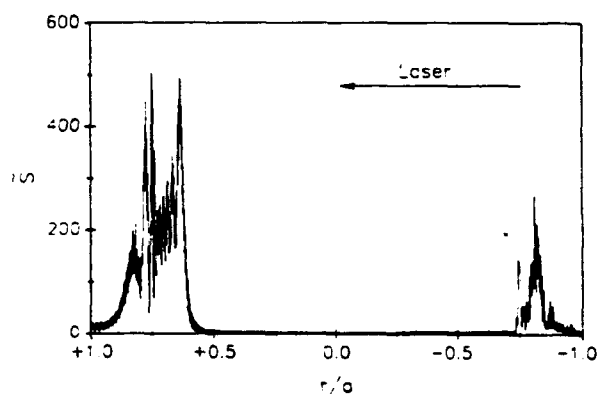


Fig. 6. Normalized internal source function for a 60-μm-diameter water droplet illuminated by $\lambda = 248$ nm incident radiation [$\bar{n} = 1.36 + (3.5 \times 10^{-8}i)$].[12]

The actual physical mechanism is further complicated by the transient scattering cross section resulting from the dynamics of the laser/aerosol interaction.

We also examined the delay time between incident pulse arrival and the initial appearance of broadband emission ($B_T$) with and without water droplets at the focal point of the KrF laser beam operating at 100 GW/cm². The results indicated that $B_T$ was approximately 5 nsec with droplets at the focal point and increased to 12 nsec when no droplets were present at the focal point. Two factors are known to contribute to this observation. First, it is well documented that the presence of the droplets serves to amplify the magnitude of the electric field near the shadow surface of a transparent droplet.[11] Second, it is possible that the presence of the droplet decreases the threshold for ionization. To resolve the latter issue it would be necessary to determine whether initial ionization occurs inside or outside of the water droplet.

To understand the dynamics of the laser/aerosol interaction better we examined typical images of the droplets at various times during the aerosol breakup. Figure 5 shows representative images of 60-μm-diameter water droplets irradiated by 3-GW/cm² KrF laser pulses. The imaging pulses used for illumination of the droplets lag the high-energy pulses by 0, 20, 50, 100, 300, and 1000 nsec. A 248-nm bandpass filter was placed in the optical path to the vidicon to eliminate the passage of broadband emission into the imaging system. The sequence of photos in Fig. 5 illustrates that material is expelled from both the illuminated and shadow hemispheres of the droplet within 100 nsec after the arrival of the high-energy pulse. The average velocity of the material ejected from the shadow hemisphere during the first 50 nsec can be estimated from the photographs to be approximately 1500 m/sec, while the material from the illuminated hemisphere is expelled at approximately 200 m/sec. At 300 nsec the expelled materials from nearby droplets begin to interact with one another. This mutual interaction between the expanding plumes of adjacent droplets results in the interesting appearance of the material at 1000 nsec.

Evidence of material ejection from both hemispheres of the droplet is not surprising, according to the theoretical Lorenz–Mie calculations of the internal source function. Figure 6, which shows a centerline plot of the normalized internal source function (proportional to the rate of volumetric heating), indicates regions of high source-function values near the shadow and the illuminated surfaces of the droplet. These high source-function values are characteristic of transparent droplets and can become extremely large under resonance conditions.[13]

References

1. J. C. Carls and J. R. Brock, Opt. Lett. 13, 273 (1988).
2. S. M. Chitanvis, J. Appl. Phys. 62, 4387 (1987).
3. A. Zardecki and R. L. Armstrong, Appl. Opt. 27, 3690 (1988).
4. R. K. Chang, J. H. Eickmans, W. Hsieh, C. F. Wood, J. Zhang, and J. Zheng, Appl. Opt. 27, 2377 (1988).
5. A. Biswas, H. Latifi, L. J. Radziemski, and R. L. Armstrong, Appl. Opt. 27, 2386 (1988).
6. V. A. Pogodaev and A. E. Roshdestvenskii, J. Sov. Laser Res. USA 5, 257 (1984).
7. K. D. Ahlers and D. R. Alexander, Opt. Eng. 24, 1060 (1985).
8. T. P. Hughes, Plasmas and Laser Light (Hilger, Bristol, UK, 1975).
9. C. Yamanaka, T. Yamanaka, T. Sasaki, K. Yoshida, and M. Waki, Phys. Rev. A 6, 2335 (1972).
10. R. G. Pinnick, P. Chylek, M. Jarzembski, E. Creegan, V. Srivastava, G. Fernandez, J. D. Pendleton, and A. Biswas, Appl. Opt. 27, 987 (1988).
11. D. S. Benincasa, P. W. Barber, J. Zhang, W. Hsieh, and R. K. Chang, Appl. Opt. 26, 1348 (1987).
12. G. Hale and M. Querry, Appl. Opt. 12, 555 (1973).
13. P. Chylek, J. D. Pendleton, and R. G. Pinnick, Appl. Opt. 24, 3940 (1985).

# Simplified scattering coefficient expressions for a spherical particle located on the propagation axis of a fifth-order Gaussian beam

Scott A. Schaub, John P. Barton, and Dennis R. Alexander

*Center for Electro-Optics, University of Nebraska–Lincoln, Lincoln, Nebraska 68588-0656*

Expanding on developments presented in an earlier paper, theoretical expressions for the scattering coefficients of a homogeneous, absorbing, spherical particle irradiated by a fifth-order Gaussian beam are presented for the special case of the particle center located on the propagation axis of the beam. For this case, evaluation of two-dimensional surface integrals, required in computing the scattering coefficients for the most general particle location, is reduced to a computationally more efficient one-dimensional integral. For a typical size parameter $\alpha = \pi d /\lambda = 17$, the CPU time required for calculation of scattering coefficients is reduced by a factor of $\sim 1500$ by using the simplified coefficient expressions. In addition, computation of electromagnetic field components is reduced from double summation to single summation expressions, further simplifying the field calculations.

The theoretical development for a plane electromagnetic wave incident on a homogeneous, absorbing, spherical particle was first presented near the turn of the century[1-3] and has been used extensively in investigating the interaction of electromagnetic waves with aerosol particles. While plane wave Lorenz–Mie theory has been adequate in many situations of practical interest, recent applications involving the use of focused laser beams have required the use of more general theories.

In earlier work, Barton et al.[4] presented a rigorous theoretical development for an arbitrarily defined electromagnetic beam incident on a homogeneous, absorbing, spherical particle which is based on an extension of the classical Lorenz–Mie approach. This theory allows calculation of both the internal and external electromagnetic fields given any incident beam for which an accurate mathematical description is known. A subsequent paper by Barton et al.[5] utilized the arbitrary beam theory along with a first-order Gaussian beam description provided by Davis[6] to investigate the effect of focal point positioning on structural resonances within spherical particles. These calculations required a generalized approach since the location of the particle was varied in and around the focal point of the beam in order to determine the location of maximum excitation of resonances. The arbitrary beam theory was also used by Schaub et al.[7] to explain experimental observations regarding the interaction of a tightly focused $CO_2$ laser beam incident on 165-$\mu$m-diam methanol droplets which were inconsistent with plane wave Lorenz–Mie theory calculations. A recent paper by Barton and Alexander[8] used an approach similar to Davis in providing fifth-order expressions for the electric and magnetic field components for a focused Gaussian beam. This description provides a significantly improved solution to Maxwell's equation as compared to the first-order description yet adds little computational complexity. The fifth-order Gaussian beam description was later used in examining net force and net torque induced on spherical particles for both linearly and circularly polarized incident light.[9]

In all calculations involving an arbitrary incident beam, the majority of the computation time is used in determining the appropriate scattering coefficients required in the series summations for the electric and magnetic field components (see Ref. 4). For the most general case of a particle located at an arbitrary position with respect to the beam focal point, the determination of scattering coefficients involves numerical evaluation of two-dimension surface integrals. Such coefficient computation can be substantially simplified for the situation when the particle center lies somewhere along the propagation axis of the Gaussian beam. This situation corresponds to several physically important cases such as optical levitation and laser fusion studies. In this letter we expand on developments from our earlier papers[4,8] and present simplified scattering coefficient expressions for the case of a spherical particle located on the propagation axis of a fifth-order Gaussian beam. These results will greatly facilitate the computation of the electromagnetic fields for a spherical particle irradiated by a Gaussian beam.

For the specific case under examination, consider the geometry shown in Fig. 1 in which the primed coordinate system has its origin at the beam focal point while the unprimed coordinate system is referenced to the sphere center which is located on the $z'$ axis. The Gaussian beam is propagating in the $+\hat{z} = +\hat{z}'$ direction with linear polarization in the $x = x'$ direction. For convenience, the scattering coefficients from Ref. 4 are rewritten as
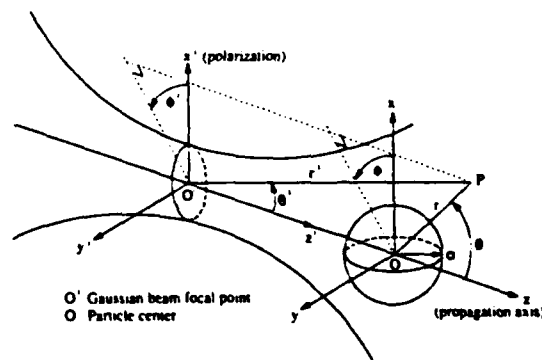


FIG. 1. Schematic of geometry.

$$a_{lm} = \frac{\psi_l'(k_{int}a)\psi_l(k_{ext}a) - \bar{n}\psi_l(k_{int}a)\psi_l'(k_{ext}a)}{\bar{n}\psi_l(k_{int}a)\xi_l^{(1)\prime}(k_{ext}a) - \psi_l'(k_{int}a)\xi_l^{(1)}(k_{ext}a)} A_{lm},$$ (1)

$$b_{lm} = \frac{\bar{n}\psi_l'(k_{int}a)\psi_l(k_{ext}a) - \psi_l(k_{int}a)\psi_l'(k_{ext}a)}{\psi_l(k_{int}a)\xi_l^{(1)\prime}(k_{ext}a) - \bar{n}\psi_l'(k_{int}a)\xi_l^{(1)}(k_{ext}a)} B_{lm},$$ (2)

$$c_{lm} = \frac{\xi_l^{(1)\prime}(k_{ext}a)\psi_l(k_{ext}a) - \xi_l^{(1)}(k_{ext}a)\psi_l'(k_{ext}a)}{\bar{n}^2\psi_l(k_{int}a)\xi_l^{(1)\prime}(k_{ext}a) - \bar{n}\psi_l'(k_{int}a)\xi_l^{(1)}(k_{ext}a)} A_{lm},$$ (3)

and

$$d_{lm} = \frac{\xi_l^{(1)\prime}(k_{ext}a)\psi_l(k_{ext}a) - \xi_l^{(1)}(k_{ext}a)\psi_l'(k_{ext}a)}{\psi_l(k_{int}a)\xi_l^{(1)\prime}(k_{ext}a) - \bar{n}\psi_l'(k_{int}a)\xi_l^{(1)}(k_{ext}a)} B_{lm},$$ (4)

where

$$A_{lm} = \frac{a^2}{l(l+1)\psi_l(k_{ext}a)}$$
$$\times \int_0^{2\pi}\int_0^\pi \sin\theta E_r^{(i)}(a,\theta,\phi) Y_{lm}^*(\theta,\phi)d\theta\,d\phi \quad (5)$$

and

$$B_{lm} = \frac{a^2}{l(l+1)\psi_l(k_{ext}a)}$$
$$\times \int_0^{2\pi}\int_0^\pi \sin\theta H_r^{(i)}(a,\theta,\phi) Y_{lm}^*(\theta,\phi)d\theta\,d\phi. \quad (6)$$

In these equations, $k = (\omega/c)\sqrt{\bar{\epsilon}}$, where $\bar{\epsilon}$ is the complex dielectric constant defined as $\bar{\epsilon} = \epsilon + i4\pi\sigma/\omega$, $\omega$ is the angular frequency, $c$ is the speed of light, and $\sigma$ is the electrical conductivity. Also, $a$ is the sphere radius and $\bar{n}$ is the complex refractive index defined by $\bar{n} = (\bar{\epsilon}_{int}/\epsilon_{ext})^{1/2}$, where the subscripts denote internal and external to the sphere, respectively. $\psi_l$ and $\xi_l^{(1)} = \psi_l - i\chi_l$ are the Riccati–Bessel functions. For complete details of the derivation the reader is referred to Ref. 4.

For brevity, only the derivation for the simplification of Eq. (5) will be presented in detail since the derivation corresponding to Eq. (6) follows in a similar manner. Expanding the radial component of the incident electric field in Eq. (5) in terms of Cartesian coordinates and using the definition of the complex conjugate of the spherical harmonic function, $Y_{lm}^*$ (Ref. 10), Eq. (5) can be rewritten as

$$A_{lm} = G_{lm}\int_0^\pi \sin\theta P_l^m(\cos\theta)\int_0^{2\pi} \left[E_x^{(i)}(a,\theta,\phi)\sin\theta\cos\phi\right.$$
$$+ E_y^{(i)}(a,\theta,\phi)\sin\theta\sin\phi + E_z^{(i)}(a,\theta,\phi)\cos\theta\Big]$$
$$\times\exp(-im\phi)d\phi\,d\theta, \quad (7)$$

where $P_l^m$ is the associated Legendre function and

$$G_{lm} = \frac{a^2}{[l(l+1)\psi_l(k_{ext}a)]}\left(\frac{2l+1(l-m)!}{4\pi(l+m)!}\right)^{1/2}. \quad (8)$$

Using the results of Barton and Alexander,[8] the incident electric field components for a fifth-order Gaussian beam can be written as

$$E_x^{(i)}/E_0 = F_1 + F_2(x'/w_0)^2, \quad (9)$$

$$E_y^{(i)}/E_0 = F_2(x'y'/w_0^2), \quad (10)$$

and

$$E_z^{(i)}/E_0 = F_3(x'/w_0). \quad (11)$$

Here, $E_0$ is the electric field amplitude at the focal point of the beam ($x' = y' = z' = 0$), $w_0$ is the beam waist, and

$$F_1 = \Gamma(1 - s^2\rho^2Q^2 + is^2\rho^4Q^3 + 2s^4\rho^4Q^4$$
$$- 3is^4\rho^6Q^5 - 0.5s^4\rho^8Q^6), \quad (12)$$

$$F_2 = \Gamma(8s^4\rho^2Q^4 - 2is^4\rho^4Q^5 - 2s^2Q^2), \quad (13)$$

$$F_3 = \Gamma(-2sQ + 6s^3\rho^2Q^3 - 2is^3\rho^4Q^4$$
$$- 20s^5\rho^4Q^5 + 10is^5\rho^6Q^6 + s^5\rho^8Q^7), \quad (14)$$

where

$$\Gamma = iQ\exp(-i\rho^2Q)\exp(-iz'/k_{ext}w_0^2s^2), \quad (15)$$

$$Q = (i + 2z'/k_{ext}w_0^2)^{-1}, \quad (16)$$

$$\rho = (x'^2 + y'^2)/w_0^2, \quad (17)$$

and

$$s = 1/k_{ext}w_0. \quad (18)$$

Noting that

$$x' = r'\sin\theta'\cos\phi' = r'\sin\theta'\cos\phi, \quad (19)$$

$$y' = r'\sin\theta'\sin\phi' = r'\sin\theta'\sin\phi, \quad (20)$$

and

$$z' = r'\cos\theta', \quad (21)$$

it is straightforward to verify that all $F$ functions [Eqs. (12)–(14)] are independent of the angle $\phi$ (note: $\phi = \phi'$ for particle center on the propagation axis). Equation (7) can now be expressed as

$$A_{lm} = E_0 G_{lm} \int_0^\pi \sin\theta P_l^m(\cos\theta)\left[ F_1 \sin\theta \int_0^{2\pi} \cos\phi \exp(-im\phi)d\phi + F_2\left(\frac{r'\sin\theta'}{w_0}\right)^2 \sin\theta \int_0^{2\pi} \cos^3\phi \exp(-im\phi)d\phi \right.$$
$$\left. + F_2\left(\frac{r'\sin\theta'}{w_0}\right)^2 \sin\theta \int_0^{2\pi}(\cos\phi - \cos^3\phi)\exp(-im\phi)d\phi + F_3\left(\frac{r'\sin\theta'}{\omega_0}\right)\cos\theta \int_0^{2\pi}\cos\phi\exp(-im\phi)d\phi \right] d\theta.$$

$$(22)$$

The two terms involving $\cos^3\phi$ are of opposite sign and will cancel. Equation (22) can be further simplified using the orthogonal properties of the cosine function:

$$\int_0^{2\pi} \cos\phi \exp(-im\phi)d\phi = \begin{cases} \pi, m = |1| \\ 0, m \neq |1|. \end{cases} \quad (23)$$

For $m = +1$ the final result can be written as

$$A_{l,+1} = \left(\frac{2l+1}{4\pi l(l+1)}\right)^{1/2} \frac{\pi E_0 a^2}{l(l+1)\psi_l(k_{ext}a)}$$

$$\times \int_0^\pi \sin\theta P_l^{(1)}(\cos\theta)\left[ F_1 \sin\theta \right.$$

$$\left. + F_2\left(\frac{r'\sin\theta'}{w_0}\right)^2 \sin\theta + F_3\left(\frac{r'\sin\theta'}{w_0}\right)\cos\theta \right] d\theta.$$

$$(24)$$

Using the relation from Ref. 10,

$$P_l^{(1)}(x) = -\frac{(l+1)!}{(l-1)!} P_l^{(-1)}(x) \quad (25)$$

for the $m = -1$ case will give the result

$$A_{l,-1} = -A_{l,+1}. \quad (26)$$

The development for $B_{lm}$ [Eq. (6)] follows in a parallel fashion yielding

$$B_{l,+1} = (-i\sqrt{\epsilon_{ext}})A_{l,+1} \quad (27)$$

and

$$B_{l,-1} = B_{l,+1}. \quad (28)$$

Equations (24) and (26)–(28) along with Eqs. (1)–(4) completely determine the scattering coefficients for a fifth-order Gaussian beam incident on a spherical particle located on the propagation axis of the beam. The results presented in this paper have reduced the required numerical integration from two-dimensional surface integrals [Eqs. (5) and (6)] to a computationally more efficient one-dimensional integral [Eq. (24)]. Comparing the two methods for a typical size parameter $\alpha = \pi d/\lambda = 17$ and complex index of refraction $\bar{n} = 1.5 + 0.01i$, the time required for computation of scattering coefficients was reduced by a factor of ~1500 by using the simplified coefficient expression. In general, the CPU savings in coefficient computation will increase at a rate approximately proportional to the size parameter. In addition, summation of electric and magnetic field components, which was previously over the two indices $l$ and $m$ (see Ref. 4), is reduced to a summation over the single index $l$, further simplifying the electromagnetic field calculations.

[1] G. Mie, Ann. Phys. 25, 377 (1908).
[2] P. Debye, Ann. Phys. 30, 57 (1909).
[3] L. Lorenz, Videnskab. Selskab. Skrifter. 6 (1890).
[4] J. P. Barton, D. R. Alexander, and S. A. Schaub, J. Appl. Phys. 64, 1632 (1988).
[5] J. P. Barton, D. R. Alexander, and S. A. Schaub, J. Appl. Phys. 65, 2900 (1989).
[6] L. W. Davis, Phys. Rev. A 19, 1177 (1979).
[7] S. A. Schaub, D. R. Alexander, J. P. Barton, and M. A. Emanuel, Appl. Opt. 28, 1666 (1989).
[8] J. P. Barton and D. R. Alexander, J. Appl. Phys. 66, 2800 (1989).
[9] J. P. Barton D. R. Alexander, and S. A. Schaub, J. Appl. Phys. 66, 4594 (1989).
[10] J. D. Jackson, Classical Electrodynamics, 2nd ed. (Wiley, New York, 1975).

# Fifth-order corrected electromagnetic field components for a fundamental Gaussian beam

J. P. Barton and D. R. Alexander

*Center for Electro-Optics, College of Engineering, University of Nebraska-Lincoln, Lincoln, Nebraska 68588-0525*

Fifth-order corrected expressions for the electromagnetic field components of a monochromatic fundamental Gaussian beam (i.e., a focused TEM$_{00}$ mode laser beam) propagating within a homogeneous dielectric media are derived and presented. Calculations of relative error indicate that the fifth-order Gaussian beam description provides a significantly improved solution to Maxwell's equations in comparison with commonly used paraxial (zeroth-order) and first-order Gaussian beam descriptions.

## I. INTRODUCTION

In two recent papers,[1,2] theoretical calculations have been presented investigating the electromagnetic interaction of a monochromatic fundamental Gaussian beam (i.e., a TEM$_{00}$ mode focused laser beam) with a homogeneous spherical particle. A mathematical description of the electromagnetic field components of the incident Gaussian beam which accurately satisfies Maxwell's equations is required for these calculations. In Refs. 1 and 2, first-order corrected expressions developed by Davis[3] were used for the incident Gaussian beam description. This first-order corrected Gaussian beam description, which is consistent with the first-order corrected expressions of Lax, Louisell, and McKnight[4] and the development of Simon, Sudarshan, and Muhunda,[5] has been found to give good results when the beam waist radius ($w_0$) is much greater than the wavelength ($\lambda$).

For tightly focused beams, where the beam waist radius is of the same order as the wavelength, the first-order corrected Gaussian beam description satisfies Maxwell's equations less accurately and the electromagnetic field calculations using the spherical particle/arbitrary beam interaction theory of Ref. 1 likewise become less accurate. In Ref. 3, Davis presents a procedure for developing a higher-order corrected Gaussian beam description and provides expressions for two of the three electric field components to third order in the parameter $s$, where

$$s = \frac{1}{kw_0} = \frac{1}{2\pi}\left(\frac{\lambda}{w_0}\right). \tag{1}$$

However, Davis's expressions are for vacuum conditions only, do not include the third electric field component or the magnetic field components, and, beyond first order, lack symmetry with regard to the electric and magnetic field components.

In this paper, a modification and extension of the procedure introduced by Davis[3] is used to derive *fifth-order* corrected expressions for all six electromagnetic field components. These expressions are symmetrical with regard to the electric and magnetic field components and are applicable for dielectric media. A comparison of relative error as a function of order and tightness of focus is also presented. These results should be of interest to anyone requiring an accurate

Gaussian beam description, particularly for tightly focused conditions.

## II. THEORETICAL DEVELOPMENT

The propagation of a monochromatic beam within isotropic, homogeneous, nonmagnetic ($\mu = 1$), nonconducting ($\sigma = 0$) dielectric media is considered. A harmonic time dependence of $e^{+i\omega t}$ is assumed. (The $e^{+i\omega t}$ is dropped from all subsequent time-dependent terms.) For these conditions, Maxwell's equations can be written in the following form:

$$\nabla \cdot \mathbf{E} = 0, \tag{2}$$

$$\nabla \times (\mathbf{H}/\sqrt{\epsilon}) - ik\,\mathbf{E} = 0, \tag{3}$$

$$\nabla \times \mathbf{E} + ik(\mathbf{H}/\sqrt{\epsilon}) = 0, \tag{4}$$

and

$$\nabla \cdot (\mathbf{H}/\sqrt{\epsilon}) = 0, \tag{5}$$

where $k = \sqrt{\epsilon}\,\omega/c = 2\pi/\lambda$ is the wave number within the media. In the Lorentz gauge, a vector potential $\mathbf{A}$ can be defined such that if $\mathbf{A}$ is a solution of the Helmholtz equation,

$$\nabla^2 \mathbf{A} + k^2 \mathbf{A} = 0, \tag{6}$$

then

$$\mathbf{E} = -(i/k)\nabla(\nabla \cdot \mathbf{A}) - ik\,\mathbf{A} \tag{7}$$

and

$$\mathbf{H}/\sqrt{\epsilon} = \nabla \times \mathbf{A} \tag{8}$$

satisfy Maxwell's equations, Eqs. (2)–(5).

Davis[3] observed that, for a beam propagating in the $+z$ axis direction, if the vector potential is assumed linearly polarized in the $x$ axis direction,

$$\mathbf{A} = A\hat{x} \tag{9}$$

where

$$A = \psi(x,y,z)e^{-ikz}, \tag{10}$$

then Eqs. (6)–(8) provide a linearly polarized (predominate electric field polarization in the $x$ axis direction) Gaussian beam. Foreseeing a solution similar to the well-established paraxial (zeroth-order) Gaussian beam solution (see, for example, Yariv[6]), the spatial coordinates transverse to

the direction of propagation are normalized relative to the beam waist radius, $\xi = x/w_0$ and $\eta = y/w_0$, and the spatial coordinate in the direction of propagation is normalized relative to the diffraction length, $\zeta = z/(kw_0^2)$. With this change of spatial variables, the expression for the vector potential becomes

$$A = \psi(\xi,\eta,\zeta)e^{-is/s}$$ (11)

and Helmholtz equation, in terms of $\psi$, can be rearranged as

$$\left(\frac{\partial^2}{\partial\xi^2} + \frac{\partial^2}{\partial\eta^2} - 2i\frac{\partial}{\partial\zeta}\right)\psi = -s^2\frac{\partial^2\psi}{\partial\zeta^2}.$$ (12)

If the parameter $s$, defined in Eq. (1), is assumed small ($w_0 \geqslant \lambda$) then from Eq. (12) it is apparent that $\psi$ can be expanded as a sum of even powers of $s$ so that

$$\psi = \psi_0 + s^2\psi_2 + s^4\psi_4 + \cdots,$$ (13)

where

$$\left(\frac{\partial^2}{\partial\xi^2} + \frac{\partial^2}{\partial\eta^2} - 2i\frac{\partial}{\partial\zeta}\right)\psi_0 = 0,$$ (14)

$$\left(\frac{\partial^2}{\partial\xi^2} + \frac{\partial^2}{\partial\eta^2} - 2i\frac{\partial}{\partial\zeta}\right)\psi_2 = -\frac{\partial^2\psi_0}{\partial\zeta^2},$$ (15)

$$\left(\frac{\partial^2}{\partial\xi^2} + \frac{\partial^2}{\partial\eta^2} - 2i\frac{\partial}{\partial\zeta}\right)\psi_4 = -\frac{\partial^2\psi_2}{\partial\zeta^2},$$ (16)

etc.

Equation (14) is the familiar paraxial beam equation,[6] which has the solution

$$\psi_0 = iQ\exp(-i\rho^2 Q),$$ (17)

where $\rho^2 = \xi^2 + \eta^2$ and $Q = 1/(i + 2\zeta)$. Substituting Eq. (17) into Eq. (15), Davis found

$$\psi_2 = (2iQ + i\rho^4 Q^3)\psi_0.$$ (18)

Continuing and substituting Eq. (18) into Eq. (16) it follows that

$$\psi_4 = (-6Q^2 - 3\rho^4 Q^4 - 2i\rho^6 Q^5 - 0.5\rho^8 Q^6)\psi_0.$$ (19)

Using

$$A \simeq (\psi_0 + s^2\psi_2 + s^4\psi_4)e^{-is/s}\hat{x}$$ (20)

with Eqs. (7) and (8) would give expressions for electromagnetic field components to fifth order in $s$. However, beyond first order, these expressions for the electric and magnetic field components lack symmetry. [Note since $A = A\hat{x}$, Eq. (8) indicates $H_x = 0$ for all orders of $s$.] In order to develop a Gaussian beam description for which the electric and magnetic field component expression have symmetry, the derivation was repeated with

$$H'/\sqrt{\epsilon} = +(i/k)\nabla(\nabla\cdot A') + ik A'$$ (21)

and

$$E' = \nabla \times A',$$ (22)

where

$$\nabla^2 A' + k^2 A' = 0$$ (23)

and

$$A' = A'\hat{y} = \psi'(x,y,z)e^{-ikz}\hat{y}.$$ (24)

The solution of Eqs. (7) and (8) was appropriately added to the solution of Eqs. (21) and (22) and the result divided by two. The resulting electromagnetic field component expressions, to fifth order in the parameter $s$, are as follows:

$$E_x = E_0\{1 + s^2(-\rho^2 Q^2 + i\rho^4 Q^3 - 2Q^2\xi^2)$$
$$+ s^4[+2\rho^4 Q^4 - 3i\rho^6 Q^5 - 0.5\rho^8 Q^6$$
$$+ (8\rho^2 Q^4 - i2\rho^4 Q^5)\xi^2]\}\psi_0 e^{-is/s^2},$$ (25)

$$E_y = E_0\{s^2(-2Q^2\xi\eta) + s^4[(8\rho^2 Q^4 - 2i\rho^4 Q^5)\xi\eta]\}\psi_0$$
$$\times e^{-is/s^2},$$ (26)

$$E_z = E_0\{s(-2Q\xi) + s^3[(+6\rho^2 Q^3 - 2i\rho^4 Q^4)\xi]$$
$$+ s^5[(-20\rho^4 Q^5 + 10i\rho^6 Q^6 + \rho^8 Q^7)\xi]\}\psi_0 e^{-is/s^2},$$ (27)

$$H_x = \sqrt{\epsilon}E_0\{s^2(-2Q^2\xi\eta) + s^4[(8\rho^2 Q^4 - 2i\rho^4 Q^5)\xi\eta]\}\psi_0$$
$$\times e^{-is/s^2},$$ (28)

$$H_y = \sqrt{\epsilon}E_0\{1 + s^2(-\rho^2 Q^2 + i\rho^4 Q^3 - 2Q^2\eta^2)$$
$$+ s^4[+2\rho^4 Q^4 - 3i\rho^6 Q^5 - 0.5\rho^8 Q^6$$
$$+ (8\rho^2 Q^4 - i2\rho^4 Q^5)\eta^2]\}\psi_0 e^{-is/s^2},$$ (29)

and

$$H_z = \sqrt{\epsilon}E_0\{s(-2Q\eta) + s^3[(+6\rho^2 Q^3 - 2i\rho^4 Q^4)\eta]$$
$$+ s^5[(-20\rho^4 Q^5 + 10i\rho^6 Q^6 + \rho^8 Q^7)\eta]\}\psi_0 e^{-is/s^2},$$ (30)

where $\psi_0$ is given by Eq. (17).

In Eqs. (25)–(30), $E_0$ is the electric field amplitude at the focal point of the beam ($\xi = \eta = \zeta = 0$) which can be related to the beam power $P$ by

$$|E_0|^2 = \frac{16P}{\sqrt{\epsilon}cw_0^2(1 + s^2 + 1.5s^4)}.$$ (31)

To zeroth order in $s$, Eqs. (25)–(30) provide the familiar paraxial Gaussian beam description.[6] To first order in $s$, Eqs. (25)–(30) are identical to the first-order corrected expressions of Davis[3] and Lax, Louisell, and McKnight[4] and the development of Simon, Sudarshan, and Mukunda.[5] Equations (25)–(30) are for a harmonic time dependence of $e^{+i\omega t}$. If a harmonic time dependence of $e^{-i\omega t}$ is assumed, then the complex conjugate of Eqs. (25)–(30) can be used.

## III. RELATIVE ACCURACY

The fifth-order corrected Gaussian beam description was verified by directly substituting the electromagnetic field components given by Eqs. (25)–(30) into Maxwell's equations, Eqs. (2)–(5), and calculating the relative percent error. [The relative percent error was computed by taking the percent deviation of the magnitude of the left-hand side of each equation from zero relative to $k|E|$ for Eqs. (2) and (3) and relative to $k|H|/\sqrt{\epsilon}$ for Eqs. (4) and (5).] Table I provides a comparison of the percent error for $s = 0.02, 0.05, 0.10, 0.20, 0.30,$ and $0.40$ for zeroth- to fifth-order Gaussian beam descriptions. Both the average percent error and the maximum percent error were calculated for 216 spatial positions surrounding the focal point consisting of all combinations of $\xi, \eta, \zeta = 0.0, 0.1, 0.2, 0.5, 1.0,$ and $1.5$. As shown in

TABLE I. Average percent error and maximum percent error of solution to Maxwell's equations for zeroth- to fifth-order Gaussian beam descriptions vs $s$. Percent error calculated for 216 points consisting of all combinations of $\xi$, $\eta$, $\zeta$ = 0.0, 0.1, 0.2, 0.5, 1.0, and 1.5.

| | $s =$ | 0.02 | 0.05 | 0.10 | 0.20 | 0.30 | 0.40 |
|---|---|---|---|---|---|---|---|
| $s^0$ | avg% | 0.817 | 2.10 | 4.37 | 9.47 | 15.3 | 21.8 |
| | max% | 3.07 | 7.94 | 16.8 | 37.0 | 60.8 | 88.0 |
| $s^1$ | avg% | $1.73 \times 10^{-2}$ | 0.111 | 0.457 | 1.90 | 4.33 | 7.74 |
| | max% | $9.28 \times 10^{-2}$ | 0.603 | 2.51 | 10.3 | 22.6 | 38.4 |
| $s^2$ | avg% | $6.43 \times 10^{-4}$ | $1.05 \times 10^{-2}$ | $8.85 \times 10^{-2}$ | 0.757 | 2.56 | 5.89 |
| | max% | $8.23 \times 10^{-3}$ | 0.133 | 1.14 | 10.7 | 31.9 | 49.3 |
| $s^3$ | avg% | $2.36 \times 10^{-5}$ | $9.58 \times 10^{-4}$ | $1.61 \times 10^{-2}$ | 0.277 | 1.44 | 4.25 |
| | max% | $1.97 \times 10^{-4}$ | $8.26 \times 10^{-3}$ | 0.144 | 2.51 | 19.1 | 36.0 |
| $s^4$ | avg% | $1.15 \times 10^{-6}$ | $1.19 \times 10^{-4}$ | $4.10 \times 10^{-3}$ | 0.148 | 1.13 | 3.85 |
| | max% | $2.46 \times 10^{-5}$ | $2.52 \times 10^{-3}$ | $8.85 \times 10^{-2}$ | 3.99 | 38.2 | 54.0 |
| $s^5$ | avg% | $5.13 \times 10^{-8}$ | $1.27 \times 10^{-5}$ | $8.69 \times 10^{-4}$ | $6.19 \times 10^{-2}$ | 0.725 | 3.34 |
| | max% | $7.58 \times 10^{-7}$ | $1.99 \times 10^{-4}$ | $1.40 \times 10^{-2}$ | 1.19 | 22.2 | 36.6 |

Table I, the fifth-order Gaussian beam description gives a significant improvement in accuracy in comparison with the commonly used zeroth- and first-order descriptions. As might be expected, the fifth-order Gaussian beam expressions become less accurate as $s$ approaches one. According to these calculations, if a deviation of 1% is acceptable, then the fifth-order description can be used for $s$ less than about 0.2. An $s$ value of 0.2 corresponds to a beam waist radius to wavelength ratio of about 0.8.

## IV. DISCUSSION

The fifth-order Gaussian beam description has been used with the spherical particle/arbitrary beam interaction theory of Ref. 1 with improved results in comparison with the previously used first-order Gaussian beam description (as evidenced by improved matching of boundary conditions across the surface of the sphere, etc.).

The procedure outlined here could be continued to develop higher-order corrected Gaussian beam descriptions. In addition, as suggested by Zauderer,[7] the transverse spatial derivatives of Eqs. (25)–(30) (and linear combinations of these derivatives) perhaps could be used to construct corrected expressions for higher-mode Gaussian beams. This advanced work is presently under consideration.

## ACKNOWLEDGMENT

[1] J. P. Barton, D. R. Alexander, and S. A. Schaub, J. Appl. Phys. 64, 1632 (1988).
[2] J. P. Barton, D. R. Alexander, and S. A. Schaub, J. Appl. Phys. 65, 2900 (1989).
[3] L. W. Davis, Phys. Rev. A 19, 1177 (1979).
[4] M. Lax, W. H. Louisell, and W. B. McKnight, Phys. Rev. A 11, 1365 (1975).
[5] R. Simon, E. C. G. Sudarshan, and N. Mukunda, J. Opt. Soc. Am. A 3, 536 (1986).
[6] A. Yariv, Introduction to Optical Electronics (Holt, Rinehart, and Winston, New York, 1976).
[7] E. Zauderer, J. Opt. Soc. Am. A 3, 465 (1986).

# Theoretical determination of net radiation force and torque for a spherical particle illuminated by a focused laser beam

J. P. Barton, D. R. Alexander, and S. A. Schaub

*Center for Electro-Optics, College of Engineering, University of Nebraska-Lincoln, Lincoln, Nebraska 68588-0525*

Series expressions for the net radiation force and torque for a spherical particle illuminated by an arbitrarily defined monochromatic beam are derived utilizing the spherical-particle/arbitrary-beam interaction theory developed in an earlier paper. Calculations of net force and torque are presented for a 5-$\mu$m-diam water droplet in air optically levitated by a tightly focused (2 $\mu$m beam waist diameter) TEM$_{00}$-mode argon-ion ($\lambda = 0.5145\,\mu$m) laser beam for on and off propagation axis, and on and off structural resonance conditions. Several features of these theoretical results are related to corresponding experimental observations.

## I. INTRODUCTION

The optical levitation of transparent micrometer-sized spherical particles using a focused TEM$_{00}$-mode laser beam was first proposed and experimentally demonstrated by Ashkin[1] in 1970. Subsequently, Ashkin,[2,3] Ashkin and Dziedzic,[4-11] and other researchers[12-18] have further investigated the various aspects and applications of optical particle levitation. As discussed in these papers, the nonintrusive precision manipulation of micrometer-sized particles offered by optical levitation can be advantageously utilized for the study of microchemistry, aerosol physics, and particle light scattering.

Theoretical expressions for the net radiation force on a homogeneous spherical particle illuminated by an electromagnetic, linearly polarized plane wave were developed by Debye[19] in 1909. (A similar, more recent, development is given in Kerker.[20]) Marston and Crichton[21,22] developed theoretical expressions for the net radiation torque induced on a homogeneous spherical particle illuminated by a circularly polarized plane wave.

For optical levitation arrangements, however, the diameters of the laser beam and the spherical particle are of the same order, and the plane-wave assumption is not appropriate. Roosen and co-workers[23-26] have performed net radiation force calculations for a spherical particle within a focused laser beam using geometrical optics. This geometrical optics analysis would not be accurate for conditions near structural resonance or when the diameter of the particle and the incident wavelength are of the same order.

Theoretical expressions for the internal and external electromagnetic fields of a homogeneous spherical particle illuminated by a focused laser beam based upon a rigorous, complete solution of Maxwell's equations have been developed, each utilizing different approaches, by Kim and Lee,[27] Gouesbet, Maheu, and Grehan,[28] and Barton, Alexander, and Schaub.[29] In the approach used by Kim and Lee,[27] the electromagnetic field of the incident beam is described using the complex-source-point method. Reference 27 contains series-form theoretical expressions for the net radiation force on the particle, in terms of this formulation, and in a later paper by Chang and Lee,[30] series expressions for the net

torque are presented. In the approach of Gouesbet and co-workers,[28] the coefficients describing the incident beam are generated using computationally difficult surface integrals over an infinite half-plane. Reference 28 presents series expressions for the net radiation force on the particle in terms of these coefficients.

In the recently developed formalism of Barton and co-workers,[29] the incident beam is arbitrarily defined, not restricted to the complex-source-point description as in Refs. 27 and 30, and the coefficients necessary to describe the incident beam are generated using finite surface integrals, which is more computationally efficient than the required integrals of Ref. 28.

Presented here are series-form theoretical expressions for the net radiation force and torque for a spherical particle illuminated by an arbitrary beam utilizing the spherical-particle/arbitrary-beam interaction theory of Barton and co-workers.[29] As an application of these equations, calculations are presented for the net radiation force and torque for a 5-$\mu$m-diam water droplet in air levitated by a single, vertically oriented, focused (2 $\mu$m beam waist diameter) TEM$_{00}$-mode argon-ion (0.5145 $\mu$m wavelength) laser beam for on and off propagation axis, and on and off structural resonance conditions. Several features of these theoretical results are related to corresponding experimental observations.

## II. THEORY

The particular problem considered is that of a homogeneous spherical particle within an infinite dielectric media illuminated by a monochromatic electromagnetic beam. Both the particle and the surrounding medium are linear, isotropic, and nonmagnetic ($\mu = 1$ is assumed throughout). Theoretical expressions for the incident, scattered, and internal electromagnetic field components are derived in Ref. 29. These equations are given, in complete nondimensional form, in Appendix A. A coordinate system with the origin at the sphere center is assumed, and all electromagnetic field components are normalized relative to an electric field magnitude characteristic of the incident beam $E_0$. The time-dependent complex exponential $e^{-i\omega t}$ is omitted from these

and all subsequent expressions. The fundamental parameters of the analysis are the dielectric constant of the surrounding medium, $\epsilon_{ext}$, the complex relative index of refraction of the particle $\bar{n} = (\bar{\epsilon}_{int}/\epsilon_{ext})^{1/2}$, and the particle size parameter $\alpha = 2\pi a/\lambda$, where $a$ is the radius of the particle and $\lambda$ is the wavelength in the surrounding medium.

The coefficients that describe the assumed known incident beam, $A_{lm}$ and $B_{lm}$, are generated using the surface integrals of Eqs. (A23) and (A24). The coefficients that describe the scattered electromagnetic field, $a_{lm}$ and $b_{lm}$, are related to $A_{lm}$ and $B_{lm}$ by Eqs. (A19) and (A20). (For an incident plane wave, all $A_{lm}$ and $B_{lm}$ are zero except for $m = \pm 1$, and the solution reduces identically to that of Mie theory.)

Assuming a steady-state condition, the net radiation force **F** on the particle can be determined by integrating the dot product of the outwardly directed normal unit vector $\hat{n}$ and Maxwell's stress tensor $\overrightarrow{T}$ over a surface enclosing the particle[31]:

$$\langle \mathbf{F} \rangle = \langle \oint_S \hat{n}\cdot\overrightarrow{T}dS \rangle, \tag{1}$$

where $\langle\ \rangle$ represents a time average. The appropriate form of Maxwell's stress tensor to use in Eq. (1) is the topic of recent reviews by Robinson[32] and Brevik.[33] Apparently, for steady-state optical conditions, the traditional Minkowski form of Maxwell's stress tensor,

$$\overrightarrow{T} = \frac{1}{4\pi}\left(\epsilon\mathbf{EE} + \mathbf{HH} - \frac{1}{2}(\epsilon E^2 + H^2)\overrightarrow{I}\right), \tag{2}$$

will give correct results. The so-called "Abraham's term" is negligible at optical frequencies, and at steady-state, electrostrictive forces are balanced by mechanical pressures. The reader is referred to Refs. 32 and 33 for further discussion.

Substituting Eq. (2) into Eq. (1) and integrating over a spherical surface $r > a$ gives

$$\langle\mathbf{F}\rangle = \frac{1}{4\pi}\int_0^{2\pi}\int_0^{\pi}\left\langle\left(\epsilon_{ext}E_r\mathbf{E} + H_r\mathbf{H}\right.\right.$$
$$\left.\left. - \frac{1}{2}(\epsilon_{ext}E^2 + H^2)\hat{r}\right)\right\rangle r^2\sin\theta\, d\theta\, d\phi\Big|_{r>a}. \tag{3}$$

In a form consistent with the nondimensionalized electromagnetic field equations given in Appendix A, Eq. (3) becomes

$$\frac{\langle\mathbf{F}\rangle}{a^2E_0^2} = \frac{1}{8\pi}\text{Re}\int_0^{2\pi}\int_0^{\pi}\left(\frac{1}{2}[\epsilon_{ext}(E_rE_r^* - E_\theta E_\theta^* - E_\phi E_\phi^*)\right.$$
$$+ (H_rH_r^* - H_\theta H_\theta^* - H_\phi H_\phi^*)]\hat{r} + (\epsilon_{ext}E_rE_\theta^*$$
$$+ H_rH_\theta^*)\hat{\theta} + (\epsilon_{ext}E_rE_\phi^* + H_rH_\phi^*)\hat{\phi}\Big)$$
$$\times \bar{r}^2\sin\theta\, d\theta\, d\phi\Big|_{\bar{r}>1}, \tag{4}$$

where, here, $\mathbf{E} = \mathbf{E}^{(i)} + \mathbf{E}^{(s)}$ and $\mathbf{H} = \mathbf{H}^{(i)} + \mathbf{H}^{(s)}$.

Numerical calculation of the surface integral of Eq. (4) can be avoided by substituting the series expressions for the electromagnetic field components (from Appendix A) and evaluating at the large radius limit ($r \gg a$), where

$$\psi_l(\alpha\bar{r}) \Rightarrow \sin(\alpha\bar{r} - l\pi/2),$$

and

$$\xi_l^{(1)}(\alpha\bar{r}) \Rightarrow -i\exp[+i(\alpha\bar{r} - l\pi/2)].$$

After a great deal of algebra and applying numerous recursion, product, and orthogonality relationships among the spherical harmonic functions, Eq. (4) can be directly integrated, and the net force on the particle can be expressed as a series over the coefficients $a_{lm}, b_{lm}, A_{lm}$, and $B_{lm}$:

$$\frac{\langle F_x\rangle + i\langle F_y\rangle}{a^2E_0^2} = +\frac{\alpha^2}{16\pi}i\sum_{l=1}^{\infty}\sum_{m=-l}^{l}\left(\sqrt{\frac{(l+m+2)(l+m+1)}{(2l+1)(2l+3)}}l(l+2)\right.$$

$$\times(2\epsilon_{ext}a_{lm}a_{l+1,m+1}^* + \epsilon_{ext}a_{lm}A_{l+1,m+1}^* + \epsilon_{ext}A_{lm}a_{l+1,m+1}^* + 2b_{lm}b_{l+1,m+1}^* + b_{lm}B_{l+1,m+1}^*$$

$$+ B_{lm}b_{l+1,m+1}^*) + \sqrt{\frac{(l-m+1)(l-m+2)}{(2l+1)(2l+3)}}l(l+2)(2\epsilon_{ext}a_{l+1,m-1}a_{lm}^* + \epsilon_{ext}a_{l+1,m-1}A_{lm}^*$$

$$+ \epsilon_{ext}A_{l+1,m-1}a_{lm}^* + 2b_{l+1,m-1}b_{lm}^* + b_{l+1,m-1}B_{lm}^* + B_{l+1,m-1}b_{lm}^*)$$

$$- \sqrt{(l+m+1)(l-m)}\sqrt{\epsilon_{ext}}(-2a_{lm}b_{l,m+1}^* + 2b_{lm}a_{l,m+1}^* - a_{lm}B_{l,m+1}^*$$

$$+ b_{lm}A_{l,m+1}^* + B_{lm}a_{l,m+1}^* - A_{lm}b_{l,m+1}^*)\Big) \tag{5}$$

and

$$\frac{\langle F_z\rangle}{a^2E_0^2} = -\frac{\alpha^2}{8\pi}\sum_{l=1}^{\infty}\sum_{m=-l}^{l}\text{Im}\left(l(l+2)\sqrt{\frac{(l-m+1)(l+m+1)}{(2l+3)(2l+1)}}\right.$$

$$\times(2\epsilon_{ext}a_{l+1,m}a_{lm}^* + \epsilon_{ext}a_{l+1,m}A_{lm}^* + \epsilon_{ext}A_{l+1,m}a_{lm}^* + 2b_{l+1,m}b_{lm}^* + b_{l+1,m}B_{lm}^*$$

$$+ B_{l+1,m}b_{lm}^*) + \sqrt{\epsilon_{ext}}m(2a_{lm}b_{lm}^* + a_{lm}B_{lm}^* + A_{lm}b_{lm}^*)\Big). \tag{6}$$

The series expressions of Eqs. (5) and (6) were verified by comparison with the numerical calculation of the surface integral of Eq. (4) for several different cases and agreement was found.

The net radiation torque N on the particle can be determined by performing a surface integral of the dot product of the outwardly directed normal unit vector $\hat{n}$ and the pseudo-tensor, $\overleftrightarrow{T} \times \mathbf{r}$, over a surface enclosing the particle[31]:

$$\langle \mathbf{N} \rangle = - \left\langle \oint_S \hat{n} \cdot (\overleftrightarrow{T} \times \mathbf{r}) dS \right\rangle. \tag{7}$$

If a spherical surface of radius $r > a$ is chosen, then

$$\langle \mathbf{N} \rangle = - \frac{1}{4\pi} \int_0^{2\pi} \int_0^{\pi} \langle [ (\epsilon_{ext} E_r E_\phi + H_r H_\phi) \hat{\theta} \\ - (\epsilon_{ext} E_r E_\theta + H_r H_\theta) \hat{\phi} ] \rangle r^3 \sin \theta \, d\theta \, d\phi |_{r > a}, \tag{8}$$

or, consistent with the form of the nondimensional electromagnetic field equations given in Appendix A,

$$\frac{\langle \mathbf{N} \rangle}{a^3 E_0^2} = - \frac{1}{8\pi} \text{Re} \int_0^{2\pi} \int_0^{\pi} [ (\epsilon_{ext} E_r E_\phi^* + H_r H_\phi^*) \hat{\theta} \\ - (\epsilon_{ext} E_r E_\theta^* + H_r H_\theta^*) \hat{\phi} ] r^3 \sin \theta \, d\theta \, d\phi |_{r > 1} \tag{9}$$

where, as before, $\mathbf{E} = \mathbf{E}^{(i)} + \mathbf{E}^{(s)}$ and $\mathbf{H} = \mathbf{H}^{(i)} + \mathbf{H}^{(s)}$. Substituting for the electromagnetic field components from Appendix A and evaluating at the large limit, Eq. (9) can be directly integrated (after a great deal of effort) to give equivalent series expressions:

$$\frac{\langle N_x \rangle}{a^3 E_0^2} = - \frac{\alpha}{8\pi} \sum_{l=1}^{\infty} \sum_{m=-l}^{l} \text{Re}\{l(l+1) \\ \times \sqrt{(l-m)(l+m+1)} \\ \times [ \epsilon_{ext} a_{lm} a_{l,m-1}^* + b_{lm} b_{l,m+1}^* \\ + \frac{1}{2}(\epsilon_{ext} a_{lm} A_{l,m+1}^* + \epsilon_{ext} a_{l,m+1} A_{lm}^* \\ + b_{lm} B_{l,m+1}^* + b_{l,m-1} B_{lm}^*)]\}. \tag{10}$$

$$\frac{\langle N_y \rangle}{a^3 E_0^2} = - \frac{\alpha}{8\pi} \sum_{l=1}^{\infty} \sum_{m=-l}^{l} \text{Im}\{l(l+1) \\ \times \sqrt{(l-m)(l+m+1)} [ \epsilon_{ext} a_{lm} a_{l,m+1}^* \\ + b_{lm} b_{l,m+1}^* + \frac{1}{2}(\epsilon_{ext} a_{lm} A_{l,m+1}^* \\ - \epsilon_{ext} a_{l,m+1} A_{lm}^* + b_{lm} B_{l,m+1}^* - b_{l,m+1} B_{lm}^*)]\}, \tag{11}$$

and

$$\frac{\langle N_z \rangle}{a^3 E_0^2} = - \frac{\alpha}{8\pi} \sum_{l=1}^{\infty} \sum_{m=-l}^{l} (l+1) m [ \epsilon_{ext} |a_{lm}|^2 + |b_{lm}|^2 \\ + \text{Re}(\epsilon_{ext} a_{lm} A_{lm}^* + b_{lm} B_{lm}^*)]. \tag{12}$$

Equations (10)–(12) were verified versus Eq. (9) for several various cases and agreement was found.

Since the power of the incident beam is directly proportional to $E_0^2$, Eqs. (5), (6) and (10)–(12) indicate that the net radiation force and torque on the particle are directly proportional to the power of the incident beam.

## III. LINEARLY POLARIZED BEAM CALCULATIONS

The theoretical expressions of Sec. II were used to determine the radiation force and torque as a function of droplet position relative to the incident beam focal point for a 5-$\mu$m-diam water droplet in air optically levitated by a single, vertically oriented, focused TEM$_{00}$-mode (Gaussian-profiled) argon-ion laser beam ($\lambda = 0.5145 \, \mu$m). The laser beam is assumed to propagate in the $+ z$-axis direction and is linearly polarized with the electric field oscillation in the $x$-axis direction. The laser beam is tightly focused to a beam waist diameter ($2w_0$) of 2 $\mu$m (less than the droplet diameter), and the $x_0$, $y_0$, and $z_0$ coordinates are used to denote the location of the droplet center relative to the focal point of the beam. The electromagnetic field components of the incident beam, necessary for the evaluation of the integrals given in Eqs. (A23) and (A24), are mathematically expressed using a fifth-order corrected Gaussian beam description[34] which is an extension of the Gaussian beam description earlier developed by Davis.[35] The characteristic electric field magnitude of the incident beam $E_0$ is the electric field magnitude at the beam focal point which can be related to the beam power $P$ by[34]

$$E_0^2 = \frac{16P}{\sqrt{\epsilon_{ext}} c w_0^2 (1 + s^2 + 1.5s^4)}, \tag{13}$$

where $s = \lambda / 2\pi w_0$. The refractive index for water at the 0.5145-$\mu$m wavelength is $\bar{n} = 1.334 + 1.2 \times 10^{-9} i$.[36]

Figure 1 shows the calculated power for levitation ($P$ such that $\langle F_z \rangle = mg$ where $m$ is the mass of the droplet and $g$ is the acceleration of gravity) as a function of droplet diameter for droplets located on the incident beam propagation axis ($x_0 = y_0 = 0$) for an elevation just below the focal point at $z_0 = - 5 \mu$m and an elevation well above the focal point at $z_0 = + 50 \, \mu$m. (These are positions of stable levitation, as will be shown, later, in Fig. 2.) At $z_0 = - 5 \, \mu$m the beam diameter is about 2.6 $\mu$m, while at $z_0 = + 50 \, \mu$m the beam diameter has spread to about 16.5 $\mu$m. As shown in Fig. 1,
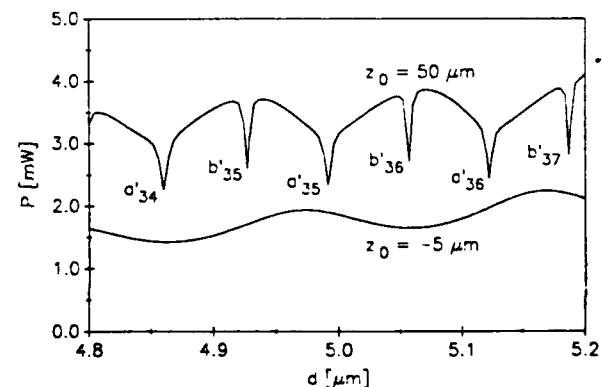


FIG. 1. Power vs droplet diameter for the optical levitation of a water droplet in air using a focused, TEM$_{00}$-mode, linearly polarized laser beam for droplet propagation axis positions of $z_0 = - 5 \, \mu$m and $+ 50 \, \mu$m. ($x_0 = y_0 = 0$, $\bar{n} = 1.334 + 1.2 \times 10^{-9} i$, $\lambda = 0.5145 \, \mu$m, and $w_0 = 1 \, \mu$m.)

μm the beam diameter is about three times that of the droplet, and plane-wave Mie theory would be expected to provide a reasonable approximation. Indeed, a calculation of required intensity to levitate using a separate Mie-theory-based computer program produced a curve essentially identical to the $z_0 = +50\,\mu$m curve of Fig. 1.

Although there is no directly comparable experimental data, the requirement of a few milliwatts of laser power to levitate a 5-$\mu$m-diam water droplet in air (as shown in Fig. 1) is consistent with measurements of Ashkin and Dziedzic[6] in which a 4-$\mu$m-diam latex sphere was levitated using $\approx 1$ mW of laser power and the levitation of a glycerol droplet evaporating from a diameter of 12–1 $\mu$m required a range of laser powers from 40 to 0.2 mW.

At an elevation of $z_0 = 50\,\mu$m, Fig. 1 indicates that at certain droplet diameters there is a decrease in the necessary power to levitate. This phenomena is a result of structural resonances within transparent water droplets at this wavelength. These structural resonances can each be associated with the excitation of particular radial modes of the general electromagnetic wave solution. The excitation of the $a_{lm}$ terms are referred to as electric wave resonances and the excitation of the $b_{lm}$ terms are referred to as magnetic wave resonances.[12,37] The presence of structural resonances in the power to levitate at a given elevation has been experimentally observed by Ashkin and Dziedzic.[9,11] Ashkin and Dziedzic[9] also observed that if the droplet is levitated near the focal point where the beam diameter is less that the diameter of the sphere, then structural resonances are not present. Figure 1 indicates a lack of structural resonances for $z_0 = -5\,\mu$m where the beam diameter (2.6 $\mu$m) is less than the droplet diameter (5 $\mu$m), consistent with Ashkin and Dziedzic's observation. As presented in a recent paper by Barton, Alexander, and Schaub,[37] structural resonances in spherical particles require edge illumination for excitation and thus would not be excited for the tightly focused conditions at $z_0 = -5\,\mu$m.

The nature (electric or magnetic), mode, and order of the structural resonances of Fig. 1 were identified, and detailed calculations were performed for the three basic types of droplets: a droplet at magnetic wave resonance (35th mode, first order, $d = 4.9266\,\mu$m), a droplet at electric wave resonance (35th mode, first order, $d = 4.9912\,\mu$m), and an intermediate nonresonance droplet ($d = 4.96\,\mu$m).

Figure 2 shows the power to levitate a droplet located on the propagation axis as a function of elevation for each of the three types of droplets. There is an increase in required laser power for droplets located near the focal point because of decreased diffraction due to the strong focusing of the beam through the center of the spherical droplet. For a given type of droplet there are then three local extrema in levitation power. A first minimum $P^1_{\min}$, which occurs below the focal point, a maximum $P_{\max}$, which occurs near the focal point, and a second minimum $P^2_{\min}$, which occurs above the focal point. (For the cases considered here, $P^1_{\min} < P^2_{\min}$.) Stable levitation occurs in regions of positive slope of $P$ vs $z_0$. From Fig. 2 it is then apparent that there are three general regimes of stable levitation. (1) If $P_{\max} < P$, then the droplet will stably levitate at a single elevation above the focal point. (2)
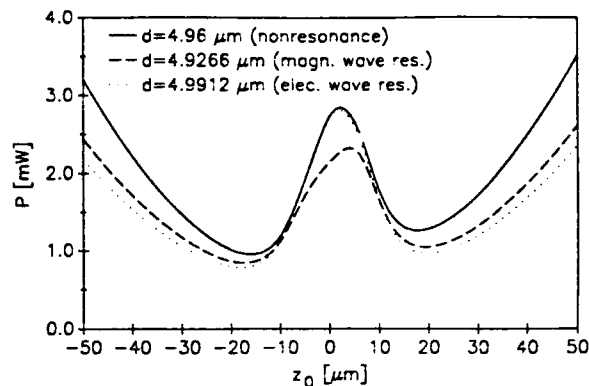


FIG. 2. Power vs propagation axis position for the optical levitation of a water droplet in air using a focused, TEM$_{00}$-mode, linearly polarized laser beam for nonresonance ($d = 4.96\,\mu$m), magnetic wave resonance ($d = 4.9266\,\mu$m), and electric wave resonance ($d = 4.9912\,\mu$m). ($x_0 = y_0 = 0$, $\bar{n} = 1.334 + 1.2\times10^{-9}i$, $\lambda = 0.5145\,\mu$m, and $w_0 = 1\,\mu$m.)

If $P^2_{\min} < P < P_{\max}$, then the droplet levitation is bistable, and the droplet can be stably levitated either above the focal point or below the focal point. (3) If $P^1_{\min} < P < P^2_{\min}$, then the droplet will stably levitate at a single elevation below the focal point. If $P < P^1_{\min}$, then the droplet cannot be stably levitated at any position. Bistable levitation for a spherical particle levitated using a tightly focused laser beam has been experimentally observed by Ashkin and Dziedzic,[5] who also observed that the particle could be easily transferred from one stable position to the other and back. If the particle begins at the above focal point position, a decrease in laser power will allow the particle to drop towards the focal point until $P = P^2_{\min}$. If the laser power is further decreased slightly, the particle will drop through the focal point to the below point position since $P^1_{\min} < P^2_{\min}$. Increasing the laser power would raise the particle towards the focal point until $P = P_{\max}$. If the laser power is further increased slightly above $P_{\max}$, the particle will rise through the focal point back to the above focal point position.

For the droplet located on the laser beam propagation axis ($z$ axis), the horizontal force components and all components of torque are zero, as is obvious from symmetry and as was verified by Eqs. (5) and (10)–(12). If the droplet is displaced in the horizontal direction, stabilizing forces act so as to push the droplet back towards the beam propagation axis. [This is true for Re($\bar{n}$) > 1, as considered here. If Re($\bar{n}$) < 1, then the horizontal forces push the droplet away from the propagation axis and there is no stable levitation.] Also, if the droplet is displaced in the horizontal direction, a torque is induced on the droplet since the beam intensity profile now presents an asymmetrical incident light distribution across the droplet. [The induced torque is dependent upon the droplets ability to absorb incident light. Consistent with the theoretical observation of Chang and Lee,[30] it was found that if the droplet is nonabsorbing, Im($\bar{n}$) = 0, then the induced torque is zero regardless of the orientation of the beam upon the droplet.] Calculations of horizontal acceleration ($a = \langle F\rangle/m$) and induced angular acceleration ($\dot{\omega} = N/I$, where $I = 2ma^2/5$) were performed for droplet

4597    J. Appl. Phys., Vol. 66, No. 10, 15 November 1989

Barton, Alexander, and Schaub    4597

displacement along both the $x$ and $y$ axes for elevations of $z_0 = +50$ and $-5\,\mu$m. Accelerations were calculated assuming a laser power necessary to levitate the droplet at the particular elevation as if the droplet were located on the propagation axis as is given in Fig. 2.

Figures 3–6 are for droplets at an elevation of $+50\,\mu$m above the focal point where the beam diameter ($2w \approx 16.5$ $\mu$m) is greater than the droplet diameter. Figure 3 shows the restoring acceleration that occurs for droplet displacement along the $x$ axis (in the direction of incident beam electric field polarization). As seen in Fig. 3, displacement of the droplet along the $x$ axis results in a force that accelerates the droplet back towards the beam propagation axis ($F_y = 0$). The force increases from zero as the droplet is moved away from the propagation axis and reaches a maximum at $x_0 \approx 4.5\,\mu$m before diminishing to zero as the droplet is moved on out of the beam. The restoring force for the nonresonance droplet is greater than the restoring force for the resonance droplets because the laser power necessary to levitate the nonresonance droplet at this elevation is greater than the laser power necessary to levitate the resonance droplets (refer to Figs. 1 and 2). Figure 4 shows the restoring acceleration for droplet displacement along the $y$ axis (perpendicular to the direction of the incident beam electric field polarization). The features for $y$-axis displacement are similar to those for $x$-axis displacement except that the restoring accelerations towards the propagation axis ($F_x = 0$) are somewhat smaller. The restoring acceleration per unit displacement very near the propagation axis is roughly 0.05 g/$\mu$m for $x$-axis displacement and roughly 0.04 g/$\mu$m for $y$-axis displacements. This compares with a restoring acceleration per unit displacement for displacements along the propagation axis (which can be found from the slope of the $P$ vs $z_0$ plot in Fig. 2) of roughly 0.03 g/$\mu$m. The horizontal and vertical stabilizing accelerations are thus of the same order for small displacements at the $z_0 = +50\,\mu$m elevation.

Figure 4 shows the $y$-component angular acceleration ($N_x = N_z = 0$) induced when the droplet is displaced along



FIG. 4. $y$-axis acceleration vs $y$-axis displacement for optical levitation of a water droplet in air using a focused, TEM$_{00}$-mode, linearly polarized ($x$-axis direction) laser beam at a droplet propagation axis position of $z_0 = 50$ $\mu$m for nonresonance ($d = 4.96\ \mu$m), magnetic wave resonance ($d = 4.9266\,\mu$m), and electric wave resonance ($d = 4.9912\,\mu$m). ($x_0 = 0$, $\bar{n} = 1.334 + 1.2\times10^{-9}i$, $\lambda = 0.5145\,\mu$m, and $w_0 = 1\,\mu$m.)

the $x$ axis at the $z_0 = +50\,\mu$m elevation. The induced angular acceleration increases from zero as the droplet is moved away from the propagation axis and reaches a maximum at roughly $x_0 = 4.5\,\mu$m before diminishing to zero as the droplet is moved on out of the beam. The induced torque is greater for the resonance droplets in comparison with the nonresonance droplet and is greater for the electric wave resonance droplet in comparison with the magnetic wave resonance droplet for $x$-axis displacements. The $x$-component angular acceleration ($N_y = N_z = 0$) induced when the droplet is displaced along the $y$ axis, shown in Fig. 6, has features similar to those for the $x$-axis displacement except that it is the magnetic wave resonance droplet that has the greatest induced torque. The increase in induced torque for the resonance droplets as the droplet is moved to the edge of the beam is consistent with the developments of Ref. 37 where it was found that structural resonances are excited by
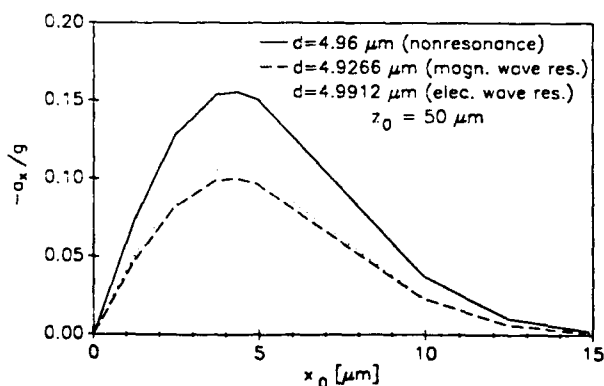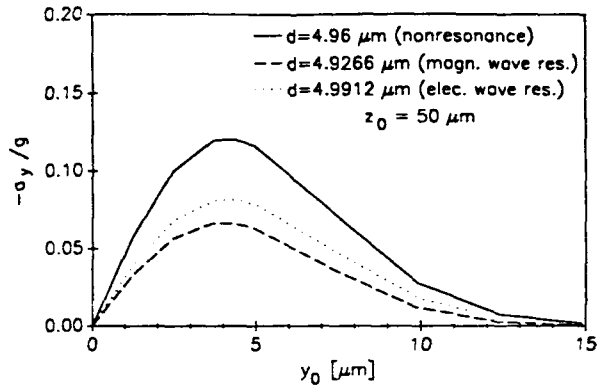


FIG. 3. $x$-axis acceleration vs $x$-axis displacement for optical levitation of a water droplet in air using a focused, TEM$_{00}$-mode, linearly polarized ($x$-axis direction) laser beam at a droplet propagation axis position of $z_0 = 50$ $\mu$m for nonresonance ($d = 4.96\,\mu$m), magnetic wave resonance ($d = 4.9266\,\mu$m), and electric wave resonance ($d = 4.9912\,\mu$m). ($y_0 = 0$, $\bar{n} = 1.334 + 1.2\times10^{-9}i$, $\lambda = 0.5145\,\mu$m, and $w_0 = 1\,\mu$m.)



FIG. 5. $y$-axis angular acceleration vs $x$-axis displacement for optical levitation of a water droplet in air using a focused, TEM$_{00}$-mode, linearly polarized ($x$-axis direction) laser beam at a droplet propagation axis position of $z_0 = 50\,\mu$m for nonresonance ($d = 4.96\,\mu$m), magnetic wave resonance ($d = 4.9266\,\mu$m), and electric wave resonance ($d = 4.9912\,\mu$m). ($y_0 = 0$, $\bar{n} = 1.334 + 1.2\times10^{-9}i$, $\lambda = 0.5145\,\mu$m, and $w_0 = 1\,\mu$m.)
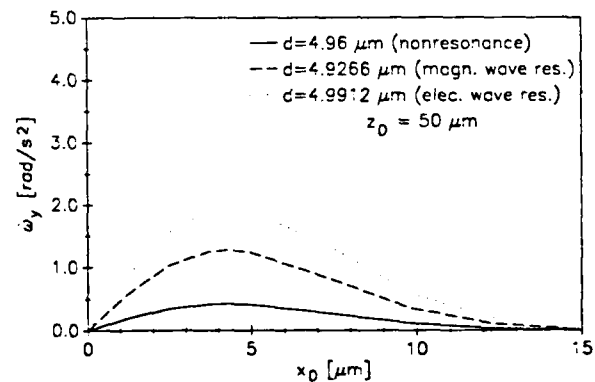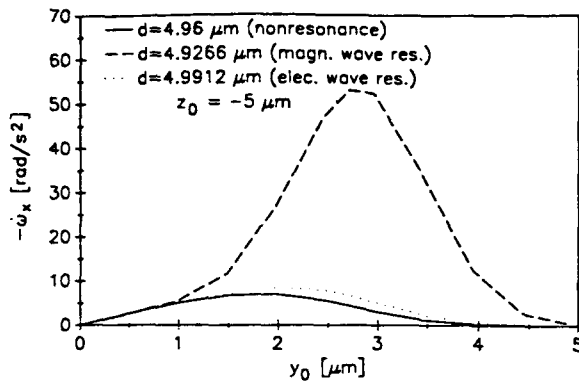
FIG. 10. x-axis angular acceleration vs y-axis displacement for optical levitation of a water droplet in air using a focused, TEM$_{00}$-mode, linearly polarized (x-axis direction) laser beam at a droplet propagation axis position of $z_0 = -5\,\mu m$ for nonresonance ($d = 4.96\,\mu m$), magnetic wave resonance ($d = 4.9266\,\mu m$), and electric wave resonance ($d = 4.9912\,\mu m$). ($x_0 = 0$, $\bar{n} = 1.334 + 1.2\times10^{-9}i$, $\lambda = 0.5145\,\mu m$, and $w_0 = 1\,\mu m$.)

eration. A circularly polarized beam, however, will induce a torque (and subsequent angular acceleration) about the propagation axis. Calculations were performed for the same conditions as considered in Sec. III, but with the beam left circularly polarized. (The fifth-order corrected, linearly polarized Gaussian beam description of Ref. 34 was rotated 90° about the propagation axis, shifted in phase by 90°, added to the original beam description, and then renormalized by dividing by $\sqrt{2}$ in order to form a mathematical description for the circularly polarized beam.) The power to levitate at a particular elevation using a circularly polarized beam was found to be identical to the power required to levitate using a linearly polarized beam for each of the three types of droplets.

Table I presents the angular acceleration about the propagation axis for droplets stably levitated at elevations of $z_0 = -5$ and $+50\,\mu m$ using a circularly polarized beam. The angular accelerations at $z_0 = +50\,\mu m$ are greater for the resonance droplets than for the nonresonance droplet. At $z_0 = -5\,\mu m$, where the beam is tightly focused through the center of the droplets, the resonances are not excited and angular accelerations are approximately equal for all three types of droplets.

TABLE I. z-axis angular acceleration for optical levitation of a water droplet in air using a focused, TEM$_{00}$-mode, left circularly polarized laser beam at droplet propagation axis positions of $z_0 = -5\,\mu m$ and $+50\,\mu m$ for nonresonance ($d = 4.96\,\mu m$), magnetic wave resonance ($d = 4.9266\,\mu m$), and electric wave resonance ($d = 4.9912$ $\mu m$). ($x = y_0 = 0$, $\bar{n} = 1.334 + 1.2\times10^{-9}i$, $\lambda = 0.5145\,\mu m$, and $w_0 = 1\,\mu m$.)

| | $\dot{\omega}_z$ [rad/s$^2$] | |
| --- | --- | --- |
| | $z_0 = -5\,\mu m$ | $z_0 = +50\,\mu m$ |
| nonresonance ($d = 4.96\,\mu m$) | 0.467 | 0.142 |
| elec. wave res. ($d = 4.9912\,\mu m$) | 0.451 | 0.235 |
| magn. wave res. ($d = 4.9266\,\mu m$) | 0.425 | 0.353 |

## V. CONCLUSIONS

Series-form theoretical expressions for the net radiation force and torque for a spherical particle illuminated by an arbitrary beam based upon the spherical-particle/arbitrary-beam interaction theory of an earlier paper[29] have been derived and presented. Calculations for a 5-$\mu m$-diam water droplet optically levitated using a 2 $\mu m$ beam waist diameter TEM$_{00}$-mode argon-ion laser beam indicate required powers to levitate, the existence of bistable levitation, and a lack of resonance near the focal point which are consistent with previous experimental observations. Additional experimental measurements are needed to provide a more direct comparison between theory and experiment, particularly with regard to the induced torque calculations.

Of interest here has been the determination of the net force and torque on the particle with no consideration with regard to how the radiation forces are actually distributed within and upon the surface of the particle. In recent experiments reported by Zhang and Chang,[38] radiation forces were sufficiently large so as to visibly distort the shape of a 100-$\mu m$-diam water droplet illuminated by a 100-mJ, 400-ns, $2w_0 \approx 200\,\mu m$, $\lambda = 0.60\,\mu m$ laser pulse. The theoretical determination of the distribution of radiation-induced forces within and upon the surface of a spherical particle illuminated by an arbitrary beam will be the topic of a later paper.

## ACKNOWLEDGMENTS

## APPENDIX A: ELECTROMAGNETIC FIELD EQUATIONS

### Incident field

$$E_r^{(i)} = \frac{1}{\bar{r}^2} \sum_{l=1}^{\infty} \sum_{m=-l}^{l} [l(l+1)A_{lm}\psi_l(\alpha\bar{r})Y_{lm}(\theta,\phi)],$$

$$E_\theta^{(i)} = \frac{\alpha}{\bar{r}} \sum_{l=1}^{\infty} \sum_{m=-l}^{l} \left( A_{lm}\psi_l'(\alpha\bar{r}) \frac{\partial Y_{lm}(\theta,\phi)}{\partial\theta} \right. \tag{A1}$$

$$\left. - \frac{m}{\sqrt{\epsilon_{ext}}} B_{lm}\psi_l(\alpha\bar{r}) \frac{Y_{lm}(\theta,\phi)}{\sin\theta} \right), \tag{A2}$$

$$E_\phi^{(i)} = \frac{\alpha}{\bar{r}} \sum_{l=1}^{\infty} \sum_{m=-l}^{l} \left( imA_{lm}\psi_l'(\alpha\bar{r}) \frac{Y_{lm}(\theta,\phi)}{\sin\theta} \right.$$

$$\left. - \frac{i}{\sqrt{\epsilon_{ext}}} B_{lm}\psi_l(\alpha\bar{r}) \frac{\partial Y_{lm}(\theta,\phi)}{\partial\theta} \right), \tag{A3}$$

$$H_r^{(i)} = \frac{1}{\bar{r}^2} \sum_{l=1}^{\infty} \sum_{m=-l}^{l} [l(l+1)B_{lm}\psi_l(\alpha\bar{r})Y_{lm}(\theta,\phi)],$$

$$H_\theta^{(i)} = \frac{\alpha}{\bar{r}} \sum_{l=1}^{\infty} \sum_{m=-l}^{l} \left( B_{lm}\psi_l'(\alpha\bar{r}) \frac{\partial Y_{lm}(\theta,\phi)}{\partial\theta} \right. \tag{A4}$$

$$\left. + m\sqrt{\epsilon_{ext}} A_{lm}\psi_l(\alpha\bar{r}) \frac{Y_{lm}(\theta,\phi)}{\sin\theta} \right), \tag{A5}$$

$$H_{\phi}^{(i)} = \frac{\alpha}{\bar{r}} \sum_{l=1}^{\infty} \sum_{m=-l}^{l} \left( imB_{lm}\psi_l(\alpha\bar{r}) \frac{Y_{lm}(\theta,\phi)}{\sin\theta} + i\sqrt{\epsilon_{ext}} A_{lm}\psi_l(\alpha\bar{r}) \frac{\partial Y_{lm}(\theta,\phi)}{\partial\theta} \right). \quad (A6)$$

### Scattered field

$$E_r^{(s)} = \frac{1}{\bar{r}^2} \sum_{l=1}^{\infty} \sum_{m=-l}^{l} [l(l+1)a_{lm}\xi_l^{(1)}(\alpha\bar{r})Y_{lm}(\theta,\phi)], \quad (A7)$$

$$E_{\theta}^{(s)} = \frac{\alpha}{\bar{r}} \sum_{l=1}^{\infty} \sum_{m=-l}^{l} \left( a_{lm}\xi_l^{(1)'}(\alpha\bar{r}) \frac{\partial Y_{lm}(\theta,\phi)}{\partial\theta} - \frac{m}{\sqrt{\epsilon_{ext}}} b_{lm}\xi_l^{(1)}(\alpha\bar{r}) \frac{Y_{lm}(\theta,\phi)}{\sin\theta} \right), \quad (A8)$$

$$E_{\phi}^{(s)} = \frac{\alpha}{\bar{r}} \sum_{l=1}^{\infty} \sum_{m=-l}^{l} \left( ima_{lm}\xi_l^{(1)'}(\alpha\bar{r}) \frac{Y_{lm}(\theta,\phi)}{\sin\theta} - \frac{i}{\sqrt{\epsilon_{ext}}} b_{lm}\xi_l^{(1)}(\alpha\bar{r}) \frac{\partial Y_{lm}(\theta,\phi)}{\partial\theta}, \quad (A9)$$

$$H_r^{(s)} = \frac{1}{\bar{r}^2} \sum_{l=1}^{\infty} \sum_{m=-l}^{l} [l(l+1)b_{lm}\xi_l^{(1)}(\alpha\bar{r})Y_{lm}(\theta,\phi)], \quad (A10)$$

$$H_{\theta}^{(s)} = \frac{\alpha}{\bar{r}} \sum_{l=1}^{\infty} \sum_{m=-l}^{l} \left( b_{lm}\xi_l^{(1)'}(\alpha\bar{r}) \frac{\partial Y_{lm}(\theta,\phi)}{\partial\theta} + m\sqrt{\epsilon_{ext}} a_{lm}\xi_l^{(1)}(\alpha\bar{r}) \frac{Y_{lm}(\theta,\phi)}{\sin\theta} \right), \quad (A11)$$

$$H_{\phi}^{(s)} = \frac{\alpha}{\bar{r}} \sum_{l=1}^{\infty} \sum_{m=-l}^{l} \left( imb_{lm}\xi_l^{(1)'}(\alpha\bar{r}) \frac{Y_{lm}(\theta,\phi)}{\sin\theta} + i\sqrt{\epsilon_{ext}} a_{lm}\xi_l^{(1)}(\alpha\bar{r}) \frac{\partial Y_{lm}(\theta,\phi)}{\partial\theta} \right). \quad (A12)$$

### Internal field

$$E_r^{(w)} = \frac{1}{\bar{r}^2} \sum_{l=1}^{\infty} \sum_{m=-l}^{l} [l(l+1)c_{lm}\psi_l(\bar{n}\alpha\bar{r})Y_{lm}(\theta,\phi)], \quad (A13)$$

$$E_{\theta}^{(w)} = \frac{\alpha}{\bar{r}} \sum_{l=1}^{\infty} \sum_{m=-l}^{l} \left( \bar{n}c_{lm}\psi_l'(\bar{n}\alpha\bar{r}) \frac{\partial Y_{lm}(\theta,\phi)}{\partial\theta} - \frac{m}{\sqrt{\epsilon_{ext}}} d_{lm}\psi_l(\bar{n}\alpha\bar{r}) \frac{Y_{lm}(\theta,\phi)}{\sin\theta} \right), \quad (A14)$$

$$E_{\phi}^{(w)} = \frac{\alpha}{\bar{r}} \sum_{l=1}^{\infty} \sum_{m=-l}^{l} \left( im\bar{n}c_{lm}\psi_l'(\bar{n}\alpha\bar{r}) \frac{Y_{lm}(\theta,\phi)}{\sin\theta} - \frac{i}{\sqrt{\epsilon_{ext}}} d_{lm}\psi_l(\bar{n}\alpha\bar{r}) \frac{\partial Y_{lm}(\theta,\phi)}{\partial\theta} \right), \quad (A15)$$

$$H_r^{(w)} = \frac{1}{\bar{r}^2} \sum_{l=1}^{\infty} \sum_{m=-l}^{l} [l(l+1)d_{lm}\psi_l(\bar{n}\alpha\bar{r})Y_{lm}(\theta,\phi)], \quad (A16)$$

$$H_{\theta}^{(w)} = \frac{\alpha}{\bar{r}} \sum_{l=1}^{\infty} \sum_{m=-l}^{l} \left( \bar{n}d_{lm}\psi_l'(\bar{n}\alpha\bar{r}) \frac{\partial Y_{lm}(\theta,\phi)}{\partial\theta} + m\sqrt{\epsilon_{ext}} \bar{n}^2 c_{lm}\psi_l(\bar{n}\alpha\bar{r}) \frac{Y_{lm}(\theta,\phi)}{\sin\theta} \right), \quad (A17)$$

$$H_{\phi}^{(w)} = \frac{\alpha}{\bar{r}} \sum_{l=1}^{\infty} \sum_{m=-l}^{l} \left( im\bar{n}d_{lm}\psi_l'(\bar{n}\alpha\bar{r}) \frac{Y_{lm}(\theta,\phi)}{\sin\theta} + i\sqrt{\epsilon_{ext}} \bar{n}^2 c_{lm}\psi_l(\bar{n}\alpha\bar{r}) \frac{\partial Y_{lm}(\theta,\phi)}{\partial\theta} \right), \quad (A18)$$

### Coefficients

$$a_{lm} = \frac{\psi_l'(\bar{n}\alpha)\psi_l(\alpha) - \bar{n}\psi_l(\bar{n}\alpha)\psi_l'(\alpha)}{\bar{n}\psi_l(\bar{n}\alpha)\xi_l^{(1)'}(\alpha) - \psi_l'(\bar{n}\alpha)\xi_l^{(1)}(\alpha)} A_{lm}, \quad (A19)$$

$$b_{lm} = \frac{\bar{n}\psi_l'(\bar{n}\alpha)\psi_l(\alpha) - \psi_l(\bar{n}\alpha)\psi_l'(\alpha)}{\psi_l(\bar{n}\alpha)\xi_l^{(1)'}(\alpha) - \bar{n}\psi_l'(\bar{n}\alpha)\xi_l^{(1)}(\alpha)} B_{lm}, \quad (A20)$$

$$c_{lm} = \frac{\xi_l^{(1)'}(\alpha)\psi_l(\alpha) - \xi_l^{(1)}(\alpha)\psi_l'(\alpha)}{\bar{n}^2\psi_l(\bar{n}\alpha)\xi_l^{(1)'}(\alpha) - \bar{n}\psi_l'(\bar{n}\alpha)\xi_l^{(1)}(\alpha)} A_{lm}, \quad (A21)$$

$$d_{lm} = \frac{\xi_l^{(1)'}(\alpha)\psi_l(\alpha) - \xi_l^{(1)}(\alpha)\psi_l'(\alpha)}{\psi_l(\bar{n}\alpha)\xi_l^{(1)'}(\alpha) - \bar{n}\psi_l'(\bar{n}\alpha)\xi_l^{(1)}(\alpha)} B_{lm}, \quad (A22)$$

where

$$A_{lm} = \frac{1}{l(l+1)\psi_l(\alpha)} \times \int_0^{2\pi} \int_0^{\pi} \sin\theta E_r^{(i)}(a,\theta,\phi) Y_{lm}^*(\theta,\phi) d\theta\, d\phi, \quad (A23)$$

and

$$B_{lm} = \frac{1}{l(l+1)\psi_l(\alpha)} \times \int_0^{2\pi} \int_0^{\pi} \sin\theta H_r^{(i)}(a,\theta,\phi) Y_{lm}^*(\theta,\phi) d\theta\, d\phi. \quad (A24)$$

$\xi_l^{(1)} = \psi_l - i\chi_l$, where $\psi_l$ and $\chi_l$ are the Riccati–Bessel functions. $Y_{lm}$ is the spherical harmonic function. $\bar{r} = r/a$ where $a$ is the sphere radius.

[1] A. Ashkin, Phys. Rev. Lett. **24**, 156 (1970).
[2] A. Ashkin, Sci. Am. **226**, 63 (1972).
[3] A. Ashkin, Science **210**, 1081 (1980).
[4] A. Ashkin and J. M. Dziedzic, Appl. Phys. Lett. **19**, 283 (1971).
[5] A. Ashkin and J. M. Dziedzic, Appl. Phys. Lett. **24**, 586 (1974).
[6] A. Ashkin and J. M. Dziedzic, Science **187**, 1073 (1975).
[7] A. Ashkin and J. M. Dziedzic, Phys. Rev. Lett. **36**, 267 (1976).
[8] A. Ashkin and J. M. Dziedzic, Appl. Phys. Lett. **28**, 333 (1976).
[9] A. Ashkin and J. M. Dziedzic, Phys. Rev. Lett. **38**, 1351 (1977).
[10] A. Ashkin and J. M. Dziedzic, Appl. Opt. **19**, 660 (1980).
[11] A. Ashkin and J. M. Dziedzic, Appl. Opt. **20**, 1803 (1981).
[12] P. Chylek, J. T. Kiehl, and M. K. W. Ko, Phys. Rev. A **18**, 2229 (1978).
[13] G. Grehan and G. Gouesbet, Appl. Opt. **19**, 2485 (1980).
[14] T. R. Lettieri, W. D. Jenkins, and D. A. Swyt, Appl. Opt. **20**, 2799 (1981).
[15] R. Thurn and W. Kiefer, Appl. Spectrosc. **38**, 78 (1984).
[16] R. Thurn and W. Kiefer, J. Raman Spectrosc. **15**, 411 (1984).
[17] R. Thurn and W. Kiefer, Appl. Opt. **24**, 1515 (1985).
[18] S. O. Park and S. S. Lee, J. Opt. Soc. Am. A **4**, 417 (1987).
[19] P. Debye, Ann. Phys. (Leipzig) **30**, 57 (1909).
[20] M. Kerker, *The Scattering of Light and Other Electromagnetic Radiation* (Academic, New York, 1969).
[21] P. L. Marston and J. H. Crichton, Phys. Rev. A **30**, 2508 (1984).
[22] P. L. Marston and J. H. Crichton, J. Opt. Soc. Am. B **1**, 528 (1984).
[23] G. Roosen and C. Imbert, Phys. Lett. **59 A**, 6 (1976).
[24] G. Roosen, Opt. Commun. **21**, 189 (1977).
[25] G. Roosen and C. Imbert, Opt. Commun. **26**, 432 (1978).
[26] G. Roosen and S. Slansky, Opt. Commun. **29**, 341 (1979).
[27] J. S. Kim and S. S. Lee, J. Opt. Soc. Am. **73**, 303 (1983).
[28] G. Gouesbet, B. Maheu, and G. Grehan, J. Opt. Soc. Am. A **5**, 1427 (1988).

[29]J. P. Barton, D. R. Alexander, and S. A. Schaub, J. Appl. Phys. **64**, 1632 (1988).

[30]S. Chang and S. S. Lee, J. Opt. Soc. Am. B **2**, 1853 (1985).

[31]J. D. Jackson, *Classical Electrodynamics*, 2nd ed. (Wiley, New York, 1975).

[32]F. N. H. Robinson, Phys. Rep. **16**, 315 (1975).

[33]I. Brevik, Phys. Rep. **52**, 133 (1979).

[34]J. P. Barton and D. R. Alexander, J. Appl. Phys. **66**, 2800 (1989).

[35]L. W. Davis, Phys. Rev. A **19**, 1177 (1979).

[36]G. M. Hale and M. R. Querry, Appl. Opt. **12**, 555 (1973).

[37]J. P. Barton, D. R. Alexander, and S. A. Schaub, J. Appl. Phys. **65**, 2900 (1989).

[38]J.-Z. Zhang and R. K. Chang, Opt. Lett. **13**, 916 (1988).

# Measurement of hypersonic velocities resulting from the laser-induced breakdown of aerosols using an excimer laser imaging system

S. A. Schaub, D. R. Alexander, D. E. Poulain, and J. P. Barton

*Center for Electro-Optics, University of Nebraska-Lincoln, Lincoln, Nebraska 68588-0656*

In this article we describe a dual-pulse excimer-laser-based imaging system used in the determination of ejected material velocities resulting from the interaction of KrF laser radiation ($\lambda = 248$ nm, pulse width FWHM $= 17$ ns, $I \approx 10^{11}$ W/cm$^2$) with 20-$\mu$m aluminum particles under vacuum ($P = 10^{-5}$ Torr) conditions. Material velocities measured 200–400 ns after arrival of the incident pulse ranged from 450 to 1200 m/s.

## INTRODUCTION

The study of the interaction of laser radiation with both solid and liquid aerosol particles has been an active research area during recent years. In particular, the use of high-energy lasers to initiate vaporization and laser-induced breakdown (LIB) of aerosols has received a great deal of attention from both a theoretical[1-3] and experimental[4-6] viewpoint. One aspect of the problem, which will be addressed in this article, is the experimental determination of material velocities during the initial stages of the laser/aerosol interaction. Determination of material velocities resulting from high-energy laser irradiation has practical importance in a variety of situations. As more sophisticated theoretical models are developed to better understand and model the fundamental physical mechanisms of the process, quantitative experimental data is needed for comparison to predicted results. The LIB process also provides a convenient method to accelerate materials to hypersonic velocities which can be used in developing instrumentation for diagnostics in research related to flows encountered during hypersonic flight. In addition, measurement of material velocities leaving the focal point of a high-energy laser is important information in examining momentum transfer between high-energy laser pulses and aerosol particles. The momentum transfer is of particular interest in research attempting to determine suitable obscurants for various types of incident laser radiation.

In earlier research by Hsieh *et al.*,[7] time-resolved streak camera images were used to measure the plasma velocities from the shadow and illuminated surfaces resulting from the LIB of water droplets irradiated by the second harmonic of a $Q$-switched Nd:YAG laser ($\lambda = 0.532\,\mu$m). At an incident irradiance of 7 GW/cm$^2$, the velocity of the plasma front propagating external to the droplet surface was measured as high as 20 000 m/s. Research conducted by Korshunov, Ustyuzhin, and Ya,[8] on the interaction of a ruby laser (0.5–1.0 J, 40-ns pulse width) with aluminum powders reported average plasma velocities of 250–1100 m/s. In this article we present an experimental technique for determination of the hypersonic velocity of material expelled during the interaction of excimer laser radiation with aerosol particles using a dual-pulse excimer-laser-based imaging system. Typical re-

sults are presented for the case of a KrF excimer laser ($\lambda = 248$ nm, pulse width FWHM $= 17$ ns, $I \approx 10^{11}$ W/cm$^2$) incident on 20-$\mu$m solid aluminum (Al) particles.

## I. EXPERIMENTAL SETUP

A schematic of the experimental setup is shown in Fig. 1. The high-energy laser beam is produced by a KrF excimer laser using unstable optics (Questek model 2860, $\lambda = 248$ nm, FWHM pulse duration $= 17$ ns) and is focused at the center of the vacuum chamber with a planoconvex lens
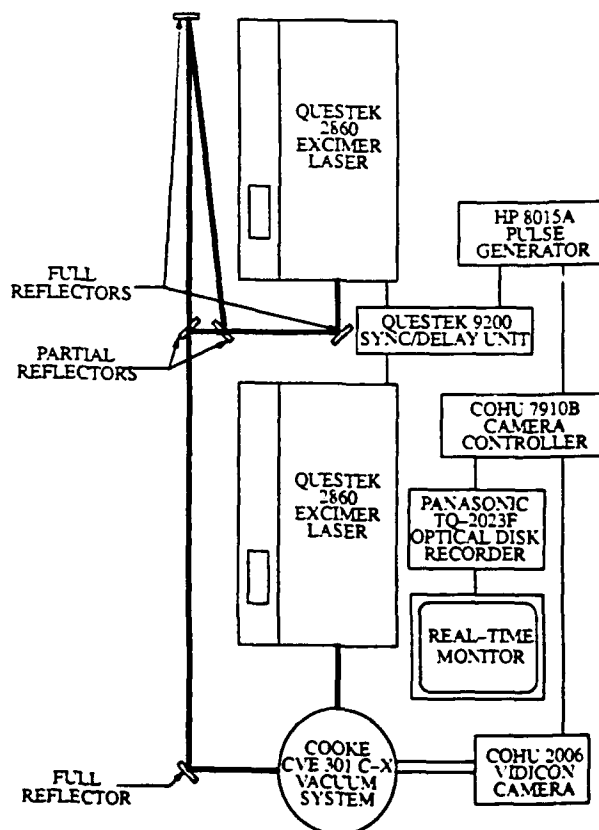


FIG. 1. Schematic of experimental arrangement.

($d = 50$ mm, $f = 250$ mm). The FWHM dimensions of the focused laser beam were determined experimentally by translating a knife edge through the focal region of the laser and were found to be 95 $\mu$m $\times$ 115 $\mu$m ($\approx 10^4$ $\mu$m$^2$). The beam from a second excimer laser, identical to the first with the exception of using stable resonator optics, is incident through an optical port on the vacuum chamber in a direction orthogonal to both the high-energy pulse and the motion of the solid particles. The imaging pulses are synchronized with the high-energy pulses by using a digital delay unit (Questek 9200 laser sync/delay unit) and serves as the illumination source for imaging studies and velocity measurements. To perform the dual-pulse imaging, the emerging pulse from the second excimer laser was split into two separate pulses, one of which was sent directly to the vacuum chamber over a minimum optical path length, and the second which was sent over an additional 45 ft of optical path (see Fig. 1). Consequently, two 17-ns pulses delayed by 45 ns provided a double exposure of the laser/aerosol interaction and allowed determination of the velocity of the expelled material by measuring the distance the material had traveled during the 45-ns time interval. Although the delay time between imaging pulses is fixed for a given optical path, the absolute delay time between the high-energy pulse and the imaging pulses could be varied by the digital delay unit.

The images were viewed using a UV-sensitive vidicon (Cohu 2006 camera system) in conjunction with a digital image-processing system.[9] Use of the image-processing system allows accurate determination of the distance the material travels during the laser/aerosol interaction. Prior to performing velocity measurements on the solid Al particles, it was necessary to position the focal region of the high-energy laser in the center of the field of view (approximately 500 $\mu$m $\times$ 400 $\mu$m) of the imaging system. To accomplish this, the breakdown of air under atmospheric conditions with no Al particles present at the focal region was imaged by increasing the gain of the camera system. After centering the breakdown region within the imaging system field of view, a 248-nm bandpass filter was placed in front of the camera to eliminate passage of broadband emission which would otherwise saturate the vidicon. The subsequent images were stored on an optical memory disk recorder (Panasonic model TQ-2023F) which was synchronized with the high-energy laser so that a single image was recorded for each high-energy pulse.

The solid particles were dispersed using a mechanical shaker which consisted of a particle reservior with a 1-mm exit hole mounted on an acoustic speaker. The input frequency and amplitude were adjusted using a function generator (Tektronix model FG 503) and a power amplifier (Nikko model Alpha 230) such that the desired particle concentration was distributed in the focal region of the high-energy laser beam. Although the diameter of single Al particles were 20 $\mu$m according to manufacturers specifications, the actual particle stream passing through the focal region of the laser frequently contained agglomerations of Al particles.

The vacuum system (Cooke CVE 301 C-X) consisted of a glass bell jar seated on a stainless-steel cylinder (11.5 in. in



FIG. 2. Interaction of KrF laser radiation ($\lambda = 248$ nm, $I \approx 10^{11}$ W/cm$^2$, pulse width FWHM = 17 ns, $E_{pulse} = 400$ mJ) with 20-$\mu$m Al spheres at $P = 10^{-5}$ Torr. Imaging pulses arrive 300 and 345 ns after high-energy pulse. A double exposure of the expelled material is shown in the upper left portion of the photograph. White spots mark the location of the aluminum spheres prior to arrival of the high-energy pulse. Laser is propagating from right to left.

diameter, 6.5 in. high) with nine optical viewing ports. Vacuum conditions were obtained using a cryogenic pump (CTI Cryogenics, Cryo-torr 100 high vacuum pump) connected to the base of the vacuum chamber through an access hole in a Newport Research Corp. optical table. Pressures within the vacuum chamber were monitored using a thermocouple and ion gauge. The lowest pressure of interest in this work was approximately $10^{-5}$ Torr.

## II. RESULTS

Figures 2 and 3 show examples of the images obtained using a single high-energy pulse ($I \approx 10^{11}$ W/cm$^2$) incident on 20-$\mu$m Al spheres using two imaging pulses separated by



FIG. 3. Interaction of KrF laser radiation ($\lambda = 248$ nm, $I \approx 10^{11}$ W/cm$^2$, pulse width FWHM = 17 ns, $E_{pulse} = 400$ mJ) with 20-$\mu$m Al spheres at $P = 10^{-5}$ Torr. Imaging pulses arrive 250 and 295 ns after high-energy pulse. A double exposure of the expelled material is shown in the left center portion of the photograph. White spots mark the location of the aluminum spheres prior to arrival of the high-energy pulse. Laser is propagating from right to left.

45 ns. The images shown in the figures were obtained at a pressure of $10^{-5}$ Torr. Note that the high-energy laser pulse is propagating from right to left in the photographs. As shown in Fig. 2, a double exposure of expelled material can be observed in the upper left portion of the photograph. The first image corresponds to the material location 300 ns after the high-energy pulse, and the second image corresponds to the location 345 ns after the high-energy pulse. In addition, the right edge of the image shows evidence of intense white areas resulting from the elastically scattered light from the high-intensity pulse which causes saturation of the vidicon. These "spatial markers" are useful in providing information about the position of the material as it is first irradiated by the high energy pulse. Due to the large amounts of expelled material shown in the photograph and multiple white spots, it is likely that this particular interaction involved a cluster of Al spheres. The velocity of the expelled material in this photograph can be determined by dividing the distance that the expelled material moved (55 $\mu$m) by the time interval between imaging pulses (45 ns), yielding a velocity of 1200 m/s traveling predominantly in the direction of the laser propagation. The uncertainty in these velocity measurements is estimated to be $\pm$ 5%, which is primarily due to the difficulty in properly identifying the material boundaries for the two images.

Figure 3 shows a similar interaction involving a smaller agglomerate of Al material. Again, the high-intensity white spot near the center of the image shows the location of Al material at the instant the high-energy laser irradiates the material. The imaging pulses in Fig. 3 arrive at 250 and 295 ns after the high-energy pulse. The resulting velocity of the material is approximately 450 m/s. The diffraction patterns which are evident in both figures are caused by aluminum particles which were outside the depth of field (out-of-focus) of the imaging system. Although the precise identification of the expelled material is a difficult problem, related experimentation on metal wires (50–150 $\mu$m in diameter) under similar conditions have shown the expelled material

to be composed of both molten metal and solid particle fragments.

The two cases shown in Figs. 2 and 3 represent typical material velocities measured for the interaction of KrF laser radiation with Al particles with nearly all velocities falling within the range of 450–1200 m/s. The different velocities measured for identical irradiance, pulse width, and material can be attributed to the fact that different areas within the focal region will exhibit different intensity values. This point is illustrated quite dramatically in Fig. 4 which was obtained using only a single imaging pulse under atmospheric conditions. Expelled material in the top center portion of the image has propagated a significantly greater distance than has material near the lower portion of the image for a given time interval (200 ns). This would indicate that the higher intensity areas within the focal region are located near the center of the image. Note also the evidence of shock propagation near the left edge of the photograph, characteristic of interactions occurring under atmospheric conditions.

## III. ADVANTAGES AND LIMITATIONS

Although velocity measurements can be accomplished using only a single imaging pulse,[10,11] the dual-imaging-pulse method has two distinct advantages over the single-pulse method. First, the relative delay between successive imaging pulses can be accurately determined using the known optical path lengths and the speed of light. This eliminates uncertainty due to the inherent jitter associated with electronic delay equipment and thyratron firing on excimer lasers. Second, both imaging pulses can be delayed relative to the high-energy pulse to provide average velocity measurements during any 45-ns time interval during the laser/aerosol interaction. The single-pulse method is restricted to measuring average velocities over time intervals corresponding to the delay between the high-energy pulse and imaging pulse.

Several factors limit the effectiveness and flexibility of the technique. For the present system, the FWHM pulse width is approximately 17 ns. For a typical material velocity of 1000 m/s, the material will move approximately 17 $\mu$m during the duration of the imaging pulse. This will result in a streaking or blurring of the image and will tend to exaggerate the spatial extent of the moving material. To remedy this problem, imaging pulses in the picosecond time regime will need to be utilized and are currently under investigation in the laboratory. The delay time between the two imaging pulses has practical limitations based on the allowable optical path length set by physical constraints and the divergence of the imaging laser (2–3 mrad for the excimer laser with stable optics). In summary, the dual-imaging-pulse method provides an accurate method of determining material velocities during the laser/aerosol interaction and is particularly attractive for situations in which jitter from the laser circuits and timing electronics would introduce unacceptable errors in velocity measurements.



FIG. 4. Interaction of 20-$\mu$m Al spheres with KrF laser radiation ($\lambda$ = 248 nm, $I \simeq 10^{11}$ W/cm$^2$, pulse width FWHM = 17 ns, $E_{pulse}$ = 400 mJ) in atmosphere, 200 ns after arrival of the high-energy pulse. Note the different material velocities depending on the location of the Al particles relative to the focal point of the high-energy beam. White spots mark the location of the aluminum spheres prior to arrival of the high-energy pulse. Laser is propagating from right to left.

[1] J. C. Carls and J. R. Brock, Opt. Lett. 13, 273 (1988).

[2] S. M. Chitanvis, J. Appl. Phys. 62, 4387 (1987).

[3] A. Zardecki and R. L. Armstrong, Appl. Opt. 27, 3690 (1988).

[4] R. K. Chang, J. H. Eickmans, W. Hseih, C. F. Wood, J. Zhang, and J. Zheng, Appl. Opt. 27, 2377 (1988).

[5] A. Biswas, H. Latifi, L. J. Radziemski, and R. L. Armstrong, Appl. Opt. 27, 2386 (1988).

[6] F. Docchio, R. Regondi, M. R. C. Capon, and J. Mellerio, Appl. Opt. 27, 3661 (1988).

[7] W.-F. Hsieh, J.-B. Zheng, C. F. Wood, B. T. Chu, and R. K. Chang, Opt. Lett. 12, 576 (1987).

[8] G. S. Korshunov, V. V. Ustyuzhin, and V. Ya. Ushakov, Sov. Phys. Tech. Phys. 30, 469 (1985).

[9] K. D. Ahlers and D. R. Alexander, Opt. Eng. 24, 1060 (1985).

[10] J.-Z. Zhang, J. K. Lamm, C. F. Wood, B. T. Chu, and R. K. Chang, Appl. Opt. 26, 4731 (1987).

[11] D. R. Alexander, S. A. Schaub, J. Zhang, D. E. Poulain, and J. P. Barton, Opt. Lett. 14, 548 (1989).

# HIGH INTENSITY ULTRAVIOLET LASER INTERACTION
# WITH A METALLIC FILAMENT

G.M. Holtmeier, D.R. Alexander, and J. P. Barton

Center for Electro-Optics

University of Nebraska

Lincoln, NE 68588-0656

## Abstract

Results of research conducted on the interaction of high intensity ultraviolet pulsed KrF laser radiation with a metallic filament are reported. Experimental results are presented on the time dependent material ejection dynamics associated with focused excimer laser beams interacting with a small diameter wire. Copper wire 75 $\mu$m in diameter was illuminated with a KrF ($\lambda = 248$ nm, pulse duration $= 17$ ns FWHM) excimer laser at an irradiance of 80 GW/cm$^2$. Interaction dynamics were recorded using both a real time and double stroked ultraviolet laser imaging technique. Temporal evolutions of both vaporized and molten material are reported. Material observed during 2-D shadow imaging on the shadow side of the wire was shown to originate from the front ablative surface without spallation of material on the shadow surface. Material emission velocities are reported utilizing two different imaging techniques. A maximum velocity of 1500 m/s was obtained for material ejected in a direction toward the ablating laser.

1

## I. Introduction

Excimer laser interaction with metals has been widely investigated utilizing generally flat targets with beam intensities near the optical breakdown thresholds[1-4] and at intensities above the breakdown thresholds[5,6]. Limited work appears in the literature on the interaction of a high intensity laser beam with metallic aerosols or small filaments. Armstrong et al.[7] performed a theoretical investigation of the propagation of a high-energy laser beam through metallic aerosols. Poulain et al.[8] performed experimental work on high intensity KrF excimer laser interaction with solid aerosols and reported interesting interaction dynamics and material breakdown thresholds for several types of solid aerosol particles. In order to overcome some of the experimental difficulties reported by Poulain et al.[8] and to better understand interaction dynamics phenomena associated with a high-energy laser beam interacting with solid aerosols, the present investigation utilized a thin metallic wire instead of solid aerosol particles in the laser beam probe volume. Thus, in this investigation, the interaction dynamics of a high intensity (80 GW/cm$^2$) KrF excimer laser beam with a 75 $\mu$m diameter copper wire were studied under atmospheric illumination conditions.

## II. Experimental Setup

A schematic of the experimental setup is shown in Figure 1. A high-energy beam was produced by a KrF excimer laser (Questek model 2860, $\lambda$ = 248 nm, pulse duration = 17 ns FWHM) using unstable optics and was focused by a plano-convex lens (d = 50 mm, f = 250 mm). The cross sectional dimensions of the high-energy beam were determined experimentally by translating a knife-edge through the focused beam[8]. A second method verified the cross sectional dimensions by measuring the illuminated damage area of a polished nickel plate placed in the focused probe volume. Dimensions of the focused high-energy beam were approximately 110 x 135 $\mu$m for this investigation. A second Questek model 2860 excimer laser, operating on ArF at $\lambda$ = 193 nm and with stable resonator optics, was used to produce an imaging beam incident in a direction orthogonal to both the high-energy pulse and the copper wire. Laser pulses used for imaging were synchronized with the high-energy pulses illuminating the targets using an analog/digital delay unit, Questek model 9200 Laser Synchronization Unit (LSU). Video timing signals produced by the camera control unit (Cohu model 8000) were sent to a pulse generator (HP model 8015A) which subsequently provided the trigger pulse for the LSU. Pulses from both lasers were simultaneously monitored using a fast photodiode (Hamamatsu model C1083) and digitizing oscilloscope (Hewlett Packard model 54200A). Analog delay controls on the LSU could be used to adjust the arrival of

2

the imaging pulse with respect to the high-energy pulse. For example, 0 ns delay indicates both imaging and high-energy pulse arrived at the same time but 10 ns delay implies that the imaging pulse occurred 10 ns after the high-energy laser ablation pulse occurred. Jitter for the system was approximately ±7 ns. The digital delay on the LSU made it possible to delay the image pulse arrival with respect to the high-energy pulse from 0–100 $\mu$s in increments of 10 ns.

Real time images of the laser beam interacting with the wire were obtained with a UV sensitive vidicon camera. Thus, the image is integrated over the laser pulse duration of 17 ns FWHM. Images were stored on an optical disk recorder (Panasonic model TQ-2023F) and processed with a digital image processing system[9] for subsequent analysis. The probe volume of the high-energy ablating pulse was positioned in the image plane of the imaging system by observing the plasma formed during air breakdown with the imaging vidicon camera. Wire targets were positioned in the imaging probe volume and centered by observing the maximum visible emission from the illuminated wire. Location of the 75 $\mu$m diameter copper wire within the imaging probe volume was maintained by feeding the wire from a spool through two glass micro-capillaries with an inside diameter of 127 $\mu$m. A mass equal to 17.5 g was connected to the bottom of the wire to keep the wire taut. A stepping motor was used to rotate the spool to feed new wire into the probe volume for each laser pulse/wire interaction.

## III. Interaction Dynamics

Experimental work to visualize the interaction dynamics was performed using a pulsed real time video imaging system to record the dynamics associated with the high-energy laser interaction with a small diameter wire. An ArF excimer laser imaging system was operated at $\lambda$=193 nm to provide high resolution images as well as to eliminate scattered 248 nm emission from the high-energy pulse by using a 193 nm bandpass filter in line with the imaging optics. Dynamic interactions were observed for a single focused 200 mJ pulse ($\lambda$ = 248 nm, pulse duration = 17 ns) incident on a 75 $\mu$m diameter copper wire. The focused beam had an 110 × 135 $\mu$m spot size giving an irradiance of 80 GW/cm$^2$. For comparative purposes, images of the wire were recorded before the high-energy pulse interaction and after the high-energy pulse interaction as shown in Figure 2. The ablating pulse was incident from right to left in Figure 2 and produced a crater on the ablated surface as a result of material removal. The term crater in this work refers to the volume of the wire removed as a result of the ablative interaction. Images recorded at various time delays during the laser beam/wire interaction process are shown in Figures 3–5. The delay time given under each

3

photograph is the delay of the image beam with respect to the arrival of the high-energy pulse. Dark regions on the left of the images were characteristic of the imaging system used and were primarily due to the optical effects associated with the bandpass filter.

The first noticeable evidence of any laser beam/wire interaction dynamics occurred at 10 ns image delay as shown in Figure 3. A cloud of material is starting to be visible at the top and bottom edges of a crater starting to form on the ablated (front) surface of the wire but not at the shadow (rear) surface. Ablated surface is used to describe the region illuminated by the high-energy ablating laser beam. At 40 ns image delay, material emission is also evident at the shadow surface and a crater is clearly forming at the ablated surface as a result of the material removal at the location of the probe volume. However, scanning electron microscope (SEM) images of the samples showed no physical material removal from the shadow surface of the wire. Thus, ejected material appearing at the shadow surface of the wire was removed from the ablated surface and propagated around the sides. At 60 ns delay, a crater on the ablated surface of the wire is clearly forming with an opaque lip forming at the top and bottom edge of the crater. In addition, the cloud of material apparent just above and below the probe volume region as shown at 40 ns image delay is absent at 60 ns delay. Lifetime of the visible plasma emission from the laser beam/wire interaction was determined to have an average value of 62 ns (FWHM). Thus, the cloud of material appearing at the ablated surface of the wire prior to 60 ns image delay is thought to be a dense plasma opaque to the imaging rays. At 100 ns delay, a dark region appears directly in front of the crater slightly beyond the location of the original wire's edge. This material is thought to be dense plasma or a cloud of vaporized material and is evident from 80–120 ns. The material observed in front of the probe volume was not evident in the images prior to 80 ns image delay since sufficient quantities do not exist to be opaque to the imaging system. After 120 ns delay, this material moves out of the field of view of the imaging system and thus does not appear on later images.

Images at longer time delays ranging from 170 ns to 600 ns are shown in Figure 4. From these images, it is evident that material has traveled from the front wire surface around the sides forming inhomogeneous clouds behind the shadow surface of the wire. This series of photographs also shows material moving away from the edges of the crater in a lateral direction along the wire surface. This laterally moving material has moved out of the field of view of the imaging system after 800 ns delay as shown in Figure 5. Material having individual particle characteristics is evident behind the shadow surface of the wire for time delays of 800 ns and longer. Current experiments are not able to distinguish whether this material formed as a result of condensation or by direct

4

emission from the ablating surface. It probably is both, however, it is our feeling that the majority is from the latter since there is clear evidence of particles forming from the molten liquid waves on the illuminated wire surface discussed later when Figure 7 is addressed. Such particles could be observed in Figure 5 for time delays up to 4.5 $\mu$s and were shown to be in a molten state by collecting them onto polished nickel plates.

SEM images are shown in Figure 6 revealing a side view (top photograph) and a shadow surface view (bottom photograph) of copper wire specimens after ablation at an irradiance of 80 GW/cm$^2$. The side view clearly shows where material removal occurred and the crater formed. In addition, molten material flow has occurred as demonstrated by the relatively smooth surface around the crater's edge. Also observed in the top photograph of Figure 6 is the rough solidification zone especially evident along the length of the wire and approximately 100 $\mu$m from the crater edge. The bottom photograph in Figure 6 provides evidence that no material was removed from the shadow surface. Further examination of the photograph shows that a lip has formed on the side of the wire from very high accelerations of ejected material.

High magnification SEM images taken of solidified material located in the rough solidification zone approximately 100 $\mu$m from the crater's edge along the length of the wire are shown in Figure 7. Particles that solidified before "pinching off" a wave surface can be identified in the top photograph. Solidification waves flowing from the front surface of the wire around the sides are clearly evident in the bottom photograph of Figure 7. Particles ejected around the wire closer to the back surface are smaller than particles forming from the surface waves formed near the front surface of the wire. Surface tension and the amplitude of the surface waves obviously are important parameters in determining the size of particles emitted.

## IV. Velocity Measurements

Velocity measurements of emitted materials from the laser beam/wire interactions were performed using single pulse ($\lambda = 193$ nm) images similar to those shown in Figures 3–5 and also by a dual pulse imaging method described in previous work by Schaub et al.[10]. Dual pulse imaging is performed by splitting the laser pulse used for imaging into two separate pulses as shown in Figure 1. One part of the imaging pulse travels directly to the imaging system while the second part travels over an additional 17.1 m (56 ft) of optical path length. Thus, two 17 ns pulses ($\lambda = 248$ nm) optically delayed by 56 ns enter the imaging system providing a double exposure image on the vidicon camera of the emitted material produced from the laser beam/wire interaction.

5

Velocity of the emitted material was determined by measuring the distance the molten material moved during the 56 ns time interval. The time interval separating the dual imaging pulses is fixed by the optical path length, however, the time delay of the first imaging pulse with respect to the high-energy pulse can be adjusted with the LSU previously described.

Figure 8 is a typical set of dual pulse images of two separate ablation cases obtained of emitted material with the first image pulse delayed 500 ns after the arrival of the high-energy pulse which was interacting at the very right edge of the photographs (wire is out of the photograph). Samples were positioned beyond the right edge of the monitor screen to eliminate scattered 248 nm emission from the laser beam/wire interaction which saturates the vidicon camera and to allow for full field of view imaging of the emitted material. Average velocities of imaged materials emitted in a direction away from the ablative laser were 570 m/s at 300 ns image delay and 460 m/s at 500 ns delay. Only a limited number of dual pulse data has been reported due to experimental difficulties in clearly identifying the same boundary edge of material in a given double exposure. Typical dual pulse images obtained at 1500 ns delay, for two separate ablative cases, are shown in Figure 9. Particles imaged in Figure 9 are approximately 10 $\mu$m in diameter and move less than 5 $\mu$m in 56 ns time delay which corresponds to a velocity less than 90 m/s.

The velocity of emitted material was also determined by utilizing a single imaging pulse and measuring the material movement for a known time delay relative to the arrival of the ablation pulse. A similar technique was used by Alexander et al.[11] to determine interaction velocities when an excimer laser beam interacted with a water droplet. For the current work, it is assumed that ejected material originates from the front of the crater region and emission starts at 0 ns image delay. The position of the wire before ablation is recorded each time to provide a reference position for subsequent velocity measurements. Results of velocity studies at three locations for ejected material from the dual and single imaging pulse techniques are presented in Figure 10. Dual and single pulse velocities should not be compared since the measurements are for different locations. Data plotted in the graphs differ only by the scale of the time (horizontal) axis. The top graph has been expanded to emphasize the acceleration and deceleration during the laser pulse. Each data point on the graphs represents the average of approximately five velocity calculations for each time frame. Error associated with the material emission velocity calculations is ±20% and is primarily due to the uncertainties in properly identifying the exact starting and ending points of boundaries in the images used to compute the velocities.

Material emission velocities in a direction back towards the ablating laser were calculated by measuring the material movement on the ablative (front) surface of the wire and in a direction

6

perpendicular to the wire. The starting position of the front wire surface was located by comparing wire images before the high-energy pulse illumination with the delayed images during illumination of the samples. Measurements of emitted material movement back toward the ablating laser could not generally be made for time delays longer than 30 ns since the material boundaries ejected out of the crater back towards ablating laser were not detected by the imaging system. However, the emission velocity was calculated for material shown in front of the probe volume at 100 ns delay in Figure 3. The average velocity of spatially emitted material toward the laser is shown to increase from 1300 m/s at 10 ns time delay to 1500 m/s at 20 ns. The time dependent acceleration is a result of the 17 ns (FWHM) high-energy pulse still depositing energy into the interaction region. A subsequent deceleration of material occurs after the end of high-energy laser pulse. Material emission velocities in a direction away from the ablating laser were calculated by the same procedure used to measure material movement towards the ablating laser. In order to obtain velocity calculations in a direction away from the ablating laser, single pulse imaging was used up to 70 ns, i.e., until the vaporized material boundaries immediately along the back edge of the wire were no longer observable. Dual pulse imaging was used for velocity measurements from 300–500 ns delay for material emission away from the ablating laser.

Lateral material emission is defined in this work as emitted material at the ablating (front) surface of the wire moving out of the crater region in a direction parallel along the length of the wire. Lateral emission velocities were obtained up to 800 ns image delay since the vaporized material moves out of the field of view of the imaging system as can be observed in Figure 4 and 5. Lateral emission velocities shown in Figure 10 remain constant at approximately 800 m/s until 130 ns image delay when deceleration to 270 m/s occurs at 300 ns delay. Deceleration occurs after the emitted material crosses the smooth interaction surface region located above and below the crater and enters the rough solidification zone shown in Figure 6. Molten material is cooling and solidifying in this zone increasing the viscous forces causing deceleration. The velocity of the lateral material emission at 300 ns image delay is approximately the speed of sound in air at atmospheric conditions.

Emitted particles appear behind the shadow surface of the wire at a time delay of 4.5 $\mu$s and are shown in Figure 5. An explanation for particles emitted microseconds after a 17 ns pulse interaction is provided by examining the thermal diffusion time and the material emission velocities. For metals interacting with an excimer laser pulse, Jervis et al.[12] report that the thermal diffusion length ($\delta$) during the pulse is given by

$$\delta = 2\sqrt{\chi\tau} \tag{1}$$

7

where $\chi$ is the thermal diffusivity and $\tau$ is the beam pulse width. For copper and a 17 ns pulse width (FWHM), $\delta = 2.2\,\mu$m. Optical skin penetration depth ($d$) of the incident beam ($\lambda = 248$ nm) into copper is calculated to be 11 nm. Since $\delta \gg d$, depth of energy distribution over the 17 ns pulse width is determined by thermal diffusion as opposed to the laser penetration depth. Therefore, thermal diffusion cannot be neglected for this investigation. Particles emitted during long time delays originated from the rough solidification zone near the front of the wire shown in Figure 7. SEM analysis of cross sections of interacted specimens revealed that the molten material in the rough surface zones can exceed 8 $\mu$m in thickness. By rearranging Eq. (1), a convenient order-of-magnitude estimation for the thermal diffusion time ($t$) through a metal surface is given by Ready[13] as

$$t = \frac{D^2}{4\chi} \tag{2}$$

where $D$ is the desired penetration thickness. For $D = 8\mu$m, thermal diffusion time ($t$) would be 200 ns. Single pulse imaging revealed molten material moving over the rough surface zone of the wire at approximately 1 $\mu$s image delay. Emitted particles from this zone were previously reported to have velocities less than 90 m/s. Since these particles originate from the front of the wire and are imaged behind the shadow surface, the total distance traveled is over 75 $\mu$m (wire diameter) and the corresponding travel time would be over 1.0 $\mu$s for a velocity under 90 m/s. Material velocities across the wire surface account for the majority of the microsecond delays of particle emission from the laser beam/wire interaction. The thermal diffusion time of approximately 200 ns contributes only a minor part to the delay in material emission.

## V. Summary

High intensity ultraviolet laser interaction with a metallic filament has been investigated. Copper wire 75 $\mu$m in diameter was illuminated with a KrF excimer laser at irradiances of 80 GW/cm$^2$. A laser imaging system showed both vaporized and molten material emitted from the laser beam/wire interaction. Emitted material imaged at the shadow surface of the wire was shown to originate from the front ablating surface and propagate around the sides of the wire. A maximum material velocity of approximately 1500 m/s was calculated for ablated material traveling in a direction back toward the ablating laser. Emitted particles were observed to be emitted up to 4.5 $\mu$s after arrival of the high-energy pulse. This delay was attributed to the material emission velocities. For example, particles ejected at 4.5 $\mu$m were shown to have a velocity of under 90 m/s.

## Acknowledgments

8

# References

1. Viswanathan, R. and Ingo Hussla, "Ablation of Metal Surfaces by Pulsed Ultraviolet Lasers Under Ultrahigh Vacuum," *J. Opt. Soc. Am. B*, Vol. 3, No. 5, p. 796, May 1986.

2. Ursu, I., I.N. Mihailescu, Al. Popa, A.M. Prokhorov, V.P. Ageev, A.A. Gorbunov and V.I. Konov, "Studies of the Change of a Metallic Surface Microrelief as a Result of Multiple-Pulse Action of Powerful UV Laser Pulses," *J. Appl. Phys.*, Vol. 58, No. 10, p. 3909, 15 November 1985.

3. Kelly, Roger and Joshua E. Rothenberg, "Laser Sputtering Part III. The Mechanism of the Sputtering of Metals at Low Energy Densities," *Nuclear Instruments and Methods in Physics Research B*, Vol. 7/8, p. 755, 1985.

4. Rosen, D.I., D.E. Hastings and G.M. Weyl, "Coupling of Pulsed $0.35$-$\mu$m Laser Radiation to Titanium Alloys," *J. Appl. Phys.*, Vol. 53, No. 8, p. 5882, August 1982.

5. Offenberger, A.A., R. Fedosejevs, P.D. Gupta, R. Popil and Y.Y. Tsui, "Experimental Results for High Intensity KrF Laser/Plasma Interaction," *Laser and Particle Beams*, Vol. 4, Parts 3 and 4, p. 329, 1986.

6. Panchenko, A.N. and V.F. Tarasenko, "Experiments on Plasma Production and Expansion During UV-Laser Irradiation of Metals," *Sov. J. Plasma Phys.*, Vol. 14, No. 6, p. 450, June 1988.

7. Armstrong, Robert L. and Andrew Zardecki, "Propagation of High Energy Laser Beams through Metallic Aerosols," *Applied Optics*, Vol. 29, No. 12, p. 1786, 20 April 1990.

8. Poulain, D.E., D.R. Alexander, J.P. Barton, S.A. Schaub and J. Zhang, "Interactions of Intense Ultraviolet Laser Radiation with Solid Aerosols," *J. Appl. Phys.*, Vol. 67, No. 5, p. 2283, 1 March 1990.

9. Ahlers, K.D. and D.R. Alexander, "Microcomputer Based Digital Image Processing System Developed to Count and Size Laser- Generated Small Particle Images," *Opt. Eng.*, Vol. 24, No. 6, p. 1060, 1985.

10. Schaub, S.A., D.R. Alexander, D.E. Poulain and J.P. Barton, "Measurement of Hypersonic Velocities Resulting from the Laser-Induced Breakdown of Aerosols Using an Excimer Laser Imaging System," *Rev. Sci. Instrum.*, Vol. 60, No. 12, p. 3688, December 1989.

11. Alexander, D.R., J.P. Barton, S.A. Schaub and G.M. Holtmeier, "Nonlinear Interactions of KrF Laser Radiation with Small Water Droplets," *Appl. Optics*, accepted for publication, 5 February 1990.

12. Jervis, T.R., M. Nastasi and T.G. Zocco, "Excimer Laser Mixing of Titanium Layers on AISI 304 Stainless Steel," *Mat. Res. Soc. Symp. Proc.*, Materials Research Society, Vol. 100, p. 621, 1988.

13. Ready, J.F., *Effects of High-Power Laser Radiation*, Academic Press, New York, 1971.

## Figures

Figure 1. Schematic of the experimental setup.

Figure 2. Images of 75 $\mu$m diameter copper wire before high-energy illumination (top) and after illumination (bottom). Irradiation was 80 GW/cm$^2$ using a KrF pulse ($\lambda = 248$ nm). Beam propagation was from right to left.

Figure 3. Interaction of KrF laser ($\lambda = 248$ nm) with a 75 $\mu$m diameter copper wire at 80 GW/cm$^2$. Time given under each photograph is the delay of the image beam with respect to the arrival of the high-energy laser pulse. Beam propagation is from right to left.

Figure 4. Interaction of KrF laser ($\lambda = 248$ nm) with a 75 $\mu$m diameter copper wire at 80 GW/cm$^2$. Time given under each photograph is the delay of the image beam with respect to the arrival of the high-energy laser pulse. Beam propagation is from right to left.

Figure 5. Interaction of KrF laser ($\lambda = 248$ nm) with a 75 $\mu$m diameter copper wire at 80 GW/cm$^2$. Time given under each photograph is the delay of the image beam with respect to the arrival of the high-energy laser pulse. Beam propagation is from right to left.

Figure 6. Photomicrographs of side view (top) and shadow surface (bottom) of an ablated 75 $\mu$m diameter copper wire. Irradiation was 80 GW/cm$^2$ by a KrF pulse ($\lambda = 248$ nm).

Figure 7. Photomicrographs of typical waves and particle formations on the front surface of an ablated 75 $\mu$m diameter copper wire. Irradiation was 80 GW/cm$^2$ by a KrF pulse ($\lambda = 248$ nm).

Figure 8. Typical dual pulse images of emitted material traveling from right to left away from the ablation area. Time delay between each imaging pulse is 56 ns providing a double exposure image. First image pulse delayed 500 ns after arrival of high-energy pulse. Irradiation was 80 GW/cm$^2$ by a KrF pulse ($\lambda = 248$ nm). Image dimensions are 280 $\mu$m square.

Figure 9. Typical dual pulse images of emitted copper particles traveling from right to left away from the ablation area. Time delay between each imaging pulse is 56 ns providing a double exposure image. First image pulse delayed 1500 ns after arrival of high-energy pulse. Irradiation was 80 GW/cm$^2$ by a KrF pulse ($\lambda = 248$ nm). Image dimensions are 165 $\times$ 230 $\mu$m.

Figure 10. Average velocities of emitted materials from interactions of KrF laser radiation at 80 GW/cm$^2$ with 75 $\mu$m diameter copper wire as a function of the image time delay. Top graph has been expanded to emphasize the acceleration during the laser pulse and the subsequent deceleration.
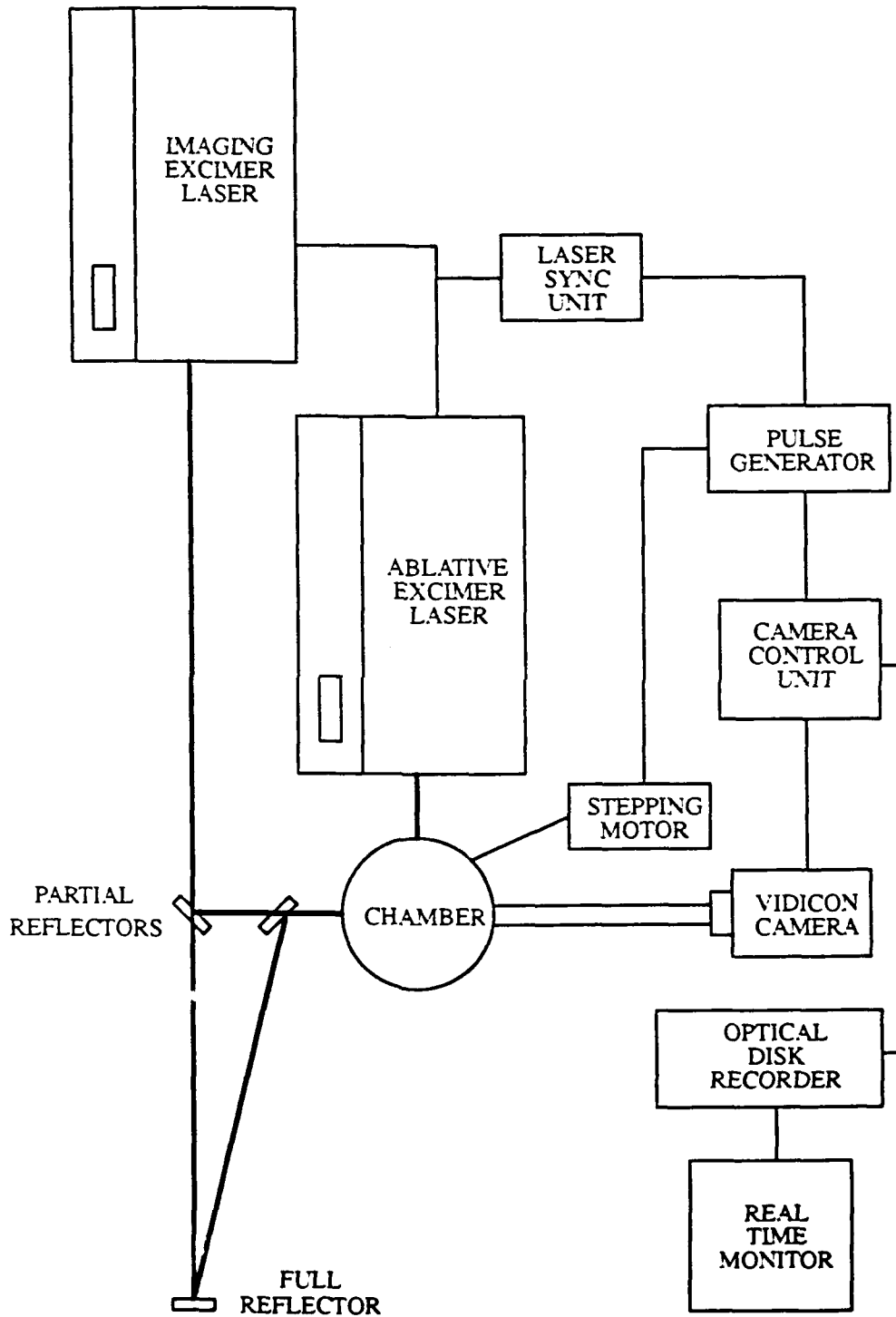
11

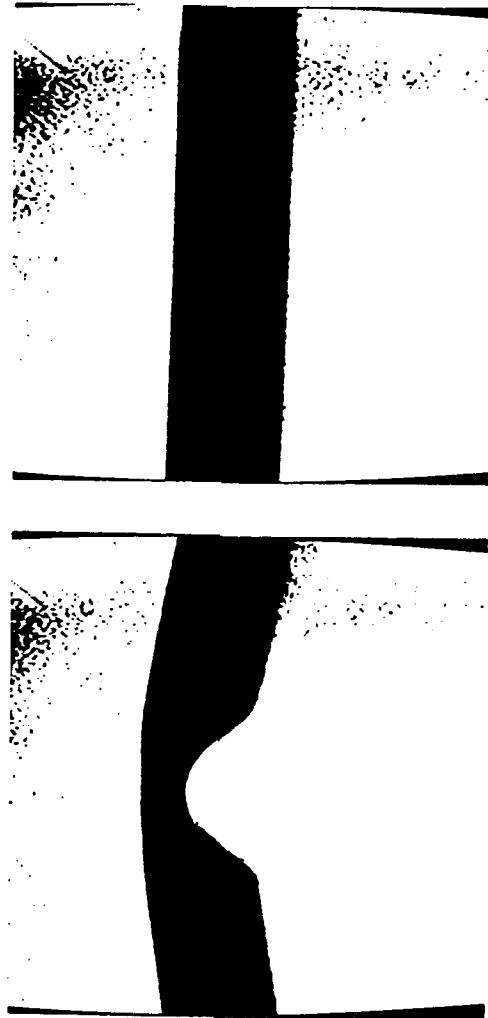Figure 1. Schematic of the experimental setup.

Figure 2. Images of 75 $\mu$m diameter copper wire before high-energy illumination (top) and after illumination (bottom). Irradiation was 80 GW/cm$^2$ using a KrF pulse ($\lambda = 248$ nm). Beam propagation was from right to left.
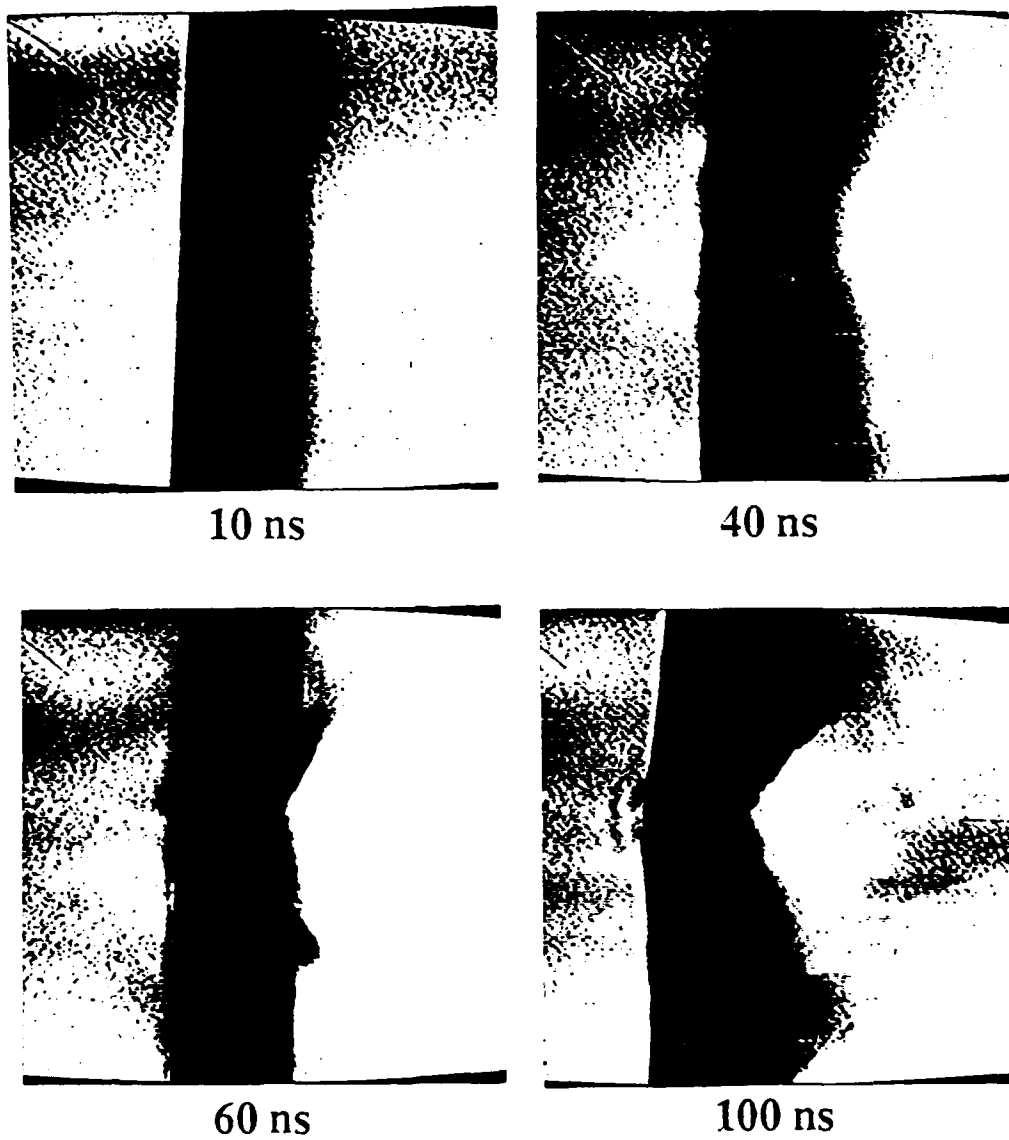
10 ns                    40 ns

60 ns                  100 ns

Figure 3. Interaction of KrF laser ($\lambda$ = 248 nm) with a 75 $\mu$m diameter copper wire at 80 GW/cm$^2$. Time given under each photograph is the delay of the image beam with respect to the arrival of the high-energy laser pulse. Beam propagation is from right to left.
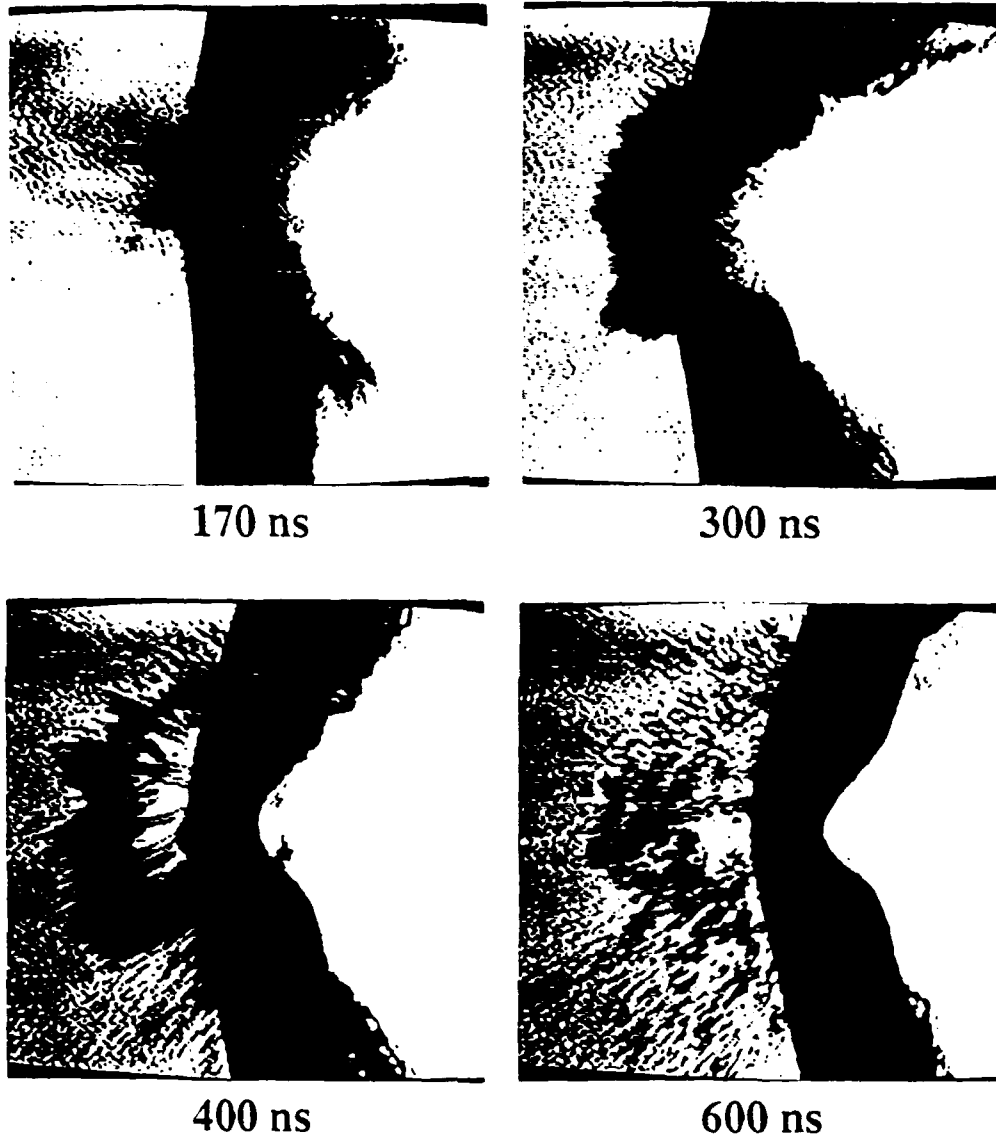
14

**170 ns**

**300 ns**

**400 ns**

**600 ns**

Figure 4. Interaction of KrF laser ($\lambda = 248$ nm) with a 75 $\mu$m diameter copper wire at 80 GW/cm$^2$. Time given under each photograph is the delay of the image beam with respect to the arrival of the high-energy laser pulse. Beam propagation is from right to left.

**800 ns**          **1400 ns**

Figure 5. Interaction of KrF laser ($\lambda = 248$ nm) with a 75 $\mu$m diameter copper wire at 80 GW/cm$^2$. Time given under each photograph is the delay of the image beam with respect to the arrival of the high-energy laser pulse. Beam propagation is from right to left.
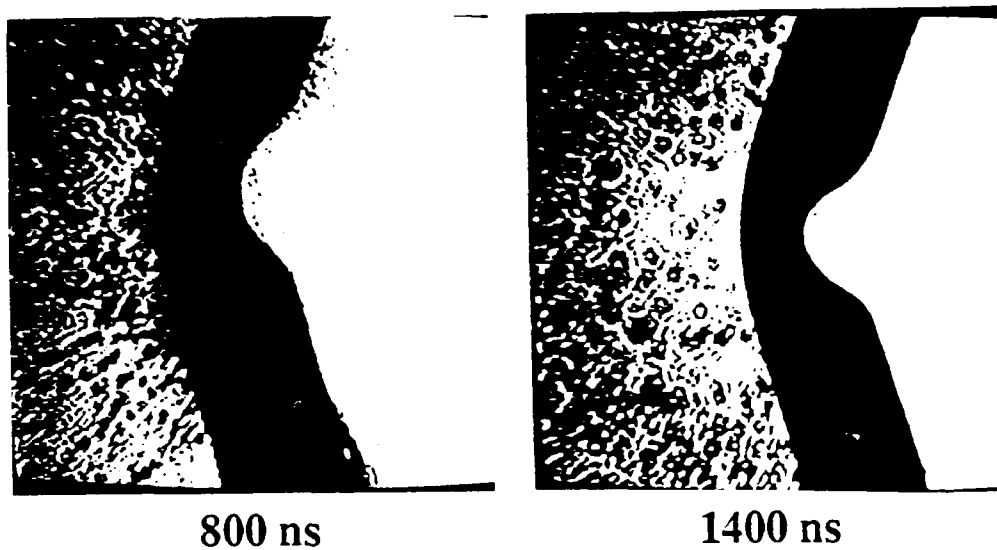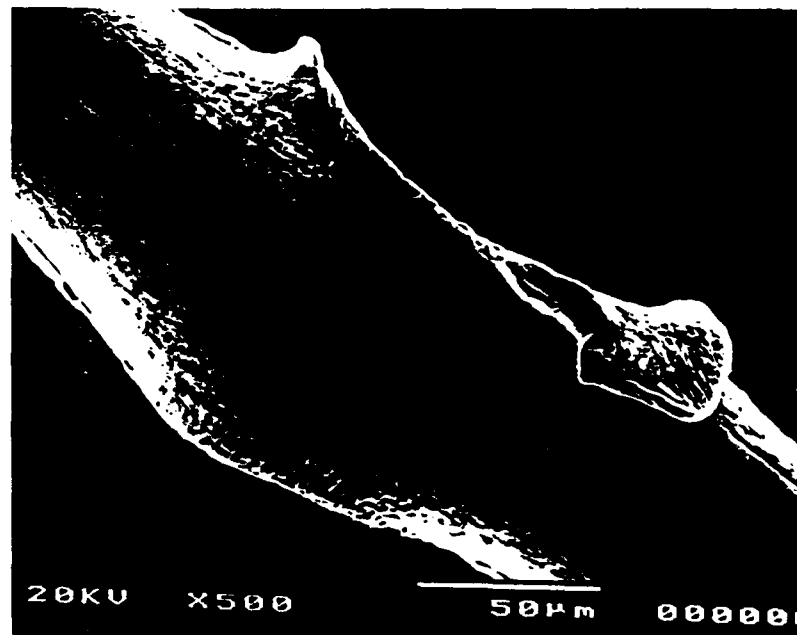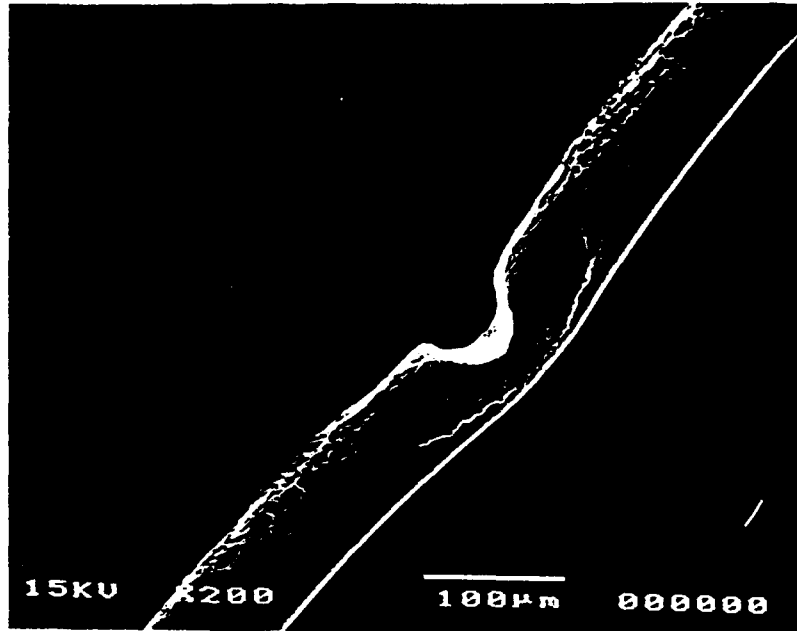
Figure 6. Photomicrographs of side view (top) and shadow surface (bottom) of an illuminated 75 $\mu$m diameter copper wire. Irradiation was 80 GW/cm$^2$ by a KrF pulse ($\lambda$ = 248 nm).
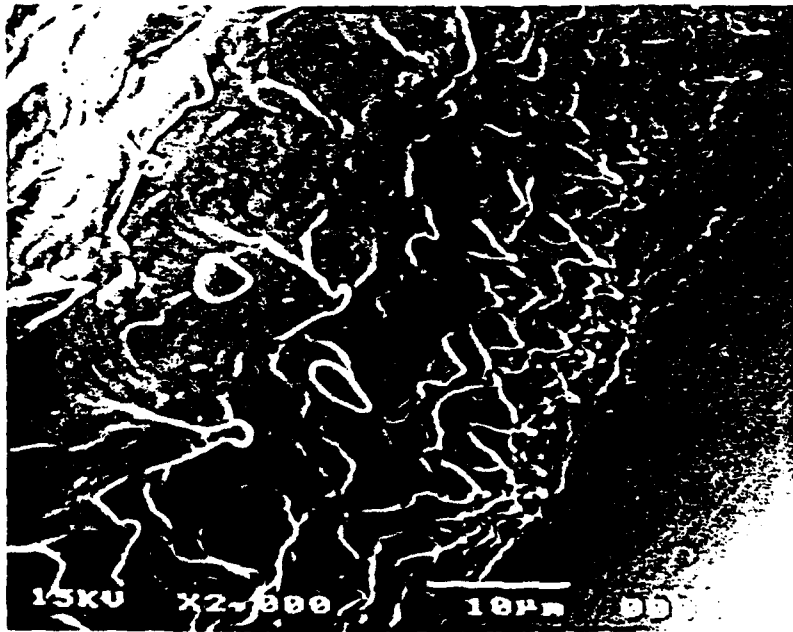
**Figure 7.** Photomicrographs of typical waves and particle formations on the front surface of an illuminated 75 μm diameter copper wire. Irradiation was 80 GW/cm² by a KrF pulse (λ = 248 nm).
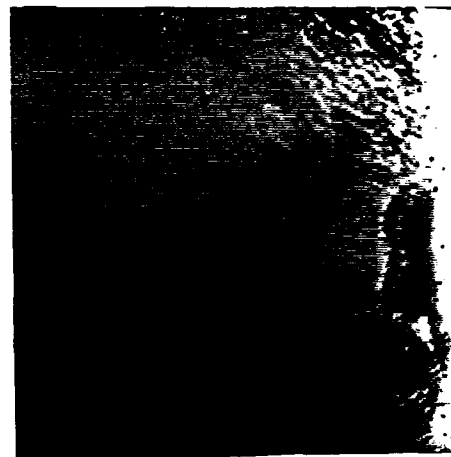
Figure 8. Typical dual pulse images of emitted material traveling from right to left away from the ablation area. Time delay between each imaging pulse is 56 ns providing a double exposure image. First image pulse delayed 500 ns after arrival of high-energy pulse. Irradiation was 80 GW/cm$^2$ by a KrF pulse ($\lambda$ = 248 nm). Image dimensions are 280 $\mu$m square.

Figure 9. Typical dual pulse images of emitted copper particles traveling from right to left away from the ablation area. Time delay between each imaging pulse is 56 ns providing a double exposure image. First image pulse delayed 1500 ns after arrival of high-energy pulse. Irradiation was 80 GW/cm$^2$ by a KrF pulse ($\lambda = 248$ nm). Image dimensions are 165 × 230 $\mu$m.

Figure 10. Average velocities of emitted materials from interactions of KrF laser radiation at 80 GW/cm$^2$ with 75 $\mu$m diameter copper wire as a function of the image time delay. Top graph has been expanded to emphasize the acceleration during the laser pulse and the subsequent deceleration.

21

# Interactions of intense ultraviolet laser radiation with solid aerosols

D. E. Poulain, D. R. Alexander, J. P. Barton, S. A. Schaub, and J. Zhang

*Center for Electro-Optics, University of Nebraska-Lincoln, Lincoln, Nebraska 68588-0525*

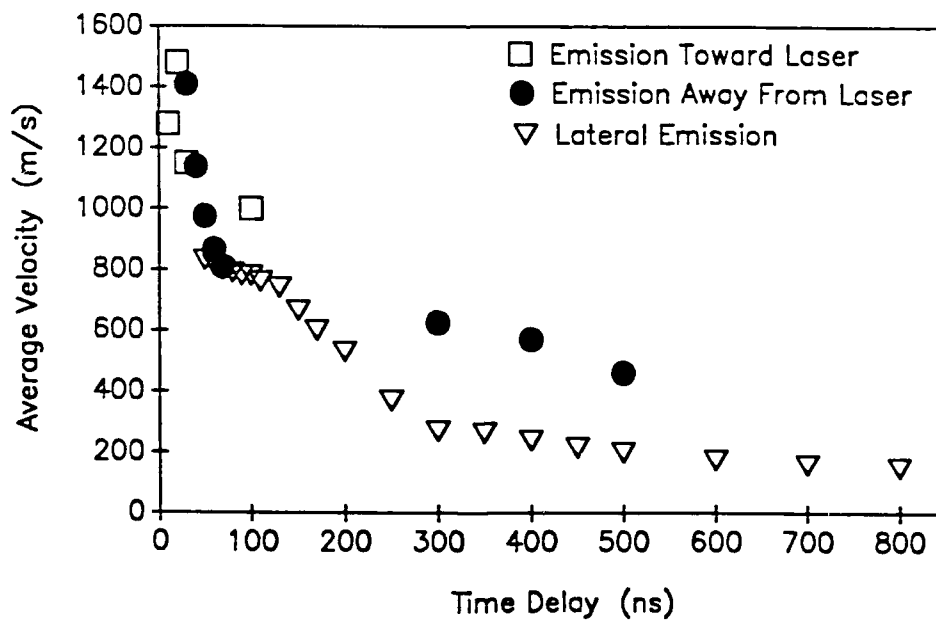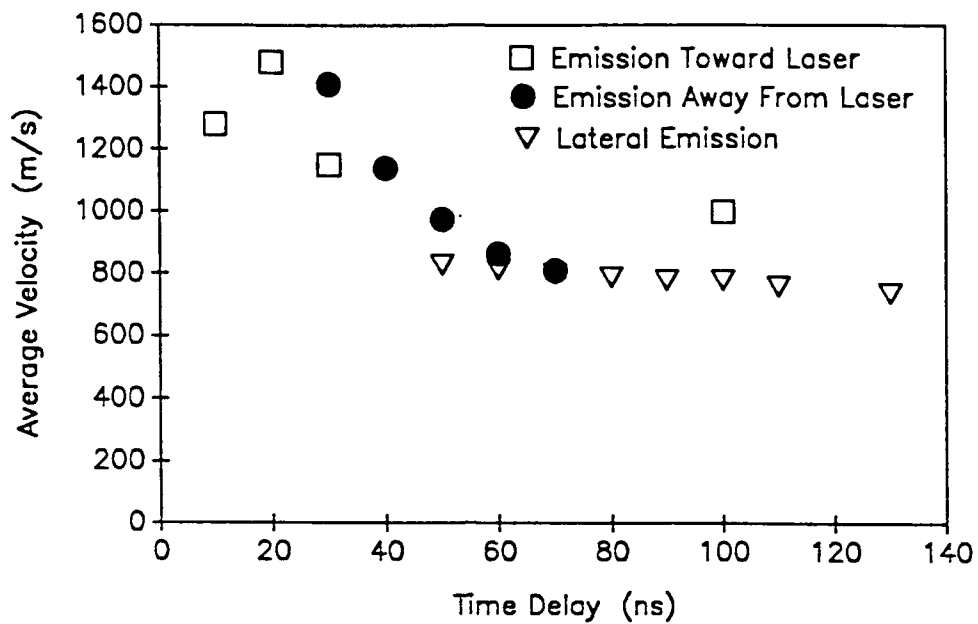Characterizations of the interaction of intense ultraviolet laser radiation ($\lambda = 248$ nm) with small solid aerosols are presented. Interaction dynamics, velocity measurements of expelled material, and thresholds for plasma formation are presented for aluminum, calcium fluoride, glass, silicon carbide, and tungsten particles. An excimer laser operating with a krypton fluoride gas mixture was used to irradiate small solid aerosol particles ($\approx 5$–$50\,\mu$m) under atmospheric and vacuum conditions down to $10^{-5}$ Torr. Focused laser radiation intensities varied from $10^7$ W/cm$^2$ to a maximum of $2 \times 10^{11}$ W/cm$^2$. Interactions of the laser radiation with the solid aerosols were recorded in real time by an ultraviolet laser imaging system. Velocities between 250 and 2000 m/s were measured for material ejected from particles undergoing laser interaction. Laser intensity thresholds for visible plasma emission ranged from a maximum of 650 MW/cm$^2$ for aluminum to a minimum of 59 MW/cm$^2$ for tungsten. Thresholds for plasma formation were determined to be relatively independent of ambient pressure.

## I. INTRODUCTION

Recently the increasing use of excimer lasers has created a growing interest in the interaction effects of intense, ultraviolet, electromagnetic radiation with solid materials. Interactions of both high-power and high-energy laser radiation with solid materials have been the subject of many theoretical[1,2] and experimental[3-6] investigations. An understanding of the processes governing photon interactions with solid aerosols is important in such fields as the study of the photoablation of semiconductor materials, creation and deposition of thin films, industrial production of powdered materials, laser machining of composites and metal matrix materials, and many other applications. A knowledge of the interaction processes for individual particles is beneficial in understanding the effects on a macroscopic scale.

In this paper the results of three related investigations are reported for the interaction of intense ultraviolet laser radiation with solid aerosols. An excimer laser imaging system was used to visualize and record the interaction dynamics of single laser pulses with individual particles (or agglomerates) approximately 5–50 $\mu$m in diameter and the subsequent laser induced breakdown of the particles. Typical velocities of material ejected from the solid particles during and subsequent to the laser pulse interaction were studied. Finally, threshold laser intensities for visible plasma emission were studied. The work reported in this paper was performed under surrounding gas pressures ranging from atmospheric pressure to $10^{-5}$ Torr in order to study the pressure dependence of the breakdown phenomena.

## II. EXPERIMENTAL PROCEDURE

The general experimental setup used for this investigation is shown schematically in Fig. 1. Two identical Questek Model 2860 excimer lasers were used to illuminate the particles. The output of the first laser, equipped with unstable resonator optics, was focused by a plano-convex lens (25.4 cm focal length, 5.08 cm diameter) through an optical port

into the vacuum chamber. The vacuum chamber consisted of a collar fitted with eight fused silica optical ports topped by a glass belljar. A cryopump was used in conjunction with a mechanical roughing pump to achieve $10^{-5}$ Torr within approximately 15 min. The output of the second laser, equipped with stable resonator optics, entered the vacuum chamber in a direction perpendicular to the beam of the first laser along the axis of a Cohu Model 2006 vidicon camera and served as the illumination source for the camera. Alignment of the imaging system probe volume and the high-energy pulse was performed using a stream of monodisperse water droplets, generated with a TSI Model 3450 vibrating orifice aerosol generator. The droplet stream was first posi-
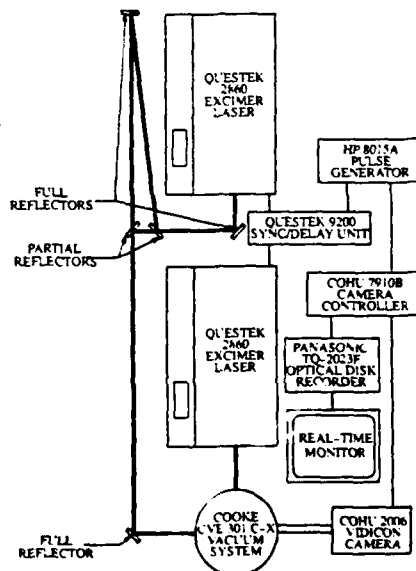


FIG 1. Schematic of the experimental arrangement.

tioned in the imaging system focal plane. The focal point of the high-energy pulse was then adjusted until maximum interaction was observed with the droplets by the real-time excimer laser imaging system. Finally, the droplet stream was removed and optical discharge in the atmosphere was observed using the imaging system to insure the proper vertical positioning of the high-energy pulse within the imaging plane. Solid particles were dispersed from a reservoir through a 500-$\mu$m orifice and allowed to fall through the probe volume. Sync signals from the Cohu 7910B camera controller were used to coordinate subsequent firing of the two excimer lasers. The camera controller sync signals were sent to an HP 8015A pulse generator and subsequently to a Questek Model 9200 Laser Sync Unit (LSU). The LSU was equipped with both analog and digital delays. The analog delay was used to adjust the laser firing times such that the imaging pulse and high-energy pulses arrived simultaneously at the probe volume. Relative delay between the imaging and high-energy pulses could then be set from 0 to 100 $\mu$s in increments of 10 ns using the digital delay.

A 248-nm bandpass filter was used in the imaging system to eliminate passage of intense visible emission that tended to saturate the vidicon camera and prevent observation of the interaction phenomena. The only observed light is thus due to the illumination beam and the elastic scattered light from the high-energy pulse.

Variation of laser intensity for threshold measurements was accomplished by varying the location of the particles along the propagation axis of the focused beam. The beam cross section was determined as a function of axial location by passing a knife edge through the beam and taking the ratio of transmitted to incident pulse energy. A Hamamatsu Slow Speed Streak Unit was used to measure the temporal characteristics of the excimer laser pulse. Average laser intensities were then computed based on pulse energy, pulse duration, and cross-sectional area of the pulse. Particles were subsequently allowed to fall through the focal point of the high-energy excimer pulse and laser intensity decreased until no visible plasma emission could be detected within the probe volume. Although a streak camera and a fast photo diode were also tried as methods for detecting the threshold values, visual observation was found to give the most consistent data.

## III. INTERACTION DYNAMICS

Experimental investigations consisted of real-time short wavelength imaging of the interaction of high-power excimer laser radiation with particles of various solid materials under atmospheric and vacuum conditions in order to determine characteristic particle breakup dynamics. Dynamic interactions were observed for aluminum, calcium fluoride, glass, silicon carbide, tungsten, aluminum oxide, and polystyrene/divinylbenzene (DVB). The materials investigated generally ranged in size from 5 to 50 $\mu$m in diameter with the exception of the polystyrene/DVB spheres which were 230 $\mu$m in diameter. Images were recorded at several time steps during the interaction process ranging from the time of arrival of the high-energy pulse up to 1 $\mu$s later. Preliminary investigations, conducted to determine the dependence of

the interaction process on the ambient pressure, revealed only minor differences in breakup dynamics for vacuum pressures between 0.1 and $10^{-5}$ Torr. Consequently, dynamic interactions are only presented for atmospheric and high-vacuum ($10^{-5}$ Torr) cases. The interactions were generally of two distinct types corresponding to absorbing (aluminum, silicon carbide, tungsten, and polystyrene/DVB) and more transparent (calcium fluoride and glass) materials. Interactions involving aluminum and calcium fluoride are presented here as representative of the two types. Images of 230-$\mu$m polystyrene/DVB particles are also included due to their unique explosive dynamics.

To serve as a control in studying the dynamics of particle breakup, images were first recorded of typical particles prior to high-energy laser interaction. Typical shadow images of aluminum and calcium fluoride particles are shown in Fig. 2. Figure 3 shows typical laser interactions with 20-$\mu$m aluminum particles at a pressure of $10^{-5}$ Torr. The laser pulse is propagating from the right- to left-hand side in all the images shown. Of particular interest are the photographs for 0 and 50 ns time delays. Material is seen being ejected from small aluminum particles in the direction of laser pulse propagation. Figure 4 shows similar laser interactions with aluminum particles under atmospheric pressure ($\approx$ 760 Torr). As with the interactions in vacuum, material is ejected in the form of plumes moving away from the bright regions in the direction of laser pulse propagation. These bright spots were determined to result from elastic scattering of the high-energy pulse by the solid particles. The resulting
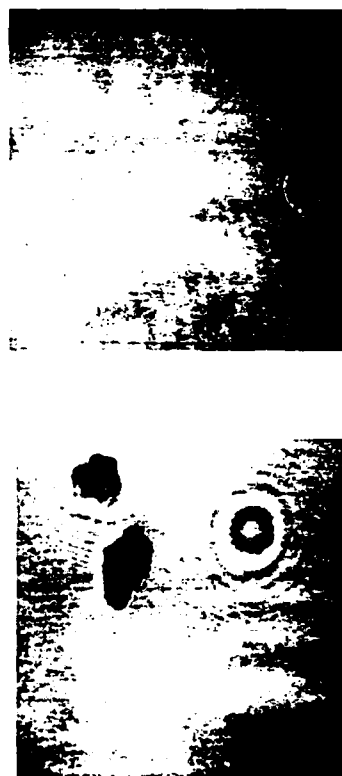


FIG. 2. Images of typical 20 $\mu$m aluminum (top) and 40 $\mu$m calcium fluoride (bottom) particles as viewed by the laser imaging system. Two out-of-focus calcium fluoride particles are visible in the bottom image. Image dimensions are 400 $\mu$m square.
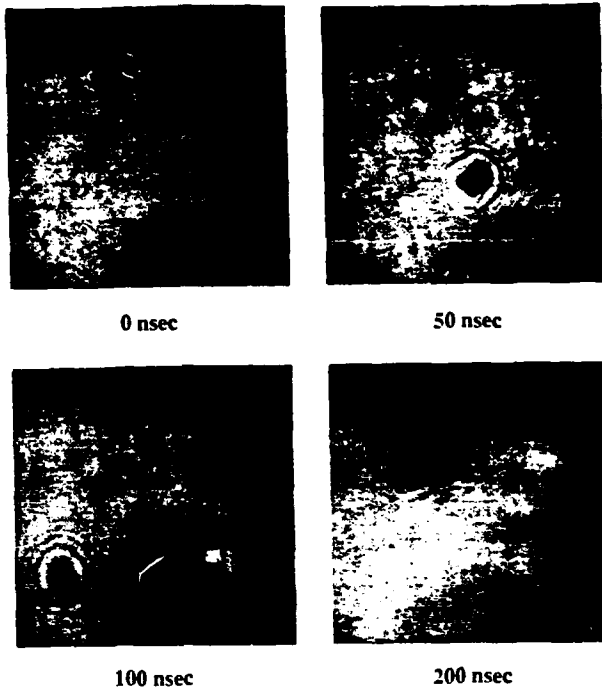
2284    J. Appl. Phys., Vol. 67, No. 5, 1 March 1990

Poulain et al.    2284

0 nsec        50 nsec

100 nsec        200 nsec

FIG. 3. Typical interactions of KrF laser ($\lambda$ = 248 nm, $I$ = 10$^{11}$ W/cm$^2$) with 20 $\mu$m aluminum particles at 10$^{-5}$ Torr. The stated times correspond to the interval between arrival of the high-energy laser pulse and the illumination pulse and vary by $\pm$ 7 ns. Laser pulse is propagating from the right- to left-hand side. Image dimensions are 400 $\mu$m square.

saturation points thus served to mark the location of initial interaction between the high-energy pulse and the solid particles. Evidence of shock waves are also apparent in the later time stages for atmospheric pressure conditions. It should be noted that the stated time delays are average values. The jitter of the system was observed to be approximately $\pm$ 7 ns.

Figure 5 shows typical laser interactions with calcium fluoride particles at an ambient pressure of 10$^{-5}$ Torr. The laser pulse is propagating from the right- to left-hand side. Evident in all the photographs is the very intense bright region corresponding to the location of the laser-particle interaction. It should be noted that the only observed light is for $\lambda$ = 248 nm passing through a bandpass filter. In contrast to the aluminum interactions, material appears to be ejected in a much more symmetric fashion from the region of interaction for calcium fluoride. Figure 6 shows similar laser interactions with calcium fluoride particles at atmospheric pressure. The breakup dynamics appear to be almost identical to those observed under vacuum conditions. The presence of a shock wave is evident in the 200-ns case for atmospheric pressure conditions.

Figure 7 shows typical laser interactions with polystyrene/DVB particles at an ambient pressure of 10$^{-5}$ Torr. Again, the laser pulse is propagating from the right- to left-hand side. Distinctive phenomena observable in these images are the pronounced jetting of material from the front surface of the particle in the 0-ns case and the absence of any observable material in the shadow region of the particle in



0 nsec        50 nsec

100 nsec        200 nsec

FIG. 4. Typical interactions of KrF laser ($\lambda$ = 248 nm, $I$ = 10$^{11}$ W/cm$^2$) with 20 $\mu$m aluminum particles at atmospheric pressure. The stated times correspond to the interval between arrival of the high-energy laser pulse and the illumination pulse and vary by $\pm$ 7 ns. Laser pulse is propagating from the right- to left-hand side. Image dimensions are 400 $\mu$m square.
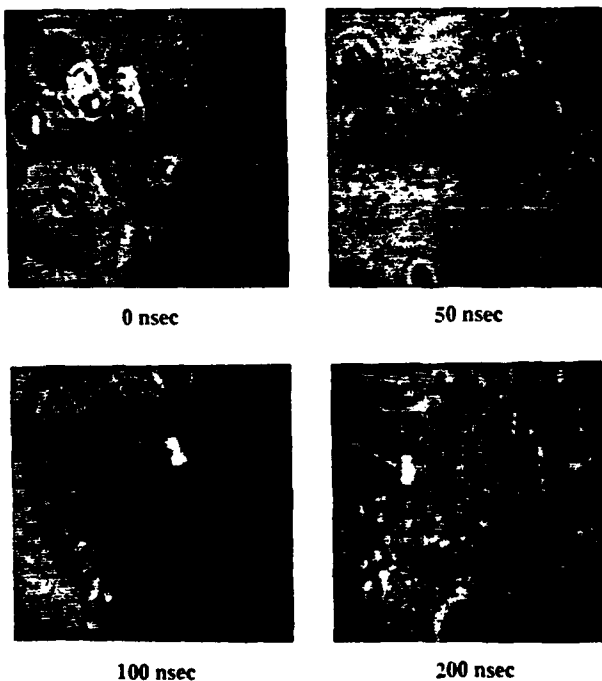


0 nsec        50 nsec

100 nsec        200 nsec

FIG. 5. Typical interactions of KrF laser ($\lambda$ = 248 nm, $I$ = 10$^{11}$ W/cm$^2$) with 40-90 $\mu$m calcium fluoride particles at 10$^{-5}$ Torr. The stated times correspond to the interval between arrival of the high-energy laser pulse and the illumination pulse and vary by $\pm$ 7 ns. Laser pulse is propagating from the right- to left-hand side. Image dimensions are 400 $\mu$m square.

**0 nsec**          **50 nsec**
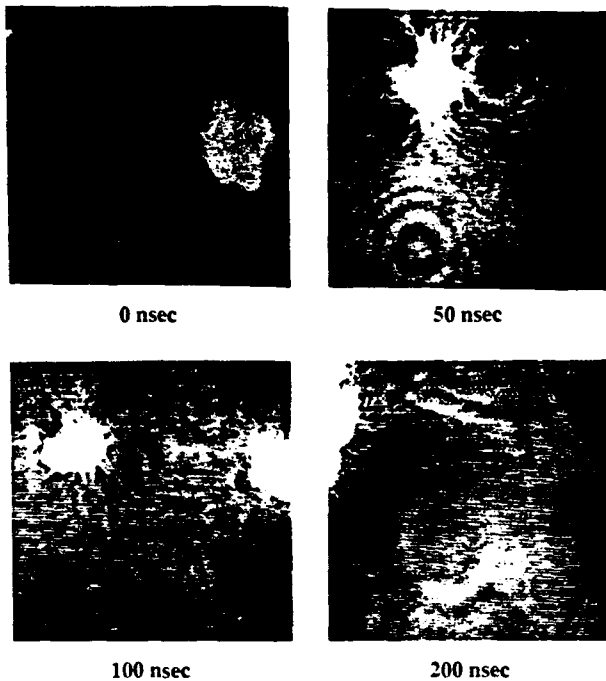


**100 nsec**          **200 nsec**

FIG. 6. Typical interactions of KrF laser ($\lambda = 248$ nm, $I = 10^{11}$ W/cm$^2$) with 40–90 $\mu$m calcium fluoride particles at atmospheric pressure. The stated times correspond to the interval between arrival of the high-energy laser pulse and the illumination pulse and vary by $\pm 7$ ns. Laser pulse is propagating from the right- to left-hand side. Image dimensions are 400 $\mu$m square.

the 100-ns case. One possible explanation of these unique dynamics is the variation in optical size parameter, $\alpha = 2\pi a/\lambda$, where $a$ is the particle radius and $\lambda$ is the wavelength of illuminating radiation, between the various materials. For the polystyrene/DVB particles, the size parameter was approximately one order of magnitude larger than that of any other material studied.

## IV. VELOCITY MEASUREMENTS

Another part of the investigation was to determine the velocity of material ejected from laser-particle interactions by imaging techniques. The output of the imaging laser was split and an optical path delay introduced for one portion of the beam, as shown in Fig. 1. Two imaging pulses, with an interval time delay of approximately 45 ns, produced dual-exposure images on the vidicon camera. Image processing and particle sizing software were then used in conjunction with a RCI Trapix 5532 image processor to determine the distance travelled by material during the interval between pulses and average velocities subsequently computed.

Figure 8 shows a typical dual image of expelled material for aluminum particles. The image shows material in the upper left-hand corner moving away from the bright interaction region on the right-hand side (laser pulse is propagating from the right- to left-hand side). The material travelled a distance of approximately 55 $\mu$m during a 45-ns pulse interval to give a velocity of 1200 m/s. Recent experiments in our laboratory using small diameter wires indicate that this material can be molten at 2 mm away from the laser-particle interaction interface.

The range of velocities measured are shown in Table I. Velocities under vacuum conditions for glass and aluminum were nearly equivalent and ranged from 440 to 2000 m/s. Velocities for glass spheres, obtained under atmospheric



**0 nsec**



**100 nsec**

FIG. 7. Typical interactions of KrF laser ($\lambda = 248$ nm, $I = 10^{11}$ W/cm$^2$) with 230 $\mu$m polystyrene-/divinylbenzene particles at $10^{-5}$ Torr. The stated times correspond to the interval between arrival of the high-energy laser pulse and the illumination pulse and vary by $\pm 7$ ns. Laser pulse is propagating from the right- to left-hand side. Image dimensions are 400 $\mu$m square.
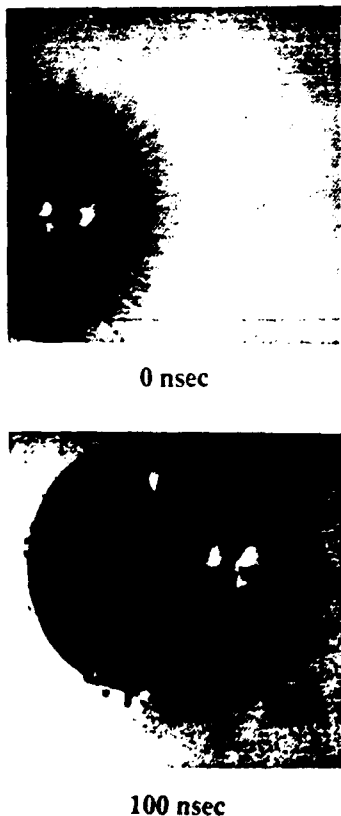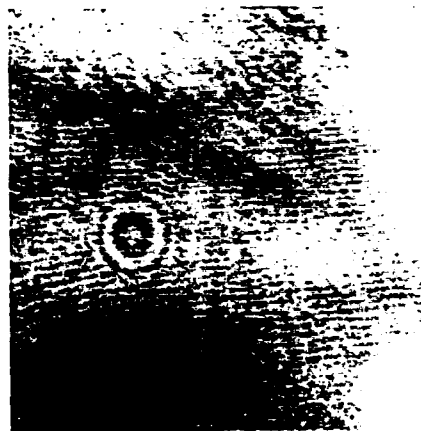


FIG. 8. Typical image used to determine velocities of material expelled from particles during interaction with KrF laser radiation. The material in the upper left of the image travelled 55 $\mu$m during the 45 ns between imaging pulses giving an average velocity of 1200 m/s. The source of the material is believed to originate from the bright region on the right-hand side where an agglomeration of aluminum particles is undergoing laser interaction. Image dimensions are 400 $\mu$m square.

| Material | Laser intensity ($W/cm^2$) | Ambient pressure (Torr) | Material velocity (m/s) |
|---|---|---|---|
| Glass (5–50 $\mu$m) | $10^{11}$ | 760 | 250–750 |
| Glass (5–50 $\mu$m) | $10^{11}$ | $10^{-5}$ | 440–2000 |
| Aluminum (20 $\mu$m) | $10^{11}$ | $10^{-5}$ | 450–1500 |

pressure, ranged from 250 to 750 m/s. Uncertainty in velocity measurements was estimated to be approximately 20%. The range of material velocities was found to be highly dependent on laser intensity (spatial location of the particle within the laser beam and pulse energy) but relatively independent of the target material. Figure 9 shows an image of the interaction of a laser pulse with three aluminum particles which demonstrates the wide variation of dynamics in and around the probe volume. The three bright regions observed on the right-hand edge of the image are due to elastic scattering of the initial high-energy laser pulse. These bright regions serve as markers for the location of the particles at the time of arrival of the incident pulse on the particles. The top bright spot demonstrates a particle that has undergone complete breakup and appears as a cloud of material to the left of the top bright spot propagating in the direction of the laser pulse. The original location of this particle coincides with the approximate center of the pulse profile, and thus the highest intensity. The next particle down is located near the edge of the pulse profile. Material is observed in the shadow region of the particle moving in the direction of the laser pulse, but the particle appears to be generally intact. The laser intensity



FIG. 9. Photograph of three 20 $\mu$m aluminum particles undergoing laser interaction. Laser pulse is propagating from the right- to left-hand side. The bright spots are due to scattered light from the initial high-energy explosive pulse and serve to mark the original location of the particles. The top particle, located in the main portion of the pulse, has undergone complete breakup and appears as a cloud of material moving from right to left. The middle particle, located near the edge of the pulse, shows material being ejected in the direction of pulse propagation. The bottom particle, located in the wings of the pulse is observed to have scattered light from the high-energy pulse but is still intact. Image dimensions are 400 $\mu$m square.

at the location of the third particle is observed to be much lower. Scattered 248-nm radiation is observed but with essentially no material in the shadow region of the particle.

## V. THRESHOLD MEASUREMENTS

Experimental investigations were performed to measure the initial thresholds for visible plasma emission from various solid materials. The dependence of the breakdown threshold on ambient pressure was investigated for pressures ranging from atmospheric to $10^{-4}$ Torr. Thresholds were determined for aluminum, calcium fluoride, soda lime glass, silicon carbide, and tungsten.

Average measured thresholds for visible plasma emission as a function of ambient pressure are shown in Fig. 10 for the materials investigated. The threshold was found to be relatively independent of ambient pressure except in the case of tungsten. The average thresholds for each material are presented in Table II. According to Shinn et al.,[4] at very high laser intensities the plasma becomes dense and highly absorbing resulting in the laser energy being absorbed in a small region. Explosive heating results and a laser-supported detonation wave is initiated. The pressure driving these waves may be on the order of several hundred bar. As a result, they state that it is reasonable to expect the ablation process to be independent of ambient gas pressure from vacuum up to 1000 Torr.

Important material and optical properties of investigated materials correlated with respective measured threshold intensities are also shown in Table II. Under vacuum conditions a vapor must first be formed from the solid material in which a plasma may then form. A review of the specific heat of the materials shows a direct correlation between increasing specific heat and threshold intensity. This suggests that as the specific heat increases more energy is required to elevate the temperature of the material to vaporize it. An investigation performed by Dreyfus, Kelly, and Walkup[7] suggested that thermal effects could not be responsible for plasma formation since they measured surface temperatures in aluminum of only 500 K, well below the temperature necessary for vaporization. However, an investigation reported by Shinn et al.[4] measured temperatures during the ablation
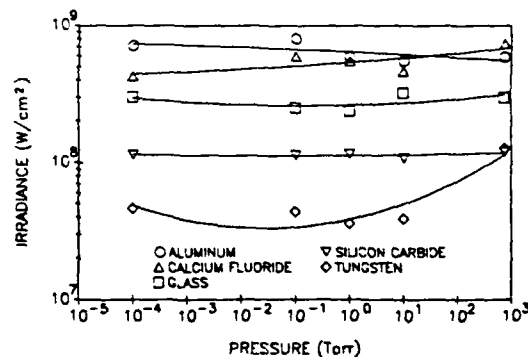


FIG. 10. Average measured threshold for visible plasma emission from the interaction of ultraviolet laser radiation ($\lambda = 248$ nm) with various solid materials as a function of ambient pressure.

TABLE II. Average measured threshold for visible plasma emission from the interaction of ultraviolet laser radiation ($\lambda = 248$ nm) with various materials and correlation to physical properties of the materials.

| Material | Measured threshold ($MW/cm^2$) | Ionization potential (eV) | Refractive index (at $\lambda = 248$ nm) | Specific heat (kJ/kg K) |
|---|---|---|---|---|
| Aluminum | 650 | 6.0[a] | 0.190[c] | 900[f] |
| Calcium fluoride | 550 | 12.5[a] | 1.468[d] | 850[g] |
| Glass | 310 | 11.6[b] | 1.44[e] | 750[h] |
| Silicon carbide | 110 | 9.0[b] | 3.16[c] | 675[h] |
| Tungsten | 59 | 7.98[c] | 3.40[c] | 134[f] |

[a] Reference 9.
[b] Reference 10.
[c] Reference 11.
[d] Reference 12.
[e] Reference 13.
[f] Reference 14.
[g] Reference 15.
[h] Reference 16.

of silicon that suggest that thermal effects in the vaporization of material may be significant.

Examination of the first ionization potentials for the materials in Table II to their relative threshold intensities also reveals a direct correlation between increasing ionization potential and threshold intensity, with the exception of aluminum. For aluminum exposed to an atmospheric environment Uhlig and Revie[8] state that a passive film of aluminum oxide 2–10 nm in thickness will be present. The optical properties of such an oxide coating on micrometer-sized aluminum particles was beyond the scope of the present investigation. However, if the penetration depth were equal to or less than the coating thickness, the interaction of bulk aluminum might be more closely approximated by the interaction of UV laser radiation with aluminum oxide. Considering the ionization potential of aluminum oxide (10.0 eV) instead of aluminum (6.0 eV) brings the correlation of threshold intensity and ionization potential more closely in agreement.

Finally, Table II shows a correlation between the real portion of the refractive index and threshold intensity. The experimental results indicate that threshold intensity increases as the real portion of the refractive index decreases at $\lambda = 248$ nm.

## VI. SUMMARY

The interactions of small solid aerosol particles with ultraviolet laser radiation ($\lambda = 248$ nm) of up to $10^{11}$ W/cm$^2$ have been investigated for the first time. Images of the dynamics of particle breakup during and subsequent to laser interaction have been presented for aluminum and calcium fluoride. The dynamics have been found to be highly variable and dependent upon the particle size, optical properties of the material, and relative location of the particle within the cross section of the laser pulse. For absorbing materials in the 5–50 μm range. particle material appears to be ejected in the direction of laser pulse propagation. Large polystyrene/DVB particles (230 μm diameter) have been found to interact entirely on the illuminated surface. Whether this is due to its unusually large size parameter or optical properties has not yet been determined since internal field calculations could not be performed since data on the index of re-

fraction at 248-nm wavelength is apparently not available in the literature. Calcium fluoride particles, which are highly transparent to the laser radiation, have been found to explode symmetrically. Velocities of material expelled from particles during laser interaction have been determined by imaging techniques. The velocity of material expelled during laser interaction has been found to be highly dependent on the incident intensity of laser radiation and to the ambient pressure, but appear to be relatively insensitive to material properties. Velocities obtained under atmospheric conditions for glass particles range from 250 to 750 m/s. Velocities obtained similarly for glass and aluminum under high vacuum conditions range from 440 to 2000 m/s. Threshold laser intensities for visible plasma emission have been determined for aluminum, calcium fluoride, glass, silicon carbide, and tungsten under pressures ranging from $10^{-4}$ Torr to atmospheric pressure. Thresholds have been found to be insensitive to ambient pressure and range from 650 MW/cm$^2$ for aluminum down to 59 MW/cm$^2$ for tungsten. Comparison of measured threshold intensities to material properties suggests a correlation of increasing specific heat. increasing ionization potential and decreasing real portion of refractive index with increasing threshold intensity. This suggests that thermal effects may play some role in the laser induced breakdown process in addition to multiphoton ionization and cascade ionization processes.

## ACKNOWLEDGMENTS

[1] D. C. Smith, J. Appl. Phys. **48**, 2217 (1977).
[2] D. Rosen, G. Weyl, D. Hastings. and J. Mittledorf. Proc. SPIE Int. Soc. Opt. Eng. **476**, 118 (1984).
[3] J. E. Rothenberg and G. Koren. Appl. Phys. Lett. **44**, 664 (1984).
[4] G. B. Shinn. F. Steigerwald. H. Stiegler. R. Sauerbrey. F. K. Tittel. and W. L. Wilson, Jr., J. Vac. Sci. Technol. B **4**, 1273 (1986).
[5] G. S. Korshunov, V. V. Ustyuzhin. and V. Ya. Ushakov. Sov. Phys. Tech. Phys. **30**, 469 (1985).
[6] R. K. Chang, "Interactions of High Energy Laser Radiation with Small Particles," Army Contract Report on Contract No. DAAL 03-86-D-0001, 1987 (unpublished).
[7] R. W. Dreyfus, R. Kelly, and R. E. Walkup. Appl. Phys. Lett. **49**, 1478 (1986).
[8] H. H. Uhlig and R. W. Revie, Corrosion and Corrosion Control. (Wiley. New York, 1985).
[9] R. D. Levin and S. G. Lias, Ionization Potential and Appearance Potential Measurements, 1971–1981. NSRDS-NBS 71 (U.S Government Printing Office. Washington, DC, 1982).
[10] H. M. Rosenstock, K. Draxl. B. W. Steiner. and J. T. Herron. J. Phys. Chem. Ref. Data **6**, 1-384. (1977).
[11] E. D. Palik. Ed.. Handbook of Optical Constants of Solids (Academic. New York. 1985).
[12] G. Callahan (private communication).
[13] W. H. Lowdermilk and D. Milam. Proc. SPIE Int. Soc. Opt. Eng. **476**, 143 (1984).
[14] R. C. Weast, Ed., CRC Handbook of Chemistry and Physics. 66th ed. (CRC, Boca Raton, FL, 1985).
[15] R. H. Perry and C. H. Chilton. Eds., Chemical Engineers' Handbook (McGraw-Hill, New York, 1973).
[16] F. P. Incropera and D. P. DeWitt, Fundamentals of Heat and Mass Transfer (Wiley, New York, 1985).

# ELECTROMAGNETIC FIELDS

# FOR AN IRREGULARLY-SHAPED, NEAR-SPHERICAL PARTICLE

# ILLUMINATED BY A FOCUSED LASER BEAM

J. P. Barton, and D. R. Alexander

Center for Electro-Optics and Department of Mechanical Engineering

College of Engineering

University of Nebraska-Lincoln

Lincoln, Nebraska 68588-0656

## ABSTRACT

A theoretical procedure is derived for the determination of the internal and external electromagnetic fields for a monochromatic beam incident upon a homogeneous particle of arbitrarily-defined shape. The procedure is best-suited for the analysis of near-spherical particles (i.e. particles which deviate from a sphere by plus or minus a few tenths of a radii). Verification and demonstration calculations are presented. Also presented are calculations investigating the effect of a surface deformation on resonance excitation within an otherwise spherical particle.

## I. INTRODUCTION

In an earlier paper,[1] equations were derived for the determination of the internal and external electromagnetic fields for a beam incident upon a homogeneous spherical particle. Presented here is a generalization of this earlier work which permits solutions for a beam incident upon a homogeneous particle of arbitrarily-defined shape. This new approach is most applicable for the analysis of near-spherical particles (i.e. particles which deviate from a sphere by plus or minus a few tenths of a radii). The procedure could be used to determine, for example, the electromagnetic fields for a laser beam focused upon a small liquid droplet which has been deformed in shape due to aerodynamic, thermal, or electromagnetic stresses.

For a plane wave incident upon a homogeneous particle, analytical solutions of the electromagnetic interaction problem exist for geometries in which Helmholz equation is separable. Solutions have been obtained for a plane wave incident upon a homogeneous sphere (Mie[2]), infinite circular cylinder (normal incidence: Lord Rayleigh,[3] oblique incidence: Wait[4]), infinite ellipsoidal cylinder (Yeh[5]), and the oblate/prolate spheroid (Oguchi[6] and Asano and Yamamoto[7]). Several approaches have been introduced for the analysis of the electromagnetic interaction of a plane wave incident upon an irregularly-shaped particle: the perturbation method,[8-14] the extended boundary condition method,[15-18] the point matching method,[6] the coupled dipole method,[19-25] the finite element method,[26-27] and the invariant imbedding T matrix method.[28] Each of these approaches for the analysis of an irregularly-shaped particle have their own associated advantages/disadvantages and regimes of applicability. The perturbation method is limited to geometries that only slightly deviate from that of a sphere. The extended boundary condition and point matching methods are restricted to geometries of limited elongation because of an eventual ill-conditioning of equations. The numerical coupled dipole and finite element methods result in large sets of simultaneous equations which restrict solutions to small objects (relative to wavelength) that can be analyzed using a small number of cells. The invariant imbedding T matrix method is a hybrid analytical/numerical approach that may provide solutions with fewer computation steps in comparison with the numerical schemes of the coupled-dipole and finite element methods.

All of the aforementioned irregularly-shaped particle efforts have been predominately concerned with the determination of the far-field scattering patterns for plane wave illumination. Yeh, Colak, and Barber[29] have considered the determination of the far-field scattering for a beam incident upon

an irregularly-shaped particle. In the approach of Yeh, Colak, and Barber,[29] the incident field is expanded in a plane wave spectrum and a superposition of plane wave solutions, obtained using the extended boundary condition method, is performed.

In our theoretical development, a focused beam solution is obtained by utilizing the incident field directly and, unlike the approach of Yeh, Colak, and Barber[29], the computationally time-consuming superposition of individual plane wave solutions is not necessary. In addition, our work concerns not only the determination of far-field scattering patterns, but also the determination of the internal and near-field electromagnetic field distributions.

## II. THEORETICAL DEVELOPMENT: GENERAL THEORY

The specific problem considered is that of a monochromatic electromagnetic beam within an infinite, nonabsorbing, dielectric medium incident upon a particle of arbitrarily-defined shape. The particle and the surrounding medium are homogeneous, linear, isotropic, and nonmagnetic ($\mu = 1$). The geometrical arrangement is shown in Fig. 1. The coordinate system origin is located within (and near the center) of the particle. The particle has an associated characteristic radius, $a$, and all spatial quantities are nondimensionalized (as indicated by a tilde) relative to this characteristic radius. Though the theoretical development is applicable for any incident beam for which a mathematical description is known, for the calculations presented in this paper, a focused, linearly-polarized, Gaussian-profiled (TEM$_{00}$ mode) beam will be assumed. A fifth-order corrected mathematical description of the electromagnetic field components for the Gaussian beam, as previously presented by Barton and Alexander,[30] is utilized for the analysis. All electromagnetic quantities are nondimensionalized relative to an electric field amplitude characteristic of the incident beam, $E_0$. For the Gaussian beam, $E_0$ is the electric field amplitude at the focal point, which can be related to the beam power by an expression given in Ref. 30.

The input parameters of the analysis are as follows: (1) the particle shape function, $\hat{r}(\theta, \phi)$ (A nondimensionalized single-valued function of the spherical coordinate angles that defines the surface of the particle. For a centered sphere, this function would equal to one.), (2) the particle size parameter, $\alpha = 2\pi a / \lambda_{ext}$ ($\lambda_{ext}$ is the wavelength within the surrounding medium.), (3) the complex relative refractive index of the particle, $\tilde{n} = \sqrt{\epsilon_{int}/\epsilon_{ext}}$, (4) the nondimensionalized beam focal point coordinates, $(\tilde{x}_0, \tilde{y}_0, \tilde{z}_0)$ (The location of the focal point of the incident beam relative to the particle.), (5) the nondimensionalized beam waist radius, $\tilde{w}_0$, (6) the beam propagation direction angle, $\theta_{bd}$ (The beam is assumed to propagate parallel to the x-z plane. $\theta_{bd}$ is the angle of beam propagation relative to the y-z plane.), and (7) the beam polarization orientation angle, $\phi_{bd}$ (For $\phi_{bd} = 0^o$, the beam electric field polarization is parallel to the x-z plane. For $\phi_{bd} = 90^o$, the beam electric field polarization is perpendicular to the x-z plane.).

The procedure for determining the electromagnetic fields for a beam incident upon a particle of arbitrarily-defined shape is a generalization of the beam incident upon a spherical particle development presented in Ref. 1. The electromagnetic field is divided into three parts: the incident field (the field that would exist in the absence of the particle), the scattered field (the difference

between the external particle field and the incident field), and the internal field (the field within the particle). The external field is the sum of the incident field (assumed known) and the scattered field: $\vec{E}^{ext} = \vec{E}^{(i)} + \vec{E}^{(s)}$ and $\vec{H}^{ext} = \vec{H}^{(i)} + \vec{H}^{(s)}$. The scattered field and the internal field are to be determined. The solution is formulated in spherical coordinates, $(r, \theta, \phi)$.

The theoretical approach used is a more mathematically rigorous variation of the point matching method,[6] and will be referred to as the boundary matching method. The electromagnetic field components of the unknown scattered and internal fields are expressed in terms of general series expansions over products of Riccati-Bessel functions $[\psi_l(kr), \chi_l(kr)]$ and spherical harmonic functions $[Y_{lm}(\theta, \phi)]$ as were derived in Ref. 1. For the particle of arbitrarily-defined shape, the forms of these series expansions for the scattered and internal fields are identical to those used for the analysis of the spherical particle, by way of the same reasoning. The $\xi_l^{(2)} = \psi_l + i\chi_l$ functions are excluded from the scattered field since, in the far-field, these functions represent incoming spherical waves and, in the far-field, the scattered field must consist of outgoing waves only. For the internal field, the $\chi_l$ functions are excluded since these functions are unbounded at the coordinate origin and the internal field must be finite everywhere within the particle, including the coordinate origin.

The coefficients of the scattered and internal field series expansions must be chosen to satisfy the boundary conditions (continuity of the tangential electromagnetic field components) at the surface of the particle. In the point matching method, the boundary conditions are imposed, not continuously over the particle surface, but at a finite number of distributed points. In the boundary matching method (used here), the boundary condition equations are expanded in spherical harmonics and matched for each angular mode. This results in a set of simultaneous algebraic equations from which the series coefficients can be determined.

Chew[31] has recently shown that the boundary matching method, as described here, is, in the end, formally equivalent to the commonly accepted extended boundary condition method. The boundary matching method would then be expected, similar to the extended boundary condition method, to exhibit an ill-conditioning of the series coefficient equations when attempting to analyze particles of appreciable elongation. (A set of linear algebraic equations is said to be ill-conditioned when a small error in the coefficient matrix will cause a large error in the solution vector.) However, the eventual ill-conditioning of the equations for the elongated object should not be interpreted as an indication of the lack of mathematical rigor for the boundary matching method (or the extended

boundary condition method), the procedure is mathematically rigorous, but not well-suited (from a computational viewpoint) for the analysis of elongated objects.

The boundary matching method procedure for the analysis of a beam incident upon a general arbitrarily-shaped particle is as follows. The electromagnetic field components of the unknown scattered and internal fields are expressed in the form of series expansions as were derived in Ref. 1 and as are given in nondimensional form (as used here) in Ref. 32. For the scattered field

$$
E_r^{(s)} = \frac{1}{\tilde{r}^2} \sum_{l=1}^{L} \sum_{m=-l}^{l} \left[ l(l+1) a_{lm} \, \xi_l^{(1)}(\alpha\tilde{r}) \, Y_{lm}(\theta,\phi) \right], \tag{1}
$$

$$
E_\theta^{(s)} = \frac{\alpha}{\tilde{r}} \sum_{l=1}^{L} \sum_{m=-l}^{l} \left[ a_{lm} \, \xi_l^{(1)\prime}(\alpha\tilde{r}) \frac{\partial Y_{lm}(\theta,\phi)}{\partial \theta} - \frac{m}{\sqrt{\epsilon_{ext}}} b_{lm} \, \xi_l^{(1)}(\alpha\tilde{r}) \frac{Y_{lm}(\theta,\phi)}{\sin\theta} \right], \tag{2}
$$

$$
E_\phi^{(s)} = \frac{\alpha}{\tilde{r}} \sum_{l=1}^{L} \sum_{m=-l}^{l} \left[ i \, m \, a_{lm} \, \xi_l^{(1)\prime}(\alpha\tilde{r}) \frac{Y_{lm}(\theta,\phi)}{\sin\theta} - \frac{i}{\sqrt{\epsilon_{ext}}} b_{lm} \, \xi_l^{(1)}(\alpha\tilde{r}) \frac{\partial Y_{lm}(\theta,\phi)}{\partial \theta} \right], \tag{3}
$$

$$
H_r^{(s)} = \frac{1}{\tilde{r}^2} \sum_{l=1}^{L} \sum_{m=-l}^{l} \left[ l(l+1) b_{lm} \, \xi_l^{(1)}(\alpha\tilde{r}) \, Y_{lm}(\theta,\phi) \right], \tag{4}
$$

$$
H_\theta^{(s)} = \frac{\alpha}{\tilde{r}} \sum_{l=1}^{L} \sum_{m=-l}^{l} \left[ b_{lm} \, \xi_l^{(1)\prime}(\alpha\tilde{r}) \frac{\partial Y_{lm}(\theta,\phi)}{\partial \theta} + m\sqrt{\epsilon_{ext}} a_{lm} \, \xi_l^{(1)}(\alpha\tilde{r}) \frac{Y_{lm}(\theta,\phi)}{\sin\theta} \right], \tag{5}
$$

and

$$
H_\phi^{(s)} = \frac{\alpha}{\tilde{r}} \sum_{l=1}^{L} \sum_{m=-l}^{l} \left[ i \, m \, b_{lm} \, \xi_l^{(1)\prime}(\alpha\tilde{r}) \frac{Y_{lm}(\theta,\phi)}{\sin\theta} + i\sqrt{\epsilon_{ext}} a_{lm} \, \xi_l^{(1)}(\alpha\tilde{r}) \frac{\partial Y_{lm}(\theta,\phi)}{\partial \theta} \right], \tag{6}
$$

and for the internal field

$$
E_r^{(w)} = \frac{1}{\tilde{r}^2} \sum_{l=1}^{L} \sum_{m=-l}^{l} \left[ l(l+1) c_{lm} \, \psi_l(\bar{n}\alpha\tilde{r}) \, Y_{lm}(\theta,\phi) \right], \tag{7}
$$

$$
E_\theta^{(w)} = \frac{\alpha}{\tilde{r}} \sum_{l=1}^{L} \sum_{m=-l}^{l} \left[ \bar{n} \, c_{lm} \, \psi_l'(\bar{n}\alpha\tilde{r}) \frac{\partial Y_{lm}(\theta,\phi)}{\partial \theta} - \frac{m}{\sqrt{\epsilon_{ext}}} d_{lm} \, \psi_l(\bar{n}\alpha\tilde{r}) \frac{Y_{lm}(\theta,\phi)}{\sin\theta} \right], \tag{8}
$$

$$
E_\phi^{(w)} = \frac{\alpha}{\tilde{r}} \sum_{l=1}^{L} \sum_{m=-l}^{l} \left[ i \, m \, \bar{n} \, c_{lm} \, \psi_l'(\bar{n}\alpha\tilde{r}) \frac{Y_{lm}(\theta,\phi)}{\sin\theta} - \frac{i}{\sqrt{\epsilon_{ext}}} d_{lm} \, \psi_l(\bar{n}\alpha\tilde{r}) \frac{\partial Y_{lm}(\theta,\phi)}{\partial \theta} \right], \tag{9}
$$

6

$$H_r^{(w)} = \frac{1}{\tilde{r}^2} \sum_{l=1}^{L} \sum_{m=-l}^{l} \left[ l(l+1) d_{lm} \, \psi_l(\bar{n}\alpha\tilde{r}) \, Y_{lm}(\theta,\phi) \right], \tag{10}$$

$$H_\theta^{(w)} = \frac{\alpha}{\tilde{r}} \sum_{l=1}^{L} \sum_{m=-l}^{l} \left[ \bar{n} \, d_{lm} \, \psi_l'(\bar{n}\alpha\tilde{r}) \frac{\partial Y_{lm}(\theta,\phi)}{\partial \theta} + m\sqrt{\epsilon_{ext}} \, \bar{n}^2 c_{lm} \, \psi_l(\bar{n}\alpha\tilde{r}) \frac{Y_{lm}(\theta,\phi)}{\sin\theta} \right], \tag{11}$$

and

$$H_\phi^{(w)} = \frac{\alpha}{\tilde{r}} \sum_{l=1}^{L} \sum_{m=-l}^{l} \left[ i\,m\,\bar{n}\,d_{lm}\,\psi_l'(\bar{n}\alpha\tilde{r}) \frac{Y_{lm}(\theta,\phi)}{\sin\theta} + i\sqrt{\epsilon_{ext}}\,\bar{n}^2 c_{lm}\,\psi_l(\bar{n}\alpha\tilde{r}) \frac{\partial Y_{lm}(\theta,\phi)}{\partial \theta} \right]. \tag{12}$$

In the above equations, $\xi_l^{(1)} = \psi_l - i\chi_l$, where $\psi_l, \chi_l$ are the Riccati-Bessel functions, and $Y_{lm}$ is the spherical harmonic function. L is the upper limit value of the radial index ($l$) necessary for series convergence. There are then

$$N = \sum_{l=1}^{L} (2l+1) \tag{13}$$

terms in each series expression. (N is the number of $lm$ combinations for a given value of L.)

The series coefficients of the scattered field, $a_{lm}, b_{lm}$, and the series coefficients of the internal field, $c_{lm}, d_{lm}$, must be determined so as to satisfy the condition of tangential electromagnetic field continuity at the particle surface. At $\tilde{r} = \hat{r}(\theta,\phi)$,

$$(\hat{n} \times \vec{E})^{ext} = (\hat{n} \times \vec{E})^{int} \tag{14}$$

and

$$(\hat{n} \times \vec{H})^{ext} = (\hat{n} \times \vec{H})^{int} \tag{15}$$

where $\hat{n}$ is a unit vector perpendicular to and outwardly directed from the particle surface. Considering tangential components in the polar angle ($\theta$) and azimuthal angle ($\phi$) directions, the boundary conditions of Eqs. (14) and (15) can be expressed as

$$(E_r \sin\hat{\theta} + E_\theta \cos\hat{\theta})^{ext} = (E_r \sin\hat{\theta} + E_\theta \cos\hat{\theta})^{int}, \tag{16}$$

7

$$[(E_r sin\theta + E_\theta cos\theta)sin\hat{\phi} + E_\phi cos\hat{\phi}]^{ext} = [(E_r sin\theta + E_\theta cos\theta)sin\hat{\phi} + E_\phi cos\hat{\phi}]^{int}, \qquad (17)$$

$$(H_r sin\hat{\theta} + H_\theta cos\hat{\theta})^{ext} = (H_r sin\hat{\theta} + H_\theta cos\hat{\theta})^{int}, \qquad (18)$$

and

$$[(H_r sin\theta + H_\theta cos\theta)sin\hat{\phi} + H_\phi cos\hat{\phi}]^{ext} = [(H_r sin\theta + H_\theta cos\theta)sin\hat{\phi} + H_\phi cos\hat{\phi}]^{int} \qquad (19)$$

where

$$\hat{\theta} = tan^{-1}\left(\frac{1}{\hat{r}}\frac{\partial \hat{r}}{\partial \theta}\right) \qquad (20)$$

and

$$\hat{\phi} = tan^{-1}\left(\frac{1}{\hat{r}sin^2\theta}\frac{\partial \hat{r}}{\partial \phi}\right) \qquad (21)$$

are angles related to the shape of the particle ($\hat{\theta}, \hat{\phi}$ are both zero for a centered sphere).

The electromagnetic field components of the scattered and internal fields given by Eqs. (1)-(12) are substituted into the boundary condition equations, Eqs. (16)-(19). Since these equations are evaluated at the surface of the particle where $\tilde{r} = \hat{r}(\theta, \phi)$, both sides of each of these equations are a function of $\theta, \phi$ only. In order to determine the series coefficients $a_{lm}, b_{lm}, c_{lm}, d_{lm}$ necessary to satisfy the boundary condition equations, Eqs. (16)-(19) are expanded in spherical harmonics ($Y_{l'm'}$), and the left and right-hand-sides of each equation are equated for each $l'm'$ mode. The result is a set of 4N linear, algebraic equations that can be solved for the 4N values of the series coefficients $a_{lm}, b_{lm}, c_{lm}, d_{lm}$:

$$\sum_{l=1}^{L}\sum_{m=-l}^{l}[-I^1_{lm,l'm'}a_{lm} + I^2_{lm,l'm'}b_{lm} + I^3_{lm,l'm'}c_{lm} - I^4_{lm,l'm'}d_{lm}] = A^1_{l'm'}, \qquad (22)$$

$$\sum_{l=1}^{L}\sum_{m=-l}^{l}[-I^5_{lm,l'm'}a_{lm} + I^6_{lm,l'm'}b_{lm} + I^7_{lm,l'm'}c_{lm} - I^8_{lm,l'm'}d_{lm}] = A^2_{l'm'}, \qquad (23)$$

8

$$\sum_{l=1}^{L}\sum_{m=-l}^{l}[-\epsilon_{ext}I_{lm,l'm'}^{2}a_{lm} - I_{lm,l'm'}^{1}b_{lm} + \bar{n}^{2}\epsilon_{ext}I_{lm,l'm'}^{4}c_{lm} + I_{lm,l'm'}^{3}d_{lm}] = B_{l'm'}^{1}, \qquad (24)$$

and

$$\sum_{l=1}^{L}\sum_{m=-l}^{l}[-\epsilon_{ext}I_{lm,l'm'}^{6}a_{lm} - I_{lm,l'm'}^{5}b_{lm} + \bar{n}^{2}\epsilon_{ext}I_{lm,l'm'}^{8}c_{lm} + I_{lm,l'm'}^{7}d_{lm}] = B_{l'm'}^{2} \qquad (25)$$

for each $l'm'$ combination.

In Eqs. (22)-(25),

$$I_{lm,l'm'}^{1} = \int_{0}^{2\pi}\int_{0}^{\pi}[\frac{sin\hat{\theta}}{\hat{r}^{2}}l(l+1)\xi_{l}^{(1)}(\alpha\hat{r})P_{lm}(\theta) + \frac{\alpha cos\hat{\theta}}{\hat{r}}\xi_{l}^{(1)\prime}(\alpha\hat{r})\frac{\partial P_{lm}}{\partial\theta}]e^{im\phi}P_{l'm'}(\theta)e^{-im'\phi}sin\hat{\nu}\hat{v}d\theta d\phi, \qquad (26)$$

$$I_{lm,l'm'}^{2} = \int_{0}^{2\pi}\int_{0}^{\pi}[\frac{\alpha cos\hat{\theta}}{\hat{r}}\frac{m}{\sqrt{\epsilon_{ext}}}\xi_{l}^{(1)}(\alpha\hat{r})\frac{P_{lm}(\theta)}{sin\theta}]e^{im\phi}P_{l'm'}(\theta)e^{-im'\phi}sin\theta d\theta d\phi, \qquad (27)$$

$$I_{lm,l'm'}^{3} = \int_{0}^{2\pi}\int_{0}^{\pi}[\frac{sin\hat{\theta}}{\hat{r}^{2}}l(l+1)\psi_{l}(\bar{n}\alpha\hat{r})P_{im}(\theta) + \frac{\alpha cos\hat{\theta}}{\hat{r}}\bar{n}\psi_{l}'(\bar{n}\alpha\hat{r})\frac{\partial P_{lm}}{\partial\theta}]e^{im\phi}P_{l'm'}(\theta)e^{-im'\phi}sin\theta d\theta d\phi, \qquad (28)$$

$$I_{lm,l'm'}^{4} = \int_{0}^{2\pi}\int_{0}^{\pi}[\frac{\alpha cos\hat{\theta}}{\hat{r}}\frac{m}{\sqrt{\epsilon_{ext}}}\psi_{l}(\bar{n}\alpha\hat{r})\frac{P_{lm}(\theta)}{sin\theta}]e^{im\phi}P_{l'm'}(\theta)e^{-im'\phi}sin\theta d\theta d\phi, \qquad (29)$$

$$I_{lm,l'm'}^{5} = \int_{0}^{2\pi}\int_{0}^{\pi}[\frac{sin\hat{\theta}sin\hat{\phi}}{\hat{r}^{2}}l(l+1)\xi_{l}^{(1)}(\alpha\hat{r})P_{lm}(\theta) + \frac{\alpha cos\hat{\theta}sin\hat{\phi}}{\hat{r}}\xi_{l}^{(1)\prime}(\alpha\hat{r})\frac{\partial P_{lm}}{\partial\theta}$$
$$+ \frac{\alpha cos\hat{\phi}}{\hat{r}}im\xi_{l}^{(1)\prime}(\alpha\hat{r})\frac{P_{lm}(\theta)}{sin\theta}]e^{im\phi}P_{l'm'}(\theta)e^{-im'\phi}sin\theta d\theta d\phi, \qquad (30)$$

$$I_{lm,l'm'}^{6} = \int_{0}^{2\pi}\int_{0}^{\pi}[\frac{\alpha cos\hat{\theta}sin\hat{\phi}}{\hat{r}}\frac{m}{\sqrt{\epsilon_{ext}}}\xi_{l}^{(1)\prime}(\alpha\hat{r})\frac{P_{lm}(\theta)}{sin\theta}$$
$$+ \frac{\alpha cos\hat{\phi}}{\hat{r}}\frac{i}{\sqrt{\epsilon_{ext}}}\xi_{l}^{(1)}(\alpha\hat{r})\frac{\partial P_{lm}}{\partial\theta}]e^{im\phi}P_{l'm'}(\theta)e^{-im'\phi}sin\theta d\theta d\phi, \qquad (31)$$

9

$$I^7_{lm,l'm'} = \int_0^{2\pi} \int_0^\pi \left[ \frac{\sin\theta\sin\hat\phi}{\hat r^2} l(l+1)\psi_l(\bar n\alpha\hat r)P_{lm}(\theta) + \frac{\alpha\cos\hat\theta\sin\hat\phi}{\hat r}\bar n\psi'_l(\bar n\alpha\hat r)\frac{\partial P_{lm}}{\partial\theta} \right.$$
$$\left. + \frac{\alpha\cos\hat\phi}{\hat r}im\bar n\psi'_l(\bar n\alpha\hat r)\frac{P_{lm}(\theta)}{\sin\theta} \right] e^{im\phi}P_{l'm'}(\theta)e^{-im'\phi}\sin\theta\,d\theta\,d\phi, \tag{32}$$

and

$$I^8_{lm,l'm'} = \int_0^{2\pi} \int_0^\pi \left[ \frac{\alpha\cos\hat\theta\sin\hat\phi}{\hat r}\frac{m}{\sqrt{\epsilon_{ext}}}\psi_l(\bar n\alpha\hat r)\frac{P_{lm}(\theta)}{\sin\theta} \right.$$
$$\left. + \frac{\alpha\cos\hat\phi}{\hat r}\frac{i}{\sqrt{\epsilon_{ext}}}\psi_l(\bar n\alpha\hat r)\frac{\partial P_{lm}}{\partial\theta} \right] e^{im\phi}P_{l'm'}(\theta)e^{-im'\phi}\sin\theta\,d\theta\,d\phi, \tag{33}$$

and

$$A^1_{l'm'} = \int_0^{2\pi} \int_0^\pi [E_r^{(i)}(\hat r,\theta,\phi)\sin\hat\theta + E_\theta^{(i)}(\hat r,\theta,\phi)\cos\hat\theta]P_{l'm'}(\theta)e^{-im'\phi}\sin\theta\,d\theta\,d\phi, \tag{34}$$

$$A^2_{l'm'} = \int_0^{2\pi} \int_0^\pi \left\{ [E_r^{(i)}(\hat r,\theta,\phi)\sin\hat\theta + E_\theta^{(i)}(\hat r,\theta,\phi)\cos\hat\theta]\sin\hat\phi \right.$$
$$\left. + E_\phi^{(i)}(\hat r,\theta,\phi)\cos\hat\phi \right\} P_{l'm'}(\theta)e^{-im'\phi}\sin\theta\,d\theta\,d\phi, \tag{35}$$

$$B^1_{l'm'} = \int_0^{2\pi} \int_0^\pi [H_r^{(i)}(\hat r,\theta,\phi)\sin\hat\theta + H_\theta^{(i)}(\hat r,\theta,\phi)\cos\hat\theta]P_{l'm'}(\theta)e^{-im'\phi}\sin\theta\,d\theta\,d\phi, \tag{36}$$

and

$$B^2_{l'm'} = \int_0^{2\pi} \int_0^\pi \left\{ [H_r^{(i)}(\hat r,\theta,\phi)\sin\hat\theta + H_\theta^{(i)}(\hat r,\theta,\phi)\cos\hat\theta]\sin\hat\phi \right.$$
$$\left. + H_\phi^{(i)}(\hat r,\theta,\phi)\cos\hat\phi \right\} P_{l'm'}(\theta)e^{-im'\phi}\sin\theta\,d\theta\,d\phi. \tag{37}$$

The $I_{lm,l'm'}$ surface integrals of Eqs. (26)-(33) are dependent solely upon the shape of the particle, $\hat r(\theta,\phi)$. The $A_{l'm'}$, $B_{l'm'}$ terms of Eqs. (34)-(37) incorporate both the shape of the particle and the nature of the incident field.

In summary, the procedure for determining the internal and external electromagnetic fields for a beam incident upon a particle of general arbitrarily-defined shape is as follows. For a given

set of input parameters $\hat{r}(\theta, \phi)$, $\alpha$, $\bar{n}$, $(\bar{x}_0, \bar{y}_0, \bar{z}_0)$, $\bar{w}_0$, $\theta_{bd}$, and $\phi_{bd}$, the $I_{lml'm'}$ and $A_{l'm'}$, $B_{l'm'}$ surface integrals of Eqs. (26)-(33) and Eqs. (34)-(37), respectively, are determined by numerical integration. The set of $4N$ linear algebraic equations of Eqs. (22)-(25) is then solved for the $4N$ values of the series coefficients $a_{lm}, b_{lm}, c_{lm}, d_{lm}$. The scattered field component equations, Eqs. (1)-(6), with the now known associated scattered field series coefficients, $a_{lm}, b_{lm}$, can then be used to determine the scattered field for any spatial position outside the particle, $\bar{r} > \hat{r}(\theta, \phi)$. The external field is the sum of the scattered field and the known incident field. The internal field component equations, Eqs. (7)-(12), with the now known internal field series coefficients, $c_{lm}, d_{lm}$, can be used to determine the internal field for any spatial position within the particle, $\bar{r} < \hat{r}(\theta, \phi)$.

As defined earlier, L is the maximum value of the radial index $(l)$ necessary for convergence of the series expressions for the electromagnetic field components given in Eqs. (1)-(12). Ideally, for a particular problem, the value of L could be successively increased until the electromagnetic field solution no longer changes significantly, and any desired degree of accuracy could be obtained. In practice, such solution convergence has been found for near-spherical geometries. For elongated geometries, however, the set of algebraic equations used to solve for the series coefficients may become increasingly ill-conditioned with increasing L and the set of algebraic equations may become unsolvable (from a computational viewpoint) before overall solution convergence occurs and, at best, only an approximate solution can be determined. Convergence and applicability of the procedure will be more fully discussed in Sec. V.

## III. THEORETICAL DEVELOPMENT: AXISYMMETRIC THEORY

The development of Sec. II. was for the general case where $\hat{r}(\theta,\phi)$. If the particle is axisymmetric and is centered about the z axis such that $\hat{r}(\theta)$ only (no $\phi$ dependence), then major simplifications in the solution procedure can be attained. If $\hat{r}$ is independent of $\phi$, then the $I_{lml'm'}$ surface integrals of Eqs. (26)-(33) are zero for $m' \neq m$. In addition, the azimuthal integrations can be performed explicitly so the surface integrals of Eqs. (26)-(39) can be reduced to line integrals:

$$I_{lml'}^{1} = 2\pi \int_{0}^{\pi} \left[ \frac{sin\theta}{\hat{r}^2}l(l+1)\xi_l^{(1)}(\alpha\hat{r})P_{lm}(\theta) + \frac{\alpha cos\theta}{\hat{r}}\xi_l^{(1)'}(\alpha\hat{r})\frac{\partial P_{lm}}{\partial\theta} \right]P_{l'm}(\theta)sin\theta d\theta, \tag{38}$$

$$I_{lml'}^{2} = 2\pi \int_{0}^{\pi} \left[ \frac{\alpha cos\theta}{\hat{r}} \frac{m}{\sqrt{\epsilon_{ext}}}\xi_l^{(1)}(\alpha\hat{r})P_{lm}(\theta) \right]P_{l'm}(\theta)d\theta, \tag{39}$$

$$I_{lml'}^{3} = 2\pi \int_{0}^{\pi} \left[ \frac{sin\theta}{\hat{r}^2}l(l+1)\psi_l(\bar{n}\alpha\hat{r})P_{lm}(\theta) + \frac{\alpha cos\theta}{\hat{r}}\bar{n}\psi_l'(\bar{n}\alpha\hat{r})\frac{\partial P_{lm}}{\partial\theta} \right]P_{l'm}(\theta)sin\theta d\theta, \tag{40}$$

$$I_{lml'}^{4} = 2\pi \int_{0}^{\pi} \left[ \frac{\alpha cos\theta}{\hat{r}} \frac{m}{\sqrt{\epsilon_{ext}}}\psi_l(\bar{n}\alpha\hat{r})P_{lm}(\theta) \right]P_{l'm}(\theta)d\theta, \tag{41}$$

$$I_{lml'}^{5} = 2\pi \int_{0}^{\pi} \left[ \frac{\alpha}{\hat{r}}im\xi_l^{(1)'}(\alpha\hat{r})P_{lm}(\theta) \right]P_{l'm}(\theta)d\theta, \tag{42}$$

$$I_{lml'}^{6} = 2\pi \int_{0}^{\pi} \left[ \frac{\alpha}{\hat{r}} \frac{i}{\sqrt{\epsilon_{ext}}}\xi_l^{(1)}(\alpha\hat{r})\frac{\partial P_{lm}}{\partial\theta} \right]P_{l'm}(\theta)sin\theta d\theta, \tag{43}$$

$$I_{lml'}^{7} = 2\pi \int_{0}^{\pi} \left[ \frac{\alpha}{\hat{r}}im\bar{n}\psi_l'(\bar{n}\alpha\hat{r})P_{lm}(\theta) \right]P_{l'm}(\theta)d\theta, \tag{44}$$

and

$$I_{lml'}^{8} = 2\pi \int_{0}^{\pi} \left[ \frac{\alpha}{\hat{r}} \frac{i}{\sqrt{\epsilon_{ext}}}\psi_l(\bar{n}\alpha\hat{r})\frac{\partial P_{lm}}{\partial\theta} \right]P_{l'm}(\theta)sin\theta d\theta. \tag{45}$$

Also, for the axisymmetric case, the 4N simultaneous equations of Eqs. (22)-(25) can be divided into subsets of linearly independent equations for each value of the angular index, $m$. For a given value of $m(\neq 0)$, Eqs. (22)-(25) become

$$\sum_{l=|m|}^{L} [-I_{lml'}^1 a_{lm} + I_{lml'}^2 b_{lm} + I_{lml'}^3 c_{lm} - I_{lml'}^4 d_{lm}] = A_{l'm}^1, \tag{46}$$

$$\sum_{l=|m|}^{L} [-I_{lml'}^5 a_{lm} + I_{lml'}^6 b_{lm} + I_{lml'}^7 c_{lm} - I_{lml'}^8 d_{lm}] = A_{l'm}^2, \tag{47}$$

$$\sum_{l=|m|}^{L} [-\epsilon_{ext} I_{lml'}^2 a_{lm} - I_{lml'}^1 b_{lm} + \bar{n}^2 \epsilon_{ext} I_{lml'}^4 c_{lm} + I_{lml'}^3 d_{lm}] = B_{l'm}^1, \tag{49}$$

and

$$\sum_{l=|m|}^{L} [-\epsilon_{ext} I_{lml'}^6 a_{lm} - I_{lml'}^5 b_{lm} + \bar{n}^2 \epsilon_{ext} I_{lml'}^8 c_{lm} + I_{lml'}^7 d_{lm}] = B_{l'm}^2 \tag{50}$$

for each $l' = |m|$ to L.

For each $m(\neq 0)$, Eqs. (46)-(50) then provide $4(L - |m| + 1)$ linear algebraic equations to solve for the $4(L - |m| + 1)$ values of $a_{lm}, b_{lm}, c_{lm}, d_{lm}$ [for a given $m(\neq 0)$].

Since $I_{lml'}^2, I_{lml'}^1, I_{lml'}^5, I_{lml'}^7$ are zero for m = 0, the solution of the $a_{l0}, b_{l0}, c_{l0}, d_{l0}$ terms must be handled separately. If m = 0 then Eqs. (22)-(25) become

$$\sum_{l=1}^{L} [-I_{l0l'}^1 a_{l0} + I_{l0l'}^3 c_{l0}] = A_{l'0}^1, \tag{51}$$

$$\sum_{l=1}^{L} [+I_{l0l'}^6 b_{l0} - I_{l0l'}^8 d_{l0}] = A_{l'0}^2. \tag{52}$$

$$\sum_{l=1}^{L} [-I_{l0l'}^1 b_{l0} + I_{l0l'}^3 d_{l0}] = B_{l'0}^1, \tag{53}$$

and

$$\sum_{l=1}^{L} [-\epsilon_{ext} I_{l0l'}^6 a_{l0} + \epsilon_{ext} \bar{n}^2 I_{l0l'}^8 c_{l0}] = B_{l'0}^2 \tag{54}$$

for each $l' = 1$ to L.

Eqs. (51) and (54) thus provide 2L linear, algebraic equations to solve for the 2L values of $a_{l0}, c_{l0}$ and Eqs. (52) and (53) provide 2L linear, algebraic equations to solve for the 2L values of $b_{l0}, d_{l0}$.

13

In summary, the procedure for determining the internal and external electromagnetic fields for a beam incident upon an axisymmetric particle is as follows. For a given set of input parameters, $\hat{r}(\theta)$, $\alpha$, $n$, $(\bar{x}_0, \bar{y}_0, \bar{z}_0)$, $\bar{w}_0$, $\theta_{bd}$, and $\phi_{bd}$, the $I_{lml'}$ line integrals of Eqs. (38)-(45) and the $A_{l'm'}$, $B_{l'm'}$ surface integrals of Eqs. (34)-(37) are determined by numerical integration. The linear algebraic equations of Eqs. (46)-(54) are then solved for the scattered field and internal field series coefficients, $a_{lm}, b_{lm}, c_{lm}, d_{lm}$. Once the series coefficients are known, Eqs. (1)-(12) can be used to determine the electromagnetic field for any spatial position inside or outside the particle.

## IV. VERIFICATION CALCULATIONS

The theoretical developments of Secs. II. and III. were verified by making direct comparisons with known solutions. Electromagnetic field calculations for a focused beam incident upon a centered sphere $[\hat{r}(\theta, \phi) = 1]$ using the general theory of Sec. II. and the axisymmetric theory of Sec. III. were found to be in agreement with corresponding electromagnetic field calculations using the spherical particle/arbitrary beam theory of Ref. 1.

For a more thorough confirmation, calculations were performed for a spherical particle displaced from the origin. Calculations of far-field scattering of a displaced sphere have previously been used by Barber and Yeh[16] for confirmation of their extended boundary condition method and by Johnson[28] for confirmation of his invariant imbedding T matrix method. If the sphere is displaced along the z-axis, then the particle shape function is a function of the polar angle, $\hat{r}(\theta)$, and, from a mathematical viewpoint, the particle appears nonspherical. For the sphere displaced along the z-axis, the axisymmetric theory of Sec. III. can be used to determine the electromagnetic field distributions. However, if plane wave illumination is assumed, the electromagnetic field distribution should be identical to that of plane wave Lorenz-Mie theory.

As an example, Fig. 2 presents a plot of the normalized source function ($S = |\vec{E}|^2/E_0^2$) distribution in the x-z plane for a $30°$ angle of incidence plane wave incident upon a centered sphere of $\alpha = 8.0$ and $n = 1.2 + 0.02i$. Figure 2 is the Lorenz-Mie theory solution rotated $30°$ about the origin in the x-z plane in order to account for the angle of incidence of the plane wave. Figure 3 was generated using the axisymmetric theory of Sec. III. for identical conditions as Fig. 2, except that the sphere has been displaced along the z-axis by a distance of $\Delta \tilde{z} = +0.25$. A comparison of Figs. 2 and 3 shows that the normalized source function distribution of the displaced sphere (Fig. 3) calculated using the axisymmetric theory of Sec. III. is identical to the normalized source function distribution of the centered sphere (Fig. 2) calculated using Lorenz-Mie theory, except that the entire solution of Fig. 3 (both internal and near-field) has been shifted along the z-axis by a distance of $\Delta \tilde{z} = 0.25$, as would be expected. (A more detailed comparison of the electromagnetic field vectors ($\vec{E}, \vec{H}$) at corresponding points also demonstrated identical agreement.)

A similar approach was used to confirm the general theory of Sec. II., except the sphere is now displaced along the x-axis so that the particle shape function is a function of both the polar and azimuthal angles, $\hat{r}(\theta, \phi)$. Figure 4 shows the normalized source function distribution for a $30°$

15

angle of incidence plane wave incident upon a centered sphere of $\alpha = 2.0$ and $\bar{n} = 1.2 + 0.02i$ as determined using Lorenz-Mie theory. Figure 5 provides the normalized source function distribution calculated using the general theory of Sec. II. for conditions identical to those of Fig. 4, except that the sphere has been displaced along the x-axis by a distance of $\Delta\tilde{x} = 0.1$. A comparison of Figs. 4 and 5 shows that the normalized source function distribution of Fig. 5 is identical to that of Fig. 4, except that the entire solution has been shifted along the x-axis by a distance of $\Delta\tilde{x}$ = +0.1, as would be expected. (Again, a more detailed comparison of the electromagnetic field vectors ($\vec{E}, \vec{H}$) at corresponding points also demonstrated identical agreement.)

Another confirmation could be obtained by making comparisons with existing nonspherical, regular geometry solutions. No results exist in the literature for internal and near-field electromagnetic field distributions other than for the centered sphere. However, comparable far-field scattering data are available. Oguchi[6] used a spheroidal function expansion solution for the plane wave incident upon an oblate spheroid problem to provide a verification of his point matching method procedure. In Ref. 6, the spheroidal function expansion solution was applied to determine the forward and backward far-field scattering for a plane wave incident upon an oblate spheroid. The plane wave was directed perpendicular to the axis of rotation of the oblate spheroid and both "horizontal" (electric field perpendicular to the axis of rotation) and "vertical" (electric field parallel to the axis of rotation) incident polarizations were considered. Oguchi presented his results in terms of a vector scattering function which, in a form consistent with the development of this paper, would be defined as

$$\vec{f}(\theta,\phi) = \lim_{r \Rightarrow \infty} \frac{r\vec{E}^{(s)}(\tilde{r},\theta,\phi)}{e^{i\alpha\tilde{r}}}. \tag{55}$$

Calculations were performed using parameters consistent with those used to generate the results of Tables 4 and 5 in Ref. 6. The incident wavelength is $\lambda_{ext} = 8.612$ mm (34.8 GHz) and the particle material has a complex relative index of refraction of $\bar{n} = 5.048 + 2.794i$ (water). A plane wave ($\tilde{w}_0 \Rightarrow \infty$) with a propagation direction angle of $\theta_{bd} = 90°$ was assumed. The forward scattered field is thus evaluated at $\theta = \pi/2, \phi = 0$ and the backward scattered field is evaluated at $\theta = \pi/2, \phi = \pi$. For "horizontal" polarization the polarization direction angle is $\phi_{bd} = 90°$ and for "vertical" polarization the polarization direction angle is $\phi_{bd} = 0°$. Calculations were performed for ten different major semiaxis and major to minor axis ratio combinations as given in Tables I.

and II. The results of the axisymmetric theory of Sec. III. and the results of the spheroidal function expansion solution as presented by Oguchi[6] are shown side-by-side for comparison. (In order to obtain consistency between the two developments, the complex conjugate of Oguchi's results are presented since, in his work, a $e^{+i\omega t}$ time dependency was assumed as opposed to a $e^{-i\omega t}$ time dependency used here.)

The "horizontal" polarization results are given in Table I. and the "vertical" polarization results are given in Table II. For the axisymmetric theory of Sec. III., four digit convergence was obtained for both the real and imaginary parts for all data presented. As can be seen in Tables I. and II., the results of the axisymmetric theory of Sec. III. and the results of the spheroidal function expansion solution of Oguchi are in agreement within an average deviation of approximately 1 part in 1000. The slight difference in the two results might be explained by the fact that Oguchi truncated his spheroidal function expansion solution at a radial index of 9, which may not be a sufficiently high value, especially for the larger size parameters.

17

## V. CONVERGENCE AND APPLICABILITY

In Sec. II., L was defined as the maximum value of the radial series index ($l$) necessary for series convergence. Ideally, for a particular problem, the value of L could be successively increased until the solution no longer changes significantly. Such convergence has been found for near-spherical particles. However, as particles of increasing elongation are considered, convergence becomes slower, and a greater number of terms are required to obtain a given degree of accuracy. For extremely elongated particles, the simultaneous algebraic equations used for the solution of the series coefficients may become increasingly ill-conditioned as L is incremented, thus making the accurate numerical solution of these equations increasingly difficult. For extremely elongated particles, the series coefficient equations may become so ill-conditioned as to be unsolvable (from a computational viewpoint) before overall solution convergence has been attained. Similar solution difficulties have been observed when applying the extended boundary condition method to severely nonspherical particles.[31,33] Note that when L is increased, not only are additional terms added to the series evaluation of the electromagnetic field components [Eqs. (1)-(12)], but, since the series coefficients are determined by the solution of simultaneous equations, the values of all the lower order series coefficients can be affected as well.

The boundary matching method used for the solution of the beam incident upon an arbitrarily-shaped particle problem is apparently best-suited for the analysis of near-spherical particles. In order to assure accuracy for any particular problem, it is necessary to verify solution convergence for the value of L chosen. A single parameter associated with solution convergence was defined. From experience, it was found that the normal electromagnetic field continuity conditions at the surface of the particle provide a sensitive solution convergence criteria. The solution procedure imposes a matching of the internal and external tangential electromagnetic field components across the surface of the particle through Eqs. (16)-(19). In addition to these tangential continuity conditions, the internal and external normal electromagnetic field components at the surface of the particle should be related by

$$E_n^{ext} = \bar{n}^2 E_n^{int} \tag{56}$$

and

$$H_n^{ext} = H_n^{int}. \tag{57}$$

The solid-angle-averaged-value of $[|E_n^{ext} - \bar{n}^2 E_n^{int}| + |H_n^{ext} - H_n^{int}|]/2$ over the surface of the particle,

$$D_n = \int_0^{2\pi} \int_0^{\pi} \left[ \frac{|E_n^{ext} - \bar{n}^2 E_n^{int}| + |H_n^{ext} - H_n^{int}|}{2} \right] sin\theta d\theta d\phi, \tag{58}$$

was defined as an empirical convergence criteria. The smaller the value of the average deviation of the normal electromagnetic field components, $D_n$, the more closely the boundary conditions at the surface of the particle are being matched and the more accurate the solution.

As a demonstration of the effect of particle shape and size on convergence, a set of calculations were performed for a $30°$ angle of incidence plane wave incident upon equal volume prolate spheroids of varying axis ratios (elongation) and two different size parameters. An index of refraction of $\bar{n} = 1.33 + 0.00i$ was assumed. Figure 6 gives the average deviation of the normal electromagnetic field components ($D_n$) as a function of axis ratio (a/b) and L for equal volume prolate spheroids with $\alpha_{sphere} = 4.0$. As shown in Fig. 6, for a sphere (a/b = 1.0), $D_n$ decreases rapidly with increasing L. The solution for elongated particles with a/b = 1.1, 1.2, and 1.3 converge, with increasing values of L, successively more slowly with increasing elongation. To obtain a value of $D_n$ less than 0.001 requires L=10 for a/b=1.1, L=14 for a/b=1.2, and L=20 for a/b=1.3. For a/b=1.4, $D_n$ gradually decreases as L is increased from 6 to 20 but then increases to a localized peak at L=24. Beyond the peak at L=24, $D_n$ for a/b=1.4 decreases rapidly with increasing L from L=26 to 34. (The eventual ill-conditioning of the equations prevented accurate solutions for L greater than 34.) For a/b=1.5, $D_n$ gradually decreases from L=6 to 12 and then increases to form a localized peak at L=20 before decreasing with increasing L from L=22 to 32 before apparently rising towards a second peak at L=34. The presence of the localized peaks in the a/b=1.4 and a/b=1.5 curves (and at the end of the a/b=1.3 curve) are an indication that solution convergence is not necessarily monotonic and care is necessary to ensure that a fully converged solution has been attained. L should be increased beyond the last of any significant peaks in $D_n$. For $\alpha_{sphere} = 4.0$ and a/b=1.5, an L value much greater than 34 is needed to obtain an accurate solution.

Figure 7 shows convergence calculations for the same arrangement as Fig. 6, but for a larger equal volume sphere size parameter of $\alpha_{sphere} = 8.0$. The general features of Figs. 6 and 7 are

19

similar. Larger size parameters require a larger value of L to obtain the same degree of convergence and the curves of Fig. 7 are roughly shifted to the right by an increment of $\Delta L=6$ in comparison with the corresponding curves of Fig. 6. In Fig. 7, the localized peak in the a/b=1.4 curve occurs at L=32 and the peak in the a/b=1.5 curve occurs at L=26. The peak in the a/b=1.3 curve has apparently shifted off the graph to an L value greater than 34. For $\alpha_{sphere} = 8.0$ and a/b=1.4 and a/b=1.5, L values much greater than 34 are needed to obtain an accurate solution.

## VI. TIGHTLY-FOCUSED BEAM ON AN OBLATE SPHEROID

In order to demonstrate the ability to determine the electromagnetic fields for a focused beam incident upon a nonspherical particle, calculations were performed for a tightly-focused beam incident upon an oblate spheroid of axis ratio a/b = 1.2, $\alpha = 15.0$, and $\bar{n} = 1.3 + 0.01i$. For the oblate spheroid, the major semiaxis (a) is used as the characteristic radius (a). The angle of incidence ($\theta_{bd}$) was held at $0°$ and the incident electric field polarization was in the x-z plane ($\phi_{bd} = 0°$). Figure 8 shows the internal normalized source function distribution in the x-z plane for an incident plane wave ($\tilde{w}_0 \Rightarrow \infty$). Only the internal field distribution is presented (the near-field values were artificially set to zero) so as to clearly show the nonspherical shape of the particle.

Figure 9 is for the same conditions as Fig. 8, but instead of plane wave incidence, a beam ($\tilde{w}_0 = 0.667$) is focused at the center of the particle ($\tilde{x}_0 = \tilde{y}_0 = \tilde{z}_0 = 0.0$). The normalized source function distribution for beam illumination is distinctly different than that for plane wave illumination, as can be seen by comparing Figs. 8 and 9. Figure 10 is for the same incident beam conditions as Fig. 9, except that the focal point of the beam has been moved up the x-axis to a position halfway along the major axis of the oblate spheroid ($\tilde{x}_0 = 0.5$, $\tilde{y}_0 = \tilde{z}_0 = 0.0$). Figure 11 shows the normalized source function distribution with the beam focused at the edge of the particle ($\tilde{x}_0 = 1.0$, $\tilde{y}_0 = \tilde{z}_0 = 0.0$).

## VII. EFFECTS OF SURFACE DEFORMATION AT RESONANCE

The beam incident upon an arbitrarily-shaped particle theory permits electromagnetic field determinations for particles of irregular geometry. As an example of an application, the axisymmetric theory of Sec. III. was used to investigate the effect of a surface deformation on resonance excitation within an otherwise spherical particle. (The effect of focal point positioning on resonance excitation was investigated in Ref. 34.) The particle is assumed spherical except for an axisymmetric surface deformation located within the polar angle interval $\pi/8 < \theta < 3\pi/8$:

$$\hat{r}(\theta) = \begin{cases} 1 \text{ for } \theta < \pi/8 \\ 1 + \epsilon/2 \big( 1 + cos[8(\theta - \pi/8) - \pi] \big) \text{ for } \pi/8 < \theta < 3\pi/8 \\ 1 \text{ for } \theta > 3\pi/8 \end{cases} \quad (59)$$

The height of the deformation, $\epsilon$, can be either positive (protrusion), negative (depression), or zero (perfect sphere). Plane wave illumination with a $0°$ angle of incidence is assumed which provides a degenerate condition such that all series coefficients except $m = \pm 1$ are identically zero. In addition, the $m = \pm 1$ terms can be combined so that the double summation electromagnetic field component expressions of Eqs. (1)-(12) reduce to single summation expressions over the radial index,

$$\sum_{l=1}^{L}, \quad (60)$$

with the associated single index series coefficients: $a_l, b_l, c_l, d_l$.

Assuming an index of refraction of $\bar{n} = 1.334 + 1.2 \times 10^{-9}i$ (0.5145 $\mu$m wavelength argon-ion laser incident upon water),[35] a spherical particle resonance was located. The resonance chosen was the 34th mode, 1st order magnetic wave (TE mode) resonance which occurs at $\alpha = 29.285$. At this size parameter, the magnitude of the 34th radial index magnetic wave internal field series coefficient ($|d_{34}|$) attains a peak value, as shown in Fig. 12.

The effect of a surface deformation on the excitation of this resonance was investigated by determining $|d_{34}|$ as a function of $\epsilon$ and $\alpha$. In Fig. 13, $|d_{34}|$ is plotted versus size parameter for $\epsilon =$

22

0.00, $\pm 0.01$, and $\pm 0.02$, and in Fig. 14, $|d_{34}|$ is plotted versus size parameter for $\epsilon = 0.00$ and $\pm 0.05$. As can be seen in Figs. 13 and 14, the presence of the surface deformation shifts the resonance to smaller size parameters for protrusions ($\epsilon > 0$) and to larger size parameters for depressions ($\epsilon < 0$). Surface deformations also decrease t! $_{\epsilon}$ quality of the resonance with protrusions ($\epsilon > 0$) having a greater effect than depressions ($\epsilon < 0$) (for these particular conditions).

For small deformations, $|\epsilon| < 0.02$, resonance is apparently retained when the circumference of the deformed particle matches the circumference of the corresponding resonant spherical particle. This observation is illustrated by the results presented in Table III.

## VII. CONCLUSION

A theoretical procedure, utilizing the boundary matching method, has been developed for the determination of the internal and external electromagnetic fields for a monochromatic beam incident upon a homogeneous particle of arbitrarily-defined shape. The procedure is apparently best-suited for the analysis of near-spherical particles and, for example, could be used to analyze laser beams interactions with liquid droplets that have been slightly distorted in shape due to aerodynamic, thermal, or electromagnetic stresses.

## ACKNOWLEDGEMENT

# REFERENCES

1. J.P. Barton, D.R. Alexander, and S.A. Schaub, J. Appl. Phys. **64**, 1632 (1988).

2. G. Mie, Ann. Phys. **25**, 377 (1908).

3. Lord Rayleigh, Philos. Mag. **36**, 365 (1918).

4. J.R. Wait, Can. J. Phys. **33**, 189 (1955).

5. C. Yeh, J. Opt. Soc. Am. **55**, 309 (1965).

6. T. Oguchi, Radio Sci. **8**, 31 (1973).

7. S. Asano and G. Yamamoto, Appl. Opt. **14**, 29 (1975).

8. C. Yeh, Phys. Rev. **135**, A1193 (1964).

9. C. Yeh, J. Math. Phys. **6**, 2008 (1965).

10. V.A. Erma, Phys. Rev. **173**, 1243 (1968).

11. V.A. Erma, Phys. Rev **176**, 1544 (1968).

12. V.A. Erma, Phys. Rev. **179**, 1238 (1969).

13. R. Schiffer, J. Opt. Soc. Am. A **6**, 385 (1989).

14. R. Schiffer, Appl. Opt. **29**, 1536 (1990).

15. P.C. Waterman, Proc. of IEEE **53**, 805 (1965).

16. P. Barber and C. Yeh, Appl. Opt. **14**, 2864 (1975).

17. M.F. Iskander, A. Lakhtakiz, and C.H. Durney, IEEE Trans. Ant. and Prop. **AP-13**, 317 (1983).

18. M.F. Iskander and A. Lakhtakia, Appl. Opt. **23**, 948 (1984).

19. E.M. Purcell and C.R. Pennypacker, Astrophys. J. **186**, 705 (1973).

20. S.D. Druger, M. Kerker, D.-S. Wang, and D.D. Cooke, Appl. Opt. **18**, 3888 (1979).

21. S.B. Singham and C.F. Bohren, Opt. Lett. **12**, 10 (1987).

22. S.B. Singham and C.F. Bohren, J. Opt. Soc. Am. A **5**, 1867 (1988).

23. S.B. Singham and C.F. Bohren, Appl. Opt. **28**, 517 (1989).

24. S.B. Singham and C.F. Bohren, Appl. Opt. **28**, 5058 (1989).

25. G.H. Goedecke and S.G. O'Brien, Appl. Opt. **27**, 2431 (1988).

26. M.A. Morgan and K.K. Mei, IEEE Trans. Ant. and Prop. **AP-27**, 202 (1979).

27. D.H. Schaubert, D.R. Wilton, and A.W. Glisson, IEEE Trans. Ant. and Prop. **AP-32**, 77 (1984).

28. B.R. Johnson, Appl. Opt. **27**, 4861 (1988).

29. C. Yeh, S. Colak, and P. Barber, Appl. Opt. **21**, 4426 (1982).

30. J.P. Barton and D.R. Alexander, J. Appl. Phys. **66**, 2800 (1989).

31. W.C. Chew, *Waves and Fields in Inhomogeneous Media*, Van Nostrand Reinhold, New York (1990), pp. 453-63.

32. J.P. Barton, D.R. Alexander, and S.A. Schaub, J. Appl. Phys. **66**, 4594 (1989).

33. A. Mugnai and W.J. Wiscombe, Appl. Opt. **25**, 1235 (1986).

34. J.P. Barton, D.R. Alexander, and S.A. Schaub, J. Appl. Phys. **65**, 2900 (1989).

35. G.M. Hale and M.R. Querry, Appl. Opt. **12**, 555 (1973).

TABLE I. Comparison between results of the boundary matching method solution and the results of a spheroidal function expansion solution as taken from Oguchi.[a] Forward and backward scattering functions for a plane wave incident upon an oblate spheroid with "horizontal" polarization. ($\lambda_{ext}$ = 8.612 mm, $\bar{n}$ = 5.048 + 2.794i, $\theta_{bd}$ = 90°, $\phi_{bd}$ = 90°.)

| Major Semiaxis [mm] | Major to Minor Axis Ratio | $f_y \times 10^3$[mm] forward backward | $(f^h)^* \times 10^3$[mm] Oguchi[a] forward backward |
|---|---|---|---|
| 0.2519 | 1.024 | 0.008271+0.0009597i <br> 0.007954+0.0003755i | 0.008273+0.0009596i <br> 0.007956+0.0003751i |
| 0.5078 | 1.048 | 0.07051+0.01985i <br> 0.06735−0.002493i | 0.07049+0.01984i <br> 0.06734−0.002496i |
| 0.7679 | 1.073 | 0.2176+0.1249i <br> 0.2735+0.007458i | 0.2175+0.1247i <br> 0.2733+0.007440i |
| 1.032 | 1.100 | 0.4106+0.4091i <br> 06117+0.2019i | 0.4107+0.4093i <br> 0.6119+0.2021i |
| 1.301 | 1.128 | 0.4732+0.8716i <br> 0.7985+0.5411i | 0.4732+0.8718i <br> 0.7986+0.54131i |
| 1.575 | 1.158 | 0.3924+1.311i <br> 0.7638+0.7480i | 0.3924+1.311i <br> 0.7639+0.7481i |
| 1.854 | 1.190 | 0.3344+1.689i <br> 0.5962+0.6882i | 0.3346+1.688i <br> 0.5964+0.6882i |
| 2.138 | 1.223 | 0.3682+2.131i <br> 0.3661+0.3323i | 0.3685+2.132i <br> 0.3659+0.3315i |
| 2.428 | 1.258 | 0.3917+2.732i <br> 0.1797−0.2809i | 0.3920+2.733i <br> 0.1796−0.2821i |
| 2.724 | 1.295 | 0.2987+3.406i <br> 0.1344−0.9398i | 0.2989+3.407i <br> 0.1344−0.9413i |

[a]See Ref. 6.

TABLE II. Comparison between results of the boundary matching method solution and the results of a spheroidal function expansion solution as taken from Oguchi.[a] Forward and backward scattering functions for a plane wave incident upon an oblate spheroid with "vertical" polarization. ($\lambda_{ext}$ = 8.612 mm, $\bar{n}$ = 5.048 + 2.794i, $\theta_{bd}$ = 90°, $\phi_{bd}$ = 0°.)

| Major Semiaxis [mm] | Major to Minor Axis Ratio | $f_z$x10³[mm] forward backward | $(f^v)^*$x10³[mm] Oguchi[a] forward backward |
|---|---|---|---|
| 0.2519 | 1.024 | 0.008048+0.0009165i<br>0.007736+0.0003465i | 0.008055+0.0009176i<br>0.007743+0.0003469i |
| 0.5078 | 1.048 | 0.06667+0.01837i<br>0.06333-0.002936i | 0.06667+0.01837i<br>0.06335-0.002937i |
| 0.7679 | 1.073 | 0.1988+0.1114i<br>0.2485-0.001941i | 0.1986+0.1112i<br>0.2483-0.001988i |
| 1.032 | 1.100 | 0.3696+0.3378i<br>0.5560+0.1363i | 0.3696+0.3379i<br>0.5561+0.1363i |
| 1.301 | 1.128 | 0.4707+0.7002i<br>0.7715+0.3895i | 0.4706+0.6998i<br>0.7715+0.3891i |
| 1.575 | 1.158 | 0.4740+1.073i<br>0.8102+0.5690i | 0.4740+1.072i<br>0.8104+0.5688i |
| 1.854 | 1.190 | 0.4765+1.396i<br>0.6986+0.5609i | 0.4761+1.397i<br>0.6991+0.5609i |
| 2.138 | 1.223 | 0.5553+1.730i<br>0.4695+0.3344i | 0.5545+1.730i<br>0.4699+0.3342i |
| 2.428 | 1.258 | 0.6870+2.152i<br>0.1712-0.009987i | 0.6863+2.154i<br>0.1732-0.09883i |
| 2.724 | 1.295 | 0.7969+2.670i<br>-0.1008-0.6429i | 0.7930+2.670i<br>-0.09991-0.6420i |

[a]See Ref. 6.

TABLE III. Circumference (in units of $\lambda_{ext}$) for spherical particle with surface deformation at the 34th, 1st order magnetic wave resonance for $\epsilon = 0.00$, $\pm 0.01$, and $\pm 0.02$. $\bar{n} = 1.334 + 1.2 \times 10^{-9}$i.

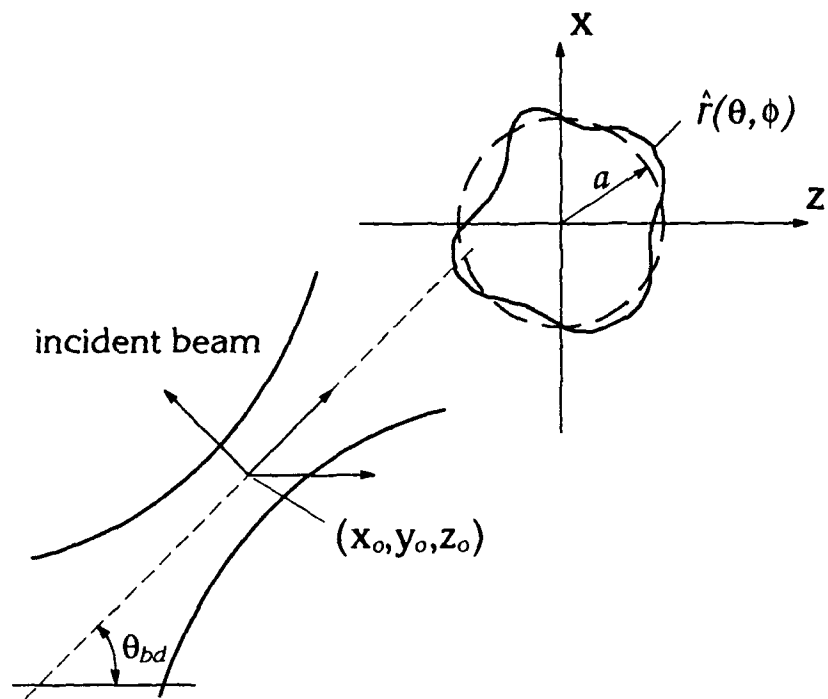| $\epsilon$ | Circumference [$\lambda_{ext}$] at $\alpha = 29.285$ | $\alpha_{res}$ | Circumference [$\lambda_{ext}$] at $\alpha_{res}$ |
|---|---|---|---|
| $-0.02$ | 29.212 | 29.355 | 29.282 |
| $-0.01$ | 29.248 | 29.321 | 29.284 |
| 0.00 | 29.285 | 29.285 | 29.285 |
| $+0.01$ | 29.322 | 29.248 | 29.285 |
| $+0.02$ | 29.358 | 29.208 | 29.281 |

# FIGURE TITLES

FIG 1. Geometrical arrangement for beam incident upon an arbitrarily-shaped particle analysis. The beam propagates parallel to the x-z plane.

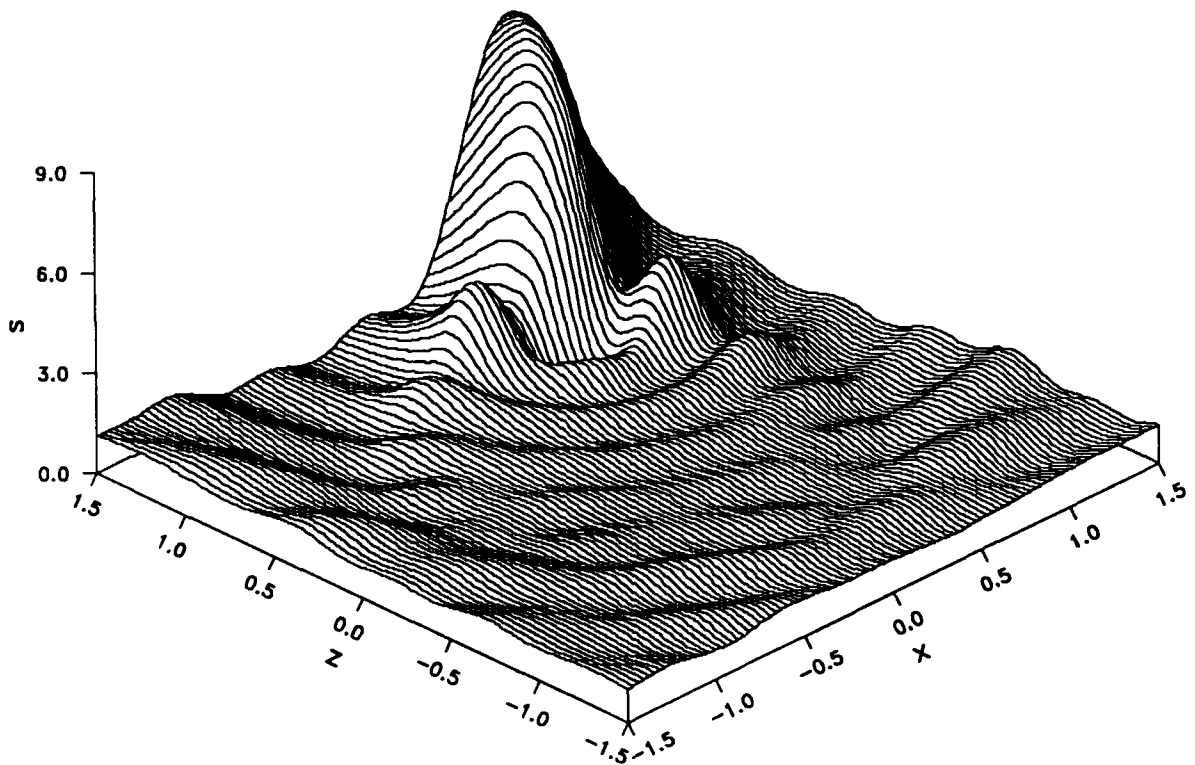FIG 2. Normalized source function distribution in the x-z plane for a $30^{\circ}$ angle of incidence plane wave incident upon a centered sphere. $\alpha = 8.0$, $\bar{n} = 1.2 + 0.02i$, $\bar{w}_0 = \infty$ (plane wave), $\theta_{bd} = 30^{\circ}$, and $\phi_{bd} = 90^{\circ}$.

FIG 3. Normalized source function distribution in the x-z plane for a $30^{\circ}$ angle of incidence plane wave incident upon a sphere displaced along the z-axis by $\Delta \bar{z} = +0.25$. $\alpha = 8.0$, $\bar{n} = 1.2 + 0.02i$, $\bar{w}_0 = \infty$ (plane wave), $\theta_{bd} = 30^{\circ}$, and $\phi_{bd} = 90^{\circ}$.

FIG 4. Normalized source function distribution in the x-z plane for a $30^{\circ}$ angle of incidence plane wave incident upon a centered sphere. $\alpha = 2.0$, $\bar{n} = 1.2 + 0.02i$, $\bar{w}_0 = \infty$ (plane wave), $\theta_{bd} = 30^{\circ}$, and $\phi_{bd} = 90^{\circ}$.
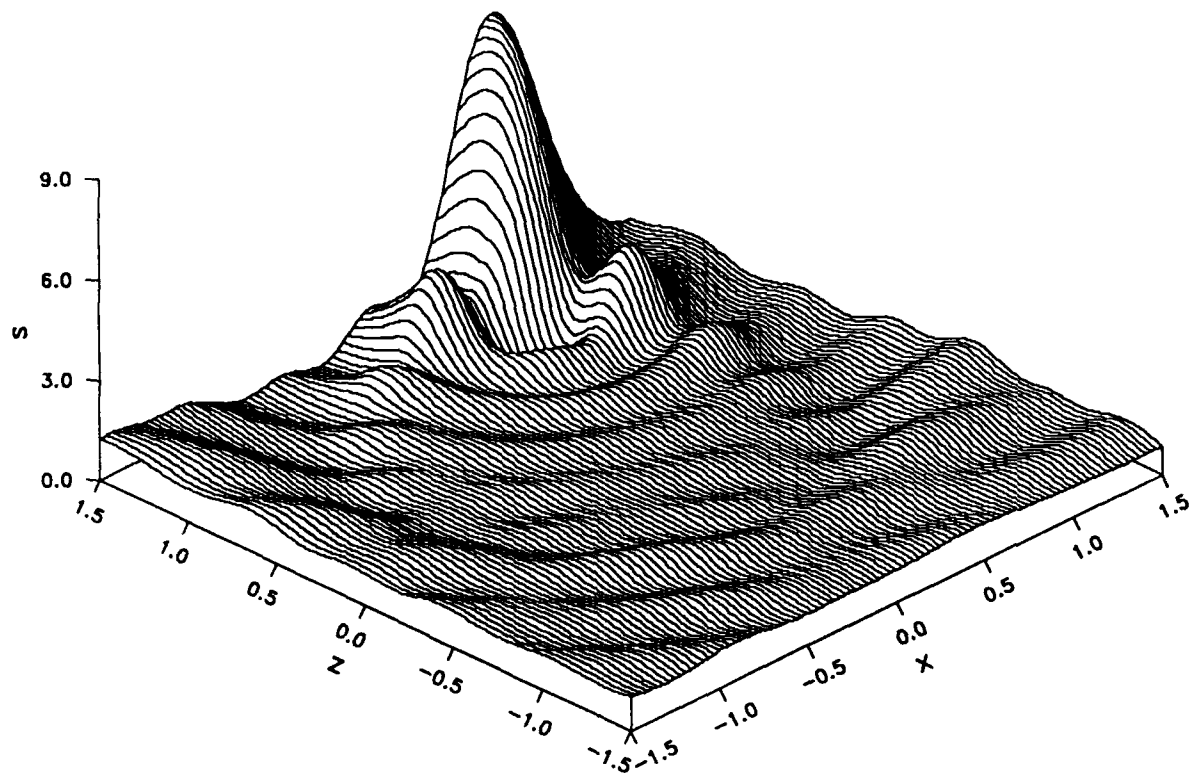
FIG 5. Normalized source function distribution in the x-z plane for a $30^{\circ}$ angle of incidence plane wave incident upon a sphere displaced along the x-axis by $\Delta \bar{x} = +0.10$. $\alpha = 2.0$, $\bar{n} = 1.2 + 0.02i$, $\bar{w}_0 = \infty$ (plane wave), $\theta_{bd} = 30^{\circ}$, and $\phi_{bd} = 90^{\circ}$.
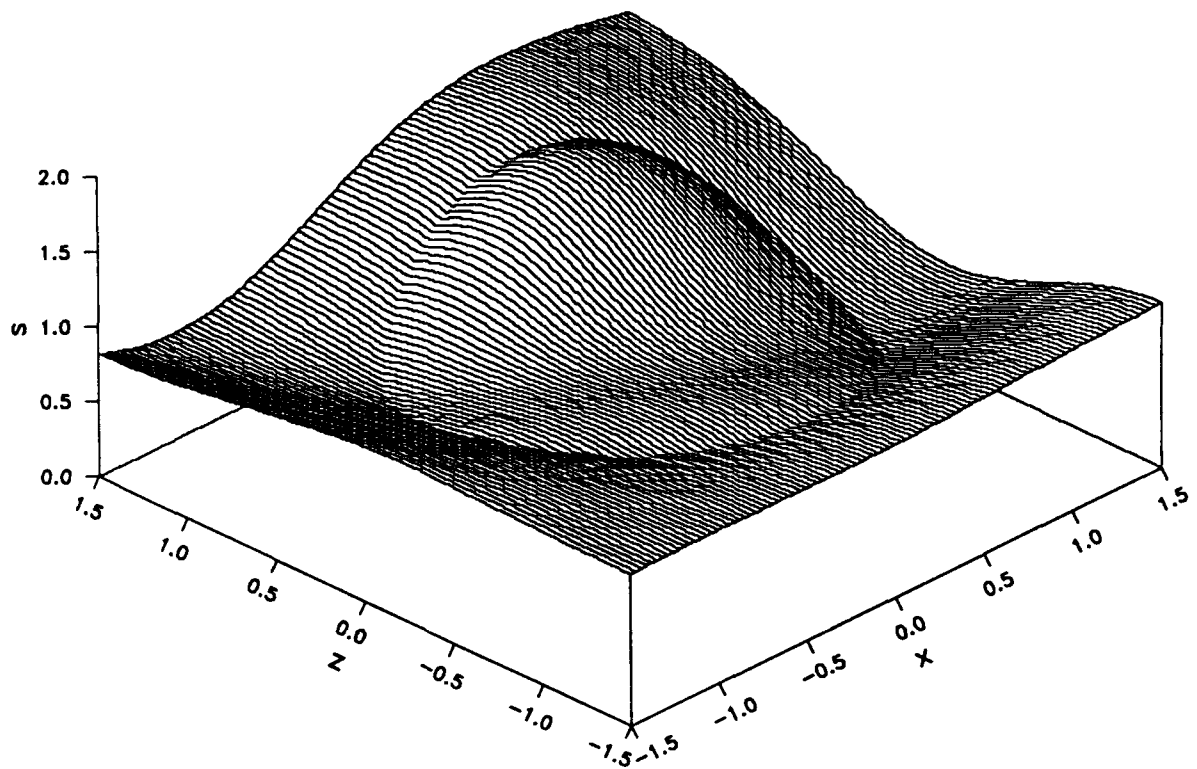
FIG 6. Average deviation of normal electromagnetic field components across surface of equal volume prolate spheroids as a function of L and axis ratio. $\alpha_{sphere} = 4.0$, $\bar{n} = 1.33 + 0.00i$, $\bar{w}_0 \Rightarrow \infty$ (plane wave), $\theta_{bd} = 30^{\circ}$, and $\phi_{bd} = 0^{\circ}$.

FIG 7. Average deviation of normal electromagnetic field components across surface of equal volume prolate spheroids as a function of L and axis ratio. $\alpha_{sphere} = 8.0$, $\bar{n} = 1.33 + 0.00i$, $\bar{w}_0 \Rightarrow \infty$ (plane wave), $\theta_{bd} = 30^{\circ}$, and $\phi_{bd} = 0^{\circ}$.

FIG 8. Internal normalized source function distribution in the x-z plane for a $0^{\circ}$ angle of incidence plane wave incident upon an oblate spheroid of axis ratio a/b = 1.2. $\alpha = 15.0$, $\bar{n} = 1.33 + 0.00i$, $\bar{w}_0 \Rightarrow \infty$ (plane wave), $\theta_{bd} = 0^{\circ}$, and $\phi_{bd} = 0^{\circ}$.

FIG 9. Internal normalized source function distribution in the x-z plane for a $0^{\circ}$ angle of incidence focused beam incident upon an oblate spheroid of axis ratio a/b = 1.2. On-center focal point positioning. $\alpha = 15.0$, $\bar{n} = 1.33 + 0.00i$, $\bar{w}_0 = 0.667$, $\bar{x}_0 = \bar{y}_0 = \bar{z}_0 = 0.0$, $\theta_{bd} = 0^{\circ}$, and $\phi_{bd} = 0^{\circ}$.

FIG 10. Internal normalized source function distribution in the x-z plane for a $0°$ angle of incidence focused beam incident upon an oblate spheroid of axis ratio $a/b = 1.2$. Mid-axis focal point positioning. $\alpha = 15.0$, $\bar{n} = 1.33 + 0.00i$, $\bar{w}_0 = 0.667$, $\tilde{x}_0 = 0.5$, $\tilde{y}_0 = \tilde{z}_0 = 0.0$, $\theta_{bd} = 0°$, and $\phi_{bd} = 0°$.

FIG 11. Internal normalized source function distribution in the x-z plane for a $0°$ angle of incidence focused beam incident upon an oblate spheroid of axis ratio $a/b = 1.2$. On-edge focal point positioning. $\alpha = 15.0$, $\bar{n} = 1.33 + 0.00i$, $\bar{w}_0 = 0.667$, $\tilde{x}_0 = 1.0$, $\tilde{y}_0 = \tilde{z}_0 = 0.0$, $\theta_{bd} = 0°$, and $\phi_{bd} = 0°$.

FIG 12. $|d_{34}|$ versus $\alpha$ for a spherical particle ($\epsilon = 0.00$). $\bar{n} = 1.334 + 1.2\times10^{-9}i$.

FIG 13. $|d_{34}|$ versus $\alpha$ for spherical particle with surface deformations of $\epsilon = 0.00$, $\pm0.01$, and $\pm0.02$. $\bar{n} = 1.334 + 1.2\times10^{-9}i$.

FIG 14. $|d_{34}|$ versus $\alpha$ for spherical particle with surface deformations of $\epsilon = 0.00$ and $\pm0.05$. $\bar{n} = 1.334 + 1.2\times10^{-9}i$.

FIG 1. Geometrical arrangement for beam incident upon an arbitrarily-shaped particle analysis. The beam propagates parallel to the x-z plane.

FIG 2. Normalized source function distribution in the x-z plane for a $30^o$ angle of incidence plane wave incident upon a centered sphere. $\alpha = 8.0$, $\bar{n} = 1.2 + 0.02i$, $\tilde{w}_0 = \infty$ (plane wave), $\theta_{bd} = 30^o$, and $\phi_{bd} = 90^o$.
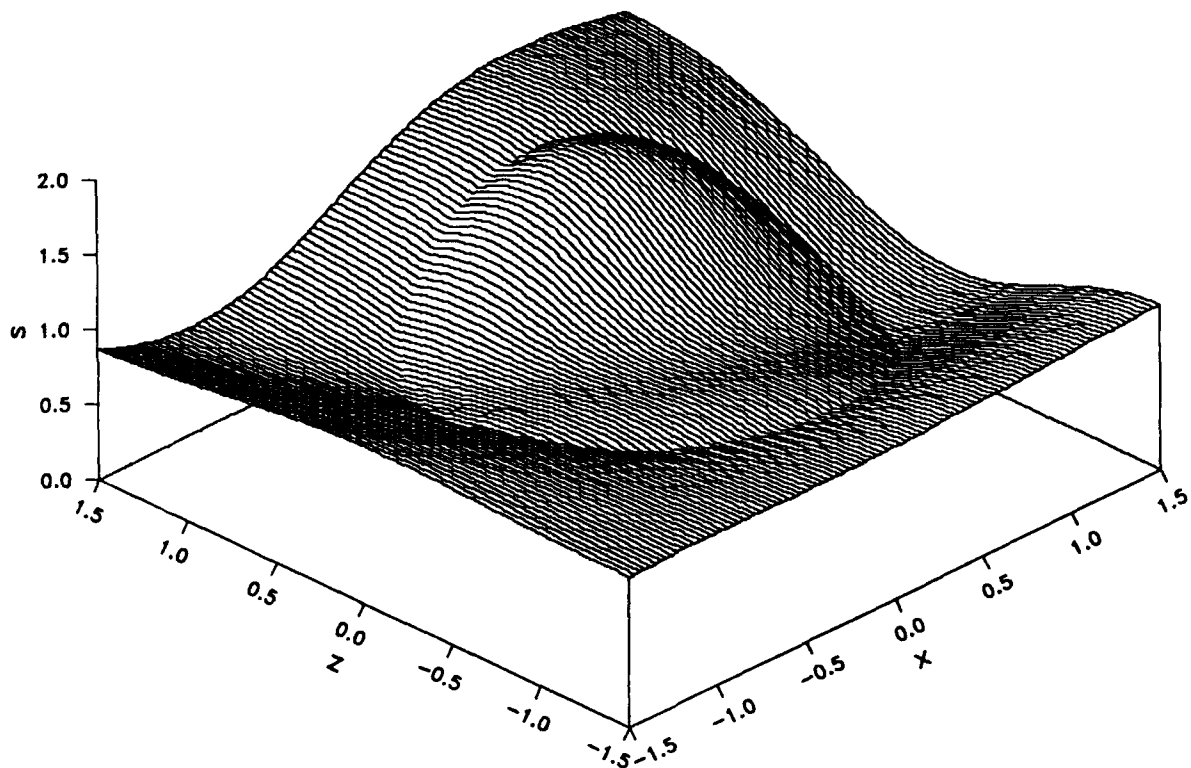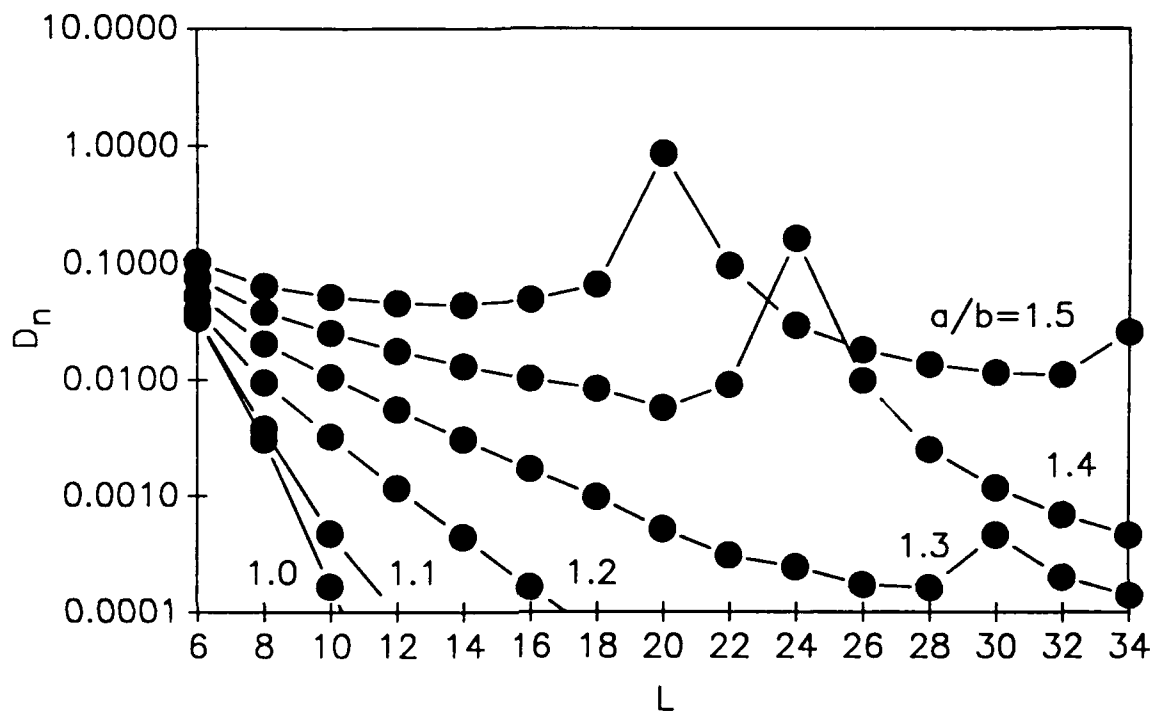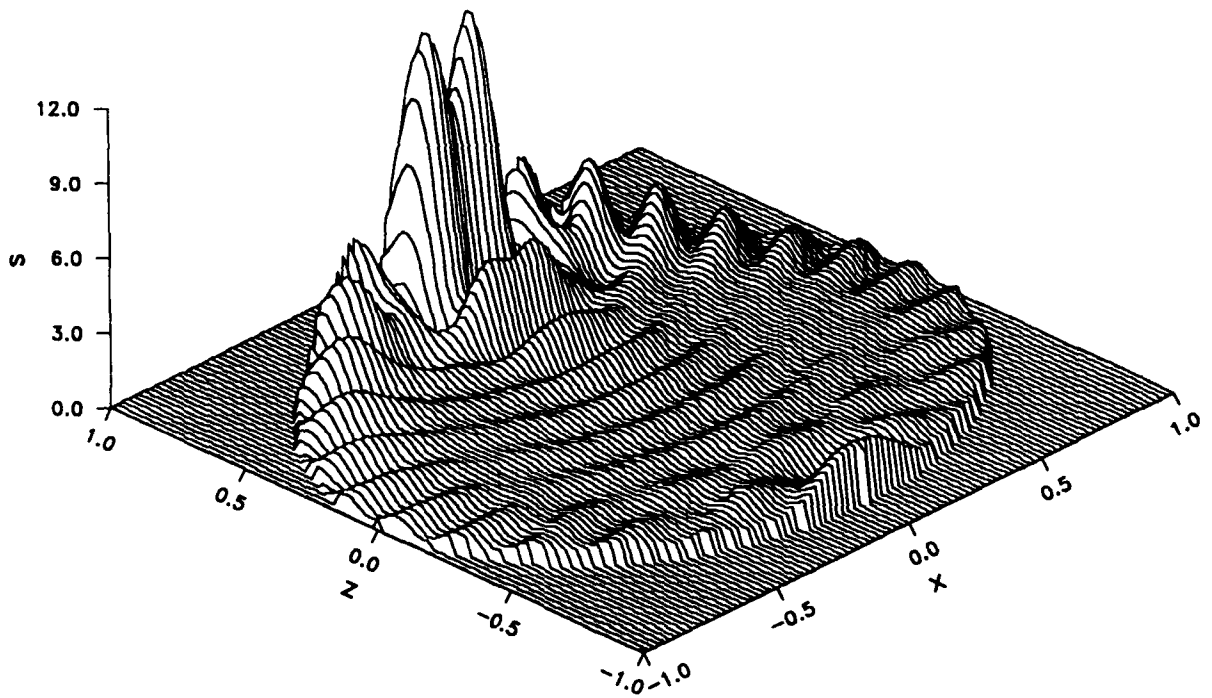
FIG 3. Normalized source function distribution in the x-z plane for a 30° angle of incidence plane wave incident upon a sphere displaced along the z-axis by $\Delta \tilde{z} = +0.25$. $\alpha = 8.0$, $\bar{n} = 1.2 + 0.02i$, $\tilde{w}_0 = \infty$ (plane wave), $\theta_{bd} = 30°$, and $\phi_{bd} = 90°$.

34

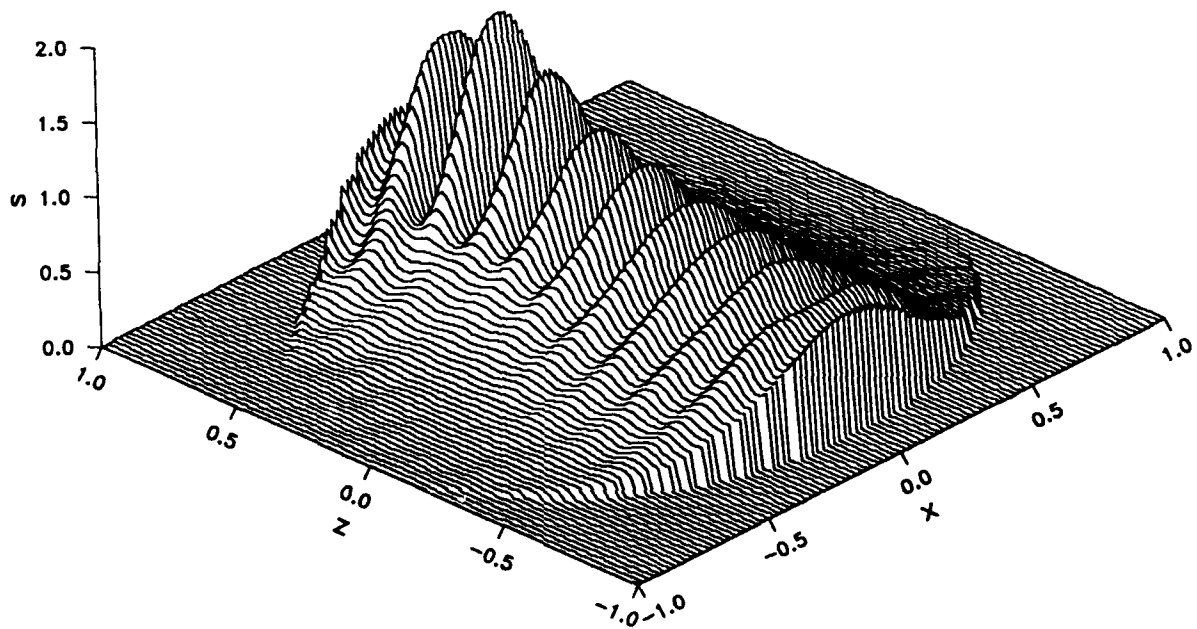FIG 4. Normalized source function distribution in the x-z plane for a 30° angle of incidence plane wave incident upon a centered sphere. $\alpha = 2.0$, $\bar{n} = 1.2 + 0.02i$, $\tilde{w}_0 = \infty$ (plane wave), $\theta_{bd} = 30°$, and $\phi_{bd} = 90°$.

FIG 5. Normalized source function distribution in the x-z plane for a $30°$ angle of incidence plane wave incident upon a sphere displaced along the x-axis by $\Delta \bar{x} = +0.10$. $\alpha = 2.0$, $\bar{n} = 1.2 + 0.02i$, $\bar{w}_0 = \infty$ (plane wave), $\theta_{bd} = 30°$, and $\phi_{bd} = 90°$.

FIG 6. Average deviation of normal electromagnetic field components across surface of equal volume prolate spheroids as a function of L and axis ratio. $\alpha_{sphere} = 4.0$, $\bar{n} = 1.33 + 0.00i$, $\tilde{w}_0 \Rightarrow \infty$ (plane wave), $\theta_{bd} = 30°$, and $\phi_{bd} = 0°$.

FIG 7. Average deviation of normal electromagnetic field components across surface of equal volume prolate spheroids as a function of L and axis ratio. $\alpha_{sphere} = 8.0$, $\bar{n} = 1.33 + 0.00i$, $\tilde{w}_0 \Rightarrow \infty$ (plane wave), $\theta_{bd} = 30^o$, and $\phi_{bd} = 0^o$.
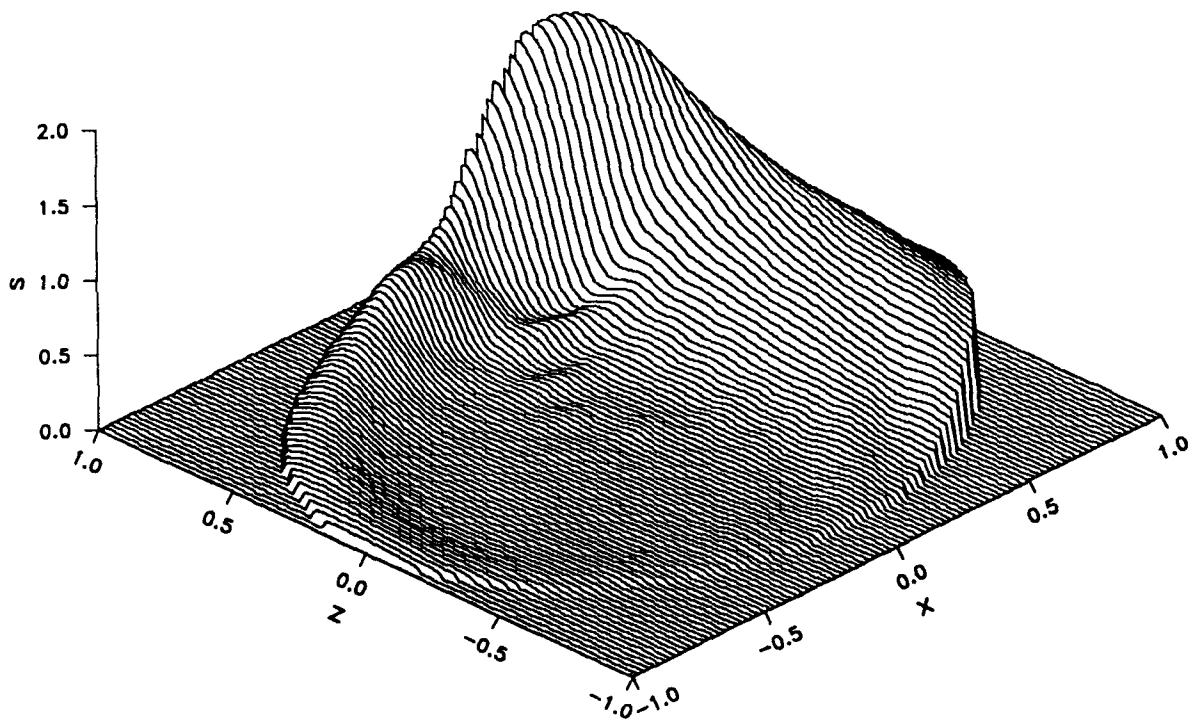
FIG 8. Internal normalized source function distribution in the x-z plane for a $0°$ angle of incidence plane wave incident upon an oblate spheroid of axis ratio a/b = 1.2. $\alpha = 15.0$, $\bar{n} = 1.33 + 0.00i$, $\tilde{w}_0 \Rightarrow \infty$ (plane wave), $\theta_{bd} = 0°$, and $\phi_{bd} = 0°$.

FIG 9. Internal normalized source function distribution in the x-z plane for a $0^o$ angle of incidence focused beam incident upon an oblate spheroid of axis ratio a/b = 1.2. On-center focal point positioning. $\alpha = 15.0$, $\bar{n} = 1.33 + 0.00i$, $\tilde{w}_0 = 0.667$, $\bar{x}_0 = \check{y}_0 = \check{z}_0 = 0.0$, $\theta_{bd} = 0^o$, and $\phi_{bd} = 0^o$.

40

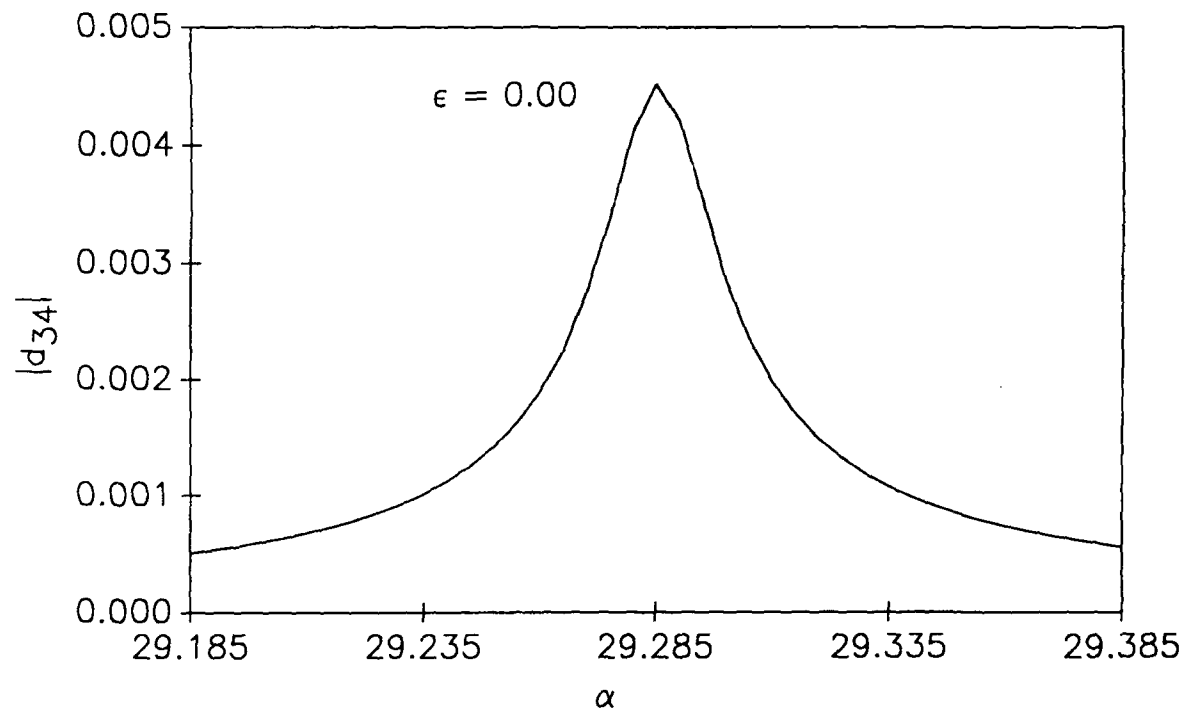FIG 10. Internal normalized source function distribution in the x-z plane for a $0^\circ$ angle of incidence focused beam incident upon an oblate spheroid of axis ratio a/b = 1.2. Mid-axis focal point positioning. $\alpha = 15.0$, $\bar{n} = 1.33 + 0.00i$, $\tilde{w}_0 = 0.667$, $\tilde{x}_0 = 0.5$, $\tilde{y}_0 = \tilde{z}_0 = 0.0$, $\theta_{bd} = 0^\circ$, and $\phi_{bd} = 0^\circ$.

FIG 11. Internal normalized source function distribution in the x-z plane for a $0^o$ angle of incidence focused beam incident upon an oblate spheroid of axis ratio a/b = 1.2. On-edge focal point positioning. $\alpha = 15.0$, $\bar{n} = 1.33 + 0.00i$, $\tilde{w}_0 = 0.667$, $\tilde{x}_0 = 1.0$, $\tilde{y}_0 = \tilde{z}_0 = 0.0$, $\theta_{bd} = 0^o$, and $\phi_{bd} = 0^o$.

FIG 12. $|d_{34}|$ versus $\alpha$ for a spherical particle ($\epsilon = 0.00$). $\bar{n} = 1.334 + 1.2 \times 10^{-9}$i.

43

FIG 13. $|d_{34}|$ versus $\alpha$ for spherical particle with surface deformations of $\epsilon = 0.00$, $\pm 0.01$, and $\pm 0.02$. $\bar{n} = 1.334 + 1.2 \times 10^{-9}$i.

FIG 14. $|d_{34}|$ versus $\alpha$ for spherical particle with surface deformations of $\epsilon = 0.00$ and $\pm 0.05$. $\bar{n} = 1.334 + 1.2 \times 10^{-9} i$.

# MODELING OF THE COHERENT IMAGING OF A SPHERICAL AEROSOL
# PARTICLE ILLUMINATED BY A PLANE WAVE AT OBLIQUE INCIDENCE

S.A. Schaub, D.R. Alexander, and J.P. Barton

Center for Electro-Optics

University of Nebraska-Lincoln

Lincoln, NE 68588-0656

(402) 472-3091

## Abstract

A theoretical model has been developed for the coherent imaging of a spherical aerosol particle illuminated by an off-axis incident plane wave. The modeling technique makes use of the arbitrary beam theory, presented by the authors in an earlier paper, to calculate the external electromagnetic field resulting from the laser/aerosol interaction. Scalar diffraction theory is used to propagate the dominant electric field component through the imaging lens and to the image plane. Demonstration calculations have been presented for both opaque and transparent particles ranging in size from 10 to 40 $\mu$m in diameter illuminated by off-axis $\lambda \approx 0.5$ $\mu$m incident radiation.

1

# 1. Introduction

Effects of off-axis light scattering by spherical aerosol particles arise in a variety of situations involving both the linear and nonlinear laser interaction with aerosol particles. [1,2,3,4,5,6] Recent investigations in the area of linear aerosol scattering has focused on the observation and prediction of glare spots resulting from the off-axis laser/aerosol interaction. [1,2] The theoretical developments utilized in these analyses have used both classical Lorenz-Mie theory [7,8] and geometrical optics. Off-axis scattering also has important implications to nonlinear laser/aerosol interaction studies. [4,5,6] For example, when performing imaging studies of the aerosol breakup dynamics resulting from high energy laser illumination, the experimental apparatus is arranged such that the imaging system axis and the high energy laser axis are not coincident (usually perpendicular). Thus, any elastically scattered light resulting from the high energy laser, which may reach the recording medium, can be considered as an off-axis contribution to the total aerosol image. Development of a theoretical model of the off-axis image contribution would provide a valuable tool in better understanding both linear and nonlinear laser/aerosol interaction processes.

One method to model the off-axis aerosol image formation would involve the use of classical Lorenz-Mie theory [7,8] to calculate the external electromagnetic field resulting from the laser/aerosol interaction. The subsequent propagation of the field through the optical components of the imaging system could be accomplished using a scalar lens transformation and the Huygens-Fresnel propagation equation. [9] This modeling approach would require evaluation of a two-dimensional integral over the entrance aperture of the imaging system and also requires storage of the electric field component terms within the aperture.

In this paper, we present an alternative theoretical approach which will allow calculation of the expected aerosol image due to off-axis illumination of a spherical particle by an incident plane wave. This alternative technique makes use of scalar diffraction theory in conjunction with the arbitrary beam theory, presented by the authors in an earlier paper. [10] The theoretical development places no restrictions on the optical properties of the particle or on the allowable degree or direction of aerosol defocus within the imaging system. Evaluation of the final expression will involve numerical

2

computation of a one-dimensional integral over the radius of the imaging system aperture. In addition, storage of the electric field component expressions at points within the aperture is not required. This development would be the preferred technique for situations in which the number of observation points is relatively small or in which computer storage is a limiting factor.

## 2. Theoretical Development

The geometry under consideration for the off-axis imaging development is shown in Fig. 1. In this arrangement, a plane wave propagating in the $+z'$ direction, is incident on a spherical absorbing particle located on the imaging system axis ($z$ axis) at plane $z_0$ (imaging system focal plane). The direction of propagation of the incident plane wave makes an angle, $\theta_r$ with respect to the imaging system axis. The polarization of the incident field is taken in either the $x'$ (referred to as the perpendicular polarization case) or $y'$ (parallel polarization case) direction. It should be noted that these two fundamental solutions provide the basis for treatment of incident fields possessing a more complex state of polarization (e.g., an elliptical polarized incident field). The external field resulting from the laser/aerosol interaction is collected by an aperture/lens combination and projected to the image plane (plane $z_3$) of the system. The modeling approach to be presented can be viewed as a hybrid technique, with the laser/aerosol interaction being examined from a vector viewpoint, while the propagation of the electric field through the imaging system is examined using a scalar development.

We begin by seeking an expression relating the electric field in the image plane (plane $z_3$) to the field present at the rear lens surface (plane $z_2$). According to Goodman, [9] provided the distance $z_{32}$ satisfies the relation,

$$z_{32}^3 = (z_3 - z_2)^3 >> \frac{\pi}{4\lambda}[(x_3 - x_2)^2 + (y_3 - y_2)^2]_{max}^2, \tag{1}$$

the electric field in plane $z_3$ can be expressed in terms of the electric field distribution in plane $z_2$ through use of the Fresnel approximation to the Huygens-Fresnel equation,

$$E_3(x_3, y_3) = \frac{\exp(ikz_{32})}{i\lambda z_{32}} \int \int_A E_2(x_2, y_2) \exp\left\{\frac{ik}{2z_{32}}\left[(x_3 - x_2)^2 + (y_3 - y_2)^2\right]\right\} dx_2 dy_2. \tag{2}$$

3

Here, $k = 2\pi/\lambda$ where $\lambda$ is the wavelength of the incident light, and the single numerical subscripts denote the $z =$ constant plane in which the particular quantity is evaluated. (e.g., $E_2$ represents the electric field evaluated in plane $z_2$.) In using scalar theory to relate the respective electric field components, one is neglecting the coupling of the electric and magnetic fields through Maxwell's equations. Thus, the final result will provide an approximate solution to the actual physical problem. Transforming to spherical coordinates, Eq. (2) can be expressed in nondimensional form (denoted by superscript tilde) as,

$$
\begin{aligned}
\tilde{E}_3(\tilde{r}_3, \phi_3) &= \tilde{P} \int_0^{\tilde{r}_a} \tilde{T}(\tilde{r}_1) \exp\left[\frac{i\alpha \tilde{r}_2(\tilde{r}_1)^2}{2\tilde{z}_{32}}\right] \tilde{r}_2(\tilde{r}_1) \\
&\times \int_0^{2\pi} \tilde{E}(\tilde{r}_1, \phi_1) \exp\left[-i\tilde{\beta}\cos(\phi_1 - \phi_3)\right] d\phi_1 d\tilde{r}_1,
\end{aligned}
\tag{3}
$$

where $\tilde{E}_1$ represents the dominant electric field component at the front lens surface (plane $z_1$), $\tilde{T}$ represents an angular independent phase transformation relating the electric field across the imaging lens,

$$
\tilde{P} = \frac{\alpha \exp(i\alpha \tilde{z}_{32}) \exp(i\alpha \tilde{r}_3^2 / 2\tilde{z}_{32})}{2\pi i \tilde{z}_{32}},
\tag{4}
$$

and

$$
\tilde{\beta} = \frac{\alpha \tilde{r}_2(\tilde{r}_1)\tilde{r}_3}{\tilde{z}_{32}}.
\tag{5}
$$

The quantity $\alpha = 2\pi a/\lambda$ is the dimensionless size parameter representing the ratio of the circumference of the droplet to the incident wavelength. In the above equations, $\tilde{r}_2$ is expressed as a function of $\tilde{r}_1$ due to refraction of the light which occurs through the imaging lens. All spatial variables are normalized by the particle radius, while the electric field expressions have been normalized by the magnitude of the incident field.

For off-axis imaging, in most practical situations, the incident field will not contribute to the image formation except for special cases when the angle between the imaging system axis and the beam propagation axis is small (i.e., $\theta_r$ is small). Even for a rather large incident beam of 10 mm in diameter along with an aperture diameter of 5 mm and lens focal length of 50 mm, the incident

4

field would be insignificant for incident angles greater than about 15 degrees. Therefore, in the following development it will be assumed that the scattered field components provide the dominant contribution to the off-axis image formation.

### E field polarized perpendicular to $y - z$ plane

Referring to Fig. 1, the incident electric field for the perpendicular polarization case can be expressed as,

$$^{\perp}\tilde{E}^{(inc)} = \exp(i\alpha\tilde{z}')\hat{i}', \tag{6}$$

where the time dependence of $\exp(-i\omega t)$ has been omitted. For an incident field polarized in the $x$ direction, one can show through direct calculation that the dominant scattered electric field component for points near the $y - z$ plane will also be in the $x$ direction. In fact, for observation points contained within the $y - z$ plane, the *only* non-zero electric field component is in the $x$ direction. The error introduced by neglecting the non-dominant field components will be related primarily to the lens focal length and the finite size of the collection aperture. Other parameters which also influence the magnitude of the respective electric field components are the size parameter, optical properties of the aerosol, and the incident beam angle. For the cases to be presented in this paper, the average of the dominant electric field component was found to be between one and two orders of magnitude larger than the average of the non-dominant components. Accepting that the aerosol image, for perpendicular incident polarization, can be expressed in terms of the $x$-component of the electric field, the term $\tilde{E}_1$ in Eq. (3) can be rewritten in terms of spherical components,

$$\begin{aligned}
\tilde{E}_1(\tilde{\rho}_{10}, \theta, \phi_1) &= \tilde{E}_r^{(sca)}(\tilde{\rho}_{10}, \theta, \phi_1)\sin\theta\cos\phi_1 + \tilde{E}_\theta^{(sca)}(\tilde{\rho}_{10}, \theta, \phi_1)\cos\theta\cos\phi_1 \\
&\quad - \tilde{E}_\phi^{(sca)}(\tilde{\rho}_{10}, \theta, \phi_1)\sin\phi_1.
\end{aligned} \tag{7}$$

The phi angles are measured with respect to the $+x$ axis in the direction of the $+y$ axis and range from 0 to $2\pi$. The only requirement in the determination of the electric field components shown in the above equation is that the radial components of the incident electric and magnetic fields be

5

known over the particle surface. [10] Substituting Eq. (7) along with the exact series expressions for the dimensionless scattered electric field components (see Ref. [10]) into the angular integral of Eq. (3), denoted by $\tilde{I}^\phi_{lm}$, gives,

$$
\begin{aligned}
\tilde{I}^\phi_{lm}(\tilde{\rho}_{10}, \theta, \phi_3) &= \left(\frac{\sin\theta}{\tilde{\rho}_{10}^2}\right) \sum_{l=1}^{\infty} \sum_{m=-l}^{l} l(l+1) a_{lm} \xi_l^{(1)}(\alpha\tilde{\rho}_{10}) F_{lm} P_l^{(m)}(\cos\theta) \int_0^{2\pi} \cos\phi_1 \exp(im\phi_1) \\
&\quad \times \ \exp[-i\tilde{\beta}\cos(\phi_1 - \phi_3)]d\phi_1 + \left(\frac{\alpha\cos\theta}{\tilde{\rho}_{10}}\right) \sum_{l=1}^{\infty} \sum_{m=-l}^{l} \Big[ a_{lm} \xi_l^{(1)\prime}(\alpha\tilde{\rho}_{10})(-\sin\theta) \\
&\quad \times \ F_{lm} P_l^{(m)\prime}(\cos\theta) - m b_{lm} \xi_l^{(1)}(\alpha\tilde{\rho}_{10}) F_{lm} P_l^{(m)}(\cos\theta)/\sin\theta \Big] \\
&\quad \times \ \int_0^{2\pi} \cos\phi_1 \exp(im\phi_1) \exp[-i\tilde{\beta}\cos(\phi_1 - \phi_3)]d\phi_1 - \left(\frac{\alpha}{\tilde{\rho}_{10}}\right) \sum_{l=1}^{\infty} \sum_{m=-l}^{l} \Big[ im a_{lm} \\
&\quad \times \ \xi_l^{(1)\prime}(\alpha\tilde{\rho}_{10}) F_{lm} P_l^{(m)}(\cos\theta)/\sin\theta - i b_{lm} \xi_l^{(1)}(\alpha\tilde{\rho}_{10}) F_{lm}(-\sin\theta) P_l^{(m)\prime}(\cos\theta) \Big] \\
&\quad \times \ \int_0^{2\pi} \sin\phi_1 \exp(im\phi_1) \exp[-i\tilde{\beta}\cos(\phi_1 - \phi_3)]d\phi_1. \quad (8)
\end{aligned}
$$

where,

$$
F_{lm} = \sqrt{\frac{2l+1}{4\pi}\frac{(l-m)!}{(l+m)!}}. \quad (9)
$$

In the above equation, $P_l^{(m)}$ is the associated Legendre function, $\xi_l^{(1)}$ is the Hankel function of the first kind which is related to the Riccati-Bessel function (i.e., $\xi_l^{(1)} = \psi_l - i\chi_l$), and $a_{lm}$ and $b_{lm}$ are the external scattering coefficients. The angular integrals shown in Eq. (8) can be evaluated exactly using the following derived integral relationships,

$$
\begin{aligned}
I_m^{\cos}(\tilde{\beta}, \phi_3) &= \int_0^{2\pi} \cos\phi_1 \exp(im\phi_1) \exp[-i\tilde{\beta}\cos(\phi_1 - \phi_3)]d\phi_1 \\
&= \pi(i)^{1-m}[-J_{m+1}(\tilde{\beta})\exp(i\phi_3) + J_{m-1}(\tilde{\beta})\exp(-i\phi_3)]\exp(im\phi_3), \quad (10)
\end{aligned}
$$

and

$$
\begin{aligned}
I_m^{\sin}(\tilde{\beta}, \phi_3) &= \int_0^{2\pi} \sin\phi_1 \exp(im\phi_1) \exp[-i\tilde{\beta}\cos(\phi_1 - \phi_3)]d\phi_1 \\
&= \pi(i)^m(-1)^{m+1}[J_{m+1}(\tilde{\beta})\exp(i\phi_3) + J_{m-1}(\tilde{\beta})\exp(-i\phi_3)]\exp(im\phi_3), \quad (11)
\end{aligned}
$$

where $J$ represents the integer order Bessel function of the first kind. The $-m$ case can be related to the $+m$ case by,

$$
I_{-m}^{\cos}(\tilde{\beta}, \phi_3) = I_m^{\cos*}(\tilde{\beta}, \phi_3)(-1)^{m-1}, \quad (12)
$$

and

$$\Gamma_{-m}^{\sin}(\tilde{\beta}, \phi_3) = \Gamma_m^{\sin *}(\tilde{\beta}, \phi_3)(-1)^{m-1}, \tag{13}$$

where the superscript asterisk denotes the complex conjugate. Using these integral relationships, Eq. (8) can then be expressed as,

$$
\begin{aligned}
\tilde{I}_{lm}^{\phi}(\tilde{\rho}_{10}, \theta, \phi_3) ={}& \left(\frac{\sin\theta}{\tilde{\rho}_{10}^2}\right) \sum_{l=1}^{\infty} \sum_{m=-l}^{l} l(l+1) a_{lm} \xi_l^{(1)}(\alpha\tilde{\rho}_{10}) F_{lm} P_l^{(m)}(\cos\theta) \Gamma_m^{\cos}(\tilde{\beta}, \phi_3) \\
&+ \left(\frac{\alpha\cos\theta}{\tilde{\rho}_{10}}\right) \sum_{l=1}^{\infty} \sum_{m=-l}^{l} \left[ a_{lm} \xi_l^{(1)\prime}(\alpha\tilde{\rho}_{10}) F_{lm}(-\sin\theta) P_l^{(m)\prime}(\cos\theta) - m b_{lm} \right. \\
&\times\; \xi_l^{(1)}(\alpha\tilde{\rho}_{10}) F_{lm} P_l^{(m)}(\cos\theta)/\sin\theta \Big] \Gamma_m^{\cos}(\tilde{\beta}, \phi_3) - \left(\frac{\alpha}{\tilde{\rho}_{10}}\right) \sum_{l=1}^{\infty} \sum_{m=-l}^{l} \Big[ i m a_{lm} \\
&\times\; \xi_l^{(1)\prime}(\alpha\tilde{\rho}_{10}) F_{lm} P_l^{(m)}(\cos\theta)/\sin\theta - i b_{lm} \xi_l^{(1)}(\alpha\tilde{\rho}_{10}) F_{lm}(-\sin\theta) \\
&\times\; P_l^{(m)\prime}(\cos\theta) \Big] \Gamma_m^{\sin}(\tilde{\beta}, \phi_3). \tag{14}
\end{aligned}
$$

Using Eq. (3), the electric field in plane $z_3$ can then be written,

$$\tilde{E}_3(\tilde{r}_3, \phi_3) = \tilde{P} \int_0^{\tilde{r}_a} \tilde{T}(\tilde{r}_1) \exp\left[ i\alpha\tilde{r}_2(\tilde{r}_1)^2 / 2\tilde{z}_{32} \right] \tilde{r}_2(\tilde{r}_1) \tilde{I}_{lm}^{\phi}(\tilde{\rho}_{10}, \theta, \phi_3) d\tilde{r}_1. \tag{15}$$

To obtain the final expression for the intensity distribution in the image plane, the thin lens transformation [9] is used to relate the electric field across the imaging lens, i.e.,

$$\tilde{T}(\tilde{r}_1) = \exp(i\alpha n_l \tilde{\Delta}_0) \exp(i\alpha\tilde{r}_1^2 / 2\tilde{f}), \tag{16}$$

and

$$\tilde{r}_2(\tilde{r}_1) = \tilde{r}_1. \tag{17}$$

Here, $\tilde{\Delta}_0$ is the normalized lens thickness, $n_l$ is the index of refraction of the lens, and $\tilde{f}$ is the dimensionless lens focal length. Note that other, more sophisticated, lens descriptions could be incorporated into the theoretical development presented. The only restriction is that the effects of the lens on the electric field be axisymmetric. For the thin lens description to qualify, the variation in the Fresnel coefficients in the angular direction have been neglected. In situations

7

where the aperture diameter is small relative to the lens focal length this turns out to be a good approximation. For these cases, all light incident on the imaging lens is nearly perpendicular to the lens surfaces, in which case the Fresnel coefficients are approximately equal for both polarization states. Substituting for $\tilde{P}$ from Eq. (4) and using the thin lens expressions given above, the electric field in the image plane can be written,

$$\tilde{E}_3(\tilde{r}_3, \phi_3) = \left[ \frac{\alpha \exp(i\alpha\tilde{z}_{32}) \exp(i\alpha\tilde{r}_3^2/2\tilde{z}_{32})}{2\pi i \tilde{z}_{32}} \right] \int_0^{\tilde{r}_a} \exp\left[ \frac{i\alpha\tilde{r}_1^2}{2} \left( \frac{1}{\tilde{z}_{32}} - \frac{1}{\tilde{f}} \right) \right] \tilde{r}_1 \tilde{I}_{lm}^\phi(\tilde{\rho}_{10}, \theta, \phi_3) d\tilde{r}_1. \quad (18)$$

In terms of intensity, the final result for perpendicular polarization can be expressed with all terms written explicitly as,

$$\begin{aligned}
{}^\perp \tilde{I}_3(\tilde{r}_3, \phi_3) &= \left( \frac{\alpha}{2\tilde{z}_{32}} \right)^2 \left| \int_0^{\tilde{r}_a} \exp\left[ \frac{i\alpha\tilde{r}_1^2}{2} \left( \frac{1}{\tilde{z}_{32}} - \frac{1}{\tilde{f}} \right) \right] \tilde{r}_1 \left\{ \left( \frac{\sin\theta}{\tilde{\rho}_{10}^2} \right) \sum_{l=1}^{\infty} \sum_{m=-l}^{l} l(l+1) a_{lm} \right. \\
&\times \quad F_{lm} \xi_l^{(1)}(\alpha\tilde{\rho}_{10}) P_l^{(m)}(\cos\theta) \left[ (i)^{1-m} \exp(im\phi_3) \left( -J_{m+1}(\tilde{\beta}) \exp(i\phi_3) \right. \right. \\
&+ \quad \left. \left. J_{m-1}(\tilde{\beta}) \exp(-i\phi_3) \right) \right] + \left( \frac{\alpha\cos\theta}{\tilde{\rho}_{10}} \right) \sum_{l=1}^{\infty} \sum_{m=-l}^{l} \left[ a_{lm} \xi_l^{(1)\prime}(\alpha\tilde{\rho}_{10}) \right. \\
&\times \quad (-\sin\theta) F_{lm} P_l^{(m)\prime}(\cos\theta) - m b_{lm} \xi_l^{(1)}(\alpha\tilde{\rho}_{10}) F_{lm} P_l^{(m)}(\cos\theta) / \sin\theta \Big] \\
&\times \quad \left[ (i)^{1-m} \exp(im\phi_3) \left( -J_{m+1}(\tilde{\beta}) \exp(i\phi_3) + J_{m-1}(\tilde{\beta}) \exp(-i\phi_3) \right) \right] \\
&- \quad \left( \frac{\alpha}{\tilde{\rho}_{10}} \right) \sum_{l=1}^{\infty} \sum_{m=-l}^{l} \left[ i m a_{lm} \xi_l^{(1)\prime}(\alpha\tilde{\rho}_{10}) F_{lm} P_l^{(m)}(\cos\theta) / \sin\theta \right. \\
&- \quad i b_{lm} \xi_l^{(1)}(\alpha\tilde{\rho}_{10})(-\sin\theta) F_{lm} P_l^{(m)\prime}(\cos\theta) \Big] \left[ (i)^m (-1)^{m+1} \exp(im\phi_3) \right. \\
&\times \quad \left. \left. \left( J_{m+1}(\tilde{\beta}) \exp(i\phi_3) + J_{m-1}(\tilde{\beta}) \exp(-i\phi_3) \right) \right] \right\} d\tilde{r}_1 \bigg|^2. \quad (19)
\end{aligned}$$

### $E$ field polarized parallel to the $y - z$ plane

The case for parallel polarization can be handled in a similar manner as was done for the perpendicular polarization case. Again referring to Fig. 1, the incident electric field now takes the form,

$$\| \tilde{E}^{(inc)} = -\exp(i\alpha\tilde{z}')\hat{j}'. \quad (20)$$

In this case, however, the $x$-component of the scattered electric field is no longer the dominant field component. For the parallel polarization case, the $y$-component of the scattered field is dominant for all $\theta_r$. Therefore, the field incident on the lens for the parallel polarization case is,

$$\bar{E}_1(\bar{\rho}_{10}, \theta, \phi_1) = \bar{E}_r^{(sca)}(\bar{\rho}_{10}, \theta, \phi_1)\sin\theta\sin\phi_1 + \bar{E}_\theta^{(sca)}(\bar{\rho}_{10}, \theta, \phi_1)\cos\theta\sin\phi_1$$
$$+ \bar{E}_\phi^{(sca)}(\bar{\rho}_{10}, \theta, \phi_1)\cos\phi_1. \tag{21}$$

Note that the only differences in the expression for the perpendicular polarization case [Eq. (7)] and the parallel polarization case [Eq. (21)] is the interchanging of the $\sin\phi$ and $\cos\phi$ terms, along with a sign change on the $\phi$ component of the expression. Thus, the derivation presented in the previous section for the perpendicular polarization case would proceed in a manner identical to the parallel polarization case, with the exception of switching the terms $I_m^{\cos}(\bar{\beta}, \phi_3)$ and $I_m^{\sin}(\bar{\beta}, \phi_3)$, and incorporating a sign change on the $\phi$ component of the final expression. The intensity in the image plane for parallel incident polarization can then be written,

$$^{\|}\bar{I}_3(\bar{r}_3, \phi_3) = \left(\frac{\alpha}{2\bar{z}_{32}}\right)^2 \left| \int_0^{\bar{r}_a} \exp\left[\frac{i\alpha\bar{r}_1^2}{2}\left(\frac{1}{\bar{z}_{32}} - \frac{1}{\bar{f}}\right)\right]\bar{r}_1 \left\{ \left(\frac{\sin\theta}{\bar{\rho}_{10}^2}\right)\sum_{l=1}^{\infty}\sum_{m=-l}^{l} l(l+1)a_{lm} \right.$$

$$\times \quad F_{lm}\xi_l^{(1)}(\alpha\bar{\rho}_{10})P_l^{(m)}(\cos\theta)\left[(i)^m(-1)^{m+1}\exp(im\phi_3)\left(J_{m+1}(\bar{\beta})\exp(i\phi_3)\right.\right.$$

$$+ \quad J_{m-1}(\bar{\beta})\exp(-i\phi_3)\bigg)\bigg] + \left(\frac{\alpha\cos\theta}{\bar{\rho}_{10}}\right)\sum_{l=1}^{\infty}\sum_{m=-l}^{l}\left[a_{lm}\xi_l^{(1)'}(\alpha\bar{\rho}_{10})\right.$$

$$\times \quad (-\sin\theta)F_{lm}P_l^{(m)'}(\cos\theta) - mb_{lm}\xi_l^{(1)}(\alpha\bar{\rho}_{10})F_{lm}P_l^{(m)}(\cos\theta)/\sin\theta\bigg]$$

$$\times \quad \left[(i)^m(-1)^{m+1}\exp(im\phi_3)\left(J_{m+1}(\bar{\beta})\exp(i\phi_3) + J_{m-1}(\bar{\beta})\exp(-i\phi_3)\right)\right]$$

$$+ \quad \left(\frac{\alpha}{\bar{\rho}_{10}}\right)\sum_{l=1}^{\infty}\sum_{m=-l}^{l}\left[ima_{lm}\xi_l^{(1)'}(\alpha\bar{\rho}_{10})F_{lm}P_l^{(m)}(\cos\theta)/\sin\theta\right.$$

$$- \quad ib_{lm}\xi_l^{(1)}(\alpha\bar{\rho}_{10})(-\sin\theta)F_{lm}P_l^{(m)'}(\cos\theta)\bigg]\bigg[(i)^{1-m}\bigg(-J_{m+1}(\bar{\beta})$$

$$\times \quad \exp(i\phi_3) + J_{m-1}(\bar{\beta})\exp(-i\phi_3)\bigg)\exp(im\phi_3)\bigg]\bigg\}d\bar{r}_1\bigg|^2. \tag{22}$$

## 2.1 Scattering Coefficient Simplification

In order to numerically evaluate Eqs. (19) and (22), the scattering coefficients $a_{lm}$ and $b_{lm}$ must first be determined. As presented in Ref. [10], this involves the numerical evaluation of

the incident field coefficients which are expressed in terms of the two-dimensional surface integrals shown below,

$$A_{lm} = \frac{1}{l(l+1)\psi_l(\alpha)} \int_0^{2\pi} \int_0^\pi \sin\theta \tilde{E}_r^{(inc)}(\tilde{\rho}=1,\theta,\phi)Y_{lm}^*(\theta,\phi)d\theta d\phi, \tag{23}$$

$$B_{lm} = \frac{1}{l(l+1)\psi_l(\alpha)} \int_0^{2\pi} \int_0^\pi \sin\theta \tilde{H}_r^{(inc)}(\tilde{\rho}=1,\theta,\phi)Y_{lm}^*(\theta,\phi)d\theta d\phi. \tag{24}$$

For the most general case, these surface integrals require substantial amounts of computation time. Fortunately, one can show that these two-dimensional integrals can be reduced to a single one-dimensional line integral for the case of a plane wave incident at an arbitrary angle on a spherical droplet.

### $E$ field polarized perpendicular to $y-z$ plane

Referring again to Fig. 1, a plane wave propagating in the $+z'$ direction with polarization in the $x$ direction (perpendicular to $y-z$ plane) is incident at an angle, $\theta_r$ with respect to the imaging system axis. Mathematically, the incident plane wave can be expressed in its time independent form as,

$$^\perp \tilde{E}^{(inc)} = \exp(i\alpha\tilde{z}')\hat{i}', \tag{25}$$

and

$$^\perp \tilde{H}^{(inc)} = \exp(i\alpha\tilde{z}')\hat{j}'. \tag{26}$$

Noting that the primed and unprimed coordinate systems can be related by,

$$\tilde{y}' = \tilde{y}\cos\theta_r + \tilde{z}\sin\theta_r, \tag{27}$$

and

$$\tilde{z}' = \tilde{z}\cos\theta_r - \tilde{y}\sin\theta_r, \tag{28}$$

the incident field can be written,

$$^\perp \tilde{E}^{(inc)}(\tilde{y},\tilde{z}) = \exp[i\alpha(\tilde{z}\cos\theta_r - \tilde{y}\sin\theta_r)]\hat{i}, \tag{29}$$

10

and

$$^{\perp}\tilde{H}^{(inc)}(\tilde{y}, \tilde{z}) = \exp[i\alpha(\tilde{z}\cos\theta_r - \tilde{y}\sin\theta_r)][\cos\theta_r\hat{j} + \sin\theta_r\hat{k}]. \tag{30}$$

As discussed earlier, to determine the incident field coefficients using the arbitrary beam theory, the radial components of the electric and magnetic fields must be known at all points on the surface of the particle under consideration. The expressions for the incident electromagnetic field can be transformed to spherical coordinates by using the relationships,

$$\tilde{y} \;=\; \tilde{\rho}\sin\theta\sin\phi, \tag{31}$$

$$\tilde{z} \;=\; \tilde{\rho}\cos\theta, \tag{32}$$

$$A_r \;=\; A_x\sin\theta\cos\phi + A_y\sin\theta\sin\phi + A_z\cos\theta, \tag{33}$$

where $A$ may represent either the electric or magnetic field. The incident electric and magnetic field components can then be written,

$$\begin{aligned}
^{\perp}\tilde{E}_r^{(inc)}(\tilde{\rho}, \theta, \phi) \;=\;& \exp[i\alpha\tilde{\rho}(\cos\theta\cos\theta_r)]\exp[-i\alpha\tilde{\rho}(\sin\theta\sin\theta_r\sin\phi)] \\
& \times\; \sin\theta\cos\phi,
\end{aligned} \tag{34}$$

and

$$\begin{aligned}
^{\perp}\tilde{H}_r^{(inc)}(\tilde{\rho}, \theta, \phi) \;=\;& \exp[i\alpha\tilde{\rho}(\cos\theta\cos\theta_r)]\exp[-i\alpha\tilde{\rho}(\sin\theta\sin\theta_r\sin\phi) \\
& \times\; (\sin\theta\cos\theta_r\sin\phi + \cos\theta\sin\theta_r)].
\end{aligned} \tag{35}$$

Expressing the off-axis incident plane wave in terms of the imaging system coordinates is required if one is to analytically integrate the phi dependence in the Fresnel propagation equation, [Eq. (8)]. The incident field coefficient expression given by Eq. (23) then becomes,

$$\begin{aligned}
^{\perp}A_{lm} \;=\;& \frac{1}{l(l+1)\psi_l(\alpha)}\int_0^\pi \exp(i\alpha\tilde{\rho}\cos\theta\cos\theta_r)\sin\theta F_{lm}P_l^{(m)}(\cos\theta)\sin\theta \\
& \times\; \int_0^{2\pi}\cos\phi\exp(-i\alpha\tilde{\rho}\sin\theta\sin\theta_r\sin\phi)\exp(-im\phi)d\phi d\theta.
\end{aligned} \tag{36}$$

11

Using Eqs. (10)-(13), the phi integral can be evaluated exactly giving the final result,

$$
\begin{aligned}
^{\perp}A_{lm} &= \frac{2\pi m(-1)^{1-m}}{l(l+1)\psi_l(\alpha)}\sqrt{\frac{2l+1}{4\pi}\frac{(l-m)!}{(l+m)!}}\frac{1}{\alpha\sin\theta_r} \\
&\times \int_0^\pi \exp(i\alpha\cos\theta\cos\theta_r)P_l^{(m)}(\cos\theta)\sin\theta J_m(\alpha\sin\theta\sin\theta_r)d\theta,
\end{aligned}
\tag{37}
$$

where, $\bar{\rho} = 1$ on the sphere surface. Note that $\sqrt{\frac{2l+1}{4\pi}\frac{(l-m)!}{(l+m)!}}P_l^{(m)}(\cos\theta)$ is equivalent to the spherical harmonics function, $Y_{lm}(\theta,\phi)$ evaluated at $\phi = 0$.

For $^{\perp}B_{lm}$, the simplification procedure is similar,

$$
\begin{aligned}
^{\perp}B_{lm} &= \frac{1}{l(l+1)\psi_l(\alpha)}\int_0^\pi exp(i\alpha\cos\theta\cos\theta_r) \\
&\times \left\{ \int_0^{2\pi} \exp(-i\alpha\sin\theta\sin\theta_r\sin\phi)\sin\theta\cos\theta_r\sin\phi\sin\theta \right. \\
&\times F_{lm}P_l^m(\cos\theta)\exp(-im\phi)d\phi + \int_0^{2\pi}\exp(-i\alpha\sin\theta\sin\theta_r\sin\phi) \\
&\times \left. \cos\theta\sin\theta_r\sin\theta F_{lm}P_l^m(\cos\theta)\exp(-im\phi)d\phi\right\}d\theta.
\end{aligned}
\tag{38}
$$

In this case, there are two phi integrals which can again be evaluated exactly using Eqs. (10)-(13) to yield the final result,

$$
\begin{aligned}
^{\perp}B_{lm} &= \frac{\pi}{l(l+1)\psi_l(\alpha)}\sqrt{\frac{2l+1}{4\pi}\frac{(l-m)!}{(l+m)!}}\int_0^\pi\exp(i\alpha\cos\theta\cos\theta_r) \\
&\times \sin\theta P_l^{(m)}(\cos\theta)\left\{\cos\theta_r\sin\theta\left[(i)^{2m-1}\left(J_{m+1}(\alpha\sin\theta\sin\theta_r)\right.\right.\right. \\
&- \left.\left.\left. J_{m-1}(\alpha\sin\theta\sin\theta_r)\right)\right] + \cos\theta\sin\theta_r\left[2J_m(\alpha\sin\theta\sin\theta_r)(-1)^m\right]\right\}d\theta.
\end{aligned}
\tag{39}
$$

The negative $m$ terms in Eqs. (37) and (39) can be related to the positive $m$ terms by using the relations, $F_{l,-m}P_l^{(-m)}(\cos\theta) = (-1)^m F_{lm}P_l^{(m)}(\cos\theta)$ [11] and $J_{-m}(\gamma) = (-1)^m J_m(\gamma)$ [12], giving

$$
^{\perp}A_{l,m} = -(^{\perp}A_{l,-m}),
\tag{40}
$$

$$
^{\perp}B_{l,m} = {}^{\perp}B_{l,-m},
\tag{41}
$$

with

$$
^{\perp}A_{l,0} = 0,
\tag{42}
$$

$$
^{\perp}B_{l,0} \neq 0.
\tag{43}
$$

### $E$ field polarized parallel to $y - z$ plane

Referring again to Fig. 1, an incident plane wave polarized parallel to the $y - z$ plane can be expressed as,

$$\parallel \bar{E}^{(inc)} = -\exp(i\alpha \tilde{z}')\hat{j}',\tag{44}$$

and

$$\parallel \bar{H}^{(inc)} = \exp(i\alpha \tilde{z}')\hat{i}'.\tag{45}$$

Comparing the incident field descriptions given by Eqs. (25) and (26) for the perpendicular polarization case, to Eqs. (44) and (45) for the parallel polarization case, one observes that the electric and magnetic field description have been transposed with a corresponding sign change in the electric field term. Therefore, the scattering coefficient evaluation for the parallel polarization case would proceed in an identical manner to the perpendicular case yielding the result,

$$
\begin{aligned}
\parallel A_{lm} = -(^{\perp}B_{lm}) \;=\; & \frac{-\pi}{l(l+1)\psi_l(\alpha)}\sqrt{\frac{2l+1}{4\pi}\frac{(l-m)!}{(l+m)!}}\int_0^{\pi}\exp(i\alpha\cos\theta\cos\theta_r)\sin\theta P_l^{(m)}(\cos\theta)\\
& \times\;\left\{\cos\theta_r\sin\theta\left[(i)^{2m-1}\Big(J_{m+1}(\alpha\sin\theta\sin\theta_r)-J_{m-1}(\alpha\sin\theta\sin\theta_r)\Big)\right]\right.\\
& +\;\left.\cos\theta\sin\theta_r\left[2J_m(\alpha\sin\theta\sin\theta_r)(-1)^m\right]\right\}d\theta,
\end{aligned}\tag{46}
$$

and

$$
\begin{aligned}
\parallel B_{lm} = {}^{\perp}A_{lm} \;=\; & \frac{2\pi m(-1)^{1-m}}{l(l+1)\psi_l(\alpha)}\sqrt{\frac{2l+1}{4\pi}\frac{(l-m)!}{(l+m)!}}\frac{1}{\alpha\sin\theta_r}\\
& \times\;\int_0^{\pi}\exp(i\alpha\cos\theta\cos\theta_r)P_l^{(m)}(\cos\theta)\sin\theta J_m(\alpha\sin\theta\sin\theta_r)d\theta.
\end{aligned}\tag{47}
$$

For the parallel polarization case, symmetry in the $+m$ and $-m$ yields,

$$\parallel A_{l,m} \;=\; \parallel A_{l,-m},\tag{48}$$

$$\parallel B_{l,m} \;=\; -(\parallel B_{l,-m}),\tag{49}$$

with

$$\parallel A_{l,0} \;\neq\; 0,\tag{50}$$

$$\parallel B_{l,0} \;=\; 0.\tag{51}$$

13

Equations (46) through (51) completely determine the incident field coefficients for a spherical particle illuminated by an off-axis plane wave. Using the remaining expressions for the coefficients given in Ref. [10], all scattering coefficients (i.e., $a_{lm}$ and $b_{lm}$ terms) for both polarization states can now be calculated for a plane wave incident at an arbitrary angle on a spherical aerosol particle.

## 2.2 Special case for $\theta_r = \pi/2$

Another useful simplification in the scattering coefficient evaluation can be implemented for the physically important case of off-axis scattering when the incident beam propagates orthogonal to the imaging system axis (i.e., $\theta_r = \pi/2$). For this case, the incident field coefficients can be further reduced to,

$$^{\perp}A_{lm} = {}^{\parallel}B_{lm} = \frac{2\pi m(-1)^{1-m}}{\alpha l(l+1)\psi_l(\alpha)} \sqrt{\frac{2l+1}{4\pi} \frac{(l-m)!}{(l+m)!}} \int_0^{\pi} P_l^{(m)}(\cos\theta) \sin\theta J_m(\alpha \sin\theta) d\theta. \qquad (52)$$

The expression given in Eq. (52) can be simplified by examining the behavior of the functions in the integrand over the interval from 0 to $\pi$. Since $\sin\theta = \sin(\pi - \theta)$ over the interval from 0 to $\pi$, the sine function is symmetric over this interval. Likewise, the function $J_m(\alpha\sin\theta)$ is also symmetric over the same interval since the dependence on the variable of integration appears explicitly in the argument $\alpha\sin\theta$. The argument of the associated Legendre function, $\cos\theta$, is anti-symmetric over the same interval [i.e., $-\cos\theta = \cos(\pi - \theta)$]. Using the identity from Arfken [13],

$$P_l^{(m)}(-\cos\theta) = (-1)^{l+m} P_l^{(m)}(\cos\theta), \qquad (53)$$

one observes that the associated Legendre function is symmetric over the interval from 0 to $\pi$ for combinations of $l$ and $m$ such that the sum $(l+m)$ is even. Therefore, both the range of integration and the limits of summation can be reduced by a factor of two giving,

$$[\text{for } (l+m) \text{ even}] \quad {}^{\perp}A_{lm} = {}^{\parallel}B_{lm} = \frac{4\pi m(-1)^{1-m}}{\alpha l(l+1)\psi_l(\alpha)} \sqrt{\frac{2l+1}{4\pi} \frac{(l-m)!}{(l+m)!}}$$

$$\times \int_0^{\pi/2} P_l^{(m)}(\cos\theta) \sin\theta J_m(\alpha \sin\theta) d\theta, \qquad (54)$$

$$[\text{for } (l+m) \text{ odd}] \quad {}^{\perp}A_{lm} = {}^{\parallel}B_{lm} = 0. \qquad (55)$$

14

The simplification for $^\perp B_{lm}$ is analogous, the only difference being the addition of the anti-symmetric cosine factor in the integrand. For this case,

$$[\text{for } (l+m) \text{ even}] \quad ^\perp B_{lm} = -(^\parallel A_{lm}) = 0, \tag{56}$$

$$[\text{for } (l+m) \text{ odd}] \quad ^\perp B_{lm} = -(^\parallel A_{lm}) = \frac{4\pi(-1)^m}{l(l+1)\psi_l(\alpha)}\sqrt{\frac{2l+1}{4\pi}\frac{(l-m)!}{(l+m)!}}$$

$$\times \int_0^{\pi/2} P_l^{(m)}(\cos\theta)\sin\theta\cos\theta J_m(\alpha\sin\theta)d\theta. \tag{57}$$

An additional computational simplification results from the fact that all the incident field coefficients become real for the $\theta_r = \pi/2$ case.

### 2.3 $m$ Summation Simplification

The numerical evaluation of Eqs. (19) and (22) can be reduced by an additional factor of two by utilizing symmetry of the terms contained within the $m$ summation.

**$E$ field polarized perpendicular to the $y - z$ plane**

Denote by $\Gamma$, $\Theta$, and $\Phi$ the portion of Eq. (19) resulting from the scattered $r$, $\theta$, and $\phi$ components, respectively. For the $r$ portion,

$$\Gamma = \sum_{m=-l}^{l} a_{lm} F_{lm} P_l^{(m)}(\cos\theta) I_m^{\cos}(\bar{\beta},\phi_3). \tag{58}$$

From previous results it was found that,

$$a_{l,-m} = -a_{lm}, \tag{59}$$

$$b_{l,-m} = b_{l,m}, \tag{60}$$

$$F_{l,-m} P_l^{(-m)}(\cos\theta) = (-1)^m F_{lm} P_l^{(m)}(\cos\theta), \tag{61}$$

$$I_{-m}^{\cos}(\bar{\beta},\phi_3) = I_m^{\cos *}(\bar{\beta},\phi_3)(-1)^{m-1}, \tag{62}$$

$$I_{-m}^{\sin}(\bar{\beta},\phi_3) = I_m^{\sin *}(\bar{\beta},\phi_3)(-1)^{m-1}, \tag{63}$$

so that Eq. (58) becomes,

$$\Gamma = 2\sum_{m=1}^{l} a_{lm} F_{lm} P_l^{(m)}(\cos\theta)\Re[I_m^{\cos}(\bar{\beta},\phi_3)], \tag{64}$$

15

where $\Re$ refers to the real part of the complex quantity. Proceeding similarly for the $\theta$ and $\phi$ portions of Eq. (19), one obtains

$$\Theta = 2 \sum_{m=1}^{l} \Re[I_m^{\cos}(\tilde{\beta}, \phi_3)] \Big[ a_{lm} \xi_l^{(1)\prime}(\alpha\tilde{\rho}_{10})(-\sin\theta) F_{lm} P_l^{(m)\prime}(\cos\theta)$$

$$- m b_{lm} \xi_l^{(1)}(\alpha\tilde{\rho}_{10}) F_{lm} P_l^{(m)}(\cos\theta)/\sin\theta \Big], \tag{65}$$

and

$$\Phi = -2 \sum_{m=1}^{l} \Im[I_m^{\sin}(\beta, \phi_3)] \Big[ m a_{lm} \xi_l^{(1)\prime}(\alpha\tilde{\rho}_{10}) F_{lm} P_l^{(m)}(\cos\theta)/\sin\theta$$

$$- b_{lm} \xi_l^{(1)}(\alpha\tilde{\rho}_{10})(-\sin\theta) F_{lm} P_l^{(m)\prime}(\cos\theta) \Big] + \Phi(m=0), \tag{66}$$

where $\Im$ refers to the imaginary part of the complex quantity and

$$\Phi(m=0) = i\, b_{l,0} \xi_l^{(1)}(\alpha\tilde{\rho}_{10})(-\sin\theta) F_{l,0} P_l^{(0)\prime}(\cos\theta)$$

$$\times \Big[ J_1\Big(\frac{\alpha\tilde{r}_1\tilde{r}_3}{\tilde{z}_{32}}\Big)\exp(i\phi_3) + J_{-1}\Big(\frac{\alpha\tilde{r}_1\tilde{r}_3}{\tilde{z}_{32}}\Big)\exp(-i\phi_3) \Big]. \tag{67}$$

Note that $\Gamma$, $\Theta$ are zero for $m=0$ because $a_{l,0}=0$, while $\Phi \neq 0$ for $m=0$. Incorporating the symmetry for $m$ into Eq. (19) gives,

$$^{\perp}\tilde{I}_3(\tilde{r}_3,\phi_3) = \Big(\frac{\alpha}{\tilde{z}_{32}}\Big)^2 \Big| \int_0^{\tilde{r}_a} \exp\Big[\frac{i\alpha\tilde{r}_1^2}{2}\Big(\frac{1}{\tilde{z}_{32}}-\frac{1}{\tilde{f}}\Big)\Big] \tilde{r}_1 \Big\langle \Big(\frac{\sin\theta}{\tilde{\rho}_{10}^2}\Big) \sum_{l=1}^{\infty}\sum_{m=1}^{l} l(l+1)\xi_l^{(1)}(\alpha\tilde{\rho}_{10})$$

$$\times\ a_{lm} F_{lm} P_l^{(m)}(\cos\theta)\Re\Big\{(i)^{1-m}\exp(im\phi_3)\Big[-J_{m+1}\Big(\frac{\alpha\tilde{r}_1\tilde{r}_3}{\tilde{z}_{32}}\Big)\exp(i\phi_3)$$

$$+\ J_{m-1}\Big(\frac{\alpha\tilde{r}_1\tilde{r}_3}{\tilde{z}_{32}}\Big)\exp(-i\phi_3)\Big]\Big\} + \Big(\frac{\alpha\cos\theta}{\tilde{\rho}_{10}}\Big)\sum_{l=1}^{\infty}\sum_{m=1}^{l}\Big[a_{lm}\xi_l^{(1)\prime}(\alpha\tilde{\rho}_{10})$$

$$\times\ (-\sin\theta) F_{lm} P_l^{(m)\prime}(\cos\theta) - m b_{lm}\xi_l^{(1)}(\alpha\tilde{\rho}_{10}) F_{lm} P_l^{(m)}(\cos\theta)/\sin\theta\Big]$$

$$\times\ \Re\Big\{(i)^{1-m}\exp(im\phi_3)\Big[-J_{m+1}\Big(\frac{\alpha\tilde{r}_1\tilde{r}_3}{\tilde{z}_{32}}\Big)\exp(i\phi_3) + J_{m-1}\Big(\frac{\alpha\tilde{r}_1\tilde{r}_3}{\tilde{z}_{32}}\Big)$$

$$\times\ \exp(-i\phi_3)\Big]\Big\} + \Big(\frac{\alpha}{\tilde{\rho}_{10}}\Big)\sum_{l=1}^{\infty}\sum_{m=1}^{l}\Big[m a_{lm}\xi_l^{(1)\prime}(\alpha\tilde{\rho}_{10}) F_{lm} P_l^{(m)}(\cos\theta)/\sin\theta$$

$$-\ b_{lm}\xi_l^{(1)}(\alpha\tilde{\rho}_{10})(-\sin\theta) F_{lm} P_l^{(m)\prime}(\cos\theta)\Big]\Im\Big\{(i)^m(-1)^{m+1}$$

$$\times\ \Big[J_{m+1}\Big(\frac{\alpha\tilde{r}_1\tilde{r}_3}{\tilde{z}_{32}}\Big)\exp(i\phi_3) + J_{m-1}\Big(\frac{\alpha\tilde{r}_1\tilde{r}_3}{\tilde{z}_{32}}\Big)\exp(-i\phi_3)\Big]\exp(im\phi_3)\Big\}$$

$$-\ \Big(\frac{\alpha}{2\tilde{\rho}_{10}}\Big)\sum_{l=1}^{\infty}\Phi(m=0)\Big\rangle d\tilde{r}_1\Big|^2. \tag{68}$$

As shown in the previous section, for $\theta_r = \pi/2$ the numerical evaluation of the above expression is simplified since $a_{lm} = 0$ for $(l+m)$ odd and $b_{lm} = 0$ for $(l+m)$ even.

### $E$ field polarized parallel to the $y-z$ plane

The simplification for the parallel polarization case follows in an identical manner to the previous development for perpendicular polarization. The only difference is that in this case the $+m$ and $-m$ scattering coefficients are related by,

$$a_{l,-m} = a_{lm}, \tag{69}$$

$$b_{l,-m} = -b_{lm}. \tag{70}$$

Thus,

$$\Gamma = 2i \sum_{m=1}^{l} a_{lm} F_{lm} P_l^{(m)}(\cos\theta) \Im[I_m^{\sin}(\tilde{\beta}, \phi_3)] + \Gamma(m=0), \tag{71}$$

where,

$$
\begin{aligned}
\Gamma(m=0) &= -l(l+1) a_{l,0} F_{l,0} P_l^{(0)}(\cos\theta) \xi_l^{(1)}(\alpha\tilde{\rho}_{10}) \\
&\quad \times \left[ J_1(\tilde{\beta}) \exp(i\phi_3) + J_{-1}(\tilde{\beta}) \exp(-i\phi_3) \right],
\end{aligned}
\tag{72}
$$

$$
\begin{aligned}
\Theta &= 2i \sum_{m=1}^{l} \Im[I_m^{\sin}(\tilde{\beta}, \phi_3)] \Big[ a_{lm} \xi_l^{(1)\prime}(\alpha\tilde{\rho}_{10})(-\sin\theta) F_{lm} P_l^{(m)\prime}(\cos\theta) \\
&\quad - m b_{lm} \xi_l^{(1)}(\alpha\tilde{\rho}_{10}) F_{lm} P_l^{(m)}(\cos\theta) / \sin\theta \Big] + \Theta(m=0),
\end{aligned}
\tag{73}
$$

where,

$$
\begin{aligned}
\Theta(m=0) &= a_{l,0} \xi_l^{(1)\prime}(\alpha\tilde{\rho}_{10})(\sin\theta) F_{l,0} P_l^{(0)\prime}(\cos\theta) \\
&\quad \times \left[ J_1(\tilde{\beta}) \exp(i\phi_3) + J_{-1}(\tilde{\beta}) \exp(-i\phi_3) \right],
\end{aligned}
\tag{74}
$$

and

$$
\begin{aligned}
\Phi &= 2i \sum_{m=1}^{l} \Re[I_m^{\cos}(\tilde{\beta}, \phi_3)] \Big[ m a_{lm} \xi_l^{(1)\prime}(\alpha\tilde{\rho}_{10}) F_{lm} P_l^{(m)}(\cos\theta) / \sin\theta \\
&\quad - b_{lm} \xi_l^{(1)}(\alpha\tilde{\rho}_{10})(-\sin\theta) F_{lm} P_l^{(m)\prime}(\cos\theta) \Big].
\end{aligned}
\tag{75}
$$

17

Here, $\Phi(m = 0) = 0$ for all $l$ since $b_{l,0} = 0$ for parallel incident polarization. Incorporating the symmetry for $m$ into the parallel polarization case gives,

$$
\begin{aligned}
^{\parallel}\tilde{I}_3(\tilde{r}_3, \phi_3) &= \left(\frac{\alpha}{\tilde{z}_{32}}\right)^2 \left| \int_0^{\tilde{r}_a} \exp\left[\frac{i\alpha\tilde{r}_1^2}{2}\left(\frac{1}{\tilde{z}_{32}} - \frac{1}{\tilde{f}}\right)\right]\tilde{r}_1 \left\langle \left(\frac{\sin\theta}{2\tilde{\rho}_{10}^2}\right)\sum_{l=1}^{\infty}\Gamma(m = 0) \right. \right. \\
&\quad + \left(\frac{i\sin\theta}{\tilde{\rho}_{10}^2}\right)\sum_{l=1}^{\infty}\sum_{m=1}^{l} l(l+1)\xi_l^{(1)}(\alpha\tilde{\rho}_{10})a_{lm}F_{lm}P_l^{(m)}(\cos\theta)\Im\left\{(i)^m(-1)^{m+1}\right. \\
&\quad \times \left. \exp(im\phi_3)\left[J_{m+1}\left(\frac{\alpha\tilde{r}_1\tilde{r}_3}{\tilde{z}_{32}}\right)\exp(i\phi_3) + J_{m-1}\left(\frac{\alpha\tilde{r}_1\tilde{r}_3}{\tilde{z}_{32}}\right)\exp(-i\phi_3)\right]\right\} \\
&\quad + \left(\frac{\alpha\cos\theta}{2\tilde{\rho}_{10}}\right)\sum_{l=1}^{\infty}\Theta(m = 0) + \left(\frac{i\alpha\cos\theta}{\tilde{\rho}_{10}}\right)\sum_{l=1}^{\infty}\sum_{m=1}^{l}\left[a_{lm}\xi_l^{(1)'}(\alpha\tilde{\rho}_{10})(-\sin\theta)\right. \\
&\quad \times \left. F_{lm}P_l^{(m)'}(\cos\theta) - mb_{lm}\xi_l^{(1)}(\alpha\tilde{\rho}_{10})F_{lm}P_l^{(m)}(\cos\theta)/\sin\theta\right]\Im\left\{(i)^m(-1)^{m+1}\right. \\
&\quad \times \left. \exp(im\phi_3)\left[J_{m+1}\left(\frac{\alpha\tilde{r}_1\tilde{r}_3}{\tilde{z}_{32}}\right)\exp(i\phi_3) + J_{m-1}\left(\frac{\alpha\tilde{r}_1\tilde{r}_3}{\tilde{z}_{32}}\right)\exp(-i\phi_3)\right]\right\} \\
&\quad + \left(\frac{i\alpha}{\tilde{\rho}_{10}}\right)\sum_{l=1}^{\infty}\sum_{m=1}^{l}\left[ma_{lm}\xi_l^{(1)'}(\alpha\tilde{\rho}_{10})F_{lm}P_l^{(m)}(\cos\theta)/\sin\theta - b_{lm}\xi_l^{(1)}(\alpha\tilde{\rho}_{10})\right. \\
&\quad \times \left. (-\sin\theta)F_{lm}P_l^{(m)'}(\cos\theta)\right]\Re\left\{(i)^{1-m}\left[-J_{m+1}\left(\frac{\alpha\tilde{r}_1\tilde{r}_3}{\tilde{z}_{32}}\right)\right.\right. \\
&\quad \times \left.\left.\left. \exp(i\phi_3) + J_{m-1}\left(\frac{\alpha\tilde{r}_1\tilde{r}_3}{\tilde{z}_{32}}\right)\exp(-i\phi_3)\right]\exp(im\phi_3)\right\}\right\rangle d\tilde{r}_1 \right|^2 .
\end{aligned}
\tag{76}
$$

Again, for $\theta_r = \pi/2$ the numerical evaluation of the above expression is further simplified since $a_{lm} = 0$ for $(l + m)$ even and $b_{lm} = 0$ for $(l + m)$ odd.

## 3. Computational Results and Discussion

As an initial verification on the theoretical development and Fortran computer codes, calculation were performed for the imaging case corresponding to $\theta_r \to 0$. For this situation, the off-axis calculations for both incident polarization states were in agreement with results generated from the Fortran codes for the on-axis imaging development (with the incident field deleted from the image) which was presented in an earlier paper. [14]

The calculations to be presented in this section will examine the influence of particle size, incident polarization, incident beam angle, and complex refractive index on the observed intensity distribution in the image plane. The major objective will be to verify that the theoretical development is providing results consistent with physical observation and previously verified theories.

18

For the cases to follow and unless otherwise stated, all particles are assumed to be in-focus with $(z_1 - z_0) = 52.5$ mm, $z_{32} = 1050$ mm, $f = 50$ mm, and $r_a = 2.5$ mm. All calculated intensity values have been normalized such that a value of unity represents the normalized intensity in the image plane for a particle with refractive index $\bar{n} = 1.0 + 0.0i$ illuminated by an on-axis plane wave. The normalized spatial coordinates in the image plane have accounted for the optical magnification of the imaging system.

A qualitative representation of the intensity distribution in the image plane can be obtained by examining the two-dimensional intensity plot shown in Fig. 2. This particular case corresponds to a 10 $\mu$m diameter droplet, illuminated by a $\lambda = 0.501$ $\mu$m plane wave, incident at $\theta_r = 90$ degrees. The complex refractive index of the particle is $\bar{n} = 1.35 + 10^{-5}i$. As shown in Fig. 2, there are two high intensity regions, or glare spots, appearing along the $\bar{y}_3$ axis. One peak appears on both the positive and negative branches of $\bar{y}_3$. Note that the intensity distribution is symmetric with respect to the $\bar{y}_3$ axis but is asymmetric with respect to the $\bar{x}_3$ axis. This plot shows general similarities to the experimental images presented by Ashkin and Dziedzic [3] for 13 $\mu$m silicone oil droplets illuminated by $\theta_r = 90$ degree visible light. Although this type of plot is useful for examining general trends, quantitative comparisons between differing cases is difficult. Therefore, the remaining calculations to be presented will examine the intensity distributions in the image plane as a function of the single spatial variable, $\bar{y}_3$. Calculations were also performed for observation points along the $\bar{x}_3$ axis but have been omitted in the results to follow since the computed intensity values are generally significantly smaller than those along the $\bar{y}_3$ axis and do not provide any significant information.

Figure 3 shows the intensity distribution in the image plane as a function of the normalized position, optical properties, and incident polarization for $\alpha = 62.706$ ($2a = 10$ $\mu$m, $\lambda = 0.501$ $\mu$m). As stated above, the intensity values were computed along the particle diameter corresponding to the $\bar{y}_3$ axis in the image plane (i.e., $\phi_3 = \pi/2, 3\pi/2$). The false contrast plot, presented in Fig. 2, is also shown in the top graph of Fig. 3. Several items are of interest in this figure. The appearance of an intensity peak, due to specular reflection at the front particle surface, is observed

19

for $\theta_r = 90$ degree incident illumination. This specular reflection would occur for light making an incident angle of 45 degrees and should appear at a normalized location of $\bar{y}_3 = -0.707$ (dotted line) in the image plane. The appearance of the intensity peak on the $-\bar{y}_3$ branch, as opposed to the $+\bar{y}_3$ branch, results from the image inversion caused by the positive imaging lens. Also note that in both the top $[\Re(\bar{n}) = n_r = 1.35]$ and bottom $[\Re(\bar{n}) = n_r = 1.50]$ graphs of Fig. 3, the peak intensity on the $-\bar{y}_3$ branch tends to move inward as $\Im(\bar{n})$ increases. This would be expected from a physical viewpoint since increasing $\Im(\bar{n})$ results in a particle with optical properties becoming more like highly conductive metals in which the reflectivity and absorptivity of the particle are high. For such a case, involving a strongly absorbing particle, one would expect that the only light observed at 90 degrees would be due to the specular reflection at the particle surface. This is, in fact, the case since the major peak in the intensity distribution for $\Im(\bar{n}) = 10^{-1}$ occurs at the specular reflection location for both $\Re(\bar{n})$ investigated. Schematically, the specular reflection is shown in Fig. 4 as the p = 0 ray. The p = 1 ray shown in the figure is representative of a ray which emerges after transmitting through the droplet. Similarly, a ray emerging after 1 internal reflection is denoted as the p = 2 ray, and so on. [15] The extremely small intensities on the $+\bar{y}_3$ branch for $\Im(\bar{n}) = 10^{-1}$ are caused by the strong absorption within the particle, greatly reducing the magnitude of the refracted light (i.e., p = 1, p = 2 ... rays) which reemerges from the particle. In contrast to the strong absorbing case $[\Im(\bar{n}) = 10^{-1}]$, the case of a transparent particle $[\Im(\bar{n}) = 10^{-5}]$ shows a definite two peak structure in the intensity distribution, with one peak appearing on each $\bar{y}_3$ branch. The existence of the peak on the $+\bar{y}_3$ branch is due to the higher order rays (i.e., p = 1, p = 2, ...) which pass through the particle and reemerge to contribute to the intensity distribution in the image plane.

Another observation which can be noted from Fig. 3 is the effect of the incident polarization on the intensity distribution in the image plane. For both transparent and absorbing particles, the peak intensity on the $-\bar{y}_3$ branch is significantly higher for perpendicular incident polarization than for parallel incident polarization. This observation can be explained by examining the behavior of the Fresnel amplitude coefficients as a function of incident angle. [16] As a first approximation,

20

one can assume that the peak on the $-\bar{y}_3$ branch receives its largest contribution from the $p = 0$ ray, incident at $\theta_i = 45$ degrees. For such a case, the amplitude reflection coefficients predict significantly higher reflected intensities for perpendicular incident polarization, consistent with the results of Fig. 3.

Another item examined was the effect, if any, that particle resonances had on the intensity distribution in the image plane. The occurrence of morphology-dependent resonances within spherical particles has been well documented in the literature [3,17,18,19] and only a brief discussion will be given here. Mathematically, a resonance condition occurs for situations in which there exists a pole in the complex scattering coefficients (i.e., $a_{lm}$ or $b_{lm}$). Physically, the resonant condition occurs for specific combinations of complex refractive index, wavelength, and particle diameter such that the incoming light is in phase with the light previously propagating within the particle. This condition results in enhanced field magnitudes both internal and external to the particle boundary. Figure 5 shows the integrated intensity at the aperture of the imaging system (plane $z_1$) as a function of the size parameter, for perpendicular incident polarization, $\bar{n} = 1.50 + 10^{-5}i$, and $\theta_r = 90$ degrees. Note that the integrated intensity, presented in Fig. 5, is representative of the total intensity collected by the imaging system but contains no information as to how the intensity will be distributed in the image plane. The two cases to be examined correspond to the nonresonance case ($\alpha = 62.706$ presented earlier) and the resonance case ($\alpha = 62.578$), each denoted by dotted vertical lines. In addition to providing enhanced scattered intensities shown in Fig. 5, the resonance case also corresponds to a peak in the particle absorption efficiency. The absorption efficiency represents the ratio of the rate at which energy is absorbed by the particle to the rate at which energy is incident on the cross-section of the particle.

The resulting images for both the resonance and nonresonance cases, for the perpendicular polarization state, is shown in Fig. 6. As might be expected, the resonance case shows an increased peak intensity and also exhibits a tendency to shift the location of the intensity peaks away from the center of the particle. The concentration of light which occurs near the outer edges of a particle under resonance conditions has been discussed previously [17], and has actually been

21

shown experimentally by Ashkin and Dziedzic [3]. Photographs presented by Ashkin and Dziedzic for a 13 $\mu$m silicone oil drop, for both on and off resonance cases, show trends similar to the calculations presented in Fig. 6. Calculations, corresponding to resonance conditions for parallel incident polarization, were also performed and showed very similar trends.

Also examined was the effect of changing the incident angle of the plane wave, $\theta_r$. Figure 7 shows the intensity distribution in the image plane for both incident polarization states as the incident beam angle is changed from 30 to 90 degrees. The particle diameter is 10 $\mu$m, index of refraction $\bar{n} = 1.50 + 10^{-5}i$, and incident wavelength 0.501 $\mu$m. For decreasing $\theta_r$, the radial location of the peak intensity on the $-\tilde{y}_3$ branch is seen to move inward toward the imaging system axis while the magnitude of the peak intensity shows a significant increase. This intensity increase is expected since small aerosol particles tend to scatter light more efficiently in the forward direction. Note that for the perpendicular polarization case, the peak intensity for the $\theta_r = 90$ degree case occurs on the $-\tilde{y}_3$ branch while all other cases show the peak occurring on the $+\tilde{y}_3$ branch.

The final set of calculations examine the influence of increasing particle size. Figure 9 presents calculations for both a 25 $\mu$m (top) and 40 $\mu$m (bottom) diameter particle with complex refractive index $\bar{n} = 1.35 + 10^{-5}i$. The incident beam angle, $\theta_r$ was fixed at 90 degrees while the incident wavelength was 0.5 $\mu$m for both cases. The results show that the peak resulting from the p = 0 ray increases in magnitude and tends to become narrower as the particle diameter increases. In contrast, however, the peak magnitudes appearing on the $+\tilde{y}_3$ branch, which results from contributions from higher order rays, remains essentially unchanged at $\approx 10^{-4}$ for particle diameters ranging from 10 to 40 $\mu$m. The existence of the intensity peak appearing near the rear hemisphere of the droplet has helped in understanding our previous experimental observations regarding high energy KrF laser interaction with water droplets. [4]

## 4. Summary

A theoretical model has been presented for calculation of the off-axis image of a spherical particle illuminated by a plane wave incident at an arbitrary angle. The technique is valid for

either transparent or opaque particle and has no restrictions on the allowable direction or degree of particle defocus within the imaging system. The model has made use of the arbitrary beam theory to calculate the external electric field resulting from the laser/aerosol interaction and scalar theory for calculation of the resulting field in the image plane. This technique provides an alternative to using the Huygens-Fresnel propagation formula which requires a two-dimensional integration over the aperture. The use of arbitrary beam theory technique is advantageous for situations in which the number of evaluation points is relatively small or for cases in which storage limitations present a problem. Calculations for both transparent and absorbing particles, ranging in size from 10 to 40 $\mu$m in diameter, illuminated by $\lambda \approx 0.5$ $\mu$m radiation, have shown results consistent with expected physical behavior and previously verified theories. The theoretical model will have important applications in interpreting results involving both linear and nonlinear laser/aerosol interaction with aerosol particles.

## 5. Acknowledgments

## 6. References

[1] H.C. van de Hulst and R.T. Wang, "Glare Spots," proceeding of the 2nd International Congress on Optical Particle Sizing, Arizona State University printing services, 40-49, March 5-8, 1990.

[2] J.A. Lock and J.R. Woodruff, "Non-Debye enhancements in the Mie scattering of light from a single water droplet," Appl. Opt., **28** (3), 523-529 (1989).

[3] A. Ashkin and J.M. Dziedzic, "Observation of optical resonances of dielectric spheres by light scattering," Appl. Opt., **20** (10), 1803-1814 (1981).

[4] D.R. Alexander, S.A. Schaub, J. Zhang, D.E. Poulain, and J.P. Barton, "Scattering of incident KrF laser radiation resulting from the laser-induced breakdown of $H_2O$ droplets," Opt. Lett. **14** (11), 548-550 (1989).

[5] R.G. Pinnick, P. Chylek, M. Jarzembski, E. Creegan, V. Srivastava, G. Fernandez, J.D. Pendleton, and A. Biswas, "Aerosol-induced laser breakdown thresholds: wavelength dependence," Appl. Opt. **27** (5), 987 (1988).

[6] P. Chylek, M.A. Jarzembski, and N.Y. Chou, "Effect of size and material of liquid spherical particles on laser-induced breakdown," Appl. Phys. Lett., **49** (21), 1475-1477 (1986).

[7] G. Mie, "Beiträge zur Optik trüber Medien, speziell kolloidaler Metallösungen," Ann. Phys. **25**, 377 (1908).

[8] P. Debye, "Der Lichtdruck auf Kugeln von beliebigem Material," Ann. Phys. **30**, 57 (1909).

[9] J.W. Goodman, *Introduction to Fourier Optics*, McGraw-Hill, New York (1968).

[10] J.P. Barton, D.R. Alexander and S.A. Schaub, "Internal and near-surface electromagnetic field for a spherical particle irradiated by a focused laser beam," J. Appl. Phys. **64** (4), 1632-1639 (1988).

[11] J.D. Jackson, *Classical Electrodynamics*, 2nd Edition, John Wiley & Sons, NY, 1975.

24

[12] *Handbook of Mathematical Function*, M. Abramowitz and I. Stegun, eds., Dover, New York, NY (1972).

[13] G. Arfken, *Mathematical Methods for Physicists*, 3rd Ed., Academic Press, Orlando, FL (1985).

[14] S.A. Schaub, D.R. Alexander, and J.P. Barton, "Theoretical model of the laser imaging of small aerosols: applications to aerosol sizing," ~~submitted for publication to~~ to be published in Appl. Opt. May 1990. X

[15] W.D. Bachalo, "Analysis and testing of a new method for drop size measurement using laser light scatter interferometry," Contract Report for NAS3-23684 (NASA Lewis), November 1983.

[16] E. Hecht, *Optics*, 2nd Edition, Addison-Wesley, Reading, MA (1987).

[17] S.C. Hill and R.E. Benner, "Morphology-dependent resonances," *Optical effects associated with small aerosol particles*, P.W. Barber and R.K. Chang, eds., 3-61, World Scientific Publ., Teanech, NJ (1988).

[18] J.P. Barton, D.R. Alexander, and S.A. Schaub, "Internal fields of a spherical particles illuminated by a tightly focused laser beam: Focal point positioning effects at resonance," J. Appl. Phys., **65** (8), 2900-2906 (1989).

[19] J-Z. Zhang, D.H. Leach, and R.K. Chang, "Photon lifetime within a droplet: temporal determination of elastic and stimulated Raman scattering," Opt. Lett., **13**, 270 (1988).
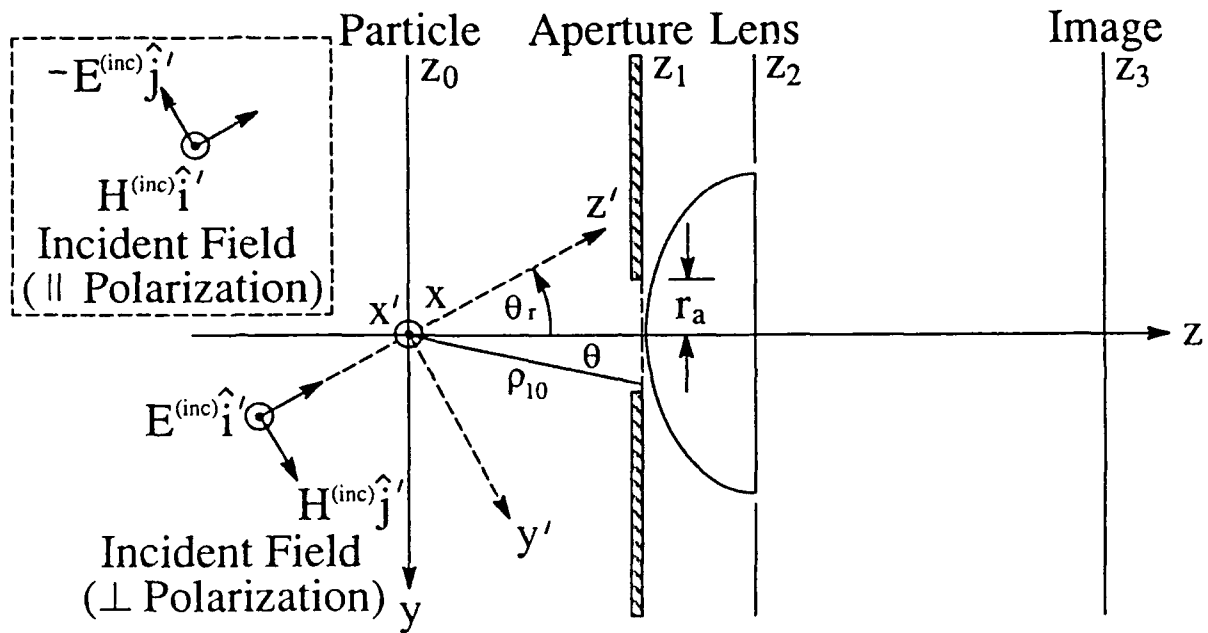
## 7. Figure Labels

Fig. 1. Imaging geometry for off-axis incident beam illumination for both perpendicular incident polarization ($\perp$) and parallel incident polarization ($\parallel$ - dotted box).
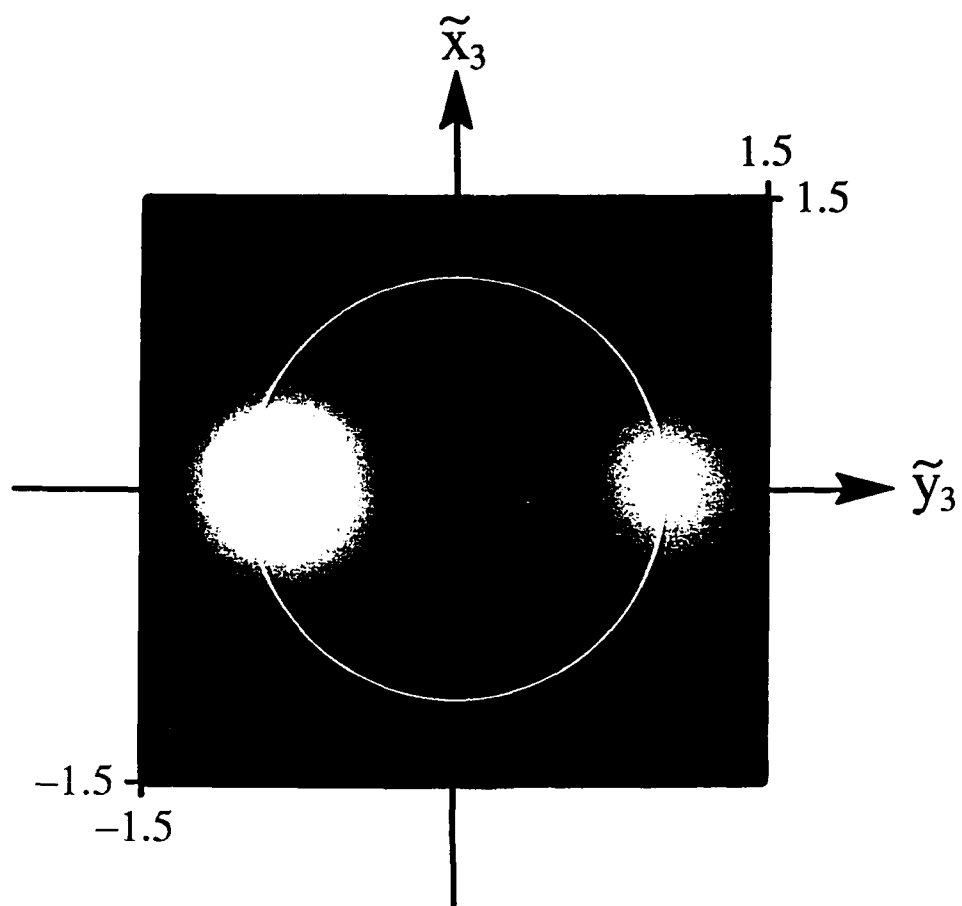
Fig. 2. Relative intensity in the image plane for a 10 $\mu$m diameter particle illuminated by a perpendicularly polarized, $\lambda = 0.501$ $\mu$m, incident plane wave. The index of refraction of the particle is $\bar{n} = 1.35 + 10^{-5}i$ and $\theta_r = 90$ degrees. White shades indicate high intensities, black shades indicate low intensities. The white circle denotes the particle boundary.

Fig. 3. Normalized intensity distribution in the image plane as a function of normalized position, incident polarization, and $\Im(\bar{n})$, for size parameter, $\alpha = 62.706$. Illuminated is by a plane wave at $\theta_r = 90$ degrees. Transparent particles with $\Im(\bar{n}) = 10^{-5}$ are denoted by T, while opaque particles with $\Im(\bar{n}) = 10^{-1}$ are denoted by O. Top graph: $\Re(\bar{n}) = 1.35$; bottom graph: $\Re(\bar{n}) = 1.50$.
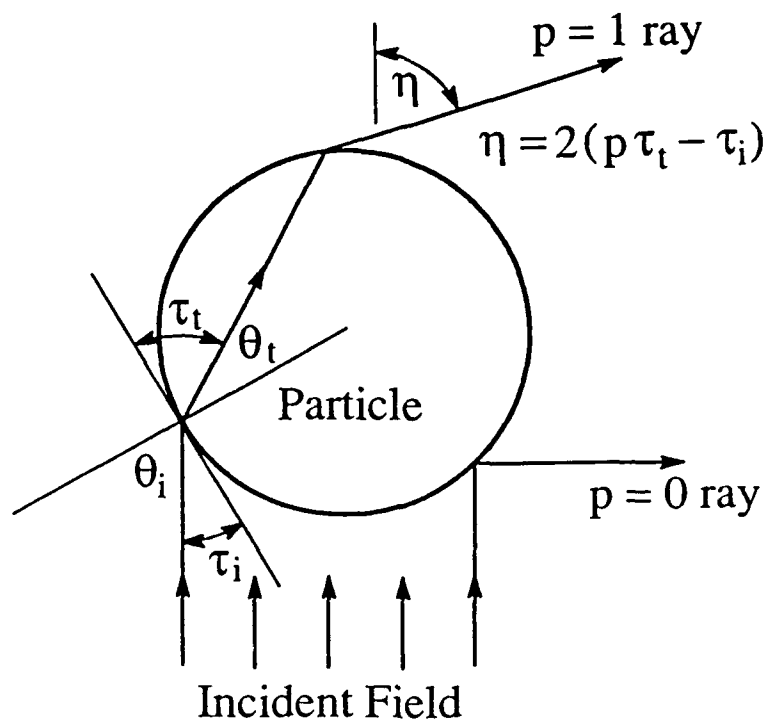
Fig. 4. Schematic showing the characterization of scattered light rays resulting from the interaction of a plane wave with a spherical particle.
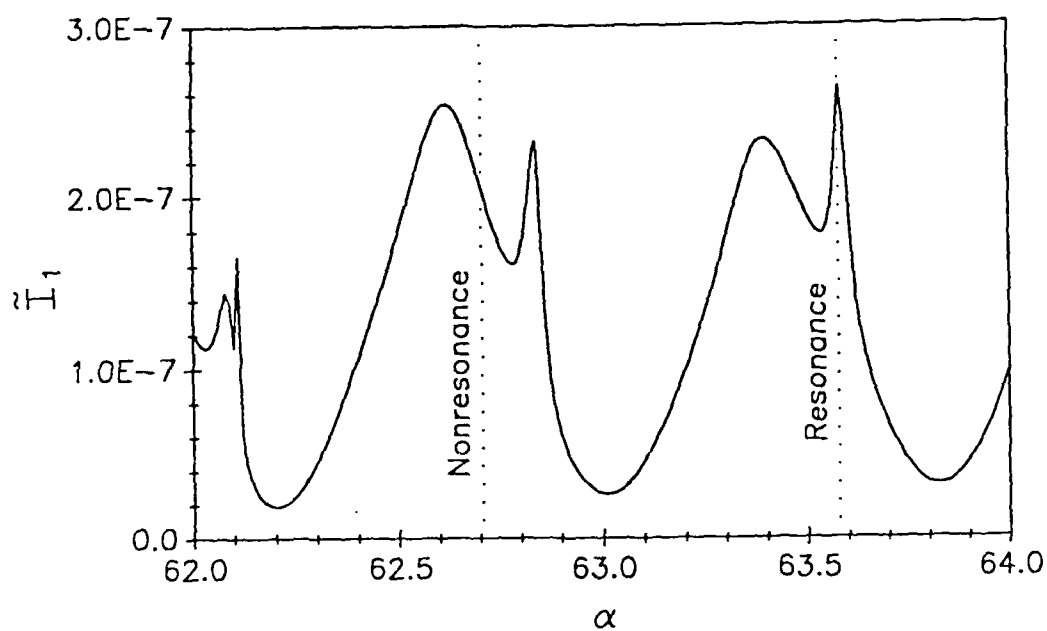
Fig. 5. Integrated intensity at the aperture of the imaging system as a function of the particle size parameter for perpendicular incident polarization, $\bar{n} = 1.50 + 10^{-5}i$, and $\theta_r = 90$ degrees.
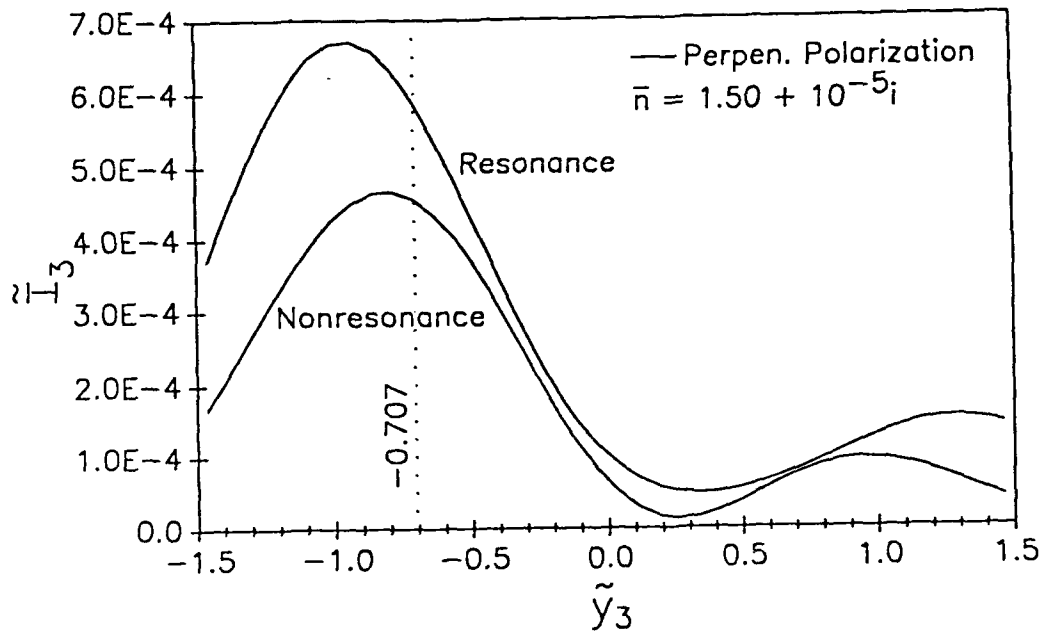
Fig. 6. Intensity as a function of radial position for perpendicular polarization and $\alpha$ (nonresonance) = 62.706 and $\alpha$ (resonance) = 63.578. The particle is 10 $\mu$m in diameter with $\bar{n} = 1.50 + 10^{-5}i$ and $\theta_r = 90$ degrees.
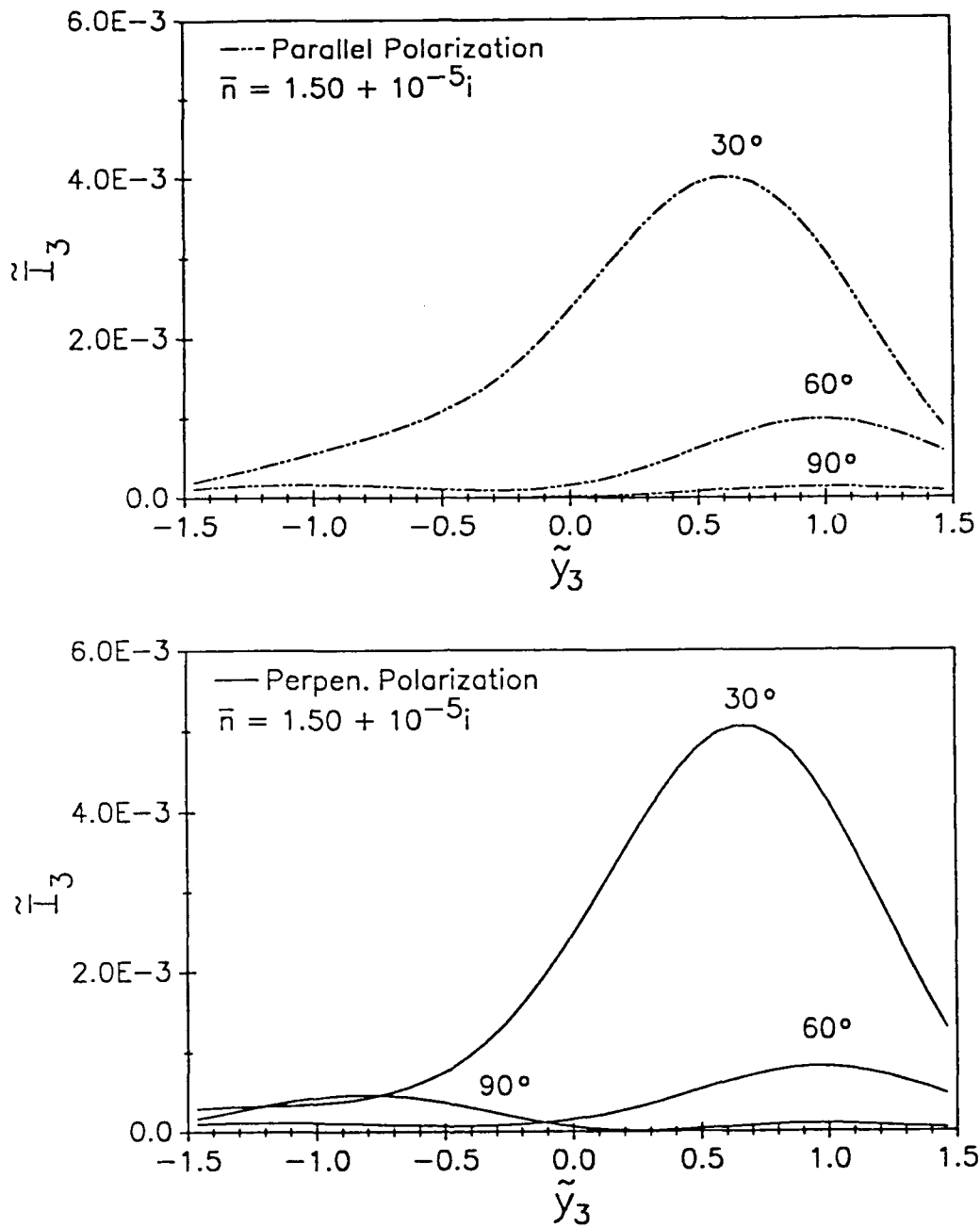
Fig. 7. Normalized intensity in the image plane as a function of normalized position and incident beam angle for both parallel and perpendicular incident polarization. The particle is 10 $\mu$m in diameter with $\bar{n} = 1.50 + 10^{-5}i$. The incident wavelength is 0.501 $\mu$m.
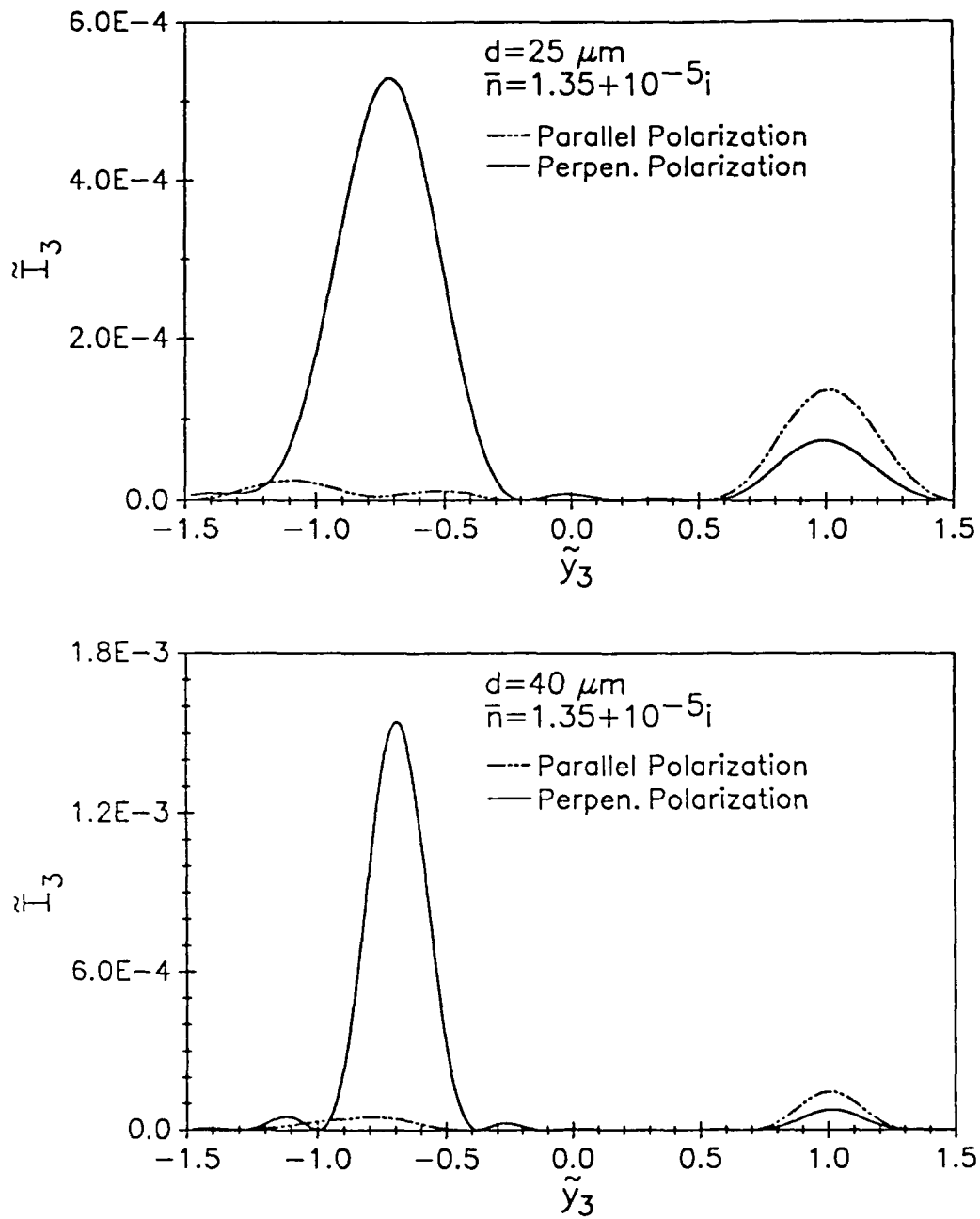
Fig. 8. Normalized intensity as a function of normalized position for a particle with complex refractive index, $\bar{n} = 1.35 + 10^{-5}$i. The particle diameters are 25 $\mu$m (top) and 40 $\mu$m (bottom). Illuminated is by a plane wave ($\lambda = 0.5$ $\mu$m) at $\theta_r = 90$ degrees.

Fig. 1. Imaging geometry for off-axis incident beam illumination for both perpendicular incident polarization ($\perp$) and parallel incident polarization ($\parallel$ - dotted box).

Fig. 2. Relative intensity in the image plane for a 10 $\mu$m diameter particle illuminated by a perpendicularly polarized, $\lambda = 0.501$ $\mu$m, incident plane wave. The index of refraction of the particle is $\bar{n} = 1.35 + 10^{-5}i$ and $\theta_r = 90$ degrees. White shades indicate high intensities, black shades indicate low intensities. The white circle denotes the particle boundary.

Fig. 3. Normalized intensity distribution in the image plane as a function of normalized position, incident polarization, and $\Im(\bar{n})$, for size parameter, $\alpha = 62.706$. Illuminated is by a plane wave at $\theta_r = 90$ degrees. Transparent particles with $\Im(\bar{n}) = 10^{-5}$ are denoted by T, while opaque particles with $\Im(\bar{n}) = 10^{-1}$ are denoted by O. Top graph: $\Re(\bar{n}) = 1.35$; bottom graph: $\Re(\bar{n}) = 1.50$.

Fig. 4. Schematic showing the characterization of scattered light rays resulting from the interaction of a plane wave with a spherical particle.

Fig. 5. Integrated intensity at the aperture of the imaging system as a function of the particle size parameter for perpendicular incident polarization, $\tilde{n} = 1.50 + 10^{-5}i$, and $\theta_r = 90$ degrees.

Fig. 6. Intensity as a function of radial position for perpendicular polarization and $\alpha$ (nonreso-
nance) = 62.706 and $\alpha$ (resonance) = 63.578. The particle is 10 $\mu$m in diameter with $\bar{n}$ =
1.50 + $10^{-5}$i and $\theta_r$ = 90 degrees.

33

Fig. 7. Normalized intensity in the image plane as a function of normalized position and incident beam angle for both parallel and perpendicular incident polarization. The particle is 10 $\mu$m in diameter with $\bar{n} = 1.50 + 10^{-5}$i. The incident wavelength is 0.501 $\mu$m.

Fig. 8. Normalized intensity as a function of normalized position for a particle with complex refractive index, $\bar{n} = 1.35 + 10^{-5}i$. The particle diameters are 25 $\mu$m (top) and 40 $\mu$m (bottom). Illuminated is by a plane wave ($\lambda = 0.5$ $\mu$m) at $\theta_r = 90$ degrees.

# ELECTROMAGNETIC FIELD FOR A BEAM INCIDENT UPON
# TWO ADJACENT SPHERICAL PARTICLES

J.P. Barton, W. Ma, S.A. Schaub, and D.R. Alexander

Center for Electro-Optics

College of Engineering and Technology

University of Nebraska

Lincoln, NE 68588-0656

## ABSTRACT

Through an application of our previously derived single spherical particle/arbitrary beam interaction theory, an iterative procedure has been developed for the determination of the electromagnetic field for a beam incident upon two adjacent spherical particles. The two particles can differ in size and composition, and can have any positioning relative to each other and relative to the focal point and propagation direction of the incident beam. Example calculations of internal and near field normalized source function ($\sim |\vec{E}|^2$) distributions are presented. Also presented are calculations demonstrating the effect of the relative positioning of the second adjacent particle on far field scattering patterns.

1

# I. INTRODUCTION

Interactive scattering between two adjacent spherical particles can result in an electromagnetic field distribution significantly different from the electromagnetic field distribution that would be obtained for a single particle. The theoretical determination of the electromagnetic field for a *plane wave* incident upon two adjacent spherical particles has been previously considered.[1-6] However, if a focused laser beam is used as the excitation source and the local beam diameter is less than or of the same order as the center-to-center separation distance of the two particles, then the plane wave assumption utilized in these earlier analyses is not valid.

By applying our single spherical particle/arbitrary beam interaction theory,[7] we have developed a procedure for determining the electromagnetic field for a *beam* incident upon two adjacent spherical particles. This analysis is general and, with no additional computational complexity, the two particles can have different sizes and different compositions, and can have any geometrical positioning relative to each other and relative to the focal point and propagation direction of the incident beam. The procedure could be straightforwardly extended to allow multiple incident beams and more than two adjacent particles, but only the single beam incident upon two adjacent particles case will be considered here.

One application of the two spherical particles/arbitrary beam interaction theory involves the determination of the internal particle and near surface electromagnetic fields for arrangements in which a laser beam is focused upon two spherical particles that have been purposely placed adjacent to each other. For example, one particle could be used to further "focus" the laser radiation onto the second particle or the two particles could be arranged to create an interacting resonance condition. Another application of the two spherical particles/arbitrary beam interaction theory is the determination of the effect of the presence of an adjacent second particle on far field scattering patterns. Certain types of particle sizing instruments, such as the phase-Doppler, utilize an analysis of scattered laser light to determine the size of individual particles within a cloud or spray. The analysis is based upon the assumption of single particle scattering. The relative motion of individual particles within a cloud or spray will, however, sporadically bring particles into close proximity of each other and the effect of cooperative scattering between particles on far field scattering characteristics and subsequent particle sizing is of interest. Preliminary calculations have been performed and are presented demonstrating both of these applications of the two spherical particles/arbitrary beam interaction theory.

2

## II. THEORETICAL DEVELOPMENT

The theoretical approach utilized is similar to the "order-of-scattering" technique introduced by Fuller and Kattawar.[5] Since our single spherical particle/arbitrary beam interaction theory[7] permits the determination of the electromagnetic field for a single particle with *any* known incident field (regardless of whether the incident field originates from an external beam, from the scattering of an adjacent particle, or from a combination of these two sources), the procedure is as follows. One particle is designated as particle 1 and the other particle is designated as particle 2. The single particle theory is used to calculate the scattered electromagnetic field of particle 1 due to the incident beam only. The scattered field of particle 1 added to the incident beam field is used as the field incident upon particle 2 and the resulting scattered field of particle 2 is calculated, again by using the single particle theory. The scattered field of particle 2 added to the incident beam field provides an updated field incident upon particle 1 and the scattered field of particle 1 is recalculated. The newly calculated scattered field of particle 1 added to the incident beam field then provides an updated field incident upon particle 2 and the scattered field of particle 2 is recalculated. These successive calculations are continued until there is no longer a significant change in the calculated electromagnetic field. For weakly interacting dual particles, such as particles spaced one or more radii apart surface-to-surface, convergence typically occurs within a few iterations.

The geometrical arrangement for the two spherical particles/arbitrary beam interaction theory is shown in Fig. 1. Consistent with the single particle theory[7] the two particles are assumed to be nonmagnetic, homogeneous spheres located within a nonabsorbing, nonmagnetic, homogeneous medium of dielectric constant, $\epsilon_{ext}$. The size (as indicated by the size parameter, $\alpha = 2\pi a/\lambda_{ext}$ where $a$ is the particle radius) and the composition (as indicated by the particle complex relative refractive index, $\bar{n}$) of the two particles may differ. The calculation is facilitated by orienting the coordinate systems of the two particles [$(x_1, y_1, z_1)$ and $(x_2, y_2, z_2)$], so that the $z$ axes align and, in terms of spherical coordinates $(r, \theta, \phi)$, the azimuthal angles of the two coordinate systems coincide $(\phi_1 = \phi_2)$.

The center of particle 1 is used as the common spatial reference point. As shown in Fig. 1, the center of particle 2 is located a distance $z_{12}$ from particle 1. The incident beam is assumed to be a focused, linearly polarized, Gaussian beam with a beam waist diameter of $2w_0$ and a focal point located at $(x_0, y_0, z_0)$ relative to particle 1. The beam has an associated coordinate system

3

$(x_b, y_b, z_b)$ with the origin at the focal point. The beam propagates in the $+z_b$ axis direction with electric field polarization in the $x_b$ axis direction. The angle $\theta_{bd}$ indicates the direction of beam propagation relative to the y-z plane of the two particles and a second beam angle, $\phi_{bd}$, indicates the direction of the electric field polarization of the beam relative to the x-z plane of the two particles. ($\phi = 0°$ indicates a beam electric field polarization in the x-z plane of the two particles and $\phi = 90°$ indicates a beam electric field polarization perpendicular to the x-z plane of the two particles.) The electromagnetic field components of the incident beam are determined using a fifth-order corrected Gaussian beam description.[8] A reference coordinate system (x,y,z) is located at $(x_{ref}, y_{ref}, z_{ref})$ relative to particle 1 and is used as the coordinate system for outputted electromagnetic field distributions. Spatial quantities are normalized (as indicated by a tilde, ˜) relative to the radius of particle 1 ($a_1$) except for the spatial coordinates of particle 2 ($x_2, y_2, z_2$, and $r_2$) which are normalized relative to the radius of particle 2 ($a_2$). Electromagnetic field components are normalized relative to the electric field magnitude at the beam focal point, $E_0$. (The beam power is directly proportional the square of $E_0$.)[8]

In summary, any arrangement of a beam incident upon two adjacent particles can be defined by the following nondimensional parameters: the size parameters of the two particles ($\alpha_1$ and $\alpha_2$), the complex relative refractive indexes of the two particles ($\bar{n}_1$ and $\bar{n}_2$), the center-to-center separation distance of the two particles ($\tilde{z}_{12}$), the beam focal point location relative to particle 1 ($\tilde{x}_0, \tilde{y}_0, \tilde{z}_0$), the beam waist radius ($\tilde{w}_0$), the beam propagation direction angle ($\theta_{bd}$), the beam polarization orientation angle ($\phi_{bd}$), the dielectric constant of the external medium ($\epsilon_{ext}$), and the location of the output coordinate system relative to particle 1 ($\tilde{x}_{ref}, \tilde{y}_{ref}, \tilde{z}_{ref}$).

The internal $[\vec{E}^{(1w)}(\tilde{r}_1, \theta_1, \phi_1), \vec{H}^{(1w)}(\tilde{r}_1, \theta_1, \phi_1)]$ and scattered $[\vec{E}^{(1s)}(\tilde{r}_1, \theta_1, \phi_1), \vec{H}^{(1s)}(\tilde{r}_1, \theta_1, \phi_1)]$ electromagnetic field components of particle 1 and the internal $[\vec{E}^{(2w)}(\tilde{r}_2, \theta_2, \phi_2), \vec{H}^{(2w)}(\tilde{r}_2, \theta_2, \phi_2)]$ and scattered $[\vec{E}^{(2s)}(\tilde{r}_2, \theta_2, \phi_2), \vec{H}^{(2s)}(\tilde{r}_2, \theta_2, \phi_2)]$ electromagnetic field components of particle 2 are each expressed as a double summation,

$$\sum_{l=1}^{\infty} \sum_{m=-l}^{l},$$

over products of Riccati-Bessel functions and spherical harmonic functions. These series expressions, in nondimensional form as used here, are given in Ref. 9. For each particle, the respective

internal field series coefficients, $c_{lm}, d_{lm}$, and scattered field series coefficients, $a_{lm}, b_{lm}$, can be directly related to the series coefficients of the field incident upon the surface of the particle, $A_{lm}, B_{lm}$, by[9]

$$a_{lm} = \frac{\psi_l'(\bar{n}\alpha)\,\psi_l(\alpha) - \bar{n}\,\psi_l(\bar{n}\alpha)\,\psi_l'(\alpha)}{\bar{n}\,\psi_l(\bar{n}\alpha)\,\xi_l^{(1)'}(\alpha) - \psi_l'(\bar{n}\alpha)\,\xi_l^{(1)}(\alpha)}\,A_{lm},$$ (1)

$$b_{lm} = \frac{\bar{n}\,\psi_l'(\bar{n}\alpha)\,\psi_l(\alpha) - \psi_l(\bar{n}\alpha)\,\psi_l'(\alpha)}{\psi_l(\bar{n}\alpha)\,\xi_l^{(1)'}(\alpha) - \bar{n}\,\psi_l'(\bar{n}\alpha)\,\xi_l^{(1)}(\alpha)}\,B_{lm},$$ (2)

$$c_{lm} = \frac{\xi_l^{(1)'}(\alpha)\,\psi_l(\alpha) - \xi_l^{(1)}(\alpha)\,\psi_l'(\alpha)}{\bar{n}^2\,\psi_l(\bar{n}\alpha)\,\xi_l^{(1)'}(\alpha) - \bar{n}\,\psi_l'(\bar{n}\alpha)\,\xi_l^{(1)}(\alpha)}\,A_{lm},$$ (3)

and

$$d_{lm} = \frac{\xi_l^{(1)'}(\alpha)\,\psi_l(\alpha) - \xi_l^{(1)}(\alpha)\,\psi_l'(\alpha)}{\psi_l(\bar{n}\alpha)\,\xi_l^{(1)'}(\alpha) - \bar{n}\,\psi_l'(\bar{n}\alpha)\,\xi_l^{(1)}(\alpha)}\,B_{lm}$$ (4)

where $A_{lm}, B_{lm}$ are determined from the electromagnetic field incident upon the particle surface $[\vec{E}^{(i)}, \vec{H}^{(i)}]$ by

$$A_{lm} = \frac{1}{l(l+1)\,\psi_l(\alpha)} \int_0^{2\pi} \int_0^{\pi} \sin\theta E_r^{(i)}(a,\theta,\phi)\,Y_{lm}^*(\theta,\phi)\,d\theta\,d\phi$$ (5)

and

$$B_{lm} = \frac{1}{l(l+1)\,\psi_l(\alpha)} \int_0^{2\pi} \int_0^{\pi} \sin\theta\, H_r^{(i)}(a,\theta,\phi)\,Y_{lm}^*(\theta,\phi)\,d\theta\,d\phi.$$ (6)

In Eqs. (1)-(6), $\xi_l^{(1)} = \psi_l - i\chi_l$ where $\psi_l, \chi_l$ are the Riccati-Bessel functions, and $Y_{lm}$ is the spherical harmonic function.

For a beam of no symmetry relative to the particle coordinate system, the surface integrals of Eqs. (5) and (6) must be numerically determined in full. However, for scattered leaving one particle and incident upon the other particle, since the coordinate systems are aligned such that $\phi_1 = \phi_2$, the azimuthal integration can be performed analytically and the surface integrals of Eqs. (5) and (6) can be reduced to numerically simpler line integrals. The detailed equations for the complete iteration procedure are presented in App. A. Once the electromagnetic field series coefficients for both particles have been determined by the iteration procedure of App. A, the

5

electromagnetic field for any spatial location, either internal or external to the particles, can be calculated. The electromagnetic field within particle 1 is determined using the associated internal field series coefficients, $c^1_{lm}, d^1_{lm}$, and the electromagnetic field within particle 2 is determined using the associated internal field series coefficients, $c^2_{lm}, d^2_{lm}$. The electromagnetic field external to the two particles is formed by a sum of the electromagnetic field of the incident beam $[\vec{E}^{(b)}, \vec{H}^{(b)}]$, the scattered field of particle 1 as determined using the associated scattered field series coefficients, $a^1_{lm}, b^1_{lm}$, and the scattered field of particle 2 as determined using the associated scattered field series coefficients, $a^2_{lm}, b^2_{lm}$:

$$\vec{E}^{ext}(\tilde{r}, \theta, \phi) = \vec{E}^{(b)}(\tilde{r}_b, \theta_b, \phi_b) + \vec{E}^{(1s)}(\tilde{r}_1, \theta_1, \phi_1) + \vec{E}^{(2s)}(\tilde{r}_2, \theta_2, \phi_2) \tag{7}$$

and

$$\vec{H}^{ext}(\tilde{r}, \theta, \phi) = \vec{H}^{(b)}(\tilde{r}_b, \theta_b, \phi_b) + \vec{H}^{(1s)}(\tilde{r}_1, \theta_1, \phi_1) + \vec{H}^{(2s)}(\tilde{r}_2, \theta_2, \phi_2). \tag{8}$$

The correctness of the two spherical particles/arbitrary beam interaction theory was verified, in the plane wave limit, by making comparisons with an existing plane wave theory. The plane wave limit for the beam theory is easily obtained by setting the beam waist parameter to a large value (e.g. $\tilde{w}_0 = 1000$). Data were generated and plotted using parameters corresponding to Figs. 2-4 in the plane wave theory paper of Fuller, Kattawar, and Wang.[4] In Figs. 2-4 of this paper,[4] the far field scattering intensity at a fixed incremental angle relative to the angle of incidence was plotted as a function of the angle of incidence for incremental angles of 70°, 90°, and 110°. This was done for a condition of the two particles in contact and for a condition of the two particles separated. Incident electric field polarization perpendicular to the plane of observation and incident electric field polarization parallel to the plane of observation were both considered. For each of these conditions, there were no perceptible differences between the plane wave limit results of the beam theory and the corresponding plane wave theory results of Fuller, Kattawar, and Wang.[4]

## II. INTERNAL AND NEAR FIELD CALCULATIONS

Example calculations of internal and near field normalized source function, $\tilde{S} = |\vec{E}|^2/E_0^2$, distributions are shown in Figs. 2, 4, 6, and 7. In Figs. 2 and 4, the normalized source function distributions are given both graphically and in false contrast visualization (white $\Leftrightarrow$ high, gray $\Leftrightarrow$ medium, black $\Leftrightarrow$ low). Only the false contrast visualization is given in Figs. 6 and 7.

Figure 2 presents the internal and near field normalized source function distribution in the x-z plane for a linearly polarized (electric field polarization perpendicular to the x-z plane, $\phi_{bd} = 90°$), 100 $\mu m$ waist diameter $CO_2$ laser beam ($\lambda = 10.6 \ \mu m$) incident upon two 45 $\mu m$ diameter water droplets ($\bar{n} = 1.179 + 0.072i$) separated by 35 $\mu m$ surface-to-surface ($z_{12} = 80 \ \mu m$). The beam is directed through the centers of the two spheres ($\theta_{bd} = 0°$, $x_0 = y_0 = 0$, $z_0 = 40 \ \mu m$). These conditions correspond to an experiment performed within our laboratory in which a $CO_2$ laser beam was directed upon two parallel streams of water droplets so that the illuminated droplet would act as a lens to focus the laser light upon the shadow side droplet.[10] This focusing effect is apparent in the theoretical calculation presented in Fig. 2 where the maximum value of the internal normalized source function occurs at the front surface (illuminated side) of the shadow side droplet. (In the false contrast visualization, the boundaries of the two particles are indicated by white-lined circles.) For these conditions, the front surface of the shadow side droplet would be preferentially heated and, for sufficiently high laser fluence, the front surface of the shadow side droplet would explosively vaporize and subsequently fragment. Figure 3 shows an experimentally obtained pulsed laser image (the imaging system is described in Ref. 11) of the fragmentation of the shadow side droplet resulting from the "focusing" of the incident $CO_2$ laser light by the illuminated side droplet.

Figure 4 provides a normalized source function distribution for a hypothetical case that demonstrates the ability to perform calculations for arrangements where the particles are unequal in size, dissimilar in composition, and located off the propagation axis of the beam. In Fig. 4, a 40 $\mu m$ waist diameter $CO_2$ laser beam is incident upon a 50 $\mu m$ diameter methanol droplet ($\bar{n}_1 = 1.395 + 0.0163i$) and a 40 $\mu m$ diameter water droplet ($\bar{n}_2 = 1.179 + 0.072i$) separated by 20 $\mu m$ surface-to-surface. The beam propagates with a directional angle of $\theta_{bd} = 30°$.

In Ref. 12, calculations were performed, using the single particle theory, demonstrating the effect of focal point positioning on the excitation of structural resonances for a tightly focused ($\bar{w}_0 < 1$) beam incident upon a spherical particle. It was found that the resonance could be most

strongly excited by positioning the propagation axis of the beam at the edge of the sphere. The two spherical particles/arbitrary beam theory was applied to investigate the interaction of two adjacent spherical particles at resonance conditions. Parameters were chosen corresponding to having a focused argon-ion laser beam ($\lambda = 0.5145\ \mu m$, $2w_0 = 2\mu m$) incident upon two equal sized water droplets ($\bar{n} = 1.334 + 1.2\times 10^{-9}$i) at the $35^{th}$ electric wave resonance ($2a = 4.9912\ \mu m$).[9] The beam was directed at the edge of particle 1 ($\theta_{bd} = 90°$, $\phi_{bd} = 0°$, $\bar{x}_0 = \bar{y}_0 = 0$, $\bar{z}_0 = -1.165$) so as to obtain maximum excitation of the resonance.[12] Particle 2 was positioned near particle 1 (on the side opposite of the beam) and the interaction was investigated as a function of surface-to-surface separation distance, $\bar{d}_{sep}$. The number of iterations necessary for three digit convergence was found to increase with decreasing separation distance, as shown in Fig. 5. For the resonant particles closely spaced together, $\bar{d}_{sep} \leq 0.13$, the iteration procedure did not converge and, in fact, diverged with increasing number of iterations. The divergence is attributed to the strong feedback between the two resonant particles that occurs at small separation distances. In contrast, for two nonresonant particles ($2a = 4.96\ \mu m$), the iteration procedure converged for all separation distances (including $\bar{d}_{sep} = 0$), as also shown in Fig. 5. For two resonant particles in close proximity, where the interaction between the two particles is strong, the iteration procedure apparently fails and a matrix inversion solution is necessary.[5]

The normalized source function distribution for the beam incident upon two adjacent particles at resonance for a separation distance of $\bar{d}_{sep} = 0.20$ is given in Fig. 6. The ring of high source function just inside the surface of particle 1 is characteristic of the edge excitation of resonance for a single particle, as discussed in Ref. 12. The scattered light from particle 1 excites the resonance in particle 2 which, in turn, feeds back into particle 1. The corresponding nonresonance case is shown in Fig. 7. At nonresonance, particle 2 is relatively unaffected by the presence of the beam incident upon particle 1.

## III. FAR FIELD SCATTERING CALCULATIONS

The far field scattering for a single spherical particle within a focused beam has been previously considered.[13-16] The two spherical particles/arbitrary beam interaction theory was applied to investigate the far field scattering patterns for two adjacent spherical particles within a focused beam. In particular, with particle 1 fixed in position at the focal point of the beam, the position of particle 2 was systematically varied, and the subsequent effect on the far field scattering pattern was studied.

Calculations were performed for parameters corresponding to a hypothetical arrangement of a linearly polarized fundamental argon-ion laser beam ($\lambda = 0.5145$ $\mu$m) of 4 $\mu$m waist diameter (divergence angle $\approx 10°$) incident upon two adjacent 1.8 $\mu$m diameter water droplets ($\bar{n}_1 = \bar{n}_2 = 1.334 + 1.2 \times 10^{-9}$i, $\alpha_1 = \alpha_2 = 11.0$, $\bar{w}_0 = 2.22$). For the cases considered here, particle 1 is fixed in position at the focal point of the beam ($\bar{x}_0 = \bar{y}_0 = \bar{z}_0 = 0$) while the position of particle 2 relative to particle 1 and relative to the propagation axis of the beam was varied. The geometrical arrangement for the far field scattering calculations is shown in Fig. 8. A far field scattering angle, $\theta_{ff}$, is defined relative to the propagation axis of the beam and a particle 2 positioning angle, $\theta_{bd2}$, is defined as the angle between the axis passing through the centers of the two particles and the beam propagation axis. (Note: $\theta_{bd2} = -\theta_{bd}$.)

In Figs. 9-15, the normalized scattering intensity, defined as

$$S_r = \lim_{\bar{r} \Rightarrow \infty} \bar{r}^2 \frac{\frac{c}{8\pi} Re(\vec{E} \times \vec{H})_r}{\frac{c}{8\pi}|E_0|^2}, \tag{9}$$

is plotted as a function of the far field scattering angle, $\theta_{ff}$, in either the $x_b$-$z_b$ plane (the plane parallel to the beam electric field polarization) or the $y_b$-$z_b$ plane (the plane perpendicular to the beam electric field polarization). Figures 9-15 are semilog plots with each vertical division representing a factor of $\times 10$. The individual curves in each Figure are unscaled relative to each other.

Figure 9 presents the reference case of a single particle at the focal point of the beam (particle 2 far removed from the beam). The scattering is shown in both the $x_b - z_b$ plane (curve a.)) and $y_b - z_b$ plane (curve c.)). For comparison, single particle scattering for the same conditions but with plane wave illumination is also given in Fig. 9 (curves b.) and d.), respectively). Since particle

9

1 is located at the focal point of the beam and the particle diameter (1.8 $\mu$m) is less than the beam waist diameter (4.0 $\mu$m), the single particle scattering patterns for beam and plane wave illumination are nearly identical.

To investigate the effect of a second adjacent particle on the far field scattering pattern, a set of calculations were performed with particle 2 placed in the $x_b - z_b$ plane and one diameter surface-to-surface away from particle 1 ($\bar{z}_{12} = 4.0, \phi_{bd} = 0°$). Figure 10 shows the far field scattering for particle 2 positioned at angles of 0° (on the $+z_b$ axis), 30°, 60°, 90° (on the $+x_b$ axis), 120°, 150°, and 180° (on the -$z_b$ axis) relative to the propagation axis of the beam. As can be observed by comparison with Fig.9a.), Fig. 10 indicates the presence of the second particle significantly affects the far field scattering distribution. The strongest effect, as would be expected, occurs when particle 2 is located well within the beam (curves a.), b.), f.), and g.) in Fig. 10) and a relatively weaker effect occurs when particle 2 is at the edge of the beam (curves c.), d.), and e.) in Fig. 10). Figure 11 presents, for the same particle positioning angles of Fig. 10, the far field scattering patterns in the $y_b - z_b$ plane.

Figure 12a.) shows the far field scattering in the $x_b$-$z_b$ plane for particle 2 located on the + $x_b$ axis (perpendicular to the beam propagation axis) one diameter surface-to-surface from particle 1 ($\bar{z}_{12} = 4.0$, $\theta_{bd2} = 90°$). At this location, particle 2 is at the edge of the beam ($\tilde{w}_0 = 2.22$) and the far field scattering distribution roughly resembles that of the corresponding single particle case of Fig 9a.). If particle 2 is further removed from the beam along the $x_b$ axis, then the far field scattering distribution more closely approaches that of a single particle as seen in curves b.) ($\bar{z}_{12} = 6.0$), c.) ($\bar{z}_{12} = 12.0$), d.) ($\bar{z}_{12} = 18.0$), and e.) ($\bar{z}_{12} \Rightarrow \infty$) of Fig. 12. In Fig. 12, particle 2 is in the same plane as the observation plane (the $x_b$-$z_b$ plane) and the far field scattering is noticeably affected even when particle 2 is removed well out of the beam. Figure 13 provides the corresponding scattering patterns in the $y_b$-$z_b$ plane for particle 2 removed along the $x_b$ axis. In Fig. 13, particle 2 is not located in the observation plane (the $y_b - z_b$ plane) and once particle 2 is removed from the main part of the beam ($\bar{z}_{12} > 6.0$), the far field scattering distribution is essentially the same as that of a single particle (Fig. 9c.)).

Figure 14a.) shows the far field scattering in the $x_b$-$z_b$ plane for particle 2 located on the beam propagation axis ($+z_b$ axis) one diameter surface-to-surface from particle 1 ($\theta_{bd2} = 0°$, $z_{12} = 4.0$). The oscillating structure in the far field scattering for this case arises due to interference between

the light scattered by the two identical particles. In the far field, the difference in path length for light leaving the two particles for this case is $|z_{12}\cos\theta_{ff}|$ and interference proportional to $[1 + \cos(\alpha\tilde{z}_{12}\cos\theta_{ff})]$ might be expected. From this expression, if particle 2 is moved further away from particle 1 along the $z_b$ axis ($\tilde{z}_{12}$ is increased) then the frequency of the oscillations in the far field scattering distribution should correspondingly increase. In addition, since the beam is diverging and the intensity incident upon particle 2 decreases as particle 2 is moved away from the focal point, the amplitude of the interference should decrease with increasing $\tilde{z}_{12}$. As particle 2 becomes far removed from particle 1, and from the focal point of the beam, the scattering distribution should converge to that of the single particle (Fig. 9a.)). As seen in Fig. 14, this is indeed observed as particle 2 is moved to $\tilde{z}_{12} = 10.$ (curve b.)), $\tilde{z}_{12} = 20.$ (curve c.)), $\tilde{z}_{12} = 50.$ (curve d.)), and $\tilde{z}_{12} = 100.$ (curve e.)). The corresponding scattering distributions in the $y_b$-$z_b$ plane are shown in Fig. 15. Calculations for particle 2 moved along the -$z_b$ axis (not shown) demonstrated nearly identical results.

11

## IV. SUMMARY

A theoretical approach has been developed for the determination of the electromagnetic field for a beam incident upon two adjacent spherical particles of arbitrary arrangement. Example calculations of internal and near field normalized source function distributions and far field normalized scattering intensity patterns have been presented. Future work will include further such "computational experimentation" and efforts to obtain direct comparisons between theoretical calculations and corresponding experimental measurements.

## ACKNOWLEDGEMENT

# APPENDIX A

## ITERATION PROCEDURE

The iteration procedure for determining the internal and scattered field series coefficients for a beam incident upon two adjacent spheres is as follows. [Note: $P_{lm}(\theta) = Y_{lm}(\theta, 0)$.]

1.) For each of the two particles, determine the incident field series coefficients for beam illumination alone:

$$A_{lm}^{(1b)} = \frac{1}{l(l+1)\psi_l(\alpha_1)} \int_0^{2\pi} \int_0^{\pi} E_{r1}^{(b)}(a_1, \theta_1, \phi_1) Y_{lm}^*(\theta_1, \phi_1) \sin\theta_1 \, d\theta_1 \, d\phi_1, \qquad (A1)$$

$$B_{lm}^{(1b)} = \frac{1}{l(l+1)\psi_l(\alpha_1)} \int_0^{2\pi} \int_0^{\pi} H_{r1}^{(b)}(a_1, \theta_1, \phi_1) Y_{lm}^*(\theta_1, \phi_1) \sin\theta_1 \, d\theta_1 \, d\phi_1, \qquad (A2)$$

$$A_{lm}^{(2b)} = \frac{1}{l(l+1)\psi_l(\alpha_2)} \int_0^{2\pi} \int_0^{\pi} E_{r2}^{(b)}(a_2, \theta_2, \phi_2) Y_{lm}^*(\theta_2, \phi_2) \sin\theta_2 \, d\theta_2 \, d\phi_2, \qquad (A3)$$

and

$$B_{lm}^{(2b)} = \frac{1}{l(l+1)\psi_l(\alpha_2)} \int_0^{2\pi} \int_0^{\pi} H_{r2}^{(b)}(a_2, \theta_2, \phi_2) Y_{lm}^*(\theta_2, \phi_2) \sin\theta_2 \, d\theta_2 \, d\phi_2. \qquad (A4)$$

2.) Determine the initial scattered field series coefficients for particle 1:

$$a_{lm}^1 = \frac{\psi_l'(\bar{n}_1 \alpha_1)\, \psi_l(\alpha_1) - \bar{n}_1 \, \psi_l(\bar{n}_1 \alpha_1)\, \psi_l'(\alpha_1)}{\bar{n}_1 \, \psi_l(\bar{n}_1 \alpha_1)\, \xi_l^{(1)\prime}(\alpha_1) - \psi_l'(\bar{n}_1 \alpha_1)\, \xi_l^{(1)}(\alpha_1)} A_{lm}^{(1b)}, \qquad (A5)$$

and

$$b_{lm}^1 = \frac{\bar{n}_1 \, \psi_l'(\bar{n}_1 \alpha_1)\, \psi_l(\alpha_1) - \psi_l(\bar{n}_1 \alpha_1)\, \psi_l'(\alpha_1)}{\psi_l(\bar{n}_1 \alpha_1)\, \xi_l^{(1)\prime}(\alpha_1) - \bar{n}_1 \, \psi_l'(\bar{n}_1 \alpha_1)\, \xi_l^{(1)}(\alpha_1)} B_{lm}^{(1b)}. \qquad (A6)$$

3.) The following equations provide the main iteration loop to determine the incident field series coefficients for the field scattered from particle 1 incident upon particle 2 $[A_{lm}^{(12)}, B_{lm}^{(12)}]$ and the incident field series coefficients for the field scattered from particle 2 incident upon particle 1 $[A_{lm}^{(21)}, B_{lm}^{(21)}]$.

Determine $A_{lm}^{(12)}, B_{lm}^{(12)}$ from the most recently calculated values of $a_{lm}^1, b_{lm}^1$:

$$A_{lm}^{(12)} = \frac{2\pi}{l(l+1)\psi_l(\alpha_2)} \int_0^\pi E_r^{(12)}(m,\theta_2) P_{lm}(\theta_2) \sin\theta_2 \, d\theta_2 \tag{A7}$$

and

$$B_{lm}^{(12)} = \frac{2\pi}{l(l+1)\psi_l(\alpha_2)} \int_0^\pi H_r^{(12)}(m,\theta_2) P_{lm}(\theta_2) \sin\theta_2 \, d\theta_2 \tag{A8}$$

where

$$E_r^{(12)}(m,\theta_2) = \sum_{l'=1}^{\infty} \left\{ \frac{1}{\tilde{r}_1^2} l'(l'+1) a_{l'm}^1 \xi_{l'}^{(1)}(\alpha_1,\tilde{r}_1) P_{l'm}(\theta_1) \cos(\theta_2 - \theta_1) \right.$$
$$\left. + \frac{\alpha_1}{\tilde{r}_1} [a_{l'm}^1 \xi_{l'}^{(1)\prime}(\alpha_1 \tilde{r}_1) \frac{dP_{l'm}(\theta_1)}{d\theta_1} - m b_{l'm}^1 \xi_{l'}^{(1)}(\alpha_1 \tilde{r}_1) \frac{P_{l'm}(\theta_1)}{\sin\theta_1}] \sin(\theta_2 - \theta_1) \right\} \tag{A9}$$

and

$$H_r^{(12)}(m,\theta_2) = \sum_{l'=1}^{\infty} \left\{ \frac{1}{\tilde{r}_1^2} l'(l'+1) b_{l'm}^1 \xi_{l'}^{(1)}(\alpha_1,\tilde{r}_1) P_{l'm}(\theta_1) \cos(\theta_2 - \theta_1) \right.$$
$$\left. + \frac{\alpha_1}{\tilde{r}_1} [b_{l'm}^1 \xi_{l'}^{(1)\prime}(\alpha_1 \tilde{r}_1) \frac{dP_{l'm}(\theta_1)}{d\theta_1} + m a_{l'm}^1 \xi_{l'}^{(1)}(\alpha_1 \tilde{r}_1) \frac{P_{l'm}(\theta_1)}{\sin\theta_1}] \sin(\theta_2 - \theta_1) \right\} \tag{A10}$$

and where

$$\theta_1 = \tan^{-1}\left[\frac{\alpha_2/\alpha_1 \sin\theta_2}{\alpha_2/\alpha_1 \cos\theta_2 + \tilde{z}_{12}}\right] \tag{A11}$$

and

$$\tilde{r}_1 = \sqrt{(\tilde{z}_{12} + \alpha_2/\alpha_1 \cos\theta_2)^2 + (\alpha_2/\alpha_1 \sin\theta_2)^2}. \tag{A12}$$

Calculate $a_{lm}^2, b_{lm}^2$ from the most recently calculated values of $A_{lm}^{(12)}, B_{lm}^{(12)}$:

$$a_{lm}^2 = \frac{\psi_l'(\bar{n}_2\alpha_2)\,\psi_l(\alpha_2) - \bar{n}_2\,\psi_l(\bar{n}_2\alpha_2)\,\psi_l'(\alpha_2)}{\bar{n}_2\,\psi_l(\bar{n}_2\alpha_2)\,\xi_l^{(1)\prime}(\alpha_2) - \psi_l'(\bar{n}_2\alpha_2)\,\xi_l^{(1)}(\alpha_2)} (A_{lm}^{(12)} + A_{lm}^{(2b)}) \tag{A13}$$

and

$$b_{lm}^2 = \frac{\bar{n}_2\,\psi_l'(\bar{n}_2\alpha_2)\,\psi_l(\alpha_2) - \psi_l(\bar{n}_2\alpha_2)\,\psi_l'(\alpha_2)}{\psi_l(\bar{n}_2\alpha_2)\,\xi_l^{(1)\prime}(\alpha_2) - \bar{n}_2\,\psi_l'(\bar{n}_2\alpha_2)\,\xi_l^{(1)}(\alpha_2)} (B_{lm}^{(12)} + B_{lm}^{(2b)}). \tag{A14}$$

14

Determine $A_{lm}^{(21)}, B_{lm}^{(21)}$ from the most recently calculated values of $a_{lm}^2, b_{lm}^2$:

$$A_{lm}^{(21)} = \frac{2\pi}{l(l+1)\psi_l(\alpha_1)} \int_0^\pi E_r^{(21)}(m,\theta_1) P_{lm}(\theta_1) \sin\theta_1 \, d\theta_1 \qquad (A15)$$

and

$$B_{lm}^{(21)} = \frac{2\pi}{l(l+1)\psi_l(\alpha_1)} \int_0^\pi H_r^{(21)}(m,\theta_1) P_{lm}(\theta_1) \sin\theta_1 \, d\theta_1 \qquad (A16)$$

where

$$E_r^{(21)}(m,\theta_1) = \sum_{l'=1}^\infty \left\{ \frac{1}{\tilde{r}_2^2} l'(l'+1) a_{l'm}^2 \xi_{l'}^{(1)}(\alpha_2, \tilde{r}_2) P_{l'm}(\theta_2) \cos(\theta_1 - \theta_2) \right.$$
$$\left. + \frac{\alpha_2}{\tilde{r}_2} [a_{l'm}^2 \xi_{l'}^{(1)\prime}(\alpha_2 \tilde{r}_2) \frac{dP_{l'm}(\theta_2)}{d\theta_2} - mb_{l'm}^2 \xi_{l'}^{(1)}(\alpha_2 \tilde{r}_2) \frac{P_{l'm}(\theta_2)}{\sin\theta_2}] \sin(\theta_1 - \theta_2) \right\} \qquad (A17)$$

and

$$H_r^{(21)}(m,\theta_1) = \sum_{l'=1}^\infty \left\{ \frac{1}{\tilde{r}_2^2} l'(l'+1) b_{l'm}^2 \xi_{l'}^{(1)}(\alpha_2, \tilde{r}_2) P_{l'm}(\theta_2) \cos(\theta_1 - \theta_2) \right.$$
$$\left. + \frac{\alpha_2}{\tilde{r}_2} [b_{l'm}^2 \xi_{l'}^{(1)\prime}(\alpha_2 \tilde{r}_2) \frac{dP_{l'm}(\theta_2)}{d\theta_2} + ma_{l'm}^2 \xi_{l'}^{(1)}(\alpha_2 \tilde{r}_2) \frac{P_{l'm}(\theta_2)}{\sin\theta_2}] \sin(\theta_1 - \theta_2) \right\} \qquad (A18)$$

and where

$$\theta_2 = \pi - \tan^{-1}\left[\frac{\sin\theta_1}{\tilde{z}_{12} - \cos\theta_1}\right] \qquad (A19)$$

and

$$\tilde{r}_2 = \alpha_1/\alpha_2 \sqrt{(\tilde{z}_{12} - \cos\theta_1)^2 + (\sin\theta_1)^2}. \qquad (A20)$$

Calculate $a_{lm}^1, b_{lm}^1$ from the most recently calculated values of $A_{lm}^{(21)}, B_{lm}^{(21)}$:

$$a_{lm}^1 = \frac{\psi_l'(\bar{n}_1\alpha_1)\psi_l(\alpha_1) - \bar{n}_1\psi_l(\bar{n}_1\alpha_1)\psi_l'(\alpha_1)}{\bar{n}_1\psi_l(\bar{n}_1\alpha_1)\xi_l^{(1)\prime}(\alpha_1) - \psi_l'(\bar{n}_1\alpha_1)\xi_l^{(1)}(\alpha_1)}(A_{lm}^{(21)} + A_{lm}^{(1b)}) \qquad (A21)$$

and

$$b_{lm}^1 = \frac{\bar{n}_1\psi_l'(\bar{n}_1\alpha_1)\psi_l(\alpha_1) - \psi_l(\bar{n}_1\alpha_1)\psi_l'(\alpha_1)}{\psi_l(\bar{n}_1\alpha_1)\xi_l^{(1)\prime}(\alpha_1) - \bar{n}_1\psi_l'(\bar{n}_1\alpha_1)\xi_l^{(1)}(\alpha_1)}(B_{lm}^{(21)} + B_{lm}^{(1b)}). \qquad (A22)$$

15

Iterate the above equations until convergence in $A_{lm}^{(21)}, B_{lm}^{(21)}$ and $A_{lm}^{(12)}, B_{lm}^{(12)}$.

4.) Once the incident field series coefficients are known, the scattered field series coefficients are determined using Eqs. (A13), (A14), (A21), and (A22). The internal field series coefficients are determined using

$$c_{lm}^1 = \frac{\xi_l^{(1)\prime}(\alpha_1)\,\psi_l(\alpha_1) - \xi_l^{(1)}(\alpha_1)\,\psi_l'(\alpha_1)}{\bar{n}_1^2\,\psi_l(\bar{n}_1\alpha_1)\,\xi_l^{(1)\prime}(\alpha_1) - \bar{n}_1\,\psi_l'(\bar{n}_1\alpha_1)\,\xi_l^{(1)}(\alpha_1)}(A_{lm}^{(21)} + A_{lm}^{(1b)}), \qquad (A23)$$

$$d_{lm}^1 = \frac{\xi_l^{(1)\prime}(\alpha_1)\,\psi_l(\alpha_1) - \xi_l^{(1)}(\alpha_1)\,\psi_l'(\alpha_1)}{\psi_l(\bar{n}_1\alpha_1)\,\xi_l^{(1)\prime}(\alpha_1) - \bar{n}_1\,\psi_l'(\bar{n}_1\alpha_1)\,\xi_l^{(1)}(\alpha_1)}(B_{lm}^{(21)} + B_{lm}^{(1b)}), \qquad (A24)$$

$$c_{lm}^2 = \frac{\xi_l^{(1)\prime}(\alpha_2)\,\psi_l(\alpha_2) - \xi_l^{(1)}(\alpha_2)\,\psi_l'(\alpha_2)}{\bar{n}_2^2\,\psi_l(\bar{n}_2\alpha_2)\,\xi_l^{(1)\prime}(\alpha_2) - \bar{n}_2\,\psi_l'(\bar{n}_2\alpha_2)\,\xi_l^{(1)}(\alpha_2)}(A_{lm}^{(12)} + A_{lm}^{(2b)}), \qquad (A25)$$

and

$$d_{lm}^2 = \frac{\xi_l^{(1)\prime}(\alpha_2)\,\psi_l(\alpha_2) - \xi_l^{(1)}(\alpha_2)\,\psi_l'(\alpha_2)}{\psi_l(\bar{n}_2\alpha_2)\,\xi_l^{(1)\prime}(\alpha_2) - \bar{n}_2\,\psi_l'(\bar{n}_2\alpha_2)\,\xi_l^{(1)}(\alpha_2)}(B_{lm}^{(12)} + B_{lm}^{(2b)}). \qquad (A26)$$

# REFERENCES

1. Bruning, J.H. and Y.T. Lo, "Multiple scattering of EM waves by spheres Part I – Multiple expansion and ray-optical solutions," IEEE Trans. Ant. and Prop. **AP-19**, 378-390 (1971).

2. Bruning, J.H. and Y.T. Lo, "Multiple scattering of EM waves by spheres Part II – Numerical and experimental results," IEEE Trans. Ant. and Prop. **AP-19**, 391-400 (1971).

3. G.W. Kattawar and C.E. Dean, "Electromagnetic scattering from two dielectric spheres: comparison between theory and experiment," J. Opt. Soc. Am. **8**, 48-50 (1983).

4. K.A. Fuller, G.W. Kattawar, and R.T. Wang, "Electromagnetic scattering from two dielectric spheres: further comparisons between theory and experiment," Appl. Opt. **25**, 2521-2529 (1986).

5. K.A. Fuller and G.W. Kattawar, "Consummate solution to the problem of classical electromagnetic scattering by an ensemble of spheres. I: Linear chains," J. Opt. Soc. Am. **13**, 90-92 (1988).

6. K.A. Fuller and G.W. Kattawar, "Consummate solution to the problem of classical electromagnetic scattering by an ensemble of spheres. II: Clusters of arbitrary configuration," J. Opt. Soc. Am. **13**, 1063-1065 (1988).

7. J.P. Barton, D.R. Alexander and S.A. Schaub, "Internal and near-surface electromagnetic for a spherical particle irradiated by a focused laser beam," J. Appl. Phys. **64**, 1632-1639 (1988).

8. J.P. Barton and D.R. Alexander, "Fifth-order corrected electromagnetic field components for a fundamental Gaussian beam," J. Appl. Phys. **66**, 2800-2802 (1989).

9. J.P. Barton, D.R. Alexander, and S.A. Schaub, "Theoretical determination of net radiation and torque for a spherical particle illuminated by a focused laser beam," J. Appl. Phys. **66**, 4594-4602 (1989).

10. D.R. Alexander, J.P. Barton, S.A. Schaub, M.A. Emanuel, and J. Zhang, "Experimental and theoretical analysis of the interaction of laser radiation with fluid cylinders and spheres," Proceedings of the 1987 U.S. Army Scientific Conference on Obscuration and Aerosol Research, Aberdeen, Maryland **CRDEC-SP-88031**, 251-272 (1987).

11. D.R. Alexander and J.G. Armstrong, "Explosive vaporization of aerosol drops under irradiation by a $CO_2$ laser beam," Appl. Opt. **26**, 533-538 (1987).

17

12. J.P. Barton, D.R. Alexander, and S.A. Schaub, "Internal fields of a spherical particle illuminated by a tightly focused laser beam: Focal point positioning effects at resonance," J. Appl. Phys. **65**, 2900-2906 (1989).

13. N. Morita, T. Tanaka, T. Yamasaki, and Y. Nakanishi, "Scattering of a beam wave by a spherical object," IEEE Trans. Antennas Propag. **AP-16**, 724-727 (1968).

14. W-C. Tsai and R.J. Pogorzelski, "Eigenfunction solution of the scattering of beam radiation by spherical objects," J. Opt. Soc. Am. **65**, 1457-1463 (1975).

15. C. Yeh, S. Colak, and P. Barber, "Scattering of sharply focused beams by arbitrarily shaped dielectric particles: an exact solution," Appl. Opt. **21**, 4426-4433 (1982).

16. G. Grehan, B. Maheu, and G. Gouesbet, "Scattering of laser beams by Mie scatter centers: numerical results using a localized approximation," Appl. Opt. **25**, 3539-3548 (1986).
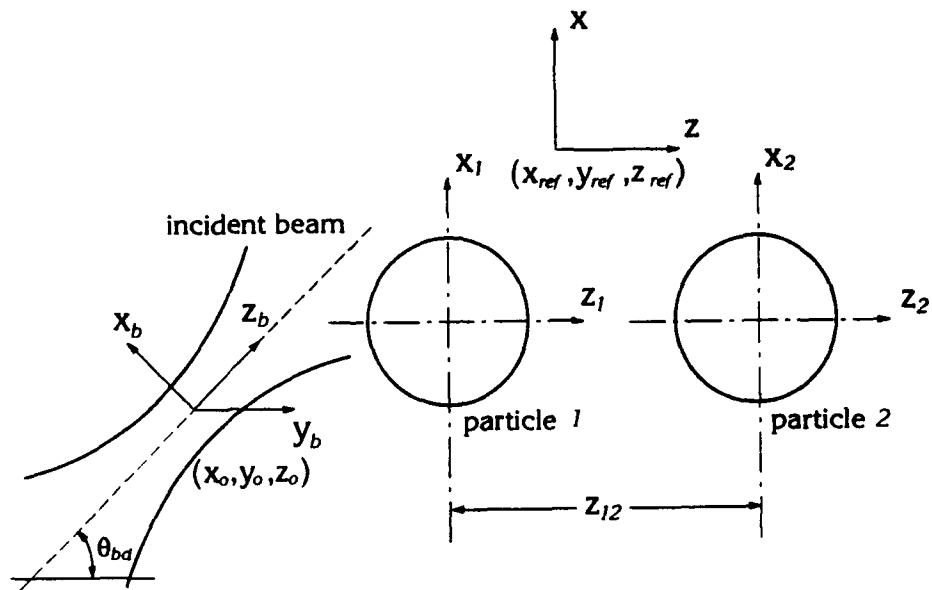
# FIGURE TITLES

FIG 1. Geometrical arrangement for two spherical particles/arbitrary beam interaction theory.

FIG 2. Normalized source function distribution in the x-z plane for a linearly polarized (electric field polarization perpendicular to the x-z plane) Gaussian beam propagating in the $\theta_{bd} = 0^o$ direction incident upon two equal size, same composition spheres. (The x,z coordinates are normalized relative to the radius of particle 1.) $\alpha_1 = \alpha_2 = 13.337$, $\bar{n}_1 = \bar{n}_2 = 1.179 + 0.072i$, $\bar{z}_{12} = 3.556$, $\bar{w}_0 = 2.222$, $\bar{x}_0 = \bar{y}_0 = 0.0$, $\bar{z}_0 = 1.778$, $\theta_{bd} = 0^o$, $\phi_{bd} = 90^o$, $\epsilon_{ext} = 1.0$, $x_{ref} = y_{ref} = 0.0$, $z_{ref} = 1.778$. [10.6 $\mu m$ wavelength ($CO_2$ laser), 100 $\mu m$ waist diameter beam incident upon two 45 $\mu m$ diameter water droplets separated along the propagation axis by 35 $\mu m$ surface-to-surface.]

FIG 3. Pulsed laser ($\Delta t = 10$ ns) image of the explosive fragmentation of the shadow side water droplet due to "focusing" of incident $CO_2$ laser radiation by the illuminated side water droplet. The $CO_2$ laser beam is incident from left-to-right. The droplets are 45 $\mu m$ in diameter and are falling from top to bottom through the focal point of the continuous $CO_2$ laser beam.
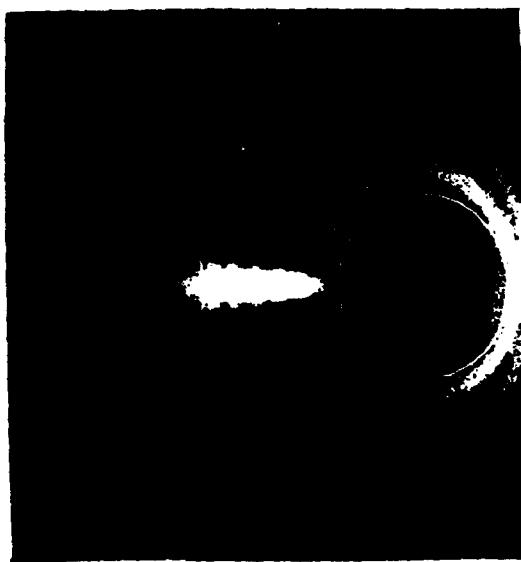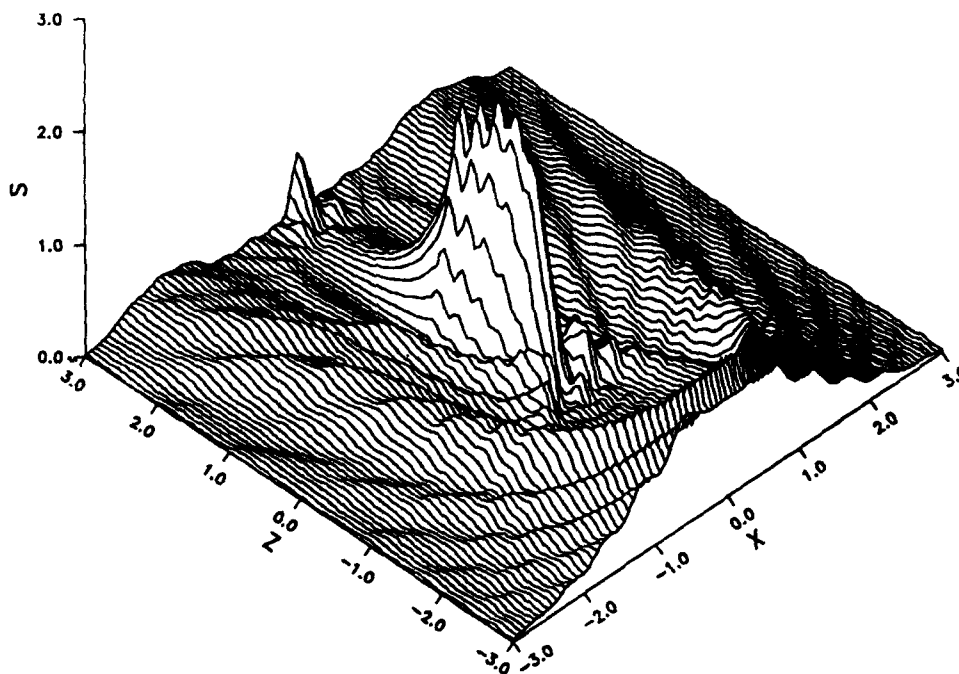
FIG 4. Normalized source function distribution in the x-z plane for a linearly polarized (electric field polarization perpendicular to the x-z plane) Gaussian beam propagating in the $\theta_{bd} = 30^o$ direction incident upon two unequal size, dissimilar composition spheres. (The x,z coordinates are normalized relative to the radius of particle 1.) $\alpha_1 = 14.82$, $\alpha_2 = 11.86$, $\bar{n}_1 = 1.395 + 0.0163i$, $\bar{n}_2 = 1.179 + 0.072i$, $\bar{z}_{12} = 2.60$, $\bar{w}_0 = 0.80$, $\bar{x}_0 = -1.0$, $\bar{y}_0 = 0.0$, $\bar{z}_0 = 0.0$, $\theta_{bd} = 30^o$, $\phi_{bd} = 90^o$, $\epsilon_{ext} = 1.0$, $x_{ref} = y_{ref} = 0.0$, $z_{ref} = 1.40$. [10.6 $\mu m$ wavelength ($CO_2$ laser), 40 $\mu m$ waist diameter beam incident upon a 50 $\mu m$ diameter methanol droplet and a 40 $\mu m$ diameter water droplet separated by 20 $\mu m$ surface-to-surface.]

FIG 5. Number of iterations required for three digit convergence for nonresonant ($\alpha = 30.286$) and resonant ($\alpha = 30.4770$) spheres as a function of surface-to-surface separation distance. $\bar{n}_1 = \bar{n}_2 = 1.334 + 1.2 \times 10^9 i$, $\bar{z}_{12} = 2.0 + \bar{d}_{sep}$, $\bar{w}_0 = 0.4007$, $\bar{x}_0 = \bar{y}_0 = 0.0$, $\bar{z}_0 = -1.165$, $\theta_{bd} = 90^o$, $\phi_{bd} = 0^o$, $\epsilon_{ext} = 1.0$.

FIG 6. Normalized source function distribution in the x-z plane for a focused beam incident upon two adjacent resonant particles. $\alpha_1 = \alpha_2 = 30.4770$, $\bar{n}_1 = \bar{n}_2 = 1.334 + 1.2 \times 10^{-9} i$, $\bar{w}_0 = 0.4007$, $\bar{x}_0 = \bar{y}_0 = 0.0$, $\bar{z}_0 = -1.165$, $\theta_{bd} = 90^o$, $\phi_{bd} = 0^o$, $\epsilon_{ext} = 1.0$, $\bar{z}_{12} = 2.2$, $\bar{x}_{ref} = \bar{y}_{ref} = 0.0$, $\bar{z}_{ref}$

19

= 1.10. [0.5145 $\mu m$ wavelength (argon-ion laser), 2 $\mu m$ waist diameter beam incident upon two 4.9912 $\mu m$ diameter water droplets ($35^{th}$ mode electric wave resonance).]

FIG 7. Normalized source function distribution in the x-z plane for a focused beam incident upon two adjacent nonresonant particles. $\alpha_1 = \alpha_2 = 30.286$, $\bar{n}_1 = \bar{n}_2 = 1.334 + 1.2\times10^{-9}i$, $\bar{w}_0 = 0.4007$, $\bar{x}_0 = \bar{y}_0 = 0.0$, $\bar{z}_0 = -1.165$, $\theta_{bd} = 90^o$, $\phi_{bd} = 0^o$, $\epsilon_{ext} = 1.0$, $\bar{z}_{12} = 2.2$, $\bar{x}_{ref} = \bar{y}_{ref} = 0.0$, $\bar{z}_{ref} = 1.10$. [0.5145 $\mu m$ wavelength (argon-ion laser), 2 $\mu m$ waist diameter beam incident upon two 4.96 $\mu m$ diameter water droplets (nonresonance).]

FIG 8. Geometrical arrangement for far field scattering calculations. Particle 1 is fixed in position at the focal point of the beam while the position of particle 2 is varied. The electric field polarization of the incident beam is in the $x_b$ axis direction. $\theta_{ff}$ is the far field scattering angle relative to the beam propagation axis. $\theta_{bd2}$ is the orientation angle of particle 2 relative to the beam propagation axis. $\alpha_1 = \alpha_2 = 1.334+1.2\times10^{-9}$, $\bar{w}_0 = 2.22$, $\bar{x}_0 = \bar{y}_0 = \bar{z}_0 = 0.0$, $\epsilon_{ext} = 1.0$, [0.5145 $\mu m$ wavelength (argon-ion laser), 4 $\mu m$ waist diameter beam incident upon two adjacent 1.8 $\mu m$ diameter water droplets.]

FIG 9. Normalized scattering intensity as a function of far field scattering angle for a single particle ($\bar{z}_{12} \Rightarrow \infty$). a.) $x_b - z_b$ plane, beam incidence, b.) $x_b - z_b$ plane, plane wave incidence, c.) $y_b - z_b$ plane, beam incidence, d.) $y_b - z_b$ plane, plane wave incidence.

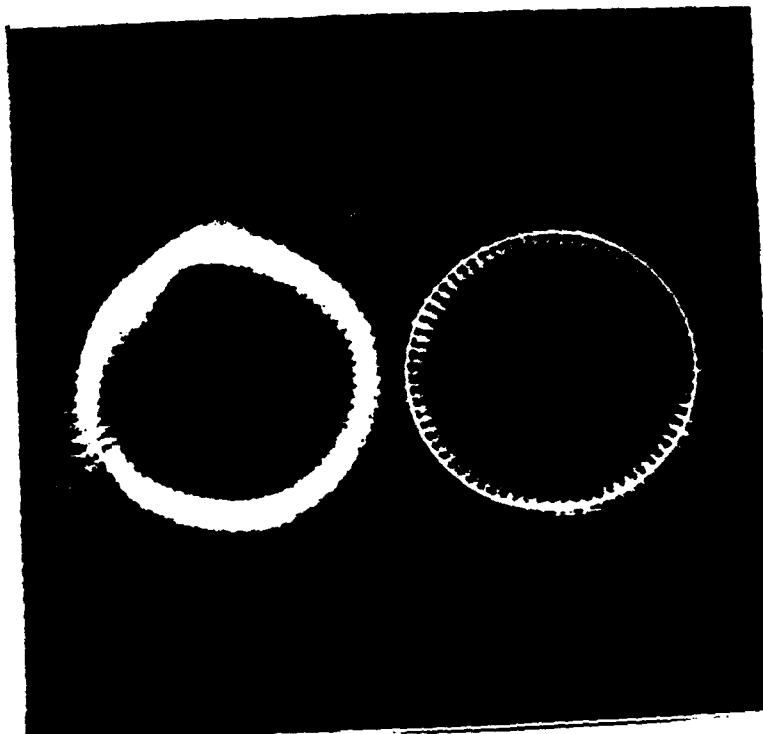FIG 10. Normalized scattering intensity in the $x_b - z_b$ plane as a function of far field scattering angle. Particle 2 in the $x_b - z_b$ plane and positioned one diameter surface-to-surface from particle 1 ($\bar{z}_{12} = 4.0$). a.) $\theta_{bd2} = 0^o$, b.) $\theta_{bd2} = 30^o$, c.) $\theta_{bd2} = 60^o$, d.) $\theta_{bd2} = 90^o$, e.) $\theta_{bd2} = 120^o$, f.) $\theta_{bd2} = 150^o$, g.) $\theta_{bd2} = 180^o$.

FIG 11. Normalized scattering intensity in the $y_b - z_b$ plane as a function of far field scattering angle. Particle 2 in the $x_b - z_b$ plane and positioned one diameter surface-to-surface from particle 1 ($\bar{z}_{12} = 4.0$). a.) $\theta_{bd2} = 0^o$, b.) $\theta_{bd2} = 30^o$, c.) $\theta_{bd2} = 60^o$, d.) $\theta_{bd2} = 90^o$, e.) $\theta_{bd2} = 120^o$, f.) $\theta_{bd2} = 150^o$, g.) $\theta_{bd2} = 180^o$.

FIG 12. Normalized scattering intensity in the $x_b - z_b$ plane as a function of far field scattering angle. Particle 2 positioned perpendicular to the beam propagation axis ($\theta_{bd2} = 90^o$). a.) $\bar{z}_{12} = 4.0$, b.) $\bar{z}_{12} = 6.0$, c.) $\bar{z}_{12} = 12.0$, d.) $\bar{z}_{12} = 18.0$, e.) $\bar{z}_{12} \Rightarrow \infty$.

FIG 13. Normalized scattering intensity in the $y_b - z_b$ plane as a function of far field scattering angle. Particle 2 positioned perpendicular to the beam propagation axis ($\theta_{bd2} = 90^o$). a.) $\bar{z}_{12} = 4.0$, b.) $\bar{z}_{12} = 6.0$, c.) $\bar{z}_{12} = 12.0$, d.) $\bar{z}_{12} = 18.0$, e.) $\bar{z}_{12} \Rightarrow \infty$.

FIG 14. Normalized scattering intensity in the $x_b - z_b$ plane as a function of far field scattering angle. Particle 2 positioned on the beam propagation axis ($\theta_{bd2} = 0^o$). a.) $\bar{z}_{12} = 4.0$, b.) $\bar{z}_{12} = 10.0$, c.) $\bar{z}_{12} = 20.0$, d.) $\bar{z}_{12} = 50.0$, e.) $\bar{z}_{12} = 100.0$, f.) $\bar{z}_{12} \Rightarrow \infty$.

FIG 15. Normalized scattering intensity in the $y_b - z_b$ plane as a function of far field scattering angle. Particle 2 positioned on the beam propagation axis ($\theta_{bd2} = 0^o$). a.) $\bar{z}_{12} = 4.0$, b.) $\bar{z}_{12} = 10.0$, c.) $\bar{z}_{12} = 20.0$, d.) $\bar{z}_{12} = 50.0$, e.) $\bar{z}_{12} = 100.0$, f.) $\bar{z}_{12} \Rightarrow \infty$.

FIG 1. Geometrical arrangement for two spherical particles/arbitrary beam interaction theory.

FIG 2. Normalized source function distribution in the x-z plane for a linearly polarized (electric field polarization perpendicular to the x-z plane) Gaussian beam propagating in the $\theta_{bd} = 0^\circ$ direction incident upon two equal size, same composition spheres. (The x,z coordinates are normalized relative to the radius of particle 1.) $\alpha_1 = \alpha_2 = 13.337$, $\bar{n}_1 = \bar{n}_2 = 1.179 + 0.072i$, $\bar{z}_{12} = 3.556$, $\bar{w}_0 = 2.222$, $\bar{x}_0 = \bar{y}_0 = 0.0$, $\bar{z}_0 = 1.778$, $\theta_{bd} = 0^\circ$, $\phi_{bd} = 90^\circ$, $\epsilon_{ext} = 1.0$, $x_{ref} = y_{ref} = 0.0$, $z_{ref} = 1.778$. [10.6 $\mu m$ wavelength ($CO_2$ laser), 100 $\mu m$ waist diameter beam incident upon two 45 $\mu m$ diameter water droplets separated along the propagation axis by 35 $\mu m$ surface-to-surface.]

FIG 3. Pulsed laser ($\Delta t = 10$ ns) image of the explosive fragmentation of the shadow side water droplet due to "focusing" of incident $CO_2$ laser radiation by the illuminated side water droplet. The $CO_2$ laser beam is incident from left-to-right. The droplets are 45 $\mu$m in diameter and are falling from top to bottom through the focal point of the continuous $CO_2$ laser beam.

FIG 4. Normalized source function distribution in the x-z plane for a linearly polarized (electric field polarization perpendicular to the x-z plane) Gaussian beam propagating in the $\theta_{bd} = 30°$ direction incident upon two unequal size, dissimilar composition spheres. (The x,z coordinates are normalized relative to the radius of particle 1.) $\alpha_1 = 14.82$, $\alpha_2 = 11.86$, $\bar{n}_1 = 1.395 + 0.0163i$, $\bar{n}_2 = 1.179 + 0.072i$, $\bar{z}_{12} = 2.60$, $\bar{w}_0 = 0.80$, $\bar{x}_0 = -1.0$, $\bar{y}_0 = 0.0$, $\bar{z}_0 = 0.0$, $\theta_{bd} = 30°$, $\phi_{bd} = 90°$, $\epsilon_{ext} = 1.0$, $x_{ref} = y_{ref} = 0.0$, $z_{ref} = 1.40$. [10.6 $\mu m$ wavelength ($CO_2$ laser), 40 $\mu m$ waist diameter beam incident upon a 50 $\mu m$ diameter methanol droplet and a 40 $\mu m$ diameter water droplet separated by 20 $\mu m$ surface-to-surface.]

25
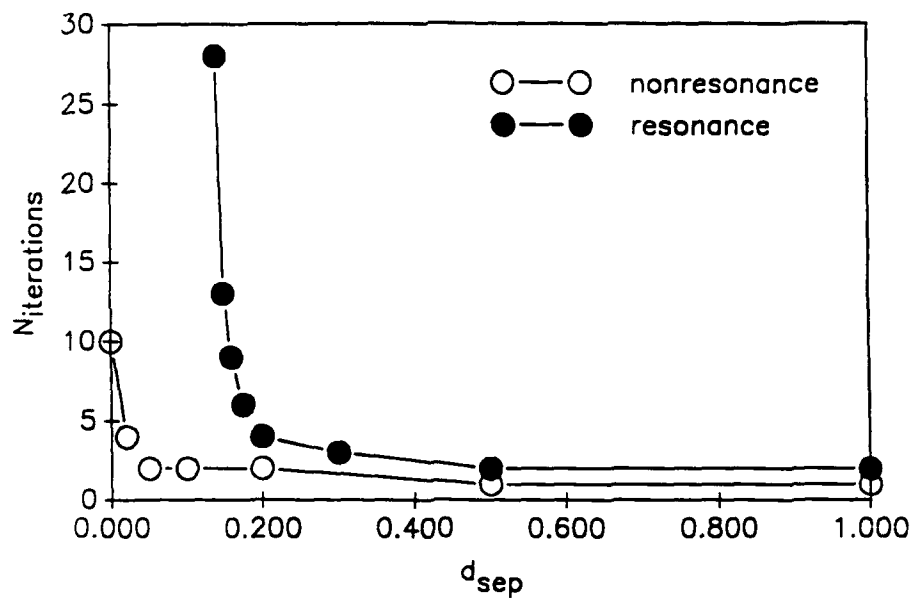
FIG 5. Number of iterations required for three digit convergence for nonresonant ($\alpha = 30.286$) and resonant ($\alpha = 30.4770$) spheres as a function of surface-to-surface separation distance. $\bar{n}_1 = \bar{n}_2 = 1.334 + 1.2 \times 10^9 i$, $\bar{z}_{12} = 2.0 + \bar{d}_{sep}$, $\bar{w}_0 = 0.4007$, $\bar{x}_0 = \bar{y}_0 = 0.0$, $\bar{z}_0 = -1.165$, $\theta_{bd} = 90°$, $\phi_{bd} = 0°$, $\epsilon_{ext} = 1.0$.

FIG 6. Normalized source function distribution in the x-z plane for a focused beam incident upon two adjacent resonant particles. $\alpha_1 = \alpha_2 = 30.4770$, $\bar{n}_1 = \bar{n}_2 = 1.334 + 1.2 \times 10^{-9}i$, $\bar{w}_0 = 0.4007$, $\bar{x}_0 = \bar{y}_0 = 0.0$, $\bar{z}_0 = -1.165$, $\theta_{bd} = 90°$, $\phi_{bd} = 0°$, $\epsilon_{ext} = 1.0$, $\bar{z}_{12} = 2.2$, $\bar{x}_{ref} = \bar{y}_{ref} = 0.0$, $\bar{z}_{ref} = 1.10$. [0.5145 $\mu m$ wavelength (argon-ion laser), 2 $\mu m$ waist diameter beam incident upon two 4.9912 $\mu m$ diameter water droplets ($35^{th}$ mode electric wave resonance).]

FIG 7. Normalized source function distribution in the x-z plane for a focused beam incident upon two adjacent nonresonant particles. $\alpha_1 = \alpha_2 = 30.286$, $\bar{n}_1 = \bar{n}_2 = 1.334 + 1.2 \times 10^{-9}\mathrm{i}$, $\tilde{w}_0 = 0.4007$, $\tilde{x}_0 = \tilde{y}_0 = 0.0$, $\tilde{z}_0 = -1.165$, $\theta_{bd} = 90°$, $\phi_{bd} = 0°$, $\epsilon_{ext} = 1.0$, $\tilde{z}_{12} = 2.2$, $\tilde{x}_{ref} = \tilde{y}_{ref} = 0.0$, $\tilde{z}_{ref} = 1.10$. [0.5145 $\mu m$ wavelength (argon-ion laser), 2 $\mu m$ waist diameter beam incident upon two 4.96 $\mu m$ diameter water droplets (nonresonance).]

FIG 8. Geometrical arrangement for far field scattering calculations. Particle 1 is fixed in position at the focal point of the beam while the position of particle 2 is varied. The electric field polarization of the incident beam is in the $x_b$ axis direction. $\theta_{ff}$ is the far field scattering angle relative to the beam propagation axis. $\theta_{bd2}$ is the orientation angle of particle 2 relative to the beam propagation axis. $\alpha_1 = \alpha_2 = 1.334 + 1.2 \times 10^{-9}$, $\tilde{w}_0 = 2.22$, $\tilde{x}_0 = \tilde{y}_0 = \tilde{z}_0 = 0.0$, $\epsilon_{ext} = 1.0$, [0.5145 $\mu$m wavelength (argon-ion laser), 4 $\mu$m waist diameter beam incident upon two adjacent 1.8 $\mu$m diameter water droplets.]

FIG 9. Normalized scattering intensity as a function of far-field scattering angle for a single particle ($\tilde{z}_{12} \Rightarrow \infty$). a.) $x_b - z_b$ plane, beam incidence, b.) $x_b - z_b$ plane, plane wave incidence, c.) $y_b - z_b$ plane, beam incidence, d.) $y_b - z_b$ plane, plane wave incidence.

FIG 10. Normalized scattering intensity in the $x_b - z_b$ plane as a function of far-field scattering angle. Particle 2 in the $x_b - z_b$ plane and positioned one diameter surface-to-surface from particle 1 ($\bar{z}_{12} = 4.0$). a.) $\theta_{bd2} = 0°$, b.) $\theta_{bd2} = 30°$, c.) $\theta_{bd2} = 60°$, d.) $\theta_{bd2} = 90°$, e.) $\theta_{bd2} = 120°$, f.) $\theta_{bd2} = 150°$, g.) $\theta_{bd2} = 180°$.

FIG 11. Normalized scattering intensity in the $y_b - z_b$ plane as a function of far-field scattering angle. Particle 2 in the $x_b - z_b$ plane and positioned one diameter surface-to-surface from particle 1 ($\bar{z}_{12} = 4.0$). a.) $\theta_{bd2} = 0°$, b.) $\theta_{bd2} = 30°$, c.) $\theta_{bd2} = 60°$, d.) $\theta_{bd2} = 90°$, e.) $\theta_{bd2} = 120°$, f.) $\theta_{bd2} = 150°$, g.) $\theta_{bd2} = 180°$.

FIG 12. Normalized scattering intensity in the $x_b - z_b$ plane as a function of far-field scattering angle. Particle 2 positioned perpendicular to the beam propagation axis ($\theta_{bd2} = 90°$). a.) $\bar{z}_{12} = 4.0$, b.) $\bar{z}_{12} = 6.0$, c.) $\bar{z}_{12} = 12.0$, d.) $\bar{z}_{12} = 18.0$, e.) $\bar{z}_{12} \Rightarrow \infty$.

FIG 13. Normalized scattering intensity in the $y_b - z_b$ plane as a function of far-field scattering angle. Particle 2 positioned perpendicular to the beam propagation axis ($\theta_{bd2} = 90°$). a.) $\bar{z}_{12} = 4.0$, b.) $\bar{z}_{12} = 6.0$, c.) $\bar{z}_{12} = 12.0$, d.) $\bar{z}_{12} = 18.0$, e.) $\bar{z}_{12} \Rightarrow \infty$.

FIG 14. Normalized scattering intensity in the $x_b - z_b$ plane as a function of far-field scattering angle. Particle 2 positioned on the beam propagation axis ($\theta_{bd2} = 0°$). a.) $\bar{z}_{12} = 4.0$, b.) $\bar{z}_{12} = 10.0$, c.) $\bar{z}_{12} = 20.0$, d.) $\bar{z}_{12} = 50.0$, e.) $\bar{z}_{12} = 100.0$, f.) $\bar{z}_{12} \Rightarrow \infty$.

FIG 15. Normalized scattering intensity in the $y_b - z_b$ plane as a function of far-field scattering angle. Particle 2 positioned on the beam propagation axis ($\theta_{bd2} = 0°$). a.) $\bar{z}_{12} = 4.0$, b.) $\bar{z}_{12} = 10.0$, c.) $\bar{z}_{12} = 20.0$, d.) $\bar{z}_{12} = 50.0$, e.) $\bar{z}_{12} = 100.0$, f.) $\bar{z}_{12} \Rightarrow \infty$.

# THEORETICAL MODEL OF THE LASER IMAGING OF SMALL AEROSOLS:
# APPLICATIONS TO AEROSOL SIZING

S.A. Schaub, D.R. Alexander, and J.P. Barton

Center for Electro-Optics

University of Nebraska

Lincoln, NE 68588-0656

(402) 472-3091

## Abstract

A theoretical model is presented for the formation of small particle shadow images in a single lens laser imaging system. The model uses a modification of classical Lorenz-Mie theory, presented by the authors in an earlier paper, to calculate the external electromagnetic fields resulting from the interaction of a Gaussian laser beam with a finite absorbing spherical particle. Propagation of the electric field through the imaging system components is developed from a scalar viewpoint using the thin lens transformation and the Fresnel approximation to the Huygens-Fresnel propagation equation. The theoretical model is valid for either transparent or absorbing spheres and has no restrictions on the allowable degree or direction of aerosol defocus. Direct comparisons between theoretical calculations and experimental observations are reported for 53 $\mu$m diameter transparent water droplets and 66 $\mu$m diameter absorbing nickel spheres for defocus ranging from -2 mm (toward lens) to +2 mm (away from lens). Theory and experiment showed good agreement in the boundary edge gradient and the location of the external peaks, while observable differences existed in the magnitude of the central spots. Theoretical results, comparing water and nickel aerosols, showed observable differences in the calculated average internal intensity (AII). In contrast, the boundary edge gradient (BEG) showed less dependence on changes in optical properties of the particle. These results indicate that criteria, such as the AII, used in focus determination must be reevaluated when applying in-focus sizing algorithms to aerosols with significantly different optical properties.

1

## I. Introduction

The problem of predicting particle images in a coherent imaging system has been addressed in several research papers during recent years. [1,2,3] The imaging problem is particularly important in the area of aerosol sizing since a number of useful diagnostic instruments in aerosol characterization studies utilize laser-based imaging systems for analysis. One of the major obstacles in using imaging systems for particle size analysis on real sprays is the development of reliable focus criteria algorithms for distinguishing in-focus from out-of-focus aerosol particles. Although empirical methods have been developed which perform adequately for particular applications, [4,5,6] an accurate theoretical model to investigate the effects of index of refraction and particle defocus on various measurable properties, would be extremely informative to researchers using laser imaging systems. Among the particle properties of interest when performing aerosol size measurements are the average internal intensity (AII) of the particle and boundary edge gradient (BEG). These properties, which change depending on the degree of particle defocus, have been used successfully for focus determination in the real-time sizing of water aerosol sprays, and direct comparison to light scattering instruments has shown good agreement. [6,7,8] Another advantage of developing an accurate theoretical model of the laser imaging problem may become apparent when attempting to extend real-time aerosol sizing technology to the submicron size range. In this size range, a theoretical model of the particle image formation may become more important for instrument calibration since there are presently no reliable calibration sources which would allow simultaneous variation of particle size and position within the test region.

In earlier attempts at similar modeling of laser imaging problems, [1,2] a necessary assumption in the developments was to treat the spherical absorbing particles as opaque disks. However, in a recent paper by English and George, [9] it was shown that the axial fields are not the same for metal spheres and conducting disks in the near field region. In an earlier paper, [3] we presented a theoretical model for incident plane wave imaging of spherical particles using classical Lorenz-Mie theory with the assumption that the $z$-component of the external electric field was axisymmetric. In this paper, we consider the more general case of an incident Gaussian beam illuminating the spherical particle. The corresponding plane wave case can always be reproduced by allowing the waist diameter of the beam to become large. In addition, the phi dependence of the $z$-component of the external electric field has been included in the present model. Direct comparisons are made between experiment and theory for absorbing nickel spheres and transparent water droplets at

various degrees of defocus. Calculations are also presented for the variation of AII and BEG as a function of aerosol size, defocus, and optical properties.

## II. Theory

The general approach to the theoretical model, which will be outlined in this section, can be summarized in three steps. The first step is to calculate the $x$-component of the external electromagnetic field resulting from the interaction of the Gaussian beam with the particle using exact series expressions presented in an earlier paper by Barton et al. [10] Appropriate phase shifts are then introduced to the portions of the external electric fields which are collected by the aperture and imaging lens. After passing through the imaging lens, the electric field can then be propagated to the image plane through the use of the Fresnel propagation equation.

The derivation for the theoretical model of this imaging problem relies on several assumptions which simplify the analytical approach. Referring to Fig. 1, a smooth, spherical, homogeneous, finite absorbing particle of radius, $a$, is located on the imaging system axis at an axial location, $z_0$. The incident electromagnetic field is taken as a Gaussian beam with waist diameter $2w_0$, and dominant electric field polarization in the $x$-direction. The beam axis and the imaging system axis are assumed coincident in the $z$-direction. Note that in the following development it is not necessary to assume the particle lies at the beam focal point, only that it is somewhere on the $z$-axis. In general, the imaging problem can be formulated for situations in which the imaging system axis and beam propagation axis are different, however, the numerical evaluation of the results becomes more time consuming. The propagation of the field from the imaging system lens to the image plane is accomplished using scalar diffraction theory. For the particular case under consideration, the $x$-component of the external electric field is assumed the dominant field component transmitted through the imaging system. This assumption can be verified by direct computation of the external field components and is physically reasonable since the incident field has dominant polarization in the $x$-direction. A great deal of previous work exists which has examined the validity of using scalar theory in modeling the propagation of electromagnetic energy. [11,12,13,14,15] In particular, the use of the Fresnel approximation to the Huygens-Fresnel equation has received considerable attention due to the computational advantages it provides. [16,17] The use of the Fresnel approximation, however, imposes certain restriction over the range in which one can expect accurate results. In this paper, the criterion of Goodman [11] has been used which states that, provided the distance $z_{32}$ satisfies the relation,

$$z_{32}^3 = (z_3 - z_2)^3 >> \frac{\pi}{4\lambda}[(x_3 - x_2)^2 + (y_3 - y_2)^2]_{max}^2, \tag{1}$$

3

the electric field distribution in plane $z_3$ (image plane) can be expressed in terms of the electric field distribution in plane $z_2$ (rear lens surface) by using the Fresnel approximation to the Huygens-Fresnel equation,

$$E_3(x_3, y_3) = \frac{\exp(ikz_{32})}{i\lambda z_{32}} \int \int_A E_2(x_2, y_2) \exp\left\{\frac{ik}{2z_{32}}\left[(x_3 - x_2)^2 + (y_3 - y_2)^2\right]\right\} dx_2 dy_2. \quad (2)$$

In this equation, $E$ denotes the $x$-component of the external electric field and the numerical subscripts denote evaluation of the particular quantity in a $z =$ constant plane. Note that for a $z =$ constant plane, $\theta = \pi/2$ so

$$x_m = r_m \cos\phi_m, \quad (3)$$

$$y_m = r_m \sin\phi_m, \quad (4)$$

where $m$ is an integer representing the particular $z =$ constant plane under consideration. The angle $\phi$ is measured with respect to the $+x$-axis in the direction of the $+y$-axis. Equation (2) can then be written,

$$\begin{aligned} E_3(r_3, \phi_3) &= \frac{\exp(ikz_{32})}{i\lambda z_{32}} \int \int_A E_2(r_2, \phi_2) \exp\left\{\frac{ik}{2z_{32}}\left[(r_3\cos\phi_3 - r_2\cos\phi_2)^2 \right.\right. \\ &\quad + \left.\left. (r_3\sin\phi_3 - r_2\sin\phi_2)^2\right]\right\} r_2 dr_2 d\phi_2. \end{aligned} \quad (5)$$

Simplifying the term in [ ], Eq. (5) becomes,

$$\begin{aligned} E_3(r_3, \phi_3) &= \frac{\exp(ikz_{32})\exp(ikr_3^2/2z_{32})}{i\lambda z_{32}} \int \int_A E_2(r_2, \phi_2) \exp\left(\frac{ikr_2^2}{2z_{32}}\right) \\ &\quad \times \exp\left[\frac{-ikr_2 r_3}{z_{32}}\cos(\phi_2 - \phi_3)\right] r_2 dr_2 d\phi_2. \end{aligned} \quad (6)$$

To relate the field at the lens back to the field incident on plane $z_1$, the imaging lens used in the system is assumed to be a pure dielectric and to possess symmetry about the imaging system axis. Probably the most straightforward approach would be to utilize the thin lens transformation as presented by Goodman[11],

$$E_2(r_2, \phi_2) = E_1(r_1, \phi_1) \exp(ikn\Delta_0) \exp\left[\frac{-ikr_1^2}{2f}\right], \quad (7)$$

where $\Delta_0$ is the lens thickness and $f$ is the focal length. In this expression, the paraxial ray approximation was utilized in which the spherical lens surface is approximated by a parabolic surface. As shown, the phase transformation introduced by the lens is composed of a constant phase delay dependent on the lens thickness and a variable phase delay which is a function of the

4

radial distance from the axis of the lens. In this expression, any refraction through the lens is neglected thus making $r_2 = r_1$. Using Eq. (7), the $x$-component of the electric field in the image plane can be written as,

$$E_3(r_3, \phi_3) = P \int_0^{r_a} \int_0^{2\pi} E_1(r_1, \phi_1) \exp\left[\frac{ikr_1^2}{2}\left(\frac{1}{z_{32}} - \frac{1}{f}\right)\right] \exp\left[\frac{-ikr_1 r_3}{z_{32}} \cos(\phi_1 - \phi_3)\right] r_1 dr_1 d\phi_1 \quad (8)$$

where,

$$P = \frac{\exp(ikn\Delta_0)\exp(ikz_{32})\exp(ikr_3^2/2z_{32})}{i\lambda z_{32}}, \quad (9)$$

and use has been made of the fact that $\phi_1 = \phi_2$ from symmetry. Note the electric field that exists within the aperture is assumed to be the same field that is incident on the aperture, which in this case is the $x$-component of the external electric field resulting from the interaction of the laser beam with the particle. For situations where the dimensions of the aperture are much larger than the wavelength, this is a reasonable assumption. Defining,

$$\tilde{\beta} = \frac{\alpha \tilde{r}_1 \tilde{r}_3}{\tilde{z}_{32}}, \quad (10)$$

Eq. (8) can be rewritten in nondimensional form as,

$$\tilde{E}_3(\tilde{r}_3, \phi_3) = \tilde{P} \int_0^{\tilde{r}_a} \exp\left[\frac{i\alpha\tilde{r}_1^2}{2}\left(\frac{1}{\tilde{z}_{32}} - \frac{1}{\tilde{f}}\right)\right] \tilde{r}_1 \int_0^{2\pi} \tilde{E}_1(\tilde{r}_1, \phi_1) \exp[-i\tilde{\beta}\cos(\phi_1 - \phi_3)] d\phi_1 d\tilde{r}_1 \quad (11)$$

where $\alpha = 2\pi a/\lambda$, and

$$\tilde{P} = \frac{\alpha \exp(i\alpha n\tilde{\Delta}_0)\exp(i\alpha\tilde{z}_{32})\exp(i\alpha\tilde{r}_3^2/2\tilde{z}_{32})}{2\pi i\tilde{z}_{32}}. \quad (12)$$

All spatial variables have been normalized by the particle radius. To greatly simplify numerical calculations, the angular integral in Eq. (11) can be evaluated exactly by first expanding the $x$-component of the external electric field in plane $z_1$ into the separate incident and scattered portions giving,

$$\tilde{E}_1(\tilde{r}_1, \phi_1) = \tilde{E}_1^{inc}(\tilde{r}_1, \phi_1) + \tilde{E}_1^{sca}(\tilde{r}_1, \phi_1). \quad (13)$$

Note that $(\tilde{r}_1, \phi_1)$ can be expressed equivalently as $(\tilde{\rho}_{10}, \theta, \phi_1)$ as shown in Fig. 1. The scattered field can be expressed in terms of spherical components,

$$\begin{aligned}
\tilde{E}_1^{sca}(\tilde{\rho}_{10}, \theta, \phi_1) &= \tilde{E}_r^{sca}(\tilde{\rho}_{10}, \theta, \phi_1) \sin\theta \cos\phi_1 \\
&+ \tilde{E}_\theta^{sca}(\tilde{\rho}_{10}, \theta, \phi_1) \cos\theta \cos\phi_1 - \tilde{E}_\phi^{sca}(\tilde{\rho}_{10}, \theta, \phi_1) \sin\phi_1. \quad (14)
\end{aligned}$$

5

Substituting the nondimensional exact series expressions for the electric field components given in Ref. [10], the scattered field can be written as,

$$\tilde{E}_1^{sca}(\rho_{10},\theta,\phi_1) = \sin\theta\cos\phi_1\left(\frac{1}{\tilde{\rho}_{10}^2}\right)\sum_{l=1}^{\infty}\sum_{m=-l}^{l}l(l+1)a_{lm}\xi_l^{(1)}(\alpha\tilde{\rho}_{10})Y_{lm}(\theta,\phi_1)$$

$$+ \cos\theta\cos\phi_1\left(\frac{\alpha}{\tilde{\rho}_{10}}\right)\sum_{l=1}^{\infty}\sum_{m=-l}^{l}\left[a_{lm}\xi_l^{(1)\prime}(\alpha\tilde{\rho}_{10})\frac{\partial}{\partial\theta}Y_{lm}(\theta,\phi_1)\right.$$

$$- \left. mb_{lm}\xi_l^{(1)}(\alpha\tilde{\rho}_{10})Y_{lm}(\theta,\phi_1)/\sin\theta\right] - \sin\phi_1\left(\frac{\alpha}{\tilde{\rho}_{10}}\right)\sum_{l=1}^{\infty}\sum_{m=-l}^{l}$$

$$\times \left[ima_{lm}\xi_l^{(1)\prime}(\alpha\tilde{\rho}_{10})Y_{lm}(\theta,\phi_1)/\sin\theta - ib_{lm}\xi_l^{(1)}(\alpha\tilde{\rho}_{10})\frac{\partial}{\partial\theta}Y_{lm}(\theta,\phi_1)\right], \quad (15)$$

where $Y_{lm}$ is the spherical harmonics function as defined by Jackson [18], $a_{lm}$ and $b_{lm}$ are the external scattering coefficients, and $\xi_l^{(1)}(\alpha\tilde{\rho}_{10}) = \psi_l(\alpha\tilde{\rho}_{10}) - i\chi_l(\alpha\tilde{\rho}_{10})$ are the Riccati-Bessel functions. Primes denote differentiation with respect to the function argument. For complete details of the derivation, the reader should refer to the paper by Barton et al. [10]. For the special case under consideration of a spherical particle located on the propagation axis of a Gaussian beam, non-zero scattering coefficients exist only for the $|m| = 1$ terms. [19] In addition, the plus and minus $m$ terms can be related by, $a_{l,1} = -a_{l,-1}$ and $b_{l,1} = b_{l,-1}$. As well as reducing the field component expressions to single summations over $l$, the evaluation of the scattering coefficients is also simplified from two-dimensional surface integrals to line integrals over theta. Equation (15) can be further simplified by noting that $Y_{l,-1}(\theta,\phi_1) = -Y_{l,1}^*(\theta,\phi_1)$, where the asterisk denotes the complex conjugate. The simplified form for the $x$-component of the scattered field can then be expressed as,

$$\tilde{E}_1^{sca}(\tilde{\rho}_{10},\theta,\phi_1) = \cos^2\phi_1\left(\frac{2\sin\theta}{\tilde{\rho}_{10}^2}\right)\sum_{l=1}^{\infty}l(l+1)\xi_l^{(1)}(\alpha\tilde{\rho}_{10})a_{l,1}F_lP_l^{(1)}(\cos\theta) - \cos^2\phi_1\left(\frac{2\alpha\cos\theta}{\tilde{\rho}_{10}}\right)$$

$$\times \sum_{l=1}^{\infty}\left[a_{l,1}\xi_l^{(1)\prime}(\alpha\tilde{\rho}_{10})F_l\sin\theta P_l^{(1)\prime}(\cos\theta) + b_{l,1}\xi_l^{(1)}(\alpha\tilde{\rho}_{10})F_lP_l^{(1)}(\cos\theta)/\sin\theta\right]$$

$$+ \sin^2\phi_1\left(\frac{2\alpha}{\tilde{\rho}_{10}}\right)\sum_{l=1}^{\infty}\left[a_{l,1}\xi_l^{(1)\prime}(\alpha\tilde{\rho}_{10})F_lP_l^{(1)}(\cos\theta)/\sin\theta\right.$$

$$+ \left. b_{l,1}\xi_l^{(1)}(\alpha\tilde{\rho}_{10})F_l\sin\theta P_l^{(1)\prime}(\cos\theta)\right], \quad (16)$$

where the coefficient $F_l$ is defined as,

$$F_l = \left[\frac{2l+1}{4\pi l(l+1)}\right]^{\frac{1}{2}}. \quad (17)$$

6

Since the phi dependence now appears explicitly, the $x$-component of the scattered electric field component can be written as,

$$\tilde{E}_1^{sca}(\tilde{\rho}_{10},\theta,\phi_1) = \cos^2\phi_1[\tilde{K}_r(\tilde{\rho}_{10},\theta) - \tilde{K}_\theta(\tilde{\rho}_{10},\theta)] + \sin^2\phi_1\tilde{K}_\phi(\tilde{\rho}_{10},\theta) \tag{18}$$

where,

$$\tilde{K}_r(\tilde{\rho}_{10},\theta) = \left(\frac{2\sin\theta}{\tilde{\rho}_{10}^2}\right)\sum_{l=1}^{\infty} l(l+1)\xi_l^{(1)}(\alpha\tilde{\rho}_{10})a_{l,1}P_l^{(1)}(\cos\theta)F_l, \tag{19}$$

$$\tilde{K}_\theta(\tilde{\rho}_{10},\theta) = \left(\frac{2\alpha\cos\theta}{\tilde{\rho}_{10}}\right)\sum_{l=1}^{\infty}\left[a_{l,1}\xi_l^{(1)\prime}(\alpha\tilde{\rho}_{10})F_l\sin\theta P_l^{(1)\prime}(\cos\theta)\right.$$
$$\left. + \; b_{l,1}\xi_l^{(1)}(\alpha\tilde{\rho}_{10})F_lP_l^{(1)}(\cos\theta)/\sin\theta\right], \tag{20}$$

and

$$\tilde{K}_\phi(\tilde{\rho}_{10},\theta) = \left(\frac{2\alpha}{\tilde{\rho}_{10}}\right)\sum_{l=1}^{\infty}\left[a_{l,1}\xi_l^{(1)\prime}(\alpha\tilde{\rho}_{10})F_lP_l^{(1)}(cos\theta)/\sin\theta\right.$$
$$\left. + \; b_{l,1}\xi_l^{(1)}(\alpha\tilde{\rho}_{10})F_lP_l^{(1)\prime}(\cos\theta)\sin\theta\right]. \tag{21}$$

To account for the incident field, we use expressions presented in earlier work [19,20] in which the incident $x$-direction electric field component for a 5th-order Gaussian beam can be written as,

$$\tilde{E}_1^{inc}(\tilde{\rho}_b,\theta_b,\phi_1) = \tilde{F}_1(\tilde{\rho}_b,\theta_b) + \tilde{F}_2(\tilde{\rho}_b,\theta_b)\left(\frac{\tilde{\rho}_b\sin\theta_b}{w_0}\right)^2\cos^2\phi_1. \tag{22}$$

The function $\tilde{F}_1$ and $\tilde{F}_2$, which define the incident Gaussian beam, have been given explicitly in Ref. [19] and will not be repeated here. The total external $x$-component of the electric field is then,

$$\tilde{E}_1(\tilde{\rho}_{10},\tilde{\rho}_b,\theta,\theta_b,\phi_1) = \tilde{F}_1(\tilde{\rho}_b,\theta_b) + \left[\tilde{F}_2(\tilde{\rho}_b,\theta_b)\left(\frac{\tilde{\rho}_b\sin\theta_b}{w_0}\right)^2\right.$$
$$\left. + \; \tilde{K}_r(\tilde{\rho}_{10},\theta) - \tilde{K}_\theta(\tilde{\rho}_{10},\theta)\right]\cos^2\phi_1 + \sin^2\phi_1\tilde{K}_\phi(\tilde{\rho}_{10},\theta) \tag{23}$$

where $\tilde{F}_1$, $\tilde{F}_2$, $\tilde{K}_r$, $\tilde{K}_\theta$ and $\tilde{K}_\phi$ are all independent of the angle $\phi_1$. Note that for a particle at the laser focal point, $\tilde{\rho}_b = \tilde{\rho}_{10}$ and $\theta_b = \theta$. Substituting into Eq. (11),

$$\tilde{E}_3(\tilde{r}_3,\phi_3) = \tilde{P}\int_0^{\tilde{r}_a}\exp\left[\frac{i\alpha\tilde{r}_1^2}{2}\left(\frac{1}{\tilde{z}_{32}} - \frac{1}{\tilde{f}}\right)\right]\tilde{r}_1\left\{\tilde{F}_1(\tilde{\rho}_b,\theta_b)\int_0^{2\pi}\exp\left[-i\tilde{\beta}\cos(\phi_3-\phi_1)\right]d\phi_1\right.$$
$$+ \; \left[\tilde{F}_2(\tilde{\rho}_b,\theta_b)\left(\frac{\tilde{\rho}_b\sin\theta_b}{\tilde{w}_0}\right)^2 + \tilde{K}_r(\tilde{\rho}_{10},\theta) - \tilde{K}_\theta(\tilde{\rho}_{10},\theta)\right]$$
$$\times \; \int_0^{2\pi}\cos^2\phi_1\exp\left[-i\tilde{\beta}\cos(\phi_3-\phi_1)\right]d\phi_1$$
$$\left. + \; \tilde{K}_\phi(\tilde{\rho}_{10},\theta)\int_0^{2\pi}\sin^2\phi_1\exp\left[-i\tilde{\beta}\cos(\phi_3-\phi_1)\right]d\phi_1\right\}d\tilde{r}_1. \tag{24}$$

7

The angular integrals in Eq. (24) can be evaluated exactly using the derived identities,

$$\int_0^{2\pi} \cos\phi_1 \, \exp(im\phi_1) \exp[-i\tilde{\beta}\cos(\phi_1 - \phi_3)] \, d\phi_1$$
$$= \pi(i)^{1-m}[-J_{m+1}(\tilde{\beta})\exp(i\phi_3) + J_{m-1}(\tilde{\beta})\exp(-i\phi_3)]\exp(im\phi_3), \tag{25}$$

and

$$\int_0^{2\pi} \sin\phi_1 \, \exp(im\phi_1) \exp[-i\tilde{\beta}\cos(\phi_1 - \phi_3)] \, d\phi_1$$
$$= \pi(i)^{m}(-1)^{m+1}[J_{m+1}(\tilde{\beta})\exp(i\phi_3) + J_{m-1}(\tilde{\beta})\exp(-i\phi_3)]\exp(im\phi_3). \tag{26}$$

Substituting for $\tilde{P}$, Eq. (24) can then be written,

$$\tilde{E}_3(\tilde{r}_3,\phi_3) = \frac{\alpha\exp(i\alpha\tilde{z}_{32})\exp(i\alpha\tilde{r}_3^2/2\tilde{z}_{32})exp(i\alpha n\tilde{\Delta}_0)}{2i\tilde{z}_{32}}\int_0^{\tilde{r}_a}\tilde{r}_1$$
$$\times \ \exp\left[\frac{i\alpha\tilde{r}_1^2}{2}\left(\frac{1}{\tilde{z}_{32}} - \frac{1}{\tilde{f}}\right)\right]\left\{J_0(\tilde{\beta})\left[2\tilde{F}_1(\tilde{\rho}_b,\theta_b) + \tilde{F}_2(\tilde{\rho}_b,\theta_b)\left(\frac{\tilde{\rho}_b\sin\theta_b}{\tilde{w}_0}\right)^2\right.\right.$$
$$+ \ \left.\tilde{K}_r(\tilde{\rho}_{10},\theta) - \tilde{K}_\theta(\tilde{\rho}_{10},\theta) + \tilde{K}_\phi(\tilde{\rho}_{10},\theta)\right] - J_2(\tilde{\beta})\left[\tilde{F}_2(\tilde{\rho}_b,\theta_b)\left(\frac{\tilde{\rho}_b\sin\theta_b}{\tilde{w}_0}\right)^2\right.$$
$$+ \ \left.\left.\tilde{K}_r(\tilde{\rho}_{10},\theta) - \tilde{K}_\theta(\tilde{\rho}_{10},\theta) - \tilde{K}_\phi(\tilde{\rho}_{10},\theta)\right]\cos(2\phi_3)\right\}d\tilde{r}_1. \tag{27}$$

where $J_0$ and $J_2$ are integer order Bessel functions of the first kind.

In terms of intensity in the image plane,

$$\tilde{I}_3(\tilde{r}_3,\phi_3) = \tilde{E}_3(\tilde{r}_3,\phi_3)\tilde{E}_3^*(\tilde{r}_3,\phi_3)$$
$$= \left(\frac{\alpha}{2\tilde{z}_{32}}\right)^2\left|\int_0^{\tilde{r}_a}r_1\exp\left[\frac{i\alpha\tilde{r}_1^2}{2}\left(\frac{1}{\tilde{z}_{32}} - \frac{1}{\tilde{f}}\right)\right]\left\{J_0(\tilde{\beta})\left[2\tilde{F}_1(\tilde{\rho}_b,\theta_b)\right.\right.\right.$$
$$+ \ \left.\tilde{F}_2(\tilde{\rho}_b,\theta_b)\left(\frac{\tilde{\rho}_b\sin\theta_b}{\tilde{w}_0}\right)^2 + \tilde{K}_r(\tilde{\rho}_{10},\theta) - \tilde{K}_\theta(\tilde{\rho}_{10},\theta) + \tilde{K}_\phi(\tilde{\rho}_{10},\theta)\right]$$
$$- \ J_2(\tilde{\beta})\left[\tilde{F}_2(\tilde{\rho}_b,\theta_b)\left(\frac{\tilde{\rho}_b\sin\theta_b}{\tilde{w}_0}\right)^2\right.$$
$$+ \ \left.\left.\tilde{K}_r(\tilde{\rho}_{10},\theta) - \tilde{K}_\theta(\tilde{\rho}_{10},\theta) - \tilde{K}_\phi(\tilde{\rho}_{10},\theta)\right]\cos(2\phi_3)\right\}d\tilde{r}_1\right|^2. \tag{28}$$

Note that the phi dependence of the intensity distribution in the image plane shows up explicitly in the form of a term involving $\cos(2\phi_3)$. This indicates that the image in plane $z_3$ is symmetric with respect to both the $x$ and $y$ axis, as would be expected for an incident beam polarized in the $x$-direction. Note also that the $F$ and $K$ functions, which appear in the equation above, are independent of the location of the observation point. Thus the values of the $F$ and $K$ terms can be calculated once for all values of $r_1$ and then later used in determining the intensity at all observation points.

### III. Experimental Arrangement

To obtain the experimental data used for comparison to the theoretical calculations, a laser-imaging system was configured as shown in Fig. 2. The illumination was provided by a Laser Energy Inc. pulsed nitrogen laser with a 10 ns pulse width and 3.0 mm Gaussian waist diameter. The shadow images of the particles were projected to a Photometrics Series 200 CCD camera head using a 50 mm focal length plano-convex lens. The CCD camera system possesses a 14 bit gray level scale and a pixel resolution of 384 by 576. Each water particle image was corrected for nonuniformities due to the laser illumination and imaging system components by subtracting a background image (no particles present) from the actual particle image. The resulting particle image was then recorded on a Panasonic TQ-3031F optical disk recorder so that later analysis could be performed. The off-line data analysis was performed using a host computer (Gateway 2000, 33 MHz-386) equipped with a Data Translation 2861 frame grabber and 2858 frame processor. All experimental data represents an average of three separate images and has been normalized to give a unity background intensity and zero intensity corresponding to absolute minimum. The monodisperse water droplets were generated using an Aerometrics Inc. vibrating orifice generator head along with a small pressure vessel which was used to supply a constant flow rate of water. The pressure vessel was used as a replacement for the standard mechanical syringe pump to provide a more uniform liquid flow rate. Previous research [21] has indicated that droplet properties such as size and shape are extremely sensitive to changes in flow rate through the orifice. Solid nickel spheres, supplied by Duke Scientific, were placed in the imaging system by distributing a small quantity on a thin microscope slide which was mounted in the focal plane of the imaging system.

### IV. Results

To generate numerical results, the expression given in Eq. (28) was implemented into a Fortran computer code. Initial checks on the code were performed by calculating the intensity distribution for small apertures (i.e., 20-100 $\mu$m) with $f \to \infty$ and particle complex refractive index $\bar{n} = 1.0 + 0.0i$. Under these conditions, the calculations were in agreement with the results expected from diffraction theory for a circular aperture. Calculations were also performed for cases when $w_0 \to \infty$ in which case, results identical to previous plane wave calculations were obtained.

Figures 3 and 4 show both the experimental data (open circles) and the theoretical calculations (solid line) for 53 $\mu$m diameter water droplets and 66 $\mu$m diameter nickel spheres, respectively. In both cases, the degree of defocus has been varied from − 2 mm (defocus toward lens) to +2

mm (defocus away from lens) for aperture sizes of 3 mm and 5 mm. The choice of water and nickel as test cases was made because of the large differences in optical properties in the ultraviolet region. In the ultraviolet, water is very transparent with complex refractive index [22], $\bar{n} = 1.345 + 8.7 \times 10^{-9}i$, while nickel is strongly absorbing with index of refraction [23], $\bar{n} = 1.66 + 2.03i$. The particular aerosol diameters selected for examination were chosen since each is representative of sizes encountered in typical sprays and is such that adequate resolution can be obtained with the imaging system described in the previous section. Other sizes in the range from 40 $\mu$m to 125 $\mu$m have been examined for both nickel and water with Figs. 3 and 4 representing typical results. Other parameters corresponding to the actual experimental setup are: lens focal length, $f = 50$ mm; distance from lens back to image plane, $z_{32} = 1039.5$ mm; distance from particle to aperture plane (in-focus), $z_{1f} = 52.5265$ mm.

As shown in Fig. 3, the theory and experiment are in good agreement for both the edge gradient of the water droplet and the location of the peaks and valleys in the intensity distribution. The theoretical calculations also show consistent trends with experimental observation as the aperture size was decreased from 5 mm to 3 mm in diameter. By decreasing the aperture size, high frequency oscillations in the intensity distribution are reduced. This damping of high frequency effects is most visible for the − 2.0 mm case. The most notable difference in experiment and theory is in the magnitude of the central spot. In most of the cases shown in Fig. 3, theory predicts a brighter central spot than that observed experimentally. There are several possible sources for the observed discrepancy. From an experimental viewpoint, it is unlikely that the falling water droplets are perfectly spherical. Previous experience has shown that water droplets exiting a vibrating orifice generator will oscillate slightly for considerable distances. Any deviation of the droplet from spherical shape would likely result in modified centerline intensities due to the lack of perfect symmetry. In addition, the theoretical approach has utilized both the idealized thin lens description and the Fresnel propagation equation to model the propagation of the electric field through the imaging system components. Previous research by Steane and Rutt [16] has reported that the Fresnel approximation does not produce the correct on-axis intensity distribution for the circular aperture case. This would suggest that the use of the Fresnel approximation may be a contributing factor to the observed differences between experiment and theory for on-axis observation points. However, the use of more general scalar diffraction expressions does not allow the analytical simplification in the angular integral shown in section II., and likewise would require substantially more computation time.

10

Figure 4 shows the corresponding data for 66 $\mu$m diameter nickel spheres. Many characteristics of the intensity distributions for nickel and water spheres are very similar, particularly as the particles become severely defocused. For these cases, both show bright central spots with surrounding diffraction rings. The two cases show significant differences, however, for the in-focus case. The water droplet, being very transparent to the incident light, shows a sharp bright spot in the center of the droplet. The nickel sphere, in contrast, remains essentially at zero intensity throughout the interior of the droplet. The oscillations in the theoretically calculated intensities far from the droplet edge, particularly significant for the 3 mm aperture calculations, also appeared in the calculations by Thompson and Malyak [1], and are caused by diffraction effects at the aperture edge. These effects do not appear for the 5 mm cases because the 3.0 mm diameter Gaussian beam provides little energy at the aperture edge. For this case, the aperture serves only to limit the collection of the scattered electric fields from the particle while not significantly influencing the incident field.

## V. Particle Sizing Applications

To better quantify the differences between images formed by transparent water droplets and absorbing nickel spheres, both the average internal intensity (AII) and boundary edge gradient (BEG) were examined as a function of particle size and particle defocus. As discussed previously, these parameters were used in the aerosol sizing systems of Bertollini et al. [4], and Wiles [6] as indicators of the degree of particle defocus. Since neither property depends directly on the magnitude of the central spot, the computations would be expected to provide reliable results.

The AII is determined by summing all intensity values which fall below 0.25 times the background intensity, $\bar{I}_b$, and dividing by the total number of contributing points. Since coherent illumination is linear with respect to complex amplitude, the threshold value of 0.25 times the background intensity was used to locate the corresponding particle edge. Note that for the calculations to be presented, $\bar{I}_b$ has been normalized to unity. The curves of AII, presented in Fig. 5, show minimum values near the imaging system focal plane and increase in value as the particles become more severely defocused. For a given aerosol size, the AII for nickel spheres is lower than that for corresponding water droplets. In addition, the curves for nickel spheres show smoother variation as the particles become defocused. Both these trends can be attributed to the fact that no refractive effects occur for opaque nickel spheres. Note that the AII for both nickel and water tends to be higher for particles defocused towards the lens (i.e., negative values of defocus).

11

The AII curves also show a decreasing intensity and a tendency to flatten as the particles size increases. Also, the percentage change in AII, as a function of particle size, decreases substantially as the particle diameters become larger. These general trends in the behavior of the AII were also observed experimentally in the work by Wiles [6] in which static opaque disks were examined at various degrees of defocus. His work showed that the change in AII as a function of size occurs very rapidly for small diameters (i.e., 10 - 30 $\mu$m diameter) but tended to decrease rapidly for diameters larger than about 60 $\mu$m. Another interesting point to be noted from Fig. 5 is the behavior of the AII curve for a particle diameter of 20 $\mu$m. As the particle defocus approaches approximately 0.3 mm, the AII curve no longer shows a uniform increase, as was the case for larger diameters, but actually begins decreasing. The point at which the AII curve begins decreasing can be identified as the allowable depth of field of the imaging system when using AII to characterize particle defocus. For this specific case, a depth of field of approximately $\pm 300$ $\mu$m would allow characterization of particles with diameters greater than 20 $\mu$m. This depth of field will decrease correspondingly as one attempts to measure smaller particle sizes.

The second aerosol property examined, which is applicable to focus determination, is the boundary edge gradient (BEG). The BEG represents the slope of the particle intensity distribution evaluated at $0.75\tilde{I}_b$ and $0.25\tilde{I}_b$. As expected, the BEG peaks for particle positions near the focal plane of the imaging system and decreases as the particles become more severely defocused. As was the case when examining the AII, the BEG curves also show asymmetry with respect to the imaging system focal plane. In contrast to the behavior of the AII, however, the BEG shows increases roughly in proportion to the diameter increase. Comparing the behavior of the BEG for water and nickel spheres indicates very little difference in the magnitude and variation in the values. This fact would suggest that the BEG is primarily a function of the droplet geometry, rather than the optical properties of the aerosol.

## VI. Conclusions

A scalar modeling technique has been developed which allows the calculation of defocused aerosol images formed in a laser-based imaging system. The technique has no restrictions on the allowable degree or direction of particle defocus and can be used for either absorbing or transparent particles. The aerosol particle can be located at any position on the z-axis of a 5th-order Gaussian beam. To examine the validity of the theoretical model, experimental images were obtained using a nitrogen laser source and CCD camera system. Direct comparison between experiment and theory,

using both 53 $\mu$m diameter water droplets and 66 $\mu$m diameter nickel spheres, has shown good agreement in the intensity distributions for positions off the optical axis. The differences observed between experiment and theory for points along the optical axis were attributed to errors introduced by the Fresnel propagation equation. Calculations of aerosol properties relevant to particle sizing have provided additional validity for the use of average internal intensity and boundary edge gradient for characterization of aerosol focus. The modeling technique also demonstrates the ability to establish depth of field for given particle sizes and imaging system geometries, based on theoretical considerations.

## VII. Acknowledgments

## VIII. References

[1] B.J. Thompson and P.H. Malyak, "Accuracy of measurement in coherent imaging of particulates in a three-dimensional sample," in *Particle Sizing and Spray Analysis*, N. Chigier and G.W. Stewart, eds., Proc. SPIE **573**, 12-20 (1985).

[2] E.A. Hovenac, "Fresnel diffraction by spherical obstacles," Am. J. of Phys., **57** (1), 79-84 (1989).

[3] S.A. Schaub, D.R. Alexander, and J.P. Barton, "Theoretical model for the image formed by a spherical particle in a coherent imaging system," Opt. Eng. **28** (5), 565-571 (1989).

[4] G.P. Bertollini, L.M. Oberdier, and Y.H. Lee, "Image processing system to analyze droplet distributions in sprays," Opt. Eng. **24** (3), 464-469 (1985).

[5] B.A. Weiss, P. Derov, D. DeBiase, and H.C. Simmons, "Fluid particle sizing using a fully automated optical imaging system," Opt. Eng. **23** (5), 561-566 (1984).

[6] K.J. Wiles, "Development of a system for secondary liquid injection into a Mach 2 supersonic flow to study drop size and distribution by video imaging techniques," Masters Thesis, Mechanical Engineering Department, University of Nebraska, Lincoln, NE (1985).

[7] K.D. Ahlers and D. R. Alexander, "Microcomputer based digital image processing system developed to count and size laser-generated small particle images," Opt. Eng. **24** (6), 1060-1065 (1985).

[8] D.R. Alexander and D.F.F. Gutierrez, "Spray characterization of a NASA MOD-1 nozzle," J. of Laser Appl. **2** (1), 49-54 (1990).

[9] R.E. English, Jr. and N. George, "Diffraction patterns in the shadows of disks and obstacles," Appl. Opt. **27** (8), 1581-1587 (1988).

[10] J.P. Barton, D.R. Alexander and S.A. Schaub, "Internal and near-surface electromagnetic field for a spherical particle irradiated by a focused laser beam," J. Appl. Phys. **64** (4), 1632-1639 (1988).

[11] J.W. Goodman, *Introduction to Fourier Optics*, McGraw-Hill, New York (1968).

[12] J.E. Harvey, "Fourier treatment of near-field scalar diffraction theory," Am. J. Phys. **47** (11), 974-980 (1979).

[13] F.D. Feiock, "Wave propagation in optical systems with large apertures," J. Opt. Soc. Am. **68** (4), 485-489 (1978).

[14] J.C. Heurtley, "Scalar Rayleigh-Sommerfeld and Kirchoff diffraction integrals: A comparison of exact evaluations for axial point," J. Opt. Soc. Am. **63** (8), 1003-1008 (1973).

[15] H.G. Kraus, "Huygens-Fresnel-Kirchoff wave-front diffraction formulation: spherical waves," J. Opt. Soc. Am. **6** (8) 1196-1205 (1989).

[16] A.M. Steane and H.N. Rutt, "Diffraction calculations in the near field and the validity of the Fresnel approximation," J. Opt. Soc. Am. **6** (12), 1809-1814 (1989).

[17] W.H. Southwell, "Validity of the Fresnel approximation in the near-field," J. Opt. Soc. Am. **71** (1), 7-14 (1981).

[18] J.D. Jackson, *Classical Electrodynamics*, 2nd Edition, John Wiley & Sons, New York, (1975).

[19] S.A. Schaub, J.P. Barton and D.R. Alexander, "Simplified scattering coefficients for a spherical particle located on the propagation axis of a fifth-order Gaussian beam," Appl. Phys. Lett., **55** (26), 2709-2711 (1989).

[20] J.P. Barton and D.R. Alexander, "Fifth-order corrected electromagnetic field components for a fundamental Gaussian beam," J. of Appl. Phys. **66** (7), 2800-2802 (1989).

[21] K. Anders, N. Roth and A. Frohn, "Operation characteristics of vibrating-orifice generators as calibration standard for sizing methods and for the study of basic phenomena," in *Proceedings of the 2nd International Congress on Optical Particle Sizing*, 325-334, (March 5-8, 1990).

[22] G.M. Hale and M.R. Querry, "Optical constants of water in the 200-nm to 200-$\mu$m wavelength region," Appl. Opt. **12** (3), 555-563 (1973).

[23] E.D. Palik, ed., *Handbook of Optical Constants of Solids*, Academic Press, New York, (1985).

**Figure Labels**

**Fig. 1** Imaging system geometry.

**Fig. 2** Experimental arrangement.
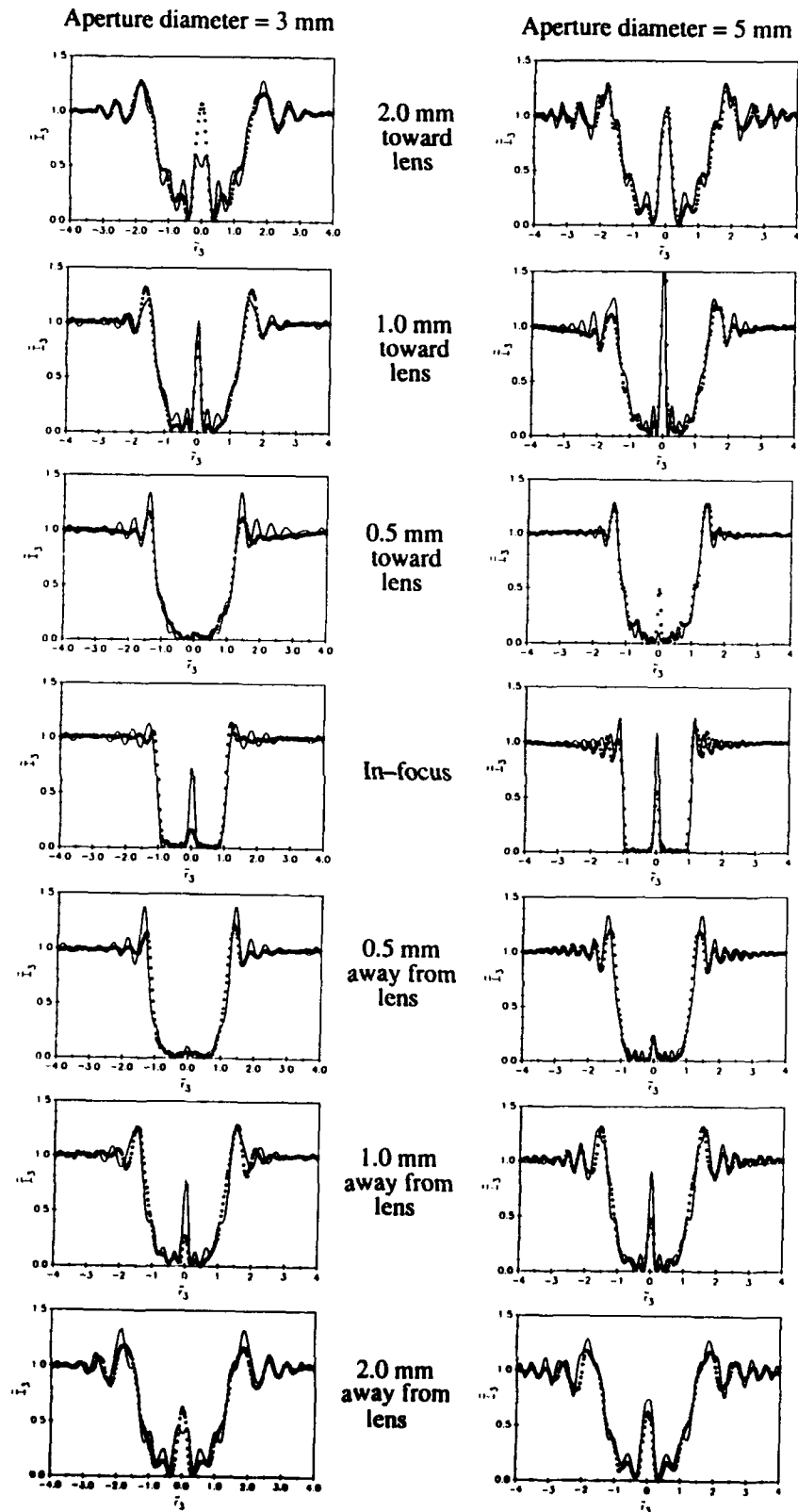
**Fig. 3** Comparison between theory(solid line) and experiment (open circles) for 53 $\mu$m diameter water droplets ($\bar{n} = 1.345 + 8.7 \times 10^{-9}i$) illuminated by a Gaussian beam ($\lambda = 337$ nm, $w_0$ = 1.5 mm) for defocus ranging from -2 mm to +2 mm. The aperture diameters, $2r_a$, used in the system were 3 mm and 5 mm, respectively.
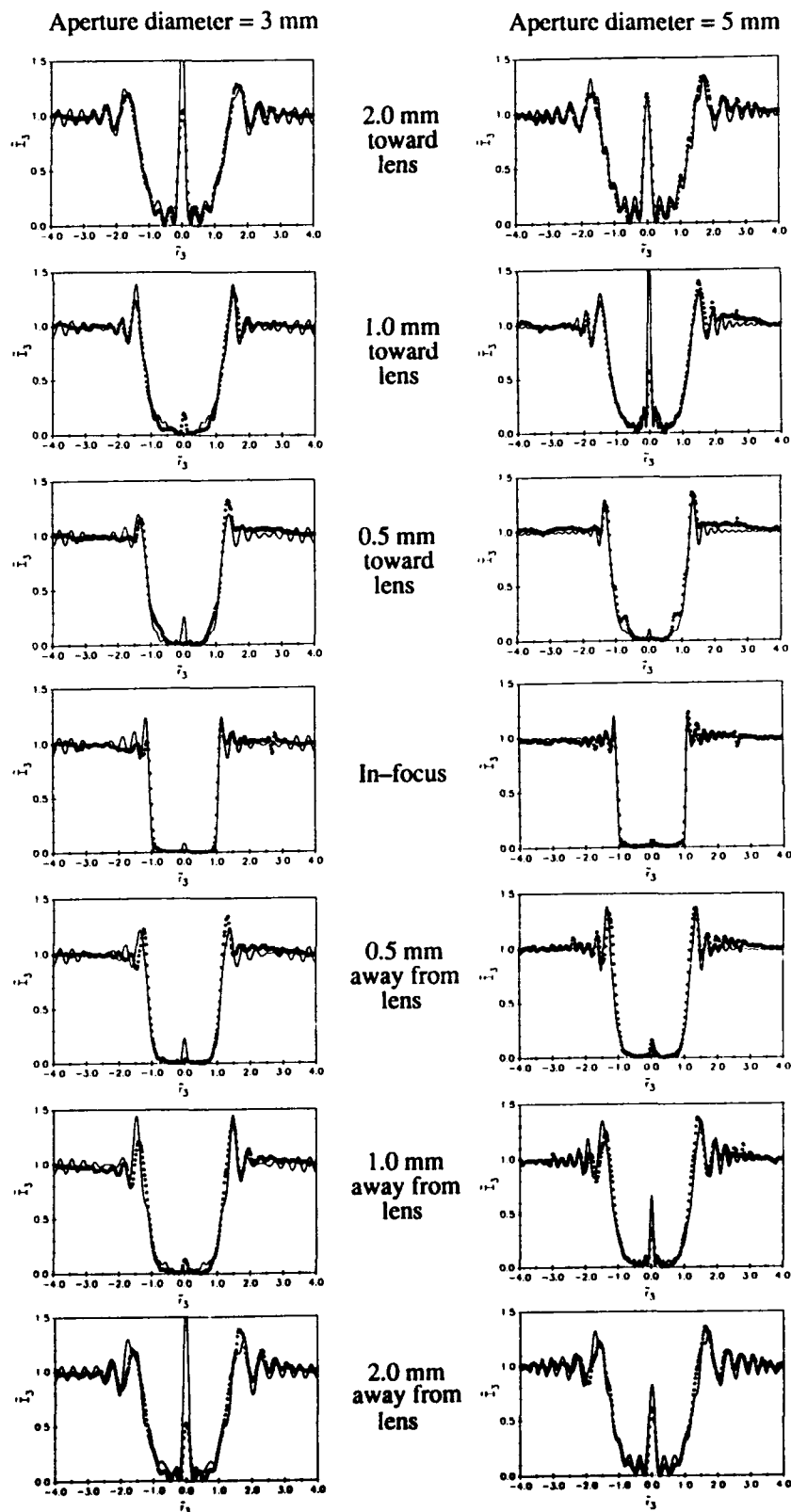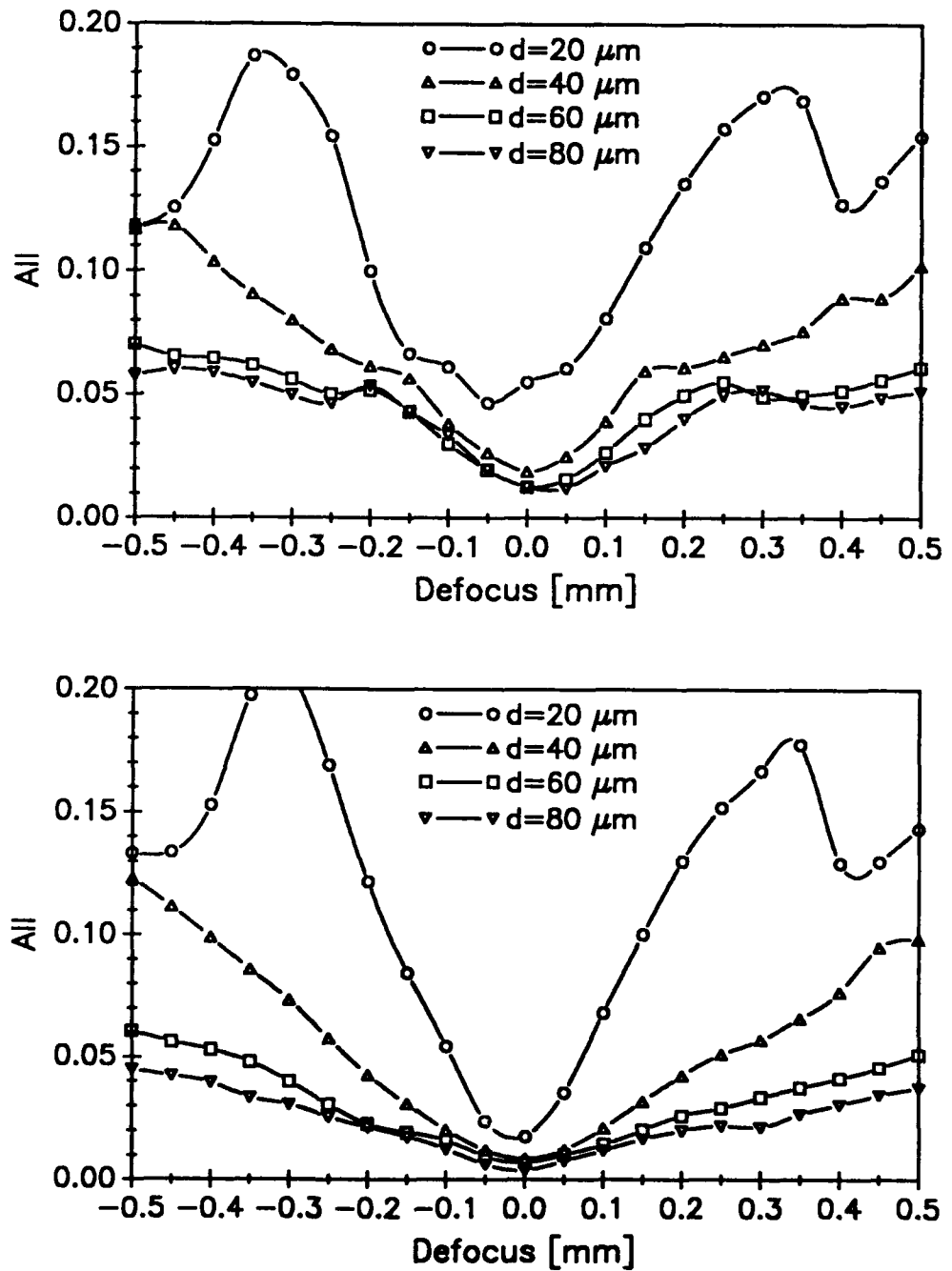
**Fig. 4** Comparison between theory(solid line) and experiment (open circles) for 66 $\mu$m diameter nickel spheres ($\bar{n} = 1.66 + 2.03i$) illuminated by a Gaussian beam ($\lambda = 337$ nm, $w_0 = 1.5$ mm) for defocus ranging from -2 mm to +2 mm. The aperture diameters, $2r_a$, used in the system were 3 mm and 5 mm, respectively.

**Fig. 5** Average internal intensity as a function of particle size and defocus for water droplets with $\bar{n} = 1.345 + 8.7 \times 10^{-9}i$ (top) and nickel spheres with $\bar{n} = 1.66 + 2.03i$ (bottom). In both cases, illumination is by a Gaussian beam ($\lambda = 337$ nm, $w_0 = 1.5$ mm) with aperture diameter, $2r_a$ = 5 mm.

**Fig. 6** Boundary edge gradient as a function of particle size and defocus for water droplets with $\bar{n} = 1.345 + 8.7 \times 10^{-9}i$ (top) and nickel spheres with $\bar{n} = 1.66 + 2.03i$ (bottom). In both cases, illumination is by a Gaussian beam ($\lambda = 337$ nm, $w_0 = 1.5$ mm) with aperture diameter, $2r_a$ = 5 mm.

**Fig. 1** Imaging system geometry.

## Data Acquisition

Test Region

Aperture

Laser Energy
N$_2$-50 Laser

Photometrics
CH220
CCD Camera

Lens

Laser Power
Supply

TSI Model 3450
Aerosol Generator

Photometrics LC200
Liquid Cooling Unit

CCD
Monitor

Computer
Monitor

Photometrics CE200
Camera Elec. Unit

Photometrics CC200
Camera Controller

AT Host Computer

Panasonic
Model TQ-3031F
Optical Disk Recor.

Digitized
Image
Monitor

Computer
Monitor

## Off-Line
## Data Reduction

Gateway 2000
33 MHz 386 Comp.

with
Data Translation 2861 Frame Grabber
Data Translation 2858 Frame Processor

**Fig. 2 Experimental arrangement.**

Aperture diameter = 3 mm

Aperture diameter = 5 mm

2.0 mm
toward
lens

1.0 mm
toward
lens

0.5 mm
toward
lens

In-focus

0.5 mm
away from
lens

1.0 mm
away from
lens

2.0 mm
away from
lens

Fig. 3 Comparison between theory(solid line) and experiment (open circles) for 53 $\mu$m diameter water droplets ($\bar{n} = 1.345 + 8.7x10^{-9}i$) illuminated by a Gaussian beam ($\lambda = 337$ nm, $w_0 = 1.5$ mm) for defocus ranging from -2 mm to +2 mm. The aperture sizes used in the system were 3 mm and 5 mm, respectively.   19

Aperture diameter = 3 mm          Aperture diameter = 5 mm



Fig. 4 Comparison between theory(solid line) and experiment (open circles) for 66 $\mu$m diameter nickel spheres ($\bar{n} = 1.66 + 2.03i$) illuminated by a Gaussian beam ($\lambda = 337$ nm, $w_0 = 1.5$ mm) for defocus ranging from -2 mm to +2 mm. The aperture diameters, $2r_a$, used in the system were 3 mm and 5 mm, respectively.     20

**Fig. 5** Average internal intensity as a function of particle size and defocus for water droplets with $\bar{n} = 1.345 + 8.7 \times 10^{-9}i$ (top) and nickel spheres with $\bar{n} = 1.66 + 2.03i$ (bottom). In both cases, illumination is by a Gaussian beam ($\lambda = 337$ nm, $w_0 = 1.5$ mm) with aperture diameter, $2r_a$ = 5 mm.

**Fig. 6** Boundary edge gradient as a function of particle size and defocus for water droplets with $\bar{n} = 1.345 + 8.7 \times 10^{-9} i$ (top) and nickel spheres with $\bar{n} = 1.66 + 2.03 i$ (bottom). In both cases, illumination is by a Gaussian beam ($\lambda = 337$ nm, $w_0 = 1.5$ mm) with aperture diameter, $2r_a$ = 5 mm.

22

# NONLINEAR INTERACTION OF KrF LASER
# RADIATION WITH SMALL WATER DROPLETS

D.R. Alexander, J.P. Barton, S.A. Schaub, and G.M. Holtmeier

Center for Electro-Optics
University of Nebraska-Lincoln
Lincoln, Nebraska 68588-0656

## Abstract

Results have been obtained for the interaction of KrF excimer laser radiation ($\lambda = 248$ nm, $t_{pulse} = 17$ ns) with 60 $\mu$m diameter distilled water droplets for irradiance values ranging from 3 to 230 GW/cm$^2$. Laser images of the droplet breakup during the time intervals from 0 to 100 ns indicate the dynamic breakup processes to be highly nonlinear. At low irradiance (3 GW/cm$^2$) material is ejected from both the illuminated and shadow hemispheres of the droplet, in qualitative agreement with the location of the electric field peaks predicted by plane wave Lorenz-Mie theory calculations. As the irradiance is increased, the interaction on the shadow hemisphere becomes stronger while the interaction on the illuminated hemisphere decreases. This nonlinear behavior is attributed to rapid electrical breakdown of the droplet near the shadow surface. The breakdown region destroys the ability of the droplet to redirect energy toward the front hemisphere of the droplet. Without this mechanism, the localized electric field maxima near the illuminated surface of the droplet cannot arise. Measurements were also taken of the average material velocities during the time intervals from 0 to 50 ns after arrival of the high energy pulse. Velocities ranged from 1000 m/s at 3 GW/cm$^2$ to 6000 m/s at 230 GW/cm$^2$.

1

## I. Introduction

The interaction of intense laser radiation with liquid droplets has been widely investigated during recent years in attempts to better understand the fundamental physics governing the interaction. Numerous experimental investigations have been performed including those examining plasma formation,[1-5] shock propagation,[6] and electrostrictive effects[7] that occur during the laser/aerosol interaction. Theoretical models have also been developed to predict the behavior of droplets under high energy laser irradiation.[8,9] Due to the complexity of the problem, most theoretical modeling of the nonlinear processes has utilized plane wave theory in the analysis. Recent work, however, has generalized the modeling of the electromagnetic field to include particles located at an arbitrary position illuminated by an arbitrarily defined incident beam.[10,11] However, accounting for the influence of spatial varying droplet properties, initial plasma formation, and heat transfer make the laser/aerosol interaction problem nonlinear and extremely complex. In this paper we present further experimental evidence of the nonlinear behavior for high energy KrF laser pulses ($\lambda$ = 248 nm) incident on distilled water droplets of diameter d = 60 $\mu$m, for irradiance values ranging from 3 GW/cm$^2$ to 230 GW/cm$^2$. We also attempt to explain the experimental observations using computational results generated from the arbitrary beam theory which was presented in an earlier paper.[10] The results presented in this paper should contribute to a better understanding of the nonlinear behavior of aerosol breakup resulting from high energy laser illumination.

## II. Experimental Setup

A schematic of the experimental setup used in the research is shown in Fig. 1. The high energy laser beam is produced by a KrF excimer laser (Questek model 2860, $\lambda$ = 248 nm) using unstable optics and is focused using a plano-convex lens (d = 50 mm, f = 200 mm). The full width at half maximum (FWHM) cross section of the high energy beam at the focal point was determined by translating a knife-edge through the probe volume and was found to be approximately 95 $\mu$m x 115 $\mu$m ($\approx 10^4$ $\mu$m$^2$). An imaging beam from a second excimer laser, identical to the first with the exception of using stable resonator optics and operating on ArF gas ($\lambda$ = 193 nm), is incident in a direction orthogonal to both the high energy pulse and the motion of the water droplets. The 193 nm imaging laser was used to obtain higher resolution real-time images as well as to

2

allow elimination of elastically scattered incident radiation from the high energy pulse by placing a 193 nm bandpass filter in line with the imaging optics. The FWHM duration of the excimer laser pulses were measured using both a fast photodiode (Hamamatsu model C1083) and streak camera (Hamamatsu M2548 slow speed streak unit) and were found to be approximately 17 ns. The imaging pulses were synchronized with the high energy pulses by using an analog/digital delay unit (Questek 9200 laser sync/delay unit) while simultaneously monitoring the output pulse using the photodiode and a digitizing oscilloscope (Hewlett Packard model 54200A). The delay between high energy pulses and imaging pulses could be varied from 0 to 100 $\mu$s in increments of 10 ns. The jitter for the entire system is approximately $\pm 7$ ns. The monodisperse water droplets were generated using a vibrating orifice generator (TSI model 3450) and were allowed to fall in the direction of the gravitational field perpendicular to both the high energy beam and the imaging beam. The real time images were viewed using a UV sensitive vidicon (Cohu 2006 camera system) in conjunction with a digital image processing system[12]. Use of the image processing system allows accurate determination of the particle size prior to explosive breakup and the distance expelled material travels during the laser/aerosol interaction. The images were stored on an optical memory disk recorder (Panasonic model TQ-2023F) so that later analysis could be performed on the images.

### III. Experimental Results

Figure 2 shows typical images of water droplets 0, 20, 40, and 100 ns after arrival of 3 GW/cm$^2$ KrF ($\lambda = 248$ nm) laser pulses. In Figs. 2-5 the laser beam is propagating from right to left in the photographs. Although the 0 ns delay was established prior to experiments by synchronizing the arrival of the high energy pulse with the imaging pulse as each reached the probe volume, it is evident in the photographs that the interaction actually begins prior to what is considered as 0 ns delay. This apparent discrepancy is caused by the finite pulse widths (FWHM = 17 ns) of the high energy and imaging pulses. For increasing irradiance, the breakup process initiates nearer the initial rise of the high energy pulse. In contrast, the photos obtained are integrated over the 17 ns duration of the imaging pulse. Also note that the images in Figs. 2-5 are not of a single droplet but of several different droplets imaged at fixed intervals after arrival of the high energy pulse. Since the vibrating orifice generator and the laser pulse characteristics change little from

3

pulse to pulse, the image variation from one pulse to the next was not significant. For 3 GW/cm2 irradiance, shown in Fig. 2, the interaction is nearly symmetric with material being expelled in a similar pattern from both the illuminated and shadow hemispheres of the droplet. Figure 3 shows, for the same delay times, a sequence of photographs for an incident irradiance of 6 GW/cm$^2$. At this irradiance, the breakup on the illuminated hemisphere relative to the shadow hemisphere is much weaker. Even at 100 ns, little material is ejected from the illuminated surface. As the irradiance is further increased to 18 GW/cm$^2$, the image shown in Fig. 4 at 0 ns shows no evidence of illuminated surface interaction. However, the breakup on the shadow surface appears stronger than for lower laser irradiances. Only at later times is there any evidence of material leaving the illuminated hemisphere. Figure 5 shows the droplet images obtained under high irradiance (230 GW/cm$^2$) conditions. In this example, the behavior is quite different. The material is ejected in a symmetric manner and appears to form thin filaments of material at 0 ns delay time.

## IV. Theoretical Supporting Work

The behavior of the droplets shown in Figs. 2-5 can be compared to the square root of the internal and near-surface electric field distributions, calculated using plane wave Lorenz-Mie theory, which are shown in Fig. 6. The square root of the electric field is plotted in efforts to emphasize smaller electric field values. As seen in Fig. 6., there appears to be four critical regions in which localized maxima appear. The absolute maximum of the electric field values occurs external to the shadow surface of the droplet and has the magnitude $|E/E_0| \approx 50$ where $|E_0|$ denotes the magnitude of the incident electric field. The high field value results from the focusing effect exhibited by droplets large compared to the incident wavelength. Internal to the droplet surface but still within the shadow hemisphere are three localized peaks each of magnitude $|E/E_0| \approx 22$. Internal to the droplet and near the illuminated surface lies the third critical region in which the magnitude is $|E/E_0| \approx 16$. External to the illuminated hemisphere is also a smaller localized peak of magnitude $|E/E_0| \approx 8$. These four regions of high electric field are characteristic of transparent droplets and have been discussed previously.[13] Provided the incident irradiance is sufficiently high, these four regions, particularly those near the shadow surface, would identify the likely locations of initial laser breakdown. Comparing the calculations in Fig. 6 to the images shown in Fig. 2, similarities are

apparent in the sense that Fig. 6 shows nearly equal (slightly higher within the shadow hemisphere) maximum electric field peaks within the two hemispheres of the droplet. Based on this linear model of the electromagnetic field distributions, one would expect to observe material expelled from both hemispheres of the droplet with the stronger interaction occurring from the shadow hemisphere. The results in Fig. 2 support this argument. In contrast however, the images in Fig. 3 show significantly less material leaving the illuminated surface of the particle suggesting that the interaction is not linear with respect to the incident irradiance.

To better understand the physics occurring during the laser/aerosol interaction, it is necessary to determine the source of the localized peaks in the electric field. As stated previously, the large electric fields near the shadow surface are a result of the focusing effect of the droplet and can be predicted by geometric optics. However, the source of the peaks near the illuminated surface is not intuitively obvious.

The following calculations serve to provide a physical picture of the origin of the localized electric field peaks in the front hemisphere and will be useful in establishing an explanation of the experimental observations. Shown in Fig. 7 is a plot of the fourth root of the magnitude of the time average Poynting vector for an 8 $\mu$m diameter water droplet illuminated by a focused KrF laser beam. The fourth root of the vector magnitude is plotted in order to emphasize and better visualize the smaller Poynting vectors within and external to the illuminated droplet. The focal point of the incident KrF beam used in the calculations has a waist diameter of approximately 1 $\mu$m and is located at the particle edge ($y = d/2$, $x = z = 0$) as shown in Fig. 7. Here, the term edge refers to the points defined by the intersection of $r = d/2$ and the $z = 0$ plane of the droplet. Note the droplet is centered at $x = y = z = 0$ and the laser is propagating in the $+z$ direction with linear polarization in the x direction. Although this particle, for which the calculations are performed, is smaller than the experimental situation under consideration, the case provides qualitative insight into the interaction process while keeping computation times within reasonable limits. A small beam waist was chosen in order to examine the behavior of the incident light over a localized region of the droplet. The theoretical details of the arbitrary beam theory used for the calculations shown in Fig. 7 has been documented previously[10,14] and will not be discussed in this paper. As one would expect, Fig. 7 shows clearly the refraction of the incident beam through the droplet and the subsequent internal reflections as well as the transmissions to the external field. In addition, Poynting vectors oriented

5

predominantly in the circumferential direction appear on both sides of the air/droplet interface indicating the propagation of surface waves. If the incident beam is positioned at different edge locations a similar pattern would be observable in the corresponding plane of the droplet. For the situation corresponding to the images of Fig. 2-5, the beam size ($\approx 100\ \mu$m) is larger than the droplet diameter (60 $\mu$m) in which case the particle is illuminated at all edge locations. These conditions provide the excitation necessary to generate a similar pattern of energy flow in all planes containing the z axis. Both the internally reflected energy and the surface waves will propagate in a predominantly circumferential direction and will tend to be concentrated near the front and rear surfaces of the droplet. The constructive interference of the energy flow will result in the localized peaks which are observed in the source function plots. Calculations for the case of the particle located at the focal point of the beam showed little flow of energy back toward the illuminated hemisphere reinforcing the idea that edge illumination is necessary to provide significant energy feedback toward the illuminated hemisphere.

Based on these theoretical calculations, we can formulate a qualitative explanation of the experimental observations. Denote the breakdown intensity for the laser/aerosol interaction as $I_b$ as shown in Fig. 8 and assume that the initial electrical breakdown occurs near the shadow surface of the droplet where the electric fields are the highest. Initial electrical breakdown along with any changes in geometry or optical properties of the material near the back surface will act to prevent internal reflections and surface wave propagation necessary for generation of high electric fields near the illuminated surface. Shown in Fig. 8 are $P_h$ and $P_l$ which represent the intensity profiles of a high energy and low energy pulse, respectively. If the droplet breakdown occurs at an intensity $I_b$, only the energy associated with the cross-hatched areas will be unaffected by the droplet breakdown. Thus a larger amount of energy can be redirected toward the front hemisphere for a low energy incident pulse. As the irradiance is increased we would expect proportionately less energy available for interaction within and near the illuminated surface of the droplet. This explanation is consistent with the observations in Figs. 2-4. For 230 GW/cm$^2$ interactions shown in Fig. 5, the 17 ns imaging pulse is not short enough to clearly resolve the early stages of the interaction process and future picosecond or femtosecond imaging work will be required to resolve the early stages of the interaction.

6

This work has shown that the prediction of aerosol dynamics resulting from laser-induced breakdown cannot be made based soley on electric field distributions calculated using linear Lorenz-Mie theory. The interaction is influenced by several factors including pulse energy and pulse rise time, which change the magnitude of illuminated hemisphere interaction.

## V. Material Velocity Measurements

The imaging system was also be used to obtain approximate average velocity measurements for the material ejected at various stages during the laser/aerosol interaction. In order to evaluate the velocity of the ejected material, it was necessary to make an assumption regarding the time at which material starts leaving the droplet surface ($\Delta t = 0$). As stated earlier in this paper and illustrated in the images, material ejection starts before what is considered 0 ns delay. For the results presented here, a time of 10 ns before the end of the imaging pulse was chosen as the time material begins leaving the droplet surface. Therefore, in calculating average velocities at 0 ns delay $\Delta t = 10$ ns was used, at 20 ns delay a $\Delta t = 30$ ns was used, etc. Although this delay value will vary depending on the incident irradiance, we have used a constant value for all irradiances since detailed resolution of these times are not presently possible in our laboratory. The average material velocity as a function of time and incident irradiance is shown in Fig. 9. The values range from approximately 1000 m/s at 3 GW/cm$^2$ to 6000 m/s at 230 GW/cm$^2$ with an uncertainty of approximately $\pm 20$ percent. This error is predominantly due to the difficulty in properly identifying the edges of the material boundaries. Only limited data could be obtained at high irradiances since the material quickly propagates out of the field of view of the imaging system.

## V. Acknowledgments

## IV. References

1. R.K. Chang, J.H. Eickmans, W.-F. Hsieh, C.F. Wood, J.- Z. Zhang, and J.-b. Zheng, "Laser-induced breakdown in large transparent water droplets," Appl. Opt., **27** (12), 2377 (1988).

2. D.R. Alexander, S.A. Schaub, J. Zhang, D.E. Poulain, and J.P. Barton, "Scattering of incident KrF laser radiation resulting from the laser-induced breakdown of $H_2O$ droplets," Opt. Lett., **14** (11), 548 (1989).

3. A. Biswas, H. Latifi, L.J. Radziemski, and R.L. Armstrong, "Irradiance and laser wavelength dependence of plasma spectra from single levitated aerosol droplets," Appl. Opt., **27** (12), 2386 (1988).

4. W.-F. Hsieh, J.H. Eickmans, and R.K. Chang, "Internal and external laser-induced avalanche breakdown of single droplets in an argon atmosphere," J. Opt. Soc. Am. B, **4** (11), 1816 (1987).

5. A. Biswas, H. Latifi, P. Shah, L. J. Radziemski, and R.L. Armstrong, "Time-resolved spectroscopy of plasmas initiated on single, levitated aerosol droplets," Opt. Lett., **12** (5), 313 (1987).

6. P. Kafalas and J. Herrmann, "Dynamics and energetics of the explosive vaporization of fog droplets by a 10.6 $\mu$m laser pulse," Appl. Opt., **12** (4), 772 (1973).

7. J.-Z. Zhang and R.K. Chang, "Shape distortion of a single water droplet by laser-induced electrostriction," Opt. Lett., **13** (10), 916 (1988).

8. J.C. Carls and J.R. Brock, "Explosive vaporization of single droplets by lasers: comparison of models with experiments," Opt. Lett., **13** (10), 919 (1988).

9. S.M. Chitanvis, "Explosive vaporization of small droplets by a high-energy laser beam," J. Appl. Phys., **62** (11), 4387 (1987).

10. J.P. Barton, D.R. Alexander, and S.A. Schaub, "Internal and near-surface electromagnetic fields for a spherical particle irradiated by a focused laser beam," J. Appl. Phys., **64** (4), 1632 (1988).

11. B. Maheu, G. Gouesbet, G. Grehan, "A concise presentation of the generalized Lorenz-Mie theory for arbitrary location of the scatterer in an arbitrary incident profile," J. Optics (Paris), **19** (2), 59 (1988).

12. K.D. Ahlers and D.R. Alexander, "Microcomputer based digital image processing system developed to count and size laser-generated small particle images," Opt. Eng., **24** (6), 1060 (1985).

13. W.-F. Hsieh, J.-B. Zheng, C.F. Wood, B.T. Chu, and R.K. Chang, "Propagation velocity of laser-induced plasma inside and outside a transparent droplet," Opt. Lett., **12** (8), 576 (1987).

14. J.P. Barton and D.R. Alexander, "Fifth-order corrected electromagnetic field components for a fundamental Gaussian beam", to be published in J. Appl. Phys., Oct. 1, 1989.

**Figure Labels**

Fig. 1. Schematic of experimental setup.

Fig. 2. Interaction of 3 GW/cm$^2$ KrF ($\lambda$ = 248 nm) laser pulses with 60 $\mu$m water droplets imaged 0, 20, 40, and 100 ns after arrival of the high energy pulse. The laser is propagating from right to left.

Fig. 3. Interaction of 6 GW/cm$^2$ KrF ($\lambda$ = 248 nm) laser pulses with 60 $\mu$m water droplets imaged 0, 20, 40, and 100 ns after arrival of the high energy pulse. The laser is propagating from right to left.

Fig. 4. Interaction of 18 GW/cm$^2$ KrF ($\lambda$ = 248 nm) laser pulses with 60 $\mu$m water droplets imaged 0, 20, 40, and 100 ns after arrival of the high energy pulse. The laser is propagating from right to left.

Fig. 5. Interaction of 230 GW/cm$^2$ KrF ($\lambda$ = 248 nm) laser pulses with 60 $\mu$m water droplets imaged 0, 20, 40, and 100 ns after arrival of the high energy pulse. The laser is propagating from right to left.

Fig. 6. Plane wave Lorenz-Mie theory calculations of the square root of the internal and near-surface electric field for a 60 $\mu$m diameter water droplet ($\bar{n}$ = 1.36 + 3.5 x 10$^{-8}$i) irradiated by a KrF laser pulse ($\lambda$ = 248 nm). Laser is propagating from right to left. Top: $\sqrt{E/E_0}$ as a function of spatial location for -1.5 < 2y/d < 1.5, -1.5 < 2z/d < 1.5 where d is the droplet radius. The laser is propagating in the +z direction with polarization in the x direction. The scale on the plot ranges from black = 0 to white $\approx$ 7. Bottom: Centerline plot for the same parameters as given above.

Fig. 7. Plot of the internal and near-surface Poynting vectors (y-z plane) for a 8 $\mu$m diameter water droplet ($\bar{n}$ = 1.36 + 3.5 x 10$^{-8}$i) illuminated by a focused KrF laser beam ($\lambda$ = 248 nm). The beam waist diameter is approximately 1 $\mu$m and the beam is incident on the right edge of the droplet (y = 1.0, x = z = 0).

Fig. 8. Graphical representation of the relationship between the incident pulse energy and the portion unaffected by the laser-induce breakdown in the shadow hemisphere for a high energy ($P_h$) and low energy ($P_l$) pulse.
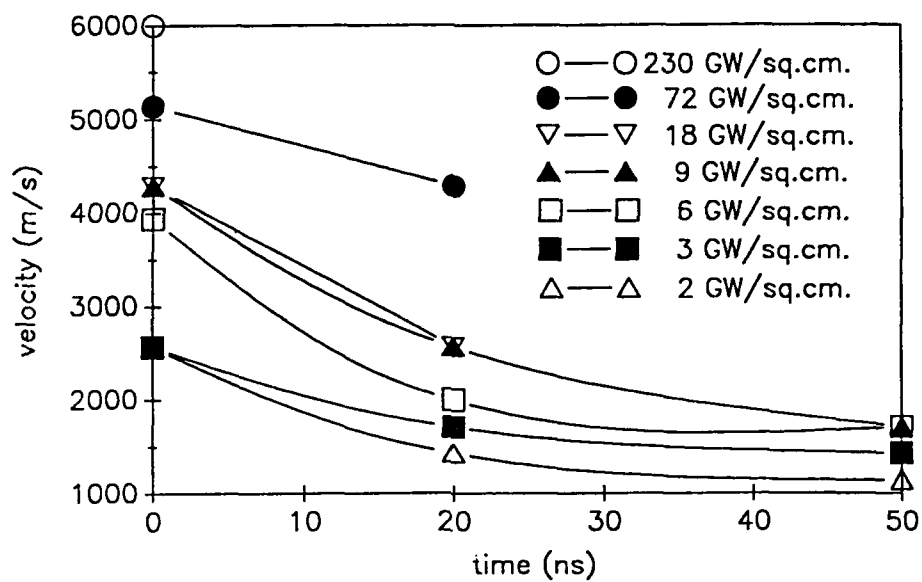
Fig. 9. Average material velocity as a function of image delay time for the interaction of KrF laser pulses ($\lambda = 248$ nm) with 60 $\mu$m diameter water droplets for laser irradiance varying from 3 to 230 GW/cm$^2$.

Fig. 1. Schematic of experimental setup.

0 ns

20 ns

40 ns

100 ns

Fig. 2. Interaction of 3 GW/cm² KrF ($\lambda$ = 248 nm) laser pulses with 60 $\mu$m water droplets imaged 0, 20, 40, and 100 ns after arrival of the high energy pulse. The laser is propagating from right to left.

13

0 ns

20 ns

40 ns

100 ns

Fig. 3. Interaction of 6 GW/cm$^2$ KrF ($\lambda$ = 248 nm) laser pulses with 60 $\mu$m water droplets imaged 0, 20, 40, and 100 ns after arrival of the high energy pulse. The laser is propagating from right to left.

14

Fig. 4. Interaction of 18 GW/cm$^2$ KrF ($\lambda$ = 248 nm) laser pulses with 60 $\mu$m water droplets imaged 0, 20, 40, and 100 ns after arrival of the high energy pulse. The laser is propagating from right to left.

15

Fig. 5. Interaction of 230 GW/cm$^2$ KrF ($\lambda = 248$ nm) laser pulses with 60 $\mu$m water droplets imaged 0, 20, 40, and 100 ns after arrival of the high energy pulse. The laser is propagating from right to left.

Fig. 6. Plane wave Lorenz-Mie theory calculations of the square root of the internal and near-surface electric field for a 60 $\mu$m diameter water droplet ($\bar{n} = 1.36 + 3.5$ x $10^{-8}$i) irradiated by a KrF laser pulse ($\lambda = 248$ nm). Laser is propagating from right to left. Top: $\sqrt{E/E_0}$ as a function of spatial location for $-1.5 < 2y/d < 1.5$, $-1.5 < 2z/d < 1.5$ where d is the droplet radius. The laser is propagating in the $+z$ direction with polarization in the x direction. The scale on the plot ranges from black = 0 to white $\approx$ 7. Bottom: Centerline plot for the same parameters as given above.

17

Fig. 7. Plot of the internal and near-surface Poynting vectors (y-z plane) for a 8 $\mu$m diameter water droplet ($\bar{n} = 1.36 + 3.5$ x $10^{-8}$i) illuminated by a focused KrF laser beam ($\lambda = 248$ nm). The beam waist diameter is approximately 1 $\mu$m and the beam is incident on the right edge of the droplet ($y = 1.0$, $x = z = 0$).

18

Fig. 8. Graphical representation of the relationship between the incident pulse energy and the portion unaffected by the laser-induce breakdown in the shadow hemisphere for a high energy ($P_h$) and low energy ($P_l$) pulse.

Fig. 9. Average material velocity as a function of image delay time for the interaction of KrF laser pulses ($\lambda = 248$ nm) with 60 $\mu$m diameter water droplets for laser irradiance varying from 3 to 230 GW/cm$^2$.

(b) Reprints of Conferences Proceedings, Item 6(b)

# EXPERIMENTAL AND THEORETICAL ANALYSIS OF LIQUID DROPLETS MOVING THROUGH A FOCUSED CO₂ LASER BEAM

J.P. Barton, D.R. Alexander, and S.A. Schaub
Center for Electro-Optics
College of Engineering
University of Nebraska-Lincoln
Lincoln, NE 68588-0525

RECENT PUBLICATIONS, SUBMITTALS FOR PUBLICATION, AND PRESENTATIONS:

A). D.R. Alexander and J.G. Armstrong, "Explosive vaporization of aerosol drops under irradiation by a CO₂ laser beam," Appl. Opt., **26**, 533 (1987).

B). D.R. Alexander, J.P. Barton, S.A. Schaub, and M.A. Fitzwater, "Beam propagation effects resulting from the electric field strengths for spheres and cylinders: internal and near field," presentation at the Workshop on the Physics of Directed Energy Propagation in the Atmosphere." U.S. Army Atmospheric Sciences Laboratory (ASL) at New Mexico State University, Las Cruces. New Mexico, January 27-28, 1987.

C). D.R. Alexander, J.P. Barton, S.A. Schaub, and M.A. Emanuel, "Experimental and theoretical analysis of the interaction of CO₂ laser radiation with fluid cylinders and adjacent spheres," presentation at the 1987 CRDEC Conference on Obscuration and Aerosol Research, June, 1987.

D). D.R. Alexander, J.P. Barton, S.A. Schaub, M.A. Emanuel, and J. Zhang, "Experimental and theoretical analysis of the interaction of laser radiation with fluid cylinders and spheres," Proceedings of the 1987 CRDEC Conference on Obscuration and Aerosol Research.

E). M.A. Emanuel, "Explosive vaporization of spherical and cylindrical aerosols: comparison between experimental results using a CO₂ laser and internal and scattered optical fields," Masters Thesis, Mechanical Engineering Department, Center for Electro-Optics, University of Nebraska-Lincoln, Lincoln, Nebraska, 68588-0525, October, 1987.

F). S.A. Schaub, D.R. Alexander, J.P. Barton, and M.A. Emanuel, "Focused laser beam interactions with methanol droplets: effects of relative beam diameter," submitted to Applied Optics. May, 1988.

G). J.P. Barton, D.R. Alexander, and S.A. Schaub, "Experimental and theoretical analysis of liquid droplets moving through a focused CO₂ laser beam," presentation at the 1988 CRDEC Conference on Obscuration and Aerosol Research, June, 1988.

H). J.P. Barton, D.R. Alexander, and S.A. Schaub, "Internal and near-surface electromagnetic fields for a spherical particle in a focused laser beam," poster presentation at the 1988 CRDEC Conference on Obscuration and Aerosol Research, June, 1988.

I). D.R. Alexander, D.E. Poulain, J.P. Barton, S.A. Schaub, and J. Zhang, "Nonlinear effects of excimer laser radiation with solid particles in a vacuum," presentation at the 1988 CRDEC Conference on Obscuration and Aerosol Research, June, 1988.

J). S.A. Schaub, D.R. Alexander, and J.P. Barton, "Theoretical model for the image formed by a spherical particle in a coherent imaging system: comparison to experiment," submitted to Optical Engineering, July, 1988.

K). J.P. Barton, D.R. Alexander, and S.A. Schaub, "Internal and near-surface electromagnetic fields for a spherical particle irradiated by a focused laser beam," J. Appl. Phys., **64**, 1632 (1988).

L). J.P. Barton, D.R. Alexander, and S.A. Schaub, "Spherical particle irradiated by a tightly-focused laser beam: focal point positioning effects at resonance conditions," submitted to the Journal of Applied Physics, September, 1988.

## Abstract

A simplified theoretical model for predicting the threshold power for explosive fragmentation of liquid droplets falling through the focal point of a tightly-focused, continuous, Gaussian-profiled laser beam has been developed. Theoretically-predicted and corresponding experimentally-measured explosive fragmentation threshold power/droplet velocity ratios are compared for $CO_2$ laser irradiated water droplets within a size parameter range of 5 to 25. The theoretical and experimental data were in agreement within a factor of about two. Future refinements of the theoretical modeling and the experimental procedure are discussed.

## I. Introduction

An experimental and theoretical analysis of the transient heating of 20 $\mu m$ to 80 $\mu m$ diameter (5 to 25 size parameter) liquid droplets falling through the focal point of a tightly-focused, fundamental ($TEM_{00}$ mode), linearly-polarized, Gaussian-profiled, 10.6 $\mu m$ dominant wavelength, continuous $CO_2$ laser beam is considered. A theoretical analysis of this problem is now possible due to our recent development of a spherical particle/arbitrarily-defined beam interaction theory[1] that permits a computationally-efficient means for determining the internal electromagnetic fields within a spherical droplet offset from the focal point of a tightly-focused Gaussian beam. Of particular interest is the development of a theoretical model to predict laser threshold power for the explosive fragmentation of the droplets, for these conditions, as a function of such parameters as beam waist diameter, droplet diameter, and droplet thermo/optical properties. An agreement between theoretically-predicted explosive fragmentation threshold power with the corresponding experimentally-measured values would support the physical mechanism assumptions of the theoretical model. Presented here is our preliminary effort at theoretically modeling falling droplet/tightly-focused laser beam heating and an initial comparison (including discussion) between theoretically-predicted and experimentally-measured explosive fragmentation threshold powers for water droplets in a size parameter range of 5 to 25.

A theoretical analysis of the transient heating of a liquid droplet irradiated by a laser pulse has been previously investigated by Prishivalko and Leiko[2] and by Pendleton.[3] In both of these analyses, monochromatic plane wave illumination upon a spherical particle was assumed, so Lorenz-Mie theory was appropriately applied to determine the internal electromagnetic field distributions necessary for the calculation of the spatially-distributed heating within the droplet. Such an incident plane wave assumption would be valid for conditions where the incident laser beam intensity is uniform over the projected area of the droplet, as might be the case if the local beam diameter

is much greater than the diameter of the droplet. Lorenz-Mie theory, and thus the analyses of Prishivalko and Leiko[2] and of Pendleton,[3] is not applicable for a spherical droplet moving through the focal point of a tightly-focused beam, as is of interest here.

Prishivalko,[4] utilizing an empirical criterion, claimed good agreement (5-10%) with experimental intensity threshold measurements for the explosive fragmentation of 20 $\mu m$ to 60 $\mu m$ diameter water droplets irradiated by a 10.6 $\mu m$ wavelength $CO_2$ laser pulse. Calculations by Pendleton[3] were consistent with the pulsed $CO_2$ laser fragmentation patterns observed by Kafalas and Ferdinand.[5] Otherwise, there appears to be little detailed theoretical/experimental comparisons for $CO_2$ laser heating of liquid droplets in the explosive fragmentation regime. To our knowledge there has been no previous detailed theoretical/experimental comparisons for liquid droplets falling through the focal point of a tightly-focused, continuous, $CO_2$ laser beam.

## II. Experimental Arrangement

The experimental arrangement and procedure are described in detail in Ref. 6; only a general description will be provided here. A schematic of the experimental arrangement is shown in Fig. 1. The fundamental ($TEM_{00}$ mode), linearly polarized, Gaussian-profiled beam from a 100 W maximum power, 10.6 $\mu m$ dominant wavelength, continuous $CO_2$ laser is focused to an estimated 100 $\mu m$ beam waist diameter. A ordered stream of monodispersed liquid droplets, produced by a vibrating orifice droplet generator, is directed through the focal point of the $CO_2$ laser beam. The droplets fall vertically downward, parallel to the electric field polarization direction of the linearly-polarized $CO_2$ laser beam. A phase/Doppler particle analyzer (not shown in Fig. 1) is used to monitor the size and velocity of the liquid droplets. Droplets enter the 100 $\mu m$ diameter $CO_2$ laser focal point with a velocity of the order 10 m/s, resulting in a beam exposure time of approximately 10 $\mu s$. The dynamics of the $CO_2$ laser/liquid droplet interaction are imaged using a back illumination, pulsed $N_2$ laser (337 nm wavelength, $\approx$ 10 ns pulse width)/vidicon camera-based imaging system.

For a particular droplet stream, it was observed that there existed a rather distinct $CO_2$ laser threshold power for explosive fragmentation of the droplets. Below the threshold power, the droplets would fall through the $CO_2$ laser beam focal point with no detectable shape distortion. Above the $CO_2$ laser threshold power the droplets would violently shatter. The threshold power for explosive fragmentation of water (distilled) droplets was experimentally measured as a function

of droplet diameter. The experimental procedure is as follows. For a particular droplet stream, the droplet diameter and velocity are measured using the phase/Doppler particle analyzer. The power of the $CO_2$ laser is then gradually increased until explosive fragmentation is observed on the pulsed $N_2$ laser imaging system. The droplet stream is then removed from the $CO_2$ laser focal point and the threshold power measured using a power meter.

Threshold power measurements were obtained for droplet diameters from 20 $\mu m$ to 80 $\mu m$. Defining the droplet size parameter, $\alpha$, as the ratio of the droplet circumference to the incident beam wavelength,

$$\alpha = \frac{2\pi a}{\lambda},$$

where a is the droplet radius, this range of droplet diameters corresponds to a size parameter range of about 5 to 25.

Typically, threshold powers for explosive fragmentation were of the order of 10 W for water droplets within the range of size parameters considered. Calculated focal point threshold intensities for these experiments are thus of the order of $10^5$ W/cm$^2$. A summary of nominal operating parameters is given in Table 1.

### III. Theoretical Modeling

Only theoretical modeling of the state of the droplet up to the time at which explosive fragmentation initiates is considered. A simplified theoretical model, appropriate for our experimental conditions, was developed as a first attempt at predicting required threshold powers for droplet explosive fragmentation as a function of such parameters as beam waist diameter, droplet diameter, and droplet thermo/optical properties. The simplified theoretical model will serve as the basis for developing more sophisticated and complete theoretical models as might be warranted by experimental comparisons and observations. Major assumptions of the simplified theoretical model are listed and discussed in the following.

**Criteria for explosive fragmentation: 0.9 $T_{cr}$ superheat temperature limit.** Similar to the approach of Prishivalko[2,4] and Pendleton,[3] it was assumed that the explosive fragmentation of the liquid droplets results from the superheating of the droplet liquid to the superheat limit, at which time spontaneous vapor nucleation occurs and the droplet is shattered by rapidly expanding vapor

bubbles. The threshold nature of the laser power necessary to explosively fragment the droplets and the observation of vapor bubbles within the liquid droplets during the initial stages of droplet fragmentation provide experimental justification for this assumption. Zemlyanov and Kuzikovskii[7] also indicate that such "shock boiling" is the correct mechanism for $CO_2$ laser irradiated water droplet explosive fragmentation for an intensity range similar to that of our experiments ($\approx 10^4$ to $10^5$ W/cm$^2$). Skripov[8] deduced that a freely suspended, pure liquid may obtain a superheated temperature of nine-tenths its critical temperature before spontaneous vapor nucleation initiates. Using this $0.9T_{cr}$ criterion, the superheat limit is then 583 K (310 °C) for water. Superheat temperatures for liquid water approximately equal to this value have been obtained during carefully controlled experiments.[9] The theoretically calculated minimum laser power required to raise the temperature of any point within the liquid droplet to $0.9\ T_{cr}$, after the droplet has fallen entirely through the focal point of the laser beam, was chosen as the criteria for predicting the explosive fragmentation threshold power.

**Neglect hydrodynamic effects.** For laser powers just below threshold for explosive fragmentation, the droplets were experimentally observed to fall through the focal point of the beam with no noticeable shape distortion. It is assumed that the heating for our conditions is sufficiently slow so that possible thermally-induced hydrodynamic effects such as thermal shock do not occur and the droplet remains spherical during heating. Thermal expansion of the droplet is also neglected, so the droplet is assumed to have a constant diameter during heating.

**Temperature independent optical properties.** The assumption of a single, uniform complex index of refraction, $\bar{n}$, for the droplet is necessary for the electromagnetic field calculations. It is recognized that the complex index of refraction of a liquid can be temperature dependent, and spatially-distributed heating within the droplet can create a spatially-distributed complex index of refraction. However, electromagnetic field calculations for such an inhomogeneous sphere are exceedingly difficult and the temperature dependence of the complex index of refraction for liquids, from room temperature to $0.9T_{cr}$, at the $CO_2$ wavelength is not well known.

**Neglect internal heat conduction and droplet surface heat convection/evaporation losses.** A characteristic time for heat conduction within the droplet can be determined in terms of the thermal diffusivity of the liquid, $\alpha_{th}$, and the droplet radius, a,

$$\Delta t = a^2/\alpha_{th}.$$

Using the room temperature thermal diffusivity of water, $1.44 \times 10^{-7}$ m$^2$/s, and a droplet radius of 10 $\mu m$ this expression gives a characteristic time for heat conduction of 694 $\mu s$, which is much greater than the approximately 10 $\mu s$ heating time of droplet beam exposure. Thus, in order to simplify the calculations, internal heat conduction is neglected during the laser heating time of the droplet. If heat conduction is neglected then droplet surface losses would not affect the interior temperatures of the droplet, and thus possible surface heat losses by either heat convection or evaporation are also neglected.

The geometrical arrangement for the theoretical calculations is shown in Fig. 2. As shown, the origin of the $(x_o, y_o, z_o)$ coordinate system is located at the focal point of the assumed focused, fundamental (TEM$_{00}$ mode), linearly-polarized, Gaussian-profiled, monochromatic beam. The focused Gaussian beam propagates in the $+z_o$ axis direction with electric field polarization in the perpendicular $x_o$ axis direction. The $(x,y,z)$ coordinate system is attached to the center of the spherical droplet. The droplet is assumed to fall at constant velocity, $v_o$, along the beam $x_o$ axis through the focal point of the beam, as shown in Fig. 2.

The electromagnetic field components of the focused Gaussian beam were determined using the first order corrected paraxial Gaussian beam description of Davis.[1,10] The electromagnetic field distribution within the droplet, which depends upon the position of the droplet relative to the focal point of the beam, was computed using the spherical particle/arbitrarily-defined beam interaction theory of our earlier paper.[1] The spatially-distributed volumetric heat rate within the droplet, $\dot{Q}'''(\vec{r}, t)$, which varies in time as the droplet falls through the profile of the beam, can be related to the electric field magnitude by

$$\dot{Q}'''(\vec{r}, t) = \frac{1}{2}\sigma|\vec{E}(\vec{r}, t)|^2, \tag{1}$$

where $\sigma$ is the electrical conductivity of the droplet liquid at the incident beam frequency. The electrical conductivity can be related to the real and imaginary parts of the liquid complex index of refraction by

$$\sigma = \frac{n_R n_I c}{\lambda} \tag{2}$$

The square of the electric field magnitude can be eliminated in terms of the normalized source function, $\tilde{S}(\vec{r}, t)$, which is defined as

$$\tilde{S}(\vec{r},t) = \frac{|\vec{E}(\vec{r},t)|^2}{|E_o|^2}, \tag{3}$$

where $|E_o|^2$, for these calculations, is the electric field magnitude squared at the focal point of the incident beam which, for a focused Gaussian beam, can be expressed in terms of the beam power. P, and the beam waist radius, $w_o$:

$$|E_o|^2 = \frac{16}{c}\frac{P}{w_o^2}. \tag{4}$$

Substituting from Eqs. (2), (3), and (4) into Eq. (1) provides an expression for $\dot{Q}'''$ in terms of more fundamental parameters,

$$\dot{Q}'''(\vec{r},t) = \frac{8 n_R n_I P}{\lambda w_o^2}\tilde{S}(\vec{r},t) \tag{5}$$

where $\tilde{S}(\vec{r},t)$ is determined using a computer program based on the spherical particle/arbitrary incident beam interaction theory discussed in Ref. 1. For our $CO_2$ laser/water droplet explosive fragmentation experiments, typical laser powers were of the order of 10 W and normalized source function values were, at the maximum, of the order of 1, which would correspond to a calculated maximum volumetric heat rate, using Eq. (5), of $\approx 3 \times 10^8$ W/cm$^3$.

As expressed in Eq. (5), the volumetric heat rate is directly proportional to the normalized source function, thus plots of the normalized source function provide an indication of the spatially-distributed heating within the droplet. Normalized source function calculations were performed for water droplets for conditions corresponding to our experimental arrangement ($\lambda = 10.6\ \mu m$, $w_o = 50\ \mu m$, and, for water, $\bar{n} = 1.179 + i0.072$). As an example, shown in Figs. 3, 4, and 5 are normalized source function distributions in the x-z plane for a 40 $\mu m$ diameter water droplet with the center of the droplet located one beam waist radius above the beam focal point (Fig. 3), one-half beam waist radius above the beam focal point (Fig. 4), and at the beam focal point (Fig. 5). In Figs. 3, 4, and 5, and all subsequent Figs., the spatial coordinates are normalized relative to the droplet radius and external normalized source function values have been artificially suppressed to zero. As can be seen in Figs. 3, 4, and 5, the normalized source function, and thus the volumetric heat rate, increases as the droplet approaches the beam axis, as would be expected for such a Gaussian-profiled beam. For droplet positioning at the beam focal point, Fig. 5, the

normalized source function distribution is similar to that for the corresponding case with plane wave illumination, shown in Fig. 6. However, for droplet positioning away from the beam focal point, there is preferential heating within the part of the droplet nearest the beam focal point as can be seen in Figs. 3 and 4.

The temperature distribution within the droplet, and the theoretically-predicted explosive fragmentation threshold power, can be determined by integrating the volumetric heating rate over time for each spatial position within the droplet. Since in the simplified theoretical model internal heat conduction and surface losses are being neglected, the general heat equation for any point within the droplet takes the form of

$$\rho \frac{\partial u(\vec{r}, t)}{\partial t} = \dot{Q}'''(\vec{r}, t)$$

or, after integration,

$$u(\vec{r}, t) - u(\vec{r}, 0) = \frac{1}{\rho} \int_0^t \dot{Q}'''(\vec{r}, t') dt' \tag{6}$$

where u is the internal energy per unit mass and $\rho$ is the liquid mass density (assumed constant). Substituting from Eq. (5) gives

$$u(\vec{r}, t) - u(\vec{r}, 0) = \frac{8 n_R n_I P}{\rho \lambda w_o^2} \int_0^t \tilde{S}(\vec{r}, t') dt'. \tag{7}$$

Since the droplet is assumed to fall at a constant velocity, $v_o$, the position of the center of the droplet on the $x_o$ axis can be related to time by

$$x_o(t) = x_o(0) - v_o t \tag{8}$$

where $x_o(0)$, the initial position of the droplet, is assumed to be well above the intensity profile of the beam. Using Eq. (8), the variable of integration of Eq. (7) can be changed so that

$$\frac{u(\vec{r}, t) - u(\vec{r}, 0)}{\frac{8 n_R n_I}{2 \pi \rho w_o^2} \frac{P}{v_o}} = \alpha \int_{\tilde{x}_o(t)}^{\tilde{x}_o(0)} \tilde{S}(\vec{r}, \tilde{x}_o') d\tilde{x}_o' = \widetilde{\Delta T}(\vec{r}, \tilde{x}_o) \tag{9}$$

where $\tilde{x}_o = x/a$ is the position of the center of the droplet normalized relative to the droplet radius and the integral of Eq. (9), which is determined numerically, is defined as $\widetilde{\Delta T}(\vec{r}, t)$ since,

if a constant specific heat is assumed, this integral provides a normalized temperature distribution within the droplet as a function of droplet position along the $x_o$ axis of the beam.

As an example, Figs. 7 - 12 show the x-z plane distribution of $\widetilde{\Delta T}$ for a 40 $\mu m$ diameter water droplet falling through the focal point of a laser beam for conditions corresponding to those of our experiments ($\lambda = 10.6$ $\mu m$, $w_o = 50$ $\mu m$, and, for water, $\bar{n} = 1.179 + i0.072$). Figures 7 - 12 are for the droplet center located one beam waist radius above the focal point (Fig. 7), one-half beam waist radius above the focal point (Fig. 8), at the focal point (Fig. 9), one-half beam radius below the focal point (Fig. 10), one beam radius below the focal point (Fig. 11), and two beam radii below the focal point (Fig. 12). After two beam radii below the focal point there is insignificant additional heating for the 40 $\mu m$ diameter water droplet for these conditions.

The sequence of Figs. 7 - 12 demonstrates the heating pattern of the droplet as it falls through the focal point of the beam. The $\widetilde{\Delta T}$ distribution increases in amplitude as the droplet falls through the Gaussian intensity profile of the beam. At the beam focal point, Fig. 9, the droplet is preferentially heated on the bottom half because this part of the droplet has been exposed to a greater fraction of the beam profile than the top half of the droplet. After falling entirely through the beam, Fig. 12, the distribution of $\widetilde{\Delta T}$ is symmetrical with regard to bottom and top halves of the droplet. (If internal heat conduction were included in the theoretical model, this would not necessarily be the case.)

The threshold power for explosive fragmentation is calculated by first determining the maximum value of $\widetilde{\Delta T}$ after the droplet has fallen entirely through the beam profile, and then evaluating, using Eq. (9), the laser power necessary to bring the temperature of this point up to $0.9T_{cr}$. Since laser power, P, and droplet velocity, $v_o$, occur as a ratio in our simplified model, the threshold criteria is expressed as the ratio of these two quantities:

$$\left. \frac{P}{v_o} \right)_{0.9T_{cr}} = \frac{\left. \Delta u \right)_{0.9T_{cr}}}{\frac{8n_R n_I}{2\pi \rho w_o^2} \widetilde{\Delta T}_{max}}, \tag{10}$$

where $\left. \Delta u \right)_{0.9T_{cr}} = u(0.9T_{cr}) - u(T_{initial})$, $T_{initial}$ is the droplet temperature before entering the beam (taken as 20 °C for our calculations), and $\widetilde{\Delta T}_{max}$ is the maximum value of $\widetilde{\Delta T}$ within the droplet after falling entirely through the beam.

Substituting values for our experimental conditions gives an explosive fragmentation threshold criteria for water of

$$\frac{P}{v_o}\Big)_{0.9T_{cr}} = \frac{30.0}{\widetilde{\Delta T}_{max}}[W/(m/s)].\tag{11}$$

For comparison, laser power/droplet velocity ratios for normal atmospheric pressure boiling were also calculated using $\Delta u_{boiling} = u(100\ ^\circ C) - u(T_{initial})$ instead of $\Delta u_{0.9T_{cr}}$ in Eq. (10) with a resulting value for water of

$$\frac{P}{v_o}\Big)_{boiling} = \frac{7.73}{\widetilde{\Delta T}_{max}}[W/(m/s)].\tag{12}$$

Continuing the example of the 40 $\mu m$ diameter water droplet for our experimental conditions, it was determined the maximum value of $\widetilde{\Delta T}$ after the droplet has fallen completely through the beam focal point, (see Fig. 12) was 28.6 . Substituting into Eq. (11), an explosive fragmentation threshold power/droplet velocity ratio of 0.95 [W/(m/s)] is theoretically-predicted for the 40 $\mu m$ diameter water droplet.

## IV. Theoretical/Experimental Comparison

A comparison between theoretically-predicted explosive fragmentation threshold power/droplet velocity ratio and the corresponding experimentally-measured values is shown in Fig. 13 for water droplets in the sized parameter range from 5 to 25. The solid line labeled "superheat" in Fig. 13 is the theoretically-predicted explosive fragmentation threshold power/droplet velocity ratio using the $0.9T_{cr}$ (310 $^\circ$C) maximum temperature criteria. The solid line labeled "boiling" is the theoretically-predicted threshold power/droplet velocity ratio necessary to raise the maximum temperature to the atmospheric pressure boiling point (100 $^\circ$C). For size parameters less than about 9 ($\approx$ 30 $\mu m$ diameter), the theoretically-predicted maximum temperature point within the water droplet occurs on the shadow (unilluminated) side of the droplet and, indeed, for water droplets of size parameter less than about 9, it was experimentally observed on the pulsed $N_2$ laser imaging system that explosive fragmentation would initiate on the shadow side. For size parameters greater than about 9, the theoretically-predicted maximum temperature point occurs on the illuminated side of the water droplet and, consistent with the theoretical model, for size parameters greater than about 9 it was experimentally observed that explosive fragmentation would initiate on the illuminated side of the droplet.

The corresponding experimentally-measured values of explosive fragmentation threshold power /droplet velocity ratio (represented in Fig. 13 by the hollow circles) demonstrated a degree of

nonrepeatability from one test day to the next beyond that expected due to normal variations in experimental conditions and procedures. Because of this, no statistical averaging of the experimental data was performed, and all individual raw data points are presented in Fig. 13. The experimental data cluster about the theoretically-predicted "superheat" line, which suggests that the liquid droplets are being significantly superheated before explosive fragmentation. The theoretically-predicted explosive fragmentation threshold power/droplet velocity ratio agrees with the experimental measurements over the 5 to 25 size parameter range within a factor of about two. The theoretically-predicted decrease in required explosive fragmentation threshold power/droplet velocity ratio for size parameter less than about 9 (when explosive fragmentation initiation goes from illuminated side to shadow side) is not seen in the experimental data.

The degree of nonrepeatability of experimental data may be a result of the influence of additional physical mechanisms not included in the simplified theoretical model which are variable from one experimental setup to the next. One concern is the quality of the droplet stream. The consistency and spherical nature of the droplet stream is monitored using the pulsed $N_2$ laser imaging system and experimental measurements are taken only when the droplet stream is of apparent high quality. Small internal oscillations of droplet shape ($\approx 1~\mu m$ and less) would be undetectable on the imaging system and may influence the required threshold power. The individual droplets may be rotating or possess internal circulation, both of which would explain the occasional higher than expected explosive fragmentation threshold power. It is also known that the droplets leaving the vibrating orifice droplet generator may be electrically-charged, which may or may not affect the path of the droplet through the laser beam focal point and the required explosive fragmentation threshold power. These and several other physical mechanisms are being considered and analyzed for their contribution to the required explosive fragmentation threshold power measurements.

## V. Summary and Future Work

A simplified theoretical model, utilizing the spherical particle/arbitrarily-defined beam interaction theory of our Ref. 1, has permitted, for the first time, a direct comparison between theoretically-predicted and experimentally-measured explosive fragmentation threshold powers for a droplet falling through a tightly-focused, continuous, laser beam. Agreement between theory and experiments would imply a good understanding of the underlying physical mechanisms of the process. For our experimental conditions, theoretically-predicted and experimentally-measured threshold

power/droplet velocity ratios were in agreement within a factor of about two for the explosive fragmentation of $CO_2$ laser irradiated water droplets in the size parameter range of 5 to 25.

Future work includes analyzing and improving the repeatability of the experimental measurements, and refining the theoretical model by including internal heat conduction and surface convection and evaporation losses. Comparisons between theory and experiment for liquids other than water (such as methanol) are also underway and being analyzed.

## Acknowledgements

## References

1. J.P. Barton, D.R. Alexander, and S.A. Schaub, "Internal and near-surface electromagnetic fields for a spherical particle irradiated by a focused laser beam," J. Appl. Phys., 64, 1632 (1988).
2. A.P. Prishivalko and S.T. Leiko, "Radiative heating and evaporation of droplets," Sov. J. App. Spectroscopy, 33, 1137 (1980).
3. J.D Pendleton, "Water droplets irradiated by a pulsed $CO_2$ laser: comparison of computed temperature contours with explosive vaporization patterns," Appl. Opt., 24, 1631 (1985).
4. A.P. Prishivalko, "Vaporization and explosion of water droplets on exposure to radiation with inhomogeneous internal heat evolution," Sov. J. Quantum Electron., 9, 851 (1979).
5. P. Kafalas and A.P. Ferdinand, Jr., "Fog droplet vaporization and fragmentation by a 10.6 $\mu m$ laser pulse," Appl. Opt., 12, 29 (1973).
6. D.R. Alexander and J.G. Armstrong, "Explosive vaporization of aerosol drops under irradiation by a $CO_2$ laser beam," Appl. Opt., 26, 533 (1987).
7. A.A. Zemlyanov and A.V. Kuzikovskii, "Modeling of the gasdynamic regime of an exploding water droplet in a high-power pulsed light field," Sov. J. Quantum Electron., 10, 876 (1980).
8. V.P. Skripov, Metastable Liquids, (Wiley, New York, 1974), p. 177.
9. J.P. Hartnett and T.F. Irvine, Jr., eds., Advances in Heat Transfer, Vol. 10, (Academic Press, New York, 1974), pp. 92-110.
10. L.W. Davis, "Theory of electromagnetic beams," Phys. Rev. A, 19, 1177 (1979).

## CO₂ Laser Experiment Arrangement

**TOP VIEW**
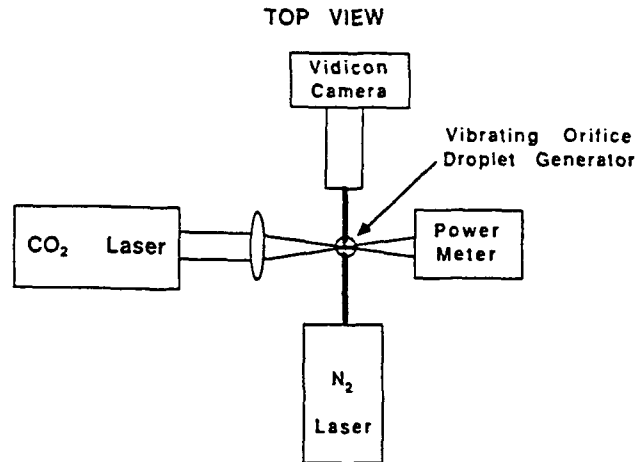


Fig. 1. Experimental arrangement for $CO_2$ laser/liquid droplet explosive fragmentation threshold power measurements.

## Geometrical Arrangement
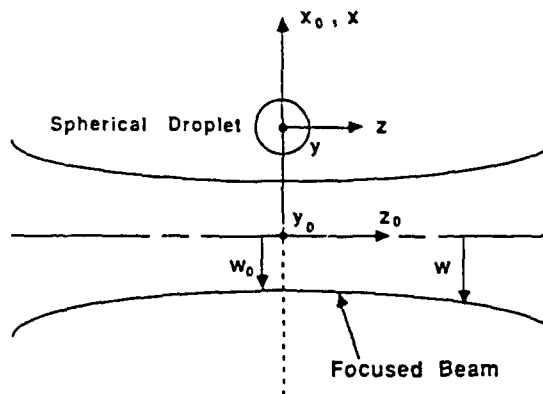


Fig. 2. Geometrical arrangement for theoretical modeling of liquid droplet falling through the focal point of a focused Gaussian laser beam.

## Nominal Operating Parameters

$CO_2$ Laser:

continuous
10.6 $\mu$m   wavelength
TEM$_{00}$  mode
Gaussian  profile
linear  polarization
$P \approx 10W$
$2w_0 = 100\mu m$
$I_0 \approx 10^5$  W/cm$^2$

Droplets:

water,  $\overline{n} = (1.179, 0.072)$
$2a = 20\mu m$  to  100 $\mu m$
$\alpha = 2\pi a /\lambda_0 = 6$ to 30
velocity,  $v \approx 10$ m/s
beam exposure time  $\approx 10$ $\mu$s

$N_2$  Laser Imaging:

337 nm  wavelength
$\approx 10$ ns pulse

Table 1. Nominal operating parameters for $CO_2$ laser/water droplet explosive fragmentation threshold power experiments.
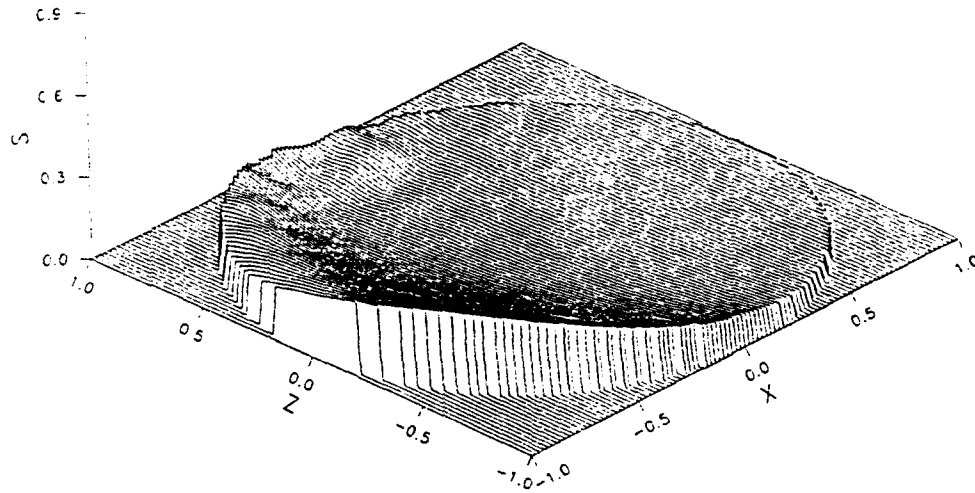
Fig. 3. Normalized source function distribution in the transverse (x-z) plane for a 40 $\mu m$ diameter water droplet located 50 $\mu m$ above the focal point of a 50 $\mu m$ beam waist radius, 10.6 $\mu m$ wavelength, focused Gaussian laser beam propagating in the + z axis direction and linearly polarized in the x axis direction.
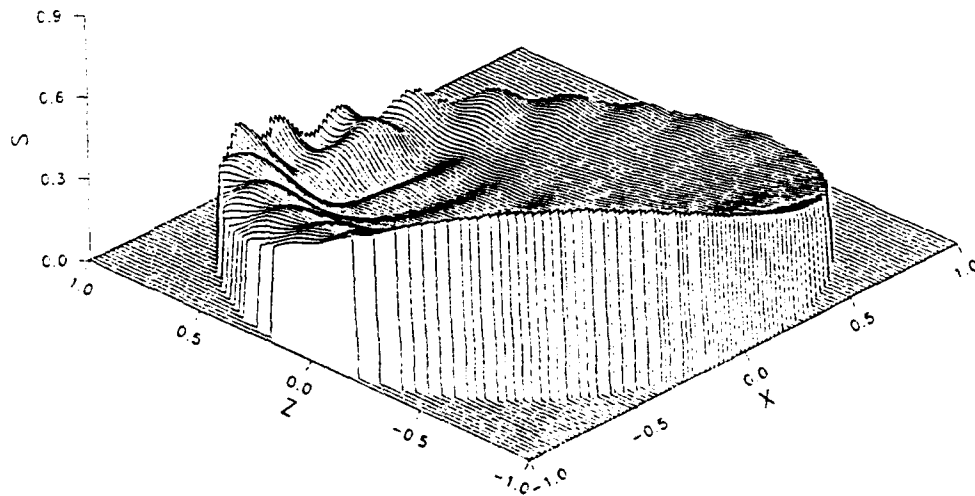


Fig. 4. Normalized source function distribution in the transverse (x-z) plane for a 40 $\mu m$ diameter water droplet located 25 $\mu m$ above the focal point of a 50 $\mu m$ beam waist radius, 10.6 $\mu m$ wavelength, focused Gaussian laser beam propagating in the + z axis direction and linearly polarized in the x axis direction.
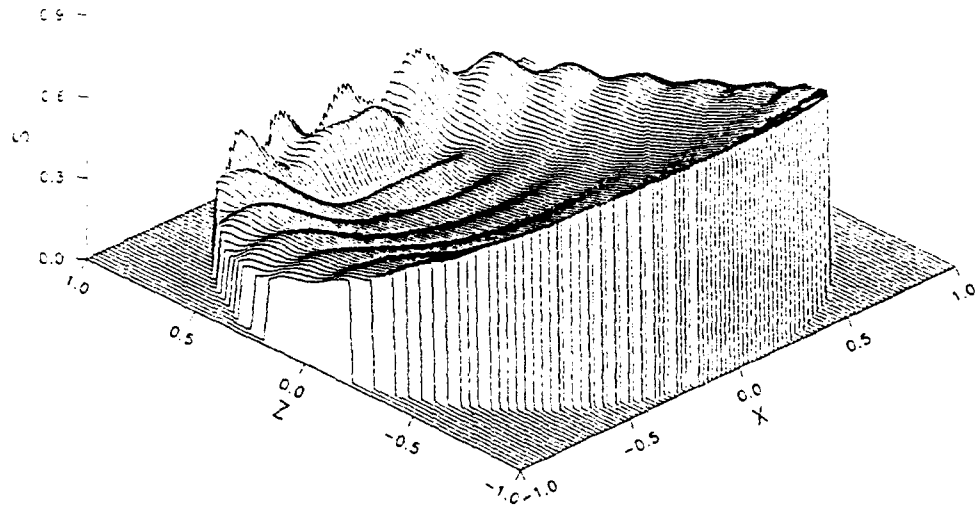
Fig. 5. Normalized source function distribution in the transverse (x-z) plane for a 40 $\mu m$ diameter water droplet located at the focal point of a 50 $\mu m$ beam waist radius, 10.6 $\mu m$ wavelength, focused Gaussian laser beam propagating in the + z axis direction and linearly polarized in the x axis direction.
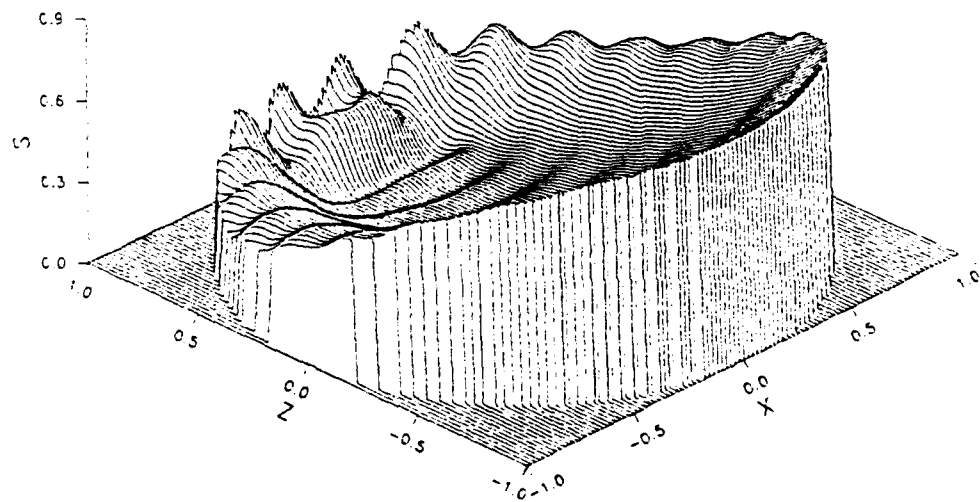


Fig. 6. Normalized source function distribution in the transverse (x-z) plane for a 40 $\mu m$ diameter water droplet irradiated by a 10.6 $\mu m$ wavelength plane electromagnetic wave propagating in the + z axis direction and linearly polarized in the x axis direction.
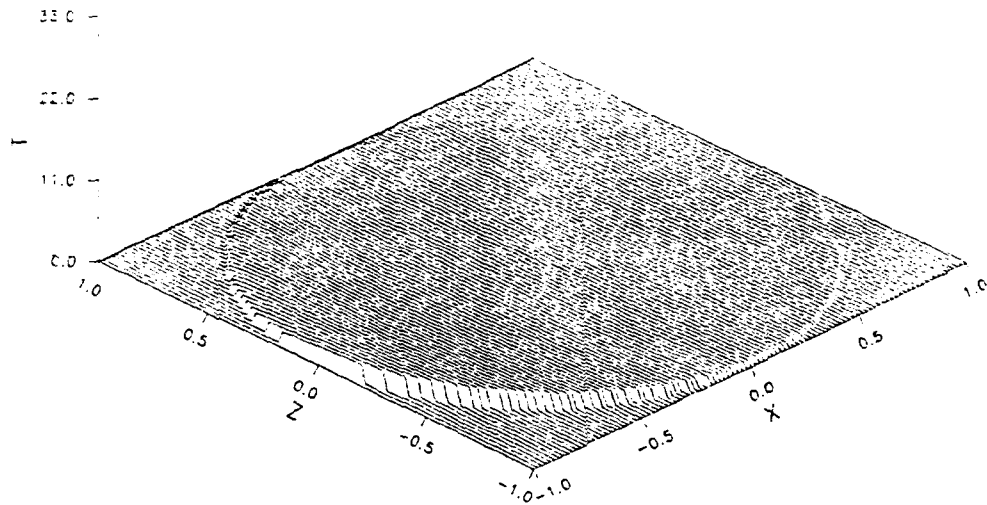
Fig. 7. $\widetilde{\Delta T}$ distribution in the transverse (x-z) plane for a 40 $\mu m$ diameter water droplet located 50 $\mu m$ above the focal point of a 50 $\mu m$ beam waist radius, 10.6 $\mu m$ wavelength, focused Gaussian laser beam propagating in the $+ z$ axis direction and linearly polarized in the x axis direction.
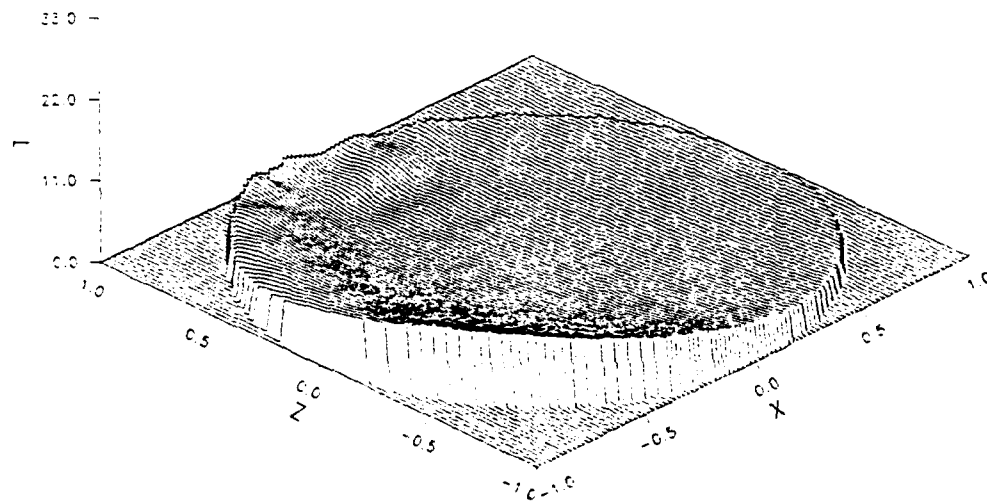


Fig. 8. $\widetilde{\Delta T}$ distribution in the transverse (x-z) plane for a 40 $\mu m$ diameter water droplet located 25 $\mu m$ above the focal point of a 50 $\mu m$ beam waist radius, 10.6 $\mu m$ wavelength, focused Gaussian laser beam propagating in the $+ z$ axis direction and linearly polarized in the x axis direction.
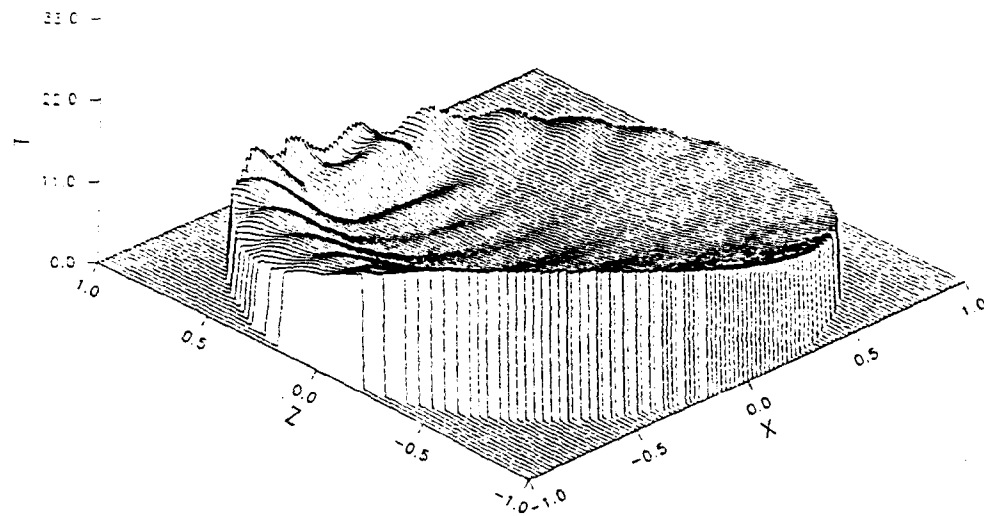
Fig. 9. $\widetilde{\Delta T}$ distribution in the transverse (x-z) plane for a 40 $\mu m$ diameter water droplet located at the focal point of a 50 $\mu m$ beam waist radius, 10.6 $\mu m$ wavelength, focused Gaussian laser beam propagating in the $+z$ axis direction and linearly polarized in the x axis direction.
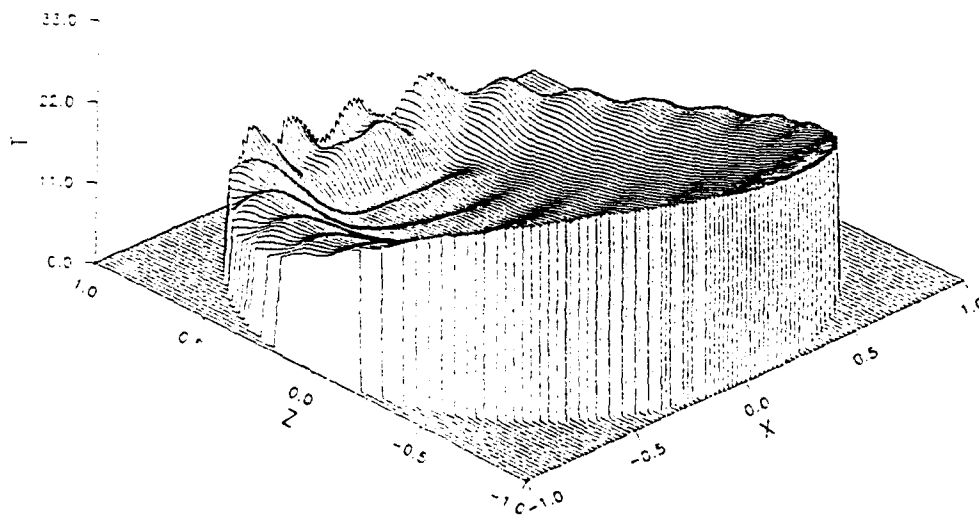


Fig. 10. $\widetilde{\Delta T}$ distribution in the transverse (x-z) plane for a 40 $\mu m$ diameter water droplet located 25 $\mu m$ below the focal point of a 50 $\mu m$ beam waist radius, 10.6 $\mu m$ wavelength, focused Gaussian laser beam propagating in the $+z$ axis direction and linearly polarized in the x axis direction.
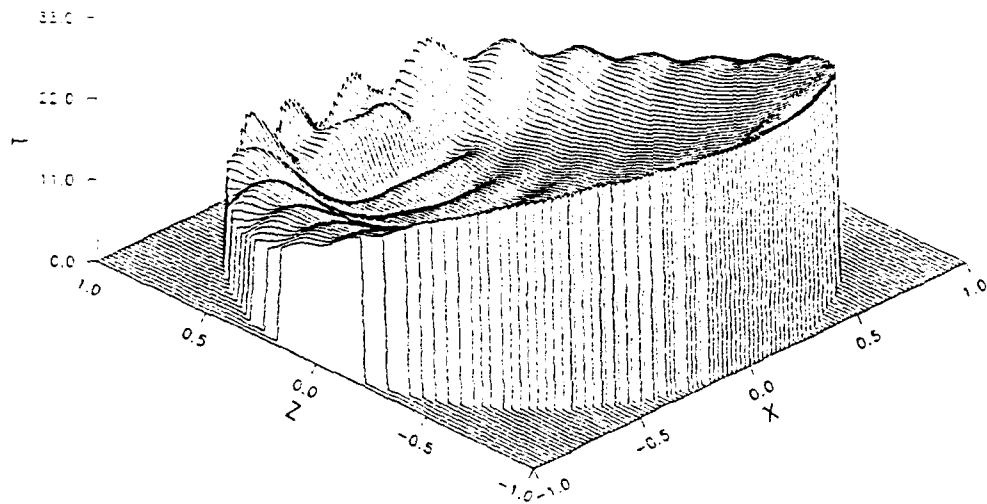
Fig. 11. $\widetilde{\Delta T}$ distribution in the transverse (x-z) plane for a 40 $\mu m$ diameter water droplet located 50 $\mu m$ below the focal point of a 50 $\mu m$ beam waist radius, 10.6 $\mu m$ wavelength, focused Gaussian laser beam propagating in the + z axis direction and linearly polarized in the x axis direction.
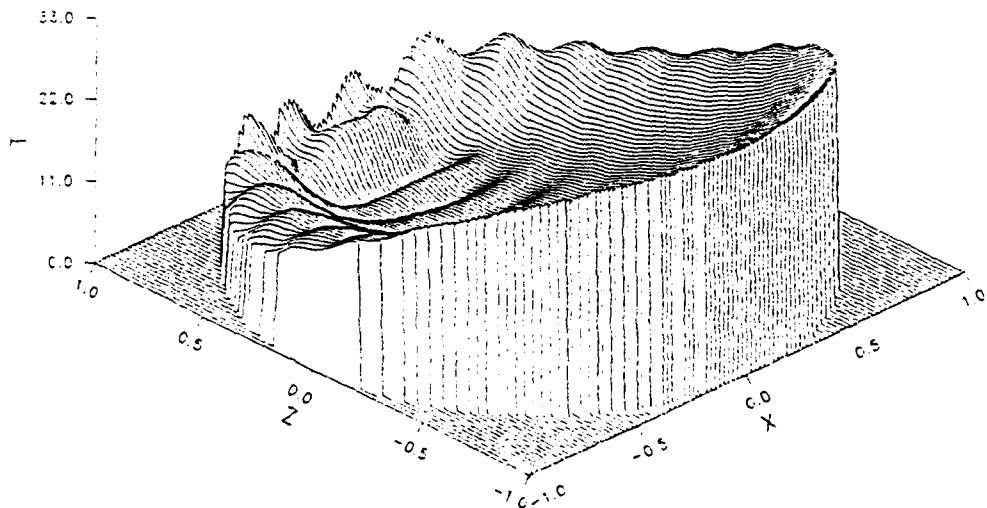


Fig. 12. $\widetilde{\Delta T}$ distribution in the transverse (x-z) plane for a 40 $\mu m$ diameter water droplet located 100 $\mu m$ below the focal point of a 50 $\mu m$ beam waist radius, 10.6 $\mu m$ wavelength, focused Gaussian laser beam propagating in the + z axis direction and linearly polarized in the x axis direction.
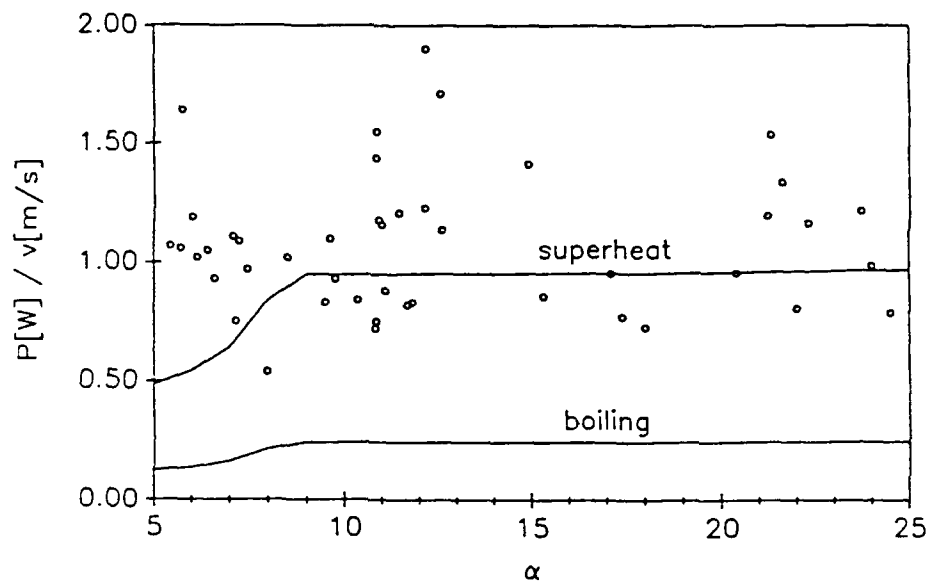
Fig. 13. Comparison between experimental and theoretical explosive fragmentation threshold power/droplet velocity ratio values for water droplets falling through the focal point of a 100 $\mu m$ beam waist diameter, 10.6 $\mu u$ dominant wavelength, linearly polarized, continuous $CO_2$ laser beam.

# INTERACTION OF EXCIMER LASER RADIATION
# WITH SOLID PARTICLES

D.R. Alexander, D.E. Poulain, J.P. Barton, S.A. Schaub, and J. Zhang

Center for Electro-Optics
University of Nebraska-Lincoln
Lincoln, Nebraska 68588-0525

## RECENT PUBLICATIONS, SUBMITTALS FOR PUBLICATION AND PRESENTATIONS

A) J.P. Barton, D.R. Alexander, and S.A. Schaub, "Spherical particle irradiated by a tightly-focused laser beam: focal point positioning effects at resonance conditions", submitted for publication in J. Appl. Phys., September 1988.

B) J.P. Barton, D.R. Alexander, and S.A. Schaub, "Internal and near-surface electromagnetic fields for a spherical particle irradiated by a focused laser beam", J. Appl. Phys., 64 (4), 15 August 1988, 1632.

C) S.A. Schaub, D.R. Alexander, and J.P. Barton, "Theoretical model for the image formed by a spherical particle in a coherent imaging system: comparison to experiment", submitted for publication to Opt. Eng., July 1988.

D) D.R. Alexander, D.E. Poulain, J.P. Barton, S.A. Schaub, and J. Zhang, "Nonlinear effects of excimer laser radiation with solid particles in a vacuum", presentation at the 1988 CRDEC Conference on Obscuration and Aerosol Research, June 1988.

E) S.A. Schaub, D.R. Alexander, and J.P. Barton, "Focused laser beam interactions with methanol droplets: effects of relative beam diameter", submitted for publication in Appl. Opt., May 1988.

F) M.A. Emanuel, "Explosive vaporization of spherical and cylindrical aerosols: comparison between experimental results using a $CO_2$ laser and internal and scattered optical fields", Masters Thesis, Mechanical Engineering Department, Center for Electro-Optics, University of Nebraska-Lincoln, Lincoln, Nebraska, 68588-0525, October 1987.

G) D.R. Alexander, J.P. Barton, S.A. Schaub, and M.A. Fitzwater, "Beam propagation effects resulting from the electric field strengths for spheres and cylinders: internal and near field", presentation at Workshop on the Physics of Directed Energy Propagation in the Atmosphere, U.S. Army Atmospheric Sciences Laboratory (ASL) at New Mexico State University, Los Cruces, New Mexico, January 27-28, 1987.

H) D.R. Alexander and J.G. Armstrong, "Explosive vaporization of aerosol drops under irradiation by a $CO_2$ laser beam", Appl. Opt., 26 1987, 533.

I) J.G. Armstrong, "Experimental study of the explosive vaporization of aerosol drops under irradiation by a $CO_2$ laser", Masters Thesis, Mechanical Engineering Department, University of Nebraska-Lincoln, Lincoln, Nebraska, 68588-0525, May 1986.

J) D.R. Alexander, "Nonlinear effects of high energy $CO_2$ laser illumination of aerosol drops", presentation at the 1986 CRDEC Conference on Obscuration and Aerosol Research, June 1986.

K) D.R. Alexander, K.J. Wiles, S.A. Schaub, and M.P. Seeman, "Effects of non-spherical drops on a phase doppler spray analyzer", SPIE 573 1985, 67.

L) D.R. Alexander, "Experimental system for real-time observation of particle dynamics at high energy", presentation at the 1985 CRDEC Conference on Obscuration and Aerosol Research, June 1985.

## Abstract

Results have been obtained for the interaction of KrF excimer laser radiation ($\lambda = 248$ nm, FWHM pulse width = 17 ns) with solid particles in air and under vacuum conditions down to approximately $10^{-5}$ Torr. Solid particles of glass spheres, Al spheres, $Al_2O_3$, W, SiC, ground fused silica (Suprasil), and polystyrene divinylbenzene have been imaged at various stages of the explosive process after interaction with the KrF laser operating at focused irradiance values of approximately $10^{11}$ W/cm$^2$. In addition to illustrating the dynamics of the explosive process, the excimer laser imaging system was also used to extract information regarding the velocities of the ejected material by the use of a dual imaging pulse. Although the velocity of the ejected material depends on several parameters, among these being the location of the particle within the focal region, typical velocities ranged from 200 to 2000 m/s. Streak camera images were also taken which revealed that the lifetime of plasma emission ranged from about 40 to 2700 ns depending on the particular material and surrounding pressure.

## Introduction

The propagation of high energy lasers through an atmosphere containing an aerosol as well as the penetration of a laser beam through particle clouds in a vacuum are of current interest. Although good progress has been made in understanding the interaction of intense laser radiation with spherical liquid aerosol particles, the open literature on the interaction of high energy laser beams with solid particles less than 100 $\mu$m in diameter is not extensive. Most of the work performed thus far appears to have been for the interaction of intense laser beams with a wide variety of thin metal films or foils.[1-6] Bol'shov, et al.[1] points out that the validity of extrapolating the results and conclusions to spherical geometry must be evaluated in each specific case.

The current paper describes experimental work on the interaction of excimer laser radiation at $\lambda = 248$ nm with solid particles in air and in vacuum conditions up to $10^{-5}$ Torr. Of particular interest in this work, was the observation of the dynamics of the laser beam interaction with several types of solid particles or clumps of solid particles. In addition, the velocity and distribution of material being ejected were also of interest.

## Experimental Setup

A schematic of the experimental setup used in the research is shown in Figure 1. The output beam (10 x 20 mm) from the front excimer laser (Questek Model 2860 operating on KrF with unstable optics, $\lambda = 248$ nm) is brought directly into the vacuum chamber where it is focused to a spot size of approximately $10^4$ $\mu$m$^2$. The spot size was determined experimentally by moving a razor blade through the focal point and taking a ratio of transmitted energy, $E_2$, to input energy, $E_1$. The energies were measured with two Molectron Model J50 detectors whose output was coupled

to an A/D board in an IBM PC AT computer for processing. The FWHM size of the focal spot as shown in Fig. 2 was 95 $\mu$m high by 115 $\mu$m wide. The maximum irradiance value used in the work reported here was approximately $10^{11}$ W/cm$^2$ which is based on a pulse length of 17 ns, pulse energy of 400 mJ, and $10^4$ $\mu$m$^2$ spot size. The second excimer laser, identical to the first except for having stable optics, is incident on the vacuum chamber in a direction orthogonal to both the high energy laser pulse used to heat the particles and the motion of the solid particles, serves as the illumination source for imaging studies and velocity measurements. The pulse from the second excimer laser was split into two separate pulses, one of which was sent directly to the vacuum chamber over a minimum optical path length, and the second which was sent over an additional 45 feet of optical path. Consequently, two 17 ns pulses delayed by approximately 45 ns allowed determination of the velocity of the expelled material by measuring the distance the material had traveled during the 45 ns interval. The absolute delay time between the firing of the second excimer (imaging) laser and the first excimer (high energy) laser was controlled by a digital delay generator incorporated into the laser sync unit and could be adjusted over a time range from 10 ns to several microseconds. Jitter in the laser circuitry, however, resulted in the absolute delay times between the two lasers to have an uncertainty of about $\pm 10$ ns (recently reduced to $\pm 7$ ns).

Images of the explosion dynamics were recorded on a vidicon (Cohu camera system) and the data stored on an optical memory disk recorder (Panasonic model TQ-2023F). The streak images were obtained using a Hamamatsu Streak Camera (Model M2548) which was oriented orthogonal to the direction of the high energy pulse and provided information regarding the duration of the plasma emission.

The solid particles were dispersed using a mechanical shaker which consisted of a particle reservoir mounted on an acoustic speaker. The input frequency and amplitude were adjusted using a Tektronixs Model FG 503 function generator and a Nikko Model Alpha 230 power amplifier so that the desired particle concentration was distributed in the focal region of the high energy laser beam.

The vacuum chamber consisted of a stainless steel cylinder (11.5 inches diameter, 6.5 inches high) with 9 optical viewing ports. High vacuum conditions were obtained using a cryogenic pump (CTI Cryogenics, Cryo-torr 100 high vacuum pump) connected to the base of the vacuum chamber through an eight-inch hole in the Newport research optical table. Pressures within the vacuum chamber were monitored using a thermocouple and ion gauge.

# Results

## Dynamics of Particle Breakup

Using the experimental arrangement described in the previous section, we investigated the laser-induced breakdown of $Al_2O_3$, W, SiC glass spheres, Al spheres, ground fused silica (Suprasil), and polystyrene divinylbenzene. Since the $Al_2O_3$, W, SiC, and ground fused silica were not spherical in form, it was difficult to distinguish material being ejected due to high energy laser interaction from additional particles in the field of view. However, the basic interactions were similar to those observed with spherical particles, and we report results only on the spherical materials. Video tapes for the other materials interacting with excimer laser radiation were given to CRDEC project monitors.

Figures 3-5 show the typical interaction of $\lambda = 248$ nm laser radiation at $I \approx 10^{11}$ W/cm$^2$ with Al spheres at pressures of 760 Torr, 0.1 Torr and $3 \times 10^{-5}$ Torr. Note the evidence of shock formation under atmospheric conditions shown in Fig. 3 which was absent for both intermediate and high vacuum conditions. The dynamics of the explosion process shown in Fig. 3 are also strongly influenced by the relative location of the particles within the focal region. Fig. 6 shows the elastically scattered $\lambda = 248$ nm radiation from the Al particles and glass spheres during the 17 ns laser heating pulse (no imaging pulse). The bright spots serve as spatial and time reference markers as illustrated in Figs. 3-5. Figures 7 and 8 show the typical interaction of glass microspheres under the same illumination conditions as for Al particles. Again, shock formation is exhibited for the atmospheric pressure case. Figure 9 shows the interaction of a large 230 $\mu$m polystrene divinylbenzene particle with $\lambda = 248$ nm radiation in air at $10^{10}$ W/cm$^2$. Filamentry formations can be observed extending outward from the plasma corona. Our work also agreed with Dhareshwar, et al.[3] where the high atomic number (Z) targets show much more pronounced plasma jetting. Velocity information of bulk material and plumes were obtained from either single delayed imaging pulses or dual delayed imaging pulses with a 45 ns optical path difference. Table 1 shows typical velocities obtained for either plumes or bulk material.

As illustrated in Figs. 3-5 and 7-8, material is being ejected from the shadow surface of the Al and glass spheres. The ejection of this material from the shadow surface was surprising since the index of refraction of Al, for example, at $\lambda = 248$ nm is n $= 0.19 + 2.942$ i and theoretical Mie calculations indicate extremely high absorption on the illuminated surface. Based on the short

Table 1. Typical Velocities Found by Dual Pulse Imaging

| Material | Power (W/cm$^2$) | Pressure (Torr) | Velocity(m/s) | |
|---|---|---|---|---|
| | | | Bulk | Plume |
| Glass Spheres (5-50 microns) | $10^{11}$ | $10^{-5}$ | NA | 440<br>460<br>690<br>760<br>2000 |
| Glass Spheres (5-50 microns) | $10^{11}$ | 760 | 250<br>250<br>270<br>300<br>330 | 510<br>550<br>750 |
| Al Spheres (20 microns) | $10^{11}$ | $10^{-5}$ | NA | 450<br>460<br>1300<br>1700<br>1800 |

time scales for the appearance of this material, a possible explanation of this material ejection is due to spallation from shock phenomena off the shadow side of the spheres. Bol'shov et al.[1] report shock velocities of $9 \times 10^4$ m/sec on the shadow surface of thick aluminum foils at $5 \times 10^{13}$ W/cm$^2$.

## Lifetimes of Plasma Emissions

Observations of laser induced time dependent plasma formation were made with a Hamamatsu streak camera. The data was obtained using the vacuum chamber with the pressure ranging from 760 Torr to $1 \times 10^{-5}$ Torr. The streak camera was set at right angles to the excimer laser beam ($\lambda = 248$ nm) used to heat and vaporize the solid particles. The broad band light emission from the plasma was focused through a fused silica lens onto the entrance slit of the streak camera with sensitivity ranging from 200 - 800 nm. Sweeping speeds of the streak camera, which could be adjusted from 10 ns to 1 ms, were used to study plasma emission times.

Figure 10 gives the result of the air breakdown initiated by the excimer laser irradiation. From Fig. 10 we see that the breakdown region extends 3.5 mm along the main beam axis. The plasma emission reached its peak intensity within the first 10-12 ns, and then decayed in time. Broad spectral emission lasted more than 100 ns after the main laser pulse ended. Figure 11 shows the results of the interaction $\lambda = 248$ nm irradiation with 20 $\mu$m diameter aluminum spheres. At atmospheric pressure (Figure 11a) with the presence of aluminum spheres, the laser-induced plasma emission was enhanced. The spatial region of the plasma extended over 4.5 mm. The peak intensity was about three times higher than that without the spheres. The emission lasted more than 800 ns after the main pulse had ceased. In vacuum, (Figure 11b) at 0.1 Torr and (Figure 11c) at $5 \times 10^{-5}$ Torr, the plasma emission showed different characteristics. For example, the spatial emission regions were more confined and the peak intensities decreased. (Note that the data in Figure 11c was taken at higher streak camera sensitivity.) The emissions in vacuum lasted only 30-50 ns, which were much shorter than that at atmospheric pressure. Figure 13 gives the plasma emission time for air, glass, and Al spheres under different pressures.

Under vacuum conditions, shown in Figs. 11 and 12, the plasma emissions showed two-peak structure. By using a band pass filter, the first peak was shown to come from the elastic scattering of the 248 nm incident light, and the second peak was the broad band emission. Batanov, et al.[7] suggest that at certain temperatures metallic conductivity ceases and liquid metal becomes a liquid dielectric and becomes almost transparent to the incident radiation. Figure 12 gives similar

results for interactions of $\lambda = 248$ nm irradiation with 5-50 micron glass spheres. The physical characteristics of the plasma emissions were very similar to aluminum spheres. However, plasma emission lifetimes increased and, in our experiments, the maximum observed lifetime was 2,700 ns.

At atmospheric pressure without particles being present, the air breakdown is initiated by multi-photon ionization (the ionization potential for air is approximately 14 eV), which provides the initial free electrons for the cascade ionization processes.[8] In air breakdown the cascade processes dominated the ionization process and accounts for the major absorption of the incident energy. However, with the presence of aluminum spheres or glass spheres, the ionization processes were enhanced. For the case where particles are also present, the lower energy required for removal of electrons from aluminum atoms where the work function of Al is 4 eV and the ionization potential is 6 eV results in more free electrons for cascade processes to initiate. In fact, the direct ionization through photoelectric effects and multi-photon ionization (for Al only 1 to 2 photons are needed) played an important role in the ionization process, under vacuum conditions since cascade ionization becomes less important[8]. In our experiments, at pressures of 0.1 Torr and lower, no air breakdown could be observed. However, at these same low pressures (0.1 Torr and $4 \times 10^{-5}$ Torr), when aluminum particles were present, strong plasma emissions were observed which indicates that the photoelectric effects and the multi-photon ionization were the main mechanisms of plasma formation in vacuum environments.

## Conclusions

The current work reports the interaction of short wavelength $\lambda = 248$ nm excimer radiation at $10^{11}$ W/cm$^2$ with solid particles in air and vacuum conditions. Material was shown to be ejected from the shadow surface of all materials studied except for the 230 $\mu$m polystyrene divinylbenzene particles. Velocities measured for the ejected material in the plumes were comparable to the sonic velocities in the materials and ranged from 200 to 2000 m/s. Plasma lifetimes decrease as the surrounding gas pressures were reduced. Plasma lifetimes ranging from 40 to 2700 ns were measured and found to decrease as the surrounding gas pressures were reduced and greatly increased with the presence of small solid particles.

## Acknowledgements

## References

1. L. A. Bol'shov, I. N. Burdonskii, A. L. Velikovich, V. V. Gavrilov, A. Yu. Gol'tsov, E. V. Zhuzhukalo, S. V. Zabyalets, V. P. Kiselev, N. G. Koval'skii, M. A. Liberman, L. S. Mkhi-tar'yan, M. I. Pergament, A. I. Yudin, and A. I. Yaroslavskii, "Acceleration of Foils by a Pulsed Laser Beam", Sov. Phys. JETP, Vol. 65, No. 6, June 1987.

2. P.D. Gupta, Y.Y. Tsui, R. Popil, R. Fedosejves, and A.A. Offenberger, "Experimental Study of KrF - Laser High -Z- Plasma Interaction Dominated by Radiation Transport," Physical Review A, Vol. 34, No. 5, 1986.

3. L.J. Dhareshwar, P.A. Naik, P.D. Nandwana, and H.C. Pant, "Characteristics of Plasma Flow from Laser Irradiated Thin Foil", J. Appl. Phys., Vol. 61, No. 9, 1987.

4. David Salzmann, Henry Szichmann, Aaron D. Krumbein and C.E. Capjack, "Radiative Preheat in Laser Produced Aluminum Plasma", Phys. Fluids, Vol. 30, No. 2, 1987.

5. G.S. Korshunov, V.V. Ustyuzhin, and V. Ya Ushakov, "Laser-Induced Formation of Long Plasma Jets from Metal Powder Targets", Sov. Phys. Tech. Phys., Vol. 30, No. 4, 1985.

6. Robert B. Raphael, "Review of Impulse Coupling with Materials", SPIE Vol. 476, p. 112, Excimer Lasers, Their Applications and New Frontiers in Lasers, 1984.

7. V. A. Batanov, F. V. Bunkin, A. M. Prokhorov, and B. V. Fedorov, "Evaporation of Matallic Targets Caused by Intense Optical Radiation", Soviet Physics JETP, Vol. 36, No. 2, 1973.

8. George Bekefi, "Principles of Laser Plasma", John Wiley and Sons, Inc., 1976.
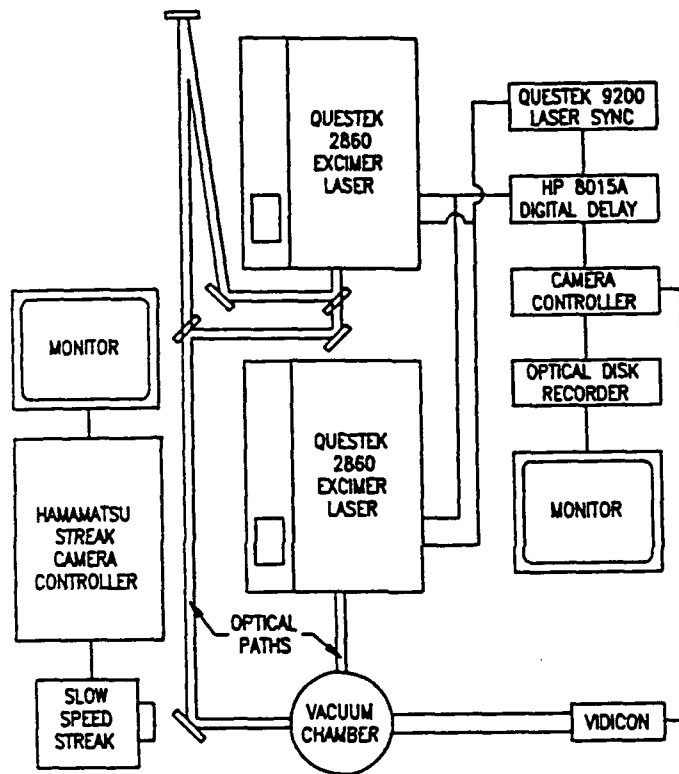
Fig. 1. Schematic of experimental setup.
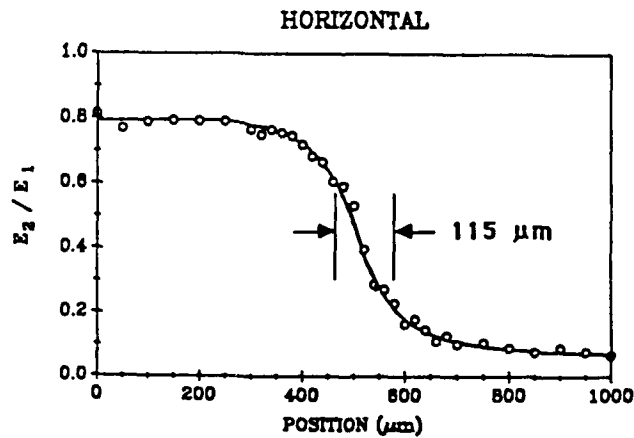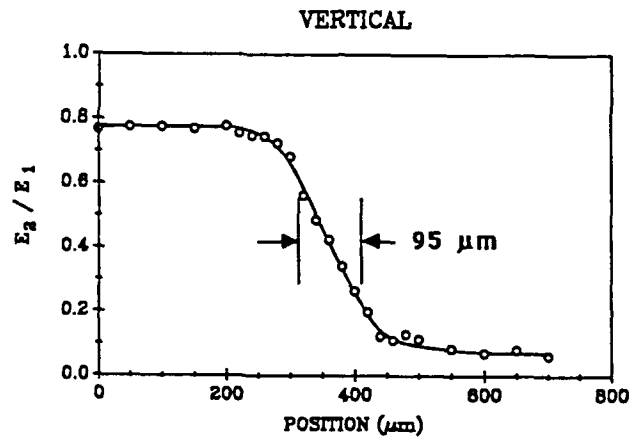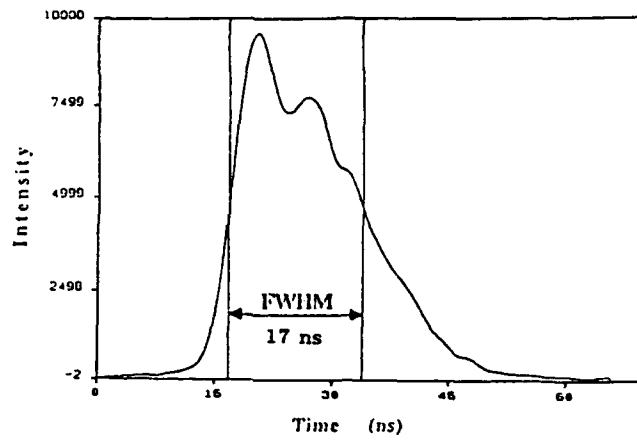
Fig. 2. (Top) Temporal profile of a typical output pulse of a Questek Model 2860 excimer laser using Krypton Fluoride ($\lambda = 248$ nm). (Bottom) Experimental determination of focused beam waist by measurement of pulse energy transmitted past a knife-edge translated through the focal point of the beam (Focusing lens: $\phi = 50$ mm, $f = 250$ mm).

20 micron Al spheres

$\lambda_{inc} = 248$ nm

$I \approx 10^{11}$ W/cm$^2$ (400 mJ/pulse)

$P = 760$ Torr

Beam propagation

Imaging pulse arrives 200 ns after high energy pulse.

Fig. 3. Interaction of 20 $\mu$m aluminum spheres with intense UV radiation ($\lambda = 248$ nm, $I \approx 10^{11}$ W/cm$^2$) in atmosphere 200 ns after arrival of the heating pulse. Note the various dynamics occurring in the probe volume relative to the focal point of the explosive beam. White spots mark the initial heating and scattering of light on illuminated surface.

20 micron Al spheres

$\lambda_{inc} = 248$ nm

$I \approx 10^{11}$ W/cm$^2$ (400 mJ/pulse)

$P = 10^{-1}$ Torr

Imaging pulse arrives 50 ns after high energy pulse.



Beam propagation →
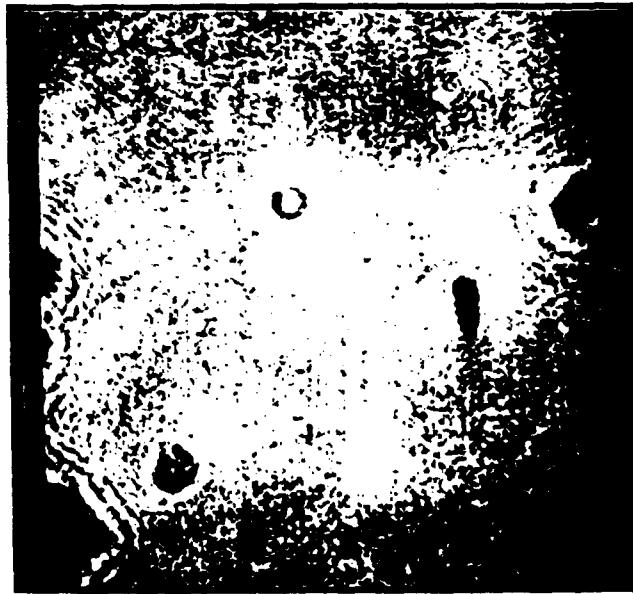
Fig. 4. Interaction of a 20 $\mu$m aluminum sphere with intense UV radiation ($\lambda = 248$ nm, $I \approx 10^{11}$ W/cm$^2$) in vacuum (0.1 torr) 50 ns after pulse incidence. Note the "jetting" of material from the sphere in the direction of beam propagation.
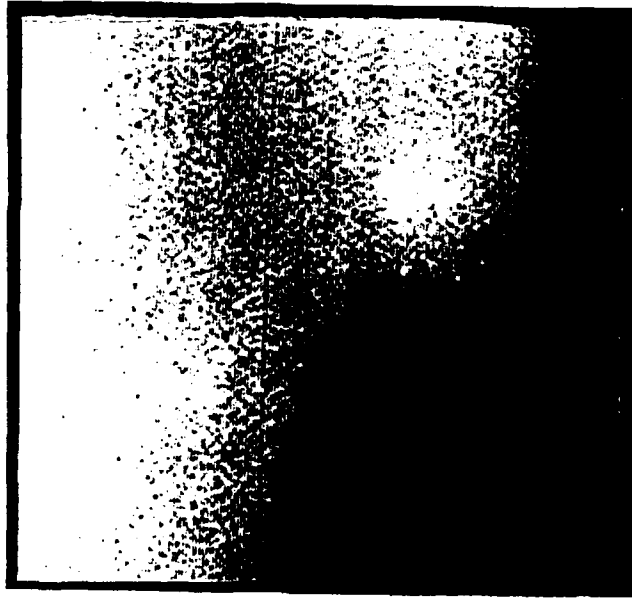
20 micron Al spheres

$\lambda_{inc} = 248$ nm

$I \approx 10^{11}$ W/cm$^2$ (400 mJ/pulse)

$P = 10^{-5}$ Torr

Imaging pulses arrive 50 ns and 95 ns after high energy pulse.

Velocity of upper plume is 1300 m/s and velocity of lower plume is 1700 m/s.



Beam propagation

Fig. 5. Dual exposure of the interaction of two adjacent 20 $\mu$m aluminum spheres with intense UV radiation ($\lambda = 248$ nm, $I \approx 10^{11}$ W/cm$^2$) 50 and 95 ns after pulse incidence. Computed velocity of the upper and lower plumes are 1300 and 1700 m/s, respectively. The bright, white spots locate the initial interaction at time = 0 ns.
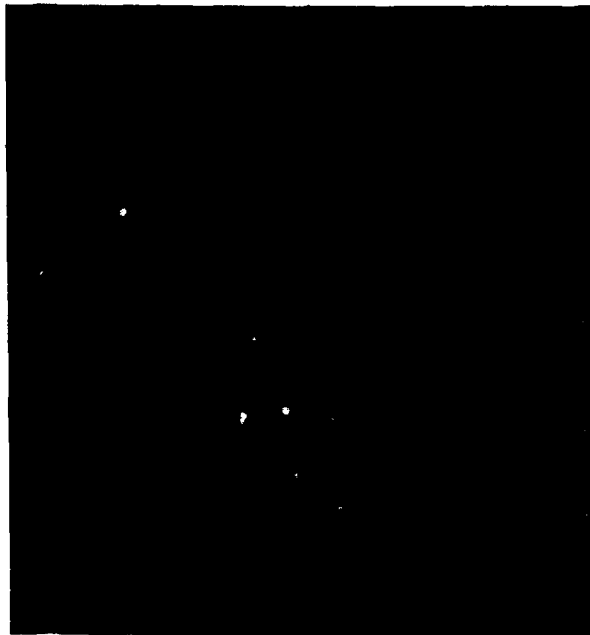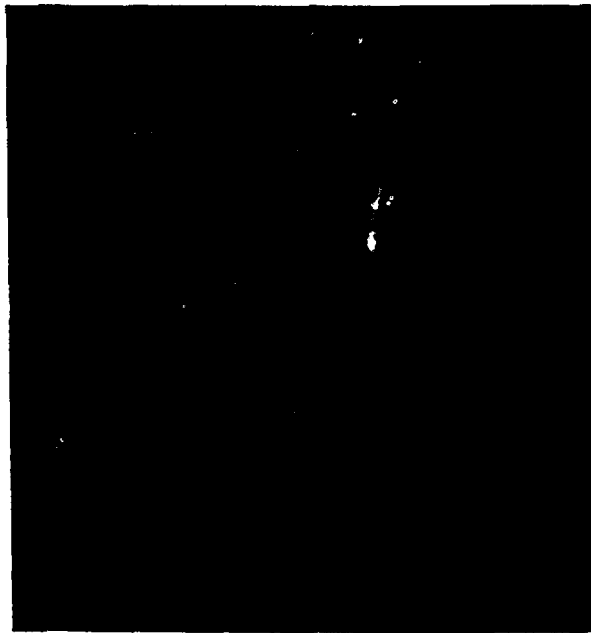
Beam propagation

Fig. 6. Images taken without any imaging beam illumination of the interaction of 20 $\mu$m aluminum spheres (top) and 5-50 $\mu$m glass spheres (bottom) with intense UV radiation ($\lambda = 248$ nm, I $\approx 10^{11}$ W/cm$^2$). The only light observed is scattered 248 nm light due to the presence of a bandpass filter.
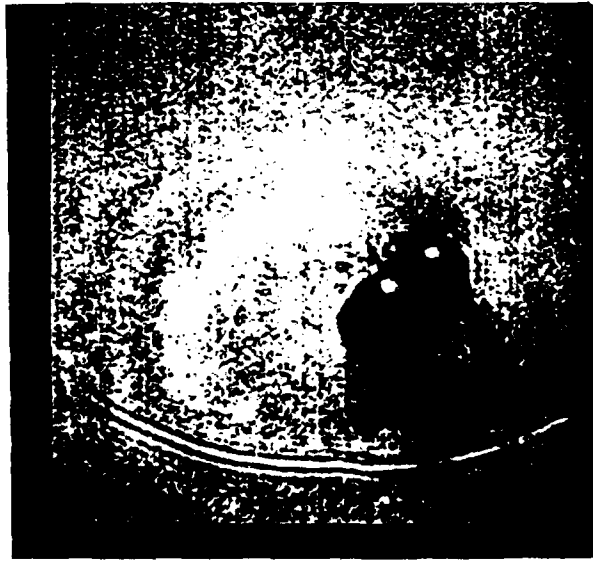
5-50 micron glass spheres

$\lambda_{inc} = 248$ nm

$I \approx 10^{11}$ W/cm$^2$ (400 mJ/pulse)

$P = 760$ Torr

Beam propagation →



Imaging pulse arrives 50 ns after high energy pulse.

Fig. 7. Interaction of 5-50 $\mu$m glass spheres with intense UV radiation ($\lambda = 2^{\prime}$ nm, $I \approx 10^{11}$ W/cm$^2$) in atmosphere 50 ns after pulse incidence. Note "jetting" of the material from the shadow hemisphere of the spheres in the direction of beam propagation, and the presence of the shock front behind the spheres.

5-50 micron glass spheres

$\lambda_{inc} = 248$ nm

$I \approx 10^{11}$ W/cm$^2$ (400 mJ/pulse)

$P = 4.5 \times 10^{-5}$ Torr

Beam propagation

Imaging pulse arrives 0 ns after high energy pulse.

Fig. 8. Interaction of a 5-50 $\mu$m glass sphere with intense UV radiation ($\lambda = 248$ nm, $I \approx 10^{11}$ W/cm$^2$) in high vacuum ($5 \times 10^{-5}$ torr) 20 ns after pulse incidence. Note "jetting" of the material from the shadow hemisphere of the sphere. The estimated velocity of the plume is 2000 m/s.

230 micron polystyrene/DVB

$\lambda_{inc} = 248$ nm

$I \approx 10^{10}$ W/cm$^2$

$P = 760$ Torr

Imaging pulse arrives 28 ns after high energy pulse.
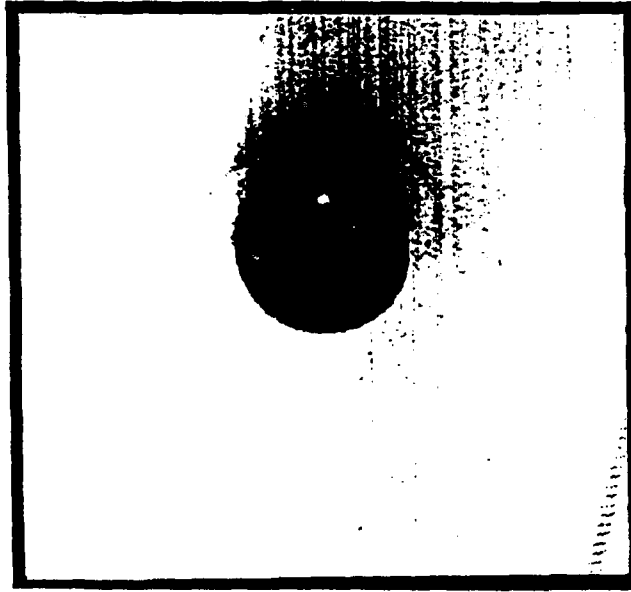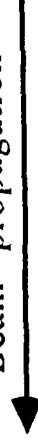


Beam propagation

Fig. 9. Interaction of a 230 $\mu$m Polystyrene/DVB sphere with intense UV radiation ($\lambda = 248$ nm, $I \approx 10^{10}$ W/cm$^2$) in atmosphere 28 ns after pulse incidence. Note the propagation of the shock front and jets/streamers of material from the illuminated hemisphere of the particle in the direction of the incident laser beam.
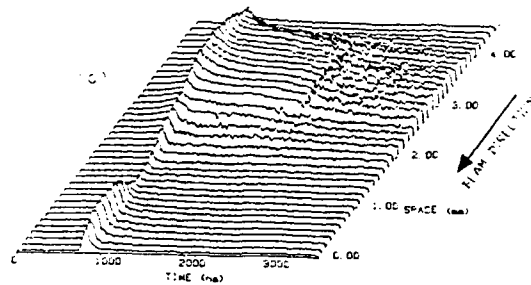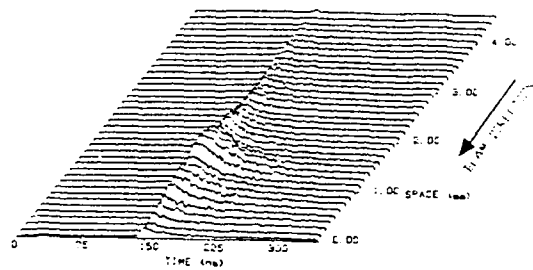
Fig. 10. Air breakdown induced by focused excimer laser radiation
($\lambda = 248$ nm, I $\approx 10^{11}$ W/cm$^2$).
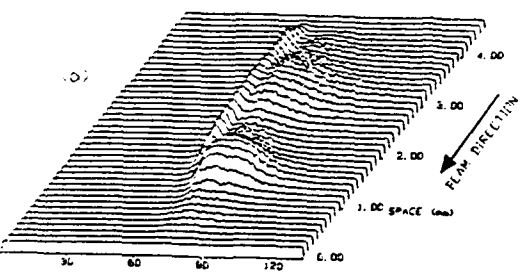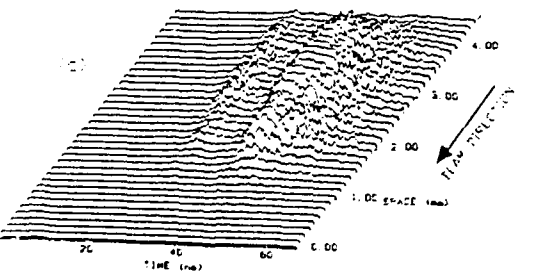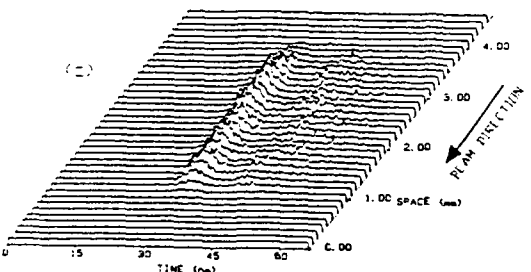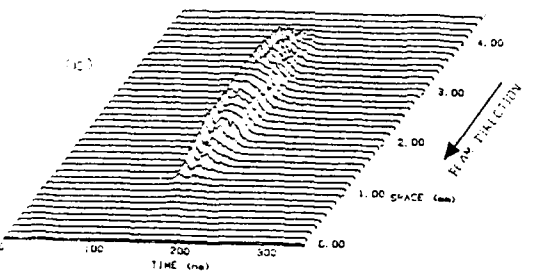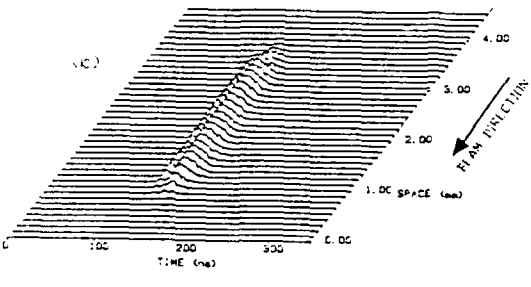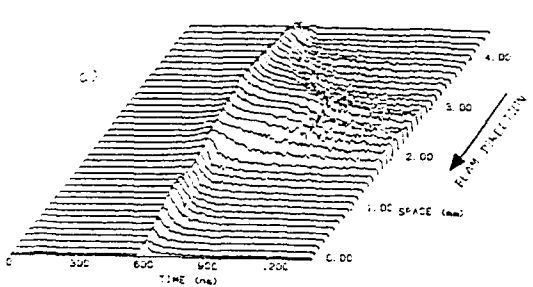
Fig. 11. 20 $\mu$m aluminum spheres irradiated by excimer laser radiation ($\lambda = 248$ nm, I $\approx 10^{11}$ W/cm$^2$) for (a) P = 760 torr, (b) P = 0.1 torr, (c) P = 4 x 10$^{-5}$ torr.

Fig. 12. 5-50 $\mu$m glass spheres irradiated by excimer laser radiation ($\lambda = 248$ nm, I $\approx 10^{11}$ W/cm$^2$) for (a) P = 760 torr, (b) P = 0.1 torr, (c) P = 5 x 10$^{-5}$ torr, (d) P = 6 x 10$^{-5}$ torr.
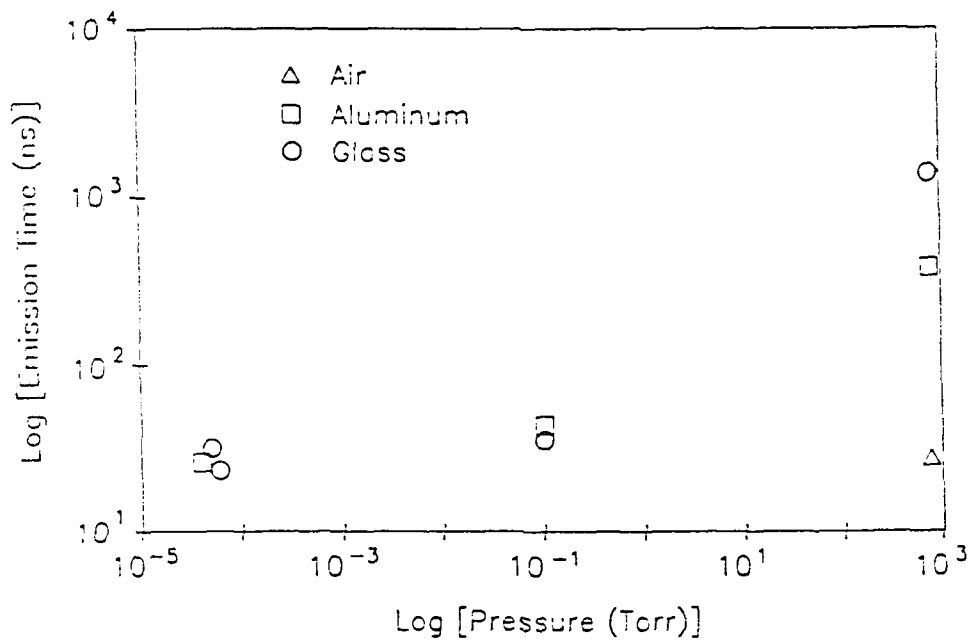
Fig. 13. Plasma emission time as a function of absolute pressure for air, and aluminum and glass spheres.

# ELECTROMAGNETIC FIELD CALCULATIONS FOR A TIGHTLY-FOCUSED LASER BEAM INCIDENT UPON A SPHERICAL PARTICLE

J.P. Barton, D.R. Alexander, and S.A. Schaub
Center for Electro-Optics
College of Engineering
University of Nebraska
Lincoln, Nebraska 68588

## RECENT PUBLICATIONS, SUBMITTALS FOR PUBLICATION, AND PRESENTATIONS:

A). J.P. Barton, D.R. Alexander, and S.A. Schaub, "Experimental and theoretical analysis of liquid droplets moving through a focused $CO_2$ laser beam," Proceedings of the 1988 CRDEC Scientific Conference on Obscuration and Aerosol Research.

B). J.P. Barton, D.R. Alexander, and S.A. Schaub, "Experimental and theoretical analysis of liquid droplets moving through a focused $CO_2$ laser beam," presentation at the 1988 CRDEC Scientific Conference on Obscuration and Aerosol Research, June, 1988.

C). J.P. Barton, D.R. Alexander, and S.A. Schaub, "Internal and near-surface electromagnetic fields for a spherical particle in a focused laser beam," poster presentation at the 1988 CRDEC Scientific Conference on Obscuration and Aerosol Research, June, 1988.

D). D.R. Alexander, D.E. Poulain, J.P. Barton, S.A. Schaub, and J. Zhang, "Nonlinear effects of excimer laser radiation with solid particles in a vacuum," presentation at the 1988 CRDEC Scientific Conference on Obscuration and Aerosol Research, June, 1988.

E). D.R. Alexander, D.E. Poulain, J.P. Barton, S.A. Schaub, and J. Zhang, "Nonlinear effects of excimer laser radiation with solid particles in a vacuum," Proceedings of the 1988 CRDEC Scientific Conference on Obscuration and Aerosol Research.

F). J.P. Barton, D.R. Alexander, and S.A. Schaub, "Internal and near-surface electromagnetic fields for a spherical particle irradiated by a focused laser beam," J. Appl. Phys. **64**, 1632 (1988).

G). S.A. Schaub, D.R. Alexander, J.P. Barton, and M.A. Emanuel, "Focused laser beam interactions with methanol droplets: effects of relative beam diameter," Appl. Opt. **28**, 1666 (1989).

H). S.A. Schaub, D.R. Alexander, and J.P. Barton, "Theoretical model for the image formed by a spherical particle in a coherent imaging system: comparison to experiment," Opt. Engr. **28**, 565 (1989).

I). J.P. Barton, D.R. Alexander, and S.A. Schaub, "Internal fields of a spherical particle illuminated by a tightly-focused laser beam: focal point positioning effects at resonance," J. Appl. Phys. **65**, 2900 (1989).

J). D.R. Alexander, S.A. Schaub, J. Zhang, D.E. Poulain, and J.P. Barton, "Scattering of incident KrF laser radiation resulting from the laser induced breakdown of $H_2O$ droplets," Opt. Lett. **14**, (1989).

K). S.A. Schaub, D.R. Alexander, D.E. Poulain, and J.P. Barton, "Measurement of hypersonic velocities resulting from the laser-induced breakdown of aerosols using an excimer laser imaging system," Rev. Sci. Instru., to be published (Dec., 1989).

L). J.P. Barton and D.R. Alexander, "Fifth-order corrected electromagnetic field components for a fundamental Gaussian beam," J. Appl. Phys., to be published (Oct. 1, 1989).

M). J.P. Barton, D.R. Alexander, and S.A. Schaub, "Theoretical determination of net radiation force and torque for a spherical particle illuminated by a focused laser beam," J. Appl. Phys., to be published (Nov. 15, 1989).

N). S.A. Schaub, J.P. Barton, and D.R. Alexander, "Simplified coefficient expression for a spherical particle located on the propagation axis of a fifth-order Gaussian beam," submitted to Appl. Phys. Lett. (1989).

O). D.E. Poulain, D.R. Alexander, J.P. Barton, and J. Zhang, "Interaction of intense ultraviolet radiation with solid aerosols," submitted to J. Appl. Phys. (1989).

P). J.P. Barton, D.R. Alexander, and S.A. Schaub, "Theoretical determination of the radiation force distribution for a spherical droplet illuminated by a focused laser beam," submitted to J.

Appl. Phys. (1989).

Q). J.P. Barton, D.R. Alexander, and S.A. Schaub, "Electromagnetic fields for a focused laser beam incident upon a spherical particle," presentation at the Workshop on the Physics of Directed Energy Propagation through the Atmosphere, Center for Atmospheric Sciences, New Mexico State University, Las Cruces, New Mexico, Feb. 28 - Mar. 1, 1989.

R). D.R. Alexander, S.A. Schaub, J. Zhang, D.E. Poulain, and J.P. Barton, "Laser induced breakdown of $H_2O$ droplets at 0.248 $\mu m$," presentation at the Workshop on the Physics of Directed Energy Propagation through the Atmosphere, Center for Atmospheric Sciences, New Mexico State University, Las Cruces, New Mexico, Feb. 28 - Mar. 1, 1989.

S). J.P. Barton, D.R. Alexander, and S.A. Schaub, "Electromagnetic field calculations for a tightly-focused laser beam incident upon a spherical particle," presentation at the 1989 CRDEC Scientific Conference on Obscuration and Aerosol Research, June, 1989.

T). D.R. Alexander, J.P. Barton, and S.A. Schaub, "Laser induced breakdown of $H_2O$ droplets and solid wires at 0.248 $\mu m$," presentation at the 1989 CRDEC Scientific Conference on Obscuration and Aerosol Research, June, 1989.

## ABSTRACT

New applications and extensions of our spherical particle/arbitrary beam electromagnetic interaction theory are presented. The topics include a further analysis of focal point positioning effects at resonance, the determination of the net radiation force and torque on the particle, the determination of the spatial distribution of radiation forces within and upon the surface of the particle, and the determination of the interactive internal and external electromagnetic fields for a beam incident upon two adjacent particles of differing size and material and of arbitrary spatial positioning. Future work will involve further refinement of these developments and an effort to obtain direct comparisons between theoretical calculations and corresponding experimental measurements.

## I. INTRODUCTION

The theoretical determination of the electromagnetic fields (and resultant electromagnetic phenomena) associated with the interaction of a tightly-focused monochromatic beam (laser beam) with a spherical particle is considered. The electromagnetic fields are calculated using our spherical particle/arbitrary beam interaction theory.[1] The spherical particle/arbitrary beam interaction theory has been previously used to investigate the heating of droplets within[2] and moving through[3] a focused laser beam, and to investigate the effects of focal point positioning on the excitation of structural resonances within a spherical particle.[4] In this paper, after giving a brief review of the spherical particle/arbitrary beam interaction theory (including the development an improved Gaussian beam description) in Sec. II., the following recent applications and extensions of the theory are presented: in Sec. III., further analysis of focal point positioning effects at resonance; in Sec. IV., net radiation force and torque on a particle; in Sec. V., radiation force distributions within and upon the surface of a particle; and in Sec. VI., beam incident upon two adjacent particles of differing size and material and of arbitrary spatial positioning.

## II. REVIEW OF SPHERICAL PARTICLE/ARBITRARY BEAM THEORY

A continuous, monochromatic beam propagating within a homogeneous, isotropic, nonmagnetic, nonabsorbing dielectric media incident upon a homogeneous, isotropic, nonmagnetic spherical particle is assumed. For a beam of arbitrary, but known, mathematical description, the electromagnetic fields internal to and external to the spherical particle can be determined using an extension of plane wave Lorenz-Mie theory which we refer to as the spherical particle/arbitrary beam interaction theory. A complete derivation of the procedure is presented in Ref. 1. The field component equations, in nondimensionalized form, are given in App. A. A spherical coordinate system with the origin at the sphere center is utilized. For the calculations of this paper, the beam is assumed to be a fundamental (TEM$_{00}$ mode) Gaussian-profiled, linearly-polarized beam propagating in the $+z$ axis direction with predominate electric field polarization in the x axis direction.

In order to calculate the electromagnetic field components internal to and external to the spherical particle, it is necessary that the electromagnetic field components of the incident beam

be known. A fifth-order corrected Gaussian beam description was derived[5] which provides an improved solution to Maxwell's equations in comparison with the previously used first-order Gaussian beam description.[1] The use of the fifth-order corrected Gaussian beam description is particularly important for calculations involving tightly-focused beams, where the beam waist diameter may be of the same order as the wavelength. The equations for the electromagnetic field components for a fifth-order corrected Gaussian beam are presented in App. B. The derivation of the these equations is given in Ref. 5.

The fundamental parameters for the analysis of a focused Gaussian beam incident upon a spherical particle are as follows: the dielectric constant of the medium, $\epsilon_{ext}$; the particle size parameter, $\alpha = 2\pi a/\lambda_{ext}$, where $a$ is the particle radius and $\lambda_{ext}$ is the wavelength of the incident beam in the external media; the complex relative refractive index of the particle, $\bar{n} = (\bar{\epsilon}_{int}/\epsilon_{ext})^{1/2}$; the beam waist diameter, $w_0$; and the coordinate location of the center of the spherical particle relative to the focal point of the incident beam, $(x_0, y_0, z_0)$. Electromagnetic field components are nondimensionalized relative to the incident beam focal point electric field, $E_0$, which can be related to the beam power by[5]

$$|E_o|^2 = \frac{16P}{\sqrt{\epsilon}cw_o^2(1 + s^2 + 1.5s^4)}$$

(1)

where s $= (1/\alpha\tilde{w}_0)$. A tilde ($\tilde{\ }$) above a spatial quantity indicates that the quantity has been nondimensionalized relative to the particle radius, $a$.

## III. FURTHER ANALYSIS OF FOCAL POINT POSITIONING EFFECTS AT RESONANCE

In a recently published paper,[4] our spherical particle/arbitrary beam interaction theory was used to investigate the effect of beam focal point positioning on the excitation of structural resonances within a spherical particle. In this work, calculations were performed using parameters corresponding to having a 1.06 $\mu m$ wavelength, 4 $\mu m$ waist diameter, linearly-polarized Gaussian beam incident upon a 10 $\mu m$ diameter water droplet ($\bar{n} = 1.33 + 5.0\times10^{-6}$i). The effect of focal point positioning on the excitation of resonances was evaluated for both a droplet at a magnetic wave resonance ($34^{th}$ mode, 1 $^{st}$ order, a = 4.954 $\mu m$, $\alpha$ = 29.365, $\tilde{w}_0$ = 0.404) and a droplet at an electric wave resonance ($34^{th}$ mode, $1^{st}$ order, a = 5.019 $\mu m$, $\alpha$ = 29.753, $\tilde{w}_0$ = 0.399). For such a tightly-focused beam (beam waist diameter less than the droplet diameter) it was found that structural resonances are not excited for on sphere center focal point positioning. Resonance excitation requires edge illumination. For the magnetic wave resonance droplet, the resonance was excited when the beam focal point was moved from the sphere center towards the surface of the sphere along the y axis (perpendicular to the direction of incident electric field polarization) and, for the electric wave resonance droplet, the resonance was excited when the beam focal point was moved from the sphere center towards the surface of the sphere along the x axis (parallel to the direction of incident electric field polarization). Maximum resonance excitation occurs when the beam focal point is located just beyond the surface of the droplet (at $\tilde{y}_0 \approx \pm 1.175$ for the magnetic wave resonance droplet and at $\tilde{x}_0 \approx \pm 1.160$ for the electric wave resonance droplet).

The excitation of resonance for edge illumination is exhibited by the development of a solid ring of increased normalized source function ($S = |\vec{E}|^2/|E_0|^2$) just inside the sphere surface. Fig. 1 shows the normalized source function distribution in the y-z plane for the magnetic wave resonance droplet with on-edge illumination ($\tilde{x}_0 = 0, \tilde{y}_0 = -1.175, \tilde{z}_0 = 0$). Further details may be found in Ref. 4.

It was suggested,[6] that the ring of increased normalized source function just within the surface of an edge illuminated, excited resonance, droplet may be the result of the droplet acting as an optical cavity with light circling near the surface of the droplet. To test this hypothesis, the calculation of Fig. 1 was repeated with two beams incident upon the droplet: the original beam at the right-hand-side of the droplet ($\tilde{y}_0 = -1.175$) and a second identical beam at the left-hand-side of the droplet ($\tilde{y}_0 = +1.175$). If the droplet is acting as an optical cavity, the two beams should produce circles of light propagating in opposite directions which will result in a pattern of constructive and destructive interference. As shown in Fig. 2, this was the obtained result. The

interference pattern for a resonance droplet with on-edge, two beam illumination is quite similar to that observed for the same resonance droplet with plane wave illumination as is given in Ref. 4.

As a further test of the optical cavity nature of a droplet at resonance, the spatial distribution of the time-averaged Poynting vector was calculated for the magnetic wave resonance droplet with single beam incident illumination corresponding to Fig. 1. A plot of the Poynting vector distribution in the y-z plane is given in Fig. 3. Since the region near the surface of the droplet is of primary interest, the plot emphasizes the near-surface and extends from $\tilde{r} = 0.8$ (at the center of the plot) to $\tilde{r} = 1.0$ (at the outer radius of the plot). As seen in Fig. 3, the Poynting vectors indicate a circular flow of energy just within the surface of the droplet.

Further calculations investigating the optical cavity nature of a droplet at resonance is in progress and will be submitted in the form of a journal paper in the near future.

## IV. NET RADIATION FORCE AND TORQUE

Series form expressions for the net radiation force and torque induced on a spherical particle illuminated by an arbitrarily-defined monochromatic beam were derived. As an example, the net force and torque for a 5 $\mu m$ diameter water droplet optically levitated by a vertically-oriented, tightly-focused ($2w_0 = 2 \mu m$), TEM$_{00}$ mode argon-ion laser beam were determined and examined for on and off propagation axis and on and off structural resonance conditions. This work is presented in a paper in press (Ref. 7) and the reader is referred to this paper for details. Only a partial summary will be provided here.

For a steady-state condition, the net radiation force, $\vec{F}$, on the particle can be determined by integrating the dot product of the outwardly-directed normal unit vector, $\hat{n}$, and the electromagnetic stress tensor, $\bar{T}$, over a surface enclosing the particle,[8]

$$< \vec{F} > = < \oint_S \hat{n} \cdot \bar{T} dS > \tag{2}$$

where $<>$ represents a time average. The appropriate form of the electromagnetic stress tensor to use in Eq. (1) is the topic of recent reviews by Robinson[9] and Brevik.[10] Apparently, for steady-state optical conditions, the traditional Minkowski form of the electromagnetic stress tensor,

$$\bar{T} = \frac{1}{4\pi}[\vec{E}\vec{D} + \vec{H}\vec{H} - \frac{1}{2}(\vec{E} \cdot \vec{D} + \vec{H} \cdot \vec{H})\bar{I}] \tag{3}$$

will give correct results. Similarly, the net radiation torque, $\vec{N}$, on the particle can be determined by performing a surface integral of the dot product of the outwardly-directed normal unit vector, $\hat{n}$, and the pseudo-tensor, $\bar{T} \times \vec{r}$, over a surface enclosing the particle,[8]

$$< \vec{N} > = - < \oint_S \hat{n} \cdot (\bar{T} \times \vec{r}) dS > . \tag{4}$$

Series form expressions for the net radiation force and torque on a spherical particle can be derived by 1.) using Eq. (3) to substitute for $\bar{T}$ in Eqs. (2) and (4), 2.) choosing the integration surface as a spherical surface in the far field ($\tilde{r} \Rightarrow \infty$), 3.) substituting for the electromagnetic field components using the series expressions of App. A, and 4.) integrating directly by applying recursion, product, and orthogonality relationships among the spherical harmonic functions. After a great deal of effort, series expressions for the components of net radiation force and torque in terms of the incident field coefficients ($A_{lm}$, $B_{lm}$) and the scattered field coefficients ($a_{lm}$, $b_{lm}$) were derived and subsequently verified. These equations are given in App. C.

The theoretical expressions of App. C were used to determine the radiation force and torque as a function of droplet position relative to the incident beam focal point for a 5 $\mu m$ diameter water droplet in air optically levitated by a single, vertically-oriented, focused TEM$_{00}$ mode (Gaussian-profiled) argon-ion laser beam ($\lambda = 0.5145 \mu m$, $\bar{n} = 1.334 + 1.2 \times 10^{-9} i$). The laser beam is tightly-focused to a beam waist diameter ($2w_0$) of 2 $\mu m$ (less than the droplet diameter).

Figure 4 shows the calculated power for levitation as a function of droplet diameter for droplets located on the incident beam propagation axis ($x_0 = y_0 = 0$) for an elevation just below the focal point at $z_0 = -5$ $\mu m$ and an elevation well above the focal point at $z_0 = +50$ $\mu m$. (These are positions of stable levitation, as will be shown later, in Fig. 5.) At $z_0 = -5$ $\mu m$, the beam diameter is about 2.6 $\mu m$ (less than the droplet diameter) while at $z_0 = +50$ $\mu m$ the beam diameter has spread to about 16.5 $\mu m$ (greater than the droplet diameter).

Although there is no directly comparable experimental data, the requirement of a few milliwatts of laser power to levitate a 5 $\mu m$ diameter water droplet in air (as shown in Fig. 4) is consistent with the measurements of Ashkin and Dziedzic[11] in which a a 4 $\mu m$ diameter latex sphere was levitated using $\approx 1$ mW of laser power and the levitation of a glycerol droplet evaporating from a diameter of 12 $\mu m$ to 1 $\mu m$ required a range of laser powers from 40 mW to 0.2 mW.

At an elevation of $z_o = 50$ $\mu m$, Fig. 4 indicates that at certain droplet diameters there is a decrease in the necessary power to levitate. This phenomena is a result of structural resonances within transparent water droplets at this wavelength. These structural resonances can each be associated with the excitation of particular radial modes of the general electromagnetic wave solution. The presence of structural resonances in the power to levitate at a given elevation has been experimentally observed by Ashkin and Dziedzic[12,13]. Ashkin and Dziedzic[12] also observed that if the droplet is levitated near the focal point where the beam diameter is less that the diameter of the sphere, then structural resonances are not present. Figure 4 indicates a lack of structural resonances for $z_o = -5$ $\mu m$ where the beam diameter (2.6 $\mu m$) is less than the droplet diameter (5 $\mu m$) consistent with Ashkin and Dziedzic's observation. As discussed in Sec. III., structural resonances in spherical particles require edge illumination for excitation and thus would not be excited for the tightly-focused conditions at $z_o = -5$ $\mu m$.

The nature (electric or magnetic), mode, and order of the structural resonances of Fig. 4 were identified, and detailed calculations were performed for the three basic types of droplets: a droplet at a magnetic wave resonance ($35^{th}$ mode, $1^{st}$ order, d = 4.9266 $\mu m$), a droplet at an electric wave resonance ($35^{th}$ mode, $1^{st}$ order, d = 4.9912 $\mu m$), and an intermediate nonresonance droplet (d = 4.96 $\mu m$).

Figure 5 shows the power to levitate a droplet located on the propagation axis as a function of elevation for each of the three types of droplets. There is an increase in required laser power for droplets located near the focal point because of decreased diffraction due to the strong focusing through the center of the spherical droplet. For a given type of droplet there are then three local extrema in levitation power. A first minimum, $P^1_{min}$, that occurs below the focal point, a maximum, $P_{max}$, that occurs near the focal point, and a second minimum, $P^2_{min}$, that occurs above the focal point. (For the cases considered here, $P^1_{min} < P^2_{min}$.) Stable levitation occurs in regions of positive slope of P versus $z_o$. From Fig. 5 it is then apparent that there are three general regimes of stable levitation. 1.) If $P_{max} < P$, then the droplet will stably levitate at a single elevation above the focal point. 2.) If $P^2_{min} < P < P_{max}$ then the droplet levitation is bistable, and the droplet can be stably levitated either above the focal point or below the focal point. 3.) If $P^1_{min} < P < P^2_{min}$ then the droplet will stably levitate at a single elevation below the focal point. If $P < P^1_{min}$ then the droplet cannot be stably levitated at any position. Bistable levitation for a spherical particle levitated using a tightly-focused laser beam has been experimentally observed by Ashkin and Dziedzic[14], who also observed that the particle could be easily transferred from one stable position to the other and back. If the particle begins at the above focal point position, a decrease in laser power will allow the particle to drop towards the focal point until $P = P^2_{min}$. If the laser power is further decreased slightly, the particle will drop through the focal point to the below focal point position since $P^1_{min} < P^2_{min}$. Increasing the laser power would raise the particle towards the focal point until $P = P_{max}$. If the laser power is further increased slightly above $P_{max}$, the particle will rise through the focal point back to the above focal point position.

For the droplet located on the laser beam propagation axis (z-axis), the horizontal force components and all components of torque are zero, as is obvious from symmetry and as was verified by the equations in App. C. If the droplet is displaced in the horizontal direction, stabilizing forces act so as to push the droplet back towards the beam propagation axis. (This is true for $Re(\bar{n}) > 1$, as considered here. If $Re(\bar{n}) < 1$, then the horizontal forces push the droplet away from the

propagation axis and there is no stable levitation.) Also, if the droplet is displaced in the horizontal direction, a torque is induced on the droplet since the beam intensity profile now presents an asymmetrical incident light distribution across the droplet. Calculations of horizontal acceleration ($a = <F>/m$) and induced angular acceleration ($\dot{\omega} = N/I$, where $I = 2ma^2/5$) were performed for droplet displacement along both the x-axis and y-axis for elevations of $z_o = +50\ \mu m$ and $z_o = -5\ \mu m$. Accelerations were calculated assuming a laser power necessary to levitate the droplet at the particular elevation **as if the droplet were located on the propagation axis** as is given in Fig. 5.

Figures 6 and 7 are for droplets at an elevation of 5 $\mu m$ below the focal point where the beam diameter ($2w_o = 2.6\ \mu m$) is less than the droplet diameter. Figure 6 shows the restoring acceleration for a droplet displacement along the x-axis. The restoring accelerations are similar for all three types of droplets and are a maximum at about 2 $\mu m$ away from the propagation axis. (Note in Figs. 4 and 5, the levitation powers for all three types of droplets are approximately equal at $z_o = -5\ \mu m$.)

Figure 7 shows the y-component angular acceleration ($N_x = N_z = 0$) induced when the droplet is displaced along the x-axis at the $z_o = -5\ \mu m$ elevation. The induced angular acceleration increases from zero as the droplet is moved away from the propagation axis and reaches a maximum before diminishing to zero as the droplet is moved on out of the beam. The induced torque is greatest for the electric wave resonance droplet for x-axis displacements. The x-component angular acceleration ($N_y = N_z = 0$) induced when the droplet is displaced along the y-axis (not shown) has features similar to those for the x-axis displacement except that it is the magnetic wave resonance droplet that has the greatest induced torque. The increase in induced torque for the resonance droplets as the droplet is moved to the edge of the beam is consistent with the developments of Ref. 4 where it was found that structural resonances are excited by on-edge illumination with electric wave resonances more strongly excited for beams moved along the x-axis (in the direction of the incident beam electric field polarization) and magnetic wave resonances more strongly excited for beams moved along the y-axis (perpendicular to the incident beam electric field polarization). Additional results and observations are presented in Ref. 7.

## V. RADIATION FORCE DISTRIBUTION

For a small particle illuminated by intense laser light, the internal absorption of the light and the reflection and refraction of the light at the surface result in changes of electromagnetic momentum which produce local forces. The theoretical determination of the *net* radiation force and torque induced on a spherical particle illuminated by a focused laser beam was considered in Sec. IV. Of additional interest is the determination of the spatial distribution of the radiation forces within and upon the surface of the particle. An understanding of the distribution of the radiation forces would be particularly useful for applications involving the laser diagnostics of liquid droplets. For liquid droplets, an asymmetrical radiation force distribution may appreciably distort the shape of the droplet, which, in turn, may affect expected light scattering patterns, structural resonance excitation, etc. Also, as suggested by Zhang and Chang,[15] radiation forces could be used to control the shape of droplets (droplets either optically levitated or within a monodispersed stream) for subsequent experimental study.

Theoretical expressions have been derived for the body forces and surface stresses that occur when a homogeneous liquid droplet is illuminated by a continuous laser beam. Using our spherical particle/arbitrary beam interaction theory to provide the required electromagnetic field components, spatial distributions of radiation forces for a spherical water droplet in air levitated by a focused laser beam (corresponding with the arrangement analyzed in Sec. IV.) have been calculated. This work has been submitted for publication.[16] A partial summary is given here.

Applying the divergence theorem to Eq. (2), the time averaged electromagnetically induced force per unit volume (body force) at any point within the liquid droplet is thus equal to the local divergence of the electromagnetic stress tensor,

$$< \vec{F}''' > = < \vec{\nabla} \cdot \vec{T} >. \tag{5}$$

For calculation purposes, Eq. (5) can be simplified by substituting for the stress tensor (from Eq. (3)), applying Maxwell's equations, and taking the time average. (Note for a homogeneous particle the dielectric constant is uniform and the local charge density is zero so $\vec{\nabla} \cdot \vec{E} = 0$.) Eq. (5) then becomes

$$< \vec{F}''' >= \frac{1}{8\pi} Re\{-i\epsilon_I (\vec{E} \cdot \vec{\nabla})\vec{E}^* - i\frac{\omega}{c}(\bar{\epsilon} - \epsilon_R)(\vec{E} \times \vec{H}^*)\} \tag{6}$$

where $\bar{\epsilon} = \epsilon + i4\pi\sigma/\omega$ and both the dielectric constant, $\epsilon = \epsilon_R + i\epsilon_I$, and the electrical conductivity, $\sigma = \sigma_R + i\sigma_I$, may be complex.

In addition to the electromagnetically induced body force, there is also an electromagnetically induced stress at the surface of the droplet. Returning to Eq. (2) and considering a cylindercal control volume of incremental cross sectional area, $\Delta S$, and incremental length, $\Delta L$, centered about a general position on the surface of the sphere, it follows in the limit that

$$< \vec{P} >= \lim_{\Delta S \to 0} \lim_{\Delta L \to 0} \frac{\vec{F}}{\Delta S} =< \hat{r} \cdot \bar{T}_{ext} - \hat{r} \cdot \bar{T}_{int} > \big|_{r=a} \tag{7}$$

where $\vec{P}$ is the electromagnetically induced surface stress. Substituting into Eq. (7) expressions for the internal (inside the sphere) and external (outside the sphere) stress tensors, utilizing the boundary conditions,

$$\epsilon_{ext} E_r^{ext} = \bar{\epsilon}_{int} E_r^{int},$$

$$E_\theta^{ext} = E_\theta^{int},$$

$$E_\phi^{ext} = E_\phi^{int},$$

$$\vec{H}_{ext} = \vec{H}_{int},$$

and taking the time average provides an expression for the surface stress in terms of the electromagnetic field components,

$$< \vec{P} >= \frac{1}{8\pi} Re\{\frac{1}{2}[(\bar{n}^2 \bar{\epsilon}_{int}^* - \epsilon_{int})|E_r^{int}|^2 + (\epsilon_{int} - \epsilon_{ext})(E_\theta^2 + E_\phi^2)]\hat{r} + (\bar{\epsilon}_{int}^* - \epsilon_{int})E_r^{int*}(E_\theta\hat{\theta} + E_\phi\hat{\phi})\}. \tag{8}$$

The theoretical expressions for the body force, Eq. (6), and the surface stress, Eq. (8), were found to be consistent with the net radiation force expressions in App. C. The net radiation force on a droplet should be equal to the sum of a volume integral of the body forces and a surface integral of the surface stresses,

$$< \vec{F} >= \int_0^a \int_0^\pi \int_0^{2\pi} < \vec{F}''' > r^2 sin\theta d\phi d\theta dr + \int_0^\pi \int_0^{2\pi} < \vec{P} > a^2 sin\theta d\phi d\theta. \tag{9}$$

Using our spherical particle/arbitrary beam interaction theory to provide the required electromagnetic field components, the integrals of Eq. (9) were numerically evaluated for several different particle size parameter, complex relative refractive index, and incident beam orientation arrangements. For each case, the net radiative force components from Eq. (9) were identical to those determined using the coefficient series expressions of App. C.

Equations (6) and (8) were used to determine the radiation force distributions for a 5 $\mu m$ water droplet optically levitated using a vertically-oriented, argon-ion laser beam corresponding with the arrangement analyzed for net force and torque in Sec. IV. The assumed continuous TEM$_{00}$ mode (Gaussian-profiled), linearly polarized laser beam is focused with a beam waist diameter of 2 $\mu m$ ($2w_o = 2\mu m$) and propagates in the $+ z$ axis direction with the electric field polarization in the x axis direction. Force distributions were calculated for the droplet both on and off the laser beam propagation axis and for the droplet 50 $\mu m$ above the beam focal point (where the beam diameter of 16.5 $\mu m$ is greater than the droplet diameter) and for the droplet 5 $\mu m$ below the beam focal

point (where the beam diameter of 2.6 $\mu m$ is less than the droplet diameter). As in Sec. IV., calculations were performed for the three basic types of droplets: a droplet at a magnetic wave resonance ($35^{th}$ mode, $1^{st}$ order, d $= 4.9266$ $\mu m$), a droplet at an electric wave resonance ($35^{th}$ mode, $1^{st}$ order, d $= 4.9912$ $\mu m$), and an intermediate nonresonance droplet (d $= 4.96$ $\mu m$).

At the 0.5145 $\mu m$ wavelength, water is a weakly absorbing dielectric with $\bar{n} = 1.334 + 1.2 \times 10^{-9}$i and thus $\epsilon_R = n_R^2 - n_I^2 = 1.780$, $\epsilon_I = 2 n_R n_I = 3.20 \times 10^{-9}$, $\sigma_R = 0$, and $\sigma_I = 0$. From Eqs. (6) and (8) it follows that $< F''' > \approx 0$, $P_\theta \approx 0$, and $P_\phi \approx 0$, so, for these conditions, the radiative forces are predominately outwardly-directed radial surface stresses.

The surface stress distributions shown in Figs. 8-12 provide the surface stress vector at $5^o$ intervals around the circumference of the droplet in the x-z plane (in Figs. 8-13 the z axis is upwards, the x axis to the right) linearly scaled relative to the maximum surface stress magnitude, $P_{max}$. The assumed laser power is that necessary to levitate the droplet at the given elevation *as if the droplet was located on the propagation axis.*

Figure 8 shows the surface stress distribution for the nonresonance droplet levitated on the beam propagation axis at an elevation of 50 $\mu m$ above the focal point. At this elevation the beam diameter is about three times the diameter of the droplet. As seen in Fig. 8, the largest forces are concentrated across the top of the droplet (in the direction of the beam propagation) with a secondary concentration of smaller forces across the bottom of the droplet. These surface forces are approximately azimuthally symmetric so that the surface force distribution in the y-z plane (plane perpendicular to the incident electric field polarization) is similar to that in the x-z plane for the nonresonance droplet.

Figure 9 shows the surface stress distribution for the electric wave resonance droplet levitated on the beam propagation axis at an elevation of 50 $\mu m$ above the focal point. As for the nonresonance droplet, the largest surface stresses are concentrated across the top of the droplet with a secondary concentration of smaller forces across the bottom of the droplet. Unlike the nonresonance droplet, however, the electric wave resonance droplet exhibits a significant surface stress over the entire circumference, not just near the top and bottom of the droplet. The maximum surface stress for the electric wave resonance droplet is also about three times larger than the maximum surface stress for the nonresonance droplet at this elevation. The excitation of the electric wave resonance, as discussed in Ref. 4, occurs predominately in the x-z plane (the plane of incident electric field polarization). The surface stress distribution for the electric wave resonance droplet is not azimuthally symmetric and is similar to that of the nonresonance droplet in the y-z plane. For the magnetic wave resonance droplet (not shown) the situation is the opposite of that of the electric wave resonance droplet: the surface stress is "excited" in the y-z plane and is not "excited" in the x-z plane.

Figure 10 presents the surface stress distribution for the nonresonance droplet levitated on the beam propagation axis at an elevation of 5 $\mu m$ below the focal point. At this elevation the beam diameter is about half the diameter of the droplet. As seen in Fig. 10, the largest surface stresses are concentrated near the top to the droplet with a secondary concentration of much smaller surface stresses near the bottom of the droplet. The maximum surface stress is about ten times greater than for the nonresonance droplet levitated at the $+ 50$ $\mu m$ elevation and the surface stress is confined to a smaller area. The surface stresses are approximately azimuthally symmetric.

Resonance excitation requires droplet edge illumination, and the electric and magnetic wave resonances are not excited for the on propagation axis location at $z_0 = - 5$ $\mu m$ where the incident beam passes through the middle of the droplet. The surface stress distributions for the electric and magnetic wave resonance droplets for the on propagation axis location at $z = - 5$ $\mu m$ (not shown) are similar to that of the nonresonance droplet.

If the droplet is horizontally displaced, there is a net restoring force that accelerates the droplet back towards the beam propagation axis (see Sec. IV.). Figure 11 presents the surface stress distribution for the nonresonance droplet levitated 5 $\mu m$ below the focal point and displaced 3 $\mu m$ along the x-axis. As shown in Fig. 11, for the displaced droplet the surface stresses are skewed towards the left which produces the net restoring force. Fig. 12 shows the same situation, but for the electric wave resonance droplet. The edge illumination caused by the horizontal displacement of the droplet excites the resonance which produces large surface stresses over the entire circumference

of the droplet in the x-z plane. For the magnetic wave resonance droplet (not shown) the resonance is excited in the y-z plane when the droplet is displaced along the y-axis.

As previously mentioned, at the 0.5145 $\mu m$ wavelength, water is weakly absorbing and body forces are small. The body forces do, however, significantly contribute for the case of the x-axis displaced electric wave resonance droplet (and the y-axis displaced magnetic wave resonance droplet) at the $z_0 = -5$ $\mu m$ elevation. As shown in Sec. IV., the x-axis displaced electric wave resonance droplet at the $z_0 = -5$ $\mu m$ elevation incurs a net torque about the negative y-axis. Since the surface stresses are essentially radial, the surface stresses do not contribute to this torque. In Sec. III. it was shown that edge illuminated droplets at resonance have an increase in electric field magnitude that forms a ring just inside the surface of the droplet. At resonance the droplet acts as an optical cavity with light circling just inside the surface. Absorption of this light results in a loss of momentum which produces a net torque about the center of the droplet.

Figure 13 shows the calculated body force distribution in the x-z plane for the electric wave resonance droplet at the $-5$ $\mu m$ elevation and displaced 3 $\mu m$ along the x-axis. Since the body forces are concentrated near the surface of the droplet, the distribution is plotted extending from $\bar{r} = 0.8$ (at the center of the plot) to $\bar{r} = 1.0$ (at the outer circumference of the plot). The body force vectors form a circling pattern which produces a net torque on the droplet. For the magnetic resonance droplet displaced along the y-axis (not shown) the body forces circle in the y-z plane.

## VI. BEAM INCIDENT UPON TWO ADJACENT SPHERES OF ARBITRARY ARRANGEMENT

Utilizing our spherical particle/arbitrary beam interaction theory, we have developed a procedure for determining the electromagnetic fields for an arbitrary beam incident upon two adjacent particles of differing size and material and of arbitrary spatial positioning. (The generalization to three or more adjacent particles would be straightforward). The two particles may be of different size, may have different composition (differing complex relative index of refractions), and may have any spatial orientation relative to each other and relative to the incident beam. It is not necessary that there be a single incident beam; having multiple beams coming from different directions would require minimal additional computation.

The theoretical approach, in the most general sense, is similar to that introduced by Fuller and Kattawar.[17,18] Since our spherical particle/arbitrary beam interaction theory permits the determination of the electromagnetic fields of a particle for *any* known incident field, the procedure is as follows. The spherical particle/arbitrary beam interaction theory is used to calculate the external electromagnetic field for the beam incident upon particle 1. The external electromagnetic field of particle 1 is used as the incident field upon particle 2 and the scattered field of particle 2 is determined. The scattered field of particle 2 is added to the incident beam to form an updated field incident upon particle 1 and the external field of particle 1 is recalculated. The newly calculated external field of particle 1 is then used as the incident field upon particle 2 and the scattered field of particle 2 is recalculated. The process is continued until there is no longer a significant change in the electromagnetic fields. For particles spaced one radius or more apart surface-to-surface, convergence typically occurs within two or three of these multiple "reflections."

The parameters of the laser beam incident upon two adjacent particles problem are then the dielectric constant of the medium ($\epsilon_{ext}$), the waist diameter of the laser beam ($w_0$), the size parameters of the two particles ($\alpha_1$ and $\alpha_2$), the complex relative index of refractions of the two particles ($\bar{n}_1$ and $\bar{n}_2$), the location of particle 1 relative to the focal point of the laser beam ($x_o$, $y_o$, $z_o$), the location of particle 2 relative to particle 1 ($x_{12}$, $y_{12}$, $z_{12}$), and the location of the plot reference relative to particle 1 ($x_{ref}$, $y_{ref}$, $z_{ref}$). Spatial quantities are normalized using the radius of particle 1 ($a_1$).

Figure 14 presents the internal and near-surface normalized source function distribution in the y-z plane for a linearly-polarized (electric field polarization in the x axis direction), 100 $\mu m$ waist diameter $CO_2$ laser beam ($\lambda = 10.6$ $\mu m$) incident upon two 45 $\mu m$ diameter water droplets separated by 35 $\mu m$ surface-to-surface along the propagation axis. These conditions correspond to an experiment performed within our Laboratory in which a $CO_2$ laser beam was directed upon two parallel streams of water droplets so that the illuminated droplet would act as a lens to focus the

laser light upon the shadow side droplet.[19] This focusing effect is apparent in Fig. 14. Figure 15 presents the same situation as Fig. 14 but with the internal field suppressed to zero. As can be seen, the maximum droplet heating rate (proportional to S) occurs at the front surface of the shadow side droplet, for this arrangement, which is in agreement with our experimental observations.[19]

Figure 16 provides a normalized source function distribution for a more general case. A 40 $\mu$m waist diameter $CO_2$ laser beam is incident upon a 50 $\mu$m diameter methanol droplet ($\bar{n}_1 = 1.395 + 0.0163i$) and a 30 $\mu$m water droplet ($\bar{n}_2 = 1.179 + 0.072i$). The droplets are offset from each other and offset from the propagation axis of the beam in the y-z plane. The effect is an interesting splitting of the beam.

Further investigation of electromagnetic phenomena associated with a beam incident upon adjacent spherical particles, including particles at resonance, is in progress.

## VII. FUTURE WORK

Besides continuing the developments discussed here, future topics that will be considered include obtaining direct comparisons between spherical particle/arbitrary beam interaction theory calculations and corresponding experimental measurements, developing an infinite cylinder/arbitrary beam interaction theory, developing an arbitrary shaped particle/arbitrary beam interaction theory, and developing a nonhomogeneous spherical particle/arbitrary beam interaction theory.

## ACKNOWLEDGEMENT

## REFERENCES

1. J.P. Barton, D.R. Alexander, and S.A. Schaub, "Internal and near-surface electromagnetic fields for a spherical particle irradiated by a focused laser beam," J. Appl. Phys. **64**, 1632 (1988).
2. S.A. Schaub, D.R. Alexander, J.P. Barton, and M.A. Emanuel, "Focused laser beam interactions with methanol droplets: effects of relative beam diameter," Appl. Opt. **28**, 1666 (1989).
3. J.P. Barton, D.R. Alexander, and S.A. Schaub, "Experimental and theoretical analysis of liquid droplets moving through a focused $CO_2$ laser beam," Proceedings of the 1988 CRDEC Scientific Conference on Obscuration and Aerosol Research.
4. J.P. Barton, D.R. Alexander, and S.A. Schaub, "Internal fields of a spherical particle illuminated by a tightly-focused laser beam: focal point positioning effects at resonance," J. Appl. Phys. **65**, 2900 (1989).
5. J.P. Barton and D.R. Alexander, "Fifth-order corrected electromagnetic field components for a fundamental Gaussian beam," J. Appl. Phys., to be published (Oct. 1, 1989).
6. R.K. Chang, personal communication (1989).
7. J.P. Barton, D.R. Alexander, and S.A. Schaub, "Theoretical determination of net radiation force and torque for a spherical particle illuminated by a focused laser beam," J. Appl. Phys., to be published (Nov. 15, 1989).
8. J.D. Jackson, *Classical Electrodynamics, 2nd ed.* (John Wiley & Sons, New York, 1975).
9. F.N.H. Robinson, "Electromagnetic stress and momentum in matter," Phys. Rep. **16**, 315 (1975).
10. I. Brevik, "Experiments in phenomenological electrodynamics and the electromagnetic energy-momentum tensor," Phys. Rep. **52**, 133 (1979).
11. A. Ashkin and J.M. Dziedzic, "Optical levitation of liquid drops by radiation pressure," Science **187**, 1073 (1975).
12. A. Ashkin and J.M. Dziedzic, "Observation of resonances in the radiation pressure on dielectric spheres," Phys. Rev. Lett. **38**, 1351 (1977).
13. A. Ashkin and J.M. Dziedzic, "Observation of optical resonances of dielectric spheres by light scattering," Appl. Opt. **20**, 1803 (1981).

14. A. Ashkin and J.M. Dziedzic, "Stability of optical levitation by radiation pressure," Appl. Phys. Lett. **24**, 586 (1974).
15. J.Z. Zhang and R.K. Chang, "Shape distortion of a single water droplet by laser-induced electrostriction," Opt. Lett. **13**, 916 (1988).
16. J.P. Barton, D.R. Alexander, and S.A. Schaub, "Theoretical determination of the radiation force distribution for a spherical droplet illuminated by a focused laser beam," submitted to J. Appl. Phys. (1989).
17. K.A. Fuller and G.W. Kattawar, "Consummate solution to the problem of classical electromagnetic scattering by an ensemble of spheres. I: Linear chains," Opt. Lett. **13**, 90 (1988).
18. K.A. Fuller and G.W. Kattawar, "Consummate solution to the problem of classical electromagnetic scattering by an ensemble of spheres. II: Clusters of arbitrary configuration," Opt. Lett. **13**, 1063 (1988).
19. D.R. Alexander, J.P. Barton, S.A. Schaub, M.A. Emanuel, and J. Zhang, "Experimental and theoretical analysis of the interaction of laser radiation with fluid cylinders and spheres," Proceedings of the 1987 CRDEC Scientific Conference on Obscuration and Aerosol Research.

# APPENDIX A: ELECTROMAGNETIC FIELD EQUATIONS

## INCIDENT FIELD

$$E_r^{(i)} = \frac{1}{\tilde{r}^2} \sum_{l=1}^{\infty} \sum_{m=-l}^{l} \left[ l(l+1) A_{lm} \psi_l(\alpha\tilde{r}) Y_{lm}(\theta,\phi) \right] \tag{A1}$$

$$E_\theta^{(i)} = \frac{\alpha}{\tilde{r}} \sum_{l=1}^{\infty} \sum_{m=-l}^{l} \left[ A_{lm} \psi_l'(\alpha\tilde{r}) \frac{\partial Y_{lm}(\theta,\phi)}{\partial\theta} - \frac{m}{\sqrt{\epsilon_{ext}}} B_{lm} \psi_l(\alpha\tilde{r}) \frac{Y_{lm}(\theta,\phi)}{\sin\theta} \right] \tag{A2}$$

$$E_\phi^{(i)} = \frac{\alpha}{\tilde{r}} \sum_{l=1}^{\infty} \sum_{m=-l}^{l} \left[ i\, m\, A_{lm} \psi_l'(\alpha\tilde{r}) \frac{Y_{lm}(\theta,\phi)}{\sin\theta} - \frac{i}{\sqrt{\epsilon_{ext}}} B_{lm} \psi_l(\alpha\tilde{r}) \frac{\partial Y_{lm}(\theta,\phi)}{\partial\theta} \right] \tag{A3}$$

$$H_r^{(i)} = \frac{1}{\tilde{r}^2} \sum_{l=1}^{\infty} \sum_{m=-l}^{l} \left[ l(l+1) B_{lm} \psi_l(\alpha\tilde{r}) Y_{lm}(\theta,\phi) \right] \tag{A4}$$

$$H_\theta^{(i)} = \frac{\alpha}{\tilde{r}} \sum_{l=1}^{\infty} \sum_{m=-l}^{l} \left[ B_{lm} \psi_l'(\alpha\tilde{r}) \frac{\partial Y_{lm}(\theta,\phi)}{\partial\theta} + m\sqrt{\epsilon_{ext}}\, A_{lm} \psi_l(\alpha\tilde{r}) \frac{Y_{lm}(\theta,\phi)}{\sin\theta} \right] \tag{A5}$$

$$H_\phi^{(i)} = \frac{\alpha}{\tilde{r}} \sum_{l=1}^{\infty} \sum_{m=-l}^{l} \left[ i\, m\, B_{lm} \psi_l'(\alpha\tilde{r}) \frac{Y_{lm}(\theta,\phi)}{\sin\theta} + i\sqrt{\epsilon_{ext}} A_{lm} \psi_l(\alpha\tilde{r}) \frac{\partial Y_{lm}(\theta,\phi)}{\partial\theta} \right] \tag{A6}$$

## SCATTERED FIELD

$$E_r^{(s)} = \frac{1}{\tilde{r}^2} \sum_{l=1}^{\infty} \sum_{m=-l}^{l} \left[ l(l+1) a_{lm} \xi_l^{(1)}(\alpha\tilde{r}) Y_{lm}(\theta,\phi) \right] \tag{A7}$$

$$E_\theta^{(s)} = \frac{\alpha}{\tilde{r}} \sum_{l=1}^{\infty} \sum_{m=-l}^{l} \left[ a_{lm} \xi_l^{(1)\prime}(\alpha\tilde{r}) \frac{\partial Y_{lm}(\theta,\phi)}{\partial\theta} - \frac{m}{\sqrt{\epsilon_{ext}}} b_{lm} \xi_l^{(1)}(\alpha\tilde{r}) \frac{Y_{lm}(\theta,\phi)}{\sin\theta} \right] \tag{A8}$$

$$E_\phi^{(s)} = \frac{\alpha}{\tilde{r}} \sum_{l=1}^{\infty} \sum_{m=-l}^{l} \left[ i\, m\, a_{lm} \xi_l^{(1)\prime}(\alpha\tilde{r}) \frac{Y_{lm}(\theta,\phi)}{\sin\theta} - \frac{i}{\sqrt{\epsilon_{ext}}} b_{lm} \xi_l^{(1)}(\alpha\tilde{r}) \frac{\partial Y_{lm}(\theta,\phi)}{\partial\theta} \right] \tag{A9}$$

$$H_r^{(s)} = \frac{1}{\tilde{r}^2} \sum_{l=1}^{\infty} \sum_{m=-l}^{l} \left[ l(l+1) b_{lm} \xi_l^{(1)}(\alpha\tilde{r}) Y_{lm}(\theta,\phi) \right] \tag{A10}$$

$$H_\theta^{(s)} = \frac{\alpha}{\tilde{r}} \sum_{l=1}^{\infty} \sum_{m=-l}^{l} \left[ b_{lm} \xi_l^{(1)\prime}(\alpha\tilde{r}) \frac{\partial Y_{lm}(\theta,\phi)}{\partial\theta} + m\sqrt{\epsilon_{ext}} a_{lm} \xi_l^{(1)}(\alpha\tilde{r}) \frac{Y_{lm}(\theta,\phi)}{\sin\theta} \right] \tag{A11}$$

$$H_\phi^{(s)} = \frac{\alpha}{\tilde{r}} \sum_{l=1}^{\infty} \sum_{m=-l}^{l} \left[ i\, m\, b_{lm}\, \xi_l^{(1)\prime}(\alpha\tilde{r}) \frac{Y_{lm}(\theta,\phi)}{\sin\theta} + i\sqrt{\epsilon_{ext}}\, a_{lm}\, \xi_l^{(1)}(\alpha\tilde{r}) \frac{\partial Y_{lm}(\theta,\phi)}{\partial\theta} \right] \tag{A12}$$

### INTERNAL FIELD

$$E_r^{(w)} = \frac{1}{\tilde{r}^2} \sum_{l=1}^{\infty} \sum_{m=-l}^{l} \left[ l(l+1)\, c_{lm}\, \psi_l(\bar{n}\alpha\tilde{r})\, Y_{lm}(\theta,\phi) \right] \tag{A13}$$

$$E_\theta^{(w)} = \frac{\alpha}{\tilde{r}} \sum_{l=1}^{\infty} \sum_{m=-1}^{l} \left[ \bar{n}\, c_{lm}\, \psi_l'(\bar{n}\alpha\tilde{r}) \frac{\partial Y_{lm}(\theta,\phi)}{\partial\theta} - \frac{m}{\sqrt{\epsilon_{ext}}}\, d_{lm}\, \psi_l(\bar{n}\alpha\tilde{r}) \frac{Y_{lm}(\theta,\phi)}{\sin\theta} \right] \tag{A14}$$

$$E_\phi^{(w)} = \frac{\alpha}{\tilde{r}} \sum_{l=1}^{\infty} \sum_{m=-l}^{l} \left[ i\, m\, \bar{n}\, c_{lm}\, \psi_l'(\bar{n}\alpha\tilde{r}) \frac{Y_{lm}(\theta,\phi)}{\sin\theta} - \frac{i}{\sqrt{\epsilon_{ext}}}\, d_{lm}\, \psi_l(\bar{n}\alpha\tilde{r}) \frac{\partial Y_{lm}(\theta,\phi)}{\partial\theta} \right] \tag{A15}$$

$$H_r^{(w)} = \frac{1}{\tilde{r}^2} \sum_{l=1}^{\infty} \sum_{m=-l}^{l} \left[ l(l+1)\, d_{lm}\, \psi_l(\bar{n}\alpha\tilde{r})\, Y_{lm}(\theta,\phi) \right] \tag{A16}$$

$$H_\theta^{(w)} = \frac{\alpha}{\tilde{r}} \sum_{l=1}^{\infty} \sum_{m=-1}^{l} \left[ \bar{n}\, d_{lm}\, \psi_l'(\bar{n}\alpha\tilde{r}) \frac{\partial Y_{lm}(\theta,\phi)}{\partial\theta} + m\sqrt{\epsilon_{ext}}\, \bar{n}^2 c_{lm}\, \psi_l(\bar{n}\alpha\tilde{r}) \frac{Y_{lm}(\theta,\phi)}{\sin\theta} \right] \tag{A17}$$

$$H_\phi^{(w)} = \frac{\alpha}{\tilde{r}} \sum_{l=1}^{\infty} \sum_{m=-l}^{l} \left[ i\, m\, \bar{n}\, d_{lm}\, \psi_l'(\bar{n}\alpha\tilde{r}) \frac{Y_{lm}(\theta,\phi)}{\sin\theta} + i\sqrt{\epsilon_{ext}}\, \bar{n}^2 c_{lm}\, \psi_l(\bar{n}\alpha\tilde{r}) \frac{\partial Y_{lm}(\theta,\phi)}{\partial\theta} \right] \tag{A18}$$

$$a_{lm} = \frac{\psi_l'(\bar{n}\alpha)\, \psi_l(\alpha) - \bar{n}\, \psi_l(\bar{n}\alpha)\, \psi_l'(\alpha)}{\bar{n}\, \psi_l(\bar{n}\alpha)\, \xi_l^{(1)\prime}(\alpha) - \psi_l'(\bar{n}\alpha)\, \xi_l^{(1)}(\alpha)}\, A_{lm} \tag{A19}$$

$$b_{lm} = \frac{\bar{n}\, \psi_l'(\bar{n}\alpha)\, \psi_l(\alpha) - \psi_l(\bar{n}\alpha)\, \psi_l'(\alpha)}{\psi_l(\bar{n}\alpha)\, \xi_l^{(1)\prime}(\alpha) - \bar{n}\, \psi_l'(\bar{n}\alpha)\, \xi_l^{(1)}(\alpha)}\, B_{lm} \tag{A20}$$

$$c_{lm} = \frac{\xi_l^{(1)\prime}(\alpha)\, \psi_l(\alpha) - \xi_l^{(1)}(\alpha)\, \psi_l'(\alpha)}{\bar{n}^2\, \psi_l(\bar{n}\alpha)\, \xi_l^{(1)\prime}(\alpha) - \bar{n}\, \psi_l'(\bar{n}\alpha)\, \xi_l^{(1)}(\alpha)}\, A_{lm} \tag{A21}$$

$$d_{lm} = \frac{\xi_l^{(1)\prime}(\alpha)\, \psi_l(\alpha) - \xi_l^{(1)}(\alpha)\, \psi_l'(\alpha)}{\psi_l(\bar{n}\alpha)\, \xi_l^{(1)\prime}(\alpha) - \bar{n}\, \psi_l'(\bar{n}\alpha)\, \xi_l^{(1)}(\alpha)}\, B_{lm} \tag{A22}$$

$$A_{lm} = \frac{1}{l(l+1)\, \psi_l(\alpha)} \int_0^{2\pi} \int_0^{\pi} \sin\theta\, E_r^{(i)}(a,\theta,\phi)\, Y_{lm}^*(\theta,\phi)\, d\theta\, d\phi \tag{A23}$$

$$B_{lm} = \frac{1}{l(l+1)\, \psi_l(\alpha)} \int_0^{2\pi} \int_0^{\pi} \sin\theta\, H_r^{(i)}(a,\theta,\phi)\, Y_{lm}^*(\theta,\phi)\, d\theta\, d\phi \tag{A24}$$

$\xi_l^{(1)} = \psi_l - i\chi_l$ where $\psi_l, \chi_l$ are the Riccati-Bessel functions. $Y_{lm}$ is the spherical harmonic function. $\tilde{r} = r/a$ where $a$ is the sphere radius.

## APPENDIX B: FIFTH-ORDER CORRECTED GAUSSIAN BEAM EQUATIONS

$$E_x = E_o \{ 1 + s^2[-\rho^2 Q^2 + i\rho^4 Q^3 - 2Q^2 \xi^2]$$
$$+ s^4[+2\rho^4 Q^4 - 3i\rho^6 Q^5 - 0.5\rho^8 Q^6 + (8\rho^2 Q^4 - i2\rho^4 Q^5)\xi^2] \} \psi_0 e^{-i\zeta/s^2}, \qquad \text{(B1)}$$

$$E_y = E_o \{ s^2[-2Q^2 \xi\eta] + s^4[(8\rho^2 Q^4 - 2i\rho^4 Q^5)\xi\eta] \} \psi_0 e^{-i\zeta/s^2}, \qquad \text{(B2)}$$

$$E_z = E_o \{ s[-2Q\xi] + s^3[(+6\rho^2 Q^3 - 2i\rho^4 Q^4)\xi$$
$$+ s^5[(-20\rho^4 Q^5 + 10i\rho^6 Q^6 + \rho^8 Q^7)\xi] \} \psi_0 e^{-i\zeta/s^2}, \qquad \text{(B3)}$$

$$H_x = \sqrt{\epsilon} E_o \{ s^2[-2Q^2 \xi\eta] + s^4[(8\rho^2 Q^4 - 2i\rho^4 Q^5)\xi\eta] \} \psi_0 e^{-i\zeta/s^2}, \qquad \text{(B4)}$$

$$H_y = \sqrt{\epsilon} E_o \{ 1 + s^2[-\rho^2 Q^2 + i\rho^4 Q^3 - 2Q^2 \eta^2]$$
$$+ s^4[+2\rho^4 Q^4 - 3i\rho^6 Q^5 - 0.5\rho^8 Q^6 + (8\rho^2 Q^4 - i2\rho^4 Q^5)\eta^2] \} \psi_0 e^{-i\zeta/s^2}, \qquad \text{(B5)}$$

and

$$H_z = \sqrt{\epsilon} E_o \{ s[-2Q\eta] + s^3[(+6\rho^2 Q^3 - 2i\rho^4 Q^4)\eta$$
$$+ s^5[(-20\rho^4 Q^5 + 10i\rho^6 Q^6 + \rho^8 Q^7)\eta] \} \psi_0 e^{-i\zeta/s^2} \qquad \text{(B6)}$$

where $\psi_0 = iQ exp(-i\rho^2 Q)$, $Q = 1/(i + 2\zeta)$, $\rho^2 = \eta^2 + \xi^2$, $s = 1/kw_0$, $\xi = x/w_0$, $\eta = y/w_0$, and $\zeta = z/kw_0^2$. Note: these equations are for an assumed time dependence of $e^{+i\omega t}$. If a time dependence of $e^{-i\omega t}$ is assumed, then the complex conjugate of the equations can be used.

# APPENDIX C: NET RADIATION FORCE AND TORQUE EQUATIONS

$$\frac{<F_x>+i<F_y>}{a^2 E_o^2} = +\frac{\alpha^2}{16\pi}i\sum_{l=1}^{\infty}\sum_{m=-l}^{l}\Bigg\{\sqrt{\frac{(l+m+2)(l+m+1)}{(2l+1)(2l+3)}}l(l+2)\times$$

$$\Big[2\epsilon_{ext}a_{lm}a_{l+1,m+1}^* + \epsilon_{ext}a_{lm}A_{l+1,m+1}^* + \epsilon_{ext}A_{lm}a_{l+1,m+1}^* + 2b_{lm}b_{l+1,m+1}^*$$

$$+ b_{lm}B_{l+1,m+1}^* + B_{lm}b_{l+1,m+1}^*\Big]$$

$$+ \sqrt{\frac{(l-m+1)(l-m+2)}{(2l+1)(2l+3)}}l(l+2)\times$$

$$\Big[2\epsilon_{ext}a_{l+1,m-1}a_{l,m}^* + \epsilon_{ext}a_{l+1,m-1}A_{l,m}^* + \epsilon_{ext}A_{l+1,m-1}a_{l,m}^* + 2b_{l+1,m-1}b_{l,m}^*$$

$$+ b_{l+1,m-1}B_{l,m}^* + B_{l+1,m-1}b_{l,m}^*\Big]$$

$$- \sqrt{(l+m+1)(l-m)}\sqrt{\epsilon_{ext}}\Big[-2a_{lm}b_{l,m+1}^* + 2b_{lm}a_{l,m+1}^* - a_{lm}B_{l,m+1}^*$$

$$+ b_{lm}A_{l,m+1}^* + B_{lm}a_{l,m+1}^* - A_{lm}b_{l,m+1}^*\Big]\Bigg\} \tag{C1}$$

$$\frac{<F_z>}{a^2 E_o^2} = -\frac{\alpha^2}{8\pi}\sum_{l=1}^{\infty}\sum_{m=-l}^{l}Im\Bigg\{l(l+2)\sqrt{\frac{(l-m+1)(l+m+1)}{(2l+3)(2l+1)}}\times$$

$$\Big[2\epsilon_{ext}a_{l+1,m}a_{lm}^* + \epsilon_{ext}a_{l+1,m}A_{lm}^* + \epsilon_{ext}A_{l+1,m}a_{lm}^* + 2b_{l+1,m}b_{lm}^* + b_{l+1,m}B_{lm}^* +$$

$$B_{l+1,m}b_{lm}^*\Big] + \sqrt{\epsilon_{ext}}m\Big[2a_{lm}b_{lm}^* + a_{lm}B_{lm}^* + A_{lm}b_{lm}^*\Big]\Bigg\} \tag{C2}$$

$$\frac{<N_x>}{a^3 E_o^2} = -\frac{\alpha}{8\pi}\sum_{l=1}^{\infty}\sum_{m=-l}^{l}Re\Bigg\{l(l+1)\sqrt{(l-m)(l+m+1)}\times$$

$$\Big[\epsilon_{ext}a_{lm}a_{l,m+1}^* + b_{lm}b_{l,m+1}^* +$$

$$\frac{1}{2}(\epsilon_{ext}a_{lm}A_{l,m+1}^* + \epsilon_{ext}a_{l,m+1}A_{lm}^* + b_{lm}B_{l,m+1}^* + b_{l,m+1}B_{lm}^*)\Big]\Bigg\} \tag{C3}$$

$$\frac{<N_y>}{a^3 E_o^2} = -\frac{\alpha}{8\pi}\sum_{l=1}^{\infty}\sum_{m=-l}^{l}Im\Bigg\{l(l+1)\sqrt{(l-m)(l+m+1)}\times$$

$$\Big[\epsilon_{ext}a_{lm}a_{l,m+1}^* + b_{lm}b_{l,m+1}^* +$$

$$\frac{1}{2}(\epsilon_{ext}a_{lm}A_{l,m+1}^* - \epsilon_{ext}a_{l,m+1}A_{lm}^* + b_{lm}B_{l,m+1}^* - b_{l,m+1}B_{lm}^*)\Big]\Bigg\} \tag{C4}$$

$$\frac{<N_z>}{a^3 E_o^2} = -\frac{\alpha}{8\pi}\sum_{l=1}^{\infty}\sum_{m=-l}^{l}(l+1)m\Big[\epsilon_{ext}|a_{lm}|^2 + |b_{lm}|^2 + Re(\epsilon_{ext}a_{lm}A_{lm}^* + b_{lm}B_{lm}^*)\Big] \tag{C5}$$

FIG 1. Normalized source function in the equatorial (y-z) plane for a transverse (x direction) polarized Gaussian beam incident upon a sphere at magnetic wave resonance. $\bar{n} = 1.33 + 5.0 \times 10^{-6} i$, $\bar{w}_o = 0.404$, $\bar{x}_o = 0.0$, $\bar{y}_o = -1.175$, $\bar{z}_o = 0.0$, and $\alpha = 29.365$. [1.06 $\mu$m wavelength, 4 $\mu$m waist diameter beam incident upon a 9.908 $\mu$m diameter (34th mode, 1st order mag. wave res.) water droplet with on edge y-axis illumination]
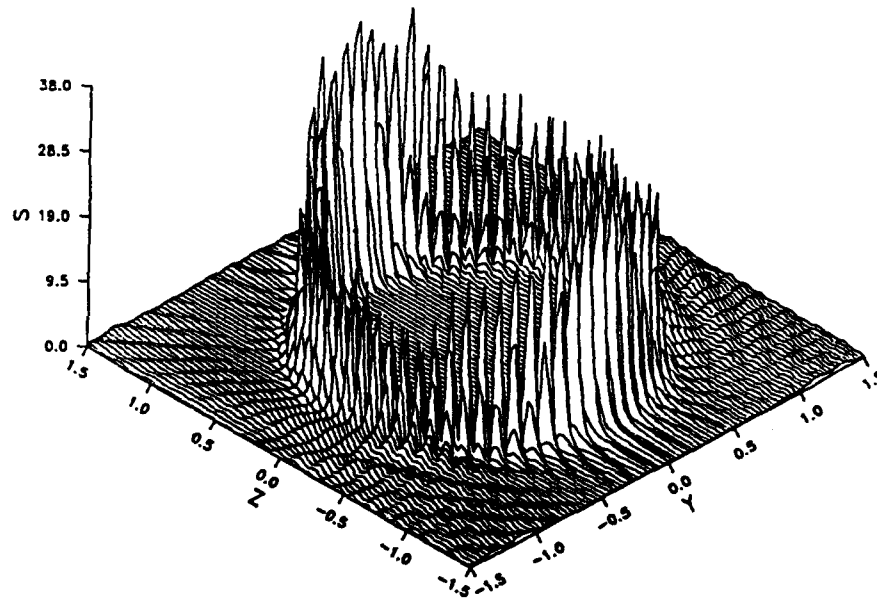


FIG 2. Normalized source function in the equatorial (y-z) plane for two transverse (x direction) polarized Gaussian beams incident upon a sphere at magnetic wave resonance. $\bar{n} = 1.33 + 5.0 \times 10^{-6} i$, $\bar{w}_o = 0.404$, $\bar{x}_o = 0.0$, $\bar{y}_o = +1.175$ and $-1.175$, $\bar{z}_o = 0.0$, and $\alpha = 29.365$. [1.06 $\mu$m wavelength, 4 $\mu$m waist diameter beams incident upon a 9.908 $\mu$m diameter (34th mode, 1st order mag. wave res.) water droplet with on edge y-axis illumination]
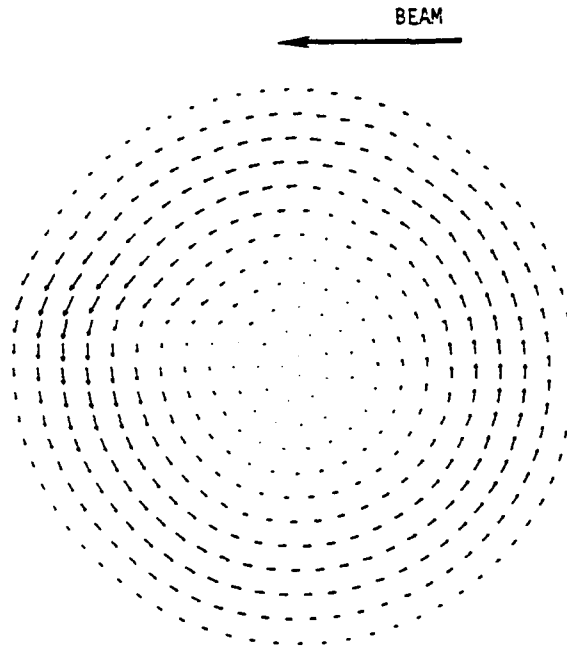
FIG 3. Poynting vector in the equatorial (y-z) plane for a transverse (x direction) polarized Gaussian beam incident upon a sphere at magnetic wave resonance. $1.0 > \bar{r} > 0.8$, $\bar{n} = 1.33 + 5.0 \times 10^{-6}i$, $\bar{w}_o = 0.404$, $\bar{x}_o = 0.0$, $\bar{y}_o = -1.175$, $\bar{z}_o = 0.0$, and $\alpha = 29.365$. [1.06 $\mu m$ wavelength, 4 $\mu m$ waist diameter beam incident upon a 9.908 $\mu m$ diameter ($34^{th}$ mode, $1^{st}$ order mag. wave res.) water droplet with on edge y-axis illumination]
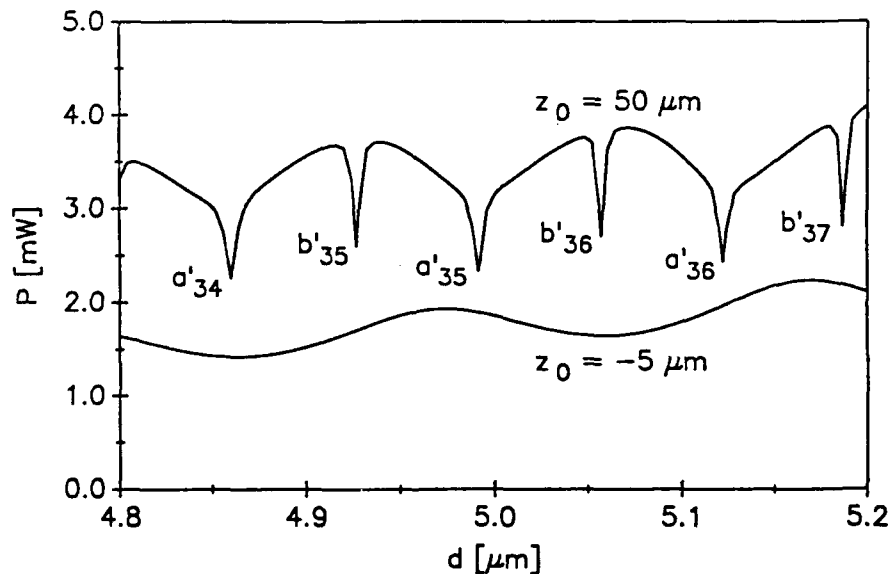


FIG. 4. Power versus droplet diameter for the optical levitation of a water droplet in air using a focused, $TEM_{00}$ mode, linearly polarized laser beam for droplet propagation axis positions of $z_o = -5\ \mu m$ and $+50\ \mu m$. ($x_o = y_o = 0$, $\bar{n} = 1.334 + 1.2 \times 10^{-9}i$, $\lambda = 0.5145\ \mu m$, and $w_o = 1\ \mu m$.)
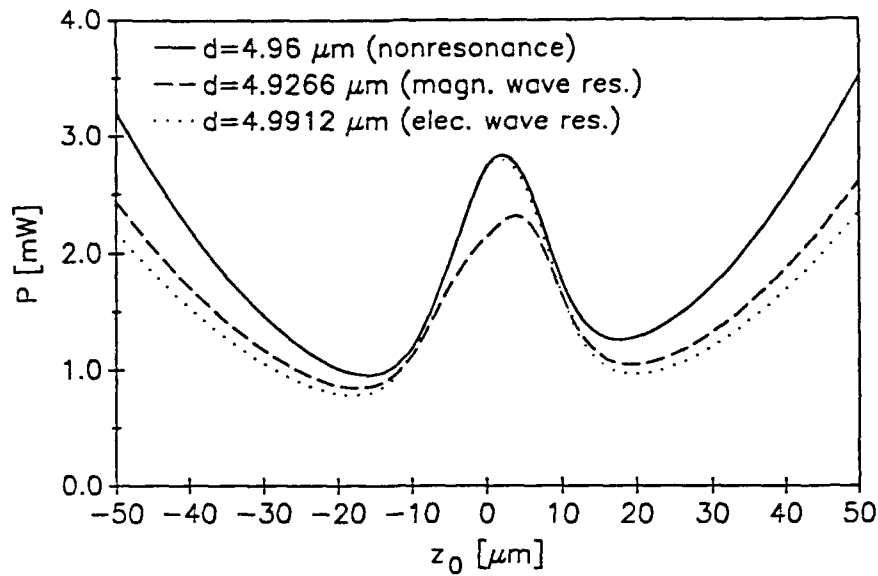
FIG. 5. Power versus propagation axis position for the optical levitation of a water droplet in air using a focused, $TEM_{00}$ mode, linearly polarized laser beam for nonresonance (d = 4.96 $\mu m$), magnetic wave resonance (d = 4.9266 $\mu m$), and electric wave resonance (d = 4.9912 $\mu m$). ($x_o = y_o = 0$, $\tilde{n} = 1.334 + 1.2 \times 10^{-9}i$, $\lambda = 0.5145$ $\mu m$, and $w_o = 1$ $\mu m$.)
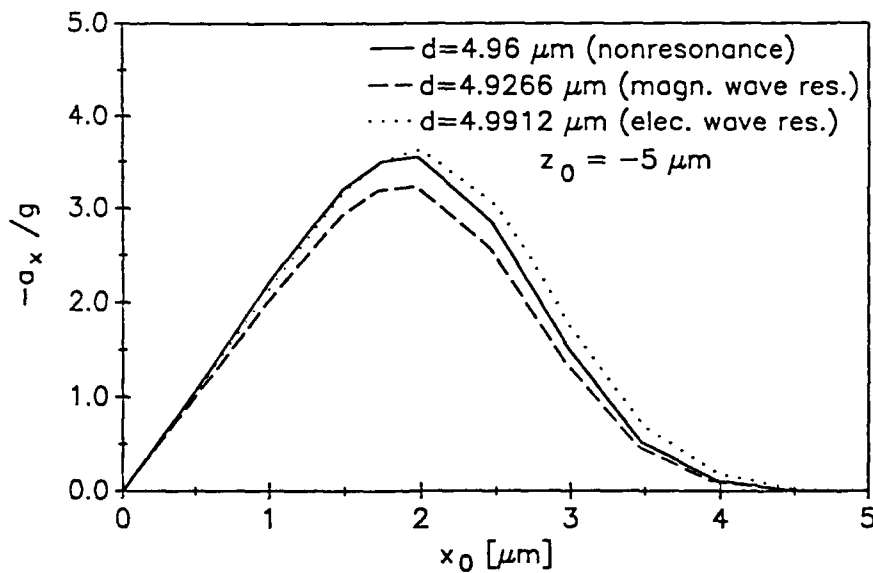


FIG. 6. x-axis acceleration versus x-axis displacement for optical levitation of a water droplet in air using a focused, $TEM_{00}$ mode, linearly polarized (x-axis direction) laser beam at a droplet propagation axis position of $z_o = -5$ $\mu m$ for nonresonance (d = 4.96 $\mu m$), magnetic wave resonance (d = 4.9266 $\mu m$), and electric wave resonance (d = 4.9912 $\mu m$). ($y_o = 0$, $\tilde{n} = 1.334 + 1.2 \times 10^{-9}i$, $\lambda = 0.5145$ $\mu m$, and $w_o = 1$ $\mu m$.)

FIG. 7. y-axis angular acceleration versus x-axis displacement for optical levitation of a water droplet in air using a focused, $TEM_{00}$ mode, linearly polarized (x-axis direction) laser beam at a droplet propagation axis position of $z_o = -5\ \mu m$ for nonresonance ($d = 4.96\ \mu m$), magnetic wave resonance ($d = 4.9266\ \mu m$), and electric wave resonance ($d = 4.9912\ \mu m$). ($y_o = 0$, $\bar{n} = 1.334 + 1.2 \times 10^{-9}i$, $\lambda = 0.5145\ \mu m$, and $w_o = 1\ \mu m$.)
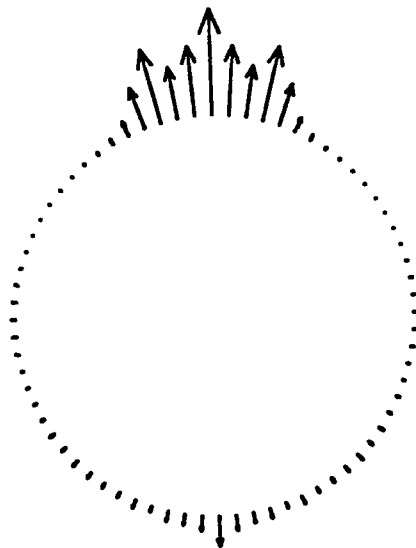


FIG. 8. Surface stress distribution in the x-z plane for a nonresonance water droplet ($d = 4.96\ \mu m$) optically levitated 50 $\mu m$ above the focal point of a 2 $\mu m$ waist diameter, 3.52 mW, argon-ion ($\lambda = 0.5145\ \mu m$) laser beam. Droplet positioned on the propagation axis. $P_{max} = 0.624$ Pa.
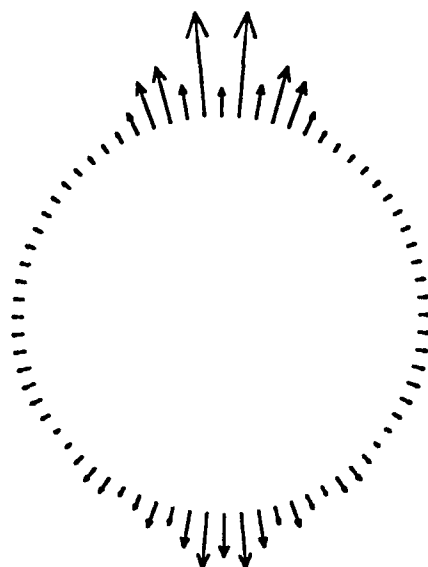
FIG. 9. Surface stress distribution in the x-z plane for an electric wave resonance water droplet (d = 4.9912 $\mu m$) optically levitated 50 $\mu m$ above the focal point of a 2 $\mu m$ waist diameter, 2.35 mW, argon-ion ($\lambda = 0.5145$ $\mu m$) laser beam. Droplet positioned on the propagation axis. $P_{max} = 1.94$ Pa.
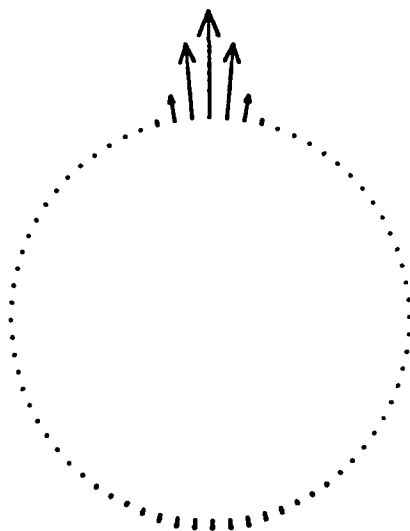


FIG. 10. Surface stress distribution in the x-z plane for a nonresonance water droplet (d = 4.96 $\mu m$) optically levitated 5 $\mu m$ below the focal point of a 2 $\mu m$ waist diameter, 1.91 mW, argon-ion ($\lambda = 0.5145$ $\mu m$) laser beam. Droplet positioned on the propagation axis. $P_{max} = 6.46$ Pa.
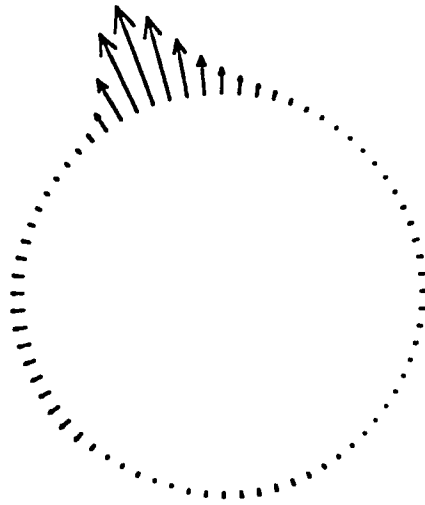
FIG. 11. Surface stress distribution in the x-z plane for a nonresonance water droplet (d = 4.96 $\mu m$) optically levitated 5 $\mu m$ below the focal point of a 2 $\mu m$ waist diameter, 1.91 mW, argon-ion ($\lambda = 0.5145$ $\mu m$) laser beam. Droplet displaced 3 $\mu m$ along the x-axis. $P_{max} = 2.12$ Pa.
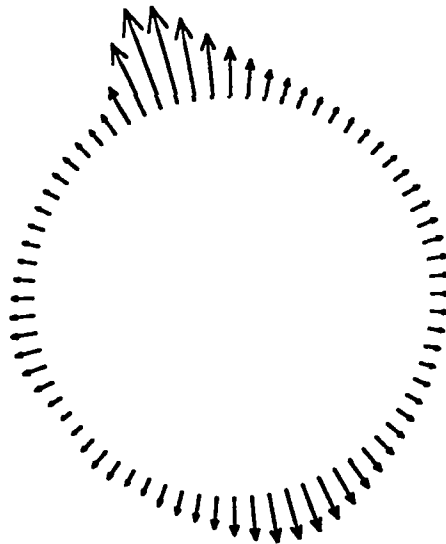


FIG. 12. Surface stress distribution in the x-z plane for an electric wave resonance water droplet (d = 4.9912 $\mu m$) optically levitated 5 $\mu m$ below the focal point of a 2 $\mu m$ waist diameter, 1.89 mW, argon-ion ($\lambda = 0.5145$ $\mu m$) laser beam. Droplet displaced 3 $\mu m$ along the x-axis. $P_{max} = 13.90$ Pa.
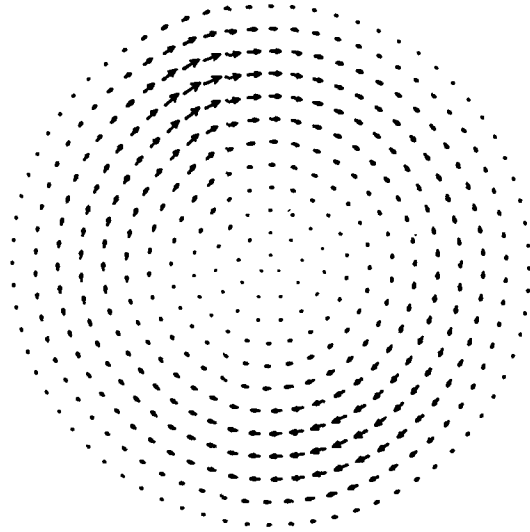
FIG. 13. Body force distribution in the x-z plane $(1.0 > r/a > 0.8)$ for an electric wave resonance water droplet $(d = 4.9912 \ \mu m)$ optically levitated 5 $\mu m$ below the focal point of a 2 $\mu m$ waist diameter, 1.89 mW, argon-ion $(0.5145 \ \mu m)$ laser beam. Droplet displaced 3 $\mu m$ along the x-axis. $F'''_{max} = 0.40 \ N/m^3$.



FIG 14. Normalized source function in the equatorial (y-z) plane for a transverse (x direction) electric field polarized Gaussian beam, propagating in the +z axis direction (right-to-left), incident upon two adjacent spheres. $\bar{n}_1 = \bar{n}_2 = 1.179 + 0.072i$, $\alpha_1 = \alpha_2 = 13.337$, $\bar{w}_o = 2.222$, $\bar{x}_o = \bar{y}_o = 0.0$, $\bar{z}_o = -1.778$, $\bar{x}_{12} = \bar{y}_{12} = 0.0$, $\bar{z}_{12} = 3.556$, $\bar{x}_{ref} = \bar{y}_{ref} = 0.0$, $\bar{z}_{ref} = 1.778$ [10.6 $\mu m$ wavelength ($CO_2$ laser), 100 $\mu m$ waist diameter beam incident upon two 45 $\mu m$ diameter water droplets separated along the propagation axis by 35 $\mu m$ surface-to-surface]

FIG 15. Normalized source function in the equatorial (y-z) plane for a transverse (x direction) electric field polarized Gaussian beam, propagating in the +z axis direction (right-to-left), incident upon two adjacent spheres. (External field suppressed.) $\bar{n}_1 = \bar{n}_2 = 1.179 + 0.072i$, $\alpha_1 = \alpha_2 = 13.337$, $\tilde{w}_o = 2.222$, $\tilde{x}_o = \tilde{y}_o = 0.0$, $\tilde{z}_o = -1.778$, $\tilde{x}_{12} = \tilde{y}_{12} = 0.0$, $\tilde{z}_{12} = 3.556$, $\tilde{x}_{ref} = \tilde{y}_{ref} = 0.0$, $\tilde{z}_{ref} = 1.778$ [10.6 $\mu$m wavelength ($CO_2$ laser), 100 $\mu$m waist diameter beam incident upon two 45 $\mu$m diameter water droplets separated along the propagation axis by 35 $\mu$m surface-to-surface.]



FIG 16. Normalized source function in the equatorial (y-z) plane for a transverse (x direction) electric field polarized Gaussian beam, propagating in the +z axis direction (right-to-left), incident upon two adjacent spheres. $\bar{n}_1 = 1.395 + 0.0163i$, $\alpha_1 = 14.82$, $\bar{n}_2 = 1.179 + 0.072i$, $\alpha_2 = 8.89$, $\tilde{w}_o = 0.8$, $\tilde{x}_o = 0.0$, $\tilde{y}_o = 1.0$, $\tilde{z}_o = 0.0$, $\tilde{x}_{12} = 0.0$, $\tilde{y}_{12} = -1.0$, $\tilde{z}_{12} = 3.0$, $\tilde{x}_{ref} = 0.0$, $\tilde{y}_{ref} = -0.5$, $\tilde{z}_{ref} = 1.5$ [10.6 $\mu$m wavelength ($CO_2$ laser), 40 $\mu$m waist diameter beam incident upon adjacent 50 $\mu$m diameter methanol and 30 $\mu$m diameter water droplets offset in the y-z plane.]

# NONLINEAR EFFECTS OF EXCIMER LASER
# INTERACTION WITH WATER DROPLETS

D.R. Alexander, J.P. Barton, S.A. Schaub, and G. Holtmeier

Center for Electro-Optics
University of Nebraska-Lincoln
Lincoln, Nebraska 68588-0525

## RECENT PUBLICATIONS, SUBMITTALS FOR PUBLICATION AND PRESENTATIONS

A) D.R. Alexander, S.A. Schaub, J. Zhang, D.E. Poulain, and J.P. Barton, "Scattering of incident KrF laser radiation resulting from the laser-induced breakdown of $H_2O$ droplets," Opt. Lett, 14 (11), (1989).

B) S.A. Schaub, D.R. Alexander, J.P. Barton, and M.A. Emanuel, "Focused laser beam interactions with methanol droplets: effects of relative beam diameter," Appl. Opt., 28 (9), (1989).

C) D.E. Poulain, "Interaction of solid aerosols with intense ultraviolet laser radiation," Masters Thesis, Mechanical Engineering Dept., Center for Electro-Optics, University of Nebraska-Lincoln, May 1989.

D) D.E. Poulain, D. R. Alexander, J.P. Barton, S.A. Schaub, and J. Zhang, "Interaction of intense ultraviolet radiation with solid aerosols," submitted for publication to J. Appl. Phys., August 1989.

E) S.A. Schaub, D.R. Alexander, D.E. Poulain, and J.P. Barton, "Measurement of hypersonic velocities resulting from the laser-induced breakdown of aerosols using and excimer laser imaging system," to be published in Rev. Sci. Instrum., December 1989.

F) S.A. Schaub, D.R. Alexander, and J.P. Barton, "Theoretical model for the image formed by a spherical particle in a coherent imaging system: comparison to experiment," Opt. Eng., 28 (5), (1989).

G) J.P. Barton, D.R. Alexander, and S.A. Schaub, "Internal and near-surface electromagnetic fields for a spherical particle irradiated by a focused laser beam," J. Appl. Phys., 64 (4), (1988).

H) J.P. Barton, D.R. Alexander, and S.A. Schaub, "Internal fields of a spherical particle illuminated by a tightly-focused laser beam: focal point positioning effects at resonance," J. Appl. Phys., 65 (8), (1989).

I) J.P. Barton and D.R. Alexander, "Fifth-order corrected electromagnetic field components for a fundamental Gaussian beam," to be published in J. Appl. Phys., October 1, 1989.

J) J.P. Barton, D.R. Alexander, and S.A. Schaub, "Theoretical determination of net radiation force and torque for a spherical particle illuminated by a focused laser beam," to be published in J. Appl. Phys., November 15, 1989.

K) S.A. Schaub, J.P. Barton, and D.R. Alexander, "Simplified coefficient expressions for a spherical particle located on the propagation axis of a fifth-order Gaussian beam," submitted for publication to Appl. Phys. Lett., July 1989.

L) J.P. Barton, D.R. Alexander, and S.A. Schaub, "Theoretical determination of the radiation force distribution for a spherical particle illuminated by a focused laser beam," submitted for publication to J. Appl. Phys., September 1989.

M) D.R. Alexander and J.P. Barton, "Interaction of high energy excimer laser radiation with small solid particles," Final Technical Report, CRDEC Contract No. DAAL03-87-K-0138, Dr. John White, Project Manager, October 1988.

N) D.R. Alexander, D.E. Poulain, J.P. Barton, S.A. Schaub, and J. Zhang, "Interaction of excimer laser radiation with solid particles," proceedings of the 1988 CRDEC Conference on Obscuration and Aerosol Research, June 1988.

O) J.P. Barton, D.R. Alexander, and S.A. Schaub, "Experimental and theoretical analysis of liquid droplets moving through a focused $CO_2$ laser beam," proceedings of the 1988 CRDEC Conference on Obscuration and Aerosol Research, June 1988.

P) D.R. Alexander and J.P. Barton, "Gaussian laser beam illumination of a spherical particle at resonance conditions," presentation at 19th European Conference on Laser Interaction with Matter, Madrid, Spain, October, 1988.

Q) D.R. Alexander, S.A. Schaub, J. Zhang, D.E. Poulain, and J.P. Barton, "Laser induced breakdown of $H_2O$ droplets at 0.248 $\mu$m," Workshop on the Physics of Directed Energy Propagation in the Atmosphere, Las Cruces, New Mexico, February 1989.

R) J.P. Barton, D.R. Alexander, and S.A. Schaub, "Electromagnetic fields for a focused laser beam incident upon a spherical particle," Workshop on the Physics of Directed Energy Propagation in the Atmosphere, Las Cruces, New Mexico, February 1989.

S) D.R. Alexander, D.E. Poulain, J.P. Barton, S.A. Schaub, and J. Zhang, "Nonlinear effects of excimer laser radiation with solid particles," presentation at the 1988 CRDEC Conference on Obscuration and Aerosol Research, Aberdeen Proving Ground, Maryland, June 1988.

T) J.P. Barton, D.R. Alexander, and S.A. Schaub, "Internal and near-surface electromagnetic fields for a spherical particle in a focused laser beam," poster presentation at the 1988 CRDEC Conference on Obscuration and Aerosol Research, Aberdeen Proving Ground, Maryland, June, 1988.

## Abstract

During this funding period results have been obtained for the interaction of KrF excimer laser radiation ($\lambda = 248$ nm, $t_{pulse} = 17$ ns) with 60 $\mu$m distilled water droplets for irradiance values ranging from 3 to 230 GW/cm$^2$. Laser images of the droplet breakup during the time interval from 0 to 100 ns indicate the dynamic breakup processes to be highly nonlinear. At low irradiance (3 GW/cm$^2$) the material is ejected from both the illuminated and shadow hemispheres of the droplet, closely resembling internal electric field strengths obtained from plane wave Lorenz-Mie theory calculations. As the irradiance is increased to 6 GW/cm$^2$ the interaction on the shadow hemisphere becomes stronger while the interaction on the illuminated hemisphere decreases. At high irradiance (230 GW/cm$^2$) the droplets fragment in essentially a symmetric manner. Average material velocity from 0 to 50 ns after arrival of the high energy pulse ranged from 1000 m/s at 3 GW/cm$^2$ to 6000 m/s at 230 GW/cm$^2$.

## I. Introduction

The interaction of intense laser radiation with liquid droplets has been widely investigated during recent years in attempts to better understand the fundamental physics governing the interaction. Experimental investigations have been performed examining plasma formation,[1-5] shock propagation,[6] and electrostrictive effects[7] that occur during the laser/aerosol interaction. Theoretical models have also been developed to predict the behavior of droplets under high energy laser irradiation.[8,9] Due to the complexity of the problem, most theories utilize plane wave theory in the analysis although recent work has generalized Lorenz-Mie theory for the case of a particle located at an arbitrary position illuminated by an arbitrarily defined incident beam.[10,11] However, accounting for the influence of spatial varying droplet properties, initial plasma formation, and heat transfer make the laser/aerosol interaction problem nonlinear and extremely complex. In this paper we present further experimental evidence of the nonlinear interactions of high energy KrF laser pulses ($\lambda = 248$ nm) with 60 $\mu$m diameter distilled water droplets for irradiance values ranging from 3 GW/cm$^2$ to 230 GW/cm$^2$.

## II. Experimental Setup

A schematic of the experimental setup used in the research is shown in Fig. 1. The high energy laser beam is produced by a KrF excimer laser (Questek model 2860, $\lambda = 248$ nm) using unstable optics and is focused at the probe volume using a plano-convex lens (d = 50 mm, f = 200 mm). The FWHM cross section of the high energy beam at the focal point was determined by translating a knife-edge through the probe volume and was found to be approximately 95 $\mu$m x 115 $\mu$m ($\approx 10^4$ $\mu$m$^2$). An imaging beam from a second excimer laser, identical to the first with the exception of using stable resonator optics and operating on ArF gas ($\lambda = 193$ nm), is incident in a direction orthogonal to both the high energy pulse and the motion of the water droplets. The use of 193 nm imaging laser was used to obtain higher resolution real-time images as well as to allow elimination of elastically scattering incident radiation by placing a 193 nm bandpass filter in line with the imaging optics. The FWHM pulse duration of the excimer laser pulses were measured using both a photodiode and streak camera and were found to be approximately 17 ns. The imaging pulses are synchronized with the high energy pulses by using an analog/digital delay unit (Questek 9200 laser sync/delay unit) while simultaneously monitoring the output pulse using a fast photodiode (Hamamatsu model C1083) and a digitizing oscilloscope (Hewlett Packard model 54200A). The delay between high energy pulses and imaging pulses could be varied from 0 to 100 $\mu$s in increments of 10 ns. The jitter for the entire system is approximately $\pm$7 ns. The monodisperse water droplets were generated using a vibrating orifice generator (TSI model 3450) and were allowed to fall in the direction of the gravitational field perpendicular to both the high energy beam and the imaging beam. The real time images were viewed using a UV sensitive vidicon (Cohu 2006 camera system) in conjunction with a digital image processing system[12]. Use

of the image processing system allows accurate determination of the particle size prior to explosive breakup and the distance expelled material travels during the laser/aerosol interaction. The images were stored on an optical memory disk recorder (Panasonic model TQ-2023F) so that later analysis could be performed on the images.

## III. Results

Figure 2 shows typical images of water droplets 0, 20, 40, and 100 ns after arrival of 3 GW/cm$^2$ KrF ($\lambda = 248$ nm) laser pulses. In Figs. 2-5 the laser beam is propagating from right to left in the photographs. Although 0 ns delay was established prior to experiments by synchronizing the arrival of the high energy pulse with the imaging pulse as they reached the probe volume, it is clearly evident in the photographs that the interaction actually begins prior to what is considered as 0 ns delay. This is caused by the finite pulse widths (FWHM = 17 ns) of the high energy and imaging pulses. For increasing irradiance, the interaction process initiates nearer the initial rise of the high energy pulse. In contrast, the image that is obtained is integrated over the 17 ns duration of the imaging pulse. Thus, although the peaks of both pulses may arrive simultaneously at the probe volume, the image contains information from the first few nanoseconds after arrival of the high energy pulse. Also note that the images in Figs. 2-5 are not of a single droplet but of several different droplets imaged at fixed times after arrival of the high energy beam. Since the vibrating orifice generator and the laser pulse characteristics change little from pulse to pulse, the image variation from one pulse to the next is not significant. For the images shown in Fig. 2, note that the interaction is nearly symmetric with material being expelled from both the illuminated and shadow hemispheres of the droplet. Figure 3 shows for the same delay times a sequence of photographs for an incident irradiance of 6 GW/cm$^2$. At this irradiance, the interaction off the illuminated hemisphere relative to the shadow hemisphere is much smaller. Even at 100 ns, little material is ejected from the illuminated surface. As the irradiance is further increased to 18 GW/cm$^2$, the image shown in Fig. 4 at 0 ns shows no evidence of illuminated surface interaction. However, the interaction on the shadow surface is stronger than for lower laser irradiance. Only at later times is there any evidence of material leaving the illuminated hemisphere. Figure 5 shows the droplet images obtained under high irradiance (230 GW/cm$^2$). In this example, the nonlinear behavior is quite different. The material is ejected in a more symmetric manner than in previous cases and appears to form thin filaments of material at 0 ns delay time.

The behavior of the droplets shown in Figs. 2-5 can be compared to the square root of the internal and near-surface electric field distributions calculated using plane wave Lorenz-Mie theory which are shown in Fig. 6. The square root of the electric field is plotted in efforts to emphasize smaller electric field values (denoted by dark shades at the top of Fig. 6). From this figure, there appears to be four critical regions in which localized maxima appear. The absolute maximum of the electric field values occurs external to the shadow surface of the droplet and has the magnitude $|E/E_0| = 50$ where $|E_0|$ denotes the magnitude of the incident electric field. The high value results

of the focusing effect of the large droplet relative to the incident wavelength. Internal to the droplet surface but still within the shadow hemisphere is three localized peaks each of magnitude $|E/E_0| = 22$. Near the illuminated surface of the droplet lies the third critical region in which the magnitude is approximately $|E/E_0| = 16$. External to the illuminated hemisphere is also a smaller localized peak of magnitude $|E/E_0| = 8$. The local maxima inside the droplet result from constructive interference of laser light reflected from the inner droplet surface and the propagation of surface waves near the air/droplet interface. These four regions of high electric field values are characteristic of transparent droplets and have been discussed previously.[13] We would expect that these four regions would identify the likely locations of initial laser breakdown. Comparing the calculations in Fig. 6 to the images shown in Fig. 2 we can see similarities in the sense that Fig. 6 shows a nearly equal (slightly higher within the shadow hemisphere) maximum electric field strength within the two hemispheres of the droplet. This would suggest that one would observe material interaction from both hemispheres of the droplet with the stronger interaction occurring from the shadow hemisphere of the droplet. The results in Fig. 2 confirm this prediction. In contrast however, the images in Fig. 3 show significantly less material leaving the illuminated surface of the particle. The dynamics of the breakup can be explained in a qualitative manner if we assume the breakdown intensity for the droplet is $I_b$ (see Fig. 7) and that the initial breakdown occurs at the location of the maximum internal electric field, which is near the shadow surface of the droplet. If it is further assumed that the breakdown of the droplet will cause the once transparent region near the shadow surface to become an absorbing plasma, the initial breakdown region in the shadow hemisphere will act to shield the incident laser light from reflecting (or propagating around the sphere in the case of surface waves) to the illuminated hemisphere. Shown in Fig. 7 are $P_h$ and $P_l$ which represent the intensity profiles of a high energy and low energy pulse, respectively. If the droplet breakdown occurs at an intensity $I_b$, only the energy associated with the cross-hatched areas will be unaffected by the plasma. Thus a larger amount of energy can be redirected toward the front hemisphere for a low energy incident pulse. As the irradiance is increased we would expect proportionately less available energy for interaction within and near the illuminated hemisphere. This agrees with the observations in Figs. 2-4. For 230 GW/cm$^2$ interactions shown in Fig. 5, the 17 ns imaging pulse is not short enough to clearly resolve the early stages of the interaction process and future picosecond or femtosecond imaging work will be required to resolve the early stages of the interaction.

The imaging system can also be used to obtain approximate average velocity measurements for the material ejected at various stages during the laser/aerosol interaction. In order to evaluate the velocity of the ejected material it was necessary to make an assumption regarding the time at which material starts leaving the droplet surface ($\Delta t = 0$). As stated earlier in this paper and illustrated in the images, material ejection starts before what is considered 0 ns delay. For the results presented here, a time of 10 ns before the end of the imaging pulse was chosen as the time material begins leaving the droplet surface. Therefore, in calculating average velocities at 0 ns delay a $\Delta t = 10$ ns was used, at 20 ns delay a $\Delta t = 30$ ns was used, etc. Although this delay value will vary depending on the incident irradiance, we have used a constant value for all irradiances

since detailed resolution of these time are not presently possible in our laboratory. The average material velocity as a function of time and incident irradiance is shown in Fig. 8. The values range from approximately 1000 at 3 $GW/cm^2$ to 6000 m/s at 230 $GW/cm^2$ with an uncertainty of approximately $\pm20$ percent which is predominantly due to the difficulty in properly identifying the material boundary. Only limited data was available at high irradiances since the material quickly propagates out of the field of view of the imaging system.

## IV. Plans for Future Work

Experimental work on the scattering of radiation in the retroreflective direction will be attempted and results compared with forward scattered radiation published in Ref. 2. Plans are to also study the $\lambda = 248$ nm interaction with nonspherical water droplets. Initial work in the area indicates aspect ratios of approximately 1.2 are required before significant effects can be observed. In order to resolve nonlinear effects at high irradiance values, we have initiated work in picosecond imaging. A femtosecond laser has been purchased and this system will be used for ultra fast diagnostics. Experimental and theoretical work will be performed on all of the above areas. Work on optical temperature measurements in aerosols continues to be pursued. Thin metal wires have to demonstrate that material is not spalled of the shadow surface of small solid aerosols. Additional theoretical modeling of $\lambda = 248$ nm interaction with solid matter will be undertaken.

## V. Acknowledgments

## IV. References

1. R.K. Chang, J.H. Eickmans, W.-F. Hsieh, C.F. Wood, J.- Z. Zhang, and J.-b. Zheng, "Laser-induced breakdown in large transparent water droplets," Appl. Opt., **27** (12), 2377 (1988).

2. D.R. Alexander, S.A. Schaub, J. Zhang, D.E. Poulain, and J.P. Barton, "Scattering of incident KrF laser radiation resulting from the laser-induced breakdown of $H_2O$ droplets," Opt. Lett., **14** (11), 548 (1989).

3. A. Biswas, H. Latifi, L.J. Radziemski, and R.L. Armstrong, "Irradiance and laser wavelength dependence of plasma spectra from single levitated aerosol droplets," Appl. Opt., **27** (12), 2386 (1988).

4. W.-F. Hsieh, J.H. Eickmans, and R.K. Chang, "Internal and external laser-induced avalanche breakdown of single droplets in an argon atmosphere," J. Opt. Soc. Am. B, **4** (11), 1816 (1987).

5. A. Biswas, H. Latifi, P. Shah, L. J. Radziemski, and R.L. Armstrong, "Time-resolved spectroscopy of plasmas initiated on single, levitated aerosol droplets," Opt. Lett., **12** (5), 313 (1987).

6. P. Kafalas and J. Herrmann, "Dynamics and energetics of the explosive vaporization of fog droplets by a 10.6 $\mu$m laser pulse," Appl. Opt., **12** (4), 772 (1973).

7. J.-Z. Zhang and R.K. Chang, "Shape distortion of a single water droplet by laser-induced electrostriction," Opt. Lett., **13** (10), 916 (1988).

8. J.C. Carls and J.R. Brock, "Explosive vaporization of single droplets be lasers: comparison of models with experiments," Opt. Lett., **13** (10), 919 (1988).

9. S.M. Chitanvis, "Explosive vaporization of small droplets by a high-energy laser beam," J. Appl. Phys., **62** (11), 4387 (1987).

10. B. Maheu, G. Gousbet, G. Grehan, "A concise presentation of the generalized Lorenz-Mie theory for arbitrary location of the scatterer in an arbitrary incident profile," J. Optics (Paris), **19** (2), 59 (1988).

11. J.P. Barton, D.R. Alexander, and S.A. Schaub, "Internal and near-surface electromagnetic fields for a spherical particle irradiated by a focused laser beam," J. Appl. Phys., **64** (4), 1632 (1988).

12. K.D. Ahlers and D.R. Alexander, "Microcomputer based digital image processing system developed to count and size laser-generated small particle images," Opt. Eng., **24** (6), 1060 (1985).

13. W.-F. Hsieh, J.-B. Zheng, C.F. Wood, B.T. Chu, and R.K. Chang, "Propagation velocity of laser-induced plasma inside and outside a transparent droplet," Opt. Lett., **12** (8), 576 (1987).

Fig. 1. Schematic of experimental setup.

0 ns

20 ns

40 ns
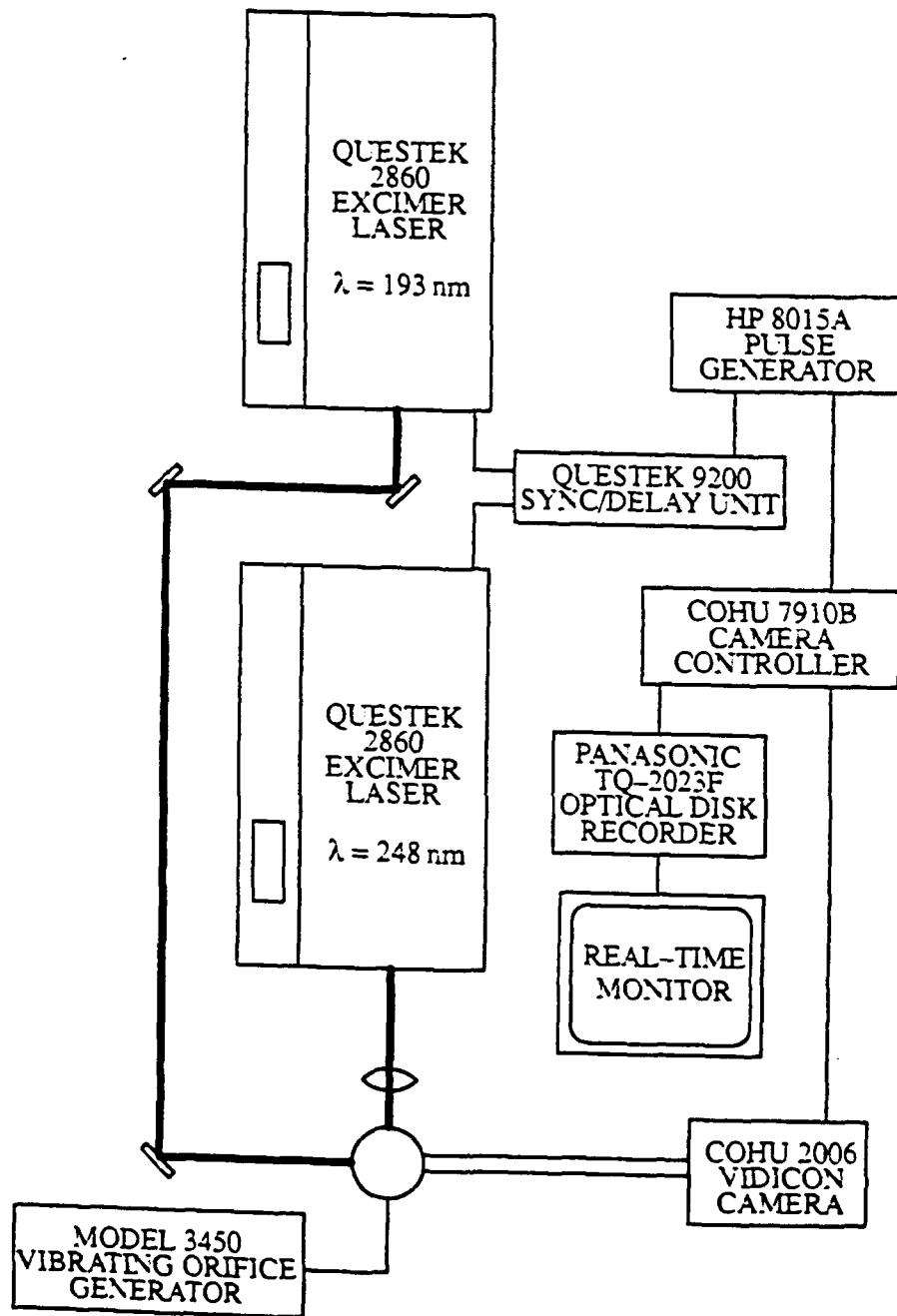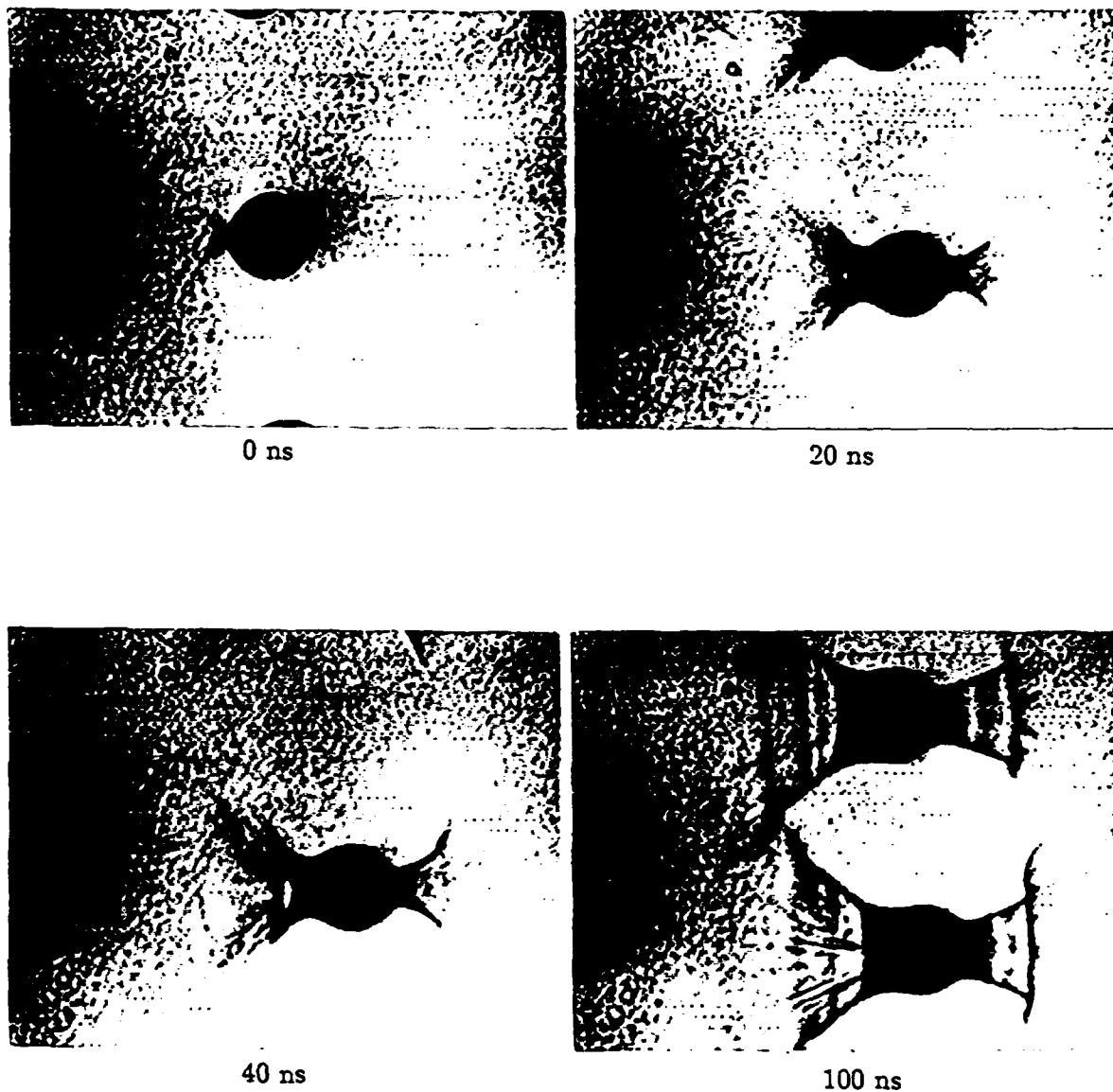
100 ns

Fig. 2. Interaction of a 3 GW/cm$^2$ KrF ($\lambda = 248$ nm) laser pulse with 60 $\mu$m water droplets seen 0, 20, 40, and 100 ns after arrival of the high energy pulse. The laser is propagating from right to left.
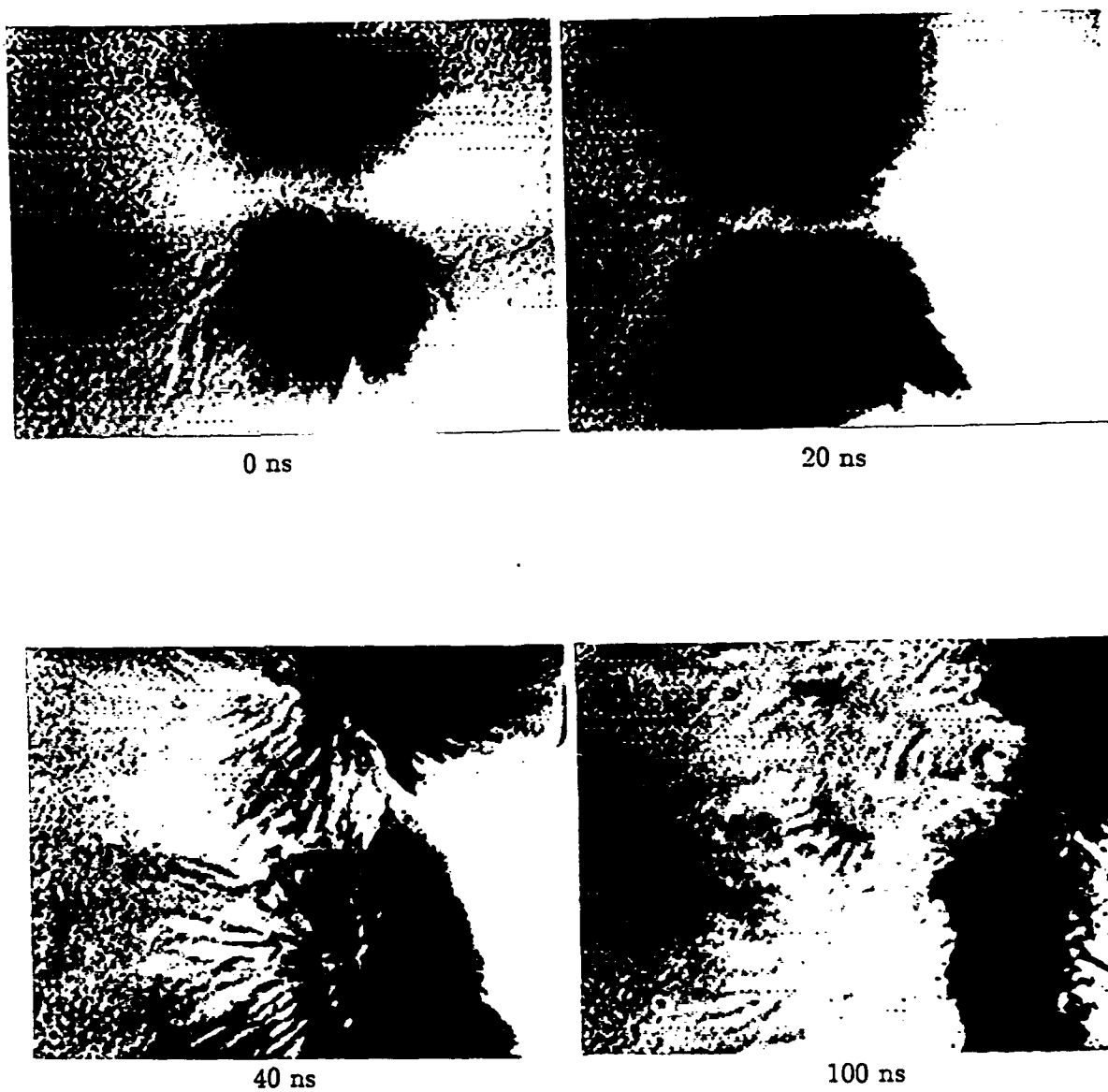
0 ns                    20 ns

40 ns                   100 ns
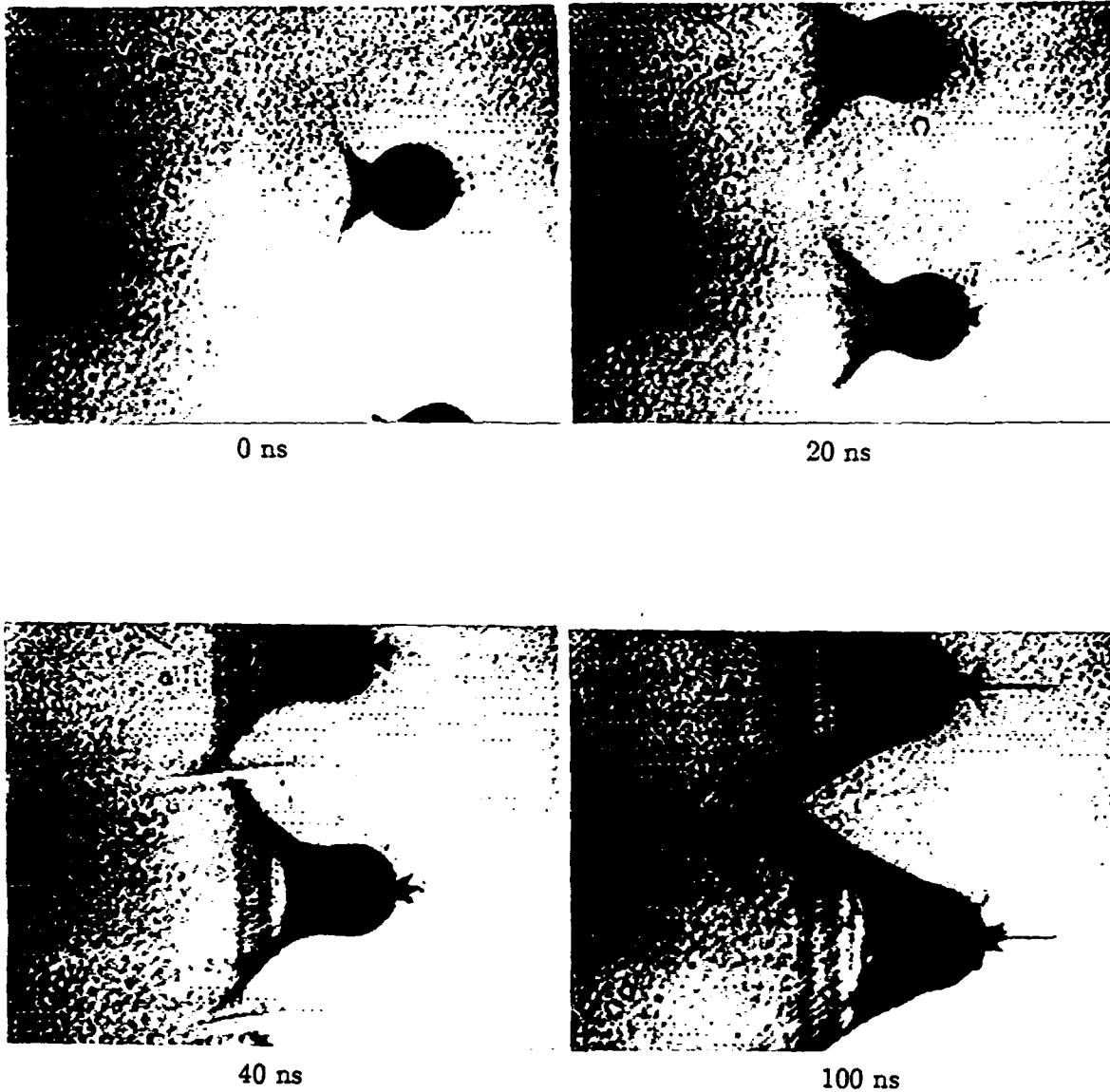
Fig. 3. Interaction of a 6 GW/cm$^2$ KrF ($\lambda = 248$ nm) laser pulse with 60 $\mu$m water droplets seen 0, 20, 40, and 100 ns after arrival of the high energy pulse. The laser is propagating from right to left.
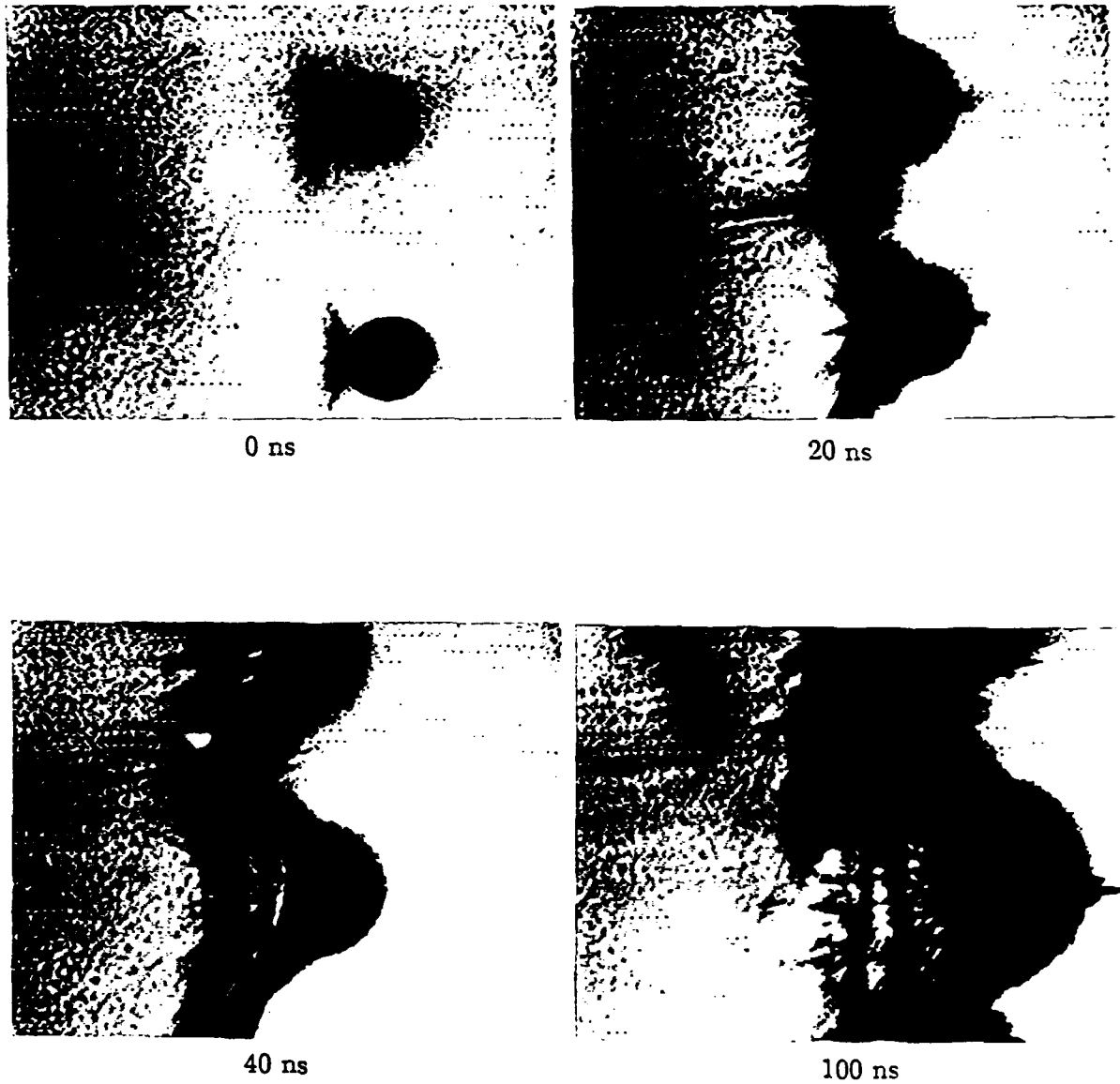
Fig. 4. Interaction of a 18 GW/cm$^2$ KrF ($\lambda = 248$ nm) laser pulse with 60 $\mu$m water droplets seen 0, 20, 40, and 100 ns after arrival of the high energy pulse. The laser is propagating from right to left.

Fig. 5. Interaction of a 230 GW/cm$^2$ KrF ($\lambda = 248$ nm) laser pulse with 60 $\mu$m water droplets seen 0, 20, 40, and 100 ns after arrival of the high energy pulse. The laser is propagating from right to left.
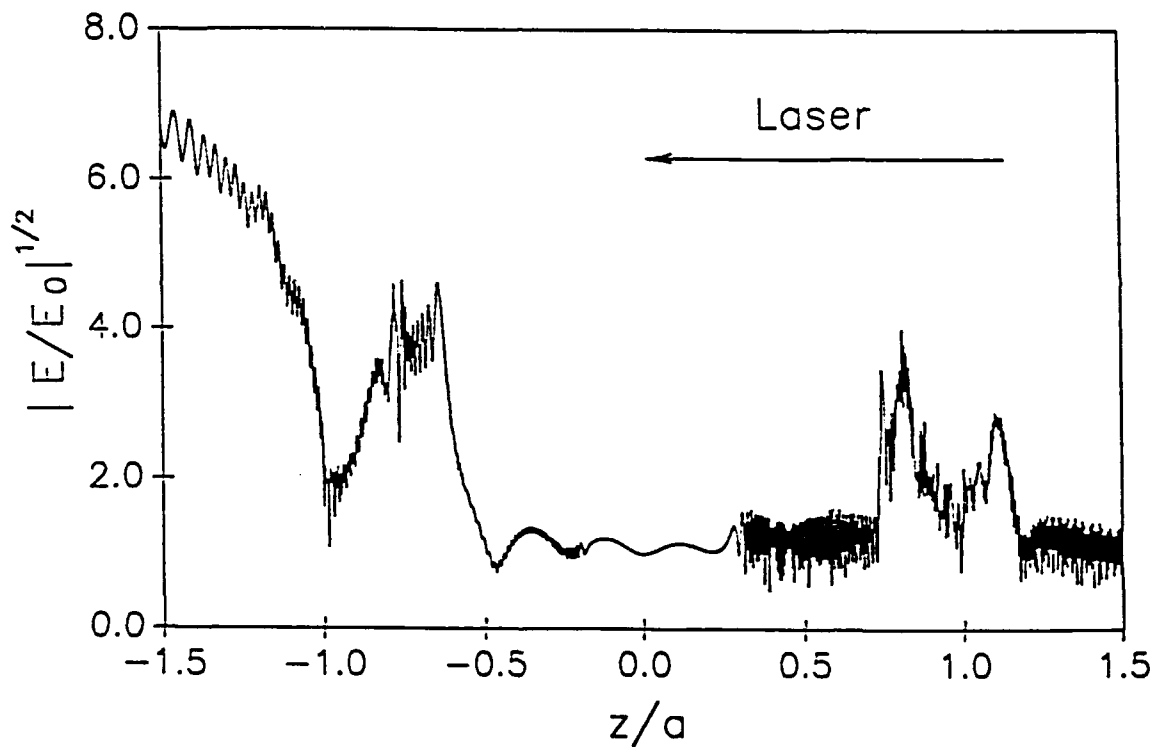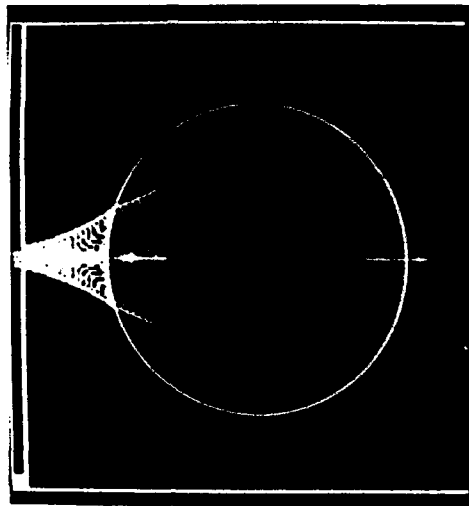
Fig. 6. Plane wave Lorenz-Mie theory calculations showing the square root of the internal and near-surface electric field distribution for a 60 $\mu$m diameter water droplet ($\bar{n} = 1.36 + 3.5 \times 10^{-8}i$) irradiated by a KrF laser pulse ($\lambda = 248$ nm). Laser is propagating from right to left. Top: Intensity (black = 0, white $\approx$ 7) plot for $-1.5 < y/a < 1.5$, $-1.5 < z/a < 1.5$ where a is the droplet radius (note the laser is propagating in the $+z$ direction with polarization in the x direction). Bottom: Centerline plot for the same parameters as given above.
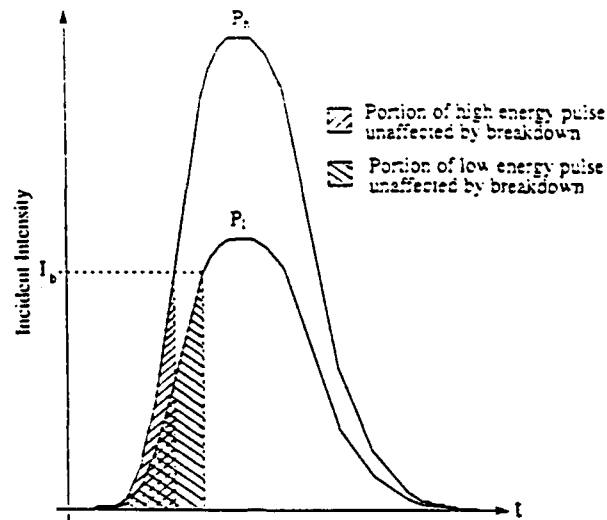
Fig. 7. Graphical representation of the relationship between the incident pulse energy and the portion unaffected by the laser-induced breakdown in the shadow hemisphere.



Fig. 8. Average material velocity as a function of image delay time for the interaction of KrF laser pulses ($\lambda = 248$ nm) with 60 $\mu$m diameter water droplets for laser irradiance varying from 3 to 230 GW/cm².

# LASER INTERACTION WITH A METALLIC FILAMENT: ABLATION DYNAMICS AND PLASMA FORMATION

D.R. Alexander, G. M. Holtmeier, Kyo-Dong Song, and J. P. Barton
Center for Electro-Optics
College of Engineering
University of Nebraska
Lincoln, NE 68588-0656

## RECENT PUBLICATIONS, SUBMITTALS FOR PUBLICATION, AND PRESENTATIONS:

A.) J.P. Barton, D.R. Alexander, and S.A. Schaub, "Electromagnetic field calculations for a tightly-focused laser beam incident upon a spherical particle." Proceedings of the 1989 U.S. Army CRDEC Scientific Conference on Obscuration and Aerosol Research, Aberdeen, Maryland, 1989.

B.) D.R. Alexander, J.P. Barton, and S.A. Schaub, "Laser induced breakdown of $H_2O$ droplets and solid wires at 0.248 $\mu$m," Proceedings of the 1989 U.S. Army CRDEC Scientific Conference on Obscuration and Aerosol Research, Aberdeen, Maryland, 1989.

C.) J.P. Barton, D.R. Alexander, and S.A. Schaub, "Theoretical determination of net radiation force and torque for a spherical particle illuminated by a focused laser beam," Journal of Applied Physics. Vol. 66, pp. 4594-4602, 1989.

D.) J.P. Barton and D.R. Alexander, "Fifth-order corrected electromagnetic field components for a fundamental Gaussian beam," Journal of Applied Physics, Vol. 66, pp. 2800-2802, 1989.

E.) J.P. Barton, D.R. Alexander, and S.A. Schaub, "Internal fields of a spherical particle illuminated by a tightly-focused laser beam: focal point positioning effects at resonance," Journal of Applied Physics, Vol. 65. pp. 2900-2906, 1989.

F.) J.P. Barton, W. Ma, S.A. Schaub, and D.R. Alexander, "Theoretical determination of the electromagnetic fields for a laser beam incident upon two adjacent spherical particles of arbitrary arrangement," Proceedings of the 2nd International Congress on Optical Particle Sizing, Tempe. Arizona, 1990.

G.) J.P. Barton, W. Ma, S.A. Schaub, and D.R. Alexander, "Electromagnetic fields for a beam incident upon two adjacent spherical particles," submitted to Applied Optics. May, 1990.

H.) J.P. Barton and D.R. Alexander, "Electromagnetic fields for an irregularly-shaped. near-spherical particle illuminated by a focused laser beam," submitted to the Journal of Applied Physics, August, 1990.

I.) D.R. Alexander, S.A. Schaub. J. Zhang, D.E. Poulain, and J.P. Barton, "Scattering of incident KrF laser radiation resulting from the laser induced breakdown of $H_2O$ droplets," Optics Letters, Vol. 14, pp. 548-550, 1989.

J.) D.R. Alexander, J.P. Barton, S.A. Schaub, and G.M. Holtmeier, "Nonlinear interactions of KrF laser radiation with small water droplets," submitted to Applied Optics, October, 1989.

K.) S.A. Schaub, D.R. Alexander, D.E. Poulain, and J.P. Barton, "Measurement of hypersonic velocities resulting from the laser induced breakdown of aerosols using an excimer laser imaging system," Review of Scientific Instruments, Vol. 60, pp. 3688-3691, 1989.

L.) S.A. Schaub, J.P. Barton, and D.R. Alexander, "Simplified scattering coefficient expressions for a spherical particle located on the propagation axis of a fifth-order Gaussian beam," Applied Physics Letters, Vol. 55, pp. 2709-2711, 1989.

M.) D.E. Poulain, D.R. Alexander, J.P. Barton, S.A. Schaub, and J. Zhang, "Interactions of intense ultraviolet laser radiation with solid aerosols," Journal of Applied Physics, Vol. 67, 1990.

N.) S.A. Schaub, D.R. Alexander, and J.P. Barton, "Theoretical model for the image formed by a spherical particle in a coherent imaging system: comparison to experiment," Optical Engineering, Vol. 28, pp. 565-571, 1989.

O.) S.A. Schaub, D.R. Alexander, J.P. Barton, and M.A. Emanuel, "Focused laser beam interactions with methanol droplets: effects of relative beam diameter," Applied Optics, Vol. 28, pp. 1666-1669, 1989.

P.) G.M. Holtmeier, D.R. Alexander, and J.P. Barton, "High intensity ultraviolet laser interaction with a metallic filament," submitted to the Journal of Applied Physics, August, 1990.

Q.) S.A. Schaub, D.R. Alexander, and J.P. Barton, "Theoretical model of the laser imaging of small aerosols: applications to aerosol sizing," submitted to Applied Optics, May, 1990.

R.) S.A. Schaub, D.R. Alexander, and J.P. Barton, "Modeling of a coherent imaging system," Proceedings of the 2nd International Congress on Optical Particle Sizing, Tempe, Arizona, 1990.

S.) J.P. Barton, D.R. Alexander, and S.A. Schaub, "Electromagnetic field calculations for a tightly-focused laser beam incident upon a spherical particle," presentation at the 1989 U.S. Army CRDEC Scientific Conference on Obscuration and Aerosol Research, Aberdeen, Maryland, June 27-30, 1989.

T.) D.R. Alexander, J.P. Barton, and S.A. Schaub, "Laser induced breakdown of $H_2O$ droplets and solid wires," presentation at the 1989 U.S. Army CRDEC Scientific Conference on Obscuration and Aerosol Research, Aberdeen, Maryland, June 27-30, 1989.

U.) J.P. Barton, W. Ma, S.A. Schaub, and D.R. Alexander, "Theoretical determination of the electromagnetic fields for a laser beam incident upon two adjacent spherical particles of arbitrary arrangement," presentation at the 2nd International Congress on Optical Particle Sizing, Tempe, Arizona, March 5-8, 1990.

V.) D.R. Alexander, S.A. Schaub, and J.P. Barton, "Modeling of a coherent imaging system: Application to focus determination in aerosol sizing," presentation at the 2nd International Congress on Optical Particle Sizing, Tempe, Arizona, March 5-8, 1990.

## ABSTRACT

Experimental results are presented on the time dependent material ejection dynamics associated with focused excimer laser beams interacting with a small diameter wire. Copper wire 75 $\mu$m in diameter was illuminated with a KrF excimer laser at an irradiance of 80 GW/cm$^2$. Interaction dynamics were recorded using both real time and double strobed ultraviolet laser imaging techniques. Temporal evolutions of both vaporous and molten material are reported for the laser beam/wire interactions. Material observed during 2-D shadow imaging on the shadow side of the wire was shown to originate from the illuminated surface without spallation of material on the shadow surface. Material emission velocities are reported utilizing two different imaging techniques. A maximum velocity of 1500 m/s was obtained for material ejected in a direction toward the illuminating laser. The elastically scattered incident radiation (ESIR) for both solid copper wires and $H_2O$ drops show a distinct two-peak structure which is dependent on the incident energy. Broad band plasma emission for copper starts at 6.5 $\pm$ 1.4 ns after the pulse arrival as compared to 11 $\pm$ 0.36 ns for water drops. Future work will include the use of a femtosecond laser to investigate laser interactions at higher irradiances (200 GW/cm$^2$) and associated nonlinear behavior.

# I. INTRODUCTION

Excimer laser interaction with metals has been widely investigated utilizing generally flat targets with beam intensities near the optical breakdown thresholds[1-4] and at intensities above the breakdown thresholds.[5,6] Limited work appears in the literature on the interaction of a high intensity laser beam with metallic aerosols or small filaments. Armstrong et al.[7] performed a theoretical investigation of the propagation of a high-energy laser beam through metallic aerosols. Poulain et al.[8] performed experimental work on high intensity KrF excimer laser interaction with solid aerosols and reported interesting interaction dynamics and material breakdown thresholds for several types of solid aerosol particles. In order to overcome some of the experimental difficulties reported by Poulain et al.[8] and to better understand interaction dynamics phenomena associated with a high-energy laser beam interacting with solid aerosols, the present investigation utilized a thin metallic wire instead of solid aerosol particles in the laser beam probe volume. Thus, in this investigation, interaction dynamics of a high intensity (80 GW/cm$^2$) KrF excimer laser beam with a 75 $\mu$m diameter copper wire were studied under atmospheric illumination conditions.

Alexander et al.[9] has previously studied the time history of ESIR and broadband emission for a water droplet illuminated by KrF laser pulse. The present work reports differences in plasma formation from copper wire targets and water droplets, i.e. time dependent plasma formations and ESIR. In this paper we present comparative data from the two distinct types of plasmas for incident laser beam irradiance ranging from 1-100 GW/cm$^2$.

# II. EXPERIMENTAL SETUP

A schematic of the experimental setup is shown in Figure 1. A high-energy beam was produced by a KrF excimer laser (Questek model 2860, $\lambda$ = 248 nm, pulse duration = 17 ns FWHM) using unstable optics and was focused by a plano-convex lens (d = 50 mm, f = 250 mm). The cross sectional dimensions of the high-energy beam were determined experimentally by translating a knife-edge through the focused beam.[8] A second method verified the cross sectional dimensions by measuring the illuminated damage area of a polished nickel plate placed in the focused probe volume. Dimensions of the focused high-energy beam were approximately 110 × 135 $\mu$m for this investigation. A second excimer laser, identical to the first with the exception of using stable resonator optics, was used to produce an imaging beam incident in a direction orthogonal to both the high-energy pulse and the copper wire. Laser pulses used for imaging were synchronized with the high-energy pulses illuminating the targets using an analog/digital delay unit, Questek model 9200 Laser Sync Unit (LSU). Sync signals from the camera control unit (Cohu model 8000) were sent to a pulse generator (HP model 8015A) which subsequently provided the trigger pulse for the LSU. Pulses from both lasers were simultaneously monitored using a fast photodiode (Hamamatsu model C1083) and digitizing oscilloscope (Hewlett Packard model 54200A). Analog delay controls on the LSU were used to calibrate arrival of the imaging pulse to be coincident with the high-energy pulse (defined as 0 ns image delay in this investigation). Jitter for the system was approximately ±7 ns. The digital delay on the LSU made it possible to delay the image pulse arrival with respect to the high-energy pulse from 0–100 $\mu$s in increments of 10 ns.

Real time images of the laser beam interacting with the wire were obtained with a UV sensitive vidicon camera. Thus, the image is integrated over the laser pulse duration of 17 ns FWHM. Images were stored on an optical disk recorder (Panasonic model TQ-2023F) and processed with a digital image processing system[10] for subsequent analysis. The probe volume of the high-energy illuminating pulse was positioned in the image plane by observing the plasma formed during air

breakdown with the vidicon camera. Wire targets were positioned in the same imaging probe volume and centered by observing the maximum visible emission from the illuminated wire. Location of the 75 $\mu$m diameter copper wire within the same probe volume was maintained by feeding the wire from a spool through two glass micro-capillaries with an inside diameter of 127 $\mu$m. A mass equal to 17.5 g was connected to the bottom of the wire to keep the wire taut. A stepping motor was used to rotate the spool to feed new wire into the probe volume for each laser pulse/wire interaction. The experimental setup used in the current work for interacting $H_2O$ droplets with the excimer laser beam and detecting the plasma emission is described in Reference 9.

## III. INTERACTION DYNAMICS

Experimental work to visualize the interaction dynamics was performed using a pulsed real time video imaging system to record the dynamics associated with the high-energy laser interaction with a small diameter wire. An ArF excimer laser imaging system was operated at $\lambda$=193 nm to provide high resolution images as well as to eliminate scattered 248 nm emission from the high-energy pulse by using a 193 nm bandpass filter in line with the imaging optics. Dynamic interactions were observed for a single 80 GW/cm$^2$ pulse ($\lambda = 248$ nm, pulse duration $= 17$ ns) incident on a 75 $\mu$m diameter copper wire. For comparative purposes, images of the wire were recorded before the high-energy pulse interaction and after the high-energy pulse interaction as shown in Figure 2. The illuminating pulse was incident from right to left in Figure 2 and produced a crater-shaped region at the illuminated surface as a result of material removal. The term crater in this work refers to the volumetric region at the illuminated surface of the wire where material has been removed as a result of the interaction. Images recorded at various time delays during the laser beam/wire interaction process are shown in Figures 3–5. Delay time given under each photograph is the delay of the image beam ($\pm$7 ns) with respect to the arrival of the high-energy pulse. Dark regions on the left of the images were characteristic of the imaging system used and were primarily due to the optical effects associated with the bandpass filter.

The first noticeable evidence of any laser beam/wire interaction dynamics was at 10 ns image delay as shown in Figure 3. A cloud of material is visible at the illuminated (front) surface of the wire but not at the shadow (rear) surface. At 40 ns image delay, material emission is evident at the shadow surface of the wire and a crater like depression is clearly forming at the illuminated surface of the wire as a result of the material removal at approximately the location of the probe volume. Scanning electron microscope (SEM) images of the samples showed no physical material removal from the shadow surface of the wire. Thus, ejected material appearing at the shadow surface of the wire was removed from the illuminated surface of the wire and propagated around the sides of the wire. At 60 ns delay, a crater on the illuminated surface of the wire is clearly defined with an opaque lip forming at the edge of the probe volume region. In addition, no cloud of material is apparent above and below the probe volume region as shown at 40 ns image delay. Lifetime of the visible plasma emission from the laser beam/wire interaction was determined to have an average value of 62 ns (FWHM). The cloud of material appearing at the illuminated surface of the wire prior to 60 ns image delay is thought to be a dense plasma. At 100 ns delay, a dark region appears directly in front of the probe volume on the illuminated side. The material is thought to be plasma or vapor and is evident from 80–120 ns. This material in front of the probe volume was not evident in the images prior to 80 ns image delay since sufficient quantities do not exist to be detected by the imaging system. After 120 ns delay, this material moves out of the field of view of the imaging system.

Images at longer time delays ranging from 170 ns to 600 ns are shown in Figure 4. From these images, it is evident that material has traveled from the illuminated front wire surface to form diffuse fans behind the shadow surface of the wire. These series of photographs show material moving along the illuminated surface away from the crater region in a lateral direction parallel to the wire surface. This lateral moving material has moved out of the field of view of the imaging system after 800 ns delay as shown in Figure 5. Material having individual particle characteristics is evident behind the shadow surface of the wire for time delays of 800 ns and longer. Particles could be observed in the photographs for time delays up to 4.5 $\mu$s and were shown to be in a molten state by collecting them onto polished nickel plates.

SEM images are shown in Figure 6 revealing a side view (top) and a shadow surface view (bottom) of copper wire samples after illumination by a KrF laser pulse ($\lambda = 248$ nm) at 80 GW/cm$^2$. The side view clearly shows where material removal occurred and the crater formed. In addition, molten material flow has occurred as demonstrated by the relatively smooth surface above and below the crater followed by a rough surface region where solidification of the material occurred. The top photograph in Figure 6 further shows material flowed in all directions from the crater region. The bottom photograph in Figure 6 provides evidence that no material was removed from the shadow surface. Further examination of the photograph shows that a lip has formed on the side of the wire from molten material exploding away from the illuminated surface as a result of high pressures.

High magnification SEM images taken of solidified material located in the rough surface region on the front of the wire are shown in Figure 7. Particles that solidified before "pinching off" a wave surface can be identified in the top photograph. Solidification waves traveling from the front surface of the wire to the sides are evident in the bottom photograph of Figure 7. Particles ejected at the sides of the wire are smaller than particles forming from the surface waves formed near the front surface of the wire. Surface tension and the height of the surface waves are important parameters in determining the size of particles formed.

## IV. VELOCITY MEASUREMENTS

Velocity measurements of emitted materials from the laser beam/wire interactions were performed using single pulse ($\lambda = 193$ nm) images similar to those shown in Figures 3–5 and also by a dual pulse imaging method described in previous work by Schaub et al.[11] Dual pulse imaging is performed by splitting the laser pulse used for imaging into two separate pulses as shown in Figure 1. One part of the imaging pulse travels directly to the imaging system while the second part travels over an additional 17.1 m (56 ft) of optical path length. Thus, two 17 ns pulses ($\lambda = 248$ nm) optically delayed by 56 ns enter the imaging system providing a double exposure image on the vidicon camera of the emitted material produced from the laser beam/wire interaction. Velocity of the emitted material was determined by measuring the distance the molten material moved during the 56 ns time interval. The time interval separating the dual imaging pulses is fixed by the optical path length, however, the time delay of the first imaging pulse with respect to the high-energy pulse can be adjusted with the LSU previously described.

Figure 8 is a typical dual pulse image obtained of emitted material with the first image pulse delayed 500 ns after the arrival of the high-energy pulse (80 GW/cm$^2$) which was incident from right to left. Samples were positioned to appear beyond the right edge of the monitor screen to eliminate scattered 248 nm emission from the laser beam/wire interaction which saturates the vidicon camera. Average velocities of materials emitted in a direction away from the illuminating laser were 570 m/s at 300 ns image delay and 460 m/s at 500 ns delay. Dual pulse images were

not obtained for image delays shorter than 300 ns since the material was not dense enough to be picked up by the imaging system and for image delays longer than 500 ns as a result of material expanding in diffuse fans covering the complete field of view. Figure 9 is a typical dual pulse image obtained at image delays of 1500 ns and longer of individual particles traveling in a direction away from the illuminating laser (right to left). Particles are approximately 10 $\mu$m in diameter and move less than 5 $\mu$m in 56 ns time delay which corresponds to a velocity less than 90 m/s.

The velocity of emitted material was also determined by utilizing a single imaging pulse and measuring the material movement for a known time delay relative to the arrival of the ablation pulse. A similar technique was used by Alexander et al.[12] to determine interaction velocities when an excimer laser beam interacted with a water droplet. For the current work, it is assumed that ejected material originates from the front of the crater region and emission starts at 0 ns image delay. Velocity calculations for ejected materials from the dual and single imaging pulse techniques are presented in Figure 10. Data plotted in the graphs differ only by the scale of the time (horizontal) axis. The top graph has been expanded to emphasize the acceleration and deceleration during the laser pulse. Each data point on the graphs represents the average of approximately five velocity calculations for each time frame. An estimated error associated with the material emission velocity calculations is ±20% and is primarily due to the uncertainties in properly identifying the exact starting and ending of material boundaries.

Material emission velocities in a direction towards the illuminating laser were calculated by measuring the material movement on the illuminated (front) surface of the wire and in a direction perpendicular to the wire. The starting position of the front wire surface was located by comparing wire images before the high- energy pulse illumination with the delayed images during illumination of the samples. Measurements of emitted material movement toward the illuminating laser could not generally be made for time delays longer than 30 ns since material boundaries could not be clearly identified. However, the emission velocity was calculated for material shown in front of the probe volume at 100 ns delay in Figure 3. The average velocity of spatially emitted material toward the laser is shown to increase from 1300 m/s at 10 ns time delay to 1500 m/s at 20 ns. The corresponding acceleration is from the 17 ns (FWHM) high-energy pulse still depositing energy into the interaction region. A subsequent deceleration of material occurs after the end of high-energy laser pulse. Material emission velocities in a direction away from the illuminating laser were calculated by the same procedure used to measure material movement on the illuminated surface of the wire. In order to obtain velocity calculations in a direction away from the illuminating laser, single pulse imaging was used up to 70 ns, i.e., until material boundaries were no longer distinguishable and dual pulse imaging was used from 300–500 ns.

Lateral material emission is defined in this work as emitted material at the illuminated surface of the wire moving out of the crater region in a direction parallel to the wire. Lateral emission velocities were obtained only up to 800 ns image delay since material moves out of the field of view of the imaging system as shown in Figure 4 and 5. As shown in Figure 10, lateral emission velocities remain constant at approximately 800 m/s until 130 ns image delay when deceleration to 270 m/s occurs at 300 ns delay. Deceleration occurs after the emitted material crosses the smooth interaction surface region located above and below the crater and enters the rough surface region shown in Figure 6. Molten material is cooling and solidifying in the rough surface region on the illuminated wire surface causing deceleration. The velocity of the lateral material emission at 300 ns image delay is comparable to the speed of sound at atmospheric conditions.

As shown in Figure 5, emitted particles appear behind the shadow surface of the wire at a time delay of 4.5 $\mu$s. An explanation for particles emitted microseconds after a 17 ns pulse interaction is

provided by examining the thermal diffusion time and the material emission velocities. For metals interacting with an excimer laser pulse, Jervis et al.[13] report that the thermal diffusion length ($\delta$) is given by

$$\delta = 2\sqrt{\chi\tau} \tag{1}$$

where $\chi$ is the thermal diffusivity and $\tau$ is the beam pulse width. For copper and a 17 ns pulse width (FWHM), $\delta = 2.2\ \mu$m. Penetration depth ($d$) of the incident beam ($\lambda = 248$ nm) into copper is calculated to be 11 nm. Since $\delta \gg d$, depth of energy distribution over the 17 ns pulse width is determined by thermal diffusion as opposed to the laser penetration depth. Therefore, thermal diffusion cannot be neglected for this investigation. Particles emitted during long time delays originated from rough surface regions of the wire shown in Figure 7. SEM analysis of cross sections of interacted specimens revealed that the molten material in the rough surface regions can exceed 8 $\mu$m in thickness. By rearranging Eq. (1), a convenient order-of-magnitude estimation for the thermal diffusion time ($t$) through a metal surface is given by Ready[14] as

$$t \approx \frac{D^2}{4\chi} \tag{2}$$

where $D$ is the desired penetration thickness. For $D = 8\mu$m, thermal diffusion time ($t$) would be 200 ns. Single pulse imaging revealed molten material moving over the rough surface region of the wire at approximately 1 $\mu$s image delay. Emitted particles from this zone were previously reported to have velocities less than 90 m/s. Since these particles originate from the front wire surface and are imaged behind the shadow surface, total distance traveled is over 75 $\mu$m (wire diameter) and the corresponding travel time would be over 1.0 $\mu$s for a velocity under 90 m/s. Therefore, thermal diffusion time and material velocities across the wire surface account for microsecond delays of particle emission from the laser beam/wire interaction.

## V. COPPER AND H₂O DROPLET PLASMA EMISSION

For our experiments at $\lambda = 248$ nm, one photon is needed to ionize copper while three are required for water and air. As shown in Figure 11 the onset of ionization and plasma formation for copper starts approximately 4 ns earlier than plasma formation in a water droplet. Several mechanisms contribute to the observed differences. Before ionization occurs in water, the molecules of $H_2O$ will breakup into $H_2$ and O which initially delays the plasma. The ionization potential for $H_2$ and O is three times greater than the ionization potential for copper. After initial electron formation by multiphoton ionization (MPI), cascade breakdown occurs. For cascade ionization to occur, electrons are needed with an energy greater than the material ionization potential. During the cascade ionization (CAI) process, energy losses such as electron diffusion, attachment to oxygen, and excitation all alter the plasma formation processes. In Figure 11, the plasma emission times for both copper and water plasma are shown. The delay in the start of the copper plasma can be explained by the $4s^1$-$3d^{10}$ transition.

The time history of ESIR behavior for copper is similar to the water case as shown in Figure 12. Figure 12 is a plot of the arbitrary intensity of the incident pulse and ESIR as a function of time for 75 $\mu$m diameter copper wire illuminated by a KrF laser pulse at 1-100 GW/cm$^2$. The arrival of the incident pulse is defined as the time when the intensity reaches $1/e^2$ of its maximum value and is used to reference all other delay times. The delay times $P_{t1}$ and $P_{t2}$ are taken from the incident pulse arrival to the first and second peak of ESIR, respectively. $V_t$ is the delay time from the incident pulse arrival to the first minimum of the ESIR. As expected, the first ESIR starts as

the incident pulse arrives. In Figure 12(a), one observes that the first ESIR is rapidly increasing within 6 ns after the incident laser pulse reaches the surface of the copper wire. ESIR peaks and then decreases as a result of the plasma formation on the surface of the material which absorbs the incident pulse energy. As the time is increased, the density of the resulting electrons and ions increase such that a dense plasma reflects the incident pulse until its reaches the peak, $P_{t2}$. At the irradiance of 100 GW/cm$^2$, the intensity of the second ESIR peak is higher than $P_{t1}$. This indicates that the higher input energy results in a higher frequency plasma as well as a more dense plasma. At the input energy of 50 GW/cm$^2$, the first ESIR appears to be dominant. At lower input energies, there is no distinct second ESIR peak which implies only a low density plasma on the surface of the copper wire. Examination of the wire surface using a stereo microscope revealed oxidation and no material removal for the lower input energies.

The delay times, $P_{t1}$, $P_{t2}$ and $V_t$ for the copper and water can be compared and are shown in Figure 13. In Figure 13, subscripts c and w refer to the copper and the water, respectively. As shown in Figure 13, there is a general trend for the delay times of the copper to be higher than for water. However, the standard deviation for the copper wire results is much higher than $P_{t2}$ and $V_t$ due to the plasma instability in time, even though the $P_{t1}$ is quite stable. As the input irradiance is increased, the delay time for plasma formation for both materials remains essentially constant. The spectral distribution of the ESIR and plasma emission in the spectral range of 440-520 nm is shown in Figure 14. The second harmonic of the ESIR is approximately 496 nm and serves as a reference wavelength. At 26 ns after the incident pulse arrival, the ESIR is less than the continuum radiation. The copper line (510.5 nm) and nitrogen (510 nm) line are both very evident in the plasma emission spectrum.

## VI. SUMMARY

High intensity ultraviolet laser interaction with a metallic filament and with $H_2O$ droplets has been investigated. A 2-D shadow imaging system showed both vaporous and molten material emitted from the laser beam/wire interaction. Material was shown to be emitted in every direction from the probe volume as a result of a high pressure region at the surface of the wire. Emitted material imaged at the shadow surface of the wire originated from the illuminated surface and propagated around the sides of the wire. A maximum material velocity of approximately 1500 m/s was calculated for ablated material in a direction back toward the illuminating laser. Emitted particles were evident 4.5 $\mu$s after arrival of the high-energy pulse. It was concluded that this delay was the resultant combination of the thermal diffusion time and material emission velocities. Particles ejected at these later times were shown to have a velocity of under 90 m/s.

The ESIR of copper wire plasma also has a two distinct peak structure which is dependent on the input energy and, except for differences in initiation times, is similar to plasma formation in $H_2O$ droplets. Plasma formation of the copper wire started 4 ns earlier as a result of the dissociation times of $H_2O$. In addition, the ionization potential of copper is around three times smaller than $H_2$ and O. However, the rise time in the copper plasma was not as fast as that observed in plasma emitted from water droplets as a result of interband transition.

## ACKNOWLEDGMENTS

# REFERENCES

1. Viswanathan, R. and Ingo Hussla, "Ablation of Metal Surfaces by Pulsed Ultraviolet Lasers Under Ultrahigh Vacuum," *J. Opt. Soc. Am. B*, Vol. 3, No. 5, p. 796, May 1986.

2. Ursu, I., I.N. Mihailescu, Al. Popa, A.M. Prokhorov, V.P. Ageev, A.A. Gorbunov and V.I. Konov, "Studies of the Change of a Metallic Surface Microrelief as a Result of Multiple-Pulse Action of Powerful UV Laser Pulses," *J. Appl. Phys.*, Vol. 58, No. 10, p. 3909, 15 November 1985.

3. Kelly, Roger and Joshua E. Rothenberg, "Laser Sputtering Part III. The Mechanism of the Sputtering of Metals at Low Energy Densities," *Nuclear Instruments and Methods in Physics Research B*, Vol. 7/8, p. 755, 1985.

4. Rosen, D.I., D.E. Hastings and G.M. Weyl, "Coupling of Pulsed 0.35-$\mu$m Laser Radiation to Titanium Alloys," *J. Appl. Phys.*, Vol. 53, No. 8, p. 5882, August 1982.

5. Offenberger, A.A., R. Fedosejevs, P.D. Gupta, R. Popil and Y.Y. Tsui, "Experimental Results for High Intensity KrF Laser/Plasma Interaction," *Laser and Particle Beams*, Vol. 4, Parts 3 and 4, p. 329, 1986.

6. Panchenko, A.N. and V.F. Tarasenko, "Experiments on Plasma Production and Expansion During UV-Laser Irradiation of Metals," *Sov. J. Plasma Phys.*, Vol. 14, No. 6, p. 450, June 1988.

7. Armstrong, Robert L. and Andrew Zardecki, "Propagation of High Energy Laser Beams through Metallic Aerosols," *Applied Optics*, Vol. 29, No. 12, p. 1786, 20 April 1990.

8. Poulain, D.E., D.R. Alexander, J.P. Barton, S.A. Schaub and J. Zhang, "Interactions of Intense Ultraviolet Laser Radiation with Solid Aerosols," *J. Appl. Phys.*, Vol. 67, No. 5, p. 2283, 1 March 1990.

9. Alexander, D.R., S.A. Schaub, J.Zhang, D.E. Poulain and J.P. Barton, "Scattering of Incident KrF Radiation Resulting From the Laser-Induced Breakdown of $H_2O$ Droplets," *Opt. Lett.*, Vol. 14, p. 548, 1989.

10. Ahlers, K.D. and D.R. Alexander, "Microcomputer Based Digital Image Processing System Developed to Count and Size Laser- Generated Small Particle Images," *Opt. Eng.*, Vol. 24, No. 6, p. 1060, 1985.

11. Schaub, S.A., D.R. Alexander, D.E. Poulain and J.P. Barton, "Measurement of Hypersonic Velocities Resulting from the Laser-Induced Breakdown of Aerosols Using an Excimer Laser Imaging System," *Rev. Sci. Instrum.*, Vol. 60, No. 12, p. 3688, December 1989.

12. Alexander, D.R., J.P. Barton, S.A. Schaub and G.M. Holtmeier, "Nonlinear Interactions of KrF Laser Radiation with Small Water Droplets," *Appl. Optics*, accepted for publication, 5 February 1990.

13. Jervis, T.R., M. Nastasi and T.G. Zocco, "Excimer Laser Mixing of Titanium Layers on AISI 304 Stainless Steel," *Mat. Res. Soc. Symp. Proc.*, Materials Research Society, Vol. 100, p. 621, 1988.

14. Ready, J.F., *Effects of High-Power Laser Radiation*, Academic Press, New York, 1971.

Figure 1. Schematic of the experimental setup.

Figure 2. Images of 75 $\mu$m diameter copper wire before high-energy illumination (top) and after illumination (bottom). Irradiation was 80 GW/cm$^2$ using a KrF pulse ($\lambda$ = 248 nm). Beam propagation was from right to left.
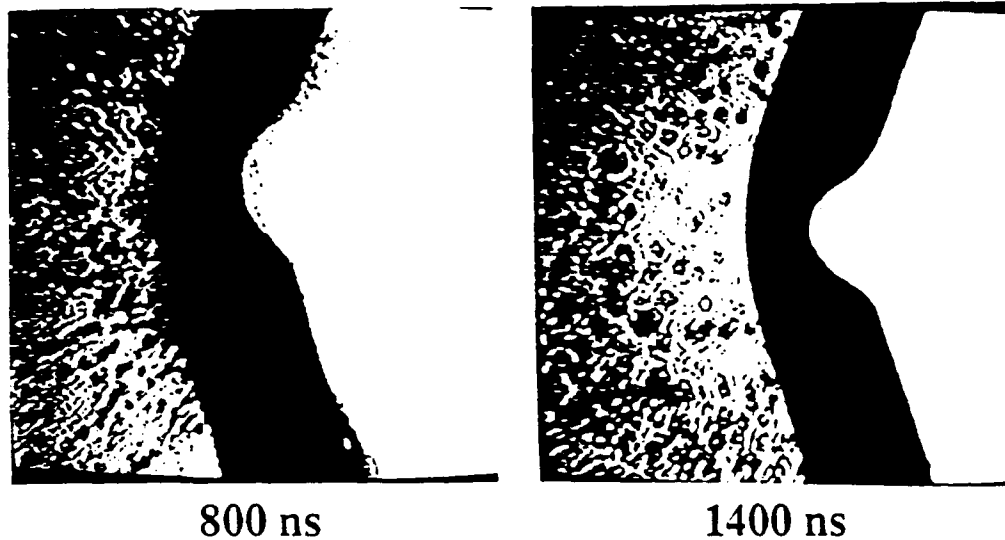
10 ns       40 ns

60 ns       100 ns

Figure 3. Interaction of KrF laser ($\lambda = 248$ nm) with a 75 $\mu$m diameter copper wire at 80 GW/cm$^2$. Time given under each photograph is the delay of the image beam with respect to the arrival of the high-energy laser pulse. Beam propagation is from right to left.

170 ns

300 ns

400 ns

600 ns

Figure 4. Interaction of KrF laser ($\lambda = 248$ nm) with a 75 $\mu$m diameter copper wire at 80 GW/cm$^2$. Time given under each photograph is the delay of the image beam with respect to the arrival of the high-energy laser pulse. Beam propagation is from right to left.

800 ns                    1400 ns

Figure 5. Interaction of KrF laser ($\lambda = 248$ nm) with a 75 $\mu$m diameter copper wire at 80 GW/cm$^2$. Time given under each photograph is the delay of the image beam with respect to the arrival of the high-energy laser pulse. Beam propagation is from right to left.

Figure 6. Photomicrographs of side view (top) and shadow surface (bottom) of an illuminated 75 $\mu$m diameter copper wire. Irradiation was 80 GW/cm$^2$ by a KrF pulse ($\lambda$ = 248 nm).

Figure 7. Photomicrographs of typical waves and particle formations on the front surface of an illuminated 75 $\mu$m diameter copper wire. Irradiation was 80 GW/cm$^2$ by a KrF pulse ($\lambda = 248$ nm).

Figure 8. Typical dual pulse images of emitted material traveling from right to left away from the ablation area. Time delay between each imaging pulse is 56 ns providing a double exposure image. First image pulse delayed 500 ns after arrival of high-energy pulse. Irradiation was 80 GW/cm$^2$ by a KrF pulse ($\lambda$ = 248 nm). Image dimensions are 280 $\mu$m square.

Figure 9. Typical dual pulse images of emitted copper particles traveling from right to left away from the ablation area. Time delay between each imaging pulse is 56 ns providing a double exposure image. First image pulse delayed 1500 ns after arrival of high-energy pulse. Irradiation was 80 GW/cm$^2$ by a KrF pulse ($\lambda$ = 248 nm). Image dimensions are 165 × 230 $\mu$m.

Figure 10. Average velocities of emitted materials from interactions of KrF laser radiation at 80 GW/cm² with 75 μm diameter copper wire as a function of the image time delay. Top graph has been expanded to emphasize the acceleration during the laser pulse and the subsequent deceleration.

Figure 11. Intensities as a function of time for the incident pulse, the broadband emissions of copper wire (75 $\mu$m dia.) and water droplet (75 $\mu$m dia.) illuminated by a 100 GW/cm² KrF laser pulse.
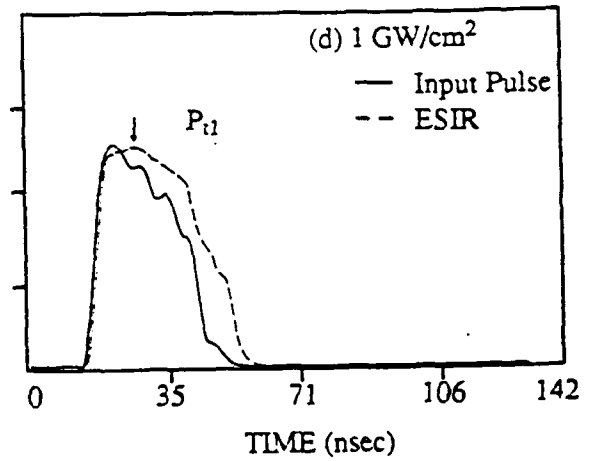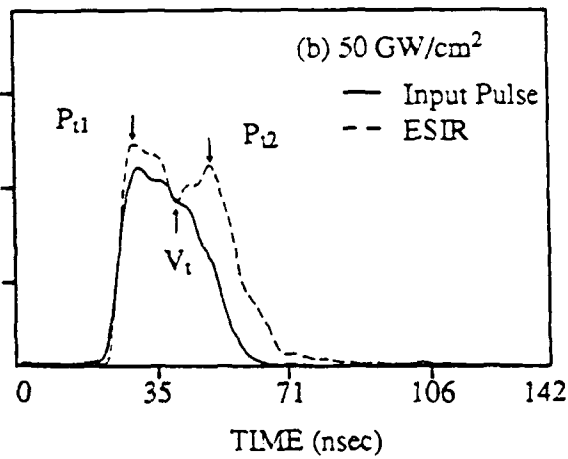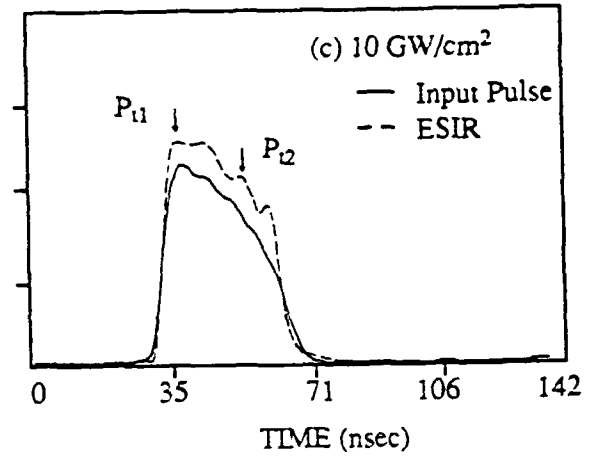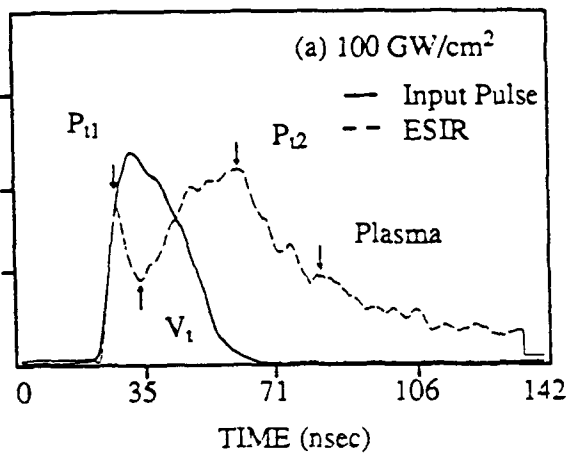
Figure 12. Intensities of the incident pulse (solid curves) and the ESIR (dashed curves) as a function of time for 75 μm diameter copper wire illuminated by a KrF laser pulse of 1-100 GW/cm². The vertical scale is in arbitrary intensity units.
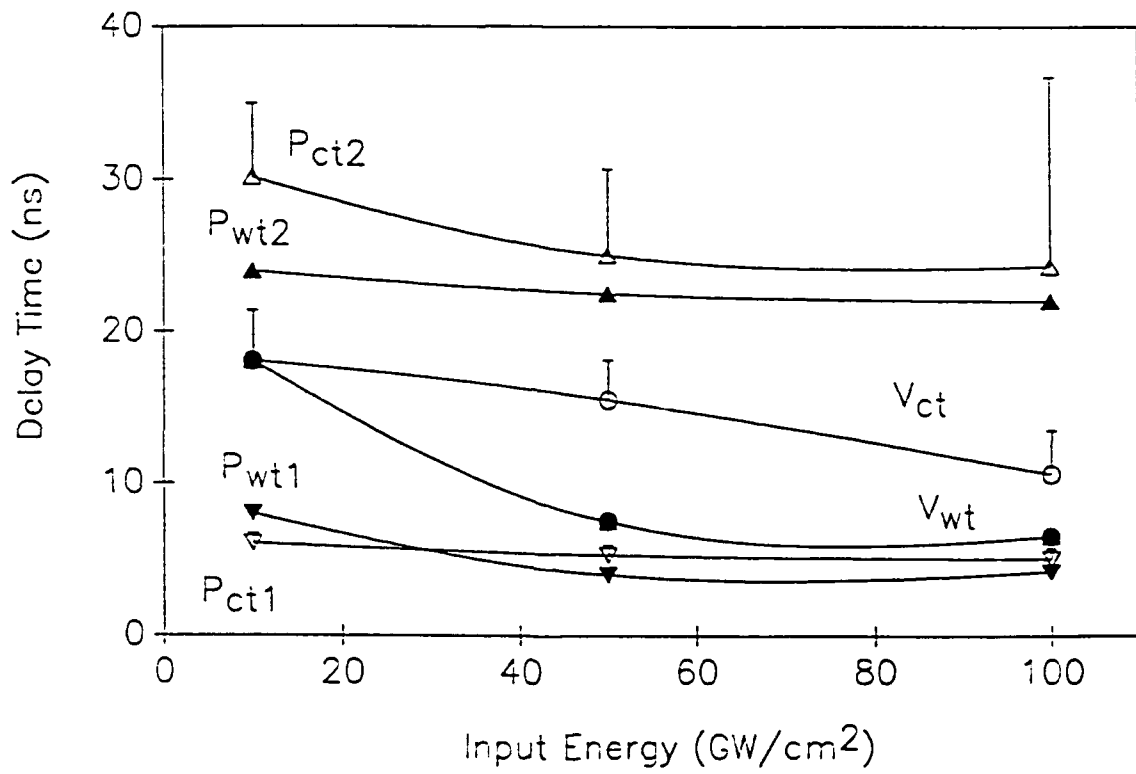
Figure 13. Delay time between the incident pulse and $P_{t1}$, $P_{t2}$ and $V_t$ for 75 $\mu$m dia. water droplet and 75 $\mu$m dia. copper wire.
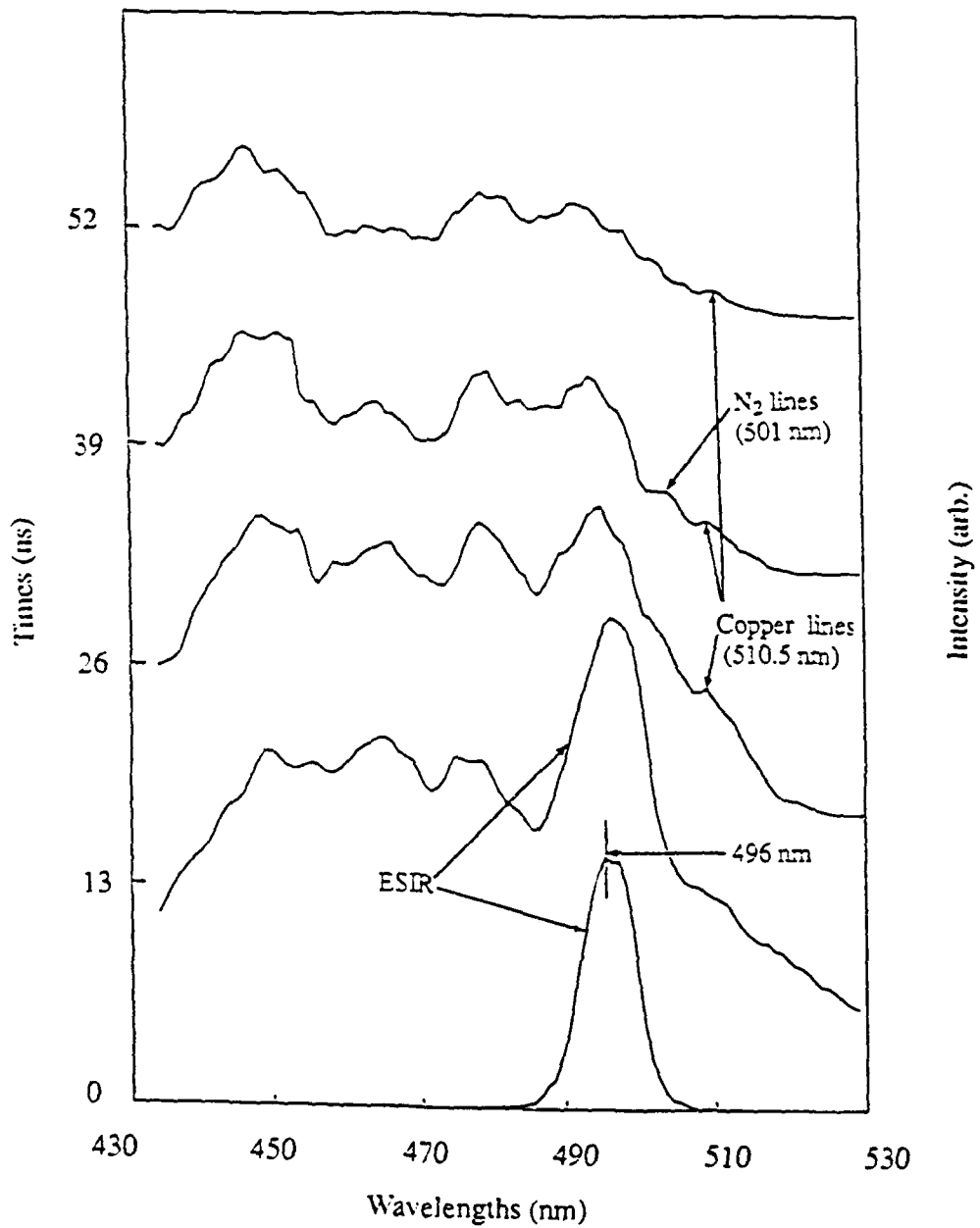
Figure 14. Spectral distributions of ESIR and plasma.

# ELECTROMAGNETIC FIELDS FOR A BEAM INCIDENT
# UPON A NONSPHERICAL PARTICLE

J.P. Barton and D.R. Alexander
Center for Electro-Optics
College of Engineering
University of Nebraska
Lincoln, Nebraska 68588-0656

## RECENT PUBLICATIONS, SUBMITTALS FOR PUBLICATION,
## AND PRESENTATIONS:

A.) J.P. Barton, D.R. Alexander, and S.A. Schaub, "Electromagnetic field calculations for a tightly-focused laser beam incident upon a spherical particle," Proceedings of the 1989 U.S. Army CRDEC Scientific Conference on Obscuration and Aerosol Research, Aberdeen, Maryland, 1989.

B.) D.R. Alexander, J.P. Barton, and S.A. Schaub, "Laser induced breakdown of $H_2O$ droplets and solid wires at 0.248 $\mu$m," Proceedings of the 1989 U.S. Army CRDEC Scientific Conference on Obscuration and Aerosol Research, Aberdeen, Maryland, 1989.

C.) J.P. Barton, D.R. Alexander, and S.A. Schaub, "Theoretical determination of net radiation force and torque for a spherical particle illuminated by a focused laser beam," Journal of Applied Physics, Vol. 66, pp. 4594-4602, 1989.

D.) J.P. Barton and D.R. Alexander, "Fifth-order corrected electromagnetic field components for a fundamental Gaussian beam," Journal of Applied Physics, Vol. 66, pp. 2800-2802, 1989.

E.) J.P. Barton, D.R. Alexander, and S.A. Schaub, "Internal fields of a spherical particle illuminated by a tightly-focused laser beam: focal point positioning effects at resonance," Journal of Applied Physics, Vol. 65, pp. 2900-2906, 1989.

F.) J.P. Barton, W. Ma, S.A. Schaub, and D.R. Alexander, "Theoretical determination of the electromagnetic fields for a laser beam incident upon two adjacent spherical particles of arbitrary arrangement," Proceedings of the 2nd International Congress on Optical Particle Sizing, Tempe, Arizona, 1990.

G.) J.P. Barton, W. Ma, S.A. Schaub, and D.R. Alexander, "Electromagnetic fields for a beam incident upon two adjacent spherical particles," submitted to Applied Optics, May, 1990.

H.) J.P. Barton and D.R. Alexander, "Electromagnetic fields for an irregularly-shaped, near-spherical particle illuminated by a focused laser beam," submitted to the Journal of Applied Physics, August, 1990.

I.) D.R. Alexander, S.A. Schaub, J. Zhang, D.E. Poulain, and J.P. Barton, "Scattering of incident KrF laser radiation resulting from the laser induced breakdown of $H_2O$ droplets," Optics Letters, Vol. 14, pp. 548-550, 1989.

J.) D.R. Alexander, J.P. Barton, S.A. Schaub, and G.M. Holtmeier, "Nonlinear interactions of KrF laser radiation with small water droplets," submitted to Applied Optics, October, 1989.

K.) S.A. Schaub, D.R. Alexander, D.E. Poulain, and J.P. Barton, "Measurement of hypersonic velocities resulting from the laser induced breakdown of aerosols using an excimer laser imaging system," Review of Scientific Instruments, Vol. 60, pp. 3688-3691, 1989.

L.) S.A. Schaub, J.P. Barton, and D.R. Alexander, "Simplified scattering coefficient expressions for a spherical particle located on the propagation axis of a fifth-order Gaussian beam," Applied Physics Letters, Vol. 55, pp. 2709-2711, 1989.

M.) D.E. Poulain, D.R. Alexander, J.P. Barton, S.A. Schaub, and J. Zhang, "Interactions of intense ultraviolet laser radiation with solid aerosols," Journal of Applied Physics, Vol. 67, 1990.

N.) S.A. Schaub, D.R. Alexander, and J.P. Barton, "Theoretical model for the image formed by a spherical particle in a coherent imaging system: comparison to experiment," Optical Engineering, Vol. 28, pp. 565-571, 1989.

O.) S.A. Schaub, D.R. Alexander, J.P. Barton, and M.A. Emanuel, "Focused laser beam interactions with methanol droplets: effects of relative beam diameter," Applied Optics, Vol. 28, pp. 1666-1669, 1989.

P.) G.M. Holtmeier, D.R. Alexander, and J.P. Barton, "High intensity ultraviolet laser interaction with a metallic filament," submitted to the Journal of Applied Physics, August, 1990.

Q.) S.A. Schaub, D.R. Alexander, and J.P. Barton, "Theoretical model of the laser imaging of small aerosols: applications to aerosol sizing," submitted to Applied Optics, May, 1990.

R.) S.A. Schaub, D.R. Alexander, and J.P. Barton, "Modeling of a coherent imaging system," Proceedings of the 2nd International Congress on Optical Particle Sizing, Tempe, Arizona, 1990.

S.) J.P. Barton, D.R. Alexander, and S.A. Schaub, "Electromagnetic field calculations for a tightly-focused laser beam incident upon a spherical particle," presentation at the 1989 U.S. Army CRDEC Scientific Conference on Obscuration and Aerosol Research, Aberdeen, Maryland, June 27-30, 1989.

T.) D.R. Alexander, J.P. Barton, and S.A. Schaub, "Laser induced breakdown of $H_2O$ droplets and solid wires," presentation at the 1989 U.S. Army CRDEC Scientific Conference on Obscuration and Aerosol Research, Aberdeen, Maryland, June 27-30, 1989.

U.) J.P. Barton, W. Ma, S.A. Schaub, and D.R. Alexander, "Theoretical determination of the electromagnetic fields for a laser beam incident upon two adjacent spherical particles of arbitrary arrangement," presentation at the 2nd International Congress on Optical Particle Sizing, Tempe, Arizona, March 5-8, 1990.

V.) D.R. Alexander, S.A. Schaub, and J.P. Barton, "Modeling of a coherent imaging system: Application to focus determination in aerosol sizing," presentation at the 2nd International Congress on Optical Particle Sizing, Tempe, Arizona, March 5-8, 1990.

## ABSTRACT

A theoretical procedure has been developed for the determination of the internal and external electromagnetic fields for a monochromatic beam incident upon a homogeneous particle of arbitrarily-defined shape. The procedure is best suited for the analysis of near-spherical particles (i.e., particles which deviate from a sphere by plus-or-minus a few tenths of a radii). Verification and demonstration calculations are presented. Also presented are calculations investigating the effect of particle shape on internal heating distributions for $CO_2$ laser heated water droplets, and calculations investigating the effect of surface deformation on resonance excitation within an otherwise spherical particle. Future work will include consideration of modifications of the theoretical procedure that would allow solutions for elongated particles, and the comparison of theoretical calculations with corresponding experimental measurements.

## I. INTRODUCTION

In an earlier work,[1] equations were derived for the theoretical determination of the internal and external electromagnetic fields for a *beam* incident upon a homogeneous *spherical* particle. A procedure has been developed that now permits the determination of the electromagnetic fields for a *beam* incident upon a homogeneous particle of *arbitrarily-defined shape*. This new approach, to be referred to as the irregularly-shaped particle/arbitrary beam theory, appears to be most applicable for the analysis of near-spherical particles (i.e., particles which deviate from a sphere by plus-or-minus a few tenths of a radii). The theory could be used, for example, to determine the electromagnetic fields for a laser beam incident upon a small liquid droplet that has been deformed in shape due to aerodynamic, thermal, or electromagnetic stresses.

Previously, Yeh, Colak, and Barber,[2] have also considered the beam incident upon an irregularly-shaped particle problem. In the approach of Yeh, Colak, and Barber,[2] the incident field is expanded in a plane wave spectrum and a superposition of plane wave solutions, obtained using the extended boundary condition method (EBCM),[3] is performed. In our theoretical development, the incident field is utilized directly, and a superposition of solutions is not necessary. In addition, the primary emphasis of the work of Yeh, Colak, and Barber[2] concerned the determination of far-field scattering patterns. In our paper, the primary emphasis is the determination of the internal and near-surface electromagnetic field distributions.

## II. THEORETICAL DEVELOPMENT

Only a general description of the irregularly-shaped particle/arbitrary beam theory will be presented here. Detailed equations are given in Ref. 4.

The specific problem considered is that of a monochromatic electromagnetic beam within an infinite, nonabsorbing, dielectric medium incident upon a particle of arbitrarily-defined shape. The particle and the surrounding medium are each homogeneous, linear, isotropic, and nonmagnetic ($\mu = 1$). The geometrical arrangement is shown in Fig. 1. The coordinate system origin is located within (and near the center) of the particle. The particle has an associated characteristic radius, $a$, and all spatial quantities are nondimensionalized (as indicated by a tilde) relative to this characteristic radius. Though the theoretical development is applicable for any incident beam for which a mathematical description is known, for the calculations presented in this paper, a focused, linearly-polarized, Gaussian-profiled (TEM$_{00}$ mode) beam will be assumed. A fifth-order corrected mathematical description of the electromagnetic field components for the Gaussian beam, as previously presented in Ref. 5, is utilized for the analysis. All electromagnetic quantities are nondimensionalized relative to an electric field magnitude characteristic of the incident beam, E$_0$. For the Gaussian beam, E$_0$ is the electric field magnitude at the focal point, which can be related to the beam power by an expression given in Ref. 5.

The input parameters of the analysis are as follows: (1) the particle shape function, $\tilde{r}(\theta, \phi)$ (A nondimensionalized single-valued function of the spherical coordinate angles that defines the surface of the particle. For a centered sphere, this function would equal to one.), (2) the particle size parameter, $\alpha = 2\pi a/\lambda_{ext}$ ($\lambda_{ext}$ is the wavelength within the surrounding medium.), (3) the complex relative refractive index of the particle, $\bar{n} = \sqrt{\bar{\epsilon}_{int}/\epsilon_{ext}}$, (4) the nondimensionalized beam focal point coordinates, $(\tilde{x}_0, \tilde{y}_0, \tilde{z}_0)$ (The location of the focal point of the incident beam relative to the particle.), (5) the nondimensionalized beam waist radius, $\tilde{w}_0$, (6) the beam propagation direction angle, $\theta_{bd}$ (The beam is assumed to propagate parallel to the x-z plane. $\theta_{bd}$ is the angle of beam propagation relative to the y-z plane.), and (7) the beam polarization orientation angle, $\phi_{bd}$ (For $\phi_{bd} = 0°$, the beam electric field polarization is parallel to the x-z plane. For $\phi_{bd} = 90°$, the beam electric field polarization is perpendicular to the x-z plane.).

The procedure for determining the electromagnetic fields for a beam incident upon a particle of arbitrarily-defined shape is a generalization of the beam incident upon a spherical particle development presented in Ref. 1. The electromagnetic field is divided into three parts: the incident field (the field that would exist in the absence of the particle), the scattered field (the difference between the external particle field and the incident field), and the internal field (the field within the particle). The external field is the sum of the incident field (assumed known) and the scattered field: $\vec{E}^{ext} = \vec{E}^{(i)} + \vec{E}^{(s)}$ and $\vec{H}^{ext} = \vec{H}^{(i)} + \vec{H}^{(s)}$. The scattered field and the internal field are to be determined. The solution is formulated in spherical coordinates, $(r, \theta, \phi)$.

The electromagnetic field components of the unknown scattered and internal fields are expressed in the form of general series expansions (obtained from a separation-of-variables solution of Maxwell's equations) involving products of radial-dependent Riccati-Bessel functions ($\psi_l, \chi_l$) and angularly-dependent spherical harmonic functions ($Y_{lm}$), as were derived in Ref. 1. It is assumed, even though the particle is not spherical, that the scattered field is appropriately expressed in terms of outgoing spherical waves ($\xi_l^{(1)} = \psi_l - i\chi_l$) and the internal field is appropriately expressed in terms of standing waves ($\psi_l$ only). The validity of these assumptions will be discussed in Sec. III. The series expansions for the electromagnetic field components are each of the form of double summations over the indexes $l$ and $m$. If $L$ is the maximum value of the index $l$ required for series convergence, there will then be

$$N = \sum_{l=1}^{L} (2l + 1) \tag{1}$$

terms in each series expansion. (N equals the number of $l$ and $m$ combinations for a given L.)

The series coefficients for the scattered field ($a_{lm}, b_{lm}$) and the series coefficients for the internal field ($c_{lm}, d_{lm}$) are determined by applying the four boundary conditions associated with the fact

that the tangential electric and magnetic field fields are continuous across the particle surface. Evaluating the four boundary conditions at a particular angular position $(\theta, \phi)$ and then expanding these equations in spherical harmonics $(Y_{l'm'})$ provides a set of 4N linear, algebraic equations for the determination of the 4N values of the series coefficients $(a_{lm}, b_{lm}, c_{lm}, d_{lm})$. Once the series coefficients for the scattered and internal fields are known, the series expansions can be used to determine the electromagnetic field anywhere internal or external to the particle.

If the particle is axisymmetric $[\hat{r}(\theta)$, independent of $\phi]$, then major simplifications in the solution procedure occur. In particular, the series coefficients for each index $m$ can be determined by solving a set of $4(L - |m| + 1)$ linear, algebraic equations (two sets of $2(L + 1)$ equations for $m = 0$). Thus, for the axisymmetric case, it is required to solve $(L + 2)$ "small" sets of linear, algebraic equations, instead of a single "large" 4N set of linear, algebraic equations, as is necessary for the general case.

## III. APPLICABILITY

As previously mentioned, it is assumed that the scattered field is appropriately expressed in terms of outgoing spherical waves $(\xi_l^{(1)} = \psi_l - i\chi_l)$ and the internal field is appropriately expressed in terms of standing waves $(\psi_l$ only). These assumptions are sometimes referred to as the "Rayleigh hypothesis." Even though the validity of the assumptions associated with the Rayleigh hypothesis can be questioned for the case of the irregularly-shaped particle, Chew[6] has recently shown that, on a fundamental level, the Rayleigh hypothesis approach and the extended-boundary-condition-method (EBCM) are essentially equivalent. For both of these methods, the resultant matrix for the solution of the series coefficients describing the fields becomes ill-conditioned (small changes in the terms of the coefficient matrix may produce large changes in the solution vector) for the analysis of elongated particles. The irregularly-shaped particle/arbitrary beam theory, similar to the EBCM, is best suited for the analysis of near-spherical particles. A further discussion of the applicability of the theory is presented in Ref. 4. All calculations in this paper, with the exceptions of Figs. 6 and 7, represent fully converged solutions.

## IV. VERIFICATION CALCULATIONS

The irregularly-shaped particle/arbitrary beam theory was verified by making direct comparisons with known solutions. Calculations were performed for a spherical particle displaced from the origin. If the sphere is displaced along the z-axis, then the particle shape function is a function of the polar angle, $\hat{r}(\theta)$, and the axisymmetric irregularly-shaped particle/arbitrary beam theory can be applied. However, if plane wave illumination is assumed, the electromagnetic field distribution should be identical to that of plane wave Lorenz-Mie theory.

As an example, Fig. 2 presents a plot of the normalized source function $(S = |\bar{E}|^2 / E_0^2)$ distribution in the x-z plane for a 30° angle of incidence plane wave incident upon a centered sphere of $\alpha = 8.0$ and $\bar{n} = 1.2 + 0.02i$. Figure 2 is the Lorenz-Mie theory solution rotated 30° about the origin in the x-z plane in order to account for the angle of incidence of the plane wave. Figure 3 was generated using the axisymmetric theory for identical conditions as Fig. 2, except that the sphere has been displaced along the z-axis by a distance of $\Delta \bar{z} = +0.25$. A comparison of Figs. 2 and 3 shows that the normalized source function distribution of the displaced sphere (Fig. 3) calculated using the axisymmetric theory is identical to the normalized source function distribution of the centered sphere (Fig. 2) calculated using Lorenz-Mie theory, except that the entire solution of Fig. 3 (both internal and near-field) has been shifted along the z-axis by a distance of $\Delta \bar{z} = 0.25$, as would be expected.

A similar approach was used to confirm the general irregularly-shaped particle/arbitrary beam theory, except the sphere is now displaced along the x-axis so that the particle shape function is a function of both the polar and azimuthal angles, $\hat{r}(\theta, \phi)$. Figure 4 shows the normalized source function distribution for a 30° angle of incidence plane wave incident upon a centered sphere of $\alpha = 2.0$ and $\bar{n} = 1.2 + 0.02i$ as determined using Lorenz-Mie theory. Figure 5 provides the normalized source function distribution calculated using the general theory for conditions identical to those of

Fig. 4, except that the sphere has been displaced along the x-axis by a distance of $\Delta\tilde{x} = 0.1$. A comparison of Figs. 4 and 5 shows that the normalized source function distribution of Fig. 5 is identical to that of Fig. 4, except that the entire solution has been shifted along the x-axis by a distance of $\Delta\tilde{x} = +0.1$, as would be expected.

Another confirmation of the arbitrarily-shaped particle theory was obtained by making comparisons with an existing nonspherical, regular geometry solution. Asano and Yamamoto[7] have developed an analytical solution for the determination of the electromagnetic fields for a plane wave incident upon a spheroidal particle. In Ref. 7, far-field scattering patterns for a 0° angle of incidence plane wave incident upon prolate and oblate spheroids of various size parameters and various axis ratios are presented. Asano and Yamamoto[7] plotted far-field normalized scattering intensity,

$$S_r = \lim_{\tilde{r} \Rightarrow \infty} \alpha^2 \tilde{r}^2 \frac{\frac{c}{8\pi} Re(\vec{E} \times \vec{H}^*)_r}{\frac{c}{8\pi}|E_0|^2}, \tag{2}$$

versus scattering angle ($\theta$) in the plane of incident electric field polarization and in the plane perpendicular to the incident electric field polarization. This was done for size parameters, c, of 1 through 7, where the c size parameter of Asano and Yamamoto[7] is related to the size parameter, $\alpha$, of this paper by

$$\alpha = \frac{c(a/b)}{\sqrt{(a/b)^2 - 1}}, \tag{3}$$

where a/b is the major to minor axis ratio. An index of refraction of $\bar{n} = 1.33 + 0.00i$ was assumed.

The axisymmetric irregularly-shaped particle/arbitrary beam theory was used to calculate far-field scattering patterns using parameters consistent with those used in Asano and Yamamoto.[7] Figure 6 presents the far-field scattering patterns for a 0° angle of incidence plane wave incident upon a prolate spheroid of a/b = 2 axis ratio as calculated using the axisymmetric theory. Figure 6 can be directly compared with Fig. 3 of Asano and Yamamoto.[7] Figure 6 is a vertically-unscaled, semi-log plot with each vertical division representing a factor of ten difference in normalized scattering intensity. The forward-scattered ($\theta = 0°$) and the back-scattered ($\theta = 180°$) normalized scattering intensity values are shown for each size parameter. The scattering patterns generated using the axisymmetric theory agreed within a few percent with those of Asano and Yamamoto.[7] For the prolate spheroid, the forward-scattered values agreed with an average deviation of 0.3% and the back-scattered values agreed with an average deviation of 3.2%.

The far-field scattering patterns for an oblate spheroid of a/b = 2 axis ratio, calculated using the axisymmetric theory, are given in Fig. 7. Figure 7 can be directly compared with Fig. 5 of Asano and Yamamoto.[7] Again, the two results were in general agreement. The back-scattered values agreed with an average deviation of 1.1% and the forward-scattered values agreed with an average deviation of 6.1%.

As was previously discussed, the theoretical procedure developed in this paper is best suited for the analysis of near-spherical particles. The far-field scattering calculations for the a/b=2 axis ratio prolate/oblate spheroids of Figs. 6 and 7 were not fully converged solutions. For each case, L was increased until the algebraic equations became too ill-conditioned to permit accurate numerical solution. For the maximum permissible value of L, the far-field scattering intensities were still changing by plus or minus a few percent for each increment in L. This lack of full convergence may explain the slight difference of the results of Figs. 6 and 7 with the comparable results of Asano and Yamamoto.[7]

## V. TIGHTLY-FOCUSED BEAM ON AN OBLATE SPHEROID

In order to demonstrate the ability to determine the electromagnetic fields for a focused beam incident upon a nonspherical particle, calculations were performed for a tightly-focused beam incident upon an oblate spheroid of axis ratio a/b = 1.2, $\alpha = 15.0$, and $\bar{n} = 1.3 + 0.01i$. The angle of incidence ($\theta_{bd}$) was held at 0° and the incident electric field polarization was in the x-z plane

($\phi_{bd} = 0°$). Figure 8 shows the internal normalized source function distribution in the x-z plane for an incident plane wave ($\tilde{w}_0 \Rightarrow \infty$). Only the internal field distribution is presented (the near-field values were artificially set to zero) so as to clearly show the nonspherical shape of the particle.

Figure 9 is for the same conditions as Fig. 8, but instead of plane wave incidence, a beam ($\tilde{w}_0 = 0.667$) is focused at the center of the particle ($\tilde{x}_0 = \tilde{y}_0 = \tilde{z}_0 = 0.0$). The normalized source function distribution for beam illumination is distinctly different than that for plane wave illumination, as can be seen by comparing Figs. 8 and 9. Figure 10 is for the same incident beam conditions as Fig. 9, except that the focal point of the beam has been moved up the x-axis to a position halfway along the major axis of the oblate spheroid ($\tilde{x}_0 = 0.5$, $\tilde{y}_0 = \tilde{z}_0 = 0.0$). Figure 11 shows the normalized source function distribution with the beam focused at the edge of the particle ($\tilde{x}_0 = 1.0$, $\tilde{y}_0 = \tilde{z}_0 = 0.0$).

## VI. CO₂ LASER HEATING OF SPHEROIDAL WATER DROPLETS

As an application of the axisymmetric irregularly-shaped particle/arbitrary beam theory, the effect of nonsphericity on the spatial heating distribution within a water droplet heated by a $CO_2$ laser beam ($\lambda = 10.6\mu m, \bar{n} = 1.179 + 0.072i$) was investigated. The heating rate per unit volume within the droplet is directly proportional to the normalized source function, $S$. Equal volume prolate/oblate spheroidal water droplets ($\alpha_{sphere} = 8.0$, $d_{sphere} \approx 27\mu m$) of major to minor axis ratios (a/b) of 1.1 and 1.2 were analyzed. Plane wave incidence ($\tilde{w}_0 \Rightarrow \infty$) was assumed and three particle orientations were considered: (Case A: $\theta_{bd} = 0°, \phi_{bd} = 0°$), (Case B: $\theta_{bd} = 90°, \phi_{bd} = 0°$), and (Case C: $\theta_{bd} = 90°, \phi_{bd} = 90°$).

For the spherical particle (a/b=1), Cases A, B, and C are indistinguishable, and the maximum normalized source function value within the spherical droplet was determined to be $S_{max} = 1.019$. The effect of particle shape and orientation on maximum source function is summarized in Table 1. For orientation A, the prolate shape results in an increased value of $S_{max}$ (relative to that of an equal volume sphere) while for orientation C, the oblate shape results in an increased value of $S_{max}$. As an example of the effect of particle shape on the spatial distribution of normalized source function (heating), Fig. 12 gives the normalized source function in the y-z plane for orientation A for a.) a sphere, b.) a prolate spheroid with a/b = 1.1, and c.) a prolate spheroid with a/b = 1.2.

## VII. EFFECTS OF SURFACE DEFORMATION AT RESONANCE

The beam incident upon an arbitrarily-shaped particle theory permits electromagnetic field determinations for particles of irregular geometry. As an example of an application, the axisymmetric theory was used to investigate the effect of a surface deformation on resonance excitation within an otherwise spherical particle. (The effect of focal point positioning on resonance excitation was investigated in Ref. 8.) The particle is assumed spherical except for an axisymmetric surface deformation located within the polar angle interval $\pi/8 < \theta < 3\pi/8$:

$$\hat{r}(\theta) = \begin{cases} 1 \text{ for } \theta < \pi/8 \\ \\ 1 + \epsilon/2\big(1 + cos[8(\theta - \pi/8) - \pi]\big) \text{ for } \pi/8 < \theta < 3\pi/8 \\ \\ 1 \text{ for } \theta > 3\pi/8 \end{cases} \qquad (4)$$

The height of the deformation, $\epsilon$, can be either positive (protrusion), negative (depression), or zero (perfect sphere). Plane wave illumination with a 0° angle of incidence is assumed which provides a degenerate condition such that all series coefficients except m = ±1 are identically zero. In

addition, the m = ±1 terms can be combined so that the double summation electromagnetic field component expansions reduce to single summations over the radial index,

$$\sum_{l=1}^{L}{}' \tag{5}$$

with the associated single index series coefficients: $a_l, b_l, c_l, d_l$.

Assuming an index of refraction of $\bar{n} = 1.334 + 1.2\times10^{-9}i$ (0.5145 $\mu$m wavelength argon-ion laser incident upon water),[9] a spherical particle resonance was located. The resonance chosen was the 34th mode, 1st order magnetic wave (TE mode) resonance which occurs at $\alpha = 29.285$. At this size parameter, the magnitude of the 34th radial index magnetic wave internal field series coefficient ($|d_{34}|$) attains a peak value, as shown in Fig. 13.

The effect of a surface deformation on the excitation of this resonance was investigated by determining $|d_{34}|$ as a function of $\epsilon$ and $\alpha$. In Fig. 14, $|d_{34}|$ is plotted versus size parameter for $\epsilon = 0.00, \pm0.01$, and $\pm0.02$, and in Fig. 15, $|d_{34}|$ is plotted versus size parameter for $\epsilon = 0.00$ and $\pm0.05$. As can be seen in Figs. 14 and 15, the presence of the surface deformation shifts the resonance to smaller size parameters for protrusions ($\epsilon > 0$) and to larger size parameters for depressions ($\epsilon < 0$). Surface deformations also decrease the quality of the resonance with protrusions ($\epsilon > 0$) having a greater effect than depressions ($\epsilon < 0$) (for these particular conditions).

For small deformations, $|\epsilon| < 0.02$, resonance is apparently retained when the circumference of the deformed particle matches the circumference of the corresponding resonant spherical particle. This observation is illustrated by the results presented in Table 2.

## VIII. CONCLUSION

A theoretical procedure has been developed for the determination of the internal and external electromagnetic fields for a monochromatic beam incident upon a homogeneous particle of arbitrarily-defined shape. The procedure is apparently best suited for the analysis of near-spherical particles and, for example, could be used to analyze laser beams interactions with liquid droplets that have been slightly distorted in shape due to aerodynamic, thermal, or electromagnetic stresses. Future work will include consideration of modifications of the theoretical procedure that would allow solutions for elongated particles, and the comparison of theoretical calculations with corresponding experimental measurements.

## ACKNOWLEDGEMENT

## REFERENCES

1. J.P. Barton, D.R. Alexander, and S.A. Schaub, "Internal and near-surface electromagnetic fields for a spherical particle irradiated by a focused laser beam," J. Appl. Phys. 64, 1632 (1988).
2. C. Yeh, S. Colak, and P. Barber, Scattering of sharply focused beams by arbitrarily shaped dielectric particles: an exact solution," Appl. Opt. 21, 4426 (1982).
3. P. Barber and C. Yeh, "Scattering of electromagnetic waves by arbitrarily shaped dielectric bodies," Appl. Opt. 14, 2864 (1975).
4. J.P. Barton and D.R. Alexander, "Electromagnetic fields for an irregularly-shaped, near-spherical particle illuminated by a focused laser beam," submitted to the Journal of Applied Physics, August, 1990.
5. J.P. Barton and D.R. Alexander, "Fifth-order corrected electromagnetic field components for a fundamental Gaussian beam," J. Appl. Phys. 66, 2800 (1989).
6. W.C. Chew, **Waves and Fields in Inhomogeneous Media**, pp. 463, Van Nostrand Reinhold, New York, 1990.
7. S. Asano and G. Yamamoto, "Light scattering by a spheroidal particle," Appl. Opt. 14, 29 (1975).
8. J.P. Barton, D.R. Alexander, and S.A. Schaub, "Internal fields of a spherical particle illuminated by a tightly-focused laser beam: focal point positioning effects at resonance," J. Appl. Phys. 65, 2900 (1989).
9. G.M. Hale and M.R. Querry, "Optical constants of water in the 200-nm to 200-$\mu$m wavelength region," Appl. Opt. 12, 555 (1973).
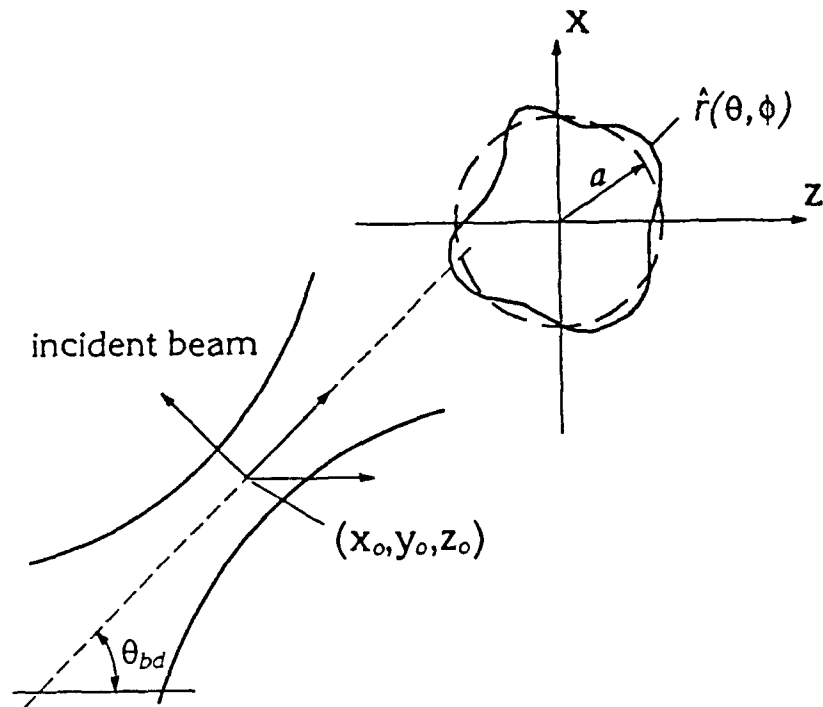
FIG 1. Geometrical arrangement for beam incident upon an arbitrarily-shaped particle analysis. The beam propagates parallel to the x-z plane.
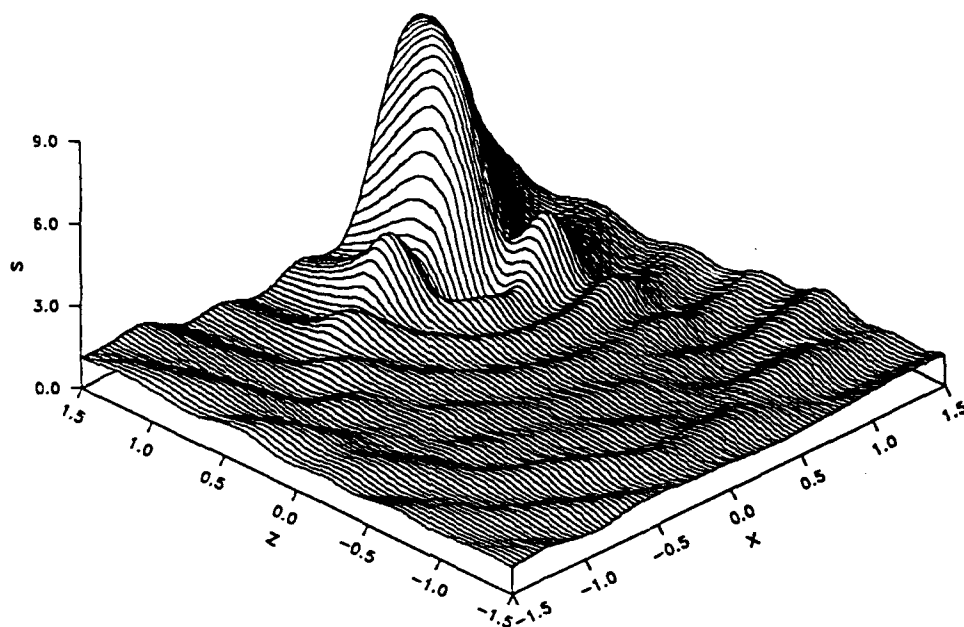
FIG 2. Normalized source function distribution in the x-z plane for a 30° angle of incidence plane wave incident upon a centered sphere. $\alpha = 8.0$, $\bar{n} = 1.2 + 0.02i$, $\bar{w}_0 = \infty$ (plane wave), $\theta_{bd} = 30°$, and $\phi_{bd} = 90°$.
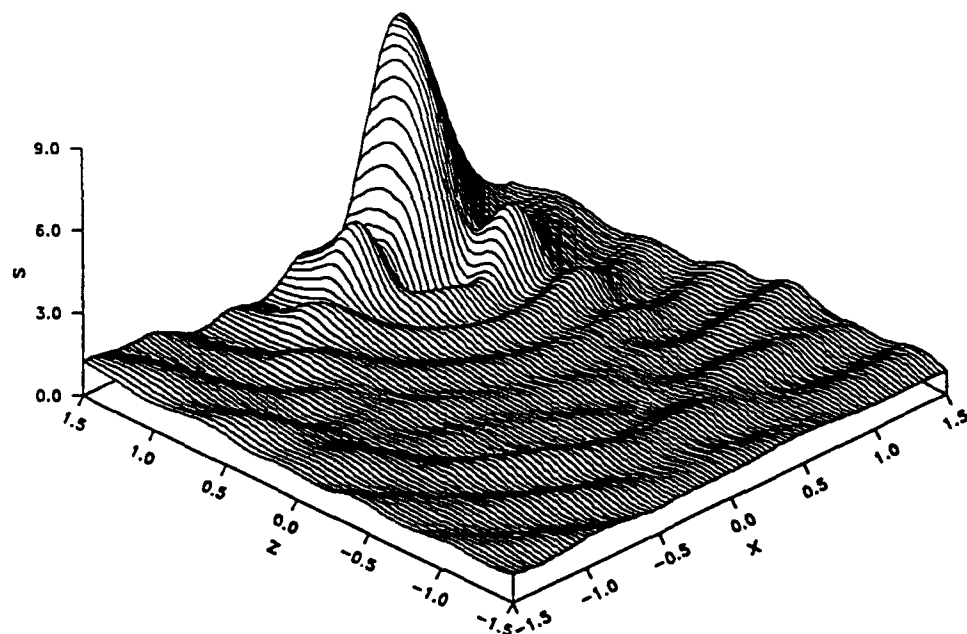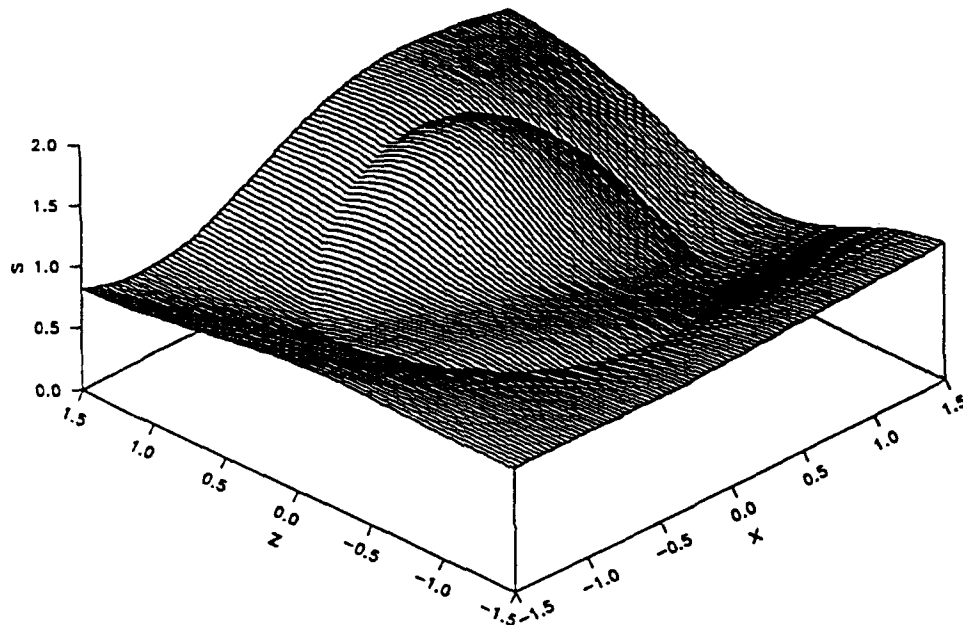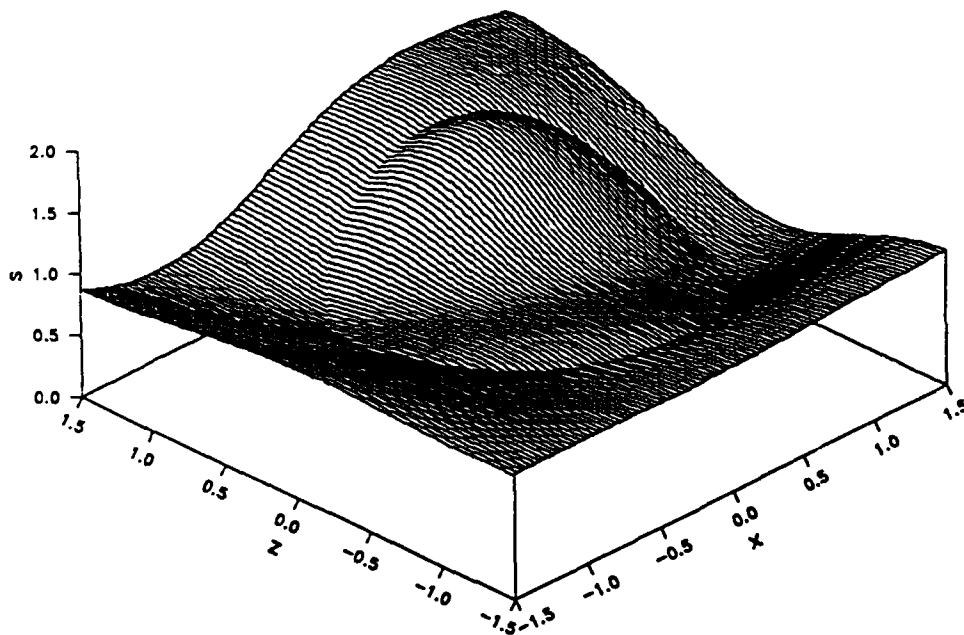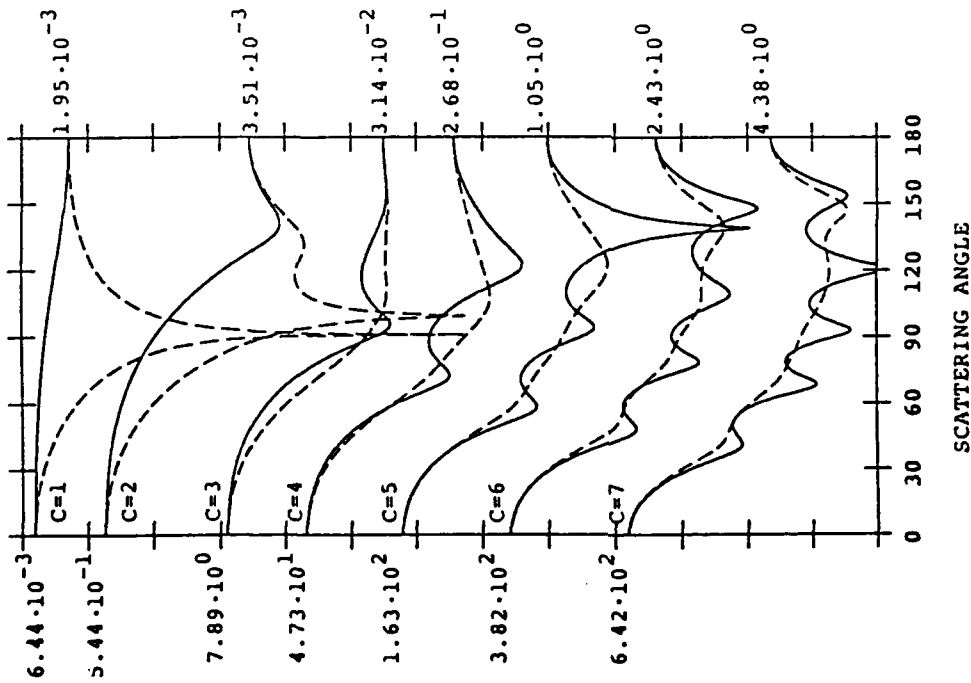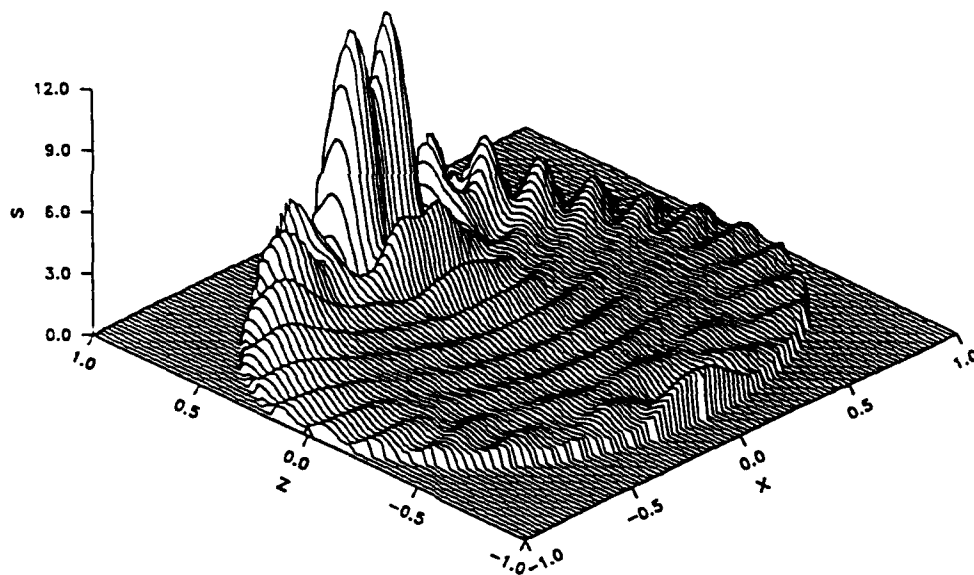


FIG 3. Normalized source function distribution in the x-z plane for a 30° angle of incidence plane wave incident upon a sphere displaced along the z-axis by $\Delta \bar{z} = +0.25$. $\alpha = 8.0$, $\bar{n} = 1.2 + 0.02i$, $\bar{w}_0 = \infty$ (plane wave), $\theta_{bd} = 30°$, and $\phi_{bd} = 90°$.

FIG 4. Normalized source function distribution in the x-z plane for a 30° angle of incidence plane wave incident upon a centered sphere. $\alpha = 2.0$, $\bar{n} = 1.2 + 0.02i$, $\bar{w}_0 = \infty$ (plane wave), $\theta_{bd} = 30°$, and $\phi_{bd} = 90°$.



FIG 5. Normalized source function distribution in the x-z plane for a 30° angle of incidence plane wave incident upon a sphere displaced along the x-axis by $\Delta\bar{x} = +0.10$. $\alpha = 2.0$, $\bar{n} = 1.2 + 0.02i$, $\bar{w}_0 = \infty$ (plane wave), $\theta_{bd} = 30°$, and $\phi_{bd} = 90°$.

FIG 6. Far-field normalized scattering intensity for a 0° angle
of incidence plane wave incident upon a a/b = 2 axis ratio proiate spheroid.
Solid line: y-z plane. Dashed line: x-z plane. $\alpha = 1.155c$,
$\bar{n} = 1.33 + 0.00i$, $\bar{w}_0 = \infty$ (plane wave), $\theta_{bd} = 0°$, and $\phi_{bd} = 0°$.
Compare with Fig. 3 of Asano and Yamamoto.[7]
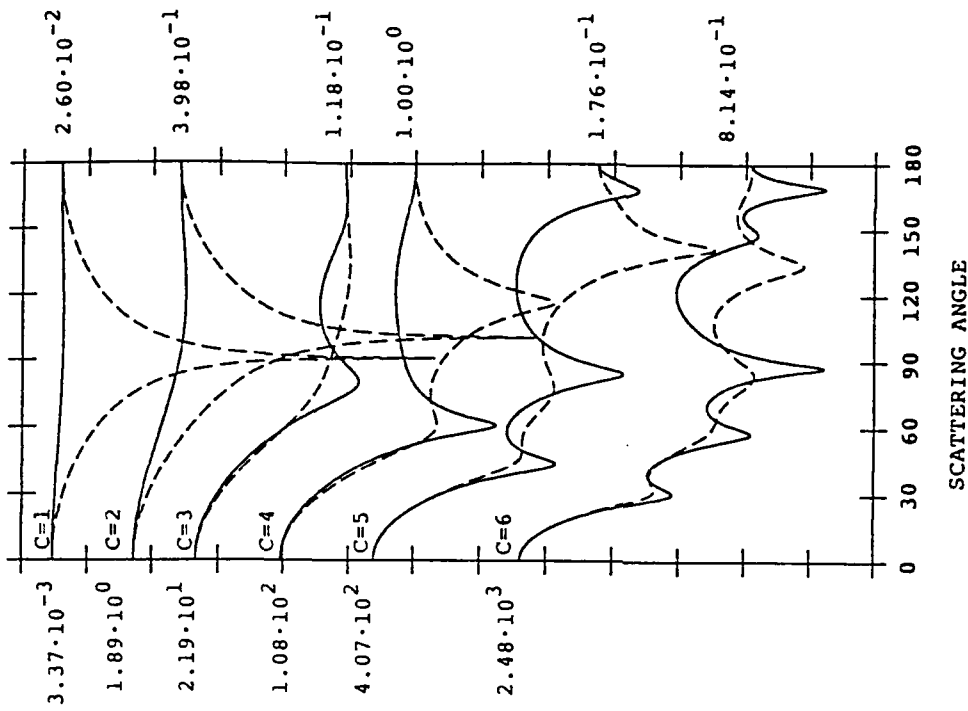


FIG 7. Far-field normalized scattering intensity for a 0° angle
of incidence plane wave incident upon a a/b = 2 axis ratio oblate spheroid.
Solid line: y-z plane. Dashed line: x-z plane. $\alpha = 1.155c$,
$\bar{n} = 1.33 + 0.00i$, $\bar{w}_0 = \infty$ (plane wave), $\theta_{bd} = 0°$, and $\phi_{bd} = 0°$.
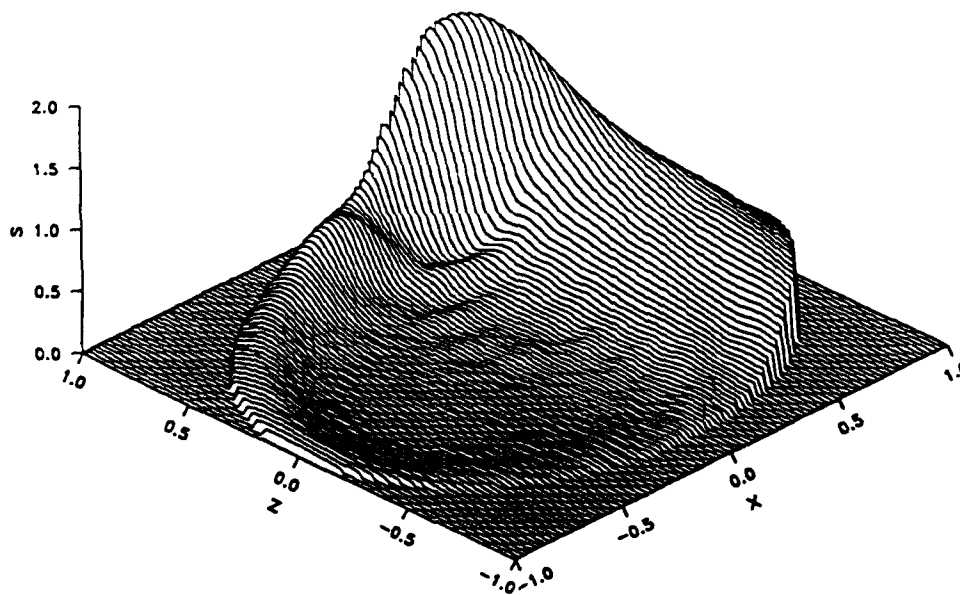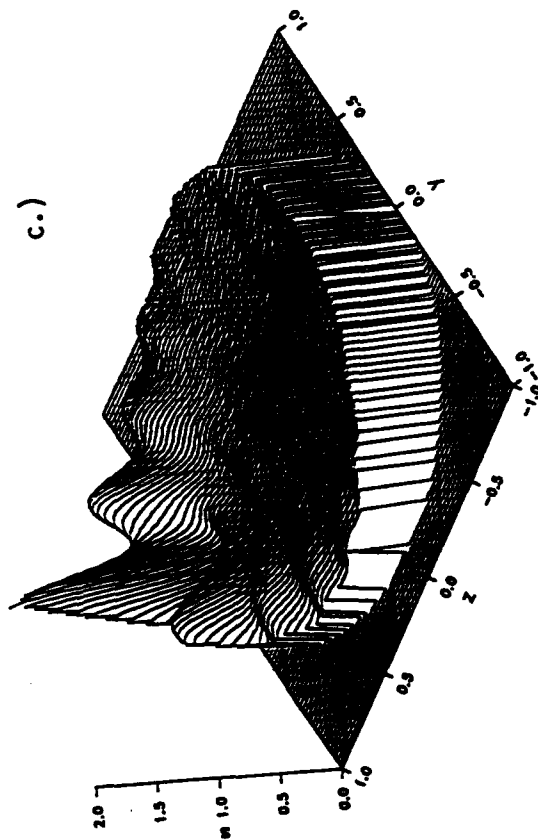Compare with Fig. 5 of Asano and Yamamoto.[7]

FIG 8. Internal normalized source function distribution in the x-z plane for a 0° angle of incidence plane wave incident upon an oblate spheroid of axis ratio a/b = 1.2. $\alpha = 15.0$, $\bar{n} = 1.33 + 0.00i$, $\bar{w}_0 \Rightarrow \infty$ (plane wave), $\bar{x}_0 = \bar{y}_0 = \dot{=}0.0$, $\theta_{bd} = 0°$, and $\phi_{bd} = 0°$.
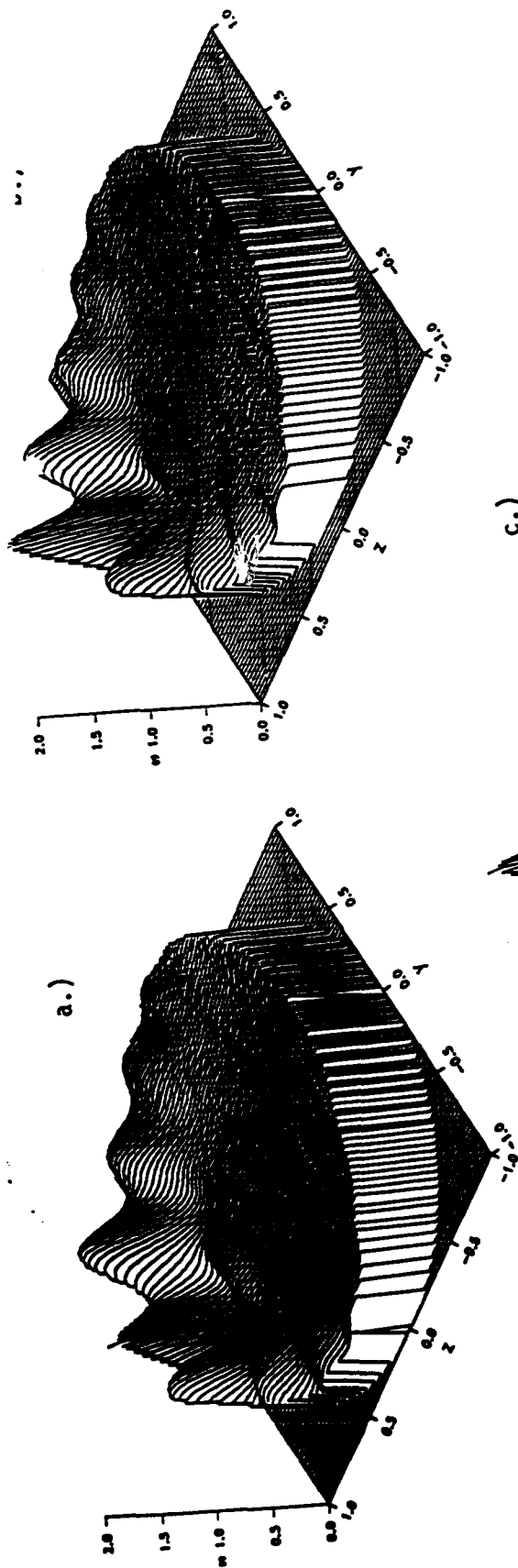


FIG 9. Internal normalized source function distribution in the x-z plane for a 0° angle of incidence focused beam incident upon an oblate spheroid of axis ratio a/b = 1.2. On-center focal point positioning. $\alpha = 15.0$, $\bar{n} = 1.33 + 0.00i$, $\bar{w}_0 = 0.667$, $\bar{x}_0 = \bar{y}_0 = \bar{z}_0 = 0.0$, $\theta_{bd} = 0°$, and $\phi_{bd} = 0°$.

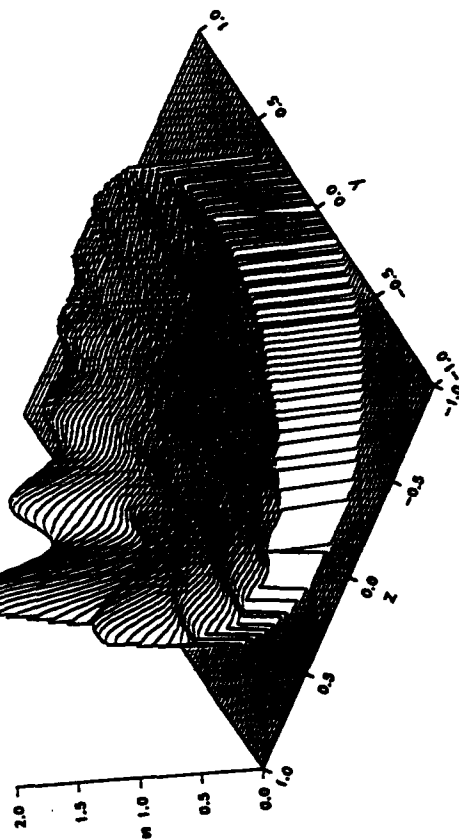FIG 10. Internal normalized source function distribution in the x-z plane for a $0°$ angle of incidence focused beam incident upon an oblate spheroid of axis ratio $a/b = 1.2$. Mid-axis focal point positioning. $\alpha = 15.0$, $\bar{n} = 1.33 + 0.00i$, $\bar{w}_0 = 0.667$, $\bar{x}_0 = 0.5$, $\bar{y}_0 = \bar{z}_0 = 0.0$, $\theta_{bd} = 0°$, and $\phi_{bd} = 0°$.



FIG 11. Internal normalized source function distribution in the x-z plane for a $0°$ angle of incidence focused beam incident upon an oblate spheroid of axis ratio $a/b = 1.2$. On-edge focal point positioning. $\alpha = 15.0$, $\bar{n} = 1.33 + 0.00i$, $\bar{w}_0 = 0.667$, $\bar{x}_0 = 1.0$, $\bar{y}_0 = \bar{z}_0 = 0.0$, $\theta_{bd} = 0°$, and $\phi_{bd} = 0°$.

FIG 12. Internal normalized source function distribution in the $y$-$z$ plane for a for a $0°$ angle of incidence plane wave incident upon equal volume a.) sphere, b.) 1.1 axis ratio prolate spheroid, and c.) 1.2 axis ratio prolate spheroid. ($CO_2$ laser incident upon a water droplet, Case $\Lambda$ orientation.) $\tilde{w}_0 \Rightarrow \infty$, $\tilde{x}_0 = \tilde{y}_0 = \tilde{z}_0 = 0.0$, $\theta_{bd} = 0°$, and $\phi_{bd} = 0°$. $\alpha_{sphere} = 8.0$, $\tilde{n} = 1.179 + 0.072i$,
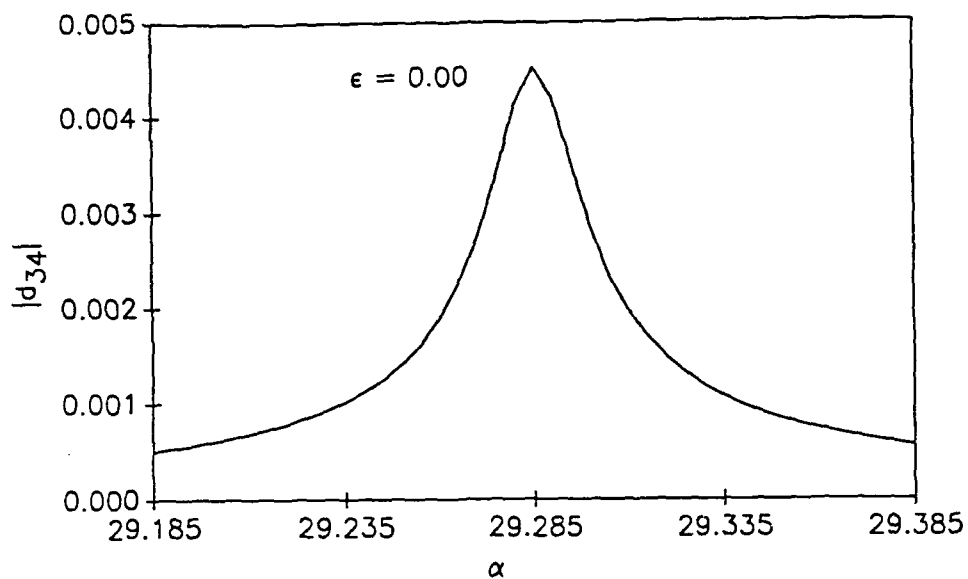
FIG 13. $|d_{34}|$ versus $\alpha$ for a spherical particle ($\epsilon = 0.00$). $\bar{n} = 1.334 + 1.2\times10^{-9}$i.
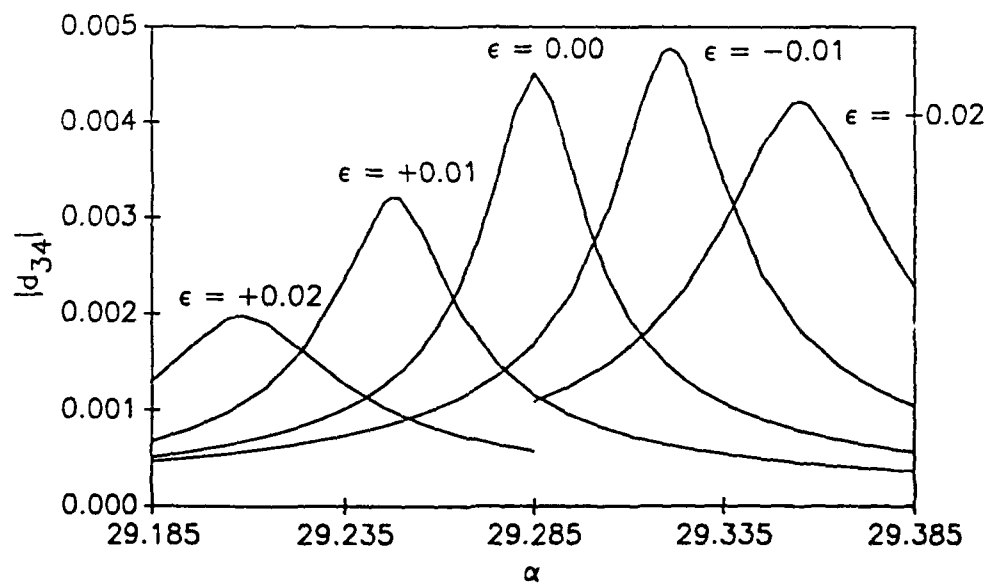


FIG 14. $|d_{34}|$ versus $\alpha$ for spherical particle with surface deformations of $\epsilon = 0.00$, $\pm0.01$, and $\pm0.02$. $\bar{n} = 1.334 + 1.2\times10^{-9}$i.
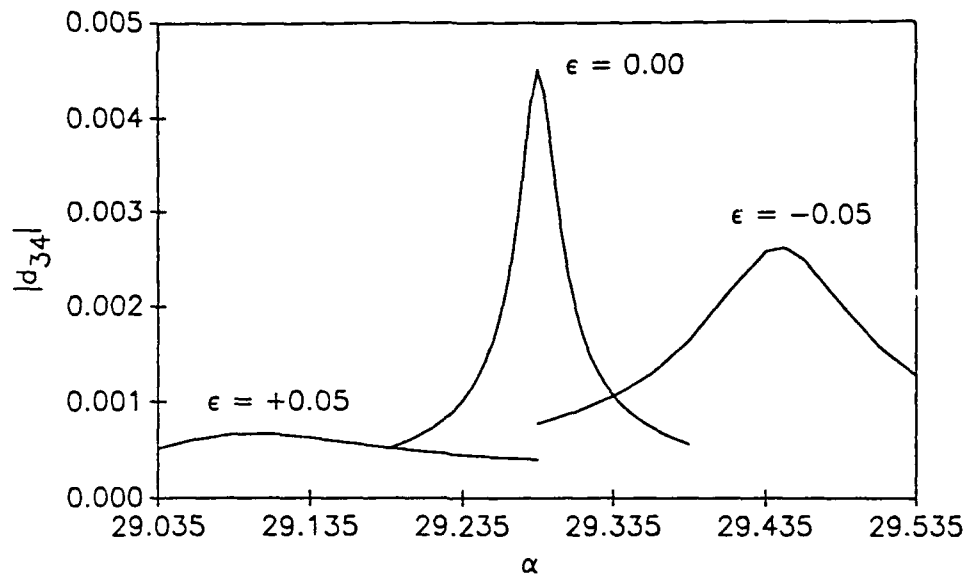
FIG 15. $|d_{34}|$ versus $\alpha$ for spherical particle with surface deformations of $\epsilon = 0.00$ and $\pm 0.05$. $\bar{n} = 1.334 + 1.2 \times 10^{-9} i$.

| | A | B | C |
|---|---|---|---|
| prolate)$_{1.1}$ | 1.405 (+38%) | 0.919 (-10%) | 1.029 (+1%) |
| prolate)$_{1.2}$ | 1.731 (+70%) | 0.889 (-13%) | 1.043 (+2%) |
| oblate)$_{1.1}$ | 0.981 (-4%) | 1.098 (+8%) | 1.280 (+26%) |
| oblate)$_{1.2}$ | 0.969 (-5%) | 1.128 (+11%) | 1.448 (+42%) |

TABLE 1. Maximum normalized source function value (and % difference from spherical particle maximum value) for equal volume prolate/oblate spheroids of major to minor axis ratios of 1.1 and 1.2 and of orientations A, B, and C for plane wave incidence. Parameters are for a $CO_2$ laser incident upon a water droplet. $\alpha_{sphere} = 8.0$ and $\bar{n} = 1.179 + 0.072i$.

| $\epsilon$ | Circumference $[\lambda_{ext}]$ at $\alpha = 29.285$ | $\alpha_{res}$ | Circumference $[\lambda_{ext}]$ at $\alpha_{res}$ |
|---|---|---|---|
| $-0.02$ | 29.212 | 29.355 | 29.282 |
| $-0.01$ | 29.248 | 29.321 | 29.284 |
| 0.00 | 29.285 | 29.285 | 29.285 |
| $+0.01$ | 29.322 | 29.248 | 29.285 |
| $+0.02$ | 29.358 | 29.208 | 29.281 |

TABLE 2. Circumference (in units of $\lambda_{ext}$) for spherical particle with surface deformation at the 34th, 1st order magnetic wave resonance for $\epsilon = 0.00$, $\pm 0.01$, and $\pm 0.02$. $\bar{n} = 1.334 + 1.2 \times 10^{-9}$i.

# THEORETICAL DETERMINATION OF THE ELECTROMAGNETIC FIELDS FOR A LASER BEAM INCIDENT UPON TWO ADJACENT SPHERICAL PARTICLES OF ARBITRARY ARRANGEMENT

J.P. Barton, W. Ma, S.A. Schaub and D.R. Alexander

Center for Electro-Optics
College of Engineering
University of Nebraska-Lincoln
Lincoln, NE 68588-0656

## ABSTRACT

Applying our previously derived spherical particle/arbitrary beam interaction theory, a procedure has been developed for the determination of the electromagnetic fields for a beam incident upon two adjacent spherical particles. Example calculations of internal and near field normalized source function ($\sim |\bar{E}|^2$) distributions are presented. Also presented are calculations demonstrating the effect of the presence and the positioning of a second adjacent particle on far field scattering patterns for beam illumination.

## I. INTRODUCTION

The relative random motion of individual particles within a cloud will sporadically bring particles into close proximity of each other. A laser beam incident upon closely spaced particles will result in cooperative scattering which may affect subsequent particle sizing measurements. An understanding of the cooperative scattering of adjacent particles illuminated by a laser beam is thus of importance.

The theoretical determination of the electromagnetic fields for a linearly-polarized, monochromatic *plane wave* incident upon adjacent spherical particles has been previously considered.[1-6] Presented plane wave calculations have primarily been for simplified arrangements where the spherical particles are of equal size and/or equal complex relative index of refraction and/or limited to small size parameter and/or located along a major incident axis.

Particle sizing, however, is often performed using focused laser beams where the local beam diameter and the particle diameter are of the same order and the plane wave assumption may not be appropriate. Utilizing our spherical particle/arbitrary beam interaction theory,[7] we have developed a procedure for determining the electromagnetic fields for a fundamental mode (Gaussian-profile) laser beam incident upon two adjacent particles of arbitrary arrangement. (The generalization to three or more adjacent particles would be straightforward). The two particles may be of different size, may have different composition (differing complex relative index of refractions), and may have any spatial orientation relative to each other and relative to the incident beam. It is not necessary that there be a single incident beam; having multiple beams coming from different directions would require minimal additional computation.

Presented here is a brief description of the theoretical development of the beam on two adjacent spheres theory followed by example internal and near field calculations and preliminary calculations showing the effect of the relative positioning of the two spheres on far field scattering distributions.

## II. THEORETICAL DEVELOPMENT

The theoretical approach, in the most general sense, is similar to that introduced by Fuller and Kattawar.[5] Since our previously derived spherical particle/arbitrary beam interaction theory permits the determination of the electromagnetic fields of a particle for *any* known incident field, the procedure is as follows. The spherical particle/arbitrary beam interaction theory is used to calculate the external electromagnetic field for the laser beam incident upon particle 1. (The electromagnetic

field components of the laser beam are mathematically expressed using our recently developed fifth-order corrected Gaussian beam description.[8]) The external electromagnetic field of particle 1 is used as the incident field upon particle 2 and the scattered field of particle 2 is determined. The scattered field of particle 2 is added to the incident beam to form an updated field incident upon particle 1 and the external field of particle 1 is recalculated. The newly calculated external field of particle 1 is then used as the incident field upon particle 2 and the scattered field of particle 2 is recalculated. The process is continued until there is no longer a significant change in the electromagnetic fields. For particles spaced one diameter or more apart surface-to-surface, convergence typically occurs within three to five of these multiple "reflections."

The parameters of the laser beam incident upon two adjacent spheres problem are the dielectric constant of the medium ($\epsilon_{ext}$), the waist diameter of the laser beam ($w_o$), the size parameters ($\alpha = 2\pi a/\lambda$) of the two particles ($\alpha_1$ and $\alpha_2$), the complex relative index of refractions of the two particles ($\bar{n}_1$ and $\bar{n}_2$), the location of particle 1 relative to the focal point of the laser beam ($x_o$, $y_o$, $z_o$), the location of particle 2 relative to particle 1 ($x_{12}$, $y_{12}$, $z_{12}$), and the location of the plot reference relative to particle 1 ($x_{ref}$, $y_{ref}$, $z_{ref}$). Spatial quantities are normalized using the radius of particle 1 ($a_1$). (A tilde ~ is used to indicate a normalized spatial quantity.)

## III. INTERNAL AND NEAR FIELD CALCULATIONS

Example calculations of internal and near field normalized source function distributions are shown in Figs. 1 and 2. The normalized source function, S, is defined as $|\bar{E}|^2/|E_o|^2$ where $E_o$ is a characteristic electric field amplitude of the incident beam. ($|E_o|^2$ is directly proportional to the laser beam power.) In Figs. 1 and 2 the normalized source function distributions are given both graphically and in false contrast visualization (white $\Leftrightarrow$ high, gray $\Leftrightarrow$ intermediate, and black $\Leftrightarrow$ low).

Figure 1 presents the internal and near field normalized source function distribution in the y-z plane for a linearly-polarized (electric field polarization in the x axis direction), 100 $\mu$m waist diameter $CO_2$ laser beam ($\lambda = 10.6$ $\mu$m) incident upon two 45 $\mu$m diameter water droplets ($\bar{n} = 1.179 + 0.072i$) separated by 35 $\mu$m surface-to-surface along the propagation axis. These conditions correspond to an experiment performed within our laboratory in which a $CO_2$ laser beam was directed upon two parallel streams of water droplets so that the illuminated droplet would act as a lens to focus the laser light upon the shadow side droplet.[9] This focusing effect is apparent in Fig. 1.

Figure 2 provides a normalized source function distribution for a more general (hypothetical) case. A 40 $\mu$m waist diameter $CO_2$ laser beam is incident upon a 50 $\mu$m diameter methanol droplet ($\bar{n}_1 = 1.395 + 0.0163i$) and a 30 $\mu$m water droplet ($\bar{n}_2 = 1.179 + 0.072i$). The droplets are offset from each other and offset from the propagation axis of the beam in the y-z plane. The effect is an interesting splitting of the beam as is most easily seen in the false contrast visualization.

## IV. FAR FIELD CALCULATIONS

Calculations of far field scattering patterns were performed for parameters corresponding to a hypothetical arrangement having a linearly-polarized, fundamental Argon-ion ($\lambda = 0.5145$ $\mu$m) laser beam of 4 $\mu$m beam waist diameter incident upon two adjacent 1.8 $\mu$m diameter water droplets ($\bar{n}_1 = \bar{n}_2 = 1.334 + 1.2 \times 10^{-9}i$,[10] $\alpha_1 = \alpha_2 = 11.0$, $\tilde{w}_0 = 2.22$). The beam propagates in the $+z$ axis direction with a divergence angle of $\approx 10°$ and with electric field polarization in the x axis direction. For the cases considered here, particle 1 is fixed in position at the focal point of the beam ($\tilde{x}_0 = \tilde{y}_0 = \tilde{z}_0 = 0$). The position of particle 2 was then systematically varied and the subsequent effect on the far field scattering pattern studied. The arrangement is shown schematically in Fig. 3. In all the Figures that follow, the normalized scattering intensity, defined as

$$S_r = \lim_{r \to \infty} \tilde{r}^2 \frac{\frac{c}{8\pi} Re(\vec{E} \times \vec{H}^*)_r}{\frac{c}{8\pi}|E_0|^2}$$

is plotted versus angle $\theta$ in the x-z plane (plane parallel to the electric field polarization.)

Figure 4 presents the reference case of a single particle at the focal point of the beam (particle 2 far removed from the beam). For comparison, Fig. 5 shows the calculated far field scattering for the same single particle condition as Fig. 4, but with plane wave illumination instead of focused beam illumination. Since the particle is located at the focal point of the beam and the particle diameter (1.8 $\mu m$) is less than the beam waist diameter (4.0 $\mu m$), the single particle scattering patterns for beam (Fig. 4) and plane wave (Fig. 5) illumination are similar.

To investigate the effect of a second adjacent particle on the far field scattering pattern, a set of calculations were performed with particle 2 placed one diameter surface-to-surface away from particle 1 ($\tilde{r}_{12} = 4$). Figures 6-12 show the far field scattering for particle 2 positioned at angles of 0° (on the +z axis, Fig. 6), 30° (Fig. 7), 60° (Fig. 8), 90° (on the +x axis, Fig. 9), 120° (Fig. 10), 150° (Fig. 11), and 180° (on the -z axis, Fig. 12) about particle 1 in the x-z plane ($\tilde{y}_{12} = 0$). The calculations of Figs. 6-12 required three iterations before convergence within a fraction of one percent. As can be observed by comparing with the single particle case of Fig. 4, Figs. 6-12 indicate the presence of the second particle significantly affects the far field scattering distribution. The strongest effect, as would be expected, occurs when particle 2 is located well within the beam (Figs. 6,7 and Figs. 11,12) and a relatively weaker effect occurs when particle 2 is at the edge of the beam (Figs. 8-10).

Figure 9 shows the far field scattering for particle 2 located on the +x axis one diameter surface-to-surface from particle 1 ($\tilde{x}_{12} = 4, \tilde{y}_{12} = 0, \tilde{z}_{12} = 0$). At this location particle 2 is at the edge of the beam ($\tilde{x}_{12} = 4.00 \approx 2\tilde{w}_0 = 4.44$) and the far field scattering distribution roughly resembles that of the single particle case of Fig. 4. If particle 2 is further removed from the beam along the x axis, then the far field scattering distribution approaches that of a single particle as seen in Fig. 13 ($\tilde{x}_{12} = 6$), Fig. 14 ($\tilde{x}_{12} = 12$), and Fig. 15 ($\tilde{x}_{12} = 18$).

Figure 6 shows the far field scattering for particle 2 located on the +z axis one diameter surface-to-surface from particle 1 ($\tilde{x}_{12} = 0, \tilde{y}_{12} = 0, \tilde{z}_{12} = 4$). The oscillating structure in the far field scattering for this case arises due to interference between the light scattered by the two identical particles. In the far field, the difference in path length for light leaving the two particles is $|z_{12}\cos\theta|$ and interference proportional to $[1 + \cos(a\tilde{z}_{12}\cos\theta)]$ might be expected. From this expression, if particle 2 is moved further away from particle 1 along the z axis ($\tilde{z}_{12}$ is increased) then the frequency of the oscillations in the far field scattering distribution should correspondingly increase. In addition, since the beam is diverging and the intensity incident upon particle 2 decreases as particle 2 is moved away from the focal point, the amplitude of the interference should decrease with increasing $\tilde{z}_{12}$. As particle 2 becomes far removed from particle 1, and from the focal point of the beam, the scattering distribution should converge to that of the single particle (Fig. 4). As seen in Fig. 16 ($\tilde{z}_{12} = 10$), Fig. 17 ($\tilde{z}_{12} = 20$), Fig. 18 ($\tilde{z}_{12} = 50$), and Fig. 19 ($\tilde{z}_{12} = 100$) this is indeed observed. Calculations for particle 2 moved along the -z axis showed near identical results.

## V. CONCLUSIONS

A theoretical approach has been developed for the determination of the electromagnetic fields for a beam incident upon two adjacent spherical particles of arbitrary arrangement. Example calculations of internal and near field normalized source function distributions and far field normalized scattering intensities have been presented. Future work will include further such "computational experimentation" and efforts to obtain direct comparisons between theoretical calculations and corresponding experimental measurements.

# REFERENCES

1. Bruning, J.H. and Y.T. Lo, "Multiple scattering of EM waves by spheres Part I – Multiple expansion and ray-optical solutions," IEEE Trans. Ant. and Prop. **AP-19**, 378-390 (1971).

2. Bruning, J.H. and Y.T. Lo, "Multiple scattering of EM waves by spheres Part II – Numerical and experimental results," IEEE Trans. Ant. and Prop. **AP-19**, 391-400 (1971).

3. G.W. Kattawar and C.E. Dean, "Electromagnetic scattering from two dielectric spheres: comparison between theory and experiment," Opt. Soc. Am. **8**, 48-50 (1983).

4. K.A. Fuller, G.W. Kattawar, and R.T. Wang, "Electromagnetic scattering from two dielectric spheres: further comparisons between theory and experiment," Appl. Opt. **25**, 2521-2529 (1986).

5. K.A. Fuller and G.W. Kattawar, "Consummate solution to the problem of classical electromagnetic scattering by an ensemble of spheres. I: Linear chains," Opt. Soc. Am. **13**, 90-92 (1988).

6. K.A. Fuller and G.W. Kattawar, "Consummate solution to the problem of classical electromagnetic scattering by an ensemble of spheres. II: Clusters of arbitrary configuration," Opt. Soc. Am. **13**, 1063-1065 (1988).

7. J.P. Barton, D.R. Alexander and S.A. Schaub, "Internal and near-surface electromagnetic fields for a spherical particle irradiated by a focused laser beam," J. Appl. Phys. **64**, 1632-1639 (1988).

8. J.P. Barton, and D.R. Alexander, "Fifth-order corrected electromagnetic field components for a fundamental Gaussian beam," J. Appl. Phys. **66**, 2800-2802 (1989).

9. D.R. Alexander, J.P. Barton, S.A. Schaub, M.A. Emanuel, and J. Zhang, "Experimental and theoretical analysis of the interaction of laser radiation with fluid cylinders and spheres," Proceedings of the 1987 U.S. Army Scientific Conference on Obscuration and Aerosol Research, Aberdeen, Maryland **CRDEC-SP-88031**, 251-272 (1987).

10. G.M. Hale and M.R. Querry, "Optical constants of water in the 200-nm to 200-$\mu$m wavelength region," Appl. Opt. **12**, 555-563 (1973).
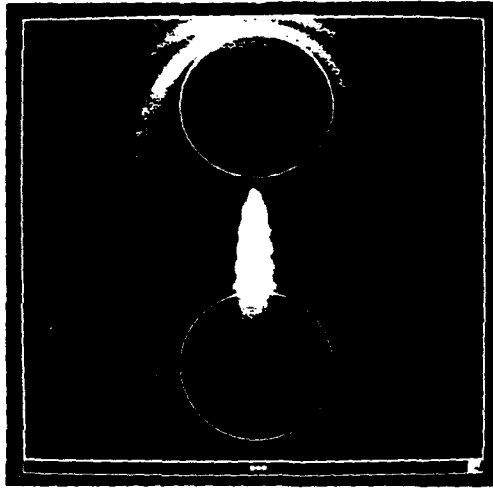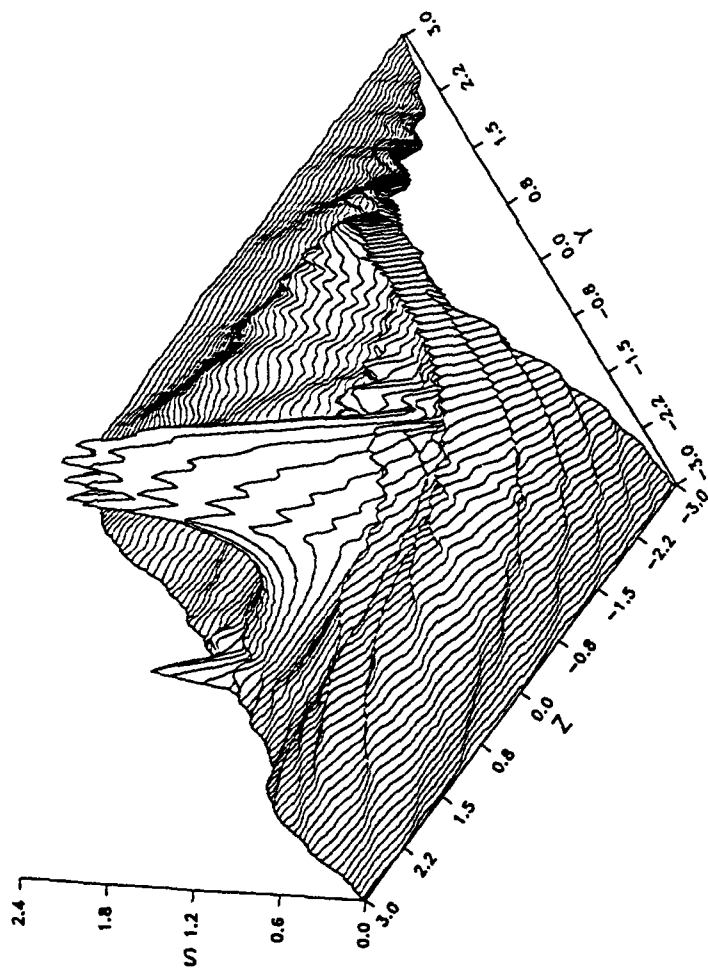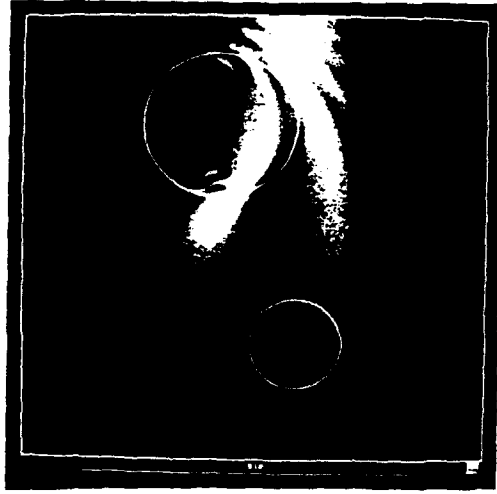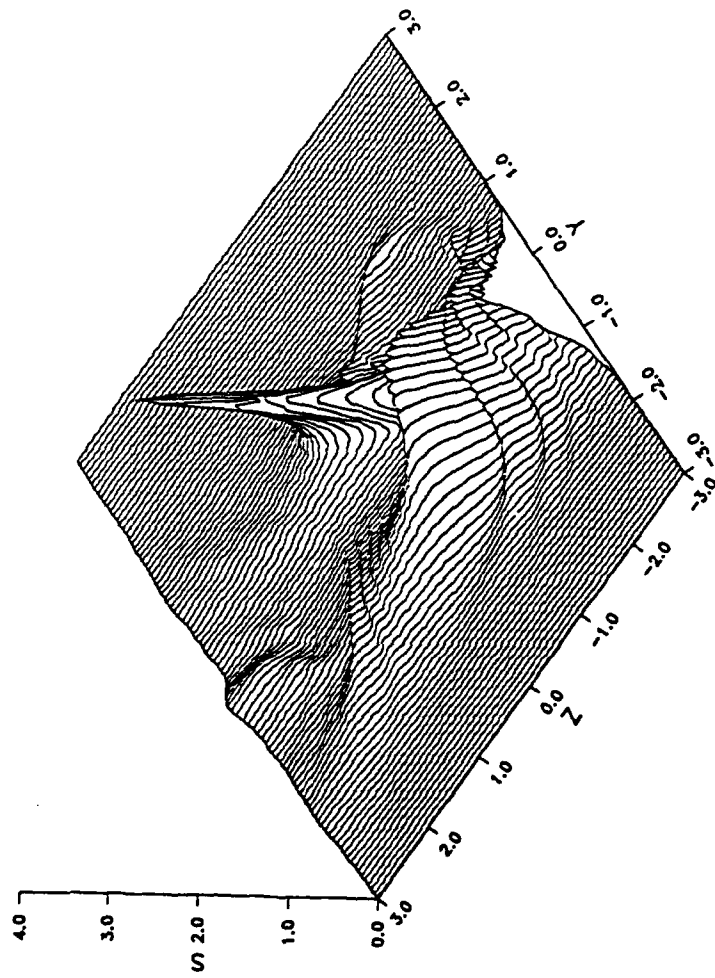
FIG 1. Normalized source function in the equatorial (y-z) plane for a transverse (x direction) electric field polarized Gaussian beam, propagating in the +z axis direction (right-to-left), incident upon two adjacent spheres. $\tilde{n}_1 = \tilde{n}_2 = 1.179 + 0.072i, \alpha_1 = \alpha_2 = 13.337, \tilde{w}_0 = 2.222, \tilde{z}_0 = \tilde{y}_0 = 0.0, \tilde{z}_0 = -1.778, \tilde{x}_{12} = \tilde{y}_{12} = 0.0, \tilde{z}_{12} = 3.556, \tilde{x}_{ref} = \tilde{y}_{ref} = 0.0, \tilde{z}_{12} = 1.778$ [10.6 $\mu m$ wavelength ($CO_2$ laser), 100 $\mu m$ waist diameter beam incident upon two 45 $\mu m$ diameter water droplets separated along the propagation axis by 35 $\mu m$ surface-to-surface.]

FIG 2. *Normalized source function in the equatorial (y-z) plane for a transverse (x direction) electric field polarized Gaussian beam, propagating in the +z axis direction (right-to-left), incident upon two adjacent spheres.* $\bar{n}_1 = 1.305 + 0.0163i, \alpha_1 = 14.82, \bar{n}_2 = 1.179 + 0.072i, \alpha_2 = 8.89, \bar{w}_0 = 0.8, \bar{x}_0 = 0.0, \bar{y}_0 = 1.0, \bar{z}_0 = 0.0, \bar{x}_{12} = 0.0, \bar{y}_{12} = -1.0, \bar{z}_{12} = 3.0, \bar{x}_{ref} = 0.0, \bar{y}_{ref} = -0.5, \bar{z}_{12} = 1.5$ *[10.6 $\mu m$ wavelength (CO$_2$ laser), 40 $\mu m$ waist diameter beam incident upon adjacent 50 $\mu m$ diameter methanol and 30 $\mu m$ diameter water droplets offset in the y-z plane.]*
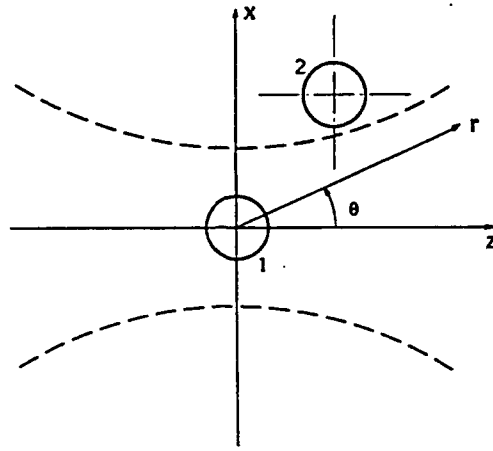
FIG 3. Arrangement for far field scattering calculations. Focused fundamental, linearly-polarized beam incident upon two adjacent spherical particles. The beam propagates in the $+z$ axis direction with electric field polarization in the x axis direction. Particle 1 is fixed in position at the focal point of the beam while the position of particle 2 is varied. An Argon-ion laser beam ($\lambda = 0.5145$ $\mu m$) with a 4 $\mu m$ beam waist diameter incident upon two adjacent 1.8 $\mu m$ diameter water droplets is assumed. $\bar{n}_1 = \bar{n}_2 = 1.334 + 1.2 \times 10^{-9}, \alpha_1 = \alpha_2 = 11.0, \bar{w}_0 = 2.22, \bar{x}_0 = \bar{y}_0 = \bar{z}_0 = 0.0$.
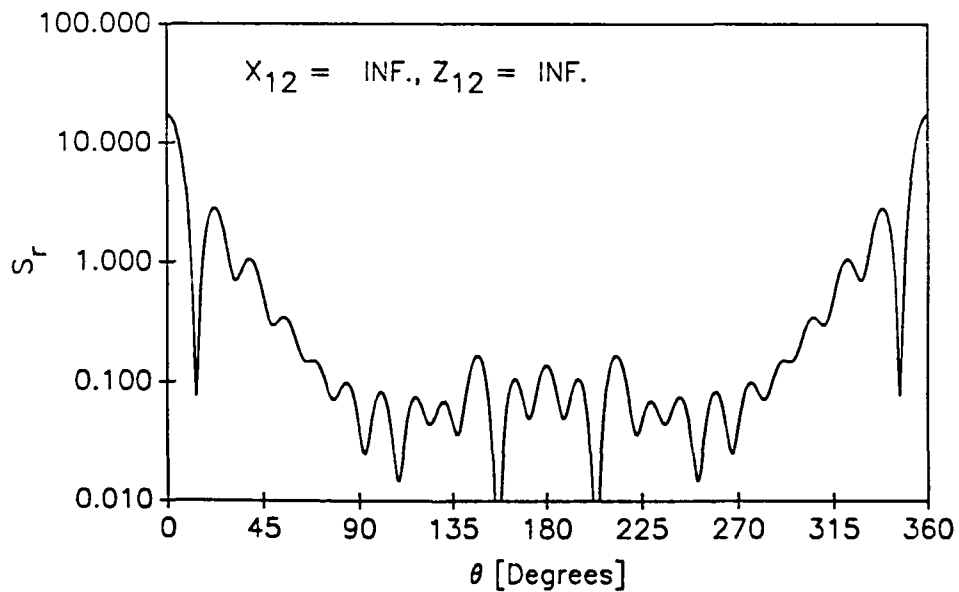


FIG 4. Normalized scattering intensity as a function of angle in the x-z plane for particle 2 far removed from the beam. (Single particle case.)
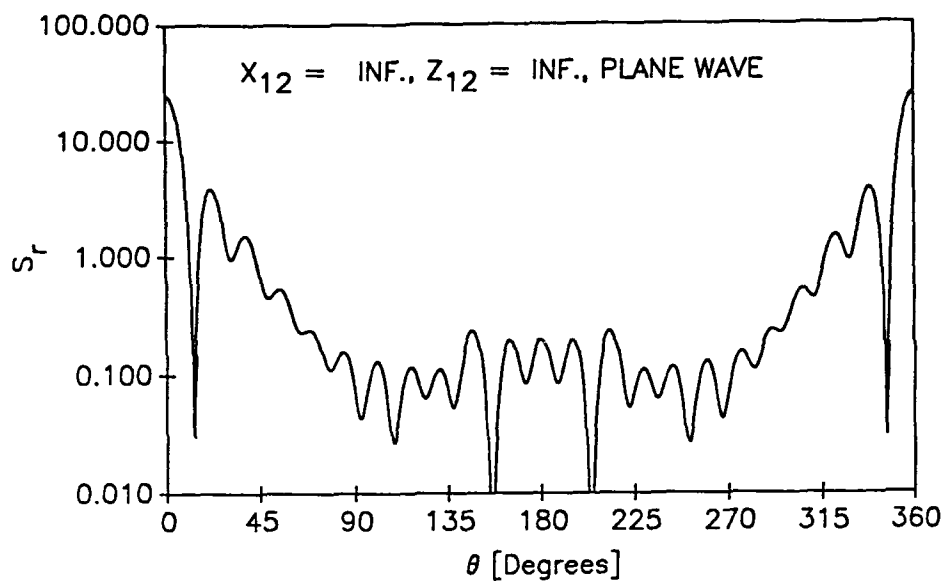
FIG 5. Normalized scattering intensity as a function of angle in the x-z plane for particle 2 far removed and plane wave illumination. (Single particle, plane wave case.)
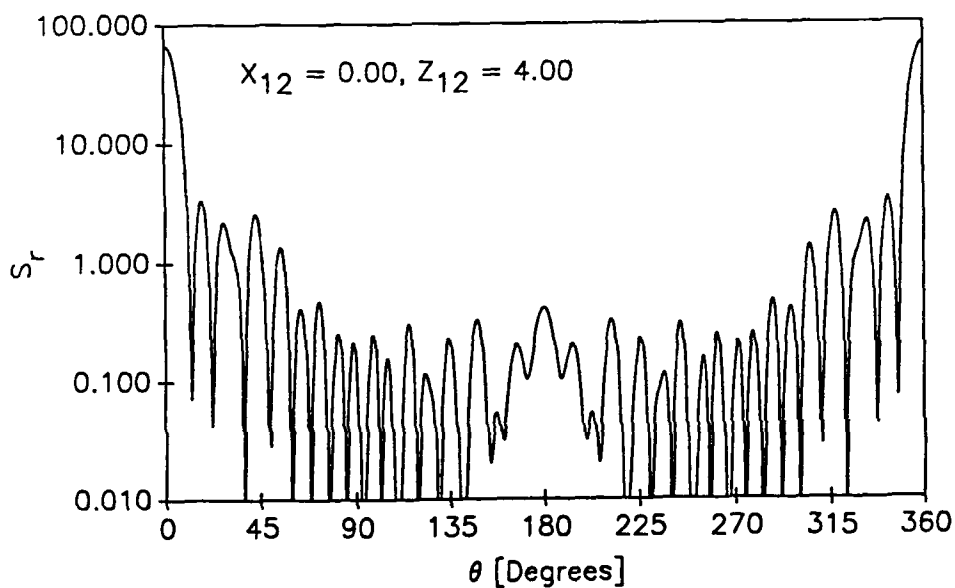


FIG 6. Normalized scattering intensity as a function of angle in the x-z plane for particle 2 positioned one diameter surface-to-surface away from particle 1 at an angle of 0° (on the + z axis). $\bar{x}_{12} = 0.0, \bar{y}_{12} = 0.0, \bar{z}_{12} = 4.00$ .
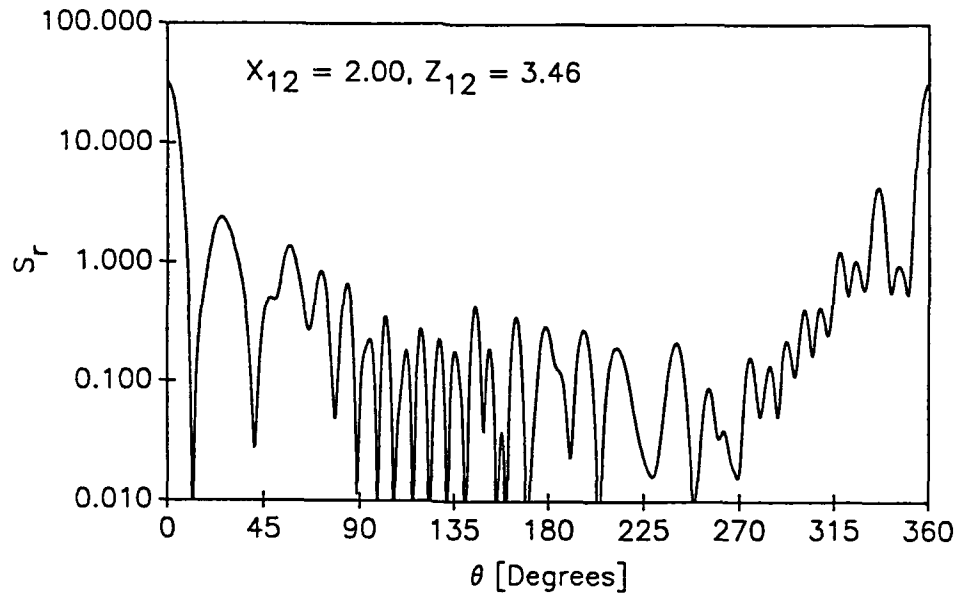
FIG 7. Normalized scattering intensity as a function of angle in the x-z plane for particle 2 positioned one diameter surface-to-surface away from particle 1 at an angle of $30^o$. $\bar{x}_{12} = 2.00, \bar{y}_{12} = 0.0, \bar{z}_{12} = 3.46$ .
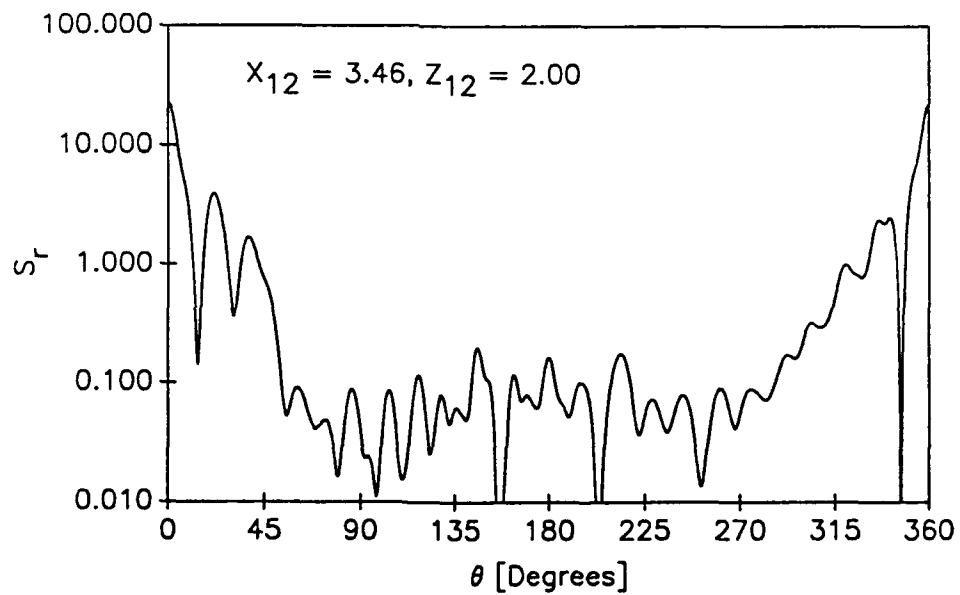


FIG 8. Normalized scattering intensity as a function of angle in the x-z plane for particle 2 positioned one diameter surface-to-surface away from particle 1 at an angle of $60^o$ . $\bar{x}_{12} = 3.46, \bar{y}_{12} = 0.0, \bar{z}_{12} = 2.00$ .
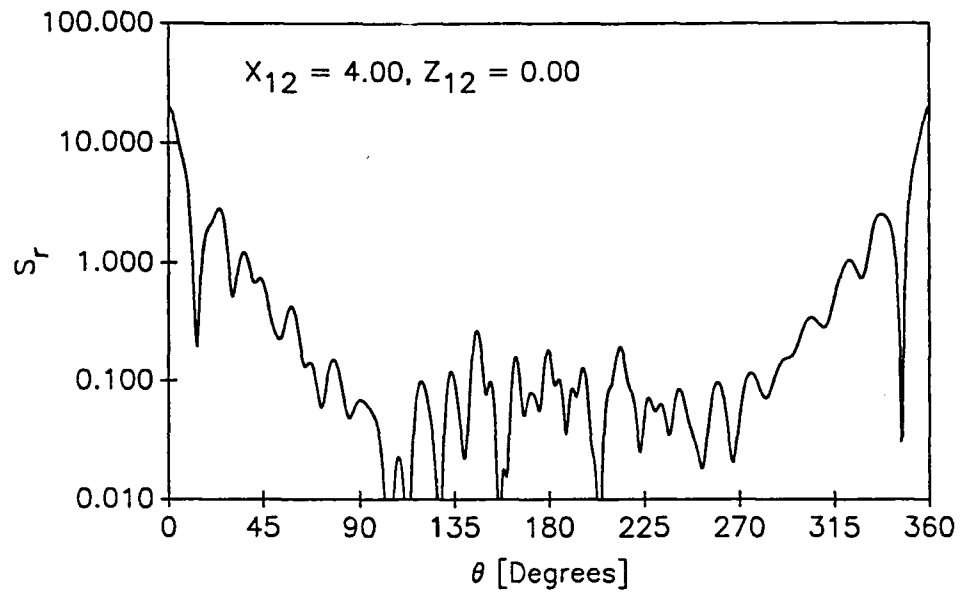
FIG 9. Normalized scattering intensity as a function of angle in the x-z plane for particle 2 positioned one diameter surface-to-surface away from particle 1 at an angle of $90°$ (on the + x axis). $\tilde{x}_{12} = 4.00, \tilde{y}_{12} = 0.0, \tilde{z}_{12} = 0.00$ .



FIG 10. Normalized scattering intensity as a function of angle in the x-z plane for particle 2 positioned one diameter surface-to-surface away from particle 1 at an angle of $120°$. $\tilde{x}_{12} = 3.46, \tilde{y}_{12} = 0.0, \tilde{z}_{12} = -2.00$ .
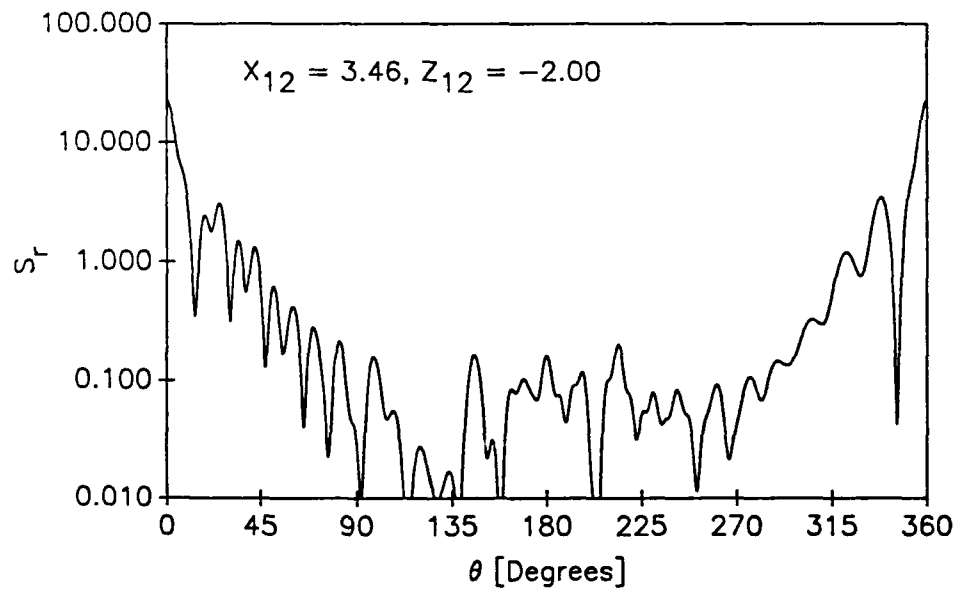
FIG 11. Normalized scattering intensity as a function of angle in the x-z plane for particle 2 positioned one diameter surface-to-surface away from particle 1 at an angle of 150° . $\bar{x}_{12} = 2.00, \bar{y}_{12} = 0.0, \bar{z}_{12} = -3.46$ .
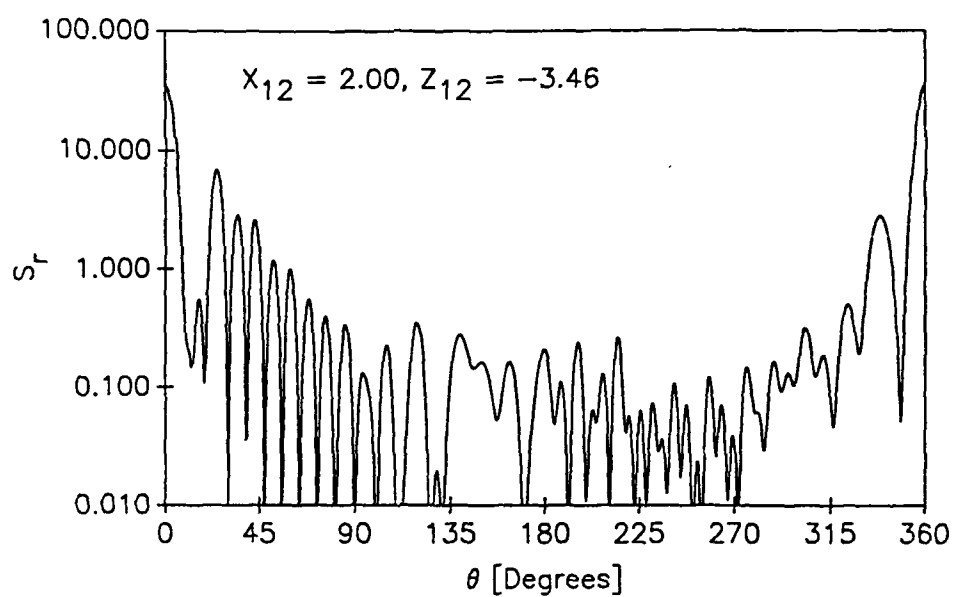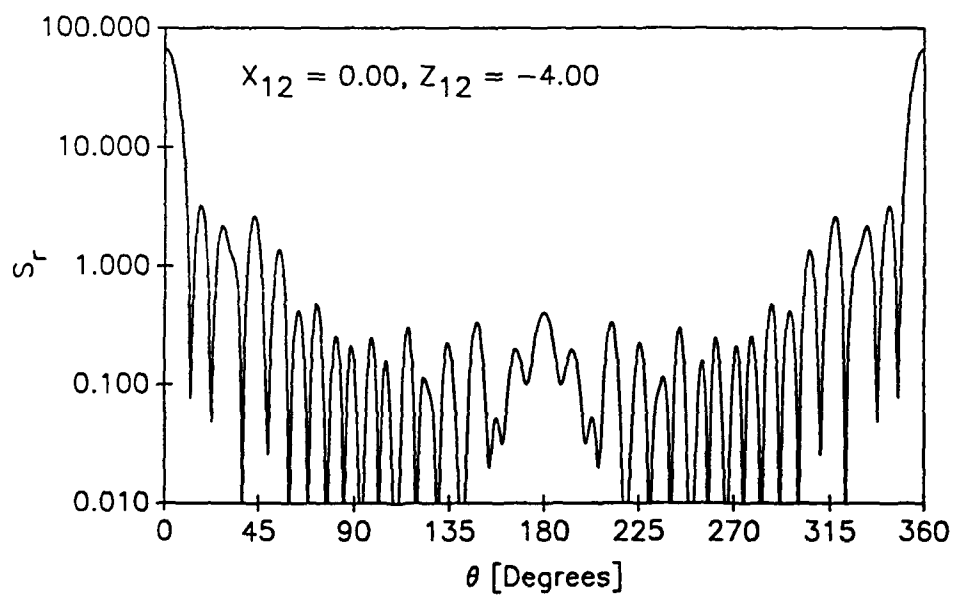


FIG 12. Normalized scattering intensity as a function of angle in the x-z plane for particle 2 positioned one diameter surface-to-surface away from particle 1 at an angle of 180° (on the - x axis). $\bar{x}_{12} = 0.0, \bar{y}_{12} = 0.0, \bar{z}_{12} = -4.00$ .

FIG 13. Normalized scattering intensity as a function of angle in the x-z plane for particle 2 positioned 6 radii along the +x axis. $\bar{x}_{12} = 6.00, \bar{y}_{12} = 0.0, \bar{z}_{12} = 0.0$ .



FIG 14. Normalized scattering intensity as a function of angle in the x-z plane for particle 2 positioned 12 radii along the +x axis. $\bar{x}_{12} = 12.0, \bar{y}_{12} = 0.0, \bar{z}_{12} = 0.0$ .

FIG 15. Normalized scattering intensity as a function of angle in the x-z plane for particle 2 positioned 18 radii along the +x axis. $\bar{x}_{12} = 18.0, \bar{y}_{12} = 0.0, \bar{z}_{12} = 0.0$ .
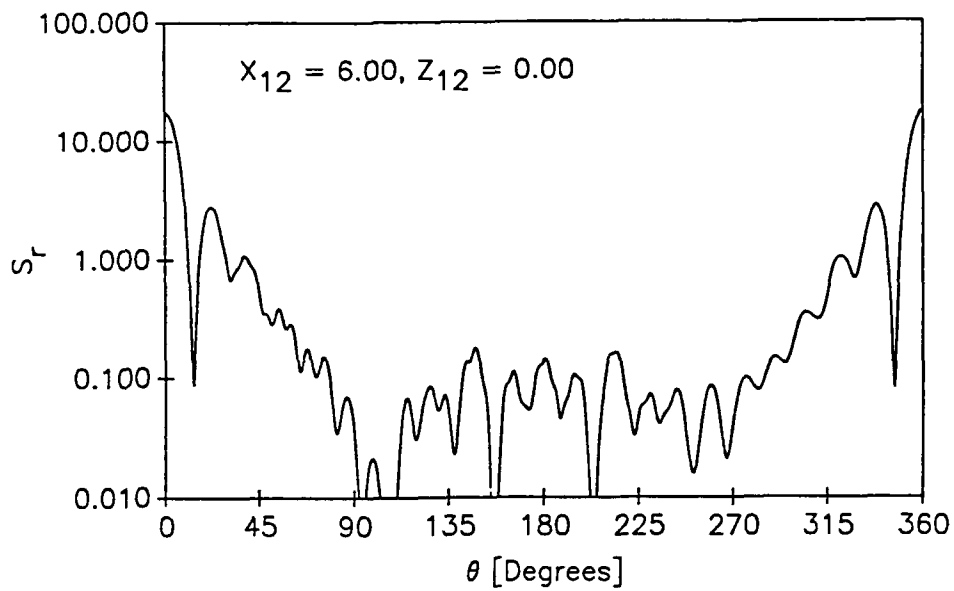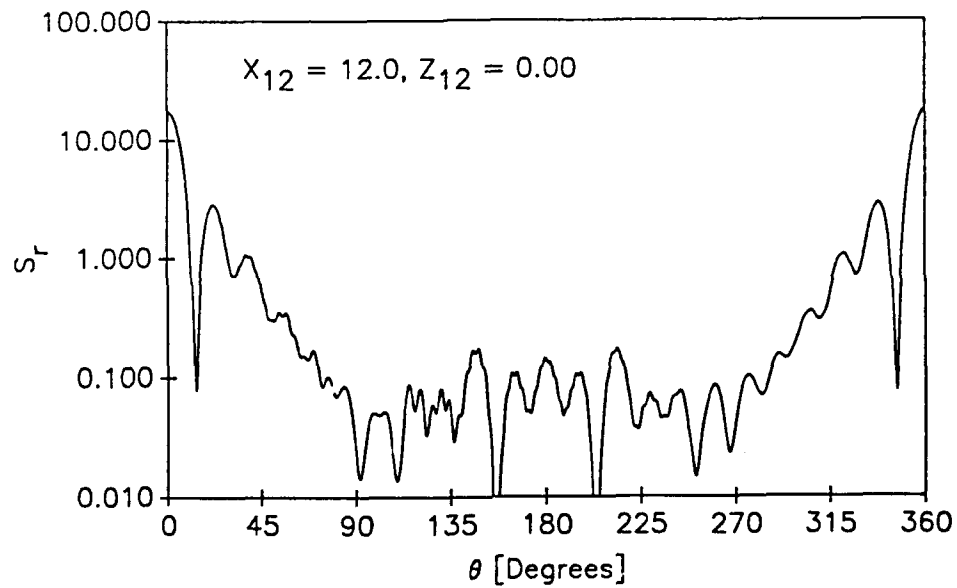


FIG 16. Normalized scattering intensity as a function of angle in the x-z plane for particle 2 positioned 10 radii along the +z axis. $\bar{x}_{12} = 0.0, \bar{y}_{12} = 0.0, \bar{z}_{12} = 10.0$ .

FIG 17. Normalized scattering intensity as a function of angle in the x-z plane for particle 2 positioned 20 radii along the +z axis. $\tilde{x}_{12} = 0.0, \tilde{y}_{12} = 0.0, \tilde{z}_{12} = 20.0$ .



FIG 18. Normalized scattering intensity as a function of angle in the x-z plane for particle 2 positioned 50 radii along the +z axis. $\tilde{x}_{12} = 0.0, \tilde{y}_{12} = 0.0, \tilde{z}_{12} = 50.0$ .
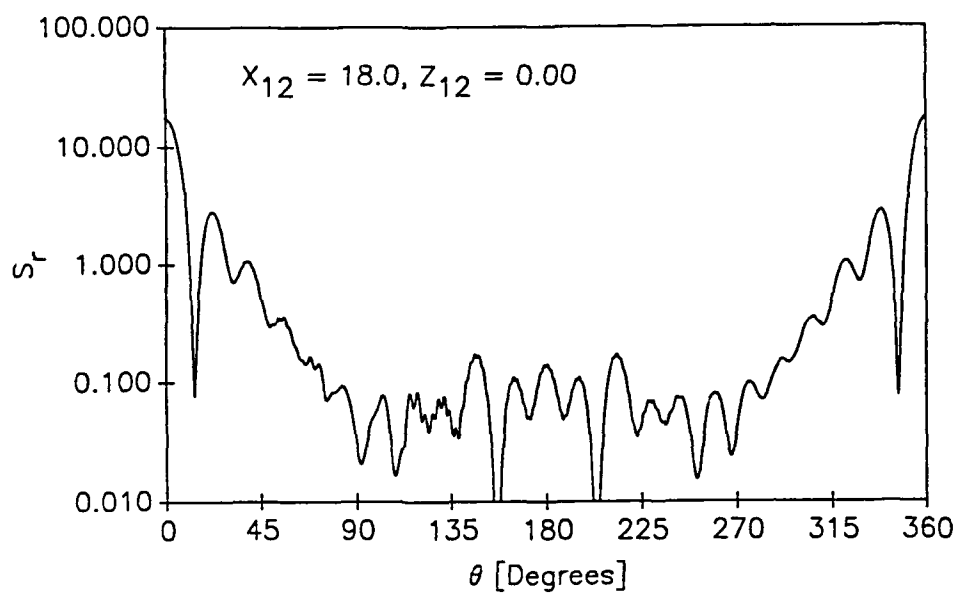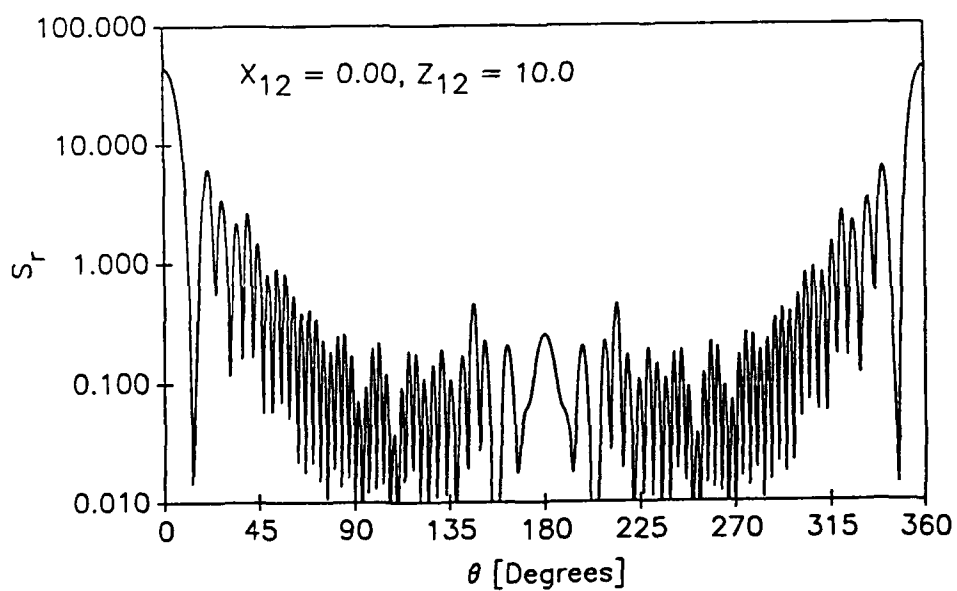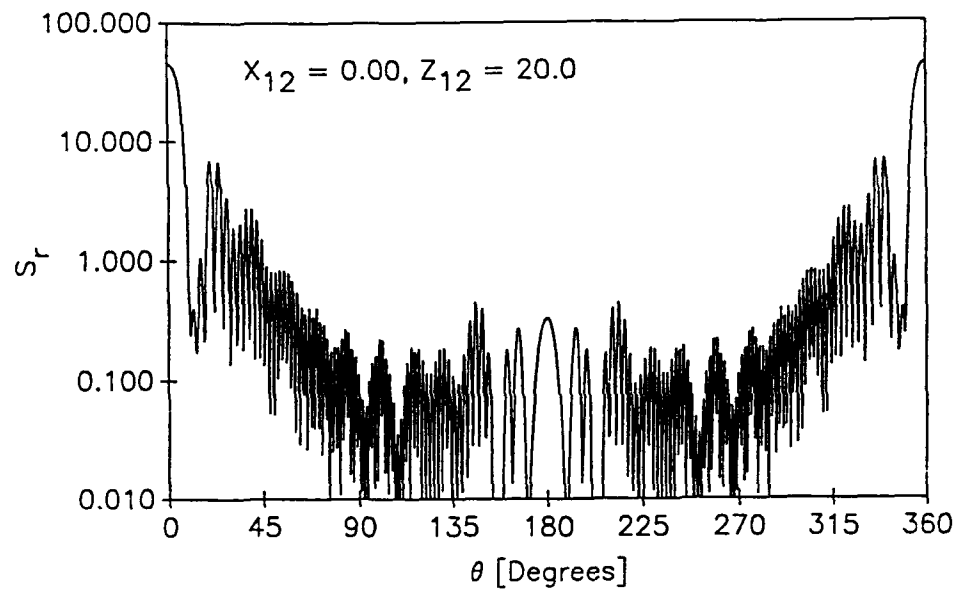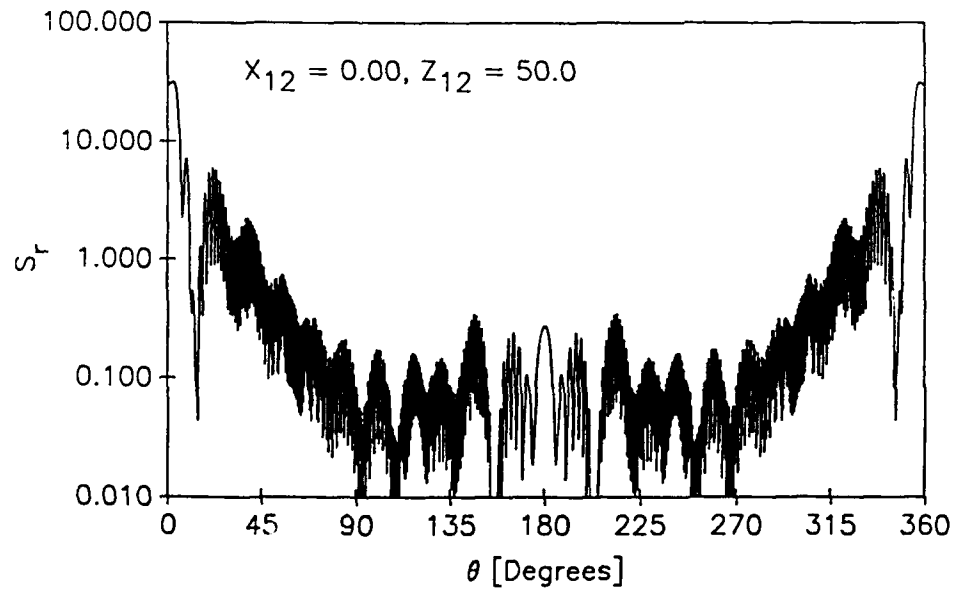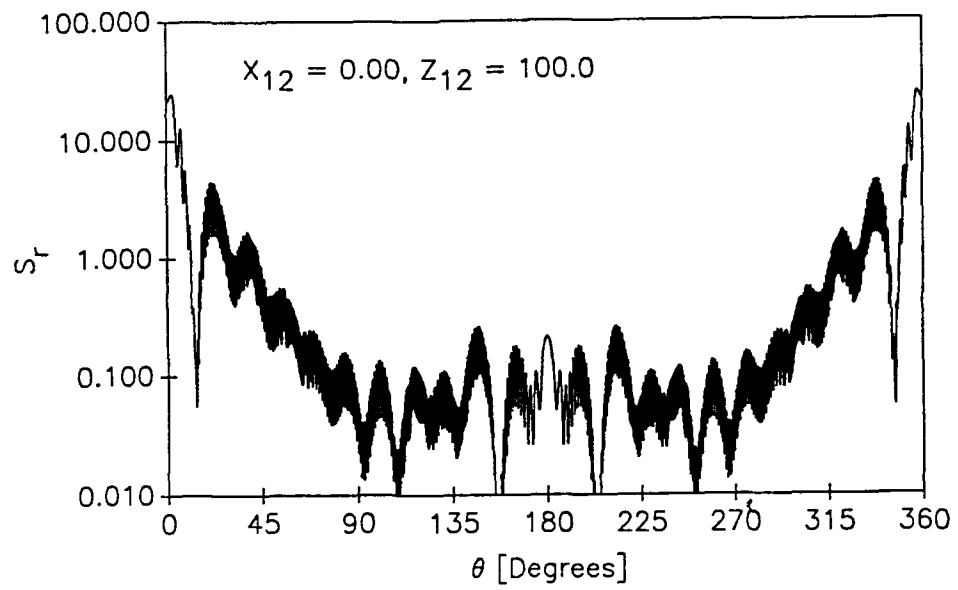
FIG 19. Normalized scattering intensity as a function of angle in the x-z plane for particle 2 positioned 100 radii along the +z axis. $\tilde{x}_{12} = 0.0, \tilde{y}_{12} = 0.0, \tilde{z}_{12} = 100.0$ .

# MODELING OF A COHERENT IMAGING SYSTEM

S.A. Schaub, D.R. Alexander, and J.P. Barton

University of Nebraska-Lincoln
Center for Electro-Optics
Lincoln, NE 68588-0656

## Abstract

A theoretical model is presented for the formation of spherical particle images in a laser-based imaging system. The model uses Lorenz-Mie theory in obtaining the electromagnetic fields at the imaging lens surface, the thin lens expression to propagate the field through the lens, and the Fresnel propagation equation to calculate the intensity distribution in the image plane. Comparisons between the theoretical calculations and experimental images are made for transparent water droplets at various degrees of particle defocus.

## I. Introduction

The problem of predicting particle images in a coherent imaging system has been addressed in several research papers during recent years. [1,2,3] The imaging problem is particularly important in the area of aerosol sizing since one of the most common instruments used in aerosol studies utilizes a laser-based imaging system for analysis. One of the major problems in using imaging systems for particle size analysis on real sprays is the development of reliable focus criteria for distinguishing in-focus from out-of-focus aerosol particles. Although empirical methods have been developed, it would be useful to have an accurate theoretical model to investigate the effects of particle defocus on various measurable parameters such as average gray level of the particle and boundary edge gradient. In this paper, results of the theoretical modeling of the laser/aerosol interaction and the subsequent propagation of the electromagnetic field through the imaging system is presented. Comparisons are made between experiment and theory for defocused water droplets generated with a monodisperse aerosol generator.

## II. Problem Description

The geometry for the single lens imaging system under consideration is shown schematically in Fig. 1. The aerosol particle of radius $a$, located at the intersection of plane $z_0$ and the imaging system axis, is assumed to be perfectly spherical, nonmagnetic, homogeneous, isotropic, and finite absorbing. The external medium is also assumed to be homogeneous, isotropic, and nonmagnetic in addition to being optically nonabsorbing. The particle is assumed to be illuminated by a monochromatic, linearly polarized laser beam propagating in the $+z$ direction with the electric field polarization in the x direction. Note that the incident laser propagation axis and the imaging system axis are coincident as shown in the figure. In general, this will not be a necessary restriction on the theoretical model. However, due to the loss of symmetry in the electromagnetic field expressions for the off-axis case, the numerical evaluation of the resulting equations would be more time consuming. The receiving optics of the imaging system consists of a single lens with focal length f and diameter $= 2r_l$. Although in this particular case a plano-convex lens is shown, the modeling technique could be used for other lens geometries provided symmetry exists about the z axis. An aperture of diameter $= 2r_a$, located at plane $z_1$, acts to limit the effective diameter of the lens. A video camera serves as the recording medium and is located at the image plane ($z_3$) of the system which is located approximately 1 meter from the lens.
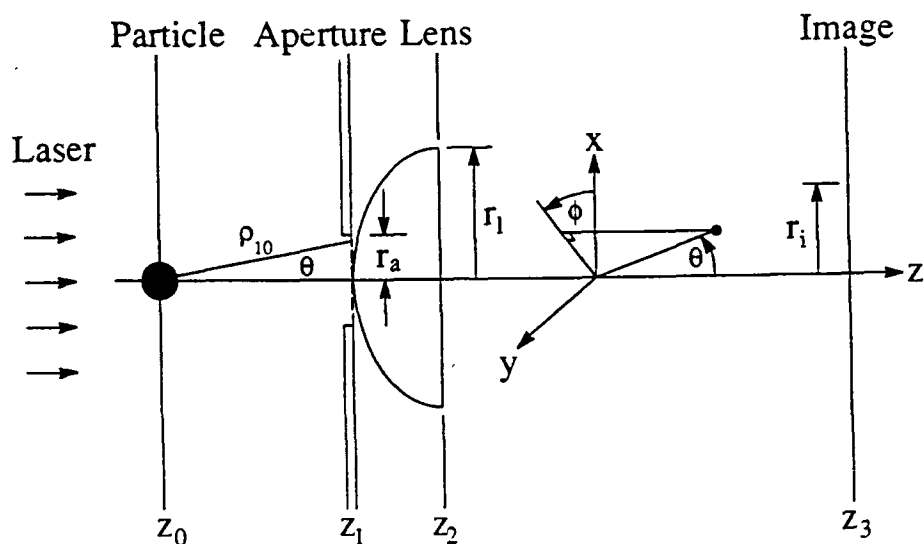
Fig. 1. Schematic of Imaging System Geometry

## III. Scalar Model

In a scalar approach to modeling the laser/aerosol imaging problem, only the scalar amplitude of one transverse component of the electric or magnetic field is considered. This neglects the fact that the electric and magnetic field components are coupled through Maxwell's equations and cannot be treated independently. In many cases, however, the scalar approach has provided satisfactory results and only through direct comparison to experimental observation can one determine if the scalar theory is applicable for a specific situation.

Figure 1 shows a schematic of the imaging system under consideration. The incident illuminating radiation is generated from a pulsed nitrogen laser ($\lambda = 337$ nm) and is modeled as a plane wave propagating in the +z direction with electric field polarization in the x direction. The theoretical development for illumination by any arbitrary electromagnetic field [4] would proceed in a similar manner although the numerical evaluation of the resulting expressions becomes more involved. In the following discussion the x-component of the electric field external to the sphere is denoted by $E_m$, where the subscript refers to the electric field evaluated at plane $z_m$. The choice of the x component of the electric field as the dominant electric field component was based on direct computation of the external field and is physically reasonable since the incident radiation is polarized predominantly in the x direction. The external electric field at plane $z_1$ can be calculated based on the exact solution provided by Lorenz-Mie theory. [5,6] A more recent derivation of the electromagnetic field equations can be found in Born and Wolf. [7] The equations for the Lorenz-Mie external field components used in the theoretical development are outlined in Appendix A.

The imaging lens used in the system is assumed a pure dielectric and to possess symmetry about the imaging system axis. From a geometrical optics point of view, the phase transformation, $T$, introduced by the lens can be expressed in the general form,

$$T(r,\phi) = A(r,\phi)e^{ikln} \tag{1}$$

where $A$ is the amplitude factor accounting for the reflection losses at the interface, $n$ is the index of refraction of the lens, $l$ is the path length of a given light ray through the lens, and $k=2\pi/\lambda$.

In general, the amplitude factor is a function of the azimuthal angle since the Fresnel coefficients, which govern the reflection losses, are different for parallel and perpendicular polarizations.

To calculate the intensities in the image plane, an expression is needed to account for the propagation of the electric field from the lens back ($z_2$) to the image plane ($z_3$). The general form for the scalar propagation is given by the Huygens-Fresnel equation, [8]

$$E_3(r_3,\phi_3) = \frac{1}{i\lambda} \int \int_A E_2(r_2,\phi_2) \frac{exp(ikr_{23})}{r_{23}} cos(\hat{n},\hat{r}_{23})\, dA, \qquad (2)$$

where $\hat{n}$ is the unit normal to the back lens surface (plane $z_2$) and $r_{23}$ represents the distance between respective points in plane $z_2$ and $z_3$. Although this expression gives good results in many applications, the difficulty in obtaining any analytical simplifications limits its usefulness. For situations, such as those under consideration, in which the distance between the source (in this case the field at plane $z_2$) and the image plane is large, certain simplifications can be utilized. When the inequality

$$(z_3 - z_2) >> \frac{\pi}{4\lambda}\left[(x_3 - x_2)^2 + (y_3 - y_2)^2\right]^2_{max}, \qquad (3)$$

holds, the Fresnel approximations can be used in which several simplifying approximations are implemented. [8] First, $r_{23}$ in the amplitude term can be replaced by the perpendicular distance, $(z_3 - z_2)$. Second, since the angle between the normal to the lens back ($\hat{n}$) and the unit vector ($\hat{r}_{23}$) is always small, the obliquity factor can be approximated by unity. The final simplification is in the phase term in which $r_{23}$ is approximated by the first two terms in the binomial expansion,

$$r_{23} = \sqrt{(z_3 - z_2)^2 + (x_3 - x_2)^2 + (y_3 - y_2)^2} \approx (z_3 - z_2)\left[1 + \frac{1}{2}\left(\frac{x_3 - x_2}{z_3 - z_2}\right)^2 + \frac{1}{2}\left(\frac{y_3 - y_2}{z_3 - z_2}\right)^2\right]. \qquad (4)$$

Using these simplifications, the external electric field at the image plane can be expressed in terms of the external electric field at the rear lens surface by the integral,

$$E_3(x_3,y_3) = \frac{exp[ik(z_3 - z_2)]}{i\lambda(z_3 - z_2)} \int \int_A E_2(x_2,y_2)\, exp\left\{\frac{ik}{2(z_3 - z_2)}\left[(x_3 - x_2)^2 + (y_3 - y_2)^2\right]\right\} dx_2 dy_2. \qquad (5)$$

where the subscript on $E$ denotes the x-component of the external electric field evaluated at a given z=constant plane. In the situation under consideration, the inequality in Eq. (3) holds by roughly one order of magnitude. As a further check on the validity of the Fresnel approximations, calculations were performed using both the Huygens-Fresnel equation (Eq. (2)) and the Fresnel propagation equation (Eq. (5)) for a plane wave illuminating the imaging lens. Results showed excellent agreement between the two expression. Due to the analytical simplifications possible using the Fresnel approximation, it will be the expression used in the following scalar model. Measuring $\phi$ with respect to the +x axis, Eq. (5) can be rewritten in terms of r-$\phi$ coordinates (i.e., $x_m = r_m \cos\phi_m$ and $y_m = r_m \sin\phi_m$ for plane $z_m$) giving,

$$\begin{aligned}E_3(r_3,\phi_3) &= \frac{exp[ik(z_3 - z_2)]}{i\lambda(z_3 - z_2)} \int \int_A E_2(r_2,\phi_2)\, exp\left\{\frac{ik}{2(z_3 - z_2)}\right. \\ &\quad \times \left.\left[(r_3\cos\phi_3 - r_2\cos\phi_2)^2 + (r_3\sin\phi_3 - r_2\sin\phi_2)^2\right]\right\} r_2\, dr_2\, d\phi_2.\end{aligned} \qquad (6)$$

Using the expression given in Eq. (1), simplifying the term in [ ] in Eq. (6), and noting that $\phi_1 = \phi_2$, Eq. (6) can be simplified yielding,

$$\begin{aligned}E_3(r_3,\phi_3) &= \frac{exp[ik(z_3 - z_2)]}{i\lambda(z_3 - z_2)}\, exp\left[\frac{ikr_3^2}{2(z_3 - z_2)}\right] \int_0^{r_a} r_2(r_1)\, exp\left[\frac{ik\, r_2(r_1)^2}{2(z_3 - z_2)}\right] \\ &\quad \times \int_0^{2\pi} T(r_1,\phi_1)\, E_1(\rho_{10},\theta,\phi_1)\, exp\left[-\frac{ik\, r_2(r_1)\, r_3}{2(z_3 - z_2)}\cos(\phi_1 - \phi_3)\right] d\phi_1\, dr_1,\end{aligned} \qquad (7)$$

where the integration is over the area bounded by the aperture. At this point we have assumed the field in the aperture can be approximated by the external field which exists at the aperture. Note that, in general, $r_2$ is expressed as function of $r_1$ due to the refraction of light through the optically denser lens. As stated earlier, the phi dependence in the phase transformation given in Eq. (1) results from the polarization dependence of the Fresnel coefficients. These differences between reflection coefficients for parallel and perpendicular polarization are most pronounced at large incident angles. For the cases under consideration, however, most rays incident on the front lens surface are nearly parallel to the lens axis and all reflections are nearly normal. Under such conditions, the phi dependence in the reflected light intensity is extremely weak. In addition, the absolute values of the intensities in the image plane are of secondary importance to the relative intensities. Based on these facts, the amplitude factor, $A$, in Eq. (1) will be assumed independent of phi and will be neglected in the following development. For this case, the phase transformation can be considered independent of phi and Eq. (7) can be rewritten as,

$$
\begin{aligned}
E_3(r_3, \phi_3) &= \frac{exp[ik(z_3 - z_2)]}{i\lambda(z_3 - z_2)} exp\left[\frac{ikr_3^2}{2(z_3 - z_2)}\right] \int_0^{r_a} r_2(r_1) exp\left[\frac{ik\, r_2(r_1)^2}{2(z_3 - z_2)}\right] \\
&\times \quad T(r_1) \int_0^{2\pi} E_1(\rho_{10}, \theta, \phi_1) exp\left[-\frac{ik\, r_2(r_1)\, r_3}{2(z_3 - z_2)} cos(\phi_1 - \phi_3)\right] d\phi_1\, dr_1.
\end{aligned}
\tag{8}
$$

To account for the phi dependence in the electric field expression, it is first necessary to expand the x-component of the external electric field in terms of spherical components of the separate incident and scattered fields,

$$
E_1 = [E_{1r}^{(inc)} + E_{1r}^{(sca)}] sin\,\theta\, cos\,\phi_1 + [E_{1\theta}^{(inc)} + E_{1\theta}^{(sca)}] cos\,\theta\, cos\,\phi_1 - [E_{1\phi}^{(inc)} + E_{1\phi}^{(sca)}] sin\,\phi_1.
\tag{9}
$$

Here the superscripts denote the incident and scattered fields while the subscripts denote the $r$, $\theta$, and $\phi$ components of the field in plane $z_1$. Using the expressions for the field components given by Lorenz-Mie theory (see Appendix A), Eq. (9) can be written as,

$$
\begin{aligned}
\tilde{E}_1(\tilde{\rho}_{10}, \theta, \phi_1) &= \left[e^{i\alpha\tilde{z}_1} sin\,\theta\, cos\,\phi_1 + \frac{cos\,\phi_1}{(\alpha\tilde{\rho}_{10})^2} \sum_{l=1}^{\infty} l(l+1)\, a_l\, \xi_l^{(1)}(\alpha\tilde{\rho}_{10})\, P_l^{(1)}(cos\,\theta)\right] sin\,\theta\, cos\,\phi_1 \\
&+ \left[e^{i\alpha\tilde{z}_1} cos\,\theta\, cos\,\phi_1 - \frac{cos\,\phi_1}{\alpha\tilde{\rho}_{10}} \sum_{l=1}^{\infty} \left(a_l\, \xi_l^{(1)'}(\alpha\tilde{\rho}_{10})\, P_l^{(1)'}(cos\,\theta)sin\,\theta\right.\right. \\
&\qquad\qquad\qquad \left.\left. -b_l\xi_l^{(1)}(\alpha\tilde{\rho}_{10})\, P_l^{(1)}(cos\,\theta)\frac{i}{sin\,\theta}\right)\right] cos\,\theta\, cos\,\phi_1 \\
&+ \left[e^{i\alpha\tilde{z}_1} sin\,\phi_1 + \frac{sin\,\phi_1}{\alpha\tilde{\rho}_{10}} \sum_{l=1}^{\infty} \left(a_l\, \xi_l^{(1)'}(\alpha\tilde{\rho}_{10})\, P_l^{(1)}(cos\,\theta)\frac{1}{sin\,\theta}\right.\right. \\
&\qquad\qquad\qquad \left.\left. -i\, b_l\xi_l^{(1)}(\alpha\tilde{\rho}_{10})\, P_l^{(1)'}(cos\,\theta)\, sin\,\theta\right)\right] sin\,\phi_1.
\end{aligned}
\tag{10}
$$

Note that Eq. (10) is expressed in terms of dimensionless variables (denoted by tilde). All spatial variable have been normalized by the radius of the particle, $a$. Factoring out the phi dependence, Eq. (10) can be expressed in the form,

$$
\tilde{E}_1(\tilde{\rho}_{10}, \theta, \phi_1) = cos^2\phi_1\, [\tilde{F}_r(\tilde{\rho}_{10}, \theta) + \tilde{F}_\theta(\tilde{\rho}_{10}, \theta)] + sin^2\phi_1\, \tilde{F}_\phi(\tilde{\rho}_{10}, \theta)
\tag{11}
$$

where,

$$\tilde{F}_r(\tilde{\rho}_{10}, \theta) = \sin^2\theta \, e^{i\alpha z_1} + \frac{\sin\theta}{(\alpha\tilde{\rho}_{10})^2} \sum_{l=1}^{\infty} l(l+1) a_l \, \xi_l^{(1)}(\alpha\tilde{\rho}_{10}) \, P_l^{(1)}(\cos\theta), \qquad (12)$$

$$\tilde{F}_\theta(\tilde{\rho}_{10}, \theta) = \cos^2\theta \, e^{i\alpha z_1} - \frac{\cos\theta}{\alpha\tilde{\rho}_{10}} \sum_{l=1}^{\infty} \left( a_l \, \xi_l^{(1)'}(\alpha\tilde{\rho}_{10}) \, P_l^{(1)'}(\cos\theta)\sin\theta \right.$$
$$\left. - b_l \, \xi_l^{(1)}(\alpha\tilde{\rho}_{10}) \, P_l^{(1)}(\cos\theta)\frac{i}{\sin\theta} \right), \qquad (13)$$

and

$$\tilde{F}_\circ(\tilde{\rho}_{10}, \theta) = e^{i\alpha z_1} + \frac{1}{\alpha\tilde{\rho}_{10}} \sum_{l=1}^{\infty} \left( a_l \, \xi_l^{(1)'}(\alpha\tilde{\rho}_{10}) \, P_l^{(1)}(\cos\theta)\frac{1}{\sin\theta} - i \, b_l \, \xi_l^{(1)}(\alpha\tilde{\rho}_{10}) \, P_l^{(1)'}(\cos\theta)\sin\theta \right).$$
$$(14)$$

Substituting Eq. (11) into Eq. (8),

$$E_3(r_3, \phi_3) = \frac{exp[ik(z_3 - z_2)]}{i\lambda(z_3 - z_2)} exp\left[\frac{ikr_3^2}{2(z_3 - z_2)}\right] \int_0^{r_a} r_2(r_1) \, exp\left[\frac{ik \, r_2(r_1)^2}{2(z_3 - z_2)}\right] T(r_1)$$

$$\times \left\{ \left[ \tilde{F}_r(\tilde{\rho}_{10}, \theta) + \tilde{F}_\theta(\tilde{\rho}_{10}, \theta) \right] \int_0^{2\pi} \cos^2\phi_1 \, exp\left[ -\frac{ik \, r_2(r_1) \, r_3}{2(z_3 - z_2)}\cos(\phi_1 - \phi_3) \right] d\phi_1 \right.$$

$$\left. + \tilde{F}_\circ(\tilde{\rho}_{10}, \theta) \int_0^{2\pi} \sin^2\phi_1 \, exp\left[ -\frac{ik \, r_2(r_1) \, r_3}{2(z_3 - z_2)}\cos(\phi_1 - \phi_3) \right] d\phi_1 \right\} dr_1. \qquad (15)$$

The phi integrals in Eq. (15) can be evaluated exactly using the relationships,

$$I_1 = \int_0^{2\pi} \cos^2\phi_1 \, exp[-i\beta\cos(\phi_1 - \phi_3)] \, d\phi_1 = \pi[J_0(\beta) - J_2(\beta)\cos(2\phi_3)], \qquad (16)$$

$$I_2 = \int_0^{2\pi} \sin^2\phi_1 \, exp[-i\beta\cos(\phi_1 - \phi_3)] \, d\phi_1 = \pi[J_0(\beta) + J_2(\beta)\cos(2\phi_3)], \qquad (17)$$

to yield,

$$E_3(r_3, \phi_3) = \frac{\pi \, exp[ik(z_3 - z_2)]}{i\lambda(z_3 - z_2)} exp\left[\frac{ikr_3^2}{2(z_3 - z_2)}\right] \int_0^{r_a} r_2(r_1) \, exp\left[\frac{ik \, r_2(r_1)^2}{2(z_3 - z_2)}\right] T(r_1)$$

$$\times \left\{ \left[ \tilde{F}_r(\tilde{\rho}_{10}, \theta) + \tilde{F}_\theta(\tilde{\rho}_{10}, \theta) \right] \left[ J_0(\beta) - J_2(\beta)\cos(2\phi_3) \right] \right.$$

$$\left. + \tilde{F}_\circ(\tilde{\rho}_{10}, \theta) \left[ J_0(\beta) + J_2(\beta)\cos(2\phi_3) \right] \right\} dr_1. \qquad (18)$$

In this expression, $J_0$ and $J_2$ are integer order Bessel functions of the first kind and,

$$\beta = \frac{k \, r_2(r_1) \, r_3}{2(z_3 - z_2)}. \qquad (19)$$

In terms of intensity,

$$I_3(r_3, \phi_3) = E_3(r_3, \phi_3) \, E_3^*(r_3, \phi_3) = \frac{\pi^2}{\lambda^2(z_3 - z_2)^2} \left| \int_0^{r_a} r_2(r_1) \, T(r_1) \right.$$

$$\times \, exp\frac{ik \, r_2(r_1)^2}{2(z_3 - z_2)} \left\{ \left[ \tilde{F}_r(\tilde{\rho}_{10}, \theta) + \tilde{F}_\theta(\tilde{\rho}_{10}, \theta) \right] \left[ J_0(\beta) - J_2(\beta)\cos(2\phi_3) \right] \right.$$

$$\left. \left. + \tilde{F}_\phi(\tilde{\rho}_{10}, \theta) \left[ J_0(\beta) + J_2(\beta)\cos(2\phi_3) \right] \right\} dr_1 \right|^2, \qquad (20)$$

where the asterisk denotes the complex conjugate. Equation (20) can be rewritten in terms of dimensionless variables to give,

$$
\begin{aligned}
\tilde{I}_3(\tilde{r}_3, \phi_3) &= \frac{a^2}{4(\tilde{z}_3 - \tilde{z}_2)^2} \left| \int_0^{\tilde{r}_a} \tilde{r}_2(\tilde{r}_1) \, \tilde{T}(\tilde{r}_1) \, exp\left[\frac{ia\tilde{r}_2(\tilde{r}_1)^2}{2(\tilde{z}_3 - \tilde{z}_2)}\right] \right. \\
&\quad \times \left\{ \left[ \tilde{F}_r(\tilde{\rho}_{10}, \theta) + \tilde{F}_\theta(\tilde{\rho}_{10}, \theta) \right] \left[ J_0(\tilde{\beta}) - J_2(\tilde{\beta}) \cos(2\phi_3) \right] \right. \\
&\quad + \left. \left. \tilde{F}_\phi(\tilde{\rho}_{10}, \theta) \left[ J_0(\tilde{\beta}) + J_2(\tilde{\beta}) \cos(2\phi_3) \right] \right\} d\tilde{r}_1 \right|^2
\end{aligned}
\tag{21}
$$

where $r$ and $z$ are normalized by the particle radius and

$$
\tilde{\beta} = \frac{\tilde{r}_2(\tilde{r}_1) \, \tilde{r}_3 \, \alpha}{(\tilde{z}_3 - \tilde{z}_2)}.
\tag{22}
$$

To generate computational results, it is necessary to determine the specific form of the phase transformation, $T$. Probably the most straightforward approach would be to utilize the thin lens transformation as presented by Goodman [8] where,

$$
T(x, y) = exp(ikn\Delta_0) \, exp\left[\frac{-ik}{2f}(x^2 + y^2)\right],
\tag{23}
$$

where $\Delta_0$ is the lens thickness and $f$ is the focal length. The phase transformation is composed of a constant phase delay dependent on the lens thickness and a variable phase delay which is a function of the radial distance from the axis of the lens. In this expression, the lens thickness and likewise any refraction through the lens is neglected thus making $r_2(r_1) = r_1$. Substituting the nondimensional form of the phase transformation given by Eq. (23) into Eq. (21) will give the result,

$$
\begin{aligned}
\tilde{I}_3(\tilde{r}_3, \phi_3) &= \frac{a^2}{4(\tilde{z}_3 - \tilde{z}_2)^2} \left| \int_0^{\tilde{r}_a} \tilde{r}_1 \, exp\left[\frac{ia\tilde{r}_1^2}{2}\left(\frac{1}{\tilde{z}_3 - \tilde{z}_2} - \frac{1}{f}\right)\right] \right. \\
&\quad \times \left\{ \left[ \tilde{F}_r(\tilde{\rho}_{10}, \theta) + \tilde{F}_\theta(\tilde{\rho}_{10}, \theta) \right] \left[ J_0(\tilde{\beta}) - J_2(\tilde{\beta}) \cos(2\phi_3) \right] \right. \\
&\quad + \left. \left. \tilde{F}_\phi(\tilde{\rho}_{10}, \theta) \left[ J_0(\tilde{\beta}) + J_2(\tilde{\beta}) \cos(2\phi_3) \right] \right\} d\tilde{r}_1 \right|^2
\end{aligned}
\tag{24}
$$

where

$$
\beta = \frac{\tilde{r}_1 \tilde{r}_3 \alpha}{(\tilde{z}_3 - \tilde{z}_2)}.
\tag{25}
$$

## IV. Computations and Experimental Comparison

To generate numerical results, the expressions given in Eqs. (12-14, 24, 25) were implemented into a Fortran computer code. Initial calculations for the case of a perfectly transparent droplet showed a significant amount of structure in the calculated image intensity. In particular, the field far from the particle edge showed evidence of periodic oscillations. This effect can also be seen in the calculation presented by Thompson and Malyak. [1] These oscillations were not consistent with experimental observation in which a uniform background was observed for plane wave illumination of the aperture (i.e., no particle in the imaging system). It was found that these oscillations could

be minimized by introducing a gradual decrease in the electric field distribution in the form of a cosine taper over the outer 2 percent of the aperture. As a check on the validity of the numerical calculations, results were generated for small apertures (i.e., 20-100 $\mu$m) with $f \rightarrow \infty$ and $\bar{n} = 1.0 + 0.0i$. Under these conditions, the calculations were in agreement with the results expected from diffraction theory for a circular aperture.

To perform the experimental comparisons, a laser-imaging system was configured as shown in Fig. 2. The illumination source was a Laser Energy Inc. pulsed nitrogen laser with a 10 ns pulse width. The image of the particles were projected to a Cohu 2006 video camera system using a 50 mm focal length plano-convex lens. The video signal was then sent to a Panasonic TQ-3031F optical disk recorder where it was recorded so that later analysis could be performed. The recorded images were later digitized using a host microcomputer (Gateway 2000, 33 MHz-386) equipped with a Data Translation 2861 frame grabber and 2858 frame processor. Averages of 10 separate images were used to generate the experimental data. The monodisperse water droplets were generated using an Aerometrics Inc. vibrating orifice generator.
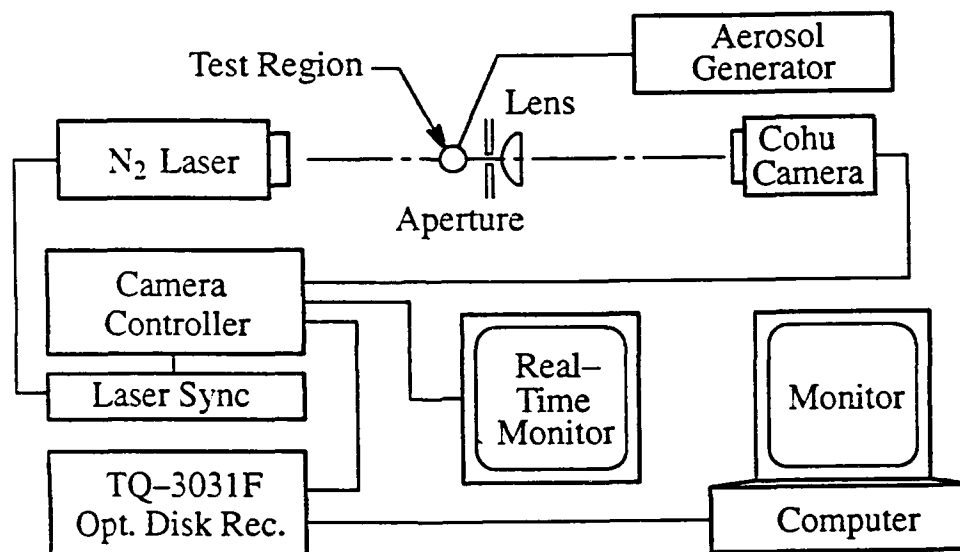


Fig. 2. Experimental Setup

Figures 3-6 show plots of the experimental data and theoretical calculations for 57 $\mu$m diameter water droplets with complex refractive index, [9] $\bar{n} = 1.345 + 8.7 \times 10^{-9}i$. Figures 3 and 4 show results for the water droplets defocused 44 and 73 diameters in a direction toward the lens. The aperture size for these cases was 4 mm. Figures 5 and 6 show the same size water droplets moved 17 and 22 diameters away from the lens, with a corresponding aperture size of 7 mm.

In general, the theoretical results were in reasonably good agreement with the experimental data. Most major features such as the boundary gradient, the first internal minimum, and the first external maximum show good agreement. The major discrepancy between the two lies in the absence of the high frequency effects which are predicted by theory. Since the theoretical model imposes several assumptions, it is unclear whether the discrepancy lies in the theoretical calculations or in the experimental data. There are several possible reasons why these high frequency effects would not be clearly observed in the experimental data. First, the motion of the droplets through the test region will tend to smear fine detail in the image. The imaging system also has
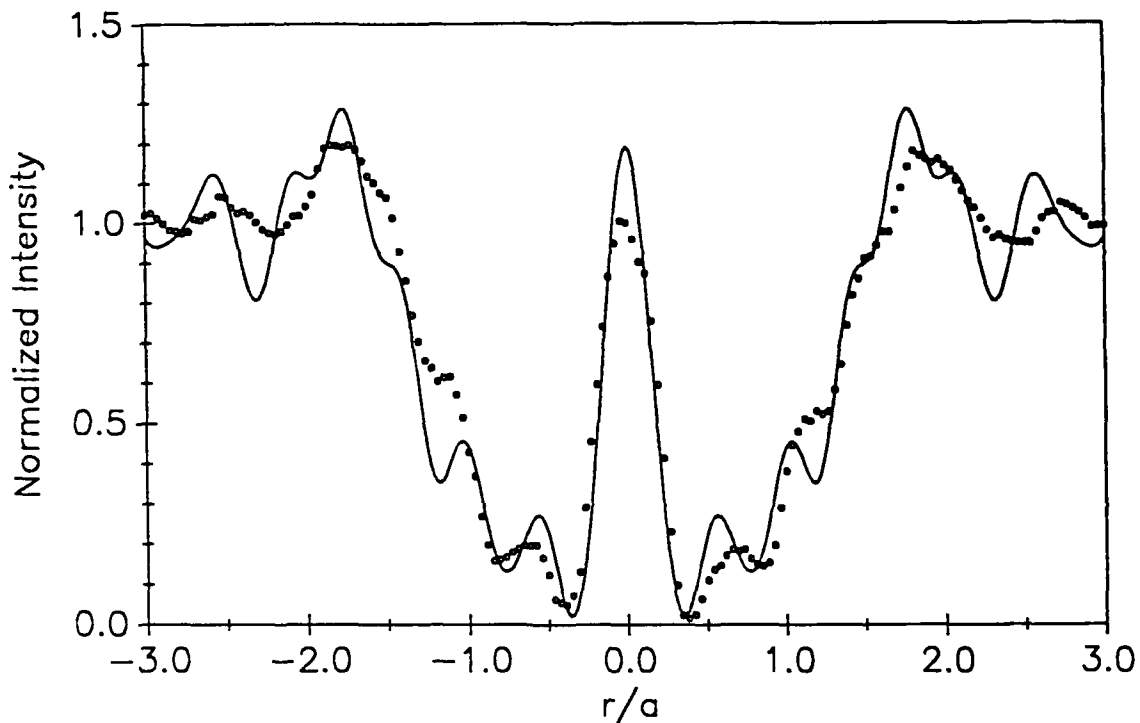
Fig. 3. Calculated (solid line) and experimental results (open circles) for a 57 $\mu$m diameter water droplets with complex refractive index of $\bar{n} = 1.345 + 8.7 \times 10^{-9}$i. The droplets are located 44 diameters out-of-focus toward the lens with an aperture size of 4 mm.



Fig. 4. Calculated (solid line) and experimental results (open circles) for a 57 $\mu$m diameter water droplets with complex refractive index of $\bar{n} = 1.345 + 8.7 \times 10^{-9}$i. The droplets are located 73 diameters out-of-focus toward the lens with an aperture size of 4 mm.

Fig. 5. Calculated (solid line) and experimental results (open circles) for a 57 μm diameter water droplets with complex refractive index of $\bar{n} = 1.345 + 8.7 \times 10^{-9}$i. The droplets are located 17 diameters out-of-focus toward the lens with an aperture size of 7 mm.
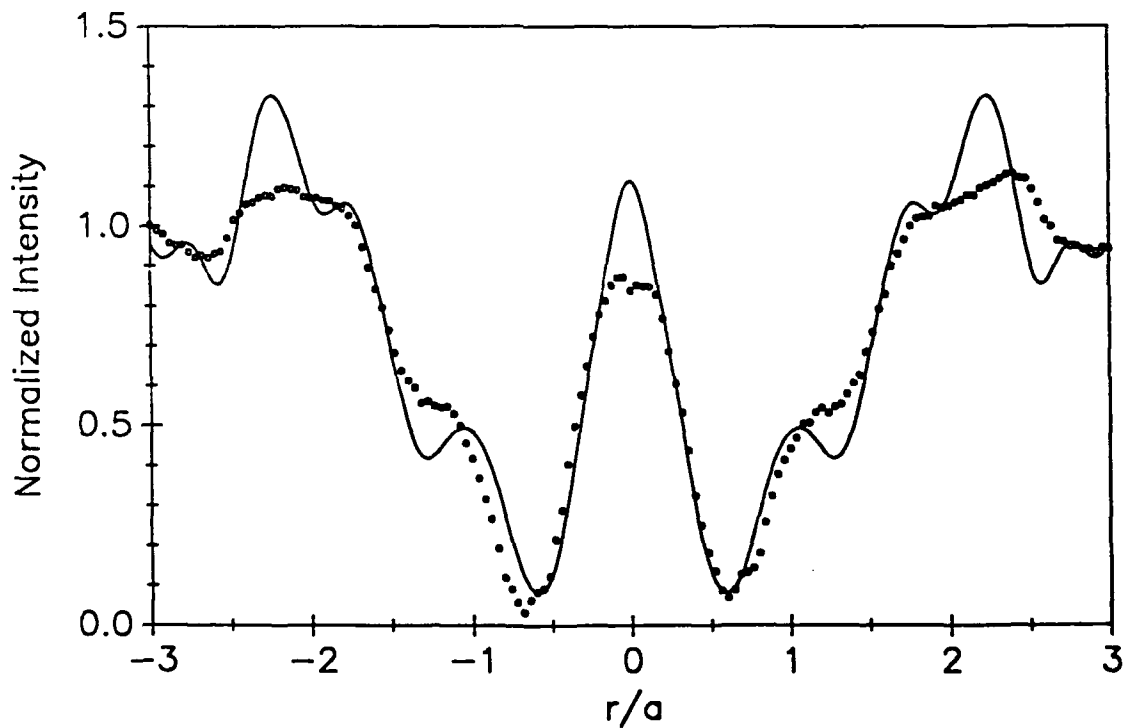


Fig. 6. Calculated (solid line) and experimental results (open circles) for a 57 μm diameter water droplets with complex refractive index of $\bar{n} = 1.345 + 8.7 \times 10^{-9}$i. The droplets are located 22 diameters out-of-focus toward the lens with an aperture size of 7 mm.
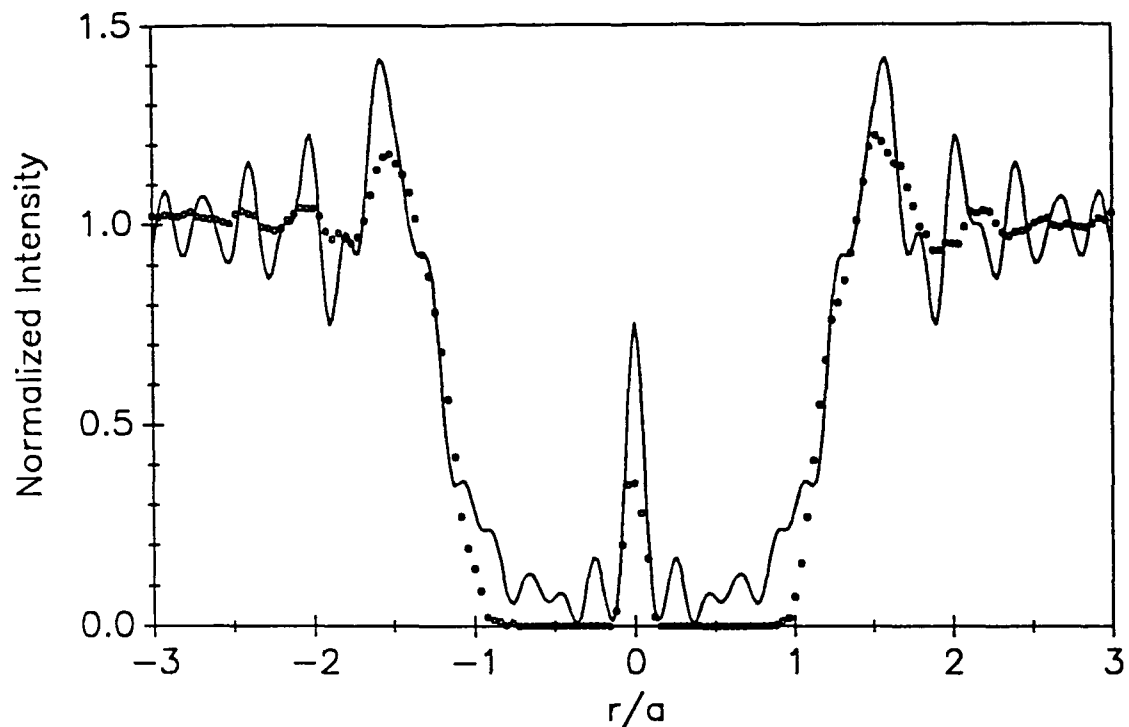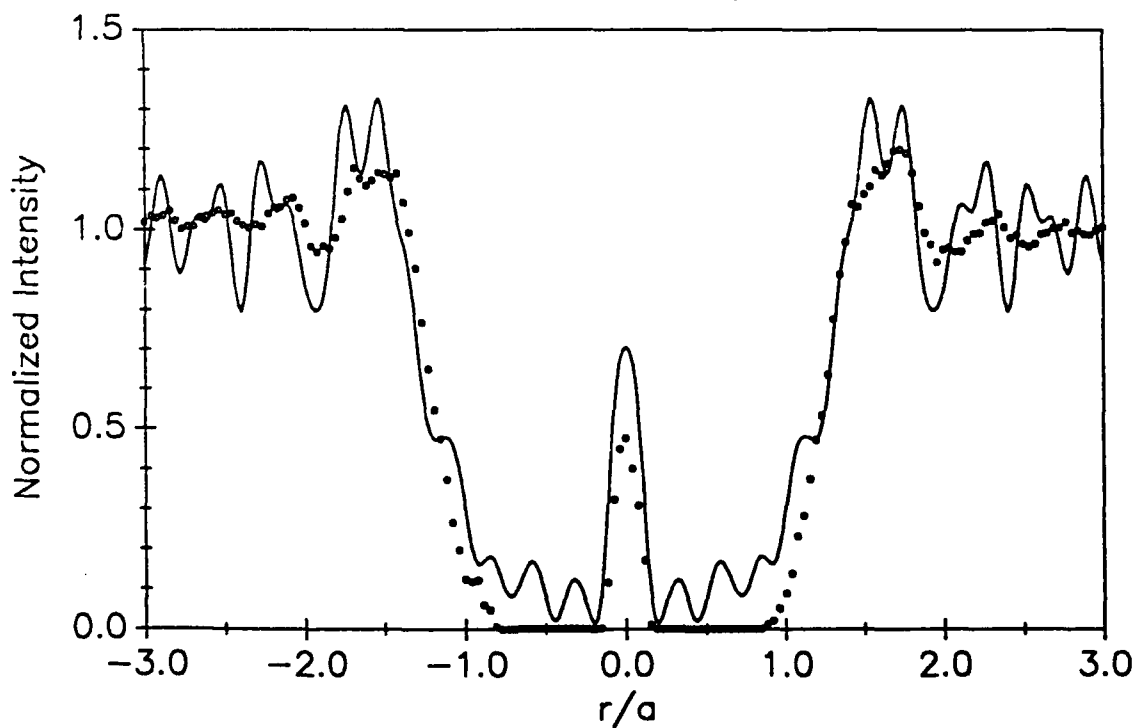
limitations due to camera nonlinearities and the finite resolution of the system which in this case is approximately 1 $\mu$m per pixel. The theoretical idealizations of plane wave illumination, thin lens optics, and perfectly spherical shaped particles will also introduce errors in the results.

## V. Conclusions

A theoretical model based on scalar theory has been presented which allows calculation of the images produced by spherical aerosol particles in a coherent imaging system. The theory is valid for either transparent or absorbing particles and has no restrictions on the allowable degree or direction of particle defocus. Comparison to experimental data has shown agreement in the main observable features, but the two differ in that the theoretical calculations show more high frequency structure. The source of these discrepancies is currently being investigated.

## VI. Future Work

Research is currently being conducted on modifying the scalar model by using a geometrical optics approach to the treatment of the electromagnetic field propagation through the lens. In addition, efforts are underway to examine the modeling of the system for the case of off-axis imaging. Such an approach would utilize an exact vector model to calculate both the free-space propagation and the propagation of the electromagnetic field through the imaging optics. The results of the theoretical model will ultimately be used to examine the validity of existing focus criteria such as measured average gray level and boundary edge gradient which are used in the sizing of dynamic aerosol sprays.

## VII. Appendix A: External Lorenz-Mie Equations

Assumptions:

1. Stationary, homogeneous, isotropic, absorbing sphere of radius a in a homogeneous, isotropic, nonabsorbing medium.

2. Both the particle and the medium are nonmagnetic ($\mu=1$).

3. Particle is illuminated by a plane, monochromatic electromagnetic wave of unit amplitude linearly polarized in the x direction, propagating in the +z direction.

4. All time dependent quantities are assumed to vary as $\exp(-i\omega t)$.

### Scattered Field

$$\tilde{E}_r^{(s)} = \frac{\cos\phi}{(\alpha\tilde{\rho})^2} \sum_{l=1}^{\infty} l(l+1)a_l\xi_l^{(1)}(\alpha\tilde{\rho})P_l^{(1)}(\cos\theta), \tag{A.1}$$

$$\tilde{E}_\theta^{(s)} = -\frac{\cos\phi}{\alpha\tilde{\rho}} \sum_{l=1}^{\infty} \left[ a_l\xi_l^{(1)\prime}(\alpha\tilde{\rho}) P_l^{(1)\prime}(\cos\theta)\sin\theta - b_l\xi_l^{(1)}(\alpha\tilde{\rho}) P_l^{(1)}(\cos\theta)\frac{i}{\sin\theta} \right], \tag{A.2}$$

and

$$\bar{E}_{\phi}^{(s)} = -\frac{\sin\phi}{\alpha\,\bar{\rho}} \sum_{l=1}^{\infty} \left[ a_l \xi_l^{(1)\prime}(\alpha\bar{\rho}) P_l^{(1)}(\cos\theta) \frac{1}{\sin\theta} - i b_l \xi_l^{(1)}(\alpha\bar{\rho}) P_l^{(1)\prime}(\cos\theta) \sin\theta \right]. \qquad (A.3)$$

The external scattering coefficients $a_l$ and $b_l$ are given by

$$a_l = \frac{i^{(l-1)}(2l+1)}{l(l+1)} \frac{\psi_l'(\bar{n}\alpha)\psi_l(\alpha) - \bar{n}\psi_l(\bar{n}\alpha)\psi_l'(\alpha)}{\bar{n}\psi_l(\bar{n}\alpha)\xi_l^{(1)\prime}(\alpha) - \psi_l'(\bar{n}\alpha)\xi_l^{(1)}(\alpha)} \qquad (A.4)$$

and

$$b_l = \frac{i^{(l-1)}(2l+1)}{l(l+1)} \frac{\bar{n}\psi_l'(\bar{n}\alpha)\psi_l(\alpha) - \psi_l(\bar{n}\alpha)\psi_l'(\alpha)}{\psi_l(\bar{n}\alpha)\xi_l^{(1)\prime}(\alpha) - \bar{n}\psi_l'(\bar{n}\alpha)\xi_l^{(1)}(\alpha)}, \qquad (A.5)$$

where $\psi_l$, $\chi_l$, and $\xi_l^{(1)} = \psi_l - i\chi_l$ are the Riccati-Bessel functions, which are related to the Bessel functions of half-integer order, $P_l^{(1)}$ is the associated Legendre function of order 1, $\bar{n}$ is the complex refractive index of the sphere, $\alpha = 2\pi a/\lambda$ is the size parameter, and $\bar{\rho} = \rho/a$ is the normalized radial coordinate. Primed quantities denote differentiation with respect to the argument of the function. Note that all electric field quantities are normalized based on an assumed uniform incident electric field of unit magnitude.

The technique used to compute the Riccati-Bessel functions is described in detail by Ross. [10] Computation of the associated Legendre function is accomplished by using standard recursion formulas such as those presented by Abramowitz and Stegun. [11]

### Incident Field

$$\bar{E}_r^{(i)} = e^{i\alpha\bar{r}\cos\theta} \sin\theta \cos\phi, \qquad (A.6)$$

$$\bar{E}_{\theta}^{(i)} = e^{i\alpha\bar{r}\cos\theta} \cos\theta \cos\phi, \qquad (A.7)$$

and

$$\bar{E}_{\phi}^{(i)} = -e^{i\alpha\bar{r}\cos\theta} \sin\phi. \qquad (A.8)$$

### External Field

In terms of cartesian coordinates,

$$\bar{E}_x^{ext} = (\bar{E}_r^{(i)} + \bar{E}_r^{(s)}) \sin\theta \cos\phi + (\bar{E}_{\theta}^{(i)} + \bar{E}_{\theta}^{(s)}) \cos\theta \cos\phi - (\bar{E}_{\phi}^{(i)} + \bar{E}_{\phi}^{(s)}) \sin\phi, \qquad (A.9)$$

$$\bar{E}_y^{ext} = (\bar{E}_r^{(i)} + \bar{E}_r^{(s)}) \sin\theta \sin\phi + (\bar{E}_{\theta}^{(i)} + \bar{E}_{\theta}^{(s)}) \cos\theta \sin\phi + (\bar{E}_{\phi}^{(i)} + \bar{E}_{\phi}^{(s)}) \cos\phi, \qquad (A.10)$$

and

$$\bar{E}_z^{ext} = (\bar{E}_r^{(i)} + \bar{E}_r^{(s)}) \cos\theta - (\bar{E}_{\theta}^{(i)} + \bar{E}_{\theta}^{(s)}) \sin\theta. \qquad (A.11)$$

## VIII. References

[1] B.J. Thompson and P.H. Malyak, "Accuracy of measurement in coherent imaging of particulates in a three-dimensional sample,"in *Particle Sizing and Spray Analysis*, N. Chigier and G.W. Stewart, eds., Proc. SPIE **573**, 12-20 (1985).

[2] E.A. Hovenac, "Fresnel diffraction by spherical obstacles," Am. J. of Phys., **57** (1), 79-84 (1989).

[3] S.A. Schaub, D.R. Alexander, and J.P. Barton,"Theoretical model for the image formed by a spherical particle in a coherent imaging system," Opt. Eng. **28** (5), 565-571 (1989).

[4] J.P. Barton, D.R. Alexander, and S.A. Schaub, "Internal and near-surface electromagnetic fields for a spherical particle irradiated by a focused laser beam," J. Appl. Phys. **64** (4), 1632-1639 (1988).

[5] G. Mie, "Beiträge zur Optik trüber Medien, speziell kolloidaler Metallösungen," Ann. Phys. **25**, 377-445 (1908).

[6] P. Debye, "Der Lichtdruck auf Kugeln von beliebigem Material," Ann. Phys. **30**, 57-136 (1909).

[7] M. Born and E. Wolf, *Principles of Optics* 6th Edition, Pergamon Press, Elmsford, New York (1986).

[8] J.W. Goodman, *Introduction to Fourier Optics*, McGraw-Hill, New York (1968).

[9] G.M. Hale and M.R. Querry, "Optical constants of water in the 200-nm to 200-$\mu$m wavelength region," Appl. Opt., **12** (3), 555-563 (1973).

[10] W.D. Ross,"Computation of Bessel functions in light scattering studies," Appl. Opt., **11** (9), 1919-1923, (1973).

[11] M. Abramowitz and I. Stegun, eds., *Handbook of Mathematical Functions*, Dover, New York (1972).

(c) Technical Reports, Item 6(d)

# PROGRESS REPORT
### (TWENTY COPIES REQUIRED)

1. **ARO PROPOSAL NUMBER** : 25615-GS

2. **PERIOD COVERED BY REPORT** : 1 July 1987 - 31 December 1987

3. **TITLE OF PROPOSAL** :
> Linear and Nonlinear Response of Liquid and
> Solid Particles to Energetic
> Radiation

4. **CONTRACT OR GRANT NUMBER** : DAAL03-87-K-0138

5. **NAME OF INSTITUTION** : UNIVERSITY OF NEBRASKA

6. **AUTHORS OF REPORT** :
> Dr. Dennis R. Alexander
> Dr. John P. Barton

7. **LIST OF MANUSCRIPTS SUBMITTED OR PUBLISHED UNDER ARO SPONSORSHIP DURING THIS REPORTING PERIOD, INCLUDING JOURNAL REFERENCES:**

1. J.P. Barton, D.R. Alexander, and S.A. Schaub, "Surface Charges on Spherical Particles Induced By Polarized Irradiation," Submitted for publication in Journal of the Optical Society of America A.
2. J.P. Barton, D.R. Alexander, and S.A. Schaub, "Internal and External Fields For A Homogeneous Sphere with an Arbitrary Incident Beam," Submitted for publication in Journal of the Optical Society of America A.

8. **SCIENTIFIC PERSONNEL SUPPORTED BY THIS PROJECT AND DEGREES AWARDED DURING THIS REPORTING PERIOD:**

Dr. Dennis R. Alexander, Principal Investigator
Dr. John P. Barton, Co-Principal Investigator
Dana Poulain, M.S.

Thesis Awarded: Mark A. Emanuel, "Laser Interaction With Spherical Aerosols and Cylindrical Fluid Columns," Masters Thesis, Mechanical Engineering Department, University of Nebraska, Lincoln, Nebraska, 68588-0525.

# BRIEF OUTLINE OF RESEARCH FINDINGS

During this funding period the experimental facility to investigate the interaction of high energy excimer laser radiation at $\lambda = 0.248\ \mu m$ has been put into operation. The Cooke vacuum chamber with optical ports is now in operation as well as the Hamamatsu streak camera. Initial results have been obtained for the interaction of $\lambda = 0.248$ radiation with water aerosols and with solid styrene divinylbenzene particles in air. The imaging work where we split off part of the beam used for the explosion process has been very successful. Dr. John White of CRDEC and Dr. Walter Flood of the Army Research Office visited the Laboratory For Electro-Optical Measurements. Video tapes of the interaction of the solid and liquid aerosol particles were provided to Dr. John White of CRDEC for presentations. Images taken at 4 nsec, 12 nsec, and 28 nsec showed the importance of being able to vary the time after the initiating pulse arrives for recording images. Liquid particles showed signs of explosive behavior at 4 ns but solid particles did not. Shock formation was observed with velocities greater than 10,000 m/sec. Future work will be to compare these air interactions with interactions in a vacuum.

In addition, we were able to make considerable progress in the theoretical calculations of an aerosol particle placed in an arbitrary beam profile. We have interacted with Dr. Richard Chang at Yale and run the case of resonance and non resonance for a particle located at various locations in a Gaussian beam. Our theoretical results are able to predict the experimental results of Dr. Chang's where the lifetimes and intensity of stimulated Raman scattering was shown to be enhanced when the particle was in the edge of the Gaussian beam. Our theoretical calculations also show a very intense ring forming around the edge of the particle when the focal point is moved to the edge of the particle. The magnitude of the intensity also increases when the focal point is moved to the outer edge of the particle.

## PROGRESS REPORT
### (TWENTY COPIES REQUIRED)

1. **ARO PROPOSAL NUMBER:** 25615-GS

2. **PERIOD COVERED BY REPORT:** 1 January 1988 - 30 June 1988

3. **TITLE OF PROPOSAL:**
   Linear and Nonlinear Response of Liquid and
   Solid Particles to Energetic Radiation

4. **CONTRACT OR GRANT NUMBER:** DAAL03-87-K-0138

5. **NAME OF INSTITUTION:** UNIVERSITY OF NEBRASKA

6. **AUTHORS OF REPORT:**
   Dr. Dennis R. Alexander
   Dr. John P. Barton

7. **LIST OF MANUSCRIPTS SUBMITTED OR PUBLISHED UNDER ARO SPONSORSHIP DURING THIS REPORTING PERIOD, INCLUDING JOURNAL REFERENCES:**

   (a) J. P. Barton, D. R. Alexander, and S. A. Schaub, "Internal and Near-Surface Electromagnetic Fields For a Spherical Particle Irradiated by a Focused Laser Beam," Accepted for Publication in Applied Physics, April 1988.

   (b) S. A. Schaub, D. R. Alexander, and J. P. Barton, "Theoretical Model For the Image Formed by a Spherical Particle in a Coherent Imaging System: Comparison to Experiment," Submitted to Optical Engineering, July 1988.

   (c) S. A. Schaub, D. R. Alexander, J. P. Barton, and M. A. Emanuel, "Focused Laser Beam Interactions with Methanol Droplets: Effects of Relative Beam Diameter, " Submitted to Applied Optics, May 1988.

8. **SCIENTIFIC PERSONNEL SUPPORTED BY THIS PROJECT AND DEGREES AWARDED DURING THIS REPORTING PERIOD:**
   Dr. Dennis R. Alexander, Principal Investigator
   Dr. John P. Barton, Co-Principal Investigator
   Dana Poulain, M. S.
   Scott Schaub, Ph. D.
   Jingyi Zhang, Ph. D.
   Greg Holtmeier, M. S.

   Thesis Awarded:
   None This Reporting Period

# BRIEF OUTLINE OF RESEARCH FINDINGS

During this funding period results have been obtained for the interaction of excimer laser radiation at $\lambda = 0.248\mu m$ with solid and liquid aerosol particles. Solid particles of $Al_2O_3$, W, SiC, Glass spheres, Al Spheres, ground fused silica (Suprasil), and styrene divinylbenzene have been imaged at 50 nsec intervals after interacting at $10^{11}$ watts/cm$^2$ at $\lambda = 0.248$ nm. Figure 1 illustrates the dynamics of the explosion process for Al spheres and the double pulse technique used to obtain the velocities shown in Table 1. Since the index of refraction for Al is $0.19 + 2.942\,i$, the amount of material ejected from the shadow side was not expected. However, this general trend was also observed for the other solid materials except ground fused silica which in its bulk form is very transparent at $\lambda = 0.248$. The fused silica seemed to explode in a symmetric fashion and spread glass fragments uniformly inside the vacuum chamber. A streak camera was used to observe the emission lifetimes of plasma plumes at various pressures. Figure 2 shows the behavior of the emission lifetimes as the pressure is reduced for Al and absorbing glass spheres.

Theoretical efforts during this funding period included the development of a theoretical analysis of the laser heating of liquid droplets moving through a focused laser beam. The arbitrary incident beam/spherical particle electromagnetic interaction theory was used to determine the spatial distribution of heating within the droplet for each position as the droplet falls through the profile of the focused laser beam. Calculations were performed corresponding with the vibrating orifice droplet generator/CW $CO_2$ laser conditions of our laboratory and prediction of explosive vaporization threshold power as a function of droplet size were in qualitative agreement with experimental observation for both water and methanol droplets.

Results of this work were presented at the 1988 CRDEC Conference on Obscuration and Aerosol Science held in June 1988. The current work has been discussed with Dr. Richard Chang at Yale, Dr. John White, Ivy Sindoni, and Jay Embury at CRDEC, and Sherwin Aminmoto at the Aerospace Corporation.
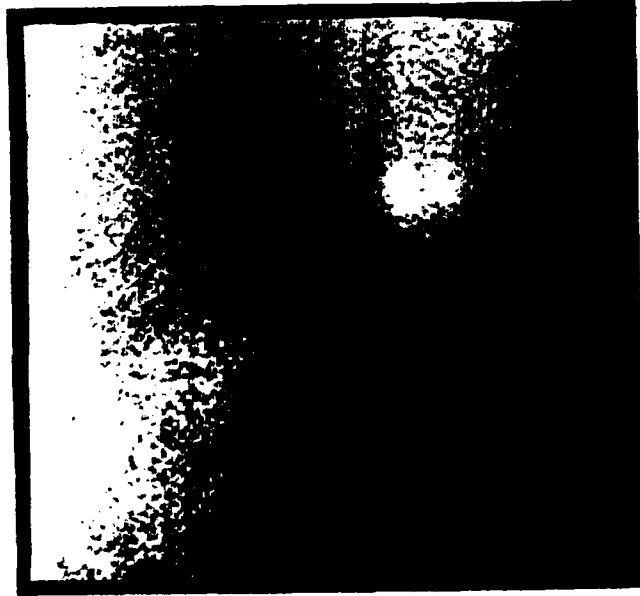
20 micron Al spheres

$\lambda_{inc} = 248$ nm

$I \approx 10^{11}$ W/cm$^2$ (400 mJ/pulse)

$P = 10^{-5}$ Torr

Imaging pulses arrive 50 ns and 95 ns after high energy pulse.

Velocity of upper plume is 1300 m/s and velocity of lower plume is 1700 m/s.



Beam propagation

Figure 1: Typical interaction of adjacent Al spheres with $\lambda = .248$nm radiation at $10^{11}$ W/cm$^2$. Bright white spots locate initial interaction location at time = 0 ns.

Table 1: Typical velocities found by dual pulse imaging.

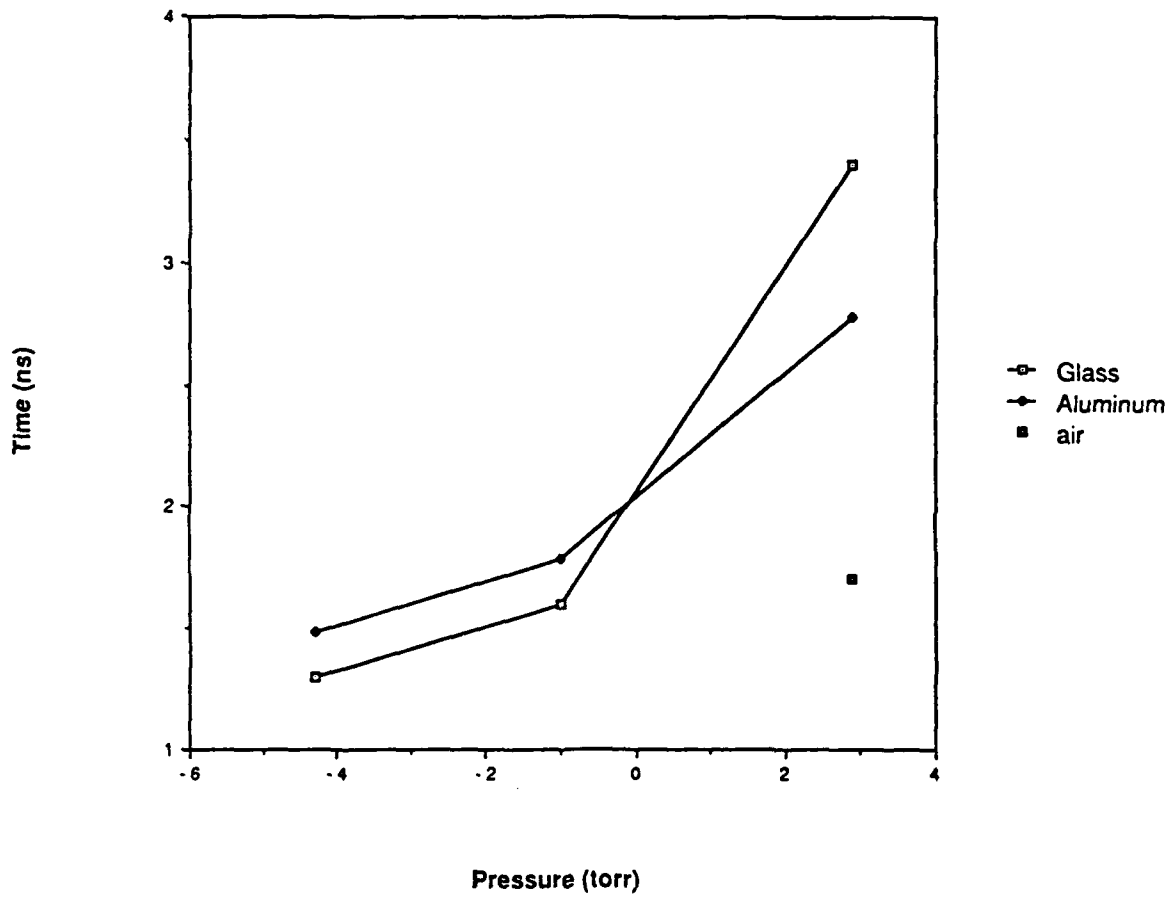| Material | Power (W/cm$^2$) | Pressure (Torr) | Velocity (m/s) | |
|---|---|---|---|---|
| | | | Bulk | Plume |
| Glass Spheres (5-50 microns) | $10^{11}$ | $10^{-5}$ | NA | 440 460 690 760 2000 |
| Glass Spheres (5-50 microns) | $10^{11}$ | 760 | 250 250 270 300 330 | 510 550 750 |
| Al Spheres (20 microns) | $10^{11}$ | $10^{-5}$ | NA | 450 460 1300 1700 1800 |

Figure 2: Emission lifetimes as a function of pressure for glass, aluminum, and air breakdowns.

## PROGRESS REPORT
### (TWENTY COPIES REQUIRED)

1. **ARO PROPOSAL NUMBER:** 25615-GS

2. **PERIOD COVERED BY REPORT:** 1 July 1988 - 31 December 1988

3. **TITLE OF PROPOSAL:**
   Linear and Nonlinear Response of Liquid and Solid Particle to Energetic Radiation

4. **CONTRACT OR GRANT NUMBER:** DAAL03-87-K-0138

5. **NAME OF INSTITUTION:** University of Nebraska

6. **AUTHORS OF REPORT:**
   Dr. Dennis R. Alexander
   Dr. John P. Barton

7. **LIST OF MANUSCRIPTS SUBMITTED OR PUBLISHED UNDER ARO SPONSORSHIP DURING THIS REPORTING PERIOD, INCLUDING JOURNAL REFERENCES:**

   (a) J.P. Barton, D.R. Alexander, and S.A. Schaub, "Internal and Near-Surface Electromagnetic Fields for a Spherical Particle Irradiated by a Focused Laser Beam," Journal of Applied Physics, 64, 1632-39 (1988).

   (b) S.A. Schaub, D.R. Alexander, and J.P. Barton, "Theoretical Model for the Image Formed by a Spherical Particle in a Coherent Imaging System: Comparison to Experiement" Accepted for publication in Optical Engineering, to be published April 1989.

   (c) J.P. Barton, D.R. Alexander, and S.A. Schaub, "Internal Fields of a Spherical Particle Illuminated by a Tightly-Focused Laser Beam: Focal Point Positioning Effects at Resonance," Accepted for publication in the Journal of Applied Physics, to be published April 15, 1989.

   (d) S.A. Schaub, D.R. Alexander, J.P. Barton, and M.A. Emanuel, "Focused Laser Beam Interactions with Methanol Droplets: Effects of Relative Beam Diameter," Accepted for Publication in Applied Optics, January 1989.

   (e) D.R. Alexander, S.A. Schaub, J. Zhang, D. Poulain, and J.P. Barton, "Scattering of Incident KrF Laser Radiation from the Laser Induced Breakdown of $H_2O$ Droplets," Submitted for publication in Optics Letters, December 1988.

   (f) D.R. Alexander, D. Poulain, J.P. Barton, S.A. Schaub, and J. Zhang, "Interaction of Excimer Laser Radiation with Solid Particles," 1988 CRDEC Proceedings.

   (g) J.P. Barton, D.R. Alexander, and S.A. Schaub, "Experimental and Theoretical Analysis of Liquid Droplets Moving Through a Focused $CO_2$ Laser Beam," 1988 CRDEC Proceedings.

8. **SCIENTIFIC PERSONNEL SUPPORTED BY THIS PROJECT AND DEGREES AWARDED DURING THIS REPORTING PERIOD:**

   Dr. Dennis R. Alexander, Principal Investigator

   Dr. John P. Barton, Co-Principal Investigator

   Dana Poulain, M.S.

   Jingyi Zhang, Ph.D.

   Gregg Holtmeier, M.S.

   Thesis Awarded: None this reporting period.

1

# BRIEF OUTLINE OF RESEARCH FINDINGS

During this funding period we concentrated our experimental research efforts on explaining the time dependent dual peak scattering of $\lambda = 248$ nm excimer laser radiation from liquid aerosol particles. This work has been submitted in a paper entitled "Scattering of Incident KrF Laser Radiation Resulting from the Laser Induced Breakdown of $H_2O$ Droplets" to Optics Letters. A copy of the manuscript has been attached. Work was also performed on the threshold for ionization for various materials as a function of surrounding pressure. Figure 1 shows the results of this work. Results were shared with Dr. Jay Embury at CRDEC.

Work was also started on trying to explain why material is being ejected off the shadow surface of solid materials interacting with $\lambda = 248$ nm. Mie calculations indicate that for metals the absorption should be entirely on the illuminated face. We have also observed that if clumps of materials are hit, the only particles showing the explosion off the shadow surface are the ones at the very back at the particle air/vacuum interface. In order to better understand this phenomena, we have started to use thin wires in the experiments.

Theoretical efforts during this funding period include the application of our spherical particle/arbitrary beam interaction theory to explore the effect of beam focal point positioning on the excitation of structural resonances within a spherical particle. A paper describing this work, entitled "Internal Fields of a Spherical Particle Illuminated by a Tightly-Focused Laser Beam: Focal Point Positioning Effects at Resonance," was submitted to the Journal of Applied Physics and has been accepted for publication (April 15, 1989). A copy of this paper is attached.

Existing spherical particle/arbitrary beam computer programs were successfully modified to allow calculations for large $\text{Im}(\bar{n}a)$. This modification was necessary in order to perform calculations corresponding with our experimental excimer laser/metal particle interaction studies. Example calculations are shown in Fig. 2.

Series expressions for the net force and torque electromagnetically-induced within a spherical particle during laser beam interaction were derived. In addition, calculations have been performed showing the spatial distribution of these forces within and on the surface of the spherical particle. These results are being assembled into paper form and will be submitted for publication.

A set of slides demonstrating the effect of beam focal point positioning on droplet heating were sent, as requested, to Dr. Ed Steubing.

Interactions with other scientists during this report period include Dr. Ed Steubing, Dr. Jay Embury, Dr. Ivy Sindoni, Dr. Walter Flood, and Dr. Shirish Chitanvis. Applications of our work were submitted under separate submission to Dr. Flood.
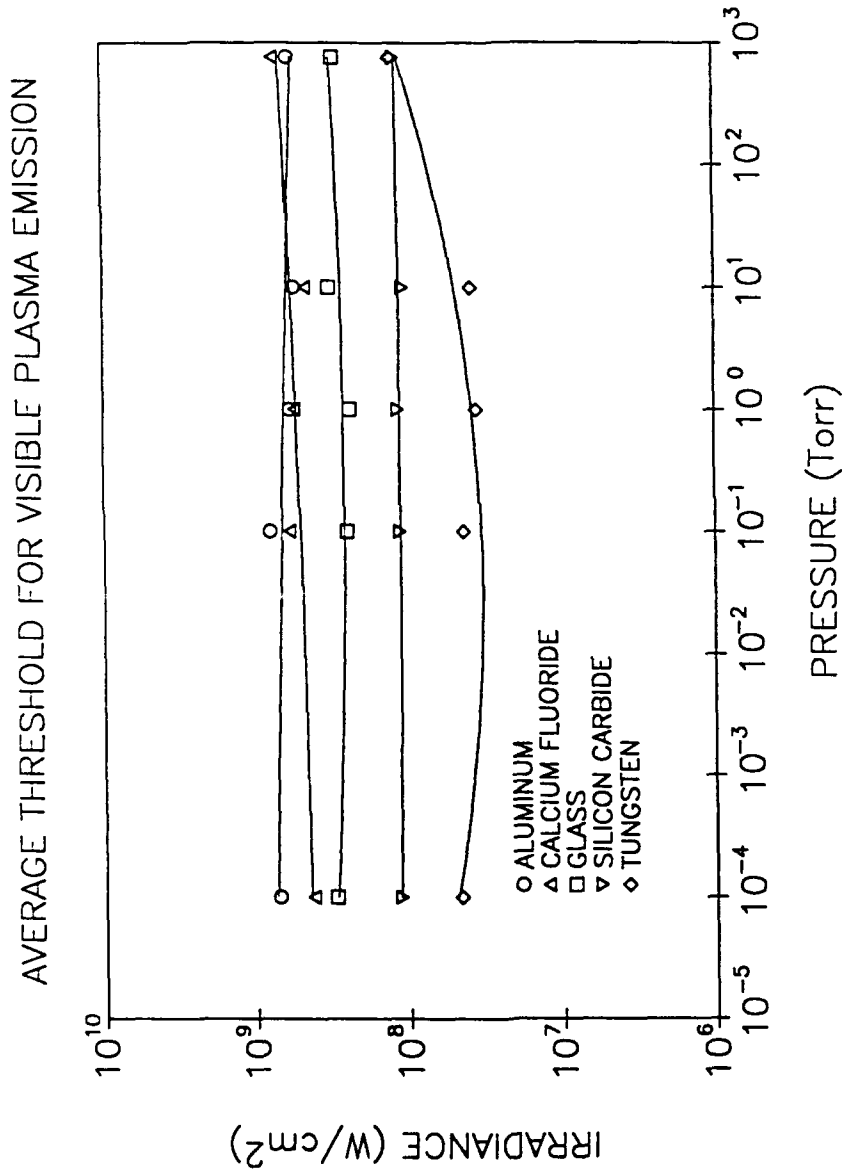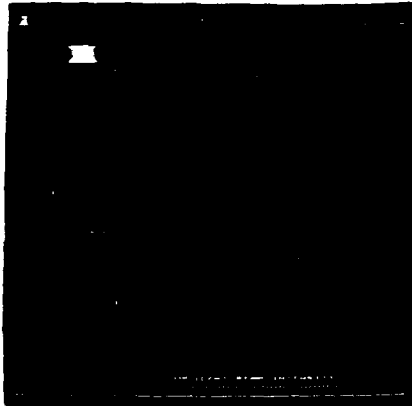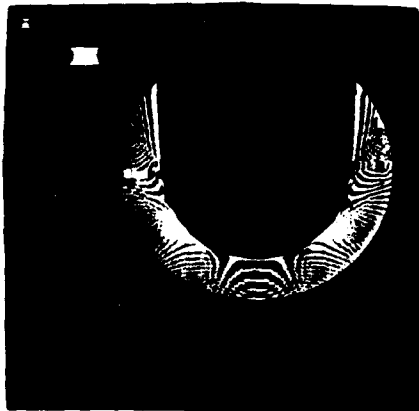
AVERAGE THRESHOLD FOR VISIBLE PLASMA EMISSION



Figure 1. Threshold values for plasma emission
for various surrounding pressures.

MATERIAL: ALUMINUM

DIAMETER: 5 μm

INDEX OF
REFRACTION: n = 0.190, k = 2.942

MAXIMUM SOURCE
FUNCTION: 9.24



MATERIAL: ALUMINUM

DIAMETER: 30 μm

INDEX OF
REFRACTION: n = 0.190, k = 2.942

MAXIMUM SOURCE
FUNCTION: 3.36

Fig. 2 False color visualization of internal and near-surface source function distribution for an aluminum sphere with plane wave illumination at $\lambda = 248$ nm. Note: for 30 μm diameter, $\bar{n}\alpha = 72.2 + 1118i$.

## PROGRESS REPORT
### (TWENTY COPIES REQUIRED)

1. **ARO PROPOSAL NUMBER:** 25615-GS

2. **PERIOD COVERED BY REPORT:** 1 January 1989 - 30 June 1989

3. **TITLE OF PROPOSAL:**
   Linear and Nonlinear Response of Liquid and Solid Particle to Energetic Radiation

4. **CONTRACT OR GRANT NUMBER:** DAAL03-87-K-0138

5. **NAME OF INSTITUTION:** University of Nebraska

6. **AUTHORS OF REPORT:**
   Dr. Dennis R. Alexander
   Dr. John P. Barton

7. **LIST OF MANUSCRIPTS SUBMITTED OR PUBLISHED UNDER ARO SPONSORSHIP DURING THIS REPORTING PERIOD, INCLUDING JOURNAL REFERENCES:**

   (a) D.R. Alexander, S.A. Schaub, J. Zhang, D.E. Poulain, and J.P. Barton, "Laser Induced Breakdown of $H_2O$ Droplets at 0.248 $\mu$m," Workshop on the Physics of Directed Energy Propagation in the Atmosphere, Las Cruces, New Mexico, February 28-March 1, 1989.

   (b) J.P. Barton, D.R. Alexander, and S.A. Schaub, "Electromagnetic Fields for a Focused Laser Beam Incident Upon a Spherical Particle," Workshop on the Physics of Directed Energy Propagation in the Atmosphere, Las Cruces, New Mexico, February 28-March 1, 1989.

   (c) J.P. Barton, D.R. Alexander, and S.A. Schaub, "Internal Fields of a Spherical Particle Illuminated by a Tightly-focused Laser Beam: Focal Point Positioning Effects at Resonance," *J. Appl. Phys.*, **65**, No. 8, April 15, 1989.

   (d) J.P. Barton and D.R. Alexander, "Fifth-order Corrected Electromagnetic Field Components for a Fundamental Gaussian Beam," accepted for publication in *J. Appl. Phys.*, July, 1989.

   (e) S. A. Schaub, D. R. Alexander, J. P. Barton, and M. A. Emanuel, "Focused Laser Beam Interactions With Methanol Droplets: Effects of Relative Beam Diameter," *Appl. Opt.*, **28**, May, 1989.

   (f) S. A. Schaub, D. R. Alexander, and J. P. Barton, "Theoretical Model for the Image Formed by a Spherical Particle in a Coherent Imaging System: Comparison to Experiment," *Optical Engineering*, **28**, No. 5, May, 1989.

   (g) S.A. Schaub, D.R. Alexander, D.E. Poulain, and J.P. Barton, "Measurement of Hypersonic Velocities Resulting from the Laser-induced Breakdown of Aerosols Using an Excimer Laser Imaging System," submitted for publication to *Rev. Sci. Instrum.*, July, 1989.

   (h) J.P. Barton, D.R. Alexander and S.A. Schaub, "Theoretical Determination of Net Radiation Force and Torque for a Spherical Particle Illuminated by a Focused Beam," accepted for publication in *J. Appl. Phys.*, July, 1989.

   (i) D.R. Alexander, S.A. Schaub, J. Zhang, D. Poulain, and J.P. Barton, "Scattering of Incident KrF Laser Radiation Resulting from the Laser Induced Breakdown of $H_2O$ Droplets," *Opt. Lett.*, **14**, No. 8, June, 1989.

   (j) J.P. Barton, D.R. Alexander and S.A. Schaub, "Electromagnetic Field Calculations for a Tightly-Focused Laser Beam Incident upon a Spherical Particle," Proceedings of the 1989 U.S. Army CRDEC Conference on Obscuration and Aerosol Research, Aberdeen Proving Ground, Maryland, June 26-30, 1989.

1

(k) D.R. Alexander, J.P. Barton, and S.A. Schaub, "Laser Induced Breakdown of $H_2O$ Droplets and Solid Wires at 0.248 $\mu$m," Proceedings of the 1989 U.S. Army CRDEC Conference on Obscuration and Aerosol Research, Aberdeen Proving Ground, Maryland, June 26-30, 1989.

(l) S.A. Schaub, J.P. Barton and D.R. Alexander, "Simplified Scattering Coefficient Expressions for a Spherical Particle Located on the Propagation Axis of a Fifth-Order Gaussian Beam," submitted for publication to *Appl. Phys. Lett.*, July 10, 1989.

(m) D.E. Poulain, D.R. Alexander, J.P. Barton, S.A. Schaub, and J. Zhang, "Interactions of Intense Ultraviolet Laser Radiation with Solid Aerosols," submitted for publication to *J. Appl. Phys.*, July, 1989.

## 8. SCIENTIFIC PERSONNEL SUPPORTED BY THIS PROJECT AND DEGREES AWARDED DURING THIS REPORTING PERIOD:

Dr. Dennis R. Alexander, Principal Investigator

Dr. John P. Barton, Co-Principal Investigator

Dana Poulain, M.S.

Jingyi Zhang, Ph.D.

Gregg Holtmeier, M.S.

Thesis Awarded: Dana E. Poulain

M.S. Thesis - "Interactions of Solid Aerosols with Intense Ultraviolet Laser Radiation," Master of Science Thesis, University of Nebraska, Lincoln, NE 68588

# BRIEF OUTLINE OF RESEARCH FINDINGS

Experimental research was conducted on the interaction of excimer laser radiation at $\lambda = 248$ nm with $H_2O$ droplets and results published in *Optics Letters* (copy attached). Additional work has recently shown that the interactions are nonlinear and are irradiance dependent. Results indicated, that as the irradiance increased, a smaller amount of energy was being deposited in the illuminated surface which cannot be explained by standard Mie scattering codes. An explanation for this nonlinear behavior is attributed to the shattering of the shadow surface which is required to scatter and focus the energy back to a hot spot near the illuminated surface. These results were presented at the CRDEC Conference and are being assembled into a paper and will be submitted for publication.

The excimer laser interaction work with solid wires has shown that what appeared to be material being ejected from the shadow surface, reported in earlier work, is actually material being blown around the sides of the wire. Collection of some of this material indicates that it is in a condensed state. Results were presented at a CRDEC meeting and are being assembled into a paper and will be submitted for publication.

Experimental work on the temperature dependence of rhodamine B dye in water solutions was performed. Experimental calibration results are shown in Figure 1. This work shows that those researchers using fluorescence imaging must take this into account when drawing conclusions about liquid and vapor areas in droplet explosion studies. Our goal is to use this method to measure temperatures in laser heated droplets as well. A paper entitled "Interactions of Intense Ultraviolet Laser Radiation with Solid Aerosols" is ready for submission to the *Journal of Applied Physics*.

Theoretical efforts during this funding period included further applications of our spherical particle/arbitrary beam interaction theory. An investigation of the net radiation force and torque induced by a tightly focused laser beam incident upon a spherical particle was concluded and results submitted as a paper to the *Journal of Applied Physics*. This paper, "Theoretical Determination of Net Radiation Force and Torque for a Spherical Particle Illuminated by a Focused Laser Beam," has been accepted for publication and a copy is attached.

A theoretical analysis of the distribution of radiation force within and upon the surface of a spherical droplet has also been conducted and results were reported at the 1989 CRDEC Conference. As an example, Fig. 2 shows the surface force distribution for an off propagation axis 5 $\mu$m diameter water droplet illuminated by a tightly focused ($2 w_o = 2$ $\mu$m) argon-ion laser beam

3

for an electric wave resonance condition. This work is being assembled into a paper that will be submitted to the *Journal of Applied Physics.*

Further calculations exploring the effect of focal point positioning on the excitation of resonances within spherical particles were performed. In order to retain accuracy while using highly focused beams ($2\,w_o \approx \lambda$), an improved Gaussian beam description was developed. A paper, "Fifth-Order Corrected Electromagnetic Field Components for a Fundamental Gaussian Beam," was submitted to the *Journal of Applied Physics* and has been accepted for publication. A copy of this paper is attached. Recent results, presented at the 1989 CRDEC Conference, have provided additional insight into the physical nature of spherical particle resonances. This work is being assembled into a paper and will be submitted as a Rapid Communications to *Applied Optics.*

A computer program was developed that allows the determination of internal and near-surface electromagnetic fields for a laser beam incident upon two adjacent spherical particles of arbitrary positioning. The particles may have different size and different complex index of refraction. Preliminary results were presented at the 1989 CRDEC Conference. As an example, Fig. 3 shows the source function distribution for a 40 $\mu$m waist diameter $CO_2$ laser beam incident upon a 50 $\mu$m diameter methanol droplet and a 30 $\mu$m diameter water droplet offset in the y-z plane. A paper on this work will be assembled and submitted to *Applied Optics.*

Interactions with other scientist included a visit to our research laboratory by Dr. Richard Chang on May 5, 1989.
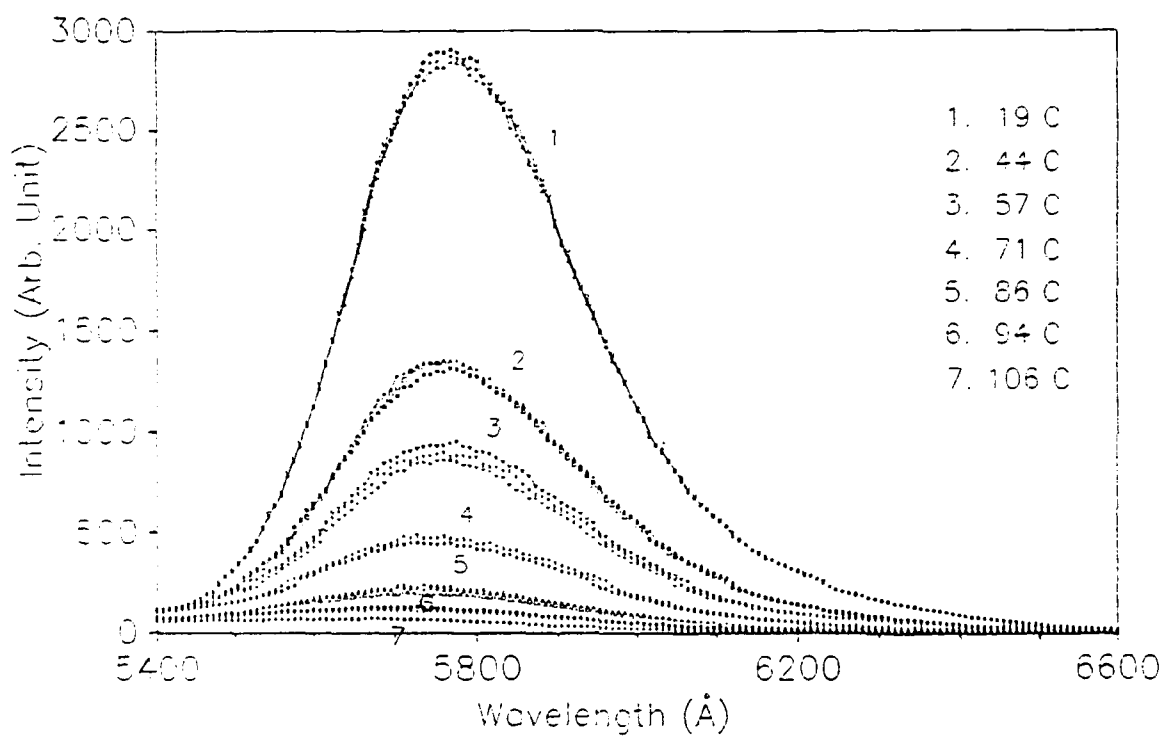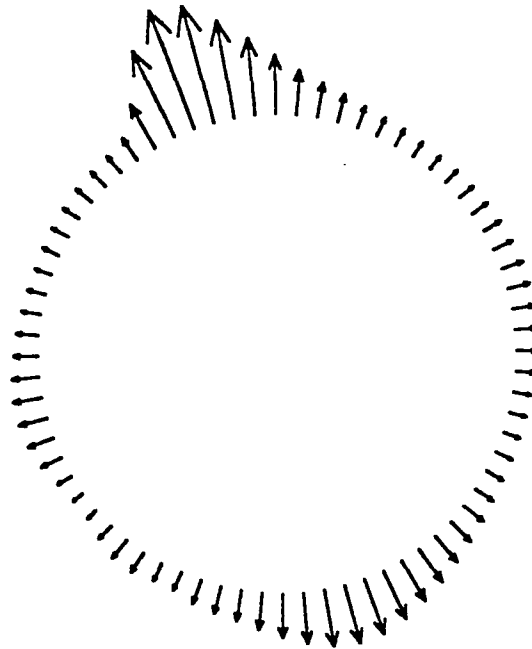
4

Figure 1. Fluorescence spectra of rhodamine B at different temperatures (excitation wavelength: 514.5nm, concentration of rhodamine B: 5.0E-6 mol in water)
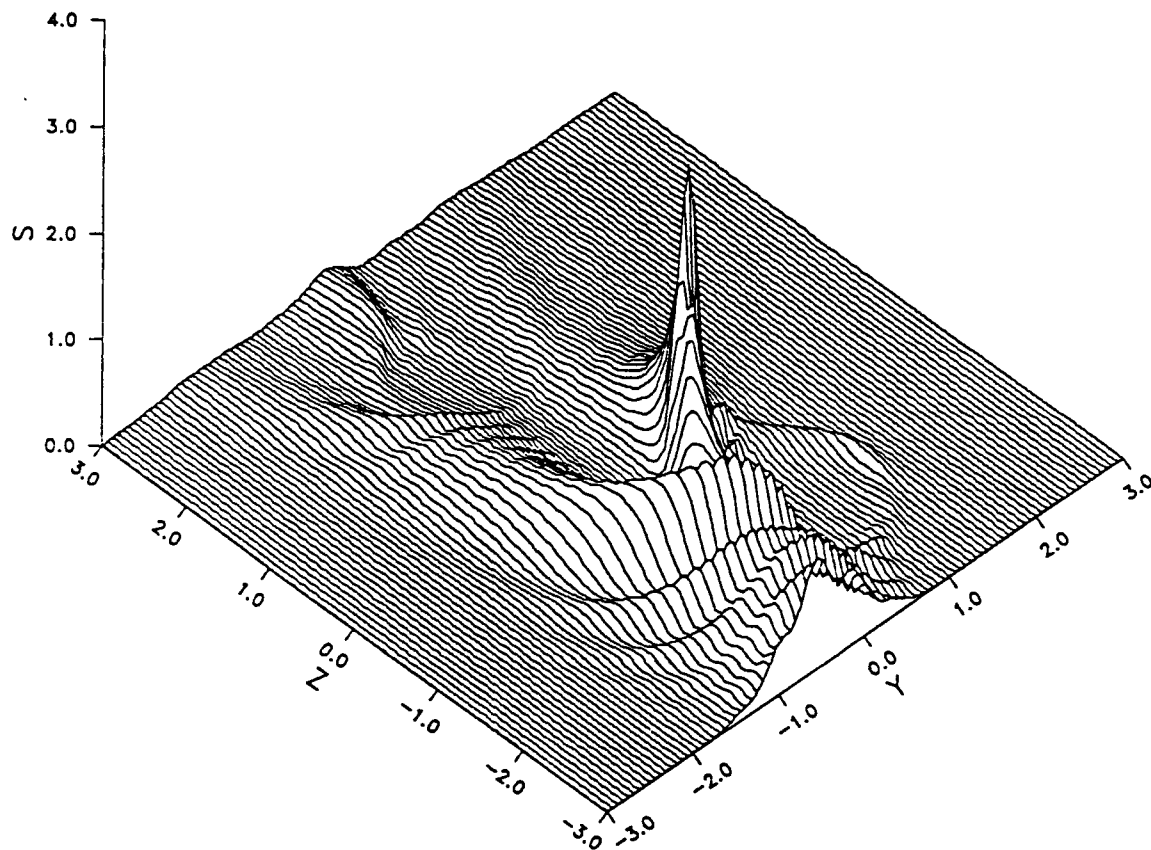
SURFACE FORCES

x-z plane, $\alpha = 30.4768$, $\bar{n} = 1.334 + 1.2 \times 10^{-9}i$

$\bar{w}_o = 0.4007$, $\bar{x}_o = 1.2021$, $\bar{y}_o = 0$, $\bar{z}_o = -2.0035$

(0.5145 $\mu$m wavelength, 2 $\mu$m waist diameter beam incident upon a 4.9912 $\mu$m diameter water droplet (elec. wave res.) for droplet positioning of 3 $\mu$m x-axis displacement at an elevation of 5 $\mu$m below the focal point)

$$P_{max} = 13.90 \text{ [Pa]}$$

Figure 2

6

Normalized source function in the equatorial (y-z) plane for a transverse (x direction) polarized Gaussian beam incident upon two adjacent spheres. $\bar{n}_1 = 1.395 + 0.0163i$, $\alpha_1 = 14.82$, $\bar{n}_2 = 1.179 + 0.072i$, $\alpha_2 = 8.89$, $\bar{w}_o = 0.8$, $\bar{x}_o = 0.0$, $\bar{y}_o = 1.0$, $\bar{z}_o = 0.0$, $\bar{x}_{12} = 0.0$, $\bar{y}_{12} = -1.0$, $\bar{z}_{12} = 3.0$, $\bar{x}_{ref} = 0.0$, $\bar{y}_{ref} = -0.5$, $\bar{z}_{ref} = 1.5$ [10.6 $\mu$m wavelength ($CO_2$ laser), 40 $\mu$m waist diameter beam incident upon adjacent 50 $\mu$m diameter methanol and 30 $\mu$m diameter water droplets offset in the y-z plane]

Figure 3

## PROGRESS REPORT
### (TWENTY COPIES REQUIRED)

1. ARO PROPOSAL NUMBER: 25615-GS

2. PERIOD COVERED BY REPORT: 1 July 1989 - 31 December 1989

3. TITLE OF PROPOSAL:
   Linear and Nonlinear Response of Liquid and Solid Particle to Energetic Radiation

4. CONTRACT OR GRANT NUMBER: DAAL03-87-K-0138

5. NAME OF INSTITUTION: University of Nebraska

6. AUTHORS OF REPORT:
   Dr. Dennis R. Alexander
   Dr. John P. Barton

7. LIST OF MANUSCRIPTS SUBMITTED OR PUBLISHED UNDER ARO SPONSORSHIP DURING THIS REPORTING PERIOD, INCLUDING JOURNAL REFERENCES:

   (a) J.P. Barton and D.R. Alexander, "Fifth-order Corrected Electromagnetic Field Components for a Fundamental Gaussian Beam," *J. Appl. Phys.*, 66, No. 7, October 1, 1989.

   (b) S.A. Schaub, D.R. Alexander, D.E. Poulain, and J.P. Barton, "Measurement of Hypersonic Velocities Resulting from the Laser-induced Breakdown of Aerosols Using an Excimer Laser Imaging System," *Rev. Sci. Instrum.*, 60, No. 12, December, 1989.

   (c) S.A. Schaub, J.P. Barton and D.R. Alexander, "Simplified Scattering Coefficient Expressions for a Spherical Particle Located on the Propagation Axis of a Fifth-Order Gaussian Beam," *Appl. Phys. Lett.*, 55, No. 26, December 25, 1989.

   (d) D.E. Poulain, D.R. Alexander, J.P. Barton, S.A. Schaub, and J. Zhang, "Interactions of Intense Ultraviolet Laser Radiation with Solid Aerosols," accepted for publication to *J. Appl. Phys.*, October, 1989.

   (e) J.P. Barton, D.R. Alexander and S.A. Schaub, "Theoretical Determination of Net Radiation Force and Torque for a Spherical Particle Illuminated by a Focused Laser Beam," *J. Appl. Phys*, 66, No. 10, November 15, 1989.

   (f) J.P. Barton, D.R. Alexander and S.A. Schaub, "Theoretical Determination of the Radiation Force Distribution for a Spherical Droplet Illuminated by a Focused Laser Beam," accepted for publication and being revised, *J. of Appl. Phys.*, August 29, 1989.

   (g) D.R. Alexander, J.P. Barton, S.A. Schaub and G. Holtmeier, "Nonlinear Interactions of KrF Laser Radiation with Small Water Droplets," submitted to *Applied Optics*, October 5, 1989.

   (h) J.P. Barton, W. Ma, S.A. Schaub and D.R. Alexander, "Theoretical Determination of the Electromagnetic Fields for a Laser Beam Incident Upon Two Adjacent Spherical Particles of Arbitrary Arrangement," accepted for inclusion in the 2nd International Congress on Optical Particle Sizing, November, 1989.

   (i) S.A. Schaub, D.R. Alexander and J.P. Barton, "Modeling of a Coherent Imaging System," accepted for inclusion in the 2nd International Congress on Optical Particle Sizing, November, 1989.

## 8. SCIENTIFIC PERSONNEL SUPPORTED BY THIS PROJECT AND DEGREES AWARDED DURING THIS REPORTING PERIOD:

Dr. Dennis R. Alexander, Principal Investigator

Dr. John P. Barton, Co-Principal Investigator

Jingyi Zhang, Ph.D.

Gregg Holtmeier, M.S.

Sik Wah Chiang, M.S.

# BRIEF OUTLINE OF RESEARCH FINDINGS

During the funding period, research was conducted on nonlinear interaction of KrF laser interaction with solid aerosols and liquid aerosols. A paper entitled, "Measurement of Hypersonic Velocities Resulting from the Laser-Induced Breakdown of Aerosols Using an Excimer Laser Imaging System," was published in *Review of Scientific Instruments*. A paper entitled, "Interactions of Intense Ultraviolet Laser Radiation with Solid Aerosols," is in press and will appear in the March issue of *Journal of Applied Physics*. Additional work on KrF $\lambda = 248$ nm interaction with liquid aerosols presented at the CRDEC meeting in June has been assembled into a paper entitled, "Nonlinear Interactions of KrF Laser Radiation with Small Water Droplets," and has been submitted to *Applied Optics*. Copies of these three papers are attached.

In our experimental work laser imaging systems are used extensively for capturing the dynamics of the laser-particle interactions. It is important to be able to understand both the experimental and theoretical aspects of particles both in and out of focus in this imaging system. We have been experimentally and theoretically modeling this imaging system. The most recent work has been assembled into a paper entitled, "Modeling of a Coherent Imaging System" which has been accepted for presentation at the Second International Congress on Optical Particle Sizing, Tempe, Arizona, March 5-8, 1990.

Experimental work showing the temperature dependence of rhodamine B dye in water has been provided in the previous progress report. In order to perform the optical temperature measurements, it is important to understand how and where the fluorescence signal in the drop is measured by the detector. This research also directly relates to optical concentration measurements in aerosols. Figure 1 demonstrates the capabilities of the computer codes written to *a priori* predict the regions in the aerosol droplet which contribute the highest probability to the detected signal. Calculations are being performed at various polarizations and view angles. Our research extends the work of Kerker et al. on "Raman and Fluorescent Scattering by Molecules Embedded in Small Particles: Numerical Results for Incoherent Optical Processes," *J. Opt. Soc. Am.*, 68, 1676-1686, 1978.

The Center for Electro-Optics purchased a CPM (colliding pulse mode) femtosecond laser (no ARO funds involved) with bow-tie amplification. I had extensive conversations with Dr. Ed Fry with regards to purchasing versus building a femtosecond laser system. The femtosecond laser will be used in performing ARO-related research in the future. As indicated in previous ARO reports,
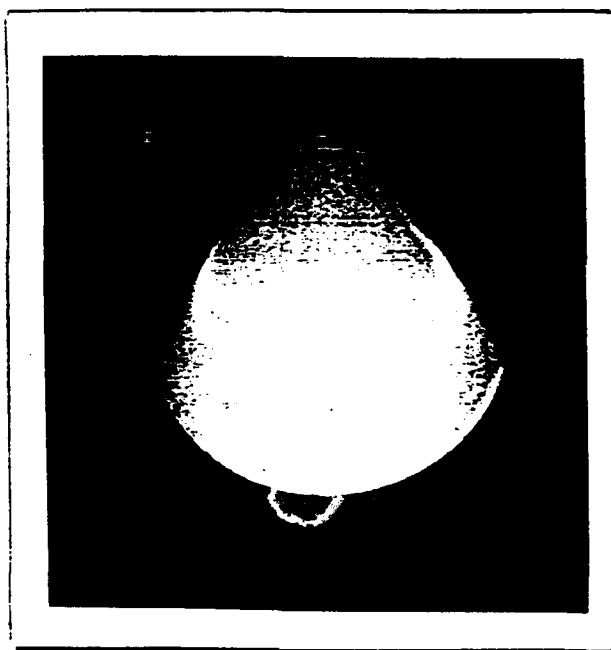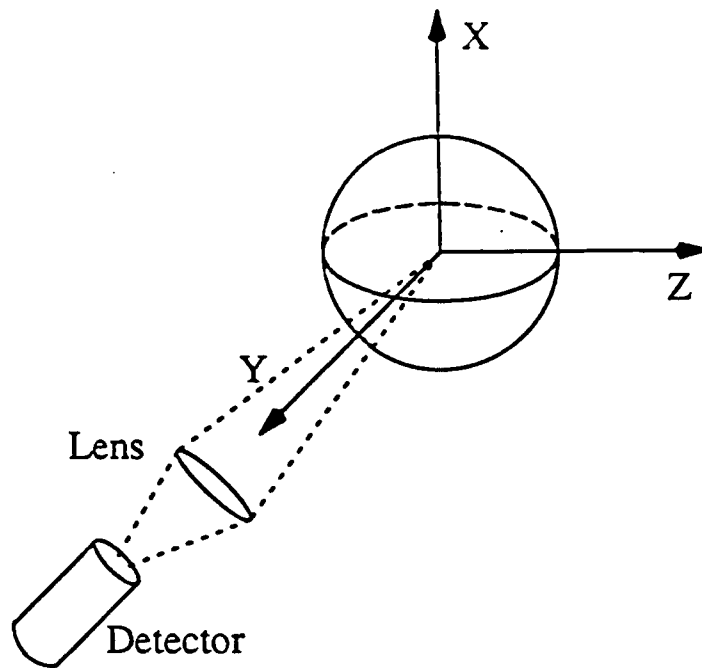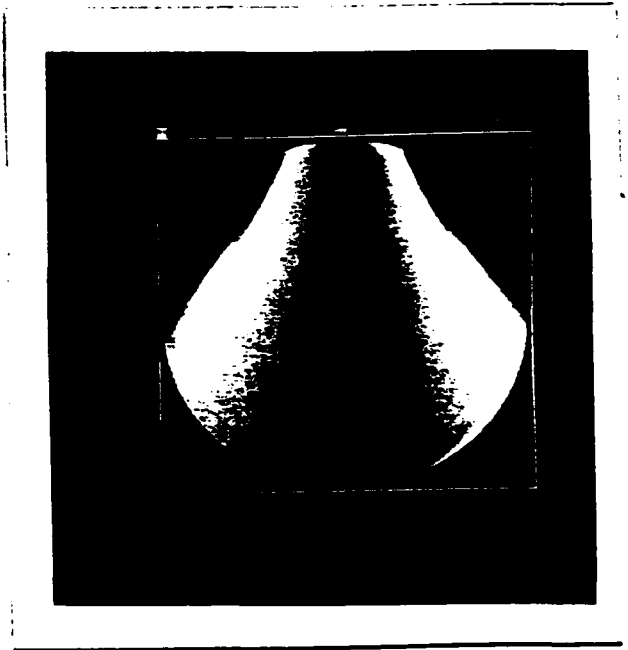
Inelastic emission polarized in X                    Inelastic emission polarized in Y

FIG. 1. Top schematic shows the geometry for calculations shown in bottom photographs. Left photograph shows spatial location of highest probability of signal reaching detector for inelastic emission polarized in X–direction. Right photograph is for the inelastic emission polarized in Y–direction. Red shows the regions of highest contribution while blue shows the least.

4

the 17 nsec pulses from our excimer lasers are not fast enough for diagnostic tools, especially at very high irradiance such as 200 $GW/cm^2$. Nonlinear effects at these high irradiance values will require picosecond and femtosecond time resolution.

More careful and extensive research work is being performed on the interaction of a $CO_2$ laser with water aerosols. One effort is to extend previous work (Mark Emanuel's M.S. Thesis) on the interaction with two adjacent spheres. Experimental work can now be compared with theoretical calculations. Although resonances should not appear for a $CO_2$ ($\lambda = 10.6$ $\mu m$) illuminating a 60 $\mu m$ stream of $H_2O$ drops, experiments clearly show evidence of a "resonance" type behavior. Research is in progress to quantify this observed behavior.

Other theoretical efforts within this funding period included further applications and developments of our beam incident upon a particle electromagnetic interaction theories. The beam on two adjacent sphere theory was used to analyze the effect of cooperative scattering on far-field scattering patterns. Systematic calculations were performed for a 4 $\mu m$ beam waist diameter Argon-ion ($\lambda = 0.5145$ $\mu m$) laser beam incident upon two adjacent 1.8 $\mu m$ diameter water droplets ($\bar{n} = 1.334$ + $1.2 \times 10^{-9}$i). The laser beam propagates in the + z axis direction and is linearly polarized with electric field polarization in the x axis direction. One particle was fixed in location at the focal point of the beam while the location of the second particle was varied and the subsequent effect on the far-field scattering pattern analyzed. Figure 2 shows the far-field scattering pattern in the x-z plane for the second particle far removed from the beam (single particle case). Figure 3 shows the far-field scattering pattern in the x-z plane for the second particle positioned at a 30° angle (referenced to the + z axis) in the x-z plane and spaced one particle diameter surface-to-surface from the focal point positioned particle. The effect of the presence of the second particle on the far-field scattering pattern can be seen by comparing Figs. 2 and 3. A paper based on this work entitled "Theoretical Determination of the Electromagnetic Fields for a Laser Beam Incident Upon Two Adjacent Spherical Particles of Arbitrary Arrangement" has been accepted for presentation at the Second International Congress on Optical Particle Sizing, Tempe, Arizona, March 5-8, 1990. A copy of this paper is attached.

The spherical particle/arbitrary beam interaction theory has been extended to now allow solutions for an arbitrary beam incident upon a homogeneous particle of arbitrarily-defined shape. The approach appears to be particularly well-suited for near-spherical particles where the shape deviates from a sphere by less than approximately ± 0.2 radii. For demonstration, Fig. 4 shows the internal normalized source function distribution ($\bar{S} = |\vec{E}|^2/E_0^2$) for a plane wave incident upon a prolate spheroid with $\alpha = 2\pi a/\lambda_{ext} = 14$, $\bar{n} = 1.363 + 3.5 \times 10^{-8}$i and b/a = 0.833 where a is
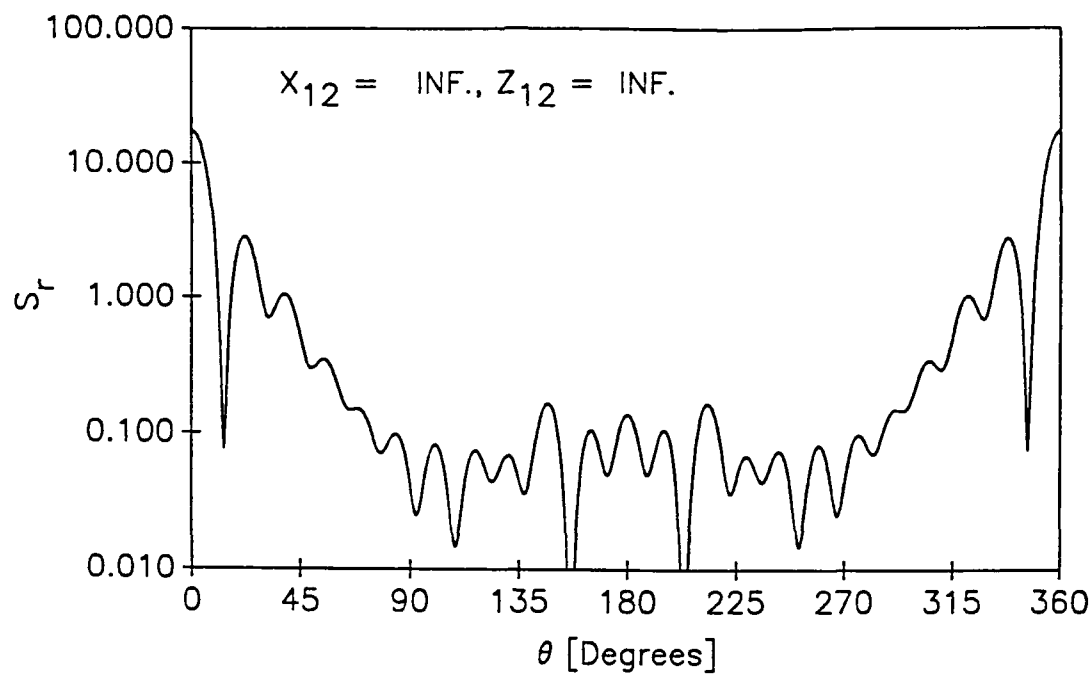
FIG 2. Normalized scattering intensity as a function of angle in the x-z plane for particle 2 far removed from the beam (single particle case).
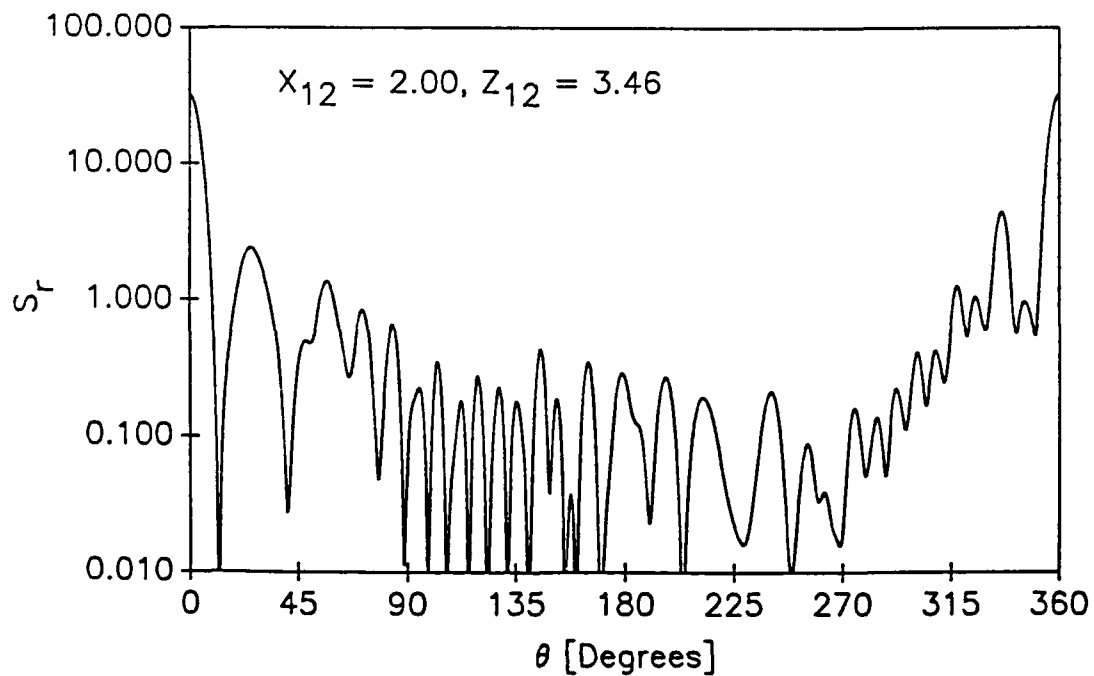


FIG 3. Normalized scattering intensity as a function of angle in the x-z plane for particle 2 positioned one diameter surface-to-surface away from particle 1 at an angle of 30°. $\bar{x}_{12} = 2.00, \bar{y}_{12} = 0.0, \bar{z}_{12} = 3.46$.
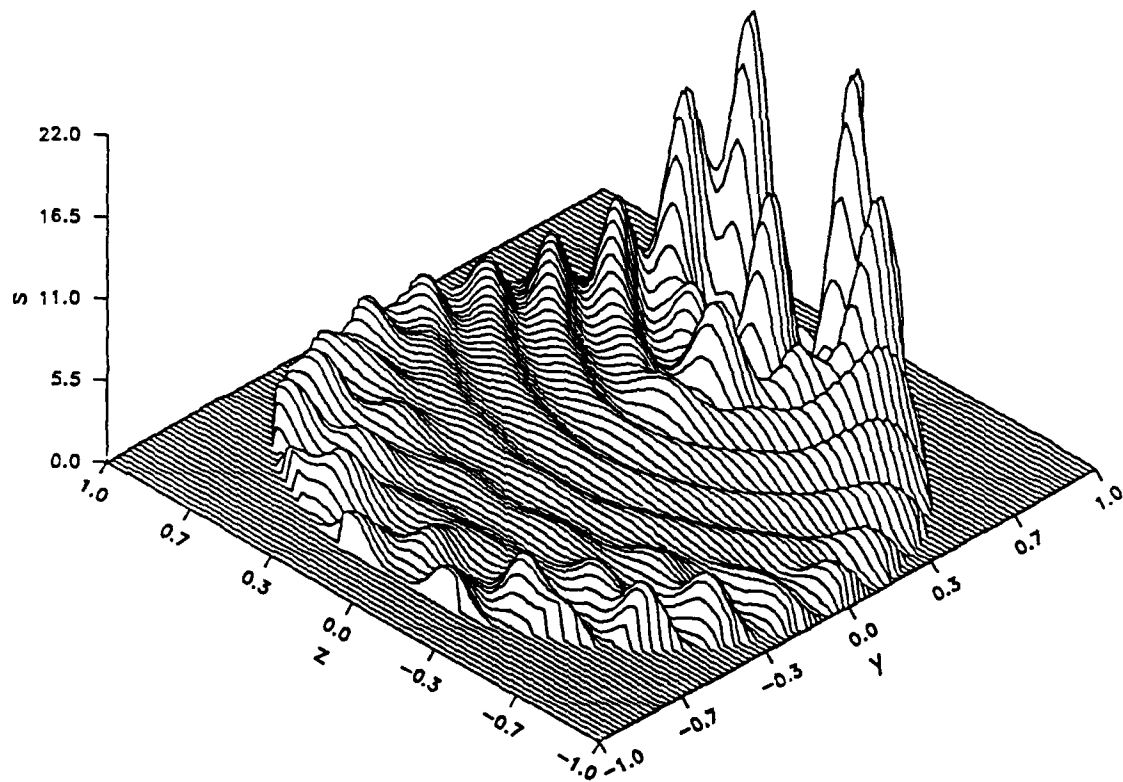
6

FIG 4. Internal normalized source function in the y-z plane for a plane wave propagating in the + y axis direction with electric field polarization in the x axis direction incident upon a prolate spheroid ($\alpha = 14.0$, $\bar{n} = 1.363 + 3.5\times10^{-8}i$, $b/a = 0.833$).

the major axis radius and b is the minor axis radius. The plane wave propagates in the $+y$ axis direction with electric field polarization in the $x$ axis direction. To our knowledge this represents the first internal field calculation for a nonspherical particle.

The nonspherical particle calculation approach permits beam as well as plane wave solutions and is not limited to "pure" geometries. The theory can be used, for example, to investigate the effect of slight nonsphericity on resonance excitation. The arbitrarily shaped particle/arbitrary beam interaction theory and subsequent computer programs are currently under final development and verification but a paper on this work will soon be assembled and submitted for publication to the *Journal of Applied Physics*.

A paper "Theoretical Determination of the Radiation Force Distribution for a Spherical Droplet Illuminated by a Focused Laser Beam" was submitted to the *Journal for Applied Physics* and has been accepted for publication with required revision. A copy of the submitted form of this paper is attached. A paper previously submitted "Simplified Scattering Coefficient Expressions for a Spherical Particle Located on the Propagation Axis of a Fifth-order Gaussian Beam" was accepted for publication and published in *Applied Physics Letters* **55**, 2709 (1989). A reprint of this paper is attached. Two papers previously submitted and accepted for publication were published during this funding period: "Fifth-order Corrected Electromagnetic Field Components for a Fundamental Gaussian Beam," *Journal of Applied Physics* **66**, 2800 (1989) and "Theoretical Determination of net Radiation Force and Torque for a Spherical Particle Illuminated by a Focused Laser Beam," *Journal of Applied Physics* **66**, 4594 (1989). Reprints of these two papers are attached.

## PROGRESS REPORT
### (TWENTY COPIES REQUIRED)

1. **ARO PROPOSAL NUMBER:** 25615-GS

2. **PERIOD COVERED BY REPORT:** 1 January 1990 - 30 June 1990

3. **TITLE OF PROPOSAL:**
   Linear and Nonlinear Response of Liquid and Solid Particle to Energetic Radiation

4. **CONTRACT OR GRANT NUMBER:** DAAL03-87-K-0138

5. **NAME OF INSTITUTION:** University of Nebraska

6. **AUTHORS OF REPORT:**
   Dr. Dennis R. Alexander
   Dr. John P. Barton

7. **LIST OF MANUSCRIPTS SUBMITTED OR PUBLISHED UNDER ARO SPONSORSHIP DURING THIS REPORTING PERIOD, INCLUDING JOURNAL REFERENCES:**

   (a) J.P. Barton, W. Ma, S.A. Schaub and D.R. Alexander, "Theoretical Determination of the Electromagnetic Fields for a Laser Beam Incident upon Two Adjacent Spherical Particles of Arbitrary Arrangement," Proceedings of the 2nd International Congress on Optical Particle Sizing, Arizona State University Printing Services, March 5-8, 1990.

   (b) S.A. Schaub, D.R. Alexander and J.P. Barton "Modeling of a Coherent Imaging System," Proceedings of the 2nd International Congress on Optical Particle Sizing, Arizona State University Printing Services, March 5-8, 1990.

   (c) D.E. Poulain, D.R. Alexander, J.P. Barton, S.A. Schaub, and J. Zhang, "Interactions of Intense Ultraviolet Laser Radiation with Solid Aerosols," *J. Appl. Phys.*, Vol. 67, No. 5, March 1, 1990.

   (d) D.R. Alexander, J.P. Barton, S.A. Schaub and G. Holtmeier, "Nonlinear Interactions of KrF Laser Radiation with Small Water Droplets," accepted for publication in *Applied Optics*, February 5, 1990.

   (e) J.P. Barton, W. Ma, S.A. Schaub and D.R. Alexander, "Electromagnetic Field for a Beam Incident Upon Two Adjacent Spherical Particles," submitted to *Appl. Opt.*, May 1, 1990.

   (f) S.A. Schaub, D.R. Alexander and J.P. Barton, "Theoretical Model of the Laser Imaging of Small Aerosols: Applications to Aerosol Sizing," submitted to *Appl. Opt.*, May 1, 1990.

   (g) D.R. Alexander, G.M. Holtmeier, K.D. Song and J.P. Barton, "KrF Laser Interactions with a Metallic Filament," Presentation at the 1990 CRDEC Scientific Conference on Obscuration and Aerosol Research, Aberdeen Proving Ground, Maryland, June 25- 28, 1990.

   (h) J.P. Barton and D.R. Alexander, "Electromagnetic Field for a Beam Incident Upon a Nonspherical Particle," Presentation at the 1990 CRDEC Scientific Conference on Obscuration and Aerosol Research, Aberdeen Proving Ground, Maryland, June 25-28, 1990.

## 8. SCIENTIFIC PERSONNEL SUPPORTED BY THIS PROJECT AND DEGREES AWARDED DURING THIS REPORTING PERIOD:

Dr. Dennis R. Alexander, Principal Investigator

Dr. John P. Barton, Co-Principal Investigator

Jingyi Zhang, Ph.D.

Gregg Holtmeier, M.S. Degree awarded. Thesis: "High Intensity Ultraviolet Laser Interaction with a Metallic Cylinder," March 1990

Sik Wah Chiang, M.S.

# BRIEF OUTLINE OF RESEARCH FINDINGS

Experimental research on the interaction of KrF excimer laser radiation at $\lambda = 248$ nm with thin metallic cylinders continued during this reporting period. Results of this work are reported in a M.S. thesis by Gregg Holtmeier entitled, "High Intensity Ultraviolet Laser Interaction with a Metallic Cylinder," (copy enclosed). A paper is ready for submission to *Journal of Applied Physics* based on Gregg's thesis. A second paper will be submitted to a metallurgical journal reporting the formation of Cu twins during the rapid cooling of the copper aerosol particles. Apparently the formation of twins by annealing processes is rare.

Experimental work continues on the excimer laser produced plasmas in copper wire targets and water droplets. Results indicate both have a distinct two-peak structure. However, initiation of broadband emission for copper starts at 6.5 ns of the arrival of the laser pulse as compared to 11 ns for water. A paper on this subject is near completion and will be submitted to *Journal of Applied Physics*.

Theoretical work continues on analyzing the signal obtained from the temperature dependence of rhodamine B dye in water aerosols. A computer code has been written to simulate the emission of photons inside a drop from fluorescence. Results are compared to Mie calculations.

Research is continuing on the theoretical modeling of the laser imaging of small aerosols. A paper entitled "Theoretical model of the laser imaging of small aerosols: applications to aerosol sizing" was presented at the 2nd International Congress on Optical Particle Sizing and subsequently submitted for publication to *Applied Optics*. (Copy attached.) Modeling of off-axis imaging is proceeding in efforts to better understand previous experimental observations regarding the excimer laser interaction with water droplets.

A femtosecond laser was purchased with State of Nebraska Research Initiative funds. The femtosecond is in operation producing 20 $\mu$joule pulses of 70 femtosecond pulse duration. Future experimental work will make use of this ultra fast laser to overcome many of the nanosecond diagnostics limitations.

Within this funding period, a paper entitled "Theoretical determination of the electromagnetic fields for a laser beam incident upon two adjacent spherical particles of arbitrary arrangement," was presented and published in the *Proceedings of the 2nd International Congress on Optical Particle Sizing*, March 5-9, 1990, Tempe, Arizona. A copy of this paper is attached. Subsequently, the beam incident upon two adjacent spherical particles theory was refined, additional calculations

3

were performed, and a paper entitled "Electromagnetic fields for a beam incident upon two adjacent spherical particles," was submitted for publication to *Applied Optics*. A copy of this submitted paper is attached.

The beam incident upon two adjacent spherical particles theory has important applications in optical particle sizing, where the effect of adjacent particle interactions on far- field scattering is of interest. The beam incident upon two adjacent particles theory can also be used to investigate the possibility of the intentional placement of one particle so as to "focus" laser light onto a second adjacent particle. Figure 1. presents a false contrast visualization (normalized source function, $\tilde{S} = |\vec{E}|^2/E_0^2$, white $\Rightarrow$ high, black $\Rightarrow$ low) of a hypothetical arrangement consisting of two identical spherical particles at resonance. The beam excites the resonance in the left-side particle which, in turn, scatters light which excites the resonance in the right-side particle.

Additional theoretical efforts included the development of further refinements and applications of the beam incident upon an arbitrarily-shaped particle theory. A presentation entitled "Electromagnetic fields for a beam incident upon a nonspherical particle," was given at the U.S. Army CRDEC Scientific Conference on Obscuration and Aerosol Research, June 25-28, Aberdeen Proving Ground, Maryland. A paper entitled "Internal and near-surface electromagnetic fields for an arbitrarily-shaped particle illuminated by a focused laser beam," is in preparation and will be submitted for publication to the *Journal of Applied Physics* in the near future. As a demonstration of the beam incident upon an arbitrarily-shaped particle theory, Fig. 2 shows the internal normalized source function distribution for a focused laser beam incident upon an oblate spheroid. The beam incident upon an arbitrarily-shaped particle theory has been applied to investigate the effect of nonsphericity on the heating patterns within $CO_2$ laser heated water droplets and to investigate the effect of slight surface deformities for a spherical particle at resonance.

Interactions with other scientists during this funding period include discussions with Richard Chang (Yale University), Steve Arnold (Polytechnic Institute of New York), Ron Pinnick and Kirk Fuller (Atmospheric Sciences Laboratory) and Larry Liou (NASA Lewis).
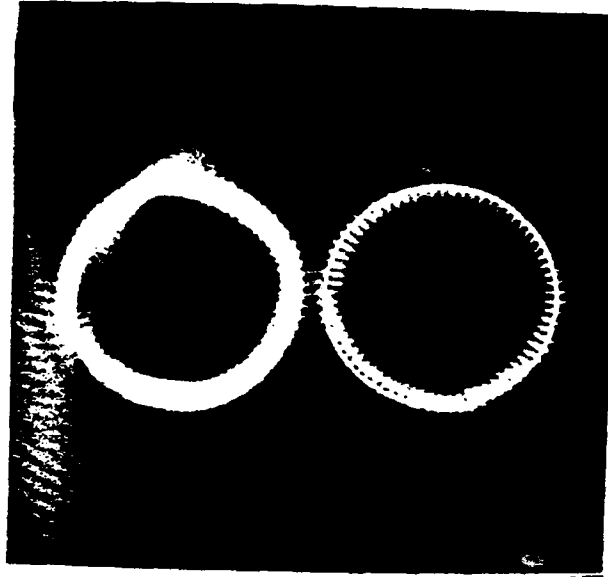
4

FIG 1. Normalized source function distribution in the x-z plane for a focused beam incident upon two adjacent resonance particles. $a_1 = a_2 = 30.4770$, $\bar{n}_1 = \bar{n}_2 = 1.334 + 1.2 \times 10^{-9}i$, $\bar{w}_0 = 0.4007$, $\bar{x}_0 = \bar{y}_0 = 0.0$, $\bar{z}_0 = -1.165$, $\theta_{bd} = 90°$, $\phi_{bd} = 0°$, $\epsilon_{ext} = 1.0$, $\bar{z}_{12} = 2.2$, $\bar{x}_{ref} = \bar{y}_{ref} = 0.0$, $\bar{z}_{ref} = 1.10$. [0.5145 $\mu m$ wavelength (argon-ion laser), 2 $\mu m$ waist diameter beam incident upon two 4.9912 $\mu m$ diameter water droplets ($35^{th}$ mode electric wave resonance).]
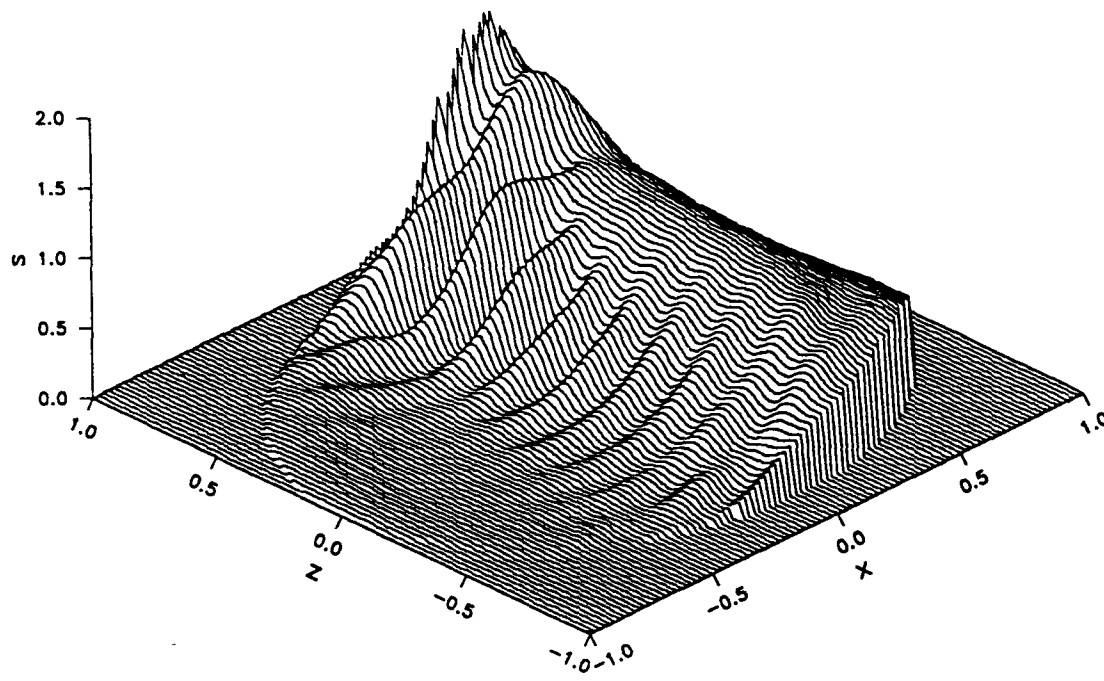
FIG 2. Internal normalized source function distribution in the x-z plane for a focused laser beam incident upon an oblate spheroid (a/b=1.2). $\alpha = 15, \bar{n} = 1.3 + 0.01i, \bar{w}_0 = 0.667, \bar{x}_0 = 0.5, \bar{y}_0 = 0.0, \bar{z}_0 = 0.0, \theta_{bd} = 0°, \phi_{bd} = 0°$.